Characterization of Low-Rank Coal Char Used in the Production of Hydrogen

R.C. Timpe, R.E. Sears, and G.G. Montgomery

University of North Dakota Energy Research Center
Box 8213 University Station, Grand Forks, ND 58202

INTRODUCTION

The production of low-cost hydrogen for use as a fuel and chemical feedstock to supplement fossil fuels and provide a feasible alternative to current hydrogen production methods is of continued interest in the energy field. The demand for hydrogen is increasing, with the need for hydrogen predicted to rise by a factor of 15 to 20 times over the next 40+ years (1).

Presently industrial quantities of hydrogen are produced primarily by either steam reforming of natural gas or partial oxidation of petroleum. However, both of the feedstocks for these processes are used more efficiently and economically in their chemically unaltered or physically refined forms. One of the most viable alternatives for hydrogen production, in terms of available feedstock, is in the use of advanced coal gasification processes. In coal gasification processes, hydrogen is produced by the following reactions:

$$C(s) + H_2O(g) \longrightarrow CO(g) + H_2(g) \quad 1)$$

$$CO(g) + H_2O(g) \longrightarrow CO_2(g) + H_2(g) \quad 2)$$

The gasification reaction 1) involves reacting coal char and steam to produce carbon monoxide and hydrogen. Additional hydrogen is produced via the water/gas shift reaction 2). The gasification step, reaction 1), is enhanced at reaction temperature by the presence of catalysts, of which the most widely studied are alkali salts (2). The alkali carbonates, bicarbonates, oxides, and hydroxides are well known as rate enhancers, while halides of the alkalis do not function nearly as well as positive catalysts. Low-rank coal offers a plentiful and relatively inexpensive substrate from which to form char that has high reactivity (higher than those of higher-rank coals) toward steam in a char-steam reaction 1) to produce hydrogen.

The thermodynamics of the water/gas shift reaction 2) require that the hydrogen production process operate at the lowest temperature possible. The limit to which the temperature may be lowered in the process is governed by the activity of the char generated at that temperature from a particular coal. Laboratory-scale experiments have shown that the 700°-800°C range at ambient pressure provide conditions for maximum production of hydrogen in the gaseous product (3). The catalytic enhancement of the rate of hydrogen production allows the operating temperature to be lowered, thus effecting greater shift and maximizing hydrogen formation.

Potassium carbonate is probably the most extensively studied of the alkali salt catalysts and is often used as a standard for comparison of catalyst effects. Other potassium compounds (except for the halides) have been shown to be excellent catalysts for the gasification of coal chars (4,5). Sodium compounds have also been studied extensively for their effect on the gasification reaction. They too have been shown to be good catalysts and in some cases were as good as the potassium compounds (5). Trona and nahcolite, naturally occuring sodium-rich minerals, have been shown in laboratory-scale experiments to be as good as potassium carbonate for catalyzing the char-steam reaction of some low-rank coals (5).

From an economic standpoint, the sodium compounds are less expensive than potassium compounds, and mineable sodium-rich minerals are even less expensive than the pure sodium compounds. However, not all low-rank coals give the same reactivity or realize the same catalytic rate enhancement under the same reaction conditions; i.e., coal-specific effects are often evident. Therefore, thorough characterization of the chars generated at the various temperatures of interest and their response to various catalysts are important in understanding the mechanism of the gasification reaction in the production of hydrogen. The research reported here involves the characterization of chars from two low-rank raw coals, Velva (North Dakota) lignite and Martin Lake (Texas) lignite. The chars were generated in the temperature range 650°-750 °C, at atmospheric pressure under inert atmosphere. Chars were also prepared from Velva and Martin Lake lignites containing added catalyst (10 wt% K_2CO_3 and Trona) at the same conditions for characterization.

EXPERIMENTAL

The reaction between low-rank coal chars and steam to produce hydrogen was studied with two different Thermogravimetric Analysis (TGA) systems. The kinetic study of weight change of carbon with time for the char-steam reaction was carried out on a DuPont 951 Thermogravimetric Analyzer (TGA) interfaced with a DuPont 1090 ThermalAnalyzer. Approximately 20 mg samples of -100 x +140 mesh uncatalyzed or catalyzed coal were devolatized under argon flowing at 160 cc/min, and the resulting char was reacted with steam ($p_{(H_2O)}$ = 0.1). Weight, time, and temperature data were recorded, and each experiment was terminated when weight loss ceased. Total gas (product gas plus carrier gas) samples were collected over the duration of the run and were analyzed by gas chromatography (GC). Selected experiments were duplicated on a large TGA so that larger gas samples could be collected, ensuring sufficiently accurate analysis. The large TGA was built at the University of North Dakota Energy Research Center (UNDERC) using a Cahn 1000 electrobalance and a 1200°C vertical tube furnace for reacting samples >1 g. Reactivity parameters, (k), for 50% carbon conversion, were calculated at each of three temperatures (T) and Arrhenius plots of ln k vs 1/T were constructed for calculating energy of activation (Ea) and frequency factor, (A), as previously described (3). Residue remaining after the reaction was analyzed by X-Ray Diffraction and X-Ray Fluorescence techniques.

Char analyzed by spectroscopic techniques was prepared as in the char-steam reaction experiments, but was cooled to room temperature under argon. In selected experiments the char was removed from the TGA under argon and stored under argon to prevent exposure to air. These samples were analyzed by Electron Spectroscopy for Chemical Analysis (ESCA) and solid state ^{13}C Cross Polarization/Magic Angle Spinning (CP/MAS) Nuclear Magnetic Resonance Spectrometry (NMR). Catalyzed and uncatalyzed samples of char were examined by Scanning Electron Microscopy (SEM), to determine surface elemental composition and to obtain photographs of the char surface. The field was scanned and representative particles were photographed and mapped to determine elemental distribution. All char samples were analyzed for active sites by gravimetric measurement of CO_2 adsorption in a manner similar to that described by Ratcliffe and Vaughn (6).

RESULTS AND DISCUSSION

There are several significant chemical differences between the coals used in this study. The Velva lignite is a northern Great Plains lignite, whereas the Martin Lake lignite is a Gulf Coast lignite and as such reflect significantly different coal-forming environments. Proximate and ultimate analyses of the two coals are listed in Table 1. The Martin Lake sample was higher in moisture and significantly lower in ash content than the Velva sample. The moisture-free (mf) oxygen value for the Martin Lake coal is 18% lower than that for the Velva, and the C/H ratio is 1.18 for Martin Lake compared to 1.30 for Velva. The normalized

product gas compositions shown in Table 2 were determined by gas chromatography (GC) on the total gas sample collected during the hydrogen production reaction carried out on both the DuPont TGA and the large laboratory TGA. The normalized hydrogen values approximated those predicted by the engineering thermodynamic model. The values obtained from the samples generated on the large TGA have somewhat less uncertainty in analysis since the dilution effect of the carrier gas was reduced.

TABLE 1

PROXIMATE AND ULTIMATE ANALYSES

Proximate Analyses	Velva	Martin Lake
Moisture %	29.3	34.8
Ash, wt % mf	13.5	8.7
Volatile Matter, wt % mf	39.3	44.0
Fixed Carbon, wt % mf	47.2	47.4
Heating Value, Btu/lb	7185	7525
Ultimate Analyses, mf		
Hydrogen	3.84	4.71
Carbon	59.93	66.46
Nitrogen	0.94	1.18
Sulfur	0.53	0.86
Oxygen (Diff)	21.26	18.09

TABLE 2

PRODUCT GAS IN MOLE % FROM VELVA LIGNITE CHAR-STEAM REACTION - LARGE TGA

Sample*	Temp. ^{o}C	H_2	CO_2	CO	CH_4
W/10 wt% Trona	750	56.23	30.13	13.64	ND
W/10 wt% Trona	700	51.73	43.51	4.55	ND
Uncatalyzed	750	57.70	35.30	6.30	0.72
Uncatalyzed	700	56.20	40.00	2.60	0.90

ND = Absent or below detection limit

*Sample sizes were between 1.0 and 1.4 grams of -100 +140 mesh "as received" coal- catalyst.

Data normalized to exclude carrier gas and air.

The inherent mineral matter of the Velva lignite had the effect of increasing the reaction rate over that of the Martin Lake lignite. Addition of either potassium or sodium compounds also increased the rate of the char-steam reaction for both the Martin Lake and the Velva char. Potassium carbonate and Trona admixed with the lignite both gave positive catalysis of the char-steam reaction. The activity parameter (k in g/hr/g) increased from 1.40 with no catalyst to 3.50 with 10 wt% K_2CO_3 and to 3.23 with 10 wt% Trona for Velva lignite at 700°C. The reactivity parameter also increased from 0.74 with no catalyst addition to 1.41 with 10 wt% K_2CO_3 and 2.37 with 10 wt% Trona for Martin Lake lignite at 700°C.

SEM photographs (Figure 1) show the surface effect, upon charring, of adding K_2CO_3 catalyst to the coals. The ragged, irregular surface and lack of apparent pores in the uncatalyzed char is in contrast to the rounded, highly porous surface on the alkali catalyzed char. The degree to which the surface changed with the addition of catalyst differed between the Velva and the Martin Lake chars. The Velva char surface is remarkably porous and contained uniform, evenly spaced nodules of approximately 0.05 μm x 0.10 μm in size. The nodules on the surface of the catalyzed Martin Lake char were neither uniform in size nor evenly spaced over the surface. The reactivities differed similarly, with the Velva having the higher reactivity. This suggests that the increase in reactivity of the catalyzed char, which may be due to mechanistic change in the chemical reaction brought about by the alkali catalyst, must also be due, at least in part, to the physical effect of producing a large increase in surface area. The result of this increase in surface area is an increase in available active sites as shown in Figures 2 and 3 for Velva char and Martin Lake char, respectively.

SEM mapping of the surface for inorganic element distribution showed that the potassium was distributed uniformly over the surface of the Velva particles. This was not the case with the Martin Lake particles. The uniform distribution of the potassium catalyst on the surface of the Velva char implies a surface wetting by a fluid consisting of, or containing, the catalyst. The Trona, however, does not exhibit this mode of distribution. Instead the element distribution map showed the sodium surface deposits as being associated with those of silicon and aluminum. The irregularly placed surface nodules of nonuniform size were located near the sodium deposits.

Carbon 13 Nuclear Magnetic Resonance (^{13}C NMR) spectra of chars prepared at temperatures from 600° to 750°C (Figure 5) indicated the absence of aliphatic groups in the char with removal of aliphatics occurring during the charring process. Aromatic CO groups and carboxyl, amide, and ester groups are absent in the chars as well. The decrease in aromatic signal strength with temperature may result from unobserved carbon in CP/MAS due to the decrease in H/C with the char (7). Table 3 shows the ESCA surface carbon/oxygen ratio on the Velva chars prepared at various temperatures. Char prepared at 750°C and exposed to air had a significantly lower surface C/O ratio than that prepared at the same temperature and protected from exposure to air. The latter sample was analyzed at the natural surface, and then at surfaces produced by removal of outer layers of char using ion "sputtering" for the time indicated on Table 3. The low C/O ratio of the exposed sample is due to the adsorption of oxygen on exposure to air. Higher oxygen contents are related to the highly activated carbon that results during the char formation. The chars formed at the other temperatures given on Table 3 exhibited little increase in C/O ratio with temperature. These results indicate that erroneous surface data can be minimized by maintaining an inert atmosphere over the char samples and a more accurate analysis can be carried out.

TABLE 3

ESCA RESULTS--VELVA LIGNITE CHAR (ELEMENT %)

Char Temp. (°C)	Sputter Time (minutes)	Element % C	O	N	C/O
750*	0	74.4	21.0	---	4.73
750	0	82.1	14.3	---	7.69
	10	82.9	13.0	---	8.52
	70	84.3	11.6	---	9.62
700	70	81.9	10.9	0.9	10.03
650	70	80.1	12.3	0.8	8.66
600	70	80.3	12.6	1.0	8.47

*Exposed to air

CONCLUSIONS

- Reactivity of low-rank coal chars are increased by factors of two to four at a given temperature with addition of catalyst.
- The increased reactivity is due to increases in surface area and active sites.
- Scanning electron microscopy shows that catalyzed chars have a much higher surface area than uncatalyzed chars.
- Potassium was distributed more uniformly than the trona over the char surface.
- The highly activated carbon created by the devolatilization of the low-rank coal necessitates the prevention of exposure to air if CO functional groups are to be accurately identified by ESCA or quantified by CP/MAS ^{13}C NMR.

REFERENCES

1. Pohani, B.P., J. Japan. Petrol. Inst., 27, 1 (1984).

2. Tomita, A., Y. Ohtsuka, Y. Tamai, Fuel, 62, 150 (1983).

3. Timpe, R.C., S.A. Farnum, S.J. Galegher, J.G. Hendrikson, M.M. Fegley, ACS Div. Fuel Preprints, 30, no. 4, p. 481 (1985).

4. Huttinger, K.J., R. Minges, Fuel, 65, 1112 (1986).

5. Sears, R.E., R.C. Timpe, S.J. Galegher, W.G. Willson, ACS Div. Fuel Preprints, 31, no. 3, 166 (1986).

6. Ratcliffe, C.T., Vaughn, S.N., ACS Div. Fuel Preprints, 30, no. 1, 304 (1985).

7. Botto, R.E., R. Wilson, and R.E. Winans, Energy and Fuels, 1, 173-181 (1987).

ACKNOWLEDGEMENTS

The authors would like to acknowledge Jan Lucht for assistance with the TGA experiments and Art Ruud for the ^{13}C NMR spectra. A special thanks is extended to Leland E. Paulson, Technical Project Officer, and Madhov Ghate, Chief, Combustion and Gasification Branch, of the Morgantown Energy Technology Center for their guidance and support.

a) Martin Lake Char - Mag. 6000X

b) Martin Lake/K_2CO_3

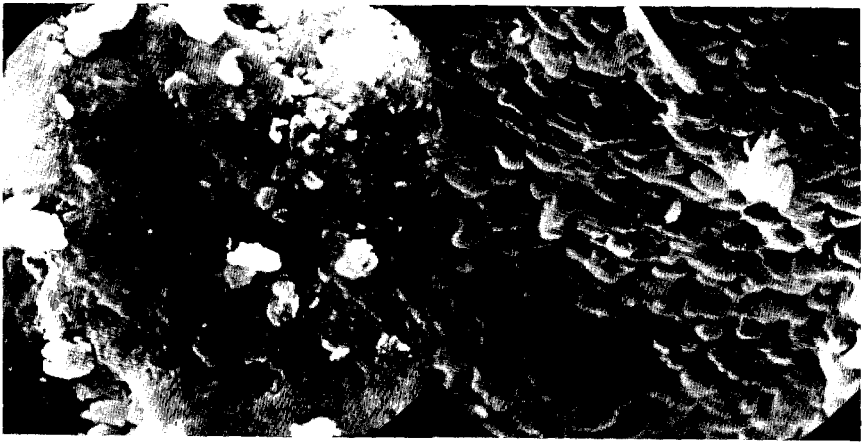

c) Velva Char - Mag. 6000X

d) Velva/M_2CO_3 Char - Mag. 6000X

Figure 1 - SEM Photographs of Coal Chars and Coal/K_2CO_3 Char Prepared at 750^{oC}

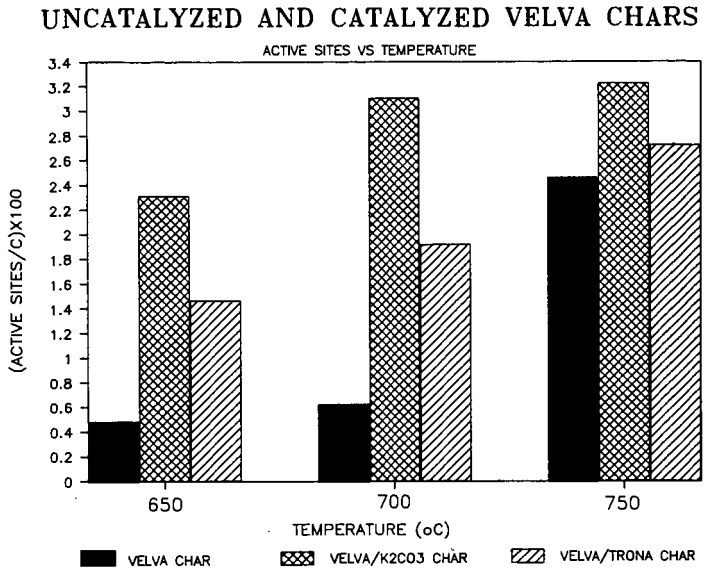

Figure 2. Number of active sites/carbon atom in Velva lignite char with and without catalyst.

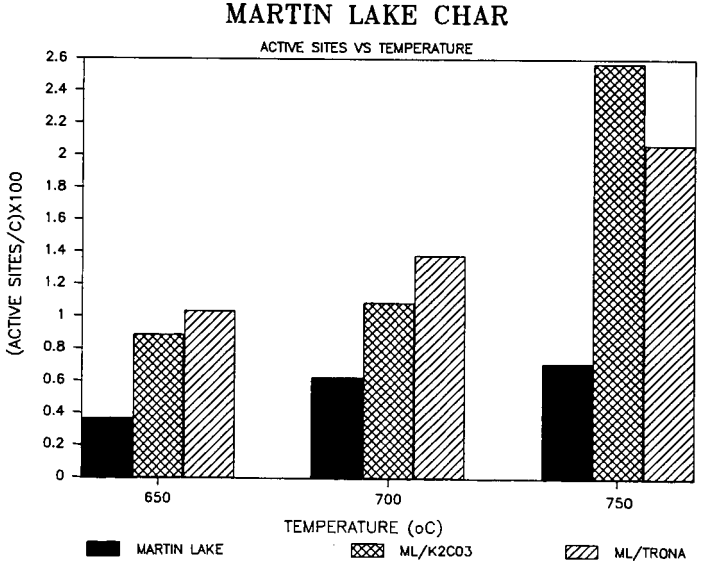

Figure 3. Number of active sites/carbon atom in Martin Lake lignite char with and without catalyst.

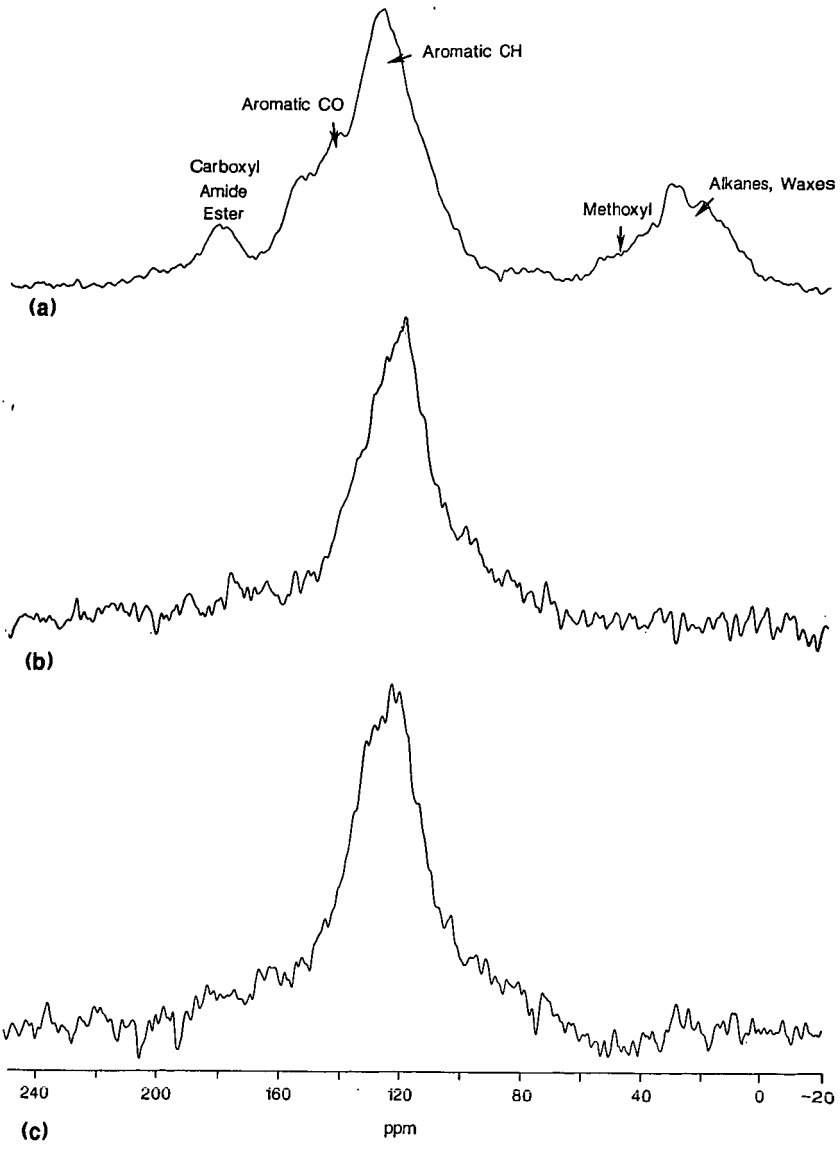

Figure 4. CP/MAS ^{13}C NMR Spectra of (a) Velva North Dakota lignite (b) Velva lignite char (750°C) and (c) Velva/Trona char 750°C.

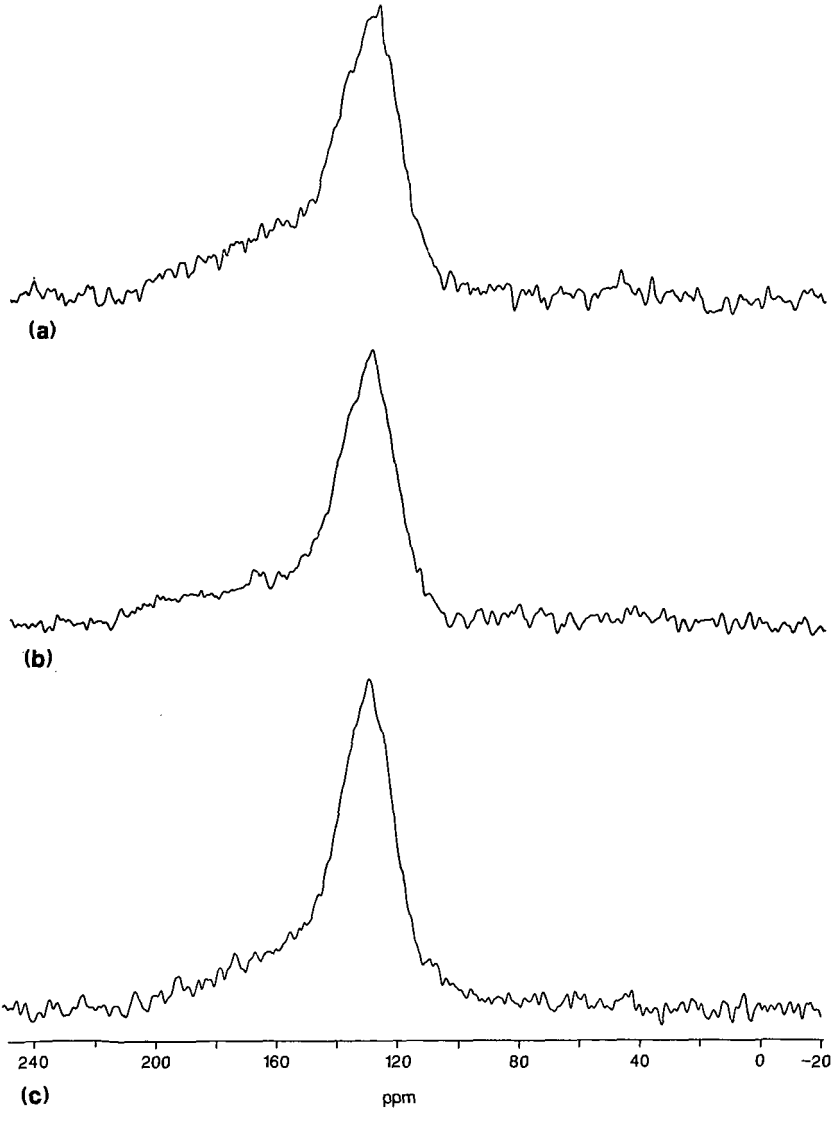

Figure 5. CP/MAS ^{13}C NMR spectra of Velva/Trona char prepared at (a) 700°C (b) 650°C, and (c) 600°C.

PYROLYSIS GC/MS ANALYSIS OF LOW-RANK COAL

David J. Miller and Steven B. Hawthorne

University of North Dakota Energy Research Center
Box 8213, University Station
Grand Forks, North Dakota 58202

ABSTRACT

The reactivity of coals under liquefaction conditions is related to their thermal decomposition. Pyrolysis GC/MS is used to determine the identity of the volatile products as the changes in coal structure occur. A Wyoming subbituminous coal (Clovis Point) and a North Dakota lignite (Indian Head) were heated under helium at four temperatures (160 °C, 250 °C, 300 °C, and 350 °C) for 30 minutes. The volatile species were cryogenically trapped in a capillary gas chromatographic column for GC/MS analysis. The two lower temperatures showed only devolatilization products (e.g., biological markers such as alkanes and terpenoids) while the higher temperatures yielded products resulting from bond-breaking (i.e., pyrolysis). The devolatilization and pyrolysis products of the two coals were similar in overall composition but markedly different in their distribution. The subbituminous coal (Clovis Point) pyrolysate contained phenol and cresols along with large amounts of C_{19} to C_{31} normal alkanes. Indian Head lignite pyrolysate contained a much larger amount of phenol, alkyl substituted phenols and dihydroxybenzene and lesser amounts of C_{19} to C_{31} alkanes.

INTRODUCTION

Pyrolysis gas chromatography/mass spectrometry has become increasingly popular for the analysis of solid fuel and fuel related materials. In recent papers, pyrolysis-GC/MS has been applied to model compounds (1), asphaltenes (2), kerogens (2), buried wood (3), coalified logs (3), and coal(4). A wide variety of techniques are employed for the pyrolysis of the sample. Most of the reported techniques employ some type of pyrolysis probe capable of rapid heating rates and temperatures in the 600 °C to >1000 °C range. The sample sizes reported were from 5 ug to 100 ug.

In order to study the products of thermal decomposition under low-severity liquefaction conditions, the maximum temperature used in this study was 350 °C. Our technique involves the use of approximately 10 mg of sample per analysis. The devolatilization and pyrolysis products are introduced into a split injector and cryogenically trapped at the head of a fused silica capillary gas chromatographic column. The use of a relatively large sample, 10 mg, and a split injector allows for a more representative sample to be collected on the capillary column. The sample is then separated and analyzed using standard GC/MS techniques.

EXPERIMENTAL

Samples

Wyoming subbituminous coal (Clovis Point) and a North Dakota lignite (Indian Head) were used in this study. Both coals were ground to -200 mesh and dried in a vacuum desiccator for 48 hours prior to pyrolysis.

Pyrolysis Gas Chromatography/Mass Spectrometry

Figure 1 shows a schematic diagram of the pyrolysis apparatus. Approximately 10 mg of coal was placed in a 30 cm x 4 mm i.d. pyrex tube. The sample was positioned approximately 5 cm from the outlet of the pyrex tube with a plug of silanized glass wool. The outlet of the tube was attached to a 1/4" x 1/16" stainless steel union fitted with a 2 in. x 0.20 mm i.d. needle. The sample tube was placed in the tube heater that had been preheated to the desired pyrolysis temperature. During the pyrolysis step, the needle was inserted into the split/splitless injection port, the helium flow was diverted from the injection port to sweep the pyrolysis products out of the pyrolysis chamber and into the injection port, and the tube heater was dropped down around the sample and union/needle assembly. The injection port was operated with a split ratio of approximately 1:100. The pyrolysate entering the fused-silica capillary chromatographic column was cryogenically trapped by holding the oven temperature at -50 ^{o}C during the 30 minutes pyrolysis. Upon completion of pyrolysis, the column oven was heated rapidly to 0 ^{o}C followed by temperature programming at 6 ^{o}C/min to 320 ^{o}C. GC/MS analysis of the pyrolysis products was performed with a Hewlett-Packard model 5985B using a 60 m x 0.25 mm i.d. (0.25 um film thickness) DB-5 fused silica capillary column (J & W Scientific, Folsom, CA). Helium was used as the carrier gas at an approximate linear flow rate of 50 cm/sec. Pyrolysis gas chromatography with flame ionization detection (GC/FID) was performed in a similar manner using a Hewlett-Packard 5890 GC.

Electron impact (EI) mass spectra were generated at 70 eV with a scan range of 35-500 amu. In the chemical ionization (CI) mode, reagent gas was introduced directly into the source through a heated transfer line colinear with the chromatographic column. Source pressure and CI tuning parameters have been reported previously (7). The structures of the dioxygen compounds (e.g., C_2 dihydroxybenzene vs C_1 methoxyphenol) were confirmed by the use of deuterated reagent chemical ionization GC/MS. In this technique, the -OH proton is exchanged for deuterium and an apparent molecular weight change occurs. For example, a C_2 dihydroxybenzene (MW = 138) would exhibit a pseudo-molecular ion at m/z 142 (ionization by D^+ and exchange of two acidic protons for deuterium), while a C_1 methoxyphenol (MW = 138) would have a pseudo-molecular ion at m/z 141 (ionization by D^+ and exchange of one acidic proton). Because of a prominent background ion at m/z

101 due to a reagent cluster ($(CH_3OD)_3D^+$), the lower limit for the mass scan range using CH_3OD CI was 104 amu.

RESULTS AND DISCUSSION

Figures 2 and 3 are the pyrolysis-GC/FID chromatograms of the Wyoming subbituminous coal and the North Dakota lignite at the four pyrolysis temperatures (160, 250, 300, and 350 °C). The numbered peaks in Figures 2 and 3 are identified in Table 1. Chromatograms for 160 °C and 250 °C show species that are thermally desorbed from the coal, and that are not pyrolysis products. This has been confirmed by the use of supercritical N_2O extraction (300 atm at 45 °C) (8) which yielded extracts that had chromatograms virtually identical to those from the 160 °C and 250 °C thermal experiments. These compounds are primarily biological markers such as alkanes, sesquiterpenes, triterpanes and steranes(5,6).

Comparison of the chromatograms obtained at 350 °C for the two coals shows marked differences in the composition of their pyrolysates. The pyrolysate yield for the lignite under the pyrolysis conditions described in the experimental section was much less then the yield for the subbituminous coal. The pyrolysate from the Wyoming subbituminous coal contains relatively larger amounts of aliphatics, aromatics, and oxygen-containing species such as phenol and alkylphenols. Catechol (1,2-dihydroxybenzene) is present in the pyrolysate of both coals, but in much lower concentration from the subbituminous coal than from the lignite. The lignite pyrolysate contains the same types of compounds as those found in the subbituminous coal pyrolysate but the distribution is very different. Alkanes in the range of C_{18} to C_{31} are present in both pyrolysates but are in much lower concentration in the lignite pyrolysis product. Anisole and C_1 anisole isomers were present in the lignite pyrolysate but not in the subbituminous pyrolysate. Larger amounts (relative to other components in the sample) of dihydroxybenzene, methoxyphenol, and their C_1 and C_2 alkyl derivatives were present in the lignite pyrolysate. This is consistent with results published by Hatcher, et al (3), and would be expected since lower rank coals have undergone less coalification and would contain organic constituents which more closely resemble structures (e.g., lignin) found in the original plant material. Several of the substituted dihydroxybenzenes and methoxyphenols were absent from the subbituminous pyrolysate.

CONCLUSION

Pyrolysis gas chromatography/mass spectrometry can be a valuable tool for evaluating candidate coals for use in synthetic fuel processes especially where separation and upgrading of the pyrolysate fraction is a concern and the chemistry of the process has a narrow operational range. Structural differences in the pyrolysates can be related to the structure of the coals. The larger sample size and split injection used in our technique

allows for a more representative sample to be analyzed.

CREDIT

The authors would like to thank the U.S. Department of Energy for support for this work under contract number DE-FG22-86PC90911.

REFERENCES

1. Bredael, P. and Vinh, T. H., Fuel, 58, 211-214 (1979).

2. Solli, H., and Leplat, P., Org. Geochem., 10, 313-329 (1986).

3. Hatcher, P. G., Lerch, H. E., Kotra, R. K., Verheyen, T. V., ACS Div. Fuel Chem. Preprints, 32(1), 85-93 (1987).

4. Siskin, M. and Aczel, T., Fuel, 62, 1321-1326 (1983).

5. van Graas, G., Org. Geochem., 10, 1127-1135 (1986).

6. Strachan, M. G., Alexander, R., Kagi, R. I., ACS Div. Fuel Chem. Preprints, 31(3), 266-274 (1986).

7. Hawthorne, S. B., and Miller, D. J., Anal. Chem., 57, 694-698 (1985).

8. Hawthorne, S. B., and Miller, D. J., Anal. Chem., (accepted for publication in June 1987).

TABLE I. Identification of Numbered Peaks from Figures 2 and 3.

Peak Number	Species
1	methylcyclopentadiene or isomer
2	benzene
3	acetic acid
4	C_2-cyclopentadiene or isomer
5	toluene
6	C_2-cyclohexane or isomer
7	C_2-benzene
8	cyclooctatetraene and C_2-benzene
9	anisole
10	phenol
11	C_1-anisole
12	C_3-benzene
13,14	cresol isomers
15	methoxyphenol
16	C_2-phenol
17	dihydroxybenzene
18	C_3-benzene
19	C_1-dihydroxybenzene and C_1-methoxyphenol
20	C_1-dihydroxybenzene
21,22	C_2-dihydroxybenzene
23	C_2-naphthalene
24	cadalene
25	M=266 biological marker
26-39	C_{18} to C_{31} alkanes
40,41,42	M=206 sesquiterpene isomers
43	M=262 biological marker
44	M=276 biological marker
45	M=270 biological marker
46	M=252 biological marker
47	M=234 biological marker
48	M=286 biological marker

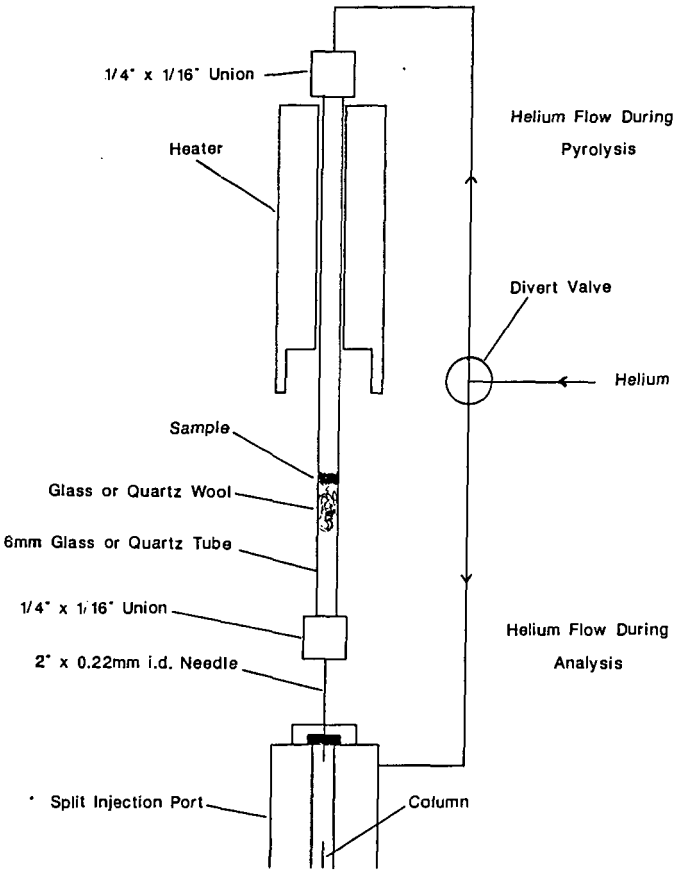

Figure 1. Pyrolysis Apparatus.

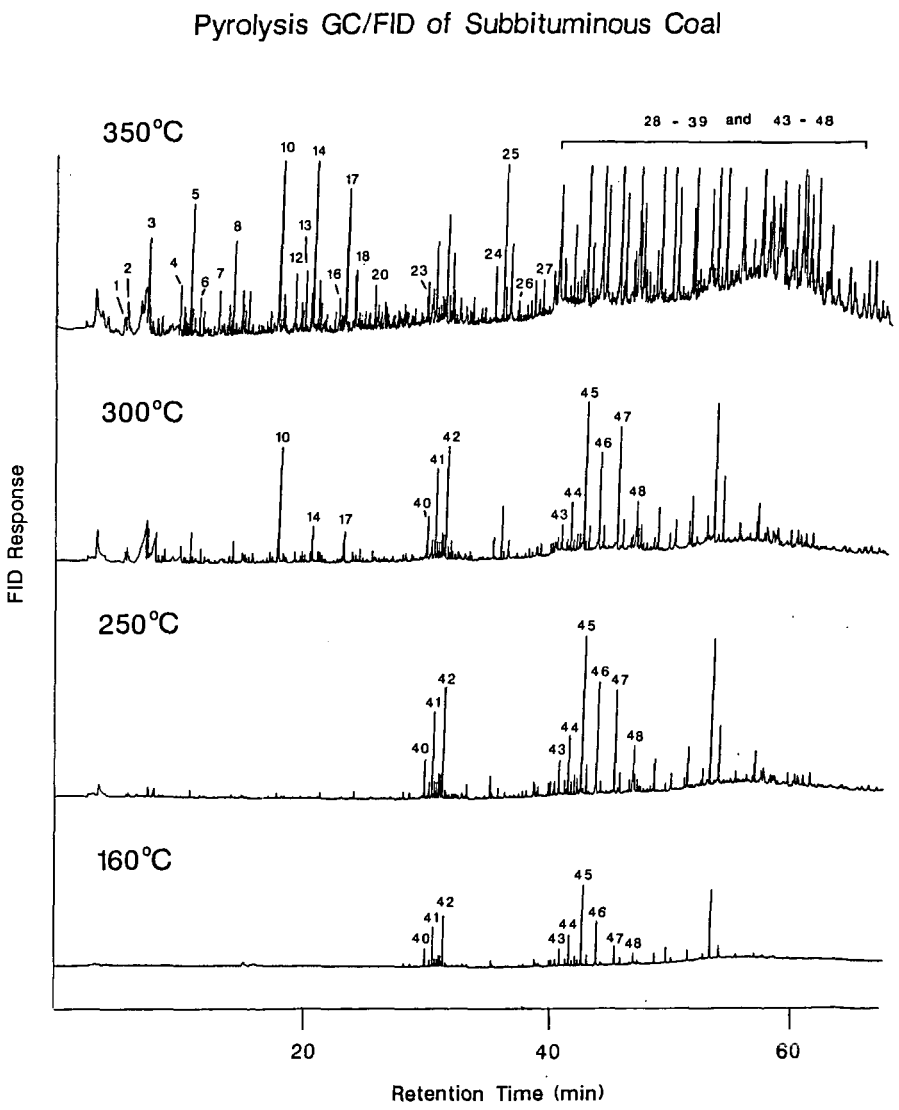

Figure 2. Pyrolysis GC/FID trace from Wyoming subbituminous coal.

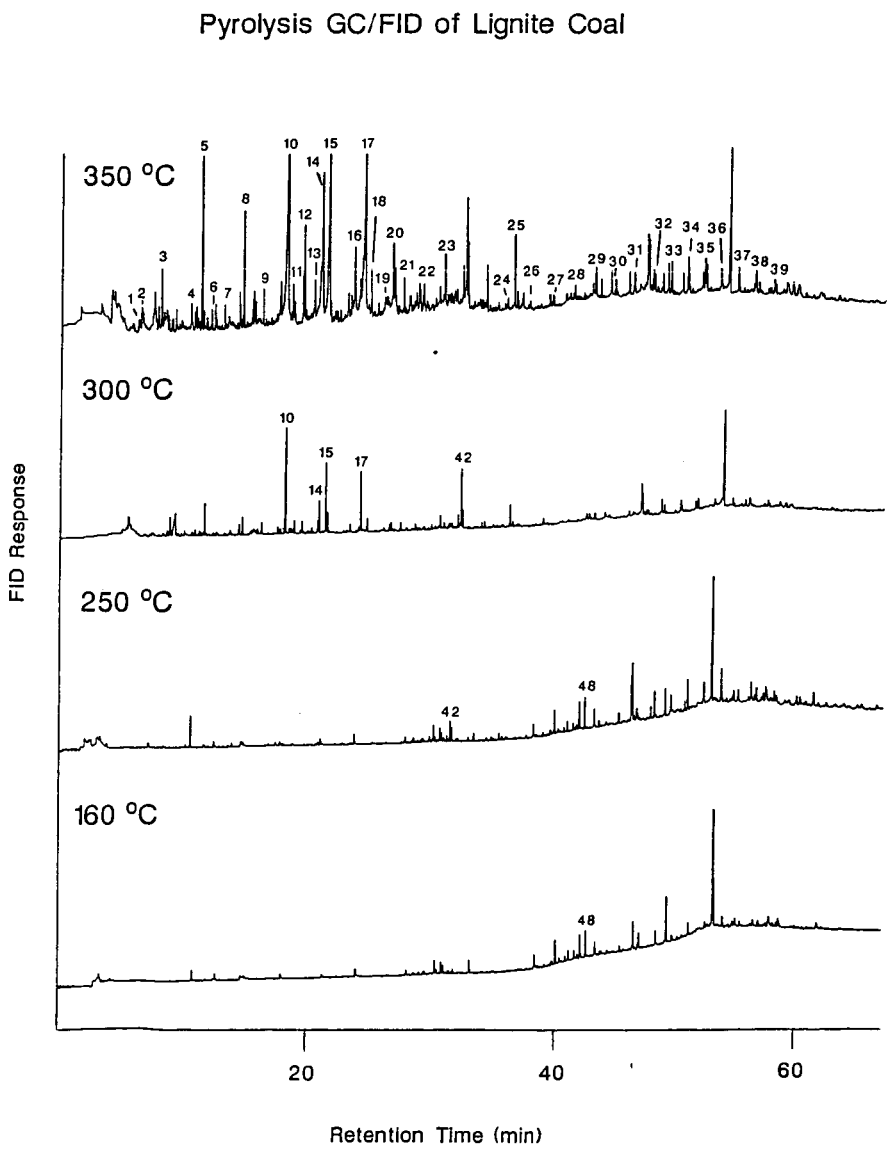

Figure 3. Pyrolysis GC/FID trace from North Dakota lignite.

COMPARISON OF DETECTORS FOR SIZE EXCLUSION CHROMATOGRAPHY OF HEAVY OIL FRACTIONS

S. COULOMBE

CANMET, Energy Research Laboratories
Energy, Mines and Resources Canada
555 Booth Street, Ottawa, Ontario K1A 0G1

INTRODUCTION

Size exclusion chromatography (SEC) is often used for the molecular weight determination of heavy oils, residues, pitches and asphaltenes because it is capable of providing the molecular weight distribution in addition to the average molecular weights. However, since these samples are very complex, results are often approximative because of three factors. First, the exclusion process separates molecules by size and shape instead of weight. Second, the sample is composed of hundreds of molecules having widely different properties which implies that additional interactions will add to the size exclusion process (1-4). Finally, the quantitation itself is approximative since usual LC detectors do not provide a signal that is independant of the molecular structure.

In this paper, the performance of a differential refractometer, an evaporative detector and a flame ionization detector for liquid chromatography is compared in terms of linearity, response factors and detection limits.

EXPERIMENTAL

The refractive index detector is a Waters 401 differential refractometer used in conjunction with a thermostated bath to keep the detector in isothermal conditions.

The flame ionization detector is a Tracor 945 LC-FID specially designed for liquid chromatography. The eluant is deposited on the belt and the solvent is evaporated before the belt enters the detector flame which will detect only the solute.

The evaporative detector is an Applied Chromatography System (ACS) 750/14 "Mass Detector" in which the eluant is nebulized at the entrance of a heated tunnel. The solvent is evaporated in this tunnel, thus leaving solute particles in a gas stream. Light scattered by the non-gaseous particles is detected by a photomultiplier.

Experiments were performed on a Varian 5000 liquid chromatograph using two types of columns: a Techsphere 5um amino column (HPLC Technology Ltd) for light standards and three Ultrastyragel styrene/divinylbenzene GPC columns (Waters) for polymer standards. All solvents were degassed before use.

RESULTS

Results are presented in terms of response factors, detection limits and linearity. Response factors are calculated according to the following equation:

$$RF = \frac{\text{area under peak X}}{\text{amount of compound X}} * \frac{\text{amount of standard}}{\text{area umder standard peak}}$$

Detection limit (DL) is calculated as the amount of compound equivalent to twice the noise level. In order to take account of different retention times and peak shapes, a time corrected detection limit (DLT) was defined as the detection limit (DL) divided by the peak width at half-height.

Finally, the linearity range was evaluated using log-log graphs of peak area vs injected amount for concentrations ranging from detection limit to solubility limit at room temperature.

Differential refractometer

This detector is the most widely used in size exclusion chromatography. Table 1 shows how response factors can vary from compound to compound. This can obviously cause errors in quantitation. Detection limits were calculated for two extreme compounds avoiding cases where solubility problems were suspected. Finally, Figure 1 shows excellent linearity over three orders of magnitude for phenanthrene.

Flame ionization detector

Figure 2 shows the signal decrease observed with time for a series of injections of a four-component mixture. Note that the time scale is not linear nor proportional. The numbers only indicate the order of injection. Pearson and Gharfeh (10) found that this decrease was caused by a gradual overheating of the block supporting the belt, thus causing evaporation of the solute before it gets to the flame. They proposed to use a fan to keep a good ventilation. In our experiments, an internal standard was used to calculate the response factors and calculations of detection limits were done on early injections.

Table 2 shows how response factors can vary between compounds. Linearity (Fig. 3) is good if one avoids high concentrations where low response was probably due to detector saturation. However, it must be noted that the relation is exponentional as shown by the slope different than 1.

Evaporative detector

Temperature is the most important operating parameter of this detector. Ideally, the evaporation tunnel is maintained at a temperature which will ensure complete evaporation of the solvent while the solute is not affected by the process. This temperature

setting is not in degrees but in arbitrary units, 0 meaning no heating. Figure 4 shows that a high temperature setting can seriously affect the response and how the variation is closely related to the molecular weight (or boiling point) of the compound. One must note here that standards selected for this study are not particularly volatile since their molecular weight is higher than 165 g/mol and their boiling point >285°C. Bartle (6) also stated that the analysis of samples having a molecular weight lower than 300 g/mol is questionable.

Response factors were calculated for several temperature settings (Table 3). At higher temperatures, response factors are extremely different. When no heating is applied, differences are less severe but still very significant. It can be observed that even without heating the response factors are still correlated with boiling points although these are relatively high (>285°C). Of course, detection limits vary to the same extent (Table 4).

Linearity plot (Fig. 5) shows some curvature. However, if one avoids a lower concentration range, the curve could be approximated to an acceptable straight line whose slope is closer to 1, which facilitates calibration. Oppenheimer and Mourey (8) already indicated that operating conditions must be carefully chosen in order to ensure linear relationship. Along with Charlesworth (5,7), they also indicated that aerosol formation influences detection. Hence, surface tension and viscosity of the solvent are important since the droplet size will influence the size of the particles that cross the light beam. It is also possible that the refractive index (7,8) and opacity of these particles have a significant influence on the output signal.

Polymers

Since the evaporative detector is mainly used in polymer analysis, response factors and linearity were investigated for selected polymers. Response factors for these polymers seem to be more uniform than for the refractometer, and also more uniform than for the individual standards analyzed in previous sections (Table 5). Linearity (Fig. 6) appears to improve slightly with polymers but again it is preferable to avoid concentrations approaching detection limits.

DISCUSSION

Performance

Linearity (Fig. 1, 3, 5 and 6) is definitely better for the refractometer than for the other detectors. Both LC-FID and evaporative detector linearity plots show curvature that could be avoided if not working with too high or too low concentrations. In the case of LC-FID, the response is clearly exponential and one must be careful in using a calibration curve.

Table 6 shows a summary of the variation of response factors for a series of components. For individual standards of molecular weight

between 165 and 300 g/mol, the refractometer showed the least scatter of data as the relative standard deviation (RSD) indicates. The evaporative detector gave the worst results because the evaporation of solute was a limiting factor. When polymers are considered, this detector seems to be slightly superior to the refractometer since evaporation of sloute is minimal.

The variety of response factors obviously influences detection limits (Table 7). However, minimum and maximum values give an overview of the range that can be expected for a given detector. One can see that the LC-FID has detection limits one order of magnitude higher than the other detectors due to high noise levels and spiking problems (see Fig. 7).

Other characteristics

The refractometer cannot be operated in a solvent gradient mode. This is not really a problem in SEC since gradients are seldom used with this type of chromatography. The nature of the detection process also implies that response factors thus quantification might be different when using different solvents. On the other hand, the refractometer is a very simple and easy-to-use detector showing good reproducibility. A definite advantage over the two other detectors is that it is suitable for both light and heavy compounds.

The evaporative detector response is partly related to the quality of the aerosol thus to physical properties of the eluant. These properties are affected by operating temperature, pressure, flow rate and solvent. For this reason, one must be careful in using gradients. As mentioned previously, volatile compounds cannot be analyzed using this detector. Finally, the evaporative detector is solid and relatively easy to use.

In comparison, the LC-FID is a fragile detector, especially the belt. It is more complicated to operate. However, once good conditions are found, they do not have to be changed. One could question the completeness of detection and of combustion by the cleaning flame when heavy compounds are analyzed.

Analysis of pitch samples

Table 8 shows the results obtained for the SEC analysis of three pitch samples while comparative chromatograms for sample 1 are given in Fig. 7. A ultraviolet detector trace was added for comparison. Obviously, a UV detector is not recommended since the extinction coefficient can be widely different between components. It can be seen here that it overestimates the contribution of the high molecular weight portion of the sample. This is indicated by very high weight average molecular weight (M_w) values since more importance is given to heavier species in the calculation of M_w. Conversely, the LC-FID does not detect high molecular weight species very well as shown by the lower M_w values. This detector also displayed severe spiking and high systematic noise that were responsible for the poor detection limits.

As shown in Table 8, average molecular weght values can differ widely and moreover the trends between samples are not always the same (see M_n for samples 2 and 3). Figure 7 shows that the refractometer detects a larger quantity of heavy material than other detectors (except UV) and that detection of the light material with the refractometer can be disturbed by the solvent front. On the other hand, the lighter components might not be detected properly by the evaporative detector. Finally, the noise level is slightly lower for the refractometer than for the evaporative detector.

SUMMARY

When considering all factors, it is very difficult to select a specific detector as the best for size exclusion chromatography of heavy oil related samples. The LC-FID was found to be unsatisfactory. The only procedure that would aid the selection between the refractometer or the evaporative detector would be to collect and weigh narrow fractions of the chromatographic effluents and to calculate the molecular weight of these less complex fractions. However, this time consuming procedure would have to be repeated for different types of samples. Current practice in our laboratory is to analyze samples with both detectors in series in order to get a better idea of the nature of the sample.

REFERENCES

1. Altgelt, K.H. in Chromatography in Petroleum Analysis, Chromatogr. Sci. Ser., v.11, 1979, p.287.

2. Cazes, J., Gaskill, D.R., Proceedings of the 6th International Seminar on Gel Permeation Chromatography, Miami Beach, Oct. 1968, p.147.

3. Albaugh, E.W., Talarico, P.C., J. Chrom., 74, 233, 1972.

4. Champagne, P.J., Manolakis, E., Ternan, M., Fuel, 64, 423, 1985.

5. Charlesworth, J.M., Anal. Chem., 50, 1414, 1978.

6. Bartle, K.D., Taylor, N., Mulligan, M.J., Mills, D.G., Gibson, C., Fuel, 62, 1181, 1983.

7. Mourey, T.H., Oppenheimer, L.E., Anal. Chem., 56, 2427, 1984.

8. Oppenheimer, L.E., Mourey, T.H., J. Chrom, 323, 297, 1985.

9. Dixon, J.B., Chimia, 38, 82, 1984.

10. Pearson, C.D., Gharfeh, S.G., Anal. Chem, 58, 307, 1986.

Table 1 - Response factors and detection limits for differential refractometer

Compound	RF	DL (10^{-7} g)	DLT (10^{-8} g/s)
Pyrene	1.0		
Phenanthrene	0.94	2.8	3.3
o-Terphenyl	0.74		
3-Methyl cholanthrene	0.95		
Dibenzofuran	0.74		
Benzophenone	0.65		
Xanthene	0.75		
Eicosanol	0.25		
Diphenyl amine	0.78		
5,6-Benzoquinoline	0.85		
Carbazole	0.34		
Dibenzothiophene	0.84		
Thianthrene	0.72		
Triphenyl methyl mercaptan	0.52	11.3	18.9

Table 2 - Response factors and detection limits for flame ionization detector

Compound	RF	DL (10^{-6} g)	DLT (10^{-7} g/s)
Pyrene	1.0		
Phenathrene	0.21		
o-Terphenyl	0.86		
3-Methyl cholanthrene	0.78		
n-C_{21}	1.58		
Dibenzofuran	0.26	4.2	3.5
Benzophenone	0.54		
Xanthene	0.54		
Eicosanol	0.87		
Diphenyl amine	0.30		
5,6-Benzoquinoline	0.59		
Carbazole	0.12		
Dibenzothiophene	0.69		
Thianthrene	0.99	2.6	2.2
Triphenyl methyl mercaptan	0.26		

Table 3 - Response factors for evaporative detector

Compound	Temperature setting			
	0	5	10	15
Pyrene	1.0	1.0	1.0	1.0
Phenanthrene			0.26	0.21
o-Terphenyl	0.53	0.46	0.31	0.62
3-Methyl cholanthrene	0.85	1.57	1.43	5.21
$n\text{-}C_{21}$			0.69	1.69
Dibenzofuran	0.027	0.014	0.011	0.004
Benzophenone	0.13	0.073	0.083	0.040
Xanthene			0.060	0.047
Eicosanol			0.80	2.75
Diphenyl amine			0.11	0.064
5,6-Benzoquinoline			0.60	0.34
Carbazole			0.76	2.45
Dibenzothiophene	0.19	0.12	0.15	0.12
Thianthrene			0.25	0.32
Triphenyl methyl mercaptan			1.04	1.94

Table 4 - Detection limits for evaporative detector

Compound	DL (10^{-6} g)				DLT (10^{-7} g/s)			
Temperature:	0	5	10	15	0	5	10	15
Dibenzofuran	2.11	37.3			3.51	62.2		
Benzophenone	1.55	14.6	9.84	34.8	1.04	9.76	8.2	29.1
Pyrene	0.741	2.24	1.73	3.45	0.617	1.87	1.44	2.88
3-Methyl cholanthrene	0.575	1.01	1.06	1.06	0.319	0.564	0.588	0.588

Table 5 - Response factors for polymers

Compound	Refractometer	Evaporative detector
Polystyrene	1.0	1.0
Polyvinyl acetate	0.19	0.44
Polysulfone	0.92	0.71
Polyethylene glycol	0.31	0.67
Polyamide	0.34	0.35
$n\text{-}C_{36}$	0.18	0.61

Table 6 - Summary of response factors

Detector	Min	Max	n	X		RSD
Standard compounds						
Refractometer	0.25	1.0	14	0.72	0.22	31%
Flame ionization	0.12	1.58	15	0.64	0.39	61%
Evaporative (T=0)	0.027	1.57	6	0.45	0.40	89%
detector (T=10)	0.011	1.43	15	0.50	0.43	86%
Polymers						
Refractometer	0.18	1.0	6	0.49	0.37	76%
Evaporative det. (T=0)	0.35	1.0	6	0.63	0.23	36%

Table 7 - Summary of detection limits

Detector	DL (ug/g)		DLT (ng/s)	
	Min	Max	Min	Max
Refractometer	0.28	1.13	33	189
Flame ionization	2.6	4.2	220	350
Evaporative det. (T=0)	0.58	2.1	32	35
(T=5)	1.0	37	56	6200

Table 8 - Average molecular weight of pitch samples

Sample	Refractometer	Evaporative det.	LC-FID	UV
	Number average molecular weight, M_n			
1	780	590	560	580
2	500	380	470	290
3	290	340	330	250
	Weight average molecular weight, M_w			
1	2730	1960	1050	3410
2	2250	1520	880	2540
3	2170	1380	630	2240

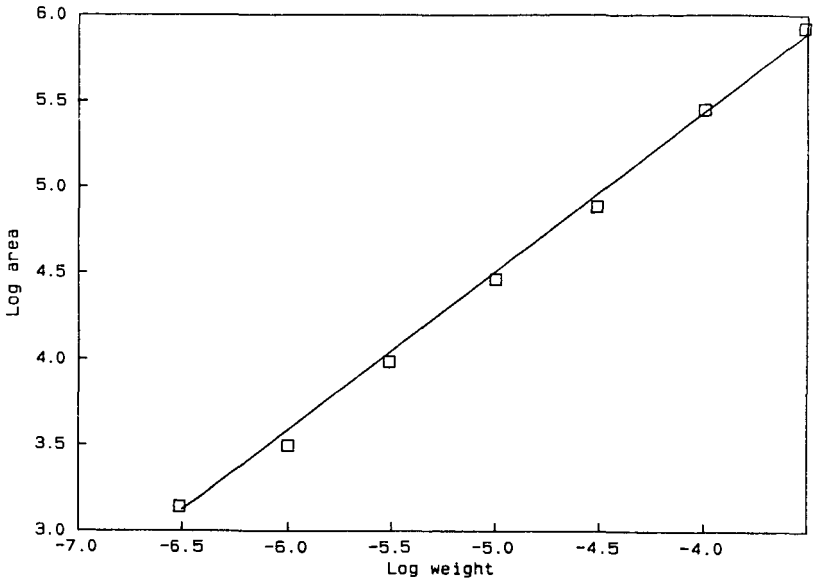

Fig.1 - Linearity of refractometer for phenanthrene (Slope=0.941, r=0.9988)

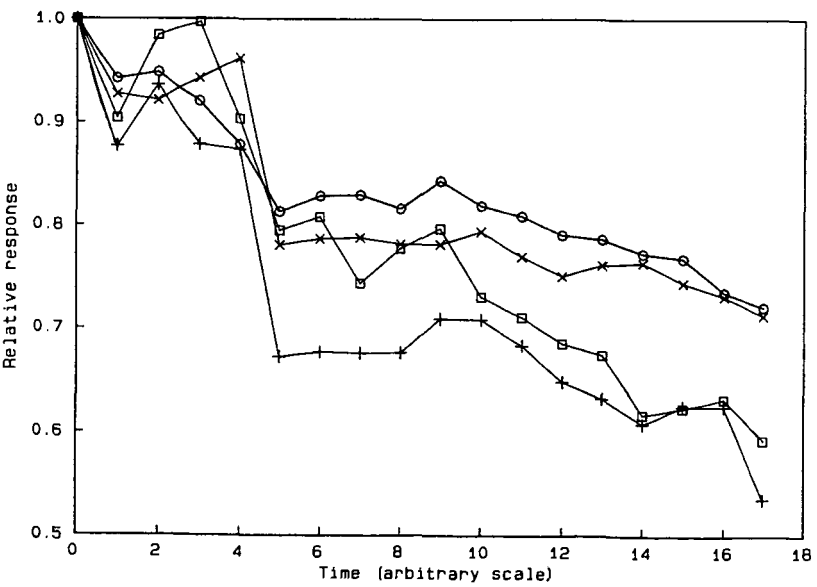

Fig.2 - Variation of signal with time for LC-FID (□ dibenzofuran, + dibenzothiphene, ○ pyrene, X benzophenone)

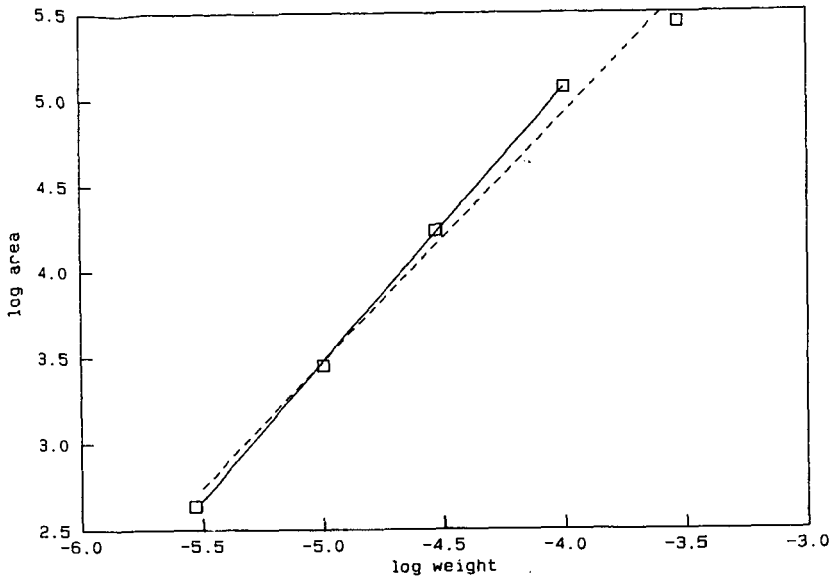

Fig.3 - Linearity of LC-FID for thianthrene (--- : slope=1.447, r=0.9946; ——— : slope=1.594, r=0.9999)

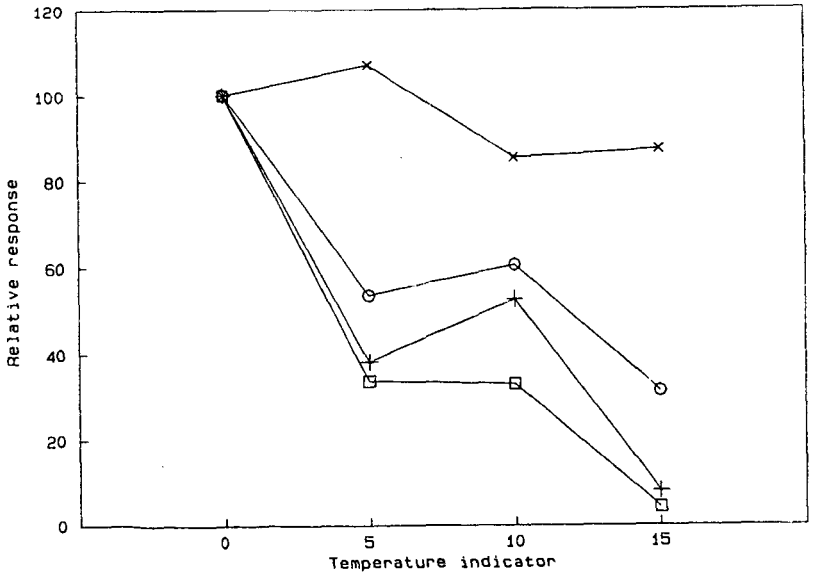

Fig.4 - Relative variation of signal with temperature setting of evaporative detector: □ dibenzofuran (MW=168), + benzophenone (MW=182), O o-terphenyl (MW=230), X 3-methyl cholanthrene (MW=268)

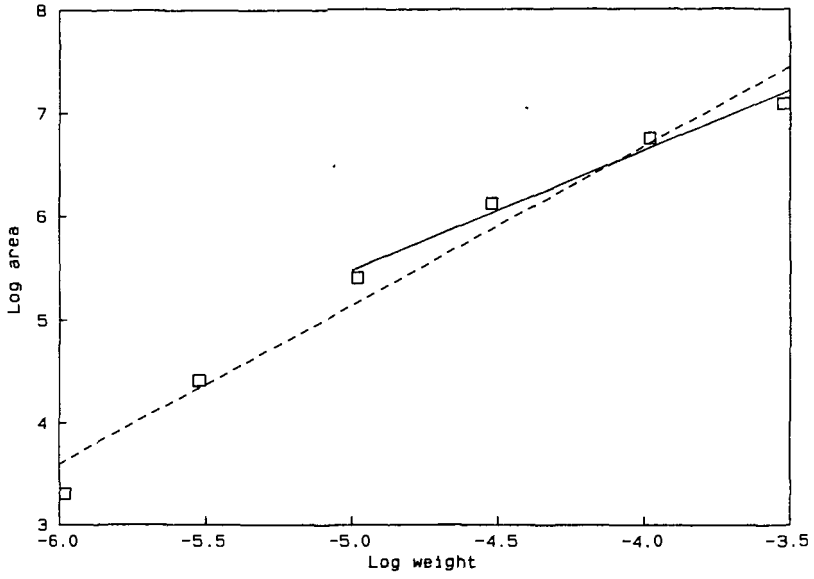

Fig.5 - Linearity of evaporative detector for pyrene (--- slope=1.537, r=0.9839;—— slope=1.161,r=0.9892)

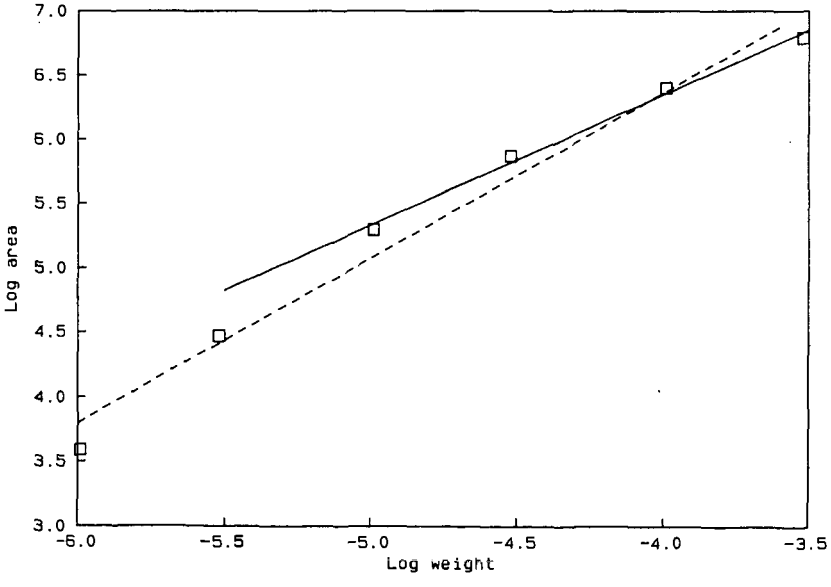

Fig.6 - Linearity of evaporative detector for polystyrene of M_w=6200 (--- slope=1.286, r=0.9888;—— slope=1.011, r=0.9969)

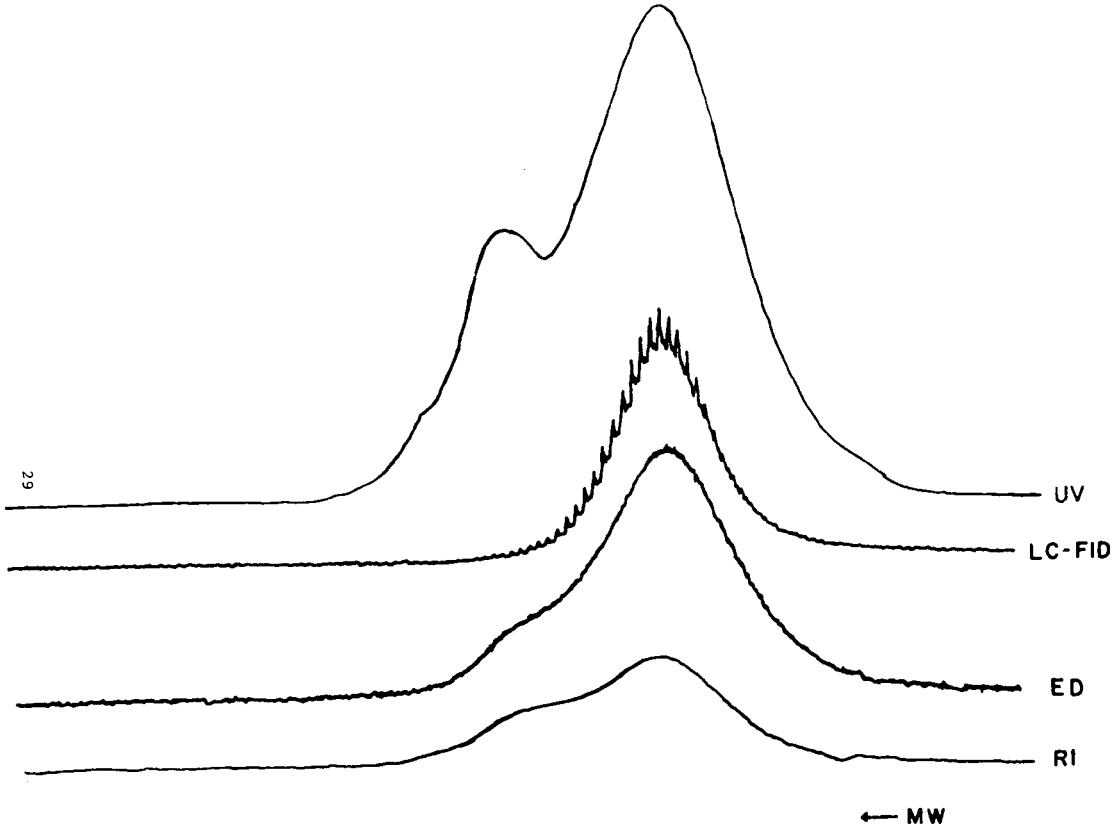

Fig.7 - SEC chromatogram of a pitch sample as detected by different detectors (UV = ultraviolet, LC-FID = flame ionization detector for liquid chromatography, ED = evaporative detector, RI = refractometer)

DETERMINATION OF AROMATICS IN HEATING OILS AND DIESEL FUELS BY SUPERCRITICAL FLUID CHROMATOGRAPHY

B.J. Fuhr, L.R. Holloway & C. Reichert

Alberta Research Council, Box 8330, Stn F
Edmonton, Alberta, Canada T6H 5X2

S.W. Lee & A.C.S. Hayden

Energy, Mines & Resources Canada, CANMET, 555 Booth Street
Ottawa, Ontario, Canada, K1A 0G1

INTRODUCTION

The presence of high quantities of aromatic compounds in middle distillate fuels causes problems for refiners and users because of the sooting propensity of such oils. Distillate fuels containing a high proportion of aromatic compounds are being produced due to the increased use of non-conventional crudes and of lower cost blending components to maximize product yield.

The method normally used in refineries for determining aromatics in oils is ASTM D 1319, the fluorescent indicator adsorption (FIA) method (1). The method uses inexpensive equipment and is simple to perform; however, it does have some limitations. The procedure is lengthly and results depend upon the operator's ability to distinguish between the colored bands, which can be difficult for colored samples. Problems have been reported with variations in dye composition and availability of the proper grade and activity of silica gel (2). Finally, the scope of the method excludes samples with final boiling points greater than 315°C.

The purpose of the present work was to develop a simple, inexpensive and precise method to determine aromatics content in heating oils and diesel fuels. It was desired that the method be applicable to samples boiling as high as 400°C, and that it be suitable for use in refinery control laboratories.

Mass spectrometry and nuclear magnetic resonance may be used for aromatics determination, but both require expensive instrumentation and highly trained operators. They are therefore unsuitable for routine refinery use.

Many methods based on high performance liquid chromatography (HPLC) have been employed for saturates and aromatics determination. Some examples are those reported by Suatoni and Swab (3), Alfredson (4) and Cookson et al (5). Generally these methods are characterized by good separation, analysis times of less than 10 minutes, and are not limited to low boiling samples. Their main disadvantage is the specificity of the usual ultraviolet (UV) and refractive index (RI) detectors, which require extensive calibration using either model compounds similar to those in the samples being analyzed, or fractions prepared from the actual samples by open column chromatography.

Two detectors thought to be preferable to the RI and UV, because of their relative uniformity of response for hydrocarbon types over a wide range of carbon numbers, are the dielectric constant (DC) detector and the flame ionization detector (FID). This uniformity of response greatly simplifies the calibration procedure. Hayes and Anderson (6) used a DC detector in conjunction with conventional HPLC

employing Partisil columns and n-butylchloride as the mobile phase to determine saturates, monoaromatics and polyaromatics in fuel distillates.

The FID presents a problem when used with conventional HPLC because of interference from commonly used solvents. Norris and Rawdon (2) have successfully coupled supercritical fluid chromatography (SFC) with FID using carbon dioxide as the mobile phase and a silica column coated with silver nitrate to determine saturates, olefins and aromatics in gasolines. Schwartz and Brownlee (7) also employed SFC/FID to determine paraffins, olefins and aromatics in gasolines employing a silica column with sulfur hexafluoride as the mobile phase.

In SFC the mobile phase is a highly compressed gas (8) with excellent solvating properties. This condition is achieved above the critical temperature and pressure of the mobile phase. Generally the density of the fluid and hence its solvating ability is increased by either increasing the pressure or decreasing the temperature. This will usually result in a loss of selectivity within a homologous series, but can be advantageous when class separations (saturates, aromatics) are desired over a wide molecular weight range. An SFC system is easily coupled to an FID with little interference from the mobile phase fluid since it rapidly desolvates before entering the detector (9).

In the present work the effects of temperature, pressure and stationary phase on the SFC/FID determination of aromatics in middle distillate fuels were investigated. The FID response to both saturates and aromatics isolated from several actual samples was determined. Results were compared to those obtained by the FIA method, and the possibilities of using SFC/FID for determining aromatics on the basis of number of rings was investigated.

EXPERIMENTAL

Instrumentation

A Varian model 8500 syringe pump was used to pressurize the carbon dioxide in the chromatographic column. Inlet pressures were between 3250 and 4200 psi (22,400 and 28,900 kPa). To facilitate filling of the pump with liquefied gas, two alternate methods were used. One employed a Lauda model K4R circulator bath to keep the syringe pump cooled. The other employed a cylinder of carbon dioxide pre-pressurized to 1200 psi with helium which allowed the pump to be filled without cooling (10). A Shimadzu model GC-8A gas chromatograph equipped with an FID contained the chromatographic column. The GC was run isothermally at temperatures ranging from 35 to 90°C; the temperature of the detector was 400°C. A Rheodyne valve model 7520 equipped with a 0.2 μL internal sample loop mounted on the exterior of the gas chromatograph was employed to introduce the sample onto the column. A Spectra-Physics model 4290 computing integrator was used for the collection and reduction of the data.

Columns and Restrictors

All columns were 250mm x 2.1mm ID (Alltech Associates). The following stationary phases were employed: 5μ silica adsorbosphere, 5μ cyano, 5μ amino, and 20% $AgNO_3$ on 5μ silica. The restrictors were flexible fused silica capillary tubing attached to the column with a 0.4mm 40% graphite ferrule with a low dead volume fitting. Either 50mm of 10μ ID tubing inserted approximately 30mm into the FID, or 130mm of 20μ ID tubing inserted approximately 90mm into the FID, as close as possible to the flame, was used. The latter arrangement was found to eliminate "spiking", a common problem in SFC (10).

Chemicals and Calibration Materials

Fisher Scientific ACS grade carbon disulfide (CS_2) was used for dilution of the samples. A modification of the column chromatographic procedure of Sawatzky et al (11) was used for the preparation of saturates and aromatics fractions from several actual samples. The saturates fraction was eluted from the silica-alumina column with n-pentane and the aromatics with toluene. Following careful air drying to remove the solvent these fractions were used for checking the FID response factors.

RESULTS AND DISCUSSION

Saturates-Aromatics Separation

A. Effect of Temperature: Retention time data, expressed as capacity factors, for a series of model compounds are shown in the first two columns of Table 1 for the silica stationary phase, mobile phase pressure of 3600 psi and temperatures of 90 and 35°C. The capacity factor, k, is defined by:

$$k = (t_R - t_o) / t_o$$

where t_R is the retention time of the given model compound, and t_o is the retention time of a compound not retained by the column which in this case is the impurity peak in the CS_2 solvent. At both temperatures, the saturates span a much smaller range of k values than do the aromatics. However, it can be seen that at 35°C the saturates as a group are better separated from the monoaromatics. For example at this temperature C_{30} has a lower k value than does benzene, but at 90°C C_{20} and toluene have approximately the same k values. The boiling points of toluene and C_{30} correspond approximately with the lowest initial boiling point and the highest final boiling point (as determined by gas chromatographic simulated distillation) of all middle distillate samples studied in the present work.

The dramatic improvement in saturates-aromatics separation upon decreasing the oven temperature is shown for an actual sample by the chromatograms in Figure 1. The sharp initial eluting peak is due to the saturates. At 35°C there is almost baseline separation between the saturates and the monoaromatic group of peaks. An added advantage of operating at the lower temperature is the shorter retention times, which would result in shorter analysis times per sample. For example, phenanthrene elutes in 11 min. at 90°C compared to 6 min. at 35°C This can be attributed to increased density of the supercritical CO_2 at the lower temperature, which increases its solvating ability (8).

B. Effect of Pressure: Data are not shown, but there was some improvement in separation between saturates and aromatics at 90°C when the pressure was increased from 3250 to 3600 psi, presumably due to the increased density of the CO_2. At 35°C, however, there was virtually no change in the separation over the pressure range of 3000 and 4200 psi.

C. Effect of Stationary Phase: Grizzle and Sablotny (12) employed HPLC with two aminosilane columns in series and hexane/methylene chloride as the mobile phase to separate saturates and aromatics. Lundanes and Greibrokk (13) reported that a silver-impregnated silica column was required to obtain complete separation of saturates and aromatics by SFC using CO_2. Based on these studies we investigated three other columns or combinations in an attempt to improve upon the separation between saturates and aromatics. The data obtained at a pressure of 3600 psi and temperature of 35°C are shown in

Table 1. It can be seen that the separation using the silica/cyano (Si/CN) combination is not as good as that of the silica at the same temperature. C_{30} and xylene have the same k value using the Si/CN, whereas C_{30} has a smaller k value than xylene with the silica alone. For the amino (NH_2) column the separation between saturates and aromatics is much poorer; in this case C_{30} has the same k value as hexamethylbenzene. From the limited number of compounds run, it appears that the series combination of silica/20% $AgNO_3$ on silica (Si/Ag) is no better than silica at 90°C. It is concluded that of the stationary phases studied in our SFC system, the best saturates-aromatics separation is obtained using a 5μ silica column.

Calibration

In order to check FID response factors for saturates and aromatics, some calibration studies were carried out. The calibration curves were determined using saturates and aromatics fractions prepared from four middle distillate samples using the procedure reported by Sawatzky et al (11). Recoveries of material from the column ranged from 81 to 99 wt%, indicating the loss of some lower boiling components. The SFC chromatograms of one of the samples and of its separate fractions using the silica column at a pressure of 3250 psi and temperature of 90°C, are shown in Figure 2. The relatively high degree of purity of each fraction implies that the separations by column chromatography and SFC are similar making the fractions suitable for calibration purposes.

The calibration curves obtained over a broad range of concentration using CS_2 solutions of the saturates and aromatics fractions are shown in Figure 3. The data points were fitted to the line: $y = A*x$. The response factors as given by the slopes of each line differ by only 5%. Differences of this order of magnitude were reported for GC/FID work on model compounds (14), from which it was concluded the response factors are more or less eqivalent.

Curvature was noted in the saturates response above approximately $100x10^6$ area counts, whereas the aromatics response was linear to $300x10^6$ area counts. The likely reason for this behavior is that the FID becomes saturated above a certain concentration. The saturates, which have a much sharper peak, saturate the detector at a lower sample size than do the aromatics. Because of this non-linear behavior, it was necessary to reduce the concentration of sample reaching the FID by dilution. CS_2 was chosen as the solvent because of its low FID response. It was found for all samples in this study that dilution by a factor of ten was sufficient to bring the saturates into the linear range.

Because of the close agreement between saturates and aromatics response for fractions obtained from actual samples, it was decided that the integrated area percentages may be used directly to quantitate saturates and aromatics provided that samples are diluted such that the components are within the linear range of the detector and that a small correction is made for the area of the impurity peak from the CS_2.

Repeatability and Accuracy

The wt% aromatics values were obtained from analyses of duplicate (1:10) dilutions in CS_2 of each of 22 samples of heating oils and diesel fuels. Standard deviations ranged from 0 to 1.4 wt%. A pooled standard deviation value of 0.4 wt% was caluculated from all data using the formula given by Snedecor and Cochran (15). According to ASTM C 670-81 (16) the standard deviation is multiplied by the factor 2.83 to obtain a repeatability. For the present data this repeatability statement is as follows: "Duplicate measurements by the same operator should be considered

suspect if they differ by more than 1.1 wt% 19 times out of 20". This repeatability compares favorably with that reported for the FIA method (1).

These particular repeatability measurements were carried out by a chemical technologist with one year of gas chromatographic experience. Three days were required for this individual to become familiar with the operation of the instrument and to perform the analyses. This indicates the relative simplicity of the technique, and suggests its suitability for use in refinery control laboratories.

The accuracy of the method could not be determined using actual samples since the absolute aromatics contents were not known. An indication of the accuracy, however, was made using known mixtures of hexadecane and naphthalene in CS_2. The differences between actual and measured values ranged from 0 to 1 wt%.

Comparison to the FIA Method

Despite its disadvantages, FIA is the most widely used standard method in the oil industry for aromatics determination. For this reason it was used as a basis for comparison of the present SFC/FID results. This comparison is shown by the plot in Figure 4. A linear regression of the data, indicated by the solid line in Figure 4, yielded a correlation coefficient of 0.9018. The 95% confidence interval for this regression is given by the dashed curves. The consistent bias of all but three of the points to higher values by SFC/FID (slope=0.97) probably reflects the fact that the output of FIA is in vol% whereas that for SFC/FID is in wt%. This has also been indicated in the work of Norris and Rawdon (2).

There are two possible explanations for the three samples whose points lie outside the confidence limits. First, these samples yielded olefins values by FIA greater than 3 vol%. High concentration of olefins do interfere with the separation between saturates and aromatics on a silica column (17), which might result in the lower aromatics values by SFC. Secondly, two of these three samples contain components boiling well above 315°C which makes the FIA results questionable for these samples.

Classification of Aromatics by Number of Rings

The capacity factor data for the silica column at both 90 and 35°C shown in Table 1 in general indicate a grouping of the aromatics according to number of rings. The only significant overlap occurs between the monoaromatics, hexamethylbenzene and octahydroanthracene, and the diaromatic compounds. It is suspected that these monoaromatics overlap because of the large amount of pi electron delocalization over the ring structures. For the model compounds considered in the present work good separation is obtained between the diaromatics and polyaromatics.

Stationary phases other than silica, such as amino-modified silica, have been employed to separate polycyclic aromatic hydrocarbons by HPLC (12,19) and by SFC (20). Our SFC data using a series combination of Si/CN stationary phases, shown in Table 1, indicate marginally better separation between mono- and diaromatics compared to silica alone, but poorer saturates-monoaromatics separation. The NH_2 column provides the best separation between mono- and diaromatics, but very poor saturates-monoaromatics separation (the k value for C_{30} is greater than most of the monoaromatic compounds as seen from Table 1). Finally, with the series combination of Si/Ag, the separation among aromatic types appears to be no better than the silica column. It is concluded that, of the stationary phases studied in the present work, a single silica column would be the one preferred for quantitation of aromatics according to number of rings.

CONCLUSIONS

A method employing SFC with FID, similar to that reported by Norris and Rawdon for the analysis of gasolines (2), has been developed for the determination of aromatics in middle distillate fuels. The method is simple, employs relatively inexpensive equipment, gives good repeatability and provides results which correlate well with those obtained by FIA. The SFC method is not affected by sample color, appears to be applicable to samples with final boiling points as high as 450°C and should be suitable for use in a refinery control laboratory. Initial indications are that the determination of aromatics according to the number of rings can be accomplished by SFC/FID.

ACKNOWLEDGEMENTS

The authors would like to thank J. Steppler and R. Dietrich of Chemex Labs (Alberta) Ltd., Calgary, AB, Canada for their assistance in this work.

REFERENCES

1. "Manual on Hydrocarbon Analysis", 3rd Edition, American Society for Testing and Materials, D 1319, Philadelphia, PA, 1977.
2. T.A. Norris and M.G. Rawdon, Anal. Chem., 56, 1767 (1984).
3. J.C. Suatoni and R.E. Swab, J. Chromatogr. Sci., 13, 361 (1975).
4. T.V. Alfredson, J. Chromatogr., 218, 715 (1981).
5. D.J. Cookson, C.J. Rix, I.M. Shaw and B.E. Smith, J. Chromatogr., 312, 237 (1984).
6. P.C. Hayes and S.D. Anderson, Anal. Chem., 57, 2094 (1985).
7. H.E. Schwartz and R.G. Brownlee, J. Chromatogr., 353, 77 (1986).
8. P.A. Peaden and M.L. Lee, J. Liq. Chromatogr., 5(Suppl. 2), 179 (1982).
9. M. Novotny, J. High Resol. Chromatogr. & Chromatogr. Comm., 9, 137 (1986).
10. H.E. Schwartz, J.W. Higgins and R.G. Brownlee, LC-GC, 4, 639 (1986).
11. H. Sawatzky, A.E. George, G.T. Smiley and D.S. Montgomery, Fuel, 55, 16 (1976).
12. P.L. Grizzle and D.M. Sablotny, Anal. Chem, 58, 2389 (1986).
13. E. Lundanes and T. Greibrokk, J. Chromatogr., 349, 439 (1985).
14. W.A. Deitz, J. of Gas Chromatography, 68, February, 1967.
15. G.W. Snedecor and W.G. Cochran, "Statistical Methods", Seventh Edition, Iowa State University Press, Ames, IO, p.91, 1980.
16. "Preparing Precision Statements for Test Methods for Construction Materials", C 670-81, Annual Book of ASTM Standards, 1984.
17. B.J. Fuhr and L.R.Holloway, Alberta Research Council, Edmonton, Alberta, unpublished data.
18. P.J. King and A. Sagarra, in "Modern Petroleum Technology", G.D. Hobson and W. Phol, Eds., 4th Ed., Institute of Petroleum, Applied Science Publication Service, 1973.
19. S.A. Wise, S.N. Chesler, H.S. Hertz, L.R. Hilpert and W.E. May, Anal. Chem., 49, 2306 (1977).
20. R.M. Campbell and M.L. Lee, Anal. Chem., 58, 2247 (1986).

TABLE 1

Comparison of Capacity Factors of Some Model Compounds Using Different Stationary Phases*

Compound	Silica 90°C	Silica 35°C	Si/CN 35°C	NH_2 35°C	Si/Ag 35°C
Saturates:					
N-pentane	-	-	-	-	0.00
N-hexane	0.00	-	-	-	-
3-Methylheptane	0.02	-	-	-	-
N-decane	0.04	0.00	-	-	-
Cyclohexane	0.04	-	-	-	-
Dimethylcyclohexane	0.05	0.04	-	0.00	-
Hexadecane	0.11	-	-	-	-
Decalin	0.13	0.05	-	-	-
Eicosane (C_{20})	0.18	0.04	-	-	0.17
Triacontane (C_{30})	-	0.09	0.15	1.12	0.26
Monoaromatics:					
Benzene	0.16	0.17	-	-	-
Toluene	0.19	0.17	-	-	-
3-Ethyltoluene	0.24	0.16	-	-	-
O-xylene	0.26	0.20	0.15	0.27	0.26
Indane	0.33	0.25	-	-	-
1-Phenydecane	0.39	0.24	-	-	-
Tetralin	0.41	-	0.27	0.62	-
Hexamethylbenzene	0.69	-	0.47	1.12	-
Octahydroanthracene	0.80	-	0.54	1.62	-
Diaromatics:					
Naphthalene	0.53	0.37	0.41	1.12	0.49
2-Methylnaphthalene	0.56	-	0.47	1.27	-
Thianaphthalene	0.56	-	0.47	1.27	-
Biphenyl	0.70	-	0.44	1.46	-
Acenaphthalene	0.80	-	0.65	-	-
Bibenzyl	0.92	-	0.57	-	-
Polyaromatics:					
Fluorene	1.02	-	-	-	-
Dibenzothiophene	1.16	-	-	-	-
Anthracene	1.22	-	-	-	-
Phenanthrene	1.27	0.85	1.15	4.85	1.08
Thianthrene	1.76	-	-	-	-
Fluoranthene	1.82	-	1.78	-	-
Pyrene	1.92	-	-	-	-
Chrysene	-	1.89	-	-	-

* All runs were carried out at a pressure of 3600 psi.

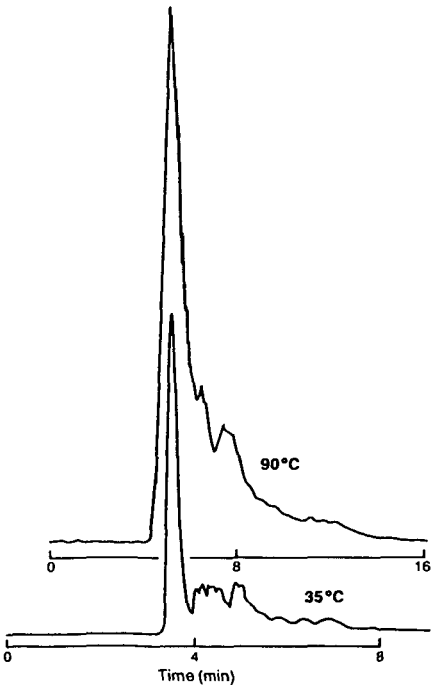

FIGURE 1: SFC chromatograms of a middle distillate sample at temperatures of 90 and 35 °C using a silica column and pressure of 3600 psi.

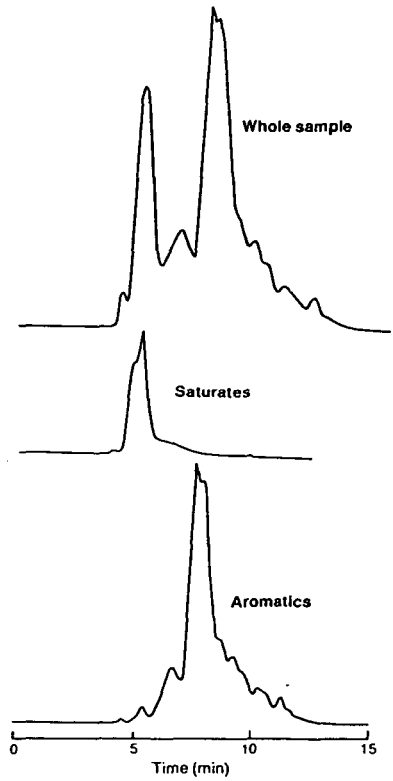

FIGURE 2: SFC chromatograms obtained at 90°C and 3250 psi of a whole middle distillate sample and of its saturates and aromatics fractions separated by column chromatography.

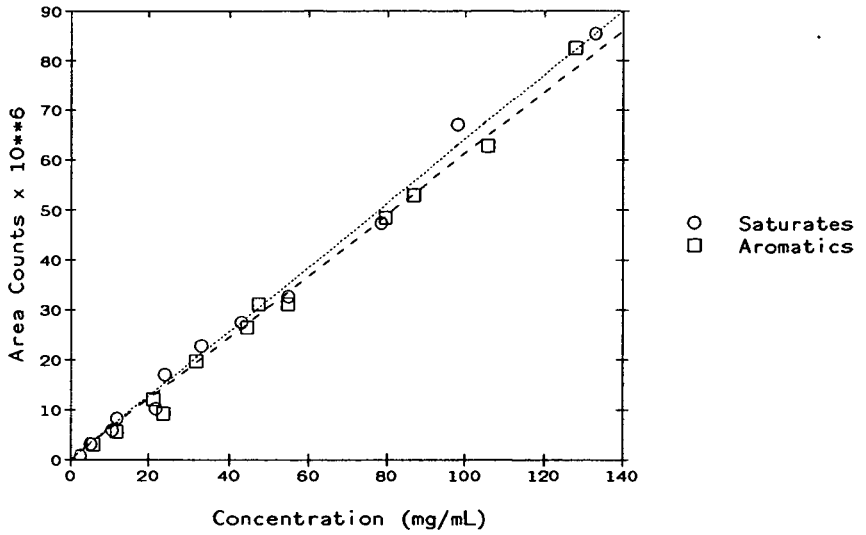

FIGURE 3: SFC calibration curves using saturates and aromatics fractions separated from middle distillates by column chromatography.

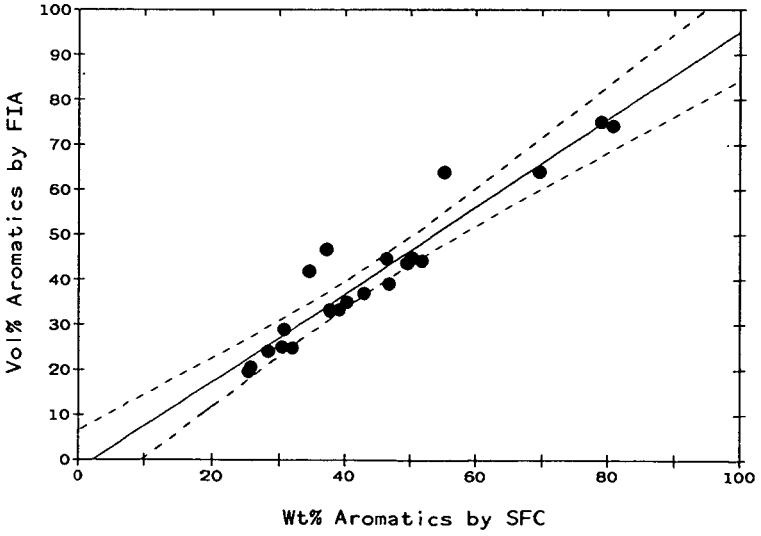

FIGURE 4: Comparison of aromatics content of middle distillates by SFC and FIA.

THE DEPOLYMERIZATION OF A MODEL COAL POLYMER

I. Lee, C. M. Sliepcevich and R. G. Mallinson

School of Chemical Engineering and Materials Science
University of Oklahoma
Norman, Oklahoma 73019

INTRODUCTION

While the macromolecular nature of the organic matter of coal has been known for some time (1), the manner in which the organic structure is held together has been a focus for a much shorter time and is still the subject of considerable scrutiny (2,3,4). It has been established that the macromolecular crosslinked structure of coal is the primary reason for its insolubility, but swellability, in organic solvents. The nature of the crosslinks, whether of a covalent or lesser type, is not really in dispute, but, rather, the relative amounts and importance of the probable interactions. The difficulties in establishing a clear concept no doubt lie in the very heterogeneous nature of coal, including the presence of trapped or "guest" molecules, and the diversity of coals of widely varying origins and ages.

The most successful approach in attempting to understand the macromolecular structure of coal has been the application of techniques and models from the field of polymer science in considering coals as crosslinked polymer networks (3,4). The difficulties of adapting a theoretical approach for ideal systems to such a heterogeneous, non-ideal, system as coal, have recently been pointed out (5,6). Nevertheless, for a pure polymer system used as a model for coal, the results should provide helpful insights into the nature of the thermal degradation of crosslinked polymer networks and coals.

In this work, a model coal polymer network has been synthesized under conditions of thermal liquefaction. The degradation of the macromolecular network and production of soluble products are followed as a function of reaction time.

EXPERIMENTAL

A crosslinked polymer network was produced using the difunctional monomers a,a'-dichloroxylene and hydroquinone with trihydroxy benzene as the trifunctional crosslinking agent. The polymer which was desired was a crosslinked aromatic based polymer in which all of the linkages, including the crosslinks, were relatively thermally labile. Thus, the linkages produced in the condensation polymerization of these monomers should all be of the benzyl phenyl ether type, which cleave readily at 350 ° C to produce phenolic hydroxyl and aromatic methyl groups when tetralin is used as a solvent (7). Figure 1 shows the monomer structures and the steps in the production of the polymer. The hydroxyl monomers were converted to their sodium salts and dissolved in water, while the dichloride was dissolved in acetone. These were then mixed and refluxed at atmospheric pressure for four hours to produce an insoluble product. The polymer which was produced was insoluble in all solvents tested, including THF and pyridine. Analysis of the polymer included carbon, hydrogen, oxygen, sodium and chlorine elemental analyses which were carried out by Huffman Laboratories, and swelling analysis. Swelling analyses were carried out in pyridine using the procedure of Larsen et al. (8).

Once the polymer had been synthesized, degradation experiments were carried out in a microtubing bomb type reactor. Approximately 0.5 grams of polymer, accurately weighed, was put into the reactor with 2.0 grams of tetralin. The reactor was then sealed and pressurized with nitrogen gas to 1000 psig. The reactor was immersed in a fluidized bed sandbath maintained at 350 ± 5 ° C. The internal reactor temperature reached the steady state temperature within one minute and, at the end of the desired reaction time, was removed from the bath and quenched in water for an essentially

instantaneous cool down.

The reactor contents were then removed and a soxhlet extraction with THF was carried out to separate soluble and insoluble materials. The THF (and tetralin) was removed from the soluble fraction by rotary evaporator and the THF removed from the insoluble matter in a vacuum oven. Both fractions were weighed and the material balance could be closed to within five percent with a few exceptions which were within ten percent. The insoluble material was then subjected to swelling analysis and hydroxyl group analysis using the acetylation technique following the procedure of Cronauer et al. (9). The soluble material was analyzed by gel permeation chromatography.

RESULTS

As mentioned above, it was initially intended that all linkages in the polymer would be of the benzyl phenyl ether type. However, the degradation results showed that after significant conversion of the initial insoluble polymer to soluble products at short reaction times, an asymptotic limit of about 40 percent was reached after which no increase in conversion was observed, as can be seen in Figure 2. After examining the elemental analysis data and the organic chemistry literature, it appeared that a side reaction involving nucleophilic attack of the aromatic rings by the hydroxyl groups was possible. This reaction altered the structure of the polymer by including diphenyl ether type structures, which are considerably more refractory than the benzyl phenyl ethers (7). This additional structure is illustrated in Figure 3 by the symbol, T. With this knowledge, the polymer structure could be broken down into the groups shown in Figure 3 for purposes of analysis. A sample of the polymer structure is shown in Figure 4 with the different structural groups outlined. The quantities of all of these groups could be determined by their algebraic relationships with the elemental analyses, including the end group analysis provided by the sodium and chlorine analyses. The reduction of the structure into groups allowed the determination of the quantities and types of crosslinks present in the polymer structure. This knowledge about the crosslinks, with the use of a modified Flory-Rehner (10,3,4) theory, provides detailed information about the network. The molecular weight between crosslinks as well as the size of the "loops" in the network may be determined.

With the appropriate parameters, the initial molecular weight between crosslinks is calculated to be 600 for the observed swelling ratio of 1.34. The interaction parameter, χ, was determined from the correlation of Lucht (11) based solely on the carbon content of the material, which was developed for coals. This parameter is currently being determined experimentally for this system. Upon degradation, the swelling behavior follows the conversion results in that the ratio increases dramatically within the first four minutes, and then levels off to an asymptotic limit of about 1.8, as may be seen in Figure 5. From the modified Flory-Rehner theory, a molecular weight between crosslinks of 900 is calculated. The behavior of both the conversion and molecular weight between crosslinks is qualitatively quite similar to what one might expect of a coal at this temperature. It follows that the more thermally labile crosslinks have been cleaved and then stabilized by the donor solvent, causing a significant amount of soluble material to be produced. At the same time the network opens up, but there remains a substantial amount of insoluble material due to the stability of the more refractory crosslinks. Figure 6 shows the hydroxyl group concentration of the polymer as a function of reaction time with the results as expected for the cleavage of the benzyl phenyl ether linkages at the conversions observed.

The soluble materials produced show a range of molecular weights from below 300 up to about 1000. Calibration of the GPC was accomplished with model compounds having molecular weights up to 532, so the values above that could have some absolute error from the extrapolation. Figure 7 shows the evolution of the molecular weight distribution with reaction time. The data are normalized per gram of initial polymer used so that the area under the curve is proportional to the mass of soluble material produced and becomes larger with higher conversions at longer reaction times. As may be seen, the general trend is for increased material of all molecular weights to be produced as the reaction

time and conversion increases. However, the lower molecular weight material, below about 300 tends to increase more rapidly than the bulk of the curve, which may be indicative of continued depolymerization within the material which has already become soluble. Also, at the higher molecular weights, above about 700, the increase is also larger than for the bulk of the curve, with a pronounced peak developing for the two longest reaction times shown. It may be that as more crosslinks are broken, larger "pieces" of structures become soluble because of increases in the numbers of hydroxyl and methyl groups per "molecular piece", which aid the solubility of such "pieces".

SUMMARY

In summary, the goal of this work has been to develop a synthetic macromolecular network which may be used as a model for coal networks, and to take advantage of the high degree of characterization available such that the network may be thermally degraded and nsights into the degradation of the networks in coal may be gained. Also, with the increased use of thermosetting polymer networks for materials applications, this knowledge is applicable to the understanding of thermal (or random) degradation and stability of these systems. This experimental work is being conducted in parallel with a modeling effort for the degradation of polymer networks.

ACKNOWLEDGEMENTS

This work was supported by the Energy Resources Institute and Oklahoma Mining and Minerals Resources Research Institute of the University of Oklahoma and in part by the U. S. Department of Energy under grant No. DE-FG01-87FE1146.

REFERENCES

(1) Van Krevelen, D. W.; *Fuel*, **44**, 229 (1965).

(2) Sanada, Y. and Honda, H.; *Fuel*, **45**, 295 (1966).

(3) Larsen, J. W. and J. Kovac; *Organic Chemistry of coal*, ACS Symposium Series 71, Chapter 2, American Chemical Society, Washington DC (1978).

(4) Lucht, L. M. and N. A. Peppas; in *Chemistry and Physics of Coal Utilization*, B. R. Cooper and L. Petrakis, Eds.; Am. Inst. Physics, New York (1981).

(5) Hsieh, S. T. and J. L. Duda; *Fuel*, **66**, 170 (1987).

(6) Painter, P., J. Nowak, M. Sobkowiak and J. Youtcheff; *ACS Fuel Chem. Div. Preprints*, **32**, #1, 576 (1987).

(7) Wooding, G. W.; M.S. Thesis, Purdue University (1982).

(8) Larsen, J. W., T. K. Green and J. Kovac; *Fuel*, **63**, 935 (1984).

(9) Cronauer, D. C. and Ruberto, R. G.; EPRI Report Number AF-442 (1977).

(10) Lee, I.; M.S. Thesis, University of Oklahoma (1986).

(11) Flory, P. J. and J. Rehner; *J. Chem. Phys.*, **11**, 521 (1943).

(12) Lucht, L. M.; Ph. D. Thesis, Purdue University (1984).

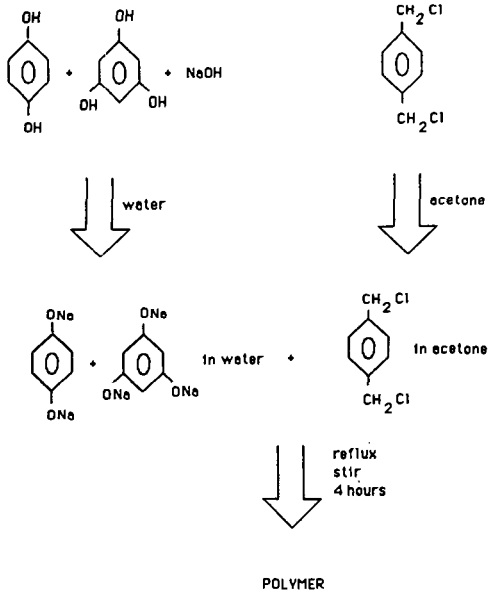

Figure 1. Preparation of the Crosslinked Polymer.

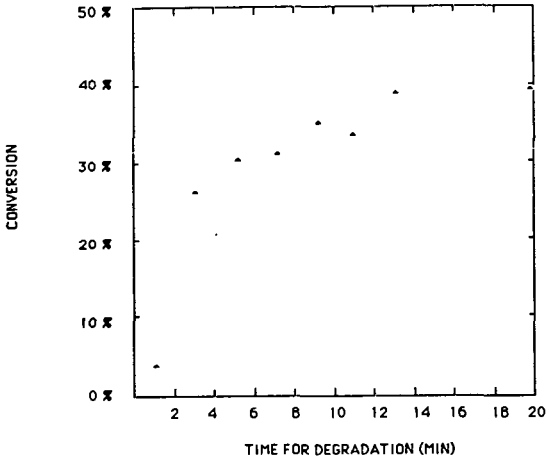

Figure 2. Conversion of the Polymer Network to Soluble Products.

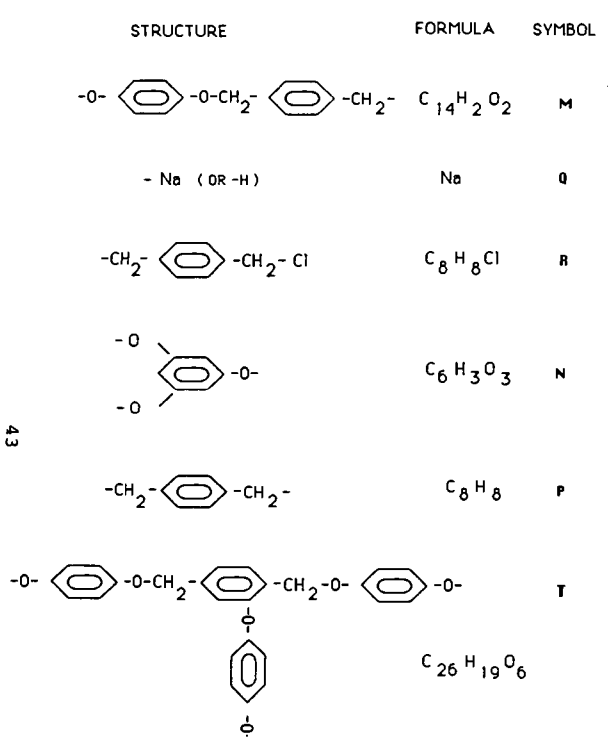

Figure 3. Basic Structural Units of the Polymer Network.

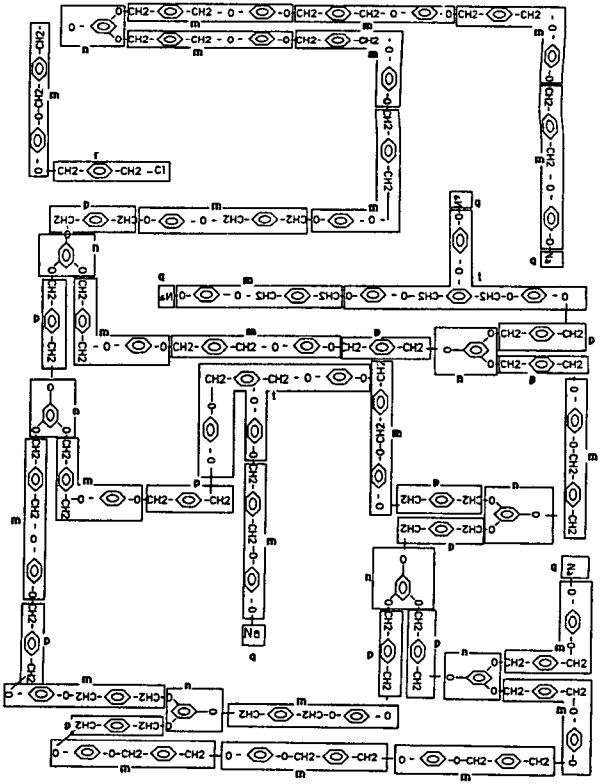

Figure 4. The Polymer Network.

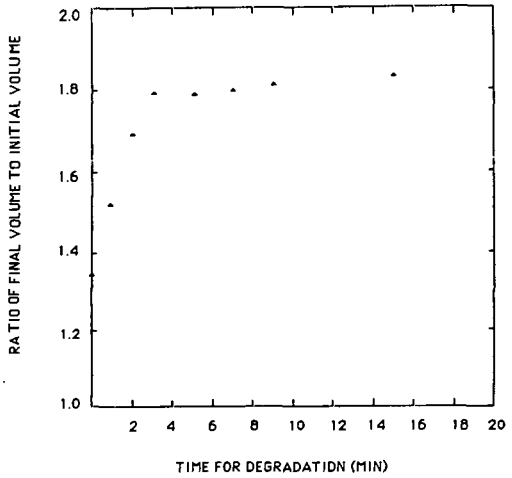

Figure 5. Swelling Ratio of the Network as a Function of Reaction Time.

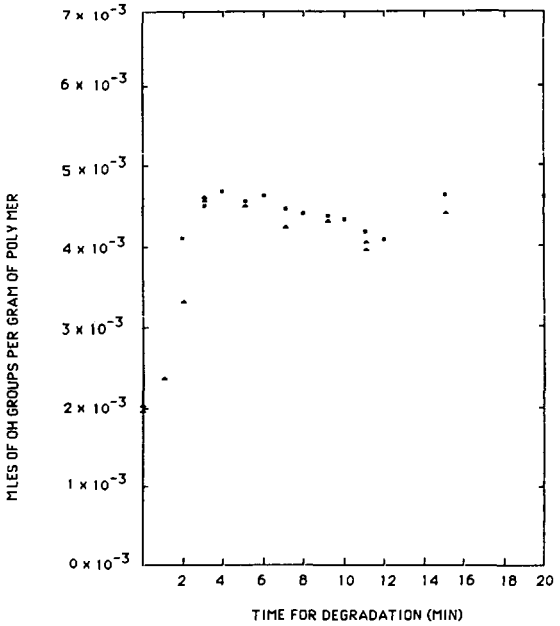

Figure 6. Hydroxyl Group Content of the Degraded Polymer.

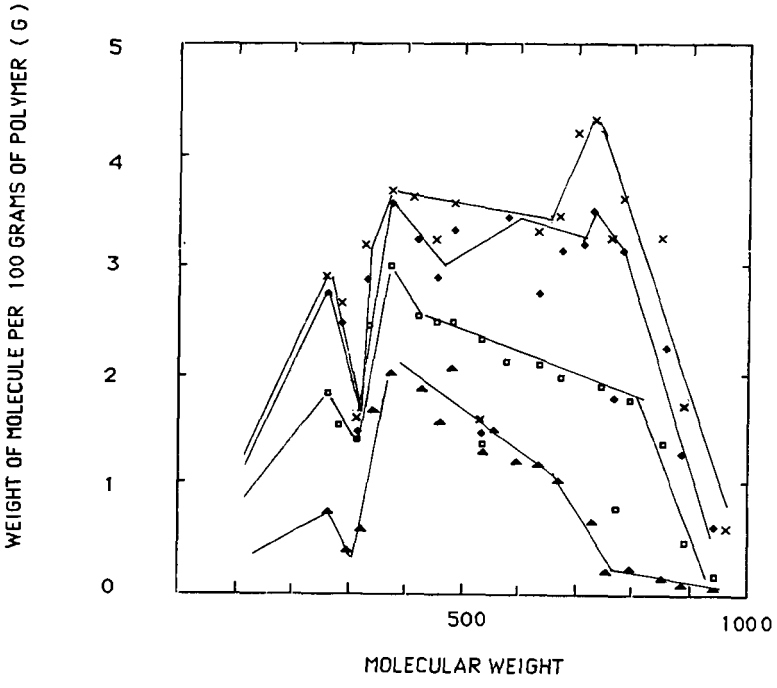

Figure 7. Molecular Weight Distributions of the Soluble Products.

Fused Salt Reactions of Organosulfur Compounds

Michael A. Nowak, Bruce R. Utz, Daniel J. Fauth
and Sidney Friedman

U.S. Department of Energy
Pittsburgh Energy Technology Center
P.O. Box 10940
Pittsburgh, PA 15236

INTRODUCTION

The treatment of coal with molten caustic is an effective method for cleaning coal (1). Molten caustic treatment removes not only mineral matter but most of the sulfur, including organic sulfur, from coal. While the chemical processes leading to the removal of inorganic sulfur have been examined (2), the mechanism of organic sulfur removal is less understood. Coal characterization studies suggest that the organosulfur moieties in coal may be largely thiophene-type ring structures (3-5). A preliminary investigation in this laboratory studied the reaction of benzothiophene with sodium and potassium hydroxides (6). Evidence was obtained that o-thiocresolates were intermediates in the desulfurization reaction (Equation 1). The overall reaction is multistep; the ring opening is a key step, since only after conversion to a thiol derivative does desulfurization take place. Our findings on the desulfurization of thiols and thiol derivatives will be discussed here.

EXPERIMENTAL

All reagents were used as purchased from commercially available sources except the thiolate salts, which were prepared as previously described (6). Potassium hydroxide contained approximately 10-12 percent moisture, and all other salts were anhydrous. An "inert fused salt diluent" (IFSD), consisting of a 36:55:9 KCl:LiCl:NaCl mixture by mole percent, was also used and had a eutectic point of 346°C. The hydroxide mixture used was a 60:40 KOH:NaOH mixture by weight (50:50 molar).

Reactions were conducted in commercially available 1/2-inch tubing unions fabricated from corrosion resistant Monel, Inconel, or Carpenter-20 alloys. Before use, the unions were washed with tetrahydrofuran and methylene chloride in order to remove any oils. One end cap was placed on the union and tightened to 30 ft lb. The half-assembled reactor was transferred into a nitrogen-purged glove box, where it was charged with approximately 0.40 gram of the organic compound and, when necessary, 2.40 grams of the powdered hydroxide(s) or salt mixture. The second end cap was placed on the reactor. After removing the reactor from the glove box, the second end cap was tightened to 30 ft lb.

The reactor was bolted in a bracket assembly and immersed in a fluidized sand bath that was preheated to the reaction temperature. For most experiments, mixing was effected by shaking the reactor assembly using a mechanical wrist action shaker. Shaking the reaction vessel had little effect on product distribution. After the specified reaction time, the reactor was cooled rapidly by immersion in tap water. The reactor was opened while submersed in 50 mL methylene chloride to dissolve volatile and neutral organic materials.

Glass reactors were prepared by sealing one end of a six-inch length of heavy-walled Pyrex tubing (12.7-mm-o.d. x 2.4-mm-i.d.). The tube was placed in the glove box and charged with approximately 0.10 gram of organic compound and, where appropriate, 0.40 gram of hydroxide(s) or salt mixture. The tube was

removed from the glove box, freeze-thaw degassed, and sealed under vacuum while the lower portion of the tube remained frozen in liquid nitrogen. After warming to room temperature, the ampoule was loaded into a 3/4-inch stainless steel reactor tee assembly (7) and pressurized to equalize the pressure buildup anticipated within the glass ampoule at reaction temperatures. The tee assembly was then submersed in a preheated fluidized sand bath for the appropriate reaction time, removed from the sand bath, and allowed to cool slowly to room temperature. The pressure was vented from the tee assembly, and the ampoule removed. The ampoule was scored and cracked open while submersed in 50 mL methylene chloride.

The methylene chloride washings were transferred into a flask containing 1,2,4,5-tetramethylbenzene as an internal standard for GLC analysis. If the reactor contained salts, it was then shaken with 50 mL distilled water containing sufficient concentrated HCl to adjust the acidity of the final solution to pH 3. The time required to dissolve the salts completely was generally 10-30 minutes. The aqueous solution was decanted into a separatory funnel, where it was extracted with two 25-mL portions of methylene chloride. The methylene chloride extracts were added to a flask containing an internal standard. Aliquots of the methylene chloride solutions were analyzed by GLC. Products were further characterized by GC/MS. Where necessary, solutions were subjected to pressure filtration through microporous membranes to remove insoluble materials (8). The presence of methylene chloride soluble polymers was determined by careful removal of solvent and volatile materials in vacuo and weighing the residues.

RESULTS AND DISCUSSION

The thermal chemistry of alkyl thiolate salts was first examined at the turn of the century (9), and since then little has been done to reveal the mechanisms of their decompositions. Most studies involved aliphatic thiolates, and only recently has anyone examined alkali metal thiolates (10,11). In general, thiolate salts are known to undergo only one pyrolysis reaction: decomposition at or near their melting point to give an organic sulfide and a metal sulfide (Equation 2).

We chose as our model compounds derivatives of the simplest aromatic thiol, thiophenol. Potassium thiophenolate or sodium thiophenolate were heated at 375°C for thirty minutes in a metal union in the presence of potassium hydroxide, sodium hydroxide, or a mixture of sodium and potassium hydroxides, or the IFSD, or as neat samples. The IFSD is molten at 375°C and was used to simulate the ionic character of the molten hydroxide media while being chemically inert towards organosulfur compounds under these conditions. By comparing the chemistry of thiophenolates in molten caustic, or IFSD, or as neat samples, we hoped to determine whether the caustic reacted with thiolate to produce a sulfur moiety more amenable to desulfurization, thus facilitating bond breaking.

We have found that, in the absence of a catalyst, neat potassium and sodium thiophenolates are stable at 375°C for extended periods of time. When potassium thiophenolate or sodium thiophenolate was treated with a molten 60:40 KOH:NaOH mixture in a corrosion-resistant union (Equation 3), a number of reaction and decomposition products were observed. Some starting material was recovered as thiophenol, and small quantities of phenyl sulfide were obtained. Significant quantities of the desulfurization product, benzene, were observed, but also some biphenyl was obtained. A number of minor products (accounting for less than 28% of the material recovered) were also observed. Methylene chloride insoluble materials that appeared as black solids were sometimes observed. Reactions conducted in the presence of hydrogen led to increased yields of benzene and lower yields of black solids (6). These observations lead us to believe that phenyl radicals are intermediates in these reactions, and that the black solids were being formed by uncontrolled polymerization of some radical species. In some cases, some methylene chloride soluble materials had insufficient volatility to be observed by GLC. These were assumed to be oligomeric materials. Products con-

taining hydroxyl groups (phenol) or several sulfhydryl groups were sometimes observed, but generally these products were insignificant. The yields of desulfurized product from the reaction of sodium thiophenolate in sodium hydroxide or potassium hydroxide (12%-16%) were lower than the yields from the reaction of potassium thiophenolate in sodium or potassium hydroxide (30%-40%).

When reactions were conducted in the same reactors using IFSD as a reaction medium, a significant difference in the chemistry of sodium thiophenolate versus potassium thiophenolate was observed. In the IFSD, diaryl sulfide formation competes with desulfurization. Phenyl sulfide was the only product observed when sodium thiophenolate decomposed in IFSD. Potassium thiophenolate decomposed in IFSD to produce the desulfurized product benzene, although a small amount of phenyl sulfide was also produced.

During the course of these studies, inconsistent results led us to observe carefully the product distributions in the different reactor vessels. Potassium thiophenolate was heated at 375°C for 30 minutes as a neat sample or in IFSD using new, "pristine" reactors. When these reactions were conducted in pristine Inconel or Carpenter-20 reactors, no desulfurization took place (Equation 4). Desulfurization was observed in experiments conducted in pristine Monel reactors. The reactors were then pretreated with molten caustic. Potassium thiophenolate was then reacted in these same reactors, and desulfurization products were observed in all cases (Equation 5). No significant increase in desulfurization was observed in experiments conducted in pretreated Monel reactors. Clearly, the metal walls of these reactors were acting as catalysts in the desulfurization mechanism or as reactants that were causing desulfurization. For Inconel and Carpenter-20 alloys, molten caustic was necessary to "activate" the metal surface.

In order to examine the catalytic effect of the metal species in these reactors, a limited systematic study was undertaken. The alloys from which these reactors were fabricated consists mainly of nickel, with individual alloys containing significant quantities of iron, copper, or chromium along with traces of manganese and other metals. Reactions were conducted in sealed glass ampoules to observe the chemistry of thiophenolates in the absence of any metals. In subsequent reactions, individual metals were added to see if they effect desulfurization. As expected, potassium thiophenolate is unreactive in the absence of any other reagents. Again, in the presence of IFSD, potassium thiophenolate provides phenyl sulfide as the major product. Some starting material was recovered. Reaction of potassium thiophenolate in the presence of caustic did not lead to desulfurization. In the presence of nickle powder or Monel shavings, with or without fused salts, significant quantities of desulfurization products (benzene and biphenyl) are obtained. Potassium thiophenolate in the presence of IFSD and iron powder does not undergo desulfurization.

In an effort to understand further the carbon-sulfur bond breaking processes, the chemistry of thiophenol and diphenyl disulfide was examined. The pyrolysis of aromatic thiols has not been studied as extensively as that of aliphatic thiols. When aromatic thiols or disulfides are heated, the major products are diaryl sulfides (12). There are several papers that report desulfurization products arising from pyrolysis of thiophenol at very high temperatures (700°C) or pyrolysis over catalysts at moderately high temperatures (300°-580°C) (13-15). Flow pyrolysis of diphenyl disulfide of 400°C yields thiophenol and diphenyl sulfide (16).

Our studies show that at 375°C, in the absence of any catalytic species, thiophenol and diphenyldisulfide decompose to phenyl sulfide. When heated in the presence of an active catalyst (Monel shavings, nickel or copper powder), thiophenol or diphenyl disulfide gives phenyl sulfide as its major product, but desulfurization products (benzene and biphenyl) are also observed.

We have observed that naphthalene thiols undergo desulfurization more readily than thiophenol. This is in agreement with observations reported in the literature (15).

CONCLUSIONS

In the presence of fused salts, an increase in the reactivity of thiolate salts is observed perhaps because the fused salts function as solvents, and increase the probability of bimolecular reactions. Bimolecular reaction giving rise to organosulfur species more resistant to desulfurization compete with desulfurization, but in coal, because of the more rigid organic matrix, it is not likely to be a problem.

Caustic is not necessary for desulfurization of thiol derivatives, although it may enhance it. An increase in desulfurization in the presence of caustic may be due to suppression of competing bimolecular reactions or some chemical process that actually speeds the desulfurization reaction. We do not have sufficient evidence to support these or other possible explanations. The desulfurization of aromatic thiols and their derivatives requires a catalyst. One of the species that catalyze these reactions is nickel, but other metals or alloys may also catalyze the desulfurization. In some cases, molten caustic is required to "activate" the catalyst. Additional studies concerning the nature of this catalysis and other possible catalytic species are under way. The chemistries of different aromatic thiols are similar, but changes in the aromatic structure influence their reactivity.

ACKNOLWEDGMENTS

We gratefully acknowledge the technical assistance of Murphy Keller, Thomas Williams, Anthony Selmeczy, and James Knoer. We also acknowledge the Oak Ridge Associated Universities Research Associate Program in which Michael Nowak, Murphy Keller, and Anthony Selmeczy participated.

DISCLAIMER

Reference in this report to any specific commercial process, product or service is to facilitate understanding and does not necessarily imply its endorsement or favoring by the United States Department of Energy.

REFERENCES

1. Masciantonio, P.X. Fuel 1965, 44, 269.

2. Chiotti, P.; Marusczewski, R. Ind. Eng. Chem., Proc. Des. Dev. 1985, 24 (4), 1137.

3. Attar, A. "An Analytical Method for the Evaluation of Sulfur Functionalities in American Coals," DOE Final Report DOE/PC/30145-T1 (DE 84007770) 1984.

4. Spiro, C.L.; Wong, J.; Lytle, F.W.; Greegor, R.B.; Maylotte, D.H.; Lamson, S.H. Science 1984, 226, 48.

5. LaCount, R.B.; Anderson, R.R.; Friedman, S.; Blaustein, B.D. Am. Chem. Soc. Div. Fuel Chem. Preprint 1986, 31(1), 70.

6. Utz, B.R.; Friedman, S.; Soboczenski, S.K. In ACS Symposium Series No. 319, "Fossil Fuels Utilization: Environmental Concerns;" Markuszewski, R., and Blaustein, B.D., Eds.; American Chemical Society: Washington, DC, 1986; Chapter 5.

7. Utz, B.R.; Appell, H.R.; Blaustein, B.D. Fuel 1986, 65, 1085.

8. Utz, B.R.; Appell, H.R.; Blaustein, B.D. Fuel 1986, 63, 1671.

9. Challenger, F. "Aspects of the Organic Chemistry of Sulfur," Butterworths Scientific, London, 1959.

10. Peach, M.E. J. Inorg. Nucl. Chem. 1979, 41, 1392.

11. Peach, M.E. J. Inorg. Nucl. Chem. 1973, 35, 1046.

12. Shagun, L.G.; Papernaya, L.K.; Deryagina, E.N.; Voronkov, M.G. Izv. Akad. Nauk SSSR, Ser. Khim. 1979, (10), 2390.

13. Robertson, H.W.; Steedman, W. Fuel 1966, 45, 375.

14. Johnson, D.E. Fuel 1987, 66, 255.

15. Tits-Skvortsova, I.N.; Danilova, T.A.; Markov, M.A.; Stepanova, I.I.; Osipenko, Ts.D. Khim. Seraorgan. Soedin., Soderzhashch. v Nefteprod., Akad. Nauk SSSR, Bashkirsk. Filial 4 1961, 141. (CA 58:3366).

16. Alnajjar, M.S.; Franz, J.A. Am. Chem. Soc. Div. Fuel Chem. Preprint 1986, 31 (1), 287.

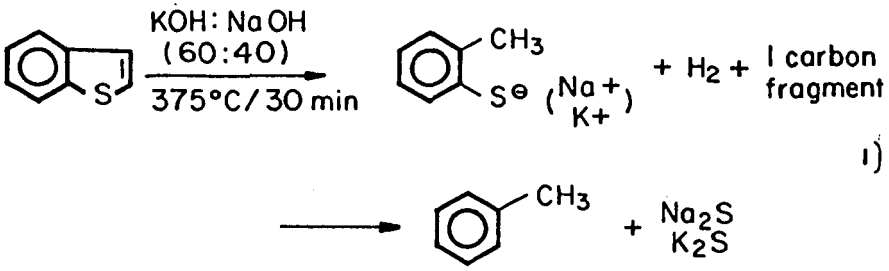
KOH: NaOH
(60:40)
375°C/30 min
CH3
S⊖ (Na+ K+)
+ H2 +
1 carbon fragment
CH3
+ Na2S K2S

1)

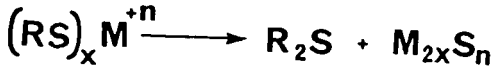
(RS)xM+n
R2S + M2xSn

2)

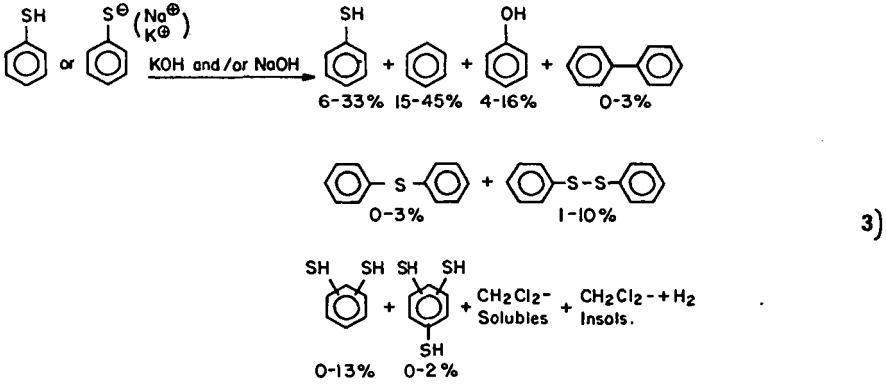
SH
or
S⊖ (Na⊕ K⊕)
KOH and/or NaOH
SH
OH
6-33%
15-45%
4-16%
0-3%
S
0-3%
S-S
1-10%
SH SH SH SH
SH
0-13%
0-2%
CH2Cl2- Solubles
CH2Cl2-+H2 Insols.

3)

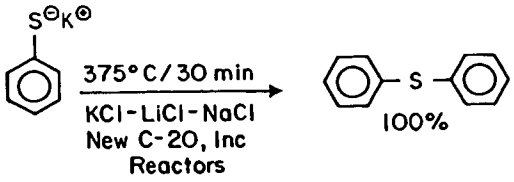
S⊖K⊕
375° C / 30 min
KCl-LiCl-NaCl
New C-20, Inc
Reactors
S
100%

4)

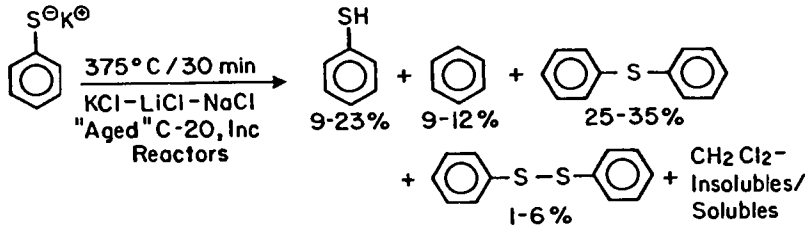
S⊖K⊕
375° C / 30 min
KCl-LiCl-NaCl
"Aged" C-20, Inc
Reactors
SH
9-23%
9-12%
S
25-35%
S
S
1-6%
CH2 Cl2-
Insolubles/
Solubles

5)

EXPERIMENTAL STUDY ON THE FORMATION OF SILICA PARTICLES IN A COUNTERFLOW DIFFUSION FLAME

Shyan-Lung Chung, Huoo-Deng Lin and Chen-Fei Kang

Department of Chemical Engineering
National Cheng Kung University
Tainan, Taiwan, R.O.C.

ABSTRACT

We describe a study on the formation of silica particles in a counterflow diffusion flame. This flame is generated in the impingement region of a fuel (H_2+N_2) and an oxidant (O_2+N_2) gas streams. SiH_4 was used as the precursor for the formation of SiO_2. It was fed into the fuel gas stream. Chemical reaction leading to the formation of SiO_2, nucleation of particles, and their initial growth all occur upstream of the flame. For a sufficiently high temperature flame, aggregates formed upstream fuse to form single, spherical particles as they pass through the flame zone. However, for a low temperature flame, aggregates remain (or partially fuse) as they pass through the flame zone. Samples of particles were collected at the exits of the burner. Particle size, shape, crystalline structure, and chemical composition were analyzed. These results will be presented.

INTRODUCTION

The formation of particles in combustion is a problem of considerable importance in many industrial processes. In coal combustion and gasification processes, formation of particles creates a serious problem of air pollution. On the other hand, formation of particles in combustion flames provides a useful technology for the manufacture of many oxide powders.

In the manufacture of powders using flame technology, the formation of particles involves the following processes: (1) The vapor of the desired material (e.g., SiO_2) is generated in the flame by oxidation of the precursor compounds (e.g., SiH_4) which is fed into the flame. (2) The vapor (in a supersaturated state) nucleates and forms initial particles. (3) The initial particles grow to form the desired powder. Since these processes all occur in the flame, the properties of the powder are greatly influenced by the structure of the flame. The structure of the flame is in term determined by the construction of the burner. The design of the burner is therefore a key element in the flame technology for the synthesis of powders.

In our laboratory, we use the counterflow diffusion flame burner designed by Shyan-Lung Chung and Joseph L. Katz [1,2] to study the formation of SiO_2 particles. A main purpose of the research is to investigate the influence of the burner design and the operating conditions (e.g., temperature, concentration, and gas flow paths) on the properties of the particles.

DESCRIPTION OF EXPERIMENT

A. Burner, Gases and Flame

As shown in Fig. 1, the burner consists of two vertically opposed tubes of rectangular cross section. The oxidant (O_2 diluted with N_2) flows downward from the upper tube, and the fuel (H_2 diluted with N_2)

flows upward from the lower tube. The two gas streams meet near the middle and then flow outward. Each tube contains three channels (separated by 0.08 mm thickness stainless steel plates): a central main channel (12.70 mm × 63.50 mm) and two side channels (12.70 mm × 6.35 mm). Fused silica plates, fitted to the outside of the two side channels, force the combustion gases to flow out along the long sides. Each of the burner tubes was designed to obtain a uniform flow of gas across its mouth by passage of the gases through a perforated plate, a bed of glass beads (1.0 mm diameter), and two stainless steel wire screens. To compensate for heat losses from the sides with fused silica windows, the oxidant and fuel streams in the side channels are enriched in O_2 and H_2, respectively, to precisely the extent required to obtain a temperature distribution which is uniform in the direction normal to the two fused silica windows (i.e., the X-direction; the X, Y, and Z directions are shown in Fig. 1). To prevent deposition of particles on the fused silica windows, no precursor compounds (i.e., SiH_4 in this research) is added to the mixtures which are fed to the side channels. Flanges fitted on each side of the burner openings minimize entrainment of surrounding air and keep the outward gas flow parallel to the burner surfaces. The distance between the two burner mouths is adjustable but has been kept at 15 mm in all the experiments presented here.

The major part of the construction of the burner as described above is the same as that designed by Chung and Katz [1,2]. However, in order to study the formation of particles, we have made some modifications. First, the main channel for the fuel gas stream was divided into three slots in the Y direction using 0.2 mm thickness stainless steel plates. Silane can be added to either the central slot or the side slots to study the effect of different flow paths on the properties of the generated particles. (Note that the dividing plates are removable. In some of the experiments, the undivided channel was used.) Second, nitrogen was added to the combustion gases at the burner exits through ten small holes on each flange. This is both to dilute the particles and to quench the effluent combustion gases so that growth of particles can be ceased at the burner exits where samples of particles are taken.

The N_2, H_2, and O_2 gases used all have the reported purities of 99%. A mixture of 10% semiconductor grade silane and 90% U.H.P. grade H_2 (99.999% purity) was used as the silane source. Each gas flows through a filter (sintered brass filter with 0.5 μm pore size) for the removal of preexisting particles. The gas flow rates were controlled and measured to about 1% accuracy using calibrated rotameters.

The burner produces a flame which is flat, stable, and rectangular in shape [1,2]. Both temperature and concentration distributions are uniform in the horizontal plane (i.e., X-Y plane) [2]. Formation of condensing species (e.g., SiO_2), nucleation of particles and their initial growth all occur upstream of the flame, where the gas flow is almost one-dimensional (i.e., Z direction). These characteristics of the flame offer great advantages for the study of the formation of particles.

B. Temperature Measurement

We used 0.05 mm diameter platinum and platinum -10% rhodium thermocouples to measure temperatures. The thermocouple wires were coated with silica to eliminate catalytic effect. The temperatures thus obtained were corrected for radiation loss.

C. Sampling and Analysis

Particles were collected at the burner exits using glass fiber

filters. The crystalline structure of the powder was examined using an X-ray diffractometer (XRD). The chemical composition was analyzed using an energy dispersive spectrometer (EDS). Particle size and shape were examined using an transmission electron micrograph (TEM). To prepare samples for TEM examinations, particles were dispersed ultrasonically in ethyl alcohol. A drop of this dispersion was placed on the TEM grid, and allowed it to dry.

RESULTS AND DISCUSSION

We describe the results of three experiments in the following. These three experiments were carried out using the same H_2-O_2 flame, i.e., the gas flow rates, and the concentrations of hydrogen and oxygen were all kept constant. The gas flow rates are listed in Table 1. In experiment one, the main channel for the fuel gas stream was not divided. In experiment two and three, this channel was equally divided into three slots. Since the dividing plates are very thin (0.1 mm), their effect on the flame is small.

Table 1.

	Fuel		Oxidizer		
	H_2	N_2	O_2	N_2	
Main channel	2260	1270	1600	1210	(cm^3/min)
Side channel	700	0	525	0	(cm^3/min)

In experiment one, the silane flow rate was 20 cm^3/min, which was equal to 0.56% of the total fuel gases. In experiment two, silane was added only to the two side slots. Its flow rate was 13.3 cm^3/min. In experiment three, silane was added only to the central slot at a flow rate of 6.7 cm^3/min. (Note that the silane concentrations in these two experiments were the same as that used in experiment one, i.e., 0.56% of the fuel gases.) The flow rate of the nitrogen used for quenching at the burner exits was 2200 cm^3/min, which decreased the temperature of the effluent gases by about 200°C.

Because the Pt and Pt-10% Rh thermocouples can not measure temperatures above 2000 K, our temperature measurement was limited to the regions outside the flame zone, where the temperatures were below 2000 K. As mentioned previously, the major construction of the burner is the same as that used by Chung and Katz [1]. The gas flow rates, and the concentrations of hydrogen and oxygen we used were also the same as those reported by Chung and Katz in one of their experiments[1,2]. We compared our thermocouple temperature measurements with theirs and found them to be in excellent agreement. We reproduced their temperature profile and showed it in figure 2.

A. Experiment One

Examination of the SiO_2 powder collected in this experiment using an XRD shows that it is amorphous in structure. Composition analysis by EDS indicates that the powder is composed of 99.6% SiO_2 and 0.4% SnO_2. In preparing samples for EDS analysis, the powder was fixed on the supporting aluminum blocks using glue containing silver . Since Ag and Sn have overlapped signals, the signal attributed to Sn may be from Ag. Further analysis is required to resolve this confusion.

Figure 3 shows three TEM micrographs of the powder. The powder can be divided into two types of particles. One is aggregates of very small particles, which are approximately 0.02 μm in diameter. The other is composed of larger, spherical particles whose diameters are approximately 0.1 μm. Some of these particles form aggregates (typically two to five together). However, some of them exist as

single particles. (It should be noted that single,spherical particles have not been found in the published studies on the formation of silica particles, using premixed flames [3,4].)

As illustrated in Fig. 4, we proposed a growth mechanism for the formation of the two types of silica particles in the counterflow diffusion flame. As the fuel gases flow out of the lower part of the burner, silane is oxidized to generate SiO_2 vapor. The SiO_2 vapor (in a supersaturated state) then nucleates and a large number of small particles are produced. These initially formed particles can grow by either vapor deposition or aggregation, or both. In the central part of the fuel gas stream, particles flow through the high-temperature flame zone. The previously formed aggregates fuse to form spherical particles as they pass through the flame zone. This process (as indicated by mechanism (a) in Fig. 4) may explain the formation of the larger, spherical particles found in this experiment. In the outer part of the fuel stream, particles do not pass through the high-temperature flame zone. The previously formed aggregates do not fuse to form spherical particles but remain as aggregates. Further formation of aggregates (or agglomerates) may occur due to interparticle collisions as the particles flow out of the burner. This process (as indicated by mechanism (b) in Fig. 4) may explain the formation of the aggregates of small particles found in this experiment.

B. Experiment Two

The TEM micrographs of the particles collected in this experiment show that all the particles are aggregates of small particles (approximately 0.02 μm in diameter) and that there is no larger, spherical particles. (see Fig. 5) Since silane was added to the side slots, particles may form by mechanism (b) as shown in Fig.4. (Therefore, all the particles are aggregates and no larger, spherical particles are formed.)

C. Experiment Three

The particles collected in this experiment also consist of two types of morphology as found in experiment one. However, there are more larger, spherical particles and less aggregates of small particles as compared with those obtained in experiment one. (See the TEM micrographs in Fig. 6) Since silane was added to the central slot, most particles may form by mechanism (a), thus leading to the formation of more larger, spherical particles. However, some particles in the outer part of the stream may form by mechanism (b), thus leading to the formation of aggregates.

CONCLUSION

Some conclusions may be drawn from the experiments described above: (1) high purity and submicron silica particles can be generated using the counterflow diffusion flame burner; (2) the original form of the burner produces two types of particles; (3) our modification of the burner offers the possibility for the control of the morphology of the particles; (4) the proposed mechanism seems to explain the formation of silica particles in the flame.

ACKNOWLEDGEMENT

Support of this research by the R.O.C. National Science Council is gratefully acknowledged.

REFERENCES

1. Shyan-Lung Chung and Joseph L. Katz, "The Counterflow Diffusion Flame Burner: A New Tool for the Study of the Nucleation of Refractory Compounds", Combustion and Flame, 61: 271 (1985).
2. Shyan-Lung Chung, "The Counterflow Diffusion Flame Burner: A New Tool for the Study of the Nucleation of Refractory Compounds", Ph.D. Dissertation, The Johns Hopkins University, Baltimore, Maryland, USA, 1985.
3. Ulrich, G.D., Riehl, J.W., "Aggregation and Growth of Submicron Oxide Particles in Flames," J. Colloid Interface Sci., 87, 257 (1982).
4. Ulrich, G.D., "Flame Synthesis of Fine Particles", Chemical and Engineering News, August 6, 1984, P. 22.

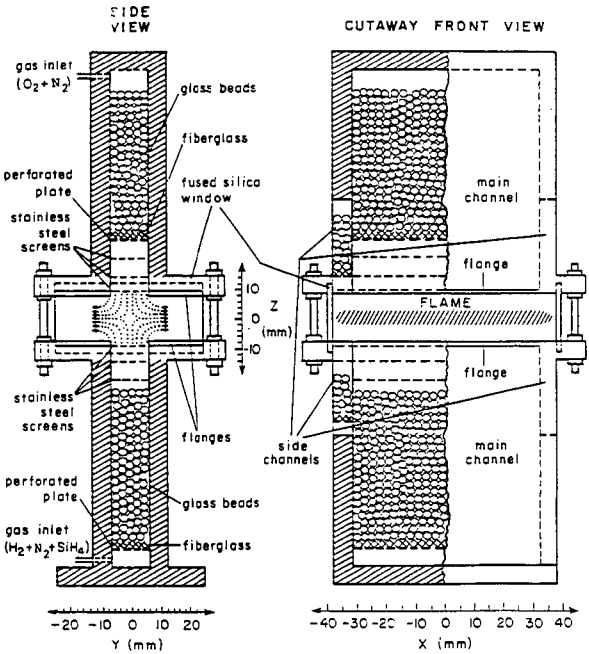

Fig. 1 The counter flow diffusion flame burner.

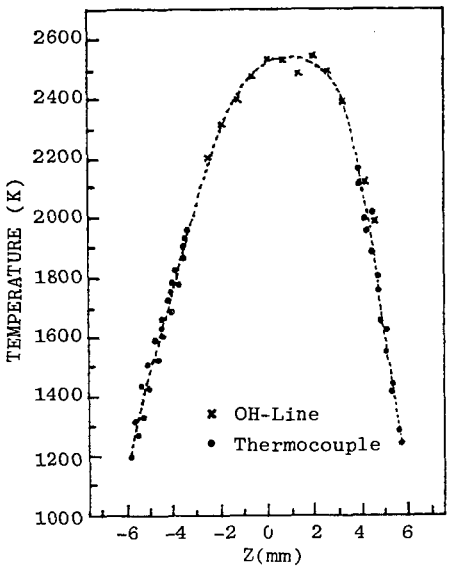

Fig. 2 Temperature distribution along the vertical direction in the counterflow diffusion flame.

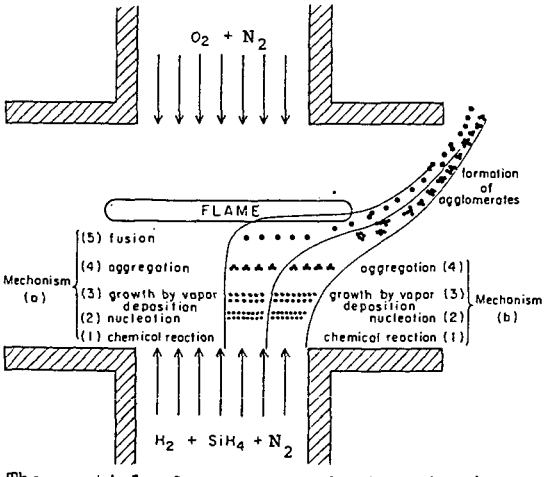

Fig. 4 The particle formation mechanisms in the counterflow diffusion flame.

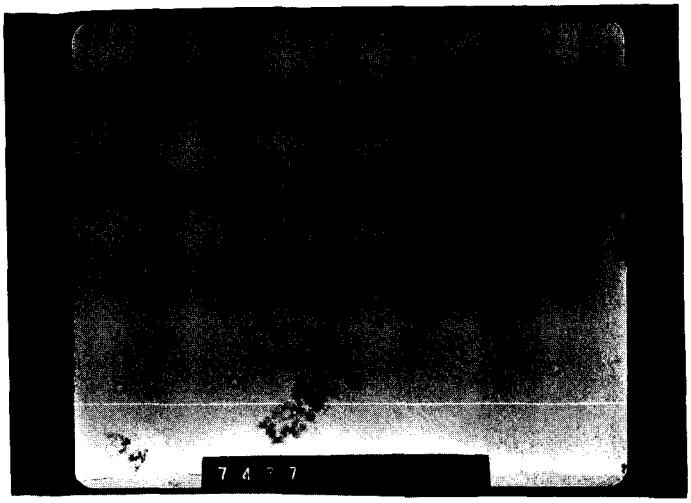

(a) 24,000×
(0.4 μm)

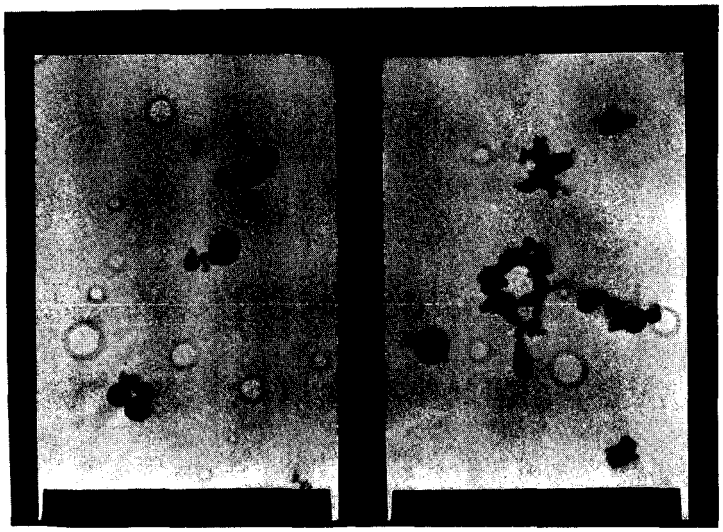

(b) 30,000×
(0.3 μm)

Fig. 3 TEM photographs of SiO_2 sample.

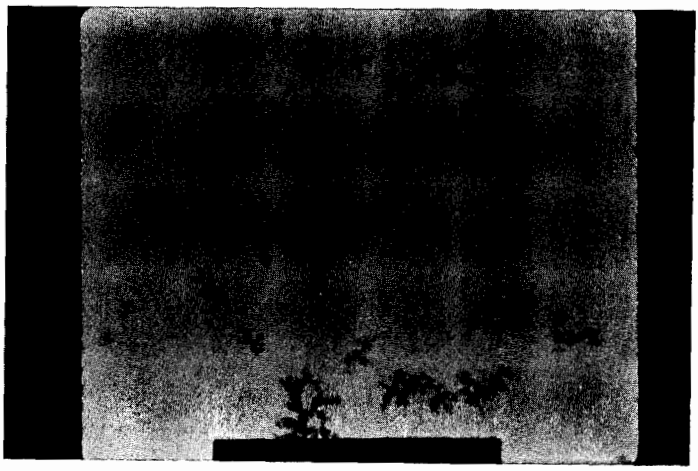

Fig. 5 TEM photograph of SiO_2 sample.
21,000× (0.4 μm)

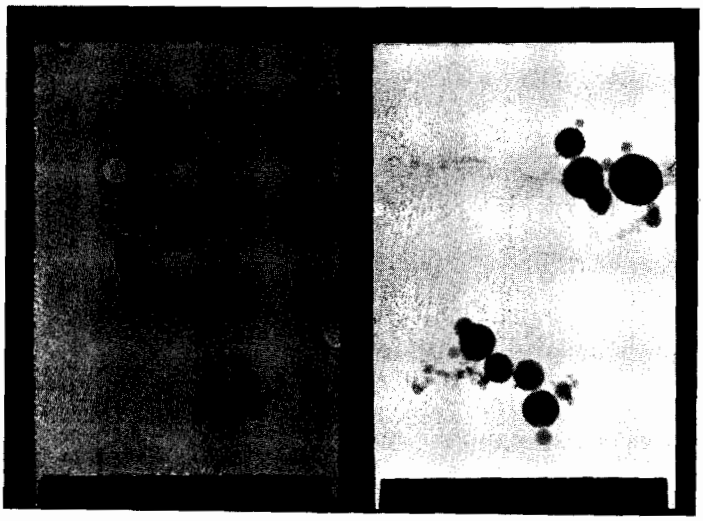

Fig. 6 TEM photographs of SiO_2 sample.
48,000× (0.2 μm)

EFFECT OF SEVERITY ON CATALYTIC HYDROPROCESSED SHALE OIL JET FUELS

N.L. MUKHERJEE

Chemical Engineering Department
Tuskegee University
Tuskegee, AL 36088

ABSTRACT

Catalytic hydroprocessed shale oil jet fuels in the USA were characterized and compared with petroleum jet fuel to demonstrate their possibility as a conventional jet fuel substitute. The shale oils (Geokinetics, Occidental, Paraho and Tosco II) were hydrotreated in a 0.0508m ID by K1.524m long reactor containing $Ni/Mo/Al_2O_3$ catalyst. The fractionated hydrogenated shale oils at jet fuel ranges (120-300^{0}C) were analyzed for composition and physical properties. The increasing hydroprocessing severity proportionally decreased nitrogen, sulfur, olefins, aromatics and increased hydrogen content. The nitrogen content was considerably higher even at high severity conditions. Sulfur and olefin contents were lower at all severities. The heat of combustion and the physical properties, except the freezing point, were comparable to petroleum jet fuels. The yields of jet fuels increased proportionally to increased severity. The study showed that high severity hydroprocessing gave better performance in processing shale oils to jet fuels.

INTRODUCTION

Shale oil jet fuels contain considerably higher nitrogen levels than petroleum jet fuels. These shale oil-derived jet fuels cannot be processed in a refinery similar to that used to obtain petroleum jet fuel because the high nitrogen content could poison the refinery catalyst. Nitrogen content greater than 5 ppm decreases fuel oil thermal stability and increases nitrogen oxide emissions during jet fuel combustion.

The present problem is to obtain a nitrogen level for jet fuel in the range of 1-5 ppm. High severity hydrodenitrification for the reduction of nitrogen content is not cost effective. The crude jet fuel cut can be chemically treated to lower the nitrogen level to an acceptable upper limit. Hydrogenation of shale oil fractions at low severity, prior to one of the chemical treatments [1] (acid washing, use of an hydrous acid, ion exchange resins, use of solvents, percolation over clays and acid absorbants, partial oxidation) has been shown to substantially lower the cost of producing jet fuel compared to severe catalytic hydrogenation. This hydrogenation operation also reduces the nitrogen level to an acceptable level (1-5 ppm). An increase of temperature [2] and pressure [3] proportionally increase the hydroprocessing severity, which facilitates the removal of nitrogen, sulfur and oxygen and the addition of hydrogen.

In the present work, shale oil hydroprocessing was performed at low, medium and high hydroprocesssing severities. The hydroprocessing severity was changed primarily by varying the temperature. Production

Table I Analysis of De-ashed/De-watered and Hydrogenated Shale Oil

	PARAHO				TOSCO II				GEOKINETICS				OCCIDENTAL			
Property	D-A/D-W	T_R=1.0	T_R=.92	T_R=.85	D-A/D-W	T_R=1.0	T_R=.92	T_R=.85	D-A/D-W	T_R=1.0	T_R=.92	T_R=.85	D-A/D-W	T_R=1.0	T_R=.92	T_R=.85
Hydrogen Content, Wt.%	11.74	14.00	13.46	12.92	11.23	13.80	13.20	12.34	12.28	13.72	13.31	12.85	12.31	13.60	13.20	12.81
Carbon Content, Wt.%	84.68	85.69	85.42	85.20	84.53	85.43	85.66	85.62	84.45	85.81	85.68	85.61	84.67	86.02	86.13	85.82
Nitrogen Content, Wt.%	2.08	0.19	0.90	1.60	2.15	0.60	0.90	1.61	1.71	0.33	0.74	1.20	1.53	0.25	0.40	1.05
Sulfur (Total), Wt.%	0.71	0.024	0.040	0.051	0.73	0.023	0.042	0.081	0.62	0.01	0.015	0.023	0.67	0.01	0.017	0.043
Density g/ml (60°C)	0.908	0.818	0.840	0.855	0.906	0.837	0.854	0.872	0.876	0.811	0.822	0.840	0.891	0.823	0.841	0.853
Pour Point, °C(°F)	21.2 (81)	23.3 (74)	23.9 (75)	23.3 (74)	20.6 (69)	19.4 (67)	19.4 (67)	21.1 (70)	12.8 (55)	25.0 (77)	23.3 (74)	16.1 (61)	12.2 (54)	23.3 (74)	4.4 (40)	6.1 (41)

of shale oil (Table I) hydroprocessing and distillation of the hydroprocessed product was carried out at NASA's Lewis Research Center bench-scale hydroprocessing facility. The process flow diagram (Figure 1) shows the jet fuel preparation from crude shale oil.

EXPERIMENTAL

De-ashed and de-watered shale oil containing 39% hydrocarbons (20% alkanes, 20% aromatics, 25% aromatic resins, 35% olefins and naphthenes) and 61% nonhydrocarbons (60% nitrogen, 10% sulfur and 30% oxygen compounds) was fractionated below 343°C. Shale oil fractions were hydrogenated in a reactor (length 1.524 m and diameter 0.0508m) containing American cynamide HDS-3A, Ni-Mo/Al_2O_3) catalyst of .025cm extrusions. The reactor contained four catalyst zones between non-reactive zones of Al_2O_3 extrusions of 0.3 cm diameter. Alumina zones equipped with wall heat-exchangers maintained nearly constant reaction temperature. The reactor's four catalyst zones were heated by four outside wall electric heaters and the hydrogen preheating (300°C) was accomplished by the electric heater at reactor top. The space velocity of the shale oil liquid in the reactor was 0.99-0.95 m^3/m^3 hr and the hydrogen comsumption was approximately 280 std. m^3/m^3 of shale oil. Shale oil fractions were hydrotreated at processing severities: (A) high=416°C and 1.413 x 10^4kpa (B) medium 382°C and 1.396 x 10^4kpa (C) low = 354°C and 1.327 x 10^4kpa. Figure 2 demonstrates hydrogen comsumption in shale oil at different processing severities. The hydroprocessed shale oil was fractionated (boiling range = 121-300°C) to produce jet fuel. Throughout the discussion, T_R is a temperature ratio indicating the severity of the run compared with high severity T_R=1.0-high severity, T_R=0.92-medium severity, T_R=0.85-low severity.

RESULTS AND DISCUSSIONS

Hydroprocessed shale oil jet fuels were distilled (ASTM D-86) at different boiling ranges (Figures 3, 4, and 5). The average boiling range of the high, medium and low severity hydroprocessed shale oil jet fuel cuts was 160-190°C for the 10 volume percent distillate and 260-270°C for the 90 volume percent distillate. Low and medium severity jet cuts have higher boiling ranges than high severity cuts because they contain more heavy hydrocarbons and heterocyclic compounds. The distillation temperatures and the volume percent recovery of the shale oil jet fuels are comparable to those of standard petroleum jet fuels (Table II). The results closely agree with the investigations of Shelton [4] who obtained a maximum boiling point of 195°C for 10 volume percent and 255°C for 90 volume percent recovery of a petroleum fuel.

Table II: Petroleum Jet Fuel Properties
(ASTM Methods)

Hydrogen content, wt%	16.00 max
Aromatics content, vol%	20 max
Nitrogen content (total), ppm	5 max
Sulfur content (mercaptan), wt%	0.003 max
Sulfur content (total), wt%	0.3 max
Naphthalenes contnt, vol%	3 max
Distillation temperature, °C	-
Initial boiling point	-
10 (vol%)	204 max

Table VII Analysis of Hydroprocessed Shale oil Jet Fuels.

PROPERTY	PARAHO			TOSCO II			GEOKINETICS			OCCIDENTAL		
	T_R=1.0	T_R=0.92	T_R=0.85	T_R=1.0	T_R=0.92	T_R=0.85	T_R=1.0	T_R=0.92	T_R=0.85	T_R=1.0	T_R=0.92	T_R=0.85
Hydrogen Content,wt%	13.85	13.53	13.33	13.78	13.50	13.14	13.68	13.64	13.29	13.78	13.64	13.45
Carbon Content,wt%	85.98	85.92	85.33	85.78	85.69	85.46	86.15	85.86	85.52	86.13	85.88	85.79
Nitrogen Content,wt%	0.122	0.418	1.16	0.366	0.655	1.16	0.140	0.428	1.06	0.038	0.355	0.725
Sulfur Content,wt%	<0.003	0.03	0.032	<0.003	0.022	0.039	<0.003	0.023	0.031	<0.003	0.021	0.025
Sulfur (Mercaptan),wt%	<0.0003	<0.0003	<0.0003	<0.0003	<0.0003	<0.0003	<0.0003	<0.0003	<0.0003	<0.0003	<0.0003	<0.0003
Aromatics Content,vol.%	19.0	19.7	19.9	22.4	22.5	23.1	19.4	22.0	22.8	20.1	22.7	23.7
Olefin Content, vol.%	0.6	3.2	4.5	1.1	1.5	3.3	1.1	1.7	2.8	1.0	2.1	2.6
Naphthalenes Content,vol.%	1.12	2.10	3.51	1.76	2.19	3.46	0.96	1.45	3.73	0.47	1.39	2.70
Flashpoint, °C (°F)	50.0 (122)	59.4 (139)	59.4 (139)	47.8 (118)	44.4 (112)	43.3 (110)	54.4 (130)	57.2 (135)	61.7 (143)	44.4 (112)	58.9 (138)	62.2 (144)
Specific Gravity, (15°C/15°C)	0.818	0.830	0.838	0.819	0.829	0.835	0.817	0.831	0.843	0.814	0.835	0.841
Freezing Point °C (°F)	-27.8 (-18)	-27.2 (-17)	-27.8 (-18)	-33.3 (-28)	-32.2 (-26)	-30.6 (-23)	-30.8 (-23.5)	-28.9 (-20)	-26.7 (-16)	-40.0 (-40)	-28.9 (-20)	-27.8 (-18)
Viscosity, $m^2/s(20^0C)$	$4.2x10^{-6}$	$4.7x10^{-6}$	$5.3x10^{-6}$	$3.5x10^{-6}$	$4.0x10^{-6}$	$5.1x10^{-6}$	$4.0x10^{-6}$	$4.5x10^{-6}$	$5.5x10^{-6}$	$2.3x10^{-6}$	$5.4x10^{-6}$	$5.7x10^{-6}$
Heat of Combustion kj/kg (Btu/lb)	42,282 (18,418)	42,998 (18,485)	42,374 (18,217)	42,549 (18,292)	42,530 (18,284)	42,246 (18,162)	43,072 (18,517)	42,356 (18,209)	42,428 (18240)	42,677 (18,347)	42,844 (18,419)	42,584 (18,307)

50 (vol%)	-
90 (vol%)	-
Final boiling point	300 max
Flashpoint, ^{0}C	38 max
Gravity (specific, 15/15^{0}C)	0.7753 to 0.8398
Freezing point, ^{0}C	-40
Viscosity at -20^{0}C, m^2/s	8×10^{-6} max
Net heat of combustion, kJ/kg (Btu/lb)	42,800 (18,400) min

Nitrogen content (Figure 6) in all severities is high in Tosco II and low in Occidental jet fuel. The amounts of Weak Base I and non-basic nitrogen compounds are variable in different types of shale oil jet fuels. High severity hydrotreatment significantly decreases [5] the nitrogen content of Weak Base I and non-basic nitrogen compounds, and Weak Base I can be removed more easily than non-basic nitrogen during hydroprocessing. High severity Occidental shale oil contains the lowest amount (0.03 wt%) of nitrogen of all shale oil jet fuels. This amount is significantly higher than that of petroleum jet fuel (1-5 ppm). The nitrogen content in low severity jet fuel is always higher than that of high severity jet fuel.

Table III shows the properties of shale oil jet fuels and also demonstrates that sulfur removal is proportional to severity. High severity jet fuels have the lowest sulfur content (0.003 wt%). Even the sulfur content in low severity jet fuels is lower than that of petroleum jet fuel (0.30 wt% maximum).

Increase of hydrogen content (Table III) in shale oil jet fuels is proportional to the severity of hydrotreatment. Severity increases saturation and cracking of hydrocarbons, thereby increasing the hydrogen/carbon ratio. Gunberger reported [6] the increase of hydrogen content from 11.40 wt% to 13.0 wt%. The hydrogen content (13-14 wt%) in shale oil jet fuel is relatively lower than that of standard petroleum jet fuel, which is 16 wt%. Aromatic content in shale jet fuels decreases with severity because of hydrocracking process. The effect of severity on aromatic content is the highest for Paraho, while Occidental shows the lowest. The aromatic content in shale oil jet fuels (except Paraho) is generally higher than in that of petroleum jet fuel, which is at maximum 20% by volume.

The freezing point of shale jet fuels is significantly higher than that of petroleum jet fuel (-40^{0}F) because shale jet fuels contain higher saturation fractions, particulary higher n-alkanes [7]. Freezing point decreases with increasing severity. Other physical properties such as flash point, viscosity, and specific gravity of the shale jet fuels decrease (Table III) with severity, and the values in all severities are within the acceptable limit of petroleum jet fuel specifications. Severity has little effect on heating values of shale jet fuels and the values are comparable to those of petroleum jet fuels.

CONCLUSION

1. High severity shale oil jet fuels constitute the hydrocarbons of more different boiling points than low and medium severity jet fuels. Aromatic and heavy hydrocarbon contents in low and medium severity are higher than in high severity jet fuels.

2. Increasing severity enhances nitrogen and sulfur removal. Nitrogen content is above, while sulfur content is much below, the acceptable limit of that of petroleum jet fuel.

3. Increasing severity increases hydrogen while it decreases aromatic content. Hydrogen content is a little lower while aromatic content is slightly higher than that of petroleum jet fuel.

4. Flash point, viscosity, and specific gravity decrease with increasing severity, and the levels in all severities are within acceptable limits. The freezing point is enhanced with increasing severity and is above the acceptable limit.

5. Increasing severity enhances yields of jet fuels. It can be concluded that high severity hydroprocessed Paraho jet fuel after processing can be considered as an alternative to conventional jet fuel.

REFERENCES

(1) Nowacki, P., Oil Shale Technical Data Handbook., Shale Oil Upgrading, Noyes Data Corporation, Park Ridge, New Jersey, 193 (1981).

(2) Cottingham, P.L., E.R. White and C.M. Frost, Hydrogenating Shale Oil to Catalytic Reforming Stock, Ind. Eng. Chem., Vol. 49, No. 4, 679-684 (1957).

(3) Frost, C.M. and P.L. Cottingham, Some Effects of Pressure on the Hydrocracking of Crude Shale Oil over Cobalt-Molybdate Catalyst, BM-PPRI-7835, Bureau of Mines (1974).

(4) Shelton, E.M., Aviation Turbine Fuels, U.S. Department of Energy, BETC/PPS-79/2 (1979).

(5) Holmes, S.A. and L.F. Thompson, Nitrogen-Type Distribution in Hydrotreated Shale Oils: Co-relation with Upgrading Process Conditions, 14th Oil Shale Symposium Proceedings, Colorado School of Mines Press, 242-243 (1981).

(6) Gunbeger, G.A. Logistics Management of Paraho Residual Shale Oil, Radian Corporation, Pasadena, CA, B-20 (1980).

(7) Newman, S.A., Shale Oil Upgrading and Refining Jet Fuel Freezing and Composition, Butterworth Publishers, Boston, 243 (1983).

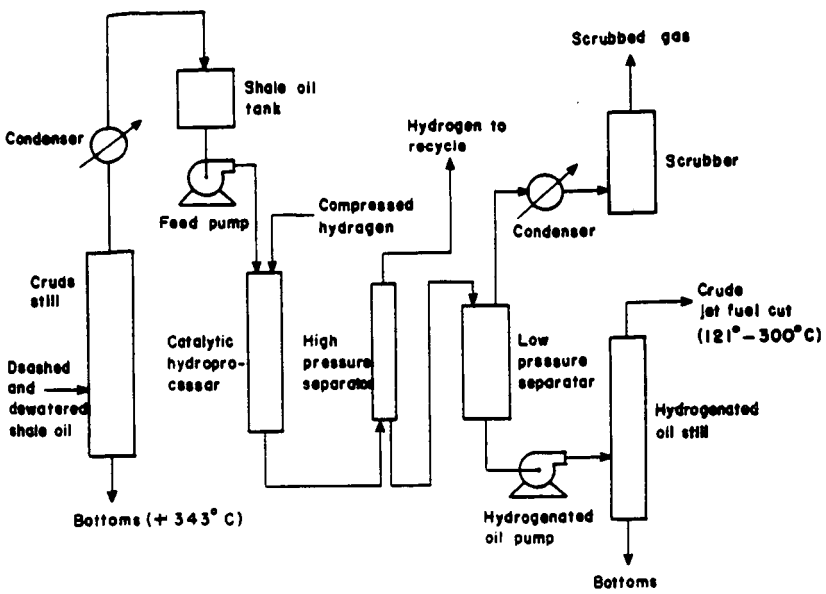

Figure 1. Process Flow Diagram to produce Shale Oil Jet Fuel

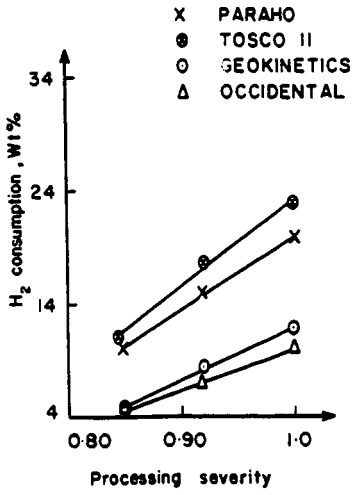

Figure 2. Hydrogen Consumption in Shale Oil Hydroprocessing

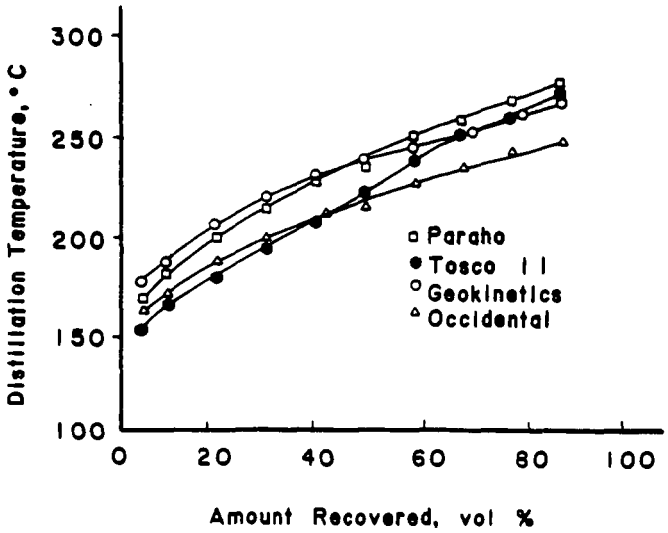

Figure 3. High severity Shale Oil Jet Fuel Distillation

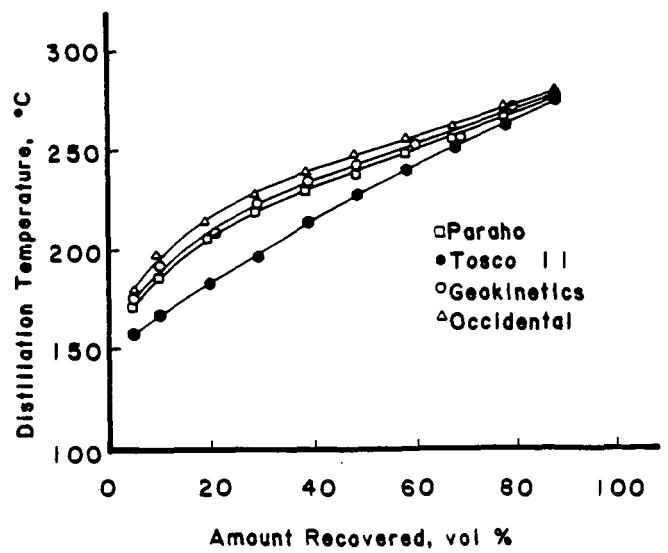

Figure 4. Medium severity Shale Oil Jet Fuel Distillation

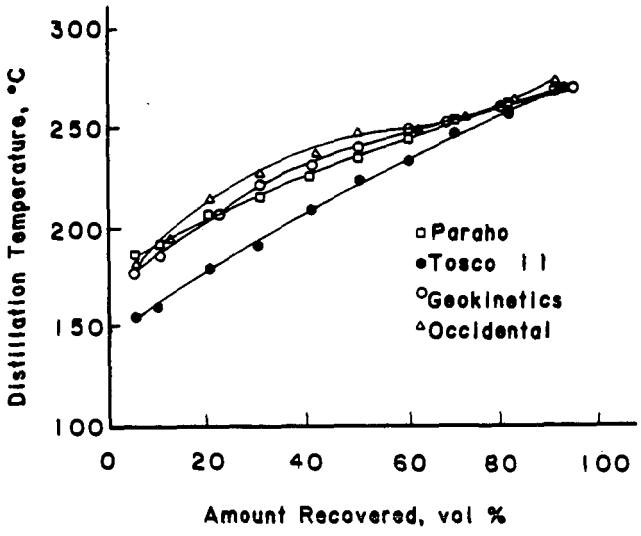

Figure 5. Low severity Shale Oil Jet Fuel Distillation

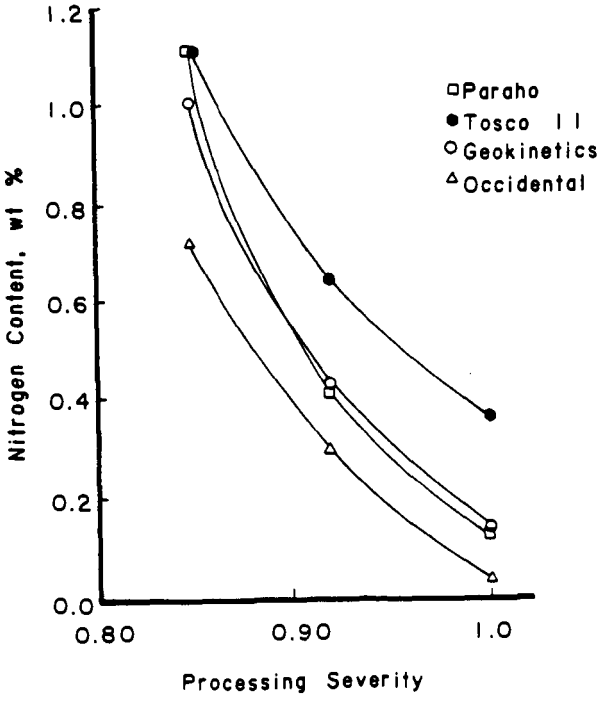

Figure 6. Nitrogen content in Shale Oil Jet Fuel

EFFECTS OF PARTICLE SIZE AND AIR FLOW RATES ON THE RUNAWAY TEMPERATURE OF BITUMINOUS COAL AT 290K < T < 700K

V. M. Malhotra* and J. C. Crelling**

* Department of Physics
** Department of Geology
Southern Illinois University, Carbondale
Illinois 62901-4401

INTRODUCTION

Spontaneous ignition and combustion of coal are major problems not only for actual mining of coal but also for its transportation and for industrial users. Most coals are prone to spontaneous combustion, but their susceptibility to ignition increases as the coal rank decreases (1). However, there are many anomalies to this straight rank order susceptibility. Chamberlain and Hall (1) have in fact, pointed out that some higher rank coals may be more susceptible to spontaneous ignition than lower rank coals.

The causes and mechanisms of spontaneous ignition are enigmatic because exceptions exist for every previously-suggested, single cause. Several models have been advanced to describe spontaneous heating (1-4), however. Among these are coal rank , electrostatic effects, geological factors, temperature, microbial ignition, the reduction in reactivity due to deterioration, air flow rates, particle size, pyrite content, porosity and water wetting of coal.

The purpose of this research was to examine the factors which may contribute to spontaneous ignition of ultrafine (particle size < 250 μm) bituminous coals and maceral enriched fractions under storage, air flow and/or dense phase pneumatic conditions and to understand physical interactions and chemical reactions pathways which may lead to spontaneous ignition of bituminois coals. We have initiated spontaneous ignition, FTIR, DSC, TGA and EPR measurements to accumulate data which can be used to propose mathematical models for spontaneous ignition of stored and pneumatically conveyed coals. In this report, we present our preliminary results on a high-volatile bituminous coal subjected to ignition temperature and FTIR measurements.

EXPERIMENTAL

To examine the effects of air flow temperature, particle size and air flow rates on the surface properties of coal, a high-volatile bituminous coal from Elkhorn #3 seam (Kentucky) was chosen. The coal samples were crushed and sieved and were divided into following particle size ranges : <44 μm , >63μm <75μm, >75μm <106μm, >106μm <150μm, >150μm <250μm, >250μm <300μm, >850μm <900μm.

The experimental arrangement used for determining the effects of air flow temperature and air flow rates on the coal's surface temperature is shown diagrammatically in Figure 1. The coal samples were packed in a quartz tube (10x120mm), and the sample tube

was inserted in the combustion tube assembly. The reaction zone was supplied with two thermocouples (T_1 and T_2) whose hot junctions were positioned along the axis of the sample bed. Thermocouple T_2 monitored the temperature of the fluid at the entrance of the sample tube; while thermocouples T_1 and T_3 monitored the temperature of the sample and exit gases, respectively. The sample tube's location in the tube (750mm length) was determined by the residence time required by the flowing gas to attain the required stable temperature at the entrance of the sample tube. The gas temperature was monitored for 1 hour before the sample tube was inserted in the combustion tube assembly. The compaction and packing of the sample in the tube plays an important role in determining whether exothermic reactions resulted or not. Therefore, every effort was made to ensure uniform compaction of the sample for each run.

Two grams of coal sample of various particle sizes were inserted in the sample tube and subjected to ignition experiments. Ignition was arbitrarily defined as the lowest air temperature which caused any part of the sample to exceed 150 K above the set temperature of the furnace. This value was chosen as an indication of a runaway reaction. Experience has shown that a rapid temperature rise, if one were to occur at all, would take place within a few minutes of the introduction of air, generally less than 20 minutes. If ignition did not occur, a fresh batch of the coal sample was used and the air temperature raised 10K higher than before air was introduced and the sequence was repeated. All FTIR spectra were obtained on an IBM IR-32 FTIR spectrometer equipped with an IBM 9000 comupter. The alkali halide pellet technique was employed to record the spectra.

RESULTS AND DISCUSSION

Ignition Experiments:

Ignition experiments on high-volatile bituminous coals showed that the ignition temperature is strongly dependent on the mode of preheating the sample to the ignition temperature point, particle size, air flow rates, and sample compaction. When using air alone for preheating, it was found to be impossible to attain a uniform sample temperature just before ignition. Accordingly, a technique was evolved to first raise the temperature of the sample close to the ignition temperature by passing a stream of hot nitrogen or carbon dioxide through the sample. Once the constant temperature of the sample was obtained, the stream of gas was switched to air. A similar inert preheating procedure has been used by Hardman et.al. (5) to determine the spontaneous ignition temperature of activated carbons.

The ignition temperatures of three, high-volatile bituminous coals from Elkhorn #3, Ohio #5 and Pittsburgh seam are reported in Table 1. These three coals were chosen because of their large differences in their petrographic composition, especially in their vitrinite and exinite content. It has been suggested (1,2) that there is a close relationship between the coal maceral type and spontaneous oxidation potential. Chamberlain and Hall (1) demonstrated this kind of role when they found that exinites oxidized much more readily than vitrinites and inertinites. If such is the case then one will expect Ohio #5 coal to show the lowest ignition temperature. In fact, Ohio

#5 shows the highest ignition temperature among the three coals examined. Our preliminary results suggest that there may not be any correlation between the petrographic composition and ignition temperature. The sample bank, on which ignition experiments are conducted, needs to be expanded before arriving at definite conclusions.

TABLE 1

Ignition Temperatures of Three High-Volatile Bituminous Coals and Their Selected Petrographic Parameters.

	Elkhorn #3 Seam	Ohio #5 Seam	Pittsburgh Seam
Air Flow Rate (cm^3/min)	900	900	900
Particle Size (μm)	<45	<45	<45
Ignition Temperature (K)	593±10	683±10	673±10
Reflectance (%)	0.93	0.74	0.79
Exinite (vol%)	9.10	26.20	3.90
Vitrinite (vol%)	75.20	55.30	84.20
Volatile Matter (wt%)	33.86	34.70	35.80
Fixed Carbon (wt%)	57.12	43.70	53.20
Moisture (wt%)	2.45	4.20	1.40
Ash (wt%)	6.57	17.40	9.60

Effects of Air Flow Temperature :

Surface reactions of coal under dense-phase pneumatic transport or under storage conditions play a crucial role in determining the initial heatup of coal. Consequently, it is of interest to determine the exothermic reaction pathways and the effects of the physical parameters on such reactions. The Elkhorn #3 seam coal was chosen to evaluate these effects since it showed the lowest ignition temperature. When coal samples of various particle size were inserted in the ignition tube assembly at temperatures lower than the ignition temperature, a typical 'particle temperature vs. time' plot is observed and is shown in Figure 2. Based on these profiles two parameters are defined:

$$\Delta T \equiv \text{Runaway Temperature} \equiv T_s' - T_g(t) \qquad 1)$$

$$\Delta t \equiv \text{Heatwidth} \equiv \text{Time period for which } T_s(t) > T_g(t), \qquad 2)$$

where T_s' is the maximum coal surface temperature, $T_s(t)$ is the coal surface temperature at time t, and $T_g(t)$ is the temperature of the flowing air at time t. Even though ΔT is arbitrarily defined, it represents the rise in coal surface temperature due to exothermic reactions under air flow conditions. In addition, ΔT and Δt measures the overall energy balance since they are related to the generation and dissipation of heat.

Figures 3 and 4 show the effect of air flow temperature ($290\ K < T_g < 700\ K$) on runaway temperature (ΔT) and heatwidth (Δt) values for Elkhorn #3 coal, respectively for three particle sizes. ΔT and Δt values were determined by using nitrogen preheat treatment before introducing air stream. The results indicate that there is a sudden jump in ΔT value at $T_g \geq 493$ K for particle size < 106 μm. As the particle size increases, the T_g value required to induce a sudden jump in ΔT value also increases. In fact, for particle size > 850 μm

no jump in ΔT value is observed at 290 K < T_g < 700 K with or without inert gas preheat treatment. This result suggests that there is a critical particle size below which Elkhorn #3 coal will be very susceptible to spontaneous ignition. This result is at variance with the recent numerical model proposed by Brooks and Glasser (3). From their numerical solution of the steady state equations, they suggested that the coal in the particle size range of (sub 1 mm) > (particle size) < (6 mm) is most susceptible to spontaneous combustion. Their prediction of the particle size effect on the spontaneous ignition is not consistent with our experimental results.

The effects of air flow rates and coal particle size on runaway temperature and heatwidth of Elkhorn #3 seam were also examined. To determine these effects, the air flow temperature T_g = 493 K was chosen since a sudden jump in ΔT value was observed at this temperature. The samples were inserted into the ignition tube assembly under air stream. The results are shown in Figures 5 and 6 for particle size and air flow rates, respectively. The experimental data suggests a power relationship between the runaway temperature (ΔT) and the particle size of coal. The coal surface temperature (T_s) under air flow rate of 900 cm^3/min suggests a relation:

$$T_s = T_g + 4726\ (\text{Particle Size, } \mu m)^{-0.84} \qquad 3)$$

Schmidt and Elder (6) have suggested a correlation between the rate of oxidation and particle size.

$$\text{Rate of oxidation} = K^3\ (\text{Specific Surface Area})^{0.5}\ , \qquad 4)$$

where K is a constant dependent on both rank and temperature. It can be seen that our results cannot be explained by equation 4 even if it is assumed that particle shape is random. Our results suggest that Elkhorn #3 coal will be most susceptible to spontaneous ignition for particle size < 150 μm. The runaway temperature shows a parabolic dependence on the air flow rates. The data shown in Figure 6 for > 63 μm < 75 μm particle size was fitted to a 3rd order polynomial:

$$T_s = T_g - 3.80 + 0.12\ (\text{Air Flow Rate}) + 8.3 \times 10^{-5}\ (\text{Air Flow Rate})^2 \qquad 5)$$

These results indicate that the susceptibility of spontaneous ignition will increase as the coal particle size decreases. In addition, there may be a critical air flow rate range for which heat generated may exceed heat dissipated.

FTIR Measurements :

FTIR measurements were carried out on the Elkhorn #3 seam bituminous coal to determine the effect of air flow temperature (T_g) on the structure of coal. The samples used for the FTIR measurements were the same samples which were subjected to air flow temperature measurements (i.e., Figure 3, < 43 μm). The samples were withdrawn from the ignition tube assembly after reacting with flowing air (900 cm^3/min) at 290 K < T < 700 K for 10 hours. Figure 7 shows the effect of air flow temperature (T_g) on the FTIR spectrum of Elkhorn #3 coal. The details of the FTIR analysis of bituminous coal and the effects of low temperature (<423K) oxidation on its vibrational spectrum have been reported earlier in the literature (7-9). The assignment of the

observed vibrational bands was based on these published works. The FTIR spectrum of unprocessed Elkhorn #3 coal can be characterized by : (a) A very broad band with maximum near ~ 3350 cm^{-1} was observed and is attributed to hydroxyl (-OH) groups. However, it was not possible to discern whether this band was due to moisture in KBr pellets, moisture in coal or hydroxyl groups which are part of organic matrix. We believe that this band is due, in fact, to a combination of the three sources mentioned above. (b) A weak absorption band at 3030 cm^{-1} was assigned to aromatic CH stretch. (c) A shoulder at 2960 cm^{-1} and two main absorption peaks at 2920 and 2850 cm^{-1} were observed and are attributed to CH_3 groups and aliphatic CH_3, CH_2, and CH groups, respectively. (d) A weak shoulder at 1700 cm^{-1} was observed and is assigned to C=O stretch. (e) The aromatic C=C bonds produced a strong absorption at 1600 cm^{-1}, and it is believed that some oxygen containing functional groups also contribute to its intensity. (f) The medium intensity band at 1445 cm^{-1} is due mainly to CH_2 groups in coal. However, CH_3 bending mode and aromatic stretching vibrations may also contribute to the intensity of this band. The weak observed band at 1375 cm^{-1} has been assigned to CH_3 groups. (g) A weak absorption at 1261 cm^{-1} has been assigned to ethers of the types C_6H_5-O-CH_3 or -CH_2O-CH_3- . In addition to 1261 cm^{-1} band, a broad weak band centered around ~ 1160 cm^{-1} was also observed and is assigned to aldehydes and/or ketones and/or ether groups in the Elkhorn coal. (h) Three absorption bands were observed in the aromatic region i.e., at 870, 812 and 754 cm^{-1}. The band at 870 cm^{-1} has been assigned to substituted benzene rings and to aromatic HCC rocking. The band at 812 cm^{-1} has been attributed to substituted benzene rings with two neighboring H, while the band at 754 cm^{-1} is assigned to monosubstituted benzene rings and O-substituted benzene rings. Additional bands due to inorganic materials were also observed but will not be discussed in this paper.

The effects of air flow temperature (T_g) on the FTIR spectra of Elkhorn #3 coal in the frequency range 4000 - 1100 cm^{-1} have been summarized in Table 2. The absorbance changes reported in this table were determined by subtracting the unprocessed coal spectrum from the processed (290K < T_g < 700K) coal spectrum. It was not possible to follow the changes in the organic bands of the processed coal at frequency < 1100 cm^{-1} due to strong overlapping inorganic bands. Attempts were made to remove the contribution of the inorganic bands by subtracting the spectrum of low temperature ash. However, this subtraction resulted in erroneous bands in the difference spectrum due to changes in the intensity and broadening of the inorganic bands at $T_g \geq$ 473K. The effect of air flow temperature on the intensity of aromatic CH stretch at 3034 cm^{-1} and aliphatic CH stretch at 2917 cm^{-1} is shown in Figures 8 and 9, respectively. Figure 10 shows the absorbance changes in the accumulative oxygen functionalities of coal as a function of air flow temperature. The y-axis of this graph represents the sum of absorbance changes at 1835, 1780 - 1700, and 1560 cm^{-1}. At $T_g \geq$ 640K, only inorganic bands were observed signifying that all the organic matter in coal has combusted. Thus the absorbance change points at $T_g \geq$ 640K in the graphs 8,9 and 10 represent a net loss of these functional groups i.e., all the organic matter is lost.

TABLE 2

The Effects of Air Flow Temperature on the Frequency of Principal Absorption Changes of Elkhorn #3 Bituminous Coal at 290K < T_g < 700K.

Air Flow Temp.(K)	Frequency (±4 cm^{-1})
343	2913(+),2845(+),1700(+),1445(+)
393	2917(-),2851(-),1835(+),1770(+),1700(+),1445(-),1375(-), 1021(-)
443	3034(-),2917(-),2851(-),1770(+),1700(+),1560(+),1445(-), 1375(-),1109(+)
493	3034(-),2917(-),2851(-),1835(+),1770(+),1725(+),1560(+), 1445(-),1219(+),1136(+)
543	3034(-),2917(-),2851(-),1835(+),1770(+),1721(+),1555(+), 1445(-),1267(+),1211(+),1100(+)
593	3034(-),2917(-),2851(-),1835(+),1770(+),1725(+),1560(+), 1451(-), *
643	3039(-),2920(-),2855(-),1698(-),1651(-),1593(-),1441(-), *, **
693	3048(-),2918(-),2857(-),1692(-),1598(-),1445(-), *, **

\+ Sign indicates that absorption increased or new bands appeared.
\- Sign indicates that absorption decreased or bands disappeared.
* At frequency < 1200 cm^{-1}, it was difficult to follow the organic bands due to overlapping inorganic bands.
** Only inorganic bands were observed.

The increase in intensity of aliphatic vibrations (i.e., at 2917, 2851, and 1445 cm^{-1}) at $T_g \leq$ 343K was most surprising. At these low temperatures a loss of some volatile matter is expected, and this loss should result in a decrease in the intensities of aliphatic vibrations. No intensity enhancement of these vibrations results if nitrogen or carbon dioxide is used under identical gas flow and temperature conditions. The intensity of the vibrational bands not only depends on the concentration of the functional groups in the sample but also on their dipole moment i.e., on the transition probability. We do not believe that the concentration of aliphatic groups has increased at $T_g \leq$ 343K, but we conjecture that an oxygen attack on coal somehow alters the dipole moment of the aliphatic groups at this temperature. At $T_g >$ 343K there is a steady decrease in the intensity of aliphatic bands at 2917, 2851 and 1445 cm^{-1}, with a major decrease located at 393K $\leq T_g \leq$ 493K. As can be seen from Figure 9, there is no correlation between the absorbance change and the runaway temperature of this coal. Similar results were observed for aliphatic bands at 2851 and 1445 cm^{-1}. These results suggest that the loss of aliphatic groups from the coal matrix, in the form of volatile products, plays a little role in the magnitude of the runaway temperature. Under air flow conditions, the volatile products are expected to be swept away from the sample toward the exhaust of the combustion tube, thus drastically decreasing the residence time of volatile products around the sample. If the volatile combusts on the coal's surface as it leaves the coal, the combustion exothermic reactions should contribute to the runaway temperature. It is possible that these exothermic reactions contribute to the early profile of heatwidth, but it seems unlikely since no correlation exists between

absorbance changes at 2917, 2851, and 1445 cm^{-1} and heatwidth. Figure 8 shows that the aromatic CH stretch vibration at 3030 cm^{-1} remains unchanged at 290K < T_g < 400K. However, it is interesting to note that as the runaway temperature increases the intensity of CH stretch vibration decreases. This decrease is mirrored along with alterations in the aromatic region's vibrations i.e., at 900 - 700 cm^{-1}. At present it is not possible to calculate the absorbance changes in this region due to interference from inorganic bands. The dependence of aromatic stretch vibration on the runaway temperature strongly suggests that it is the oxidation of the aromatic groups that results in major contribution to the runaway temperature. As T_g increases from 293K, the C=O stretch vibration at 1700 cm^{-1} increases and shows maximum contribution at 443K. Mirrored with the increase in C=O stretch at 1700 cm^{-1} a very broad, weak band is observed in OH stretch, suggesting the formation of carboxylic acid groups largely of aliphatic type. It seems that the oxidation of aliphatic groups attached to the aromatic structure contributes very little to the runaway temperature. At 493K $\leq T_g \leq$ 593K, strong absorbance bands at 1835, 1770, 1725, 1560, 1300 - 1100 cm^{-1} appear in the spectrum, indicating massive oxidation reactions in coal which leads to the formation of anhydrides, aldehydes, lactones, esters, ketones and ethers. Figure 10 shows the effect of air flow temperature on the accumulative absorbance changes in the oxygen functional groups at 1835, 1770, 1725, 1700, and 1560 cm^{-1} of Elkhorn #3 coal. These results clearly show that these oxidation reactions make major contribution to the heat generated i.e., to runaway temperature. It was surprising that at T_g = 493K, with the coal's surface temperature reaching 790K, complete combustion of the sample did not result. It appears that the oxygen functional groups generated on the surface of coal inhibit complete combustion reaction at $T_g \leq$ 593K. Diffuse reflectance - and photoacoustic - FTIR studies are in progress on these samples to evaluate the effects of incomplete combustion reactions and runaway temperature.

ACKNOWLEDGEMENTS

This work was supported in part by U.S. Department of Energy under contract No. DE-SC22-86PC91272.

REFERENCES

1. E. A. C. Chamberlain and D. A. Hall, Colliery Guardian 221, 65 (1973).
2. J. R. Herring and F. C. Rich, " Spontaneous Coal Combustion; Mechanisms and Prediction" , Proc. 1983 International Conf. on Coal Science, August 15-19, Pittsburgh, p753 (1983)
3. K. Brooks and D. Glasser, Fuel 65, 1035 (1986).
4. J. M. Bell and R. Roche, " The European Experience With Indirect Firing of Pulverized Coal and United State Applications", Proc. Pittsburgh Coal Conf., Pittsburgh, p713 (1984).
5. J. S. Hardman, C. J. Lawn and P. J. Street, Fuel 62, 632 (1983).
6. L. Schmidt and E. Elder, Ind. Eng. Chem. 32, 249 (1940).
7. J. S. Gethner, Applied Spectroscopy 41, 50 (1987).
8. N. E. Cooke, O. M. Fuller and R. P. Gaikwad, Fuel 65, 1254 (1986).
9. P. C. Painter, R. W. Snyder, M. Starsinic, M. M. Coleman, D. W. Kuehn and A. Davis, Applied Spectroscopy 35, 475 (1981).

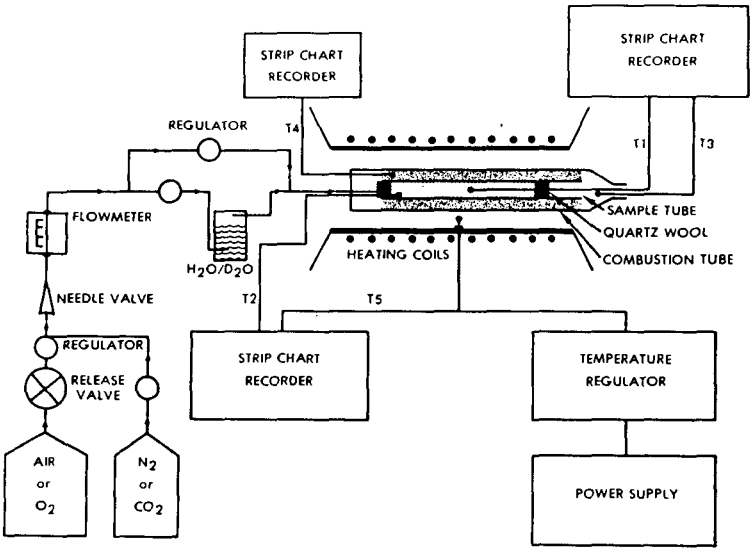

Fig. 1 Combustion tube assembly.

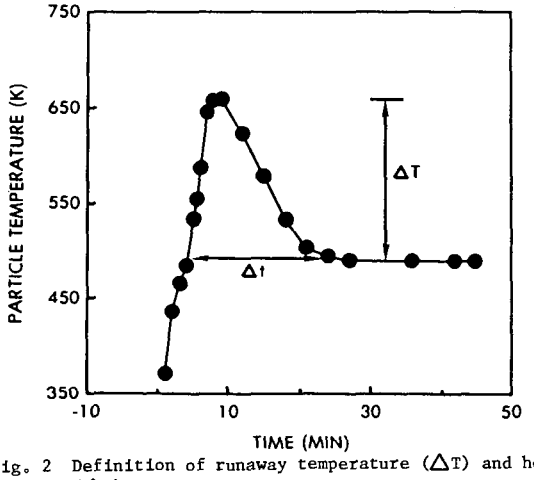

Fig. 2 Definition of runaway temperature (ΔT) and heatwidth (Δt).

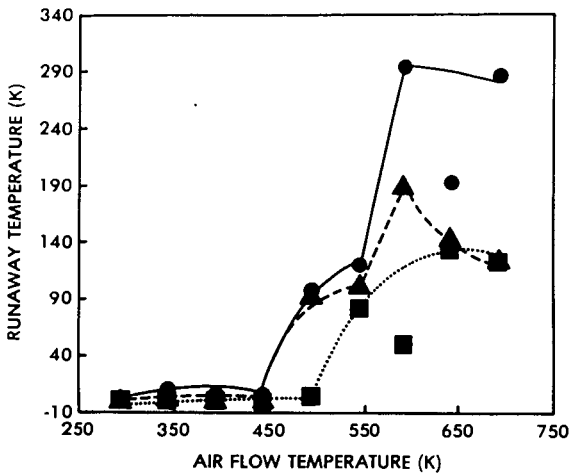

Fig. 3 Effect of air flow temperature on the runaway temperature of Elkhorn Coal. Air flow rate = 900 cc/min., ●<45 μm, ▲ 75> <105 μm, ■ 150> <250 μm.

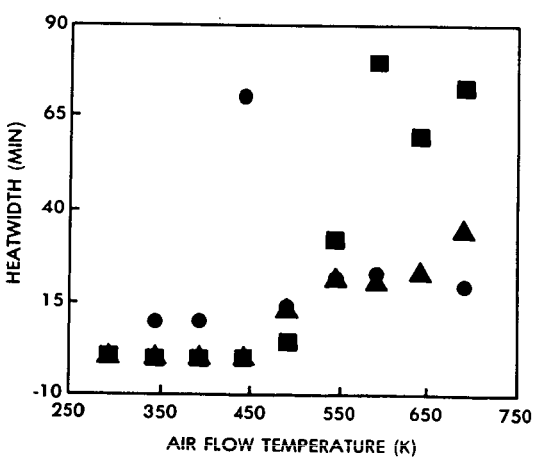

Fig. 4 Effect of air flow temperature on the heatwidth of Elkhorn coal. Air flow rate = 900 cc/min., ●<45 μm, ▲75> <105 μm, ■ 150> <250 μm.

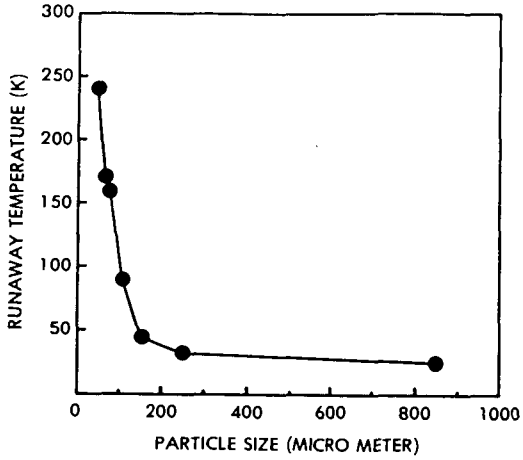

Fig. 5 Effect of particle size on the runaway temperature . $T_g \doteq$ 493K, air flow rate = 900 cc/min.

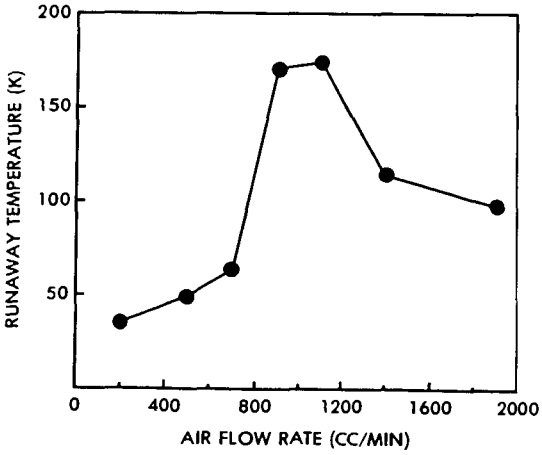

Fig. 6 Effect of air flow rate on the runaway temperature. T_g = 493K, particle size = $\lesssim$45 μm.

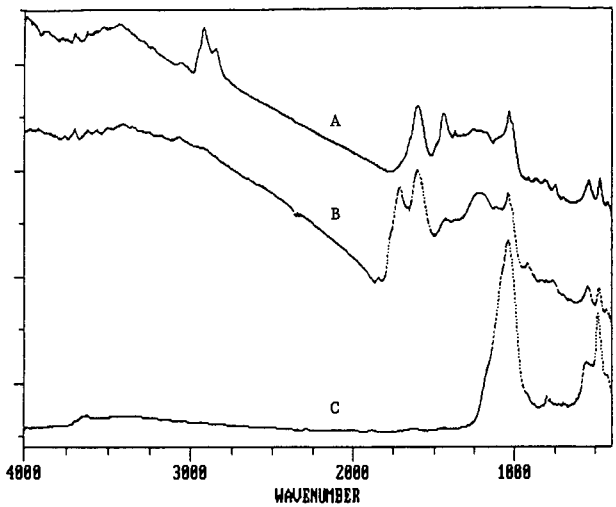

Fig. 7 FTIR spectrum of Elkhorn coal subjected to air flow experiments. (A) 293K, (B) 493K, and (C) 693K.

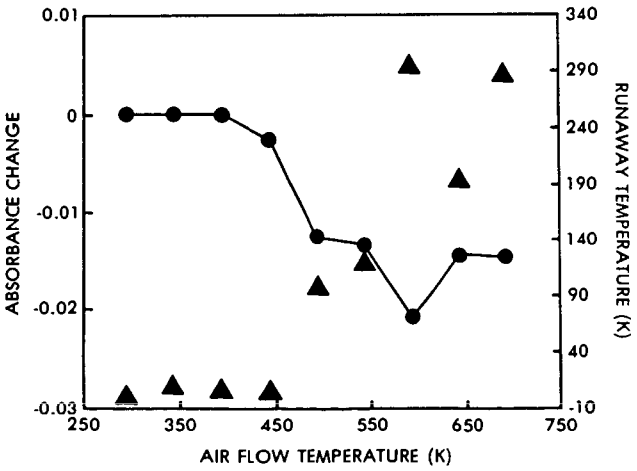

Fig. 8 Effect of air flow temperature on the absorbance of 3034 cm^{-1} band (●) and runaway temperature (▲).

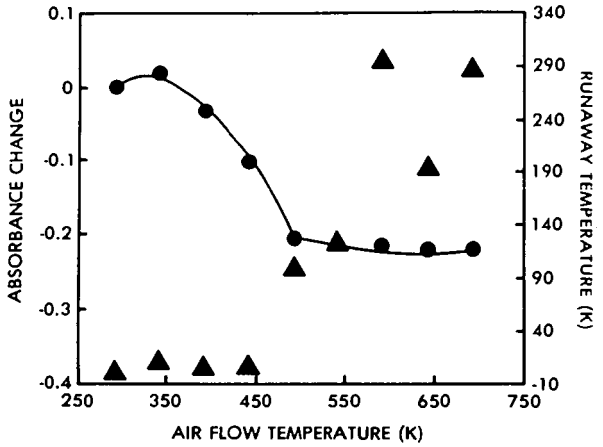

Fig. 9 Effect of air flow temperature on absorbance of 2917 cm^{-1} band (●) and runaway temperature (▲).

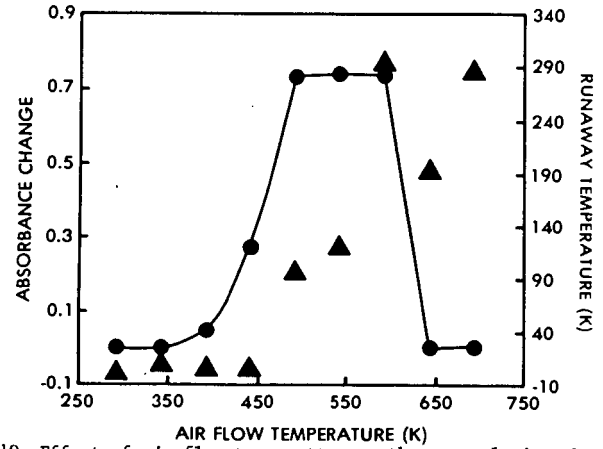

Fig. 10 Effect of air flow temperature on the accumulative absorbance of 1835, 1770, 1725, 1700 and 1560 cm^{-1} bands (●) and runaway temperature (▲).

COAL-WATER MIXTURE COMBUSTION USING OXYGEN-ENRICHED AIR AND STAGED FIRING

Y.C. Fu, G.T. Bellas, and J.I. Joubert

U.S. Department of Energy
Pittsburgh Energy Technology Center
P.O. Box 10940
Pittsburgh, Pennsylvania 15236

ABSTRACT

Coal-water mixture (CWM) combustion experiments using oxygen-enriched air were conducted in an oil-designed 700-hp watertube boiler using a bituminous CWM. The results indicated that the use of oxygen-enriched air increased carbon burnout, reduced uncontrolled fly ash emissions, and reduced combustion air preheating requirements. The boiler efficiency increased because of reduced flue gas heat losses. The improvement in boiler performance compared to an experiment without oxygen enrichment was significant when using only 2-3 percent enrichment of air (23-24 volume percent oxygen). Using combustion air enriched to 22.7 percent oxygen by volume, the required air preheating temperature was reduced to 192°F as compared to 325°F required with no oxygen enrichment, while the carbon conversion efficiency at full boiler load was increased from 95.0 percent to 97.4 percent.

Experiments on CWM combustion were also conducted using staged firing with and without oxygen-enriched air. The NO_x reduction achieved at a first-stage air/fuel stoichiometric ratio of 0.76 was about 33 percent, but it was accompanied by a reduction in combustion efficiency and an increase in particulate emissions. The use of oxygen-enriched air in the burner zone increased flame stability and carbon burnout while maintaining the effectiveness of staged combustion; however, additional experiments are needed to optimize burner-operating parameters to achieve significant NO_x reduction.

INTRODUCTION

The use of oxygen-enriched air for coal-water mixture (CWM) combustion could result in several positive effects on boiler performance: (1) preheated air requirements should be reduced or eliminated, thereby permitting the use of CWM in smaller industrial boilers that do not usually have high-temperature air preheaters; (2) the volume and velocity of the flue gas will be reduced, decreasing potential erosion problems in the boiler convection banks; and (3) boiler efficiency should increase because of reduced stack heat losses, partially compensating for loss in boiler efficiency owing to water in the slurry. Taschler et al. examined the impact of these effects on boiler operating economics and steam generation capacity in large-scale boilers (1).

Coal-water mixture combustion experiments using oxygen-enriched air were conducted at Pittsburgh Energy Technology Center (PETC) in a 700-hp watertube boiler using a commercial CWM fuel prepared from bituminous coal. The objectives of these tests were to determine (1) the optimal point of oxygen injection, (2) the minimal oxygen concentration required to stabilize the CWM flame without preheating the combustion air, and (3) the effects of boiler load conditions on oxygen enrichment requirements.

The CWM combustion experiments were also conducted using staged firing with and without oxygen-enriched air. Staged combustion is one of the most commonly applied NO_x-control techniques for coal-fired boilers (2-4). The boiler is operated with a primary fuel-rich combustion zone, in which both thermal and fuel NO_x formation is minimized. The initial combustion step is then followed by a

fuel-lean zone to complete the combustion of the residual fuel. Staged combustion in the PETC boiler was achieved by introducing the first-stage air through the burner air register, and the second-stage air through three air ports installed on a side wall of the boiler.

EXPERIMENTAL

The test unit is a Nebraska 700-hp "D"-type watertube industrial boiler originally designed for No. 6 oil firing. The boiler generates about 24,000 lb/hr of steam at full load. Figure 1 is a sectional plan view through the firebox and convection section of the boiler. Preheated combustion air is provided by an external source. The Coen single-air-zone register provided with the boiler was modified for these experiments. One of two modifications made to the air register was a diameter change of the sheet metal shroud, which increased the secondary-air linear velocities at the exit throat of the register. The other simple change was the insertion of a center air tube to establish a stable flame front. The center tube has a fixed air spinner, and both the center-tube-air and secondary-air feeds have independent flow-control systems. This allows considerable flexibility in burner-operating capabilities (5). Extensive instrumentation and a computer-controlled data acquisition system provide a large amount of data for detailed analysis and evaluation of the experiments.

Tertiary (second-stage) air is injected through three ports installed at approximately one third of the furnace length from the front wall. The port design incorporates removable sleeves to allow changing of port size to permit control of the second-stage air flow and the injection pattern.

Figure 2 is a cross-sectional view of the burner used for oxygen-enrichment tests. Oxygen is introduced through a specially fabricated oxygen guide tube (3 1/2-inch schedule-10 Monel pipe) surrounding the burner-gun guide tube. A Coen nozzle with eight 15/64-inch holes and a 60° spray angle was used. A 30° cocurrent center-air diffuser and a 45° cocurrent oxygen-guide-tube diffuser were installed during the combustion experiments.

CWM COMBUSTION USING OXYGEN-ENRICHED AIR

The use of oxygen-enriched combustion air reduces the amount of nitrogen flowing through a combustion process, resulting in elevated flame temperatures. Figure 3 shows adiabatic flame temperatures for the combustion of CWM with oxygen-enriched air at an oxygen/fuel stoichiometric ratio of 1.15. Theoretical flame temperature curves were generated at combustion air preheating temperatures of 77° (ambient), 300°, and 500°F using the PETC Multiphase Equilibrium Program for a CWM containing 70 percent Pittsburgh seam bituminous coal. The adiabatic flame temperature using normal air (O_2 = 20.69 volume percent) preheated to 500°F is 3393°F; the same flame temperature can be achieved by using 23.25 volume percent oxygen-enriched air at ambient temperature.

Because of the reduction in the amount of nitrogen per unit quantity of fuel flowing through the furnace, the amount of flue gas from the combustion of CWM using oxygen enrichment will be decreased. The decrease in flue gas volume, expressed in standard cubic feet per pound of CWM (at 70°F and 14.7 psia), is illustrated in Figure 4. For example, at 23 volume percent and 25 volume percent oxygen concentrations in the combustion air, and an oxidizer/fuel stoichiometric ratio of 1.15, the flue gas quantities decrease by 8 percent and 15 percent, respectively, compared to the quantity produced when using normal air.

Oxygen enrichment should reduce combustion air preheat requirements and reduce flue gas heat losses. Oxygen enrichment should also provide a greater range of flammability and improved flame stability compared to combustion air preheating.

A commercial CWM, ARC-COAL, produced by the Atlantic Research Corporation and containing 70 percent Eastern U.S. bituminous coal, was used in the oxygen enrichment experiments (see Table 1). Analysis of the experimental results indicates that the addition of oxygen to the combustion air results in higher carbon conversion and boiler efficiencies. Using 500°F combustion air at an oxygen level equivalent to 22.9 percent by volume in air, a carbon conversion efficiency of 97.0 percent and a boiler efficiency of 81.3 percent were obtained (see test 2 in Table 2). The base-line test (test 1) at 500°F preheating without oxygen enrichment resulted in 95.0 percent carbon conversion and 79.3 percent boiler efficiency. Because of the improvement in carbon burnout with oxygen enrichment, the carbon content of the fly ash decreased by more than 25 percent (Table 3). As a consequence, particulate emissions were also reduced. With oxygen enrichment, however, NO_x emissions increased from 0.69 to 1.00 lb NO_2/MMBtu (tests 1 and 2 in Table 3). The increased flame temperature due to oxygen enrichment apparently increased the formation of thermal NO_x.

Test 3 of Tables 2 and 3 was conducted at reduced boiler load (~70 percent of maximum capacity) using oxygen-enriched air. A slight improvement (1%) in carbon conversion was obtained compared to test 2, which was conducted at full load.

Test 4 was carried out at full load and at minimum combustion air preheat temperature (192°F) using 22.7 percent oxygen-enriched air. An improvement in boiler performance compared to the test without oxygen enrichment (test 1) is noticeable, even though the preheating temperature was reduced substantially. The minimum combustion air preheating required for a stable flame is affected by a number of variables, including CWM volatility, heating value, and oxygen enrichment (flame temperature). Other variables, such as excess oxygen level and combustion air swirl, are also important. With increased oxygen concentration in the oxygen-enriched air, the combustion air flow per unit quantity of fuel at a constant oxidizer/fuel ratio is reduced. This would reduce the intensity of the combustion air swirl and possibly adversely affect the flame stability.

CWM COMBUSTION USING STAGED FIRING

Combustion experiments were conducted at full boiler load and at total air/fuel stoichiometric ratios of 1.15 to 1.21 using combustion air preheated to about 490°F (see Tables 4 and 5). Stoichiometric ratios of the first-stage air (atomizing air plus center-tube air plus secondary air) to fuel were varied between 0.76 and 0.97 while the remaining air (tertiary air) was diverted through the side wall ports. Boiler operation could not be sustained at a stoichiometric ratio less than 0.75 in the primary combustion zone because of flame instabilities.

A base-line experiment performed without air staging (with the tertiary air ports blocked) produced NO_x emission levels of 0.77 lb/MMBtu (see test 1, Tables 4 and 5). As primary-zone stoichiometry was reduced, emissions of NO_x declined; the NO_x reduction achieved with the primary-zone stoichiometry of 0.76 was about 33 percent. The reduction in NO_x emissions, however, was achieved with some decrease in combustion efficiency. As the first-stage stoichiometric ratio was reduced from 1.15 to 0.76, the carbon conversion efficiency decreased from 95.7 percent to 92.2 percent.

It is apparent that the conditions created by deep staging (primary zone stoichiometry of less than 0.75) tend to be opposite of those conducive to good flame stability and high carbon-conversion efficiencies. Improvements in combustion efficiency may be attainable by changing the tertiary-air port location and/or velocity to increase the efficiency of tertiary-air mixing in the second stage. However, because of limitations in primary-zone temperature and residence time, it may be difficult to achieve large reductions in NO_x emissions while

firing coal or CWM in an oil-designed boiler without exacerbating the problem of fuel burnout.

CWM COMBUSTION USING STAGED FIRING AND OXYGEN-ENRICHED AIR

One approach to increasing the primary-zone temperature, flame stability, and carbon burnout under deep-staging conditions is to use oxygen-enriched air. Tables 6 and 7 show the results of CWM combustion experiments using both staged firing and oxygen-enriched air. Oxygen was introduced into the primary combustion zone through the burner oxygen guide tube (see Figure 2). These experiments were conducted using 356°F to 413°F combustion air at 1.14 to 1.16 overall oxygen/fuel stoichiometric ratio and at an overall oxygen concentration of about 26 percent by volume. Carbon conversion efficiencies ranging from 95.6 percent to 97.8 percent and boiler efficiencies ranging from 81.0 percent to 82.8 percent were obtained as the oxygen/fuel stoichiometric ratio in the primary combustion zone was varied from 1.14 (unstaged) to 0.76.

Carbon conversion efficiency was reduced only slightly and the boiler efficiency remained high as the degree of staging increased. However, a reduction in NO_x emissions was observed when the primary-stage stoichiometry was reduced to 0.76, as shown in Figure 5. With oxygen enrichment, the measured NO_x emissions at all primary-stage stoichiometries were higher than those measured in experiments conducted with no oxygen enrichment, even though the oxidizer was preheated to a higher temperature in the latter experiments.

These results suggest that the problem of reduced carbon burnout in staged combustion can be alleviated with the use of oxygen-enriched air in the burner zone while achieving a moderate reduction in NO_x emissions. However, even the experiment that provided the greatest reduction in NO_x emissions resulted in levels that are quite high (>0.6 lb NO_2/MMBtu). To further reduce NO_x emissions, it would be necessary to decrease the primary-stage stoichiometry (for this furnace, to less than 0.76). Additional experiments are required to determine if a significant reduction of NO_x emissions can indeed be achieved using oxygen-enriched air in a staged combustion system while maintaining a high level of carbon conversion efficiency.

CONCLUDING REMARKS

The combustion experiments conducted in the 700-hp watertube boiler with bituminous CWM indicate that the use of oxygen-enriched air resulted in a decrease in the level of air preheating required and an improvement in carbon burnout. The reduction in the volume of flue gas lowered heat losses and increased boiler efficiency. Using combustion air enriched to 22.7 percent oxygen by volume, the air preheating temperature could be reduced to 192°F as compared to ~325°F required with no oxygen enrichment. The improvement in boiler performance compared to the test without oxygen enrichment was noticeable even with the use of only 2-3 percent enrichment of air (23-24 volume percent oxygen).

By using staged air admission during CWM combustion in the oil-designed boiler, a reduction in NO_x emissions on the order of 1/3 was achieved. The reduction in NO_x emissions, however, was achieved with some decrease in combustion efficiency. Using 490°F combustion air at 15-21 percent excess, as the primary-stage stoichiometry was reduced from 1.15 to 0.76, NO_x emissions decreased from 0.77 lb/MMBtu to 0.52 lb/MMBtu while the carbon conversion efficiency decreased from 95.7 percent to 92.2 percent.

The use of oxygen-enriched air in the primary combustion stage increased the flame stability and diminished the problem of reduced carbon burnout while achieving moderate reduction of overall NO_x emissions. Using 356°F to 413°F combustion air at 14-16 percent excess and at an overall oxygen concentration of about 26

volume percent, NO_x emissions decreased from 0.88 lb/MMBtu to 0.65 lb/MMBtu as the primary-stage stoichiometry decreased from 1.14 to 0.76. The carbon conversion and boiler efficiencies, however, remained high and were in the ranges of 96-98 percent and 81-83 percent, respectively.

DISCLAIMER

Reference in this paper to any specific commercial product, process, or service is to facilitate understanding and does not necessarily imply its endorsement or favoring by the United States Department of Energy.

REFERENCES

1. Taschler, D.R., Nolte, F.S., and Stringfellow, T.E., "The Impact of Oxygen-Enriched Combustion of Coal Water Slurries on the Economics and Performance of Large Scale Boilers," Sixth International Symposium on Coal Slurry Combustion and Technology, Orlando, Florida, June 25-27, 1984.

2. Perkinson, G., "NO_x Controls: Many New Systems Undergo Trials," Chem. Eng., March 9, 1981.

3. Pruce, L., "Reducing NO_x Emissions at the Burner, in the Furnace, and After Combustion," Power, 125, No. 1, 33, January 1981.

4. Itse, D.C., and Penterson, D.C., "NO_x Control Technology for Industrial Combustion System," American Flame Research Committee Symposium on Combustion Diagnostics from Fuel Bunker to Stack, October 5, 1983.

5. Fu, Y.C., Bellas, G.T., and Joubert, J.I., "Combustion Testing of Coal-Water and Coal-Methanol-Water Mixtures in Oil-Designed Boilers," ASME Winter Annual Meeting, New Orleans, Louisiana, December 9-14, 1984, ASME paper 84-WA/RT-93.

Table 1. Typical Analyses of ARC-Coal

	As Received	Dry Basis
Weight Percent Coal	70.59	
Particle Size Consist (% minus-200-mesh)	89	
Proximate Analysis (%)		
Moisture	29.41	--
Volatile Matter	22.40	31.73
Fixed Carbon	42.81	60.65
Ash	5.38	7.62
Ultimate Analysis (%)		
Hydrogen	6.82	5.04
Carbon	56.86	80.53
Nitrogen	1.08	1.53
Sulfur	0.53	0.75
Oxygen	29.33	4.53
Ash	5.38	7.62
Heating Value (Btu/lb)	10,140	14,365
Viscosity (cP @ 100 sec^{-1} after 50 seconds, 79°-81°F)	584	
Ash Fusion Temperatures (°F)		
Initial Deformation Temp.	2580	
Softening Temp.	2670	
Fluid Temp.	2700	

Table 2. Operating Conditions and Boiler Performance, CWM Tests with Oxygen Enrichment

Test Number	1	2	3	4
O_2 Vol. % in Comb. Air	20.69	22.91	22.83	22.68
Overall Oxygen/Fuel Stoichiometric Ratio	1.16	1.15	1.14	1.25
O_2 Injected (lb/hr)	0	598	385	618
Fuel Flow (lb/hr)	2791	2733	1843	2833
Steam Flow (lb/hr)	24250	24390	16540	24010
Thermal Input (MMBtu/hr)	30.20	29.22	19.67	30.04
Combustion-Air Temp. (^oF)	501	491	490	192
Total Air Flow (lb/hr)	24656	21423	14379	25052
Atomizing-Air Flow (lb/hr)	1287	1316	1312	1338
Atomizing-Air Pressure (psig)	128	126	129	130
Fuel Pressure at Burner (psig)	109	105	88	148
Center-Tube-Air Flow (lb/hr)	4910	4749	4516	5804
Avg. Flue Gas Temp. (^oF)	500	509	463	503
Carbon Conversion Eff. (%)	95.0	97.0	98.1	97.4
Boiler Eff. (%) (Heat Loss Method)	79.3	81.3	82.2	80.0
Heat Loss Due to H_2O in Fuel (%)	3.21	3.26	3.21	3.24
Heat Loss from Burning Hydrogen in Fuel (%)	3.74	3.79	3.74	3.95

Table 3. Flue Gas Emissions in CWM Tests with Oxygen Enrichment

Test Number	1	2	3	4
Flue Gas Analysis				
O_2 (%)	2.9	3.1	3.9	4.2
CO_2 (%)	15.1	17.1	16.2	15.7
CO (ppm)	72	50	55	51
SO_2 (ppm)	646	693	667	662
(lb/MMBtu)	1.24	1.20	1.24	1.23
NO_x *(ppm)	499	800	753	703
(lb/MMBtu)	0.69	1.00	1.00	0.94
THC (ppm)	1.7	0.8	1.0	3.0
Particulate Emissions (Uncontrolled)				
(lb/hr)	168	133	45	124
(lb/MMBtu)	6.07	4.91	2.49	4.26
C in Fly Ash (%)	46.6	34.6	41.4	33.9

*As ppm of NO + ppm of NO_2; calculated as lb of NO_2/MMBtu.

Table 4. Operating Conditions and Boiler Performance, CWM Tests with Staged Combustion

Test Number	1	2	3	4
Total Air/Fuel Stoichiometric Ratio	1.15	1.20	1.21	1.15
First-Stage Air/Fuel Stoichiometric Ratio	1.15	0.97	0.85	0.76
Fuel Flow (lb/hr)	2888	2969	2940	3026
Steam Flow (lb/hr)	23990	24630	24080	24000
Thermal Input (MMBtu/hr)	30.74	31.77	31.45	32.40
Combustion-Air Temp. (^{o}F)	491	490	481	494
Total Air Flow (lb/hr)	25380	27170	27210	26460
Secondary-Air Flow (lb/hr)	17740	15360	13300	12110
Center-Tube-Air Flow (lb/hr)	6096	5340	4682	4122
Tertiary-Air Flow (lb/hr)	--	5264	8046	8985
Atomizing-Air Flow (lb/hr)	1164	1206	1182	1243
Atomizing-Air Pressure (psig)	127	126	129	125
Fuel Pressure at Burner (psig)	114	119	117	124
Avg. Flue Gas Temp. (^{o}F)	525	542	528	519
Carbon Conversion Eff. (%)	95.7	95.5	93.8	92.2
Boiler Eff. (%) (Heat-Loss Method)	77.5	77.6	76.9	76.0
Heat Loss Due to H_2O in Fuel (%)	3.55	3.55	3.53	3.51
Heat Loss from Burning Hydrogen in Fuel (%)	3.81	3.81	3.79	3.77

Table 5. Flue Gas Emissions in CWM Tests with Staged Combustion

Test Number	1	2	3	4
Flue Gas Analysis				
O_2 (%)	2.1	3.5	3.7	3.4
CO_2 (%)	15.8	14.5	14.5	14.5
CO (ppm)	81	74	92	124
SO_2 (ppm)	608	597	610	658
(lb/MMBtu)	1.10	1.19	1.20	1.28
NO_x (ppm)*	560	532	469	375
(lb/MMBtu)*	0.77	0.76	0.66	0.52
THC (ppm)	0.8	3.1	2.1	3.3
Particulate Emissions (uncontrolled)				
(lb/hr)	209	185	203	248
(lb/MMBtu)	7.37	6.33	7.01	8.33
C in Fly Ash (%)	48.9	40.7	50.4	53.3

*As ppm of NO + ppm of NO_2; calculated as lb of NO_2/MMBtu.

Table 6. Operating Conditions and Boiler Performance, CWM Tests with Staged Combustion and Oxygen Enrichment

Test Number	1	2	3	4
O_2vol.% in Combustion Air	26.2	26.3	26.4	26.0
Overall Oxygen/Fuel Stoichio-Ratio	1.14	1.16	1.16	1.14
First-Stage Oxygen/Fuel Stoichiometric Ratio	1.14	1.02	0.88	0.76
Oxygen Injected (lb/hr)	1448	1505	1564	1433
Fuel Flow (lb/hr)	2871	2890	2949	2953
Steam Flow (lb/hr)	23330	23400	23660	23500
Thermal Input (MMBtu/hr)	30.32	30.65	31.77	31.99
Combustion-Air Temp. (°F)	375	356	411	413
Total Air Flow (lb/hr)	18405	18872	19068	19143
Secondary-Air Flow (lb/hr)	12960	10910	8767	7263
Center-Tube-Air Flow (lb/hr)	4293	3638	2944	2389
Tertiary-Air Flow (lb/hr)	--	3166	6213	8299
Atomizing-Air Flow (lb/hr)	1152	1158	1144	1192
Atomizing-Air Pressure (psig)	130	130	131	130
Fuel Pressure at Burner (psig)	117	113	119	122
Avg. Flue Gas Temp. (°F)	489	493	499	496
Carbon Conversion Eff. (%)	97.8	96.8	95.6	96.0
Boiler Eff. (%) (Heat-Loss Method)	82.8	81.8	81.0	81.3
Heat Loss Due to H_2O in Fuel (%)	3.54	3.54	3.50	3.48
Heat Loss From Burning Hydrogen in Fuel (%)	3.51	3.51	3.46	3.44

Table 7. Flue Gas Emissions in CWM Tests with Staged Combustion and Oxygen Enrichment

Test Number	1	2	3	4
Flue Gas Analysis				
O_2 (%)	4.3	5.1	6.1	5.2
CO_2 (%)	19.7	19.0	18.5	18.3
CO (ppm)	64	77	64	79
SO_2 (ppm)	795	818	809	774
(lb/MMBtu)	1.18	1.25	1.25	1.21
NO_x (ppm)*	806	792	814	604
(lb/MMBtu)*	0.88	0.87	0.89	0.65
THC (ppm)	2.2	2.6	2.3	2.3
Particulate Emissions (uncontrolled)				
(lb/hr)	82	110	166	122
(lb/MMBtu)	2.70	3.59	5.23	3.81
C in Fly Ash (%)	44.1	47.8	44.5	55.2

*As ppm of NO + ppm of NO_2; calculated as lb of NO_2/MMBtu.

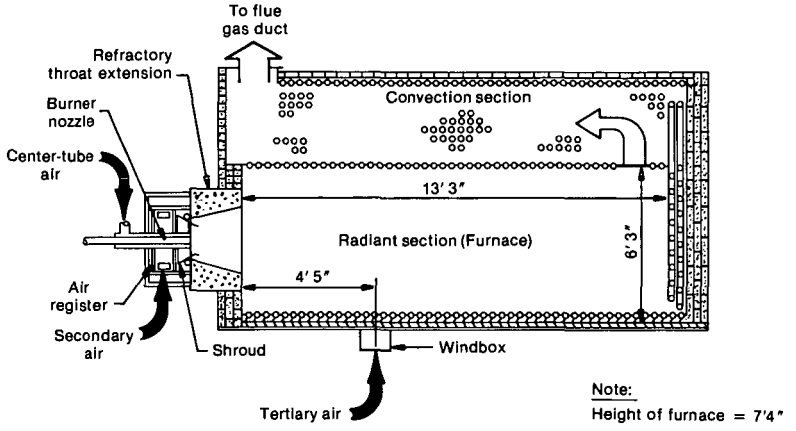

Figure 1. Horizontal cross-sectional view of 700-hp watertube boiler

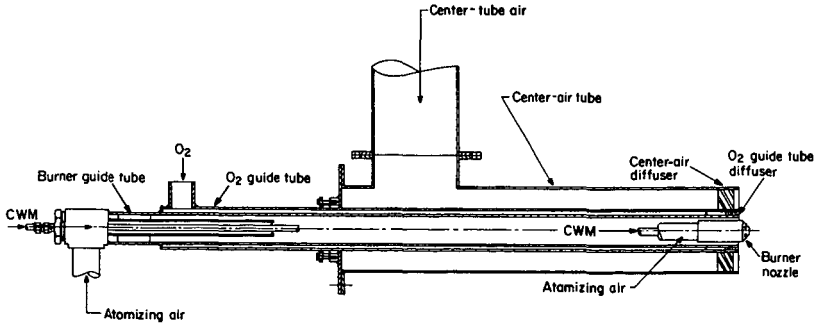

Figure 2. Burner used in oxygen enrichment tests

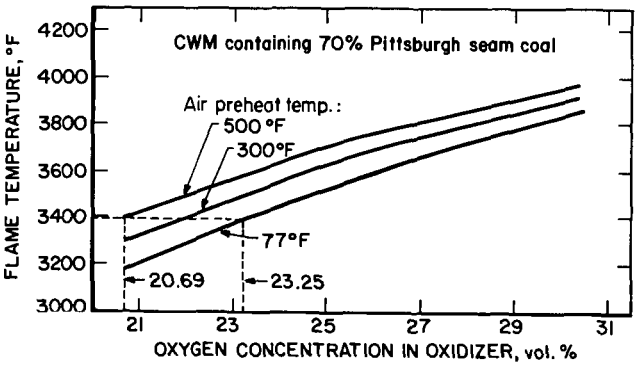

Figure 3. Adiabatic CWM flame temperature with oxygen-enriched air at various combustion air preheat temperatures (oxygen/fuel stoichiometric ratio = 1.15)

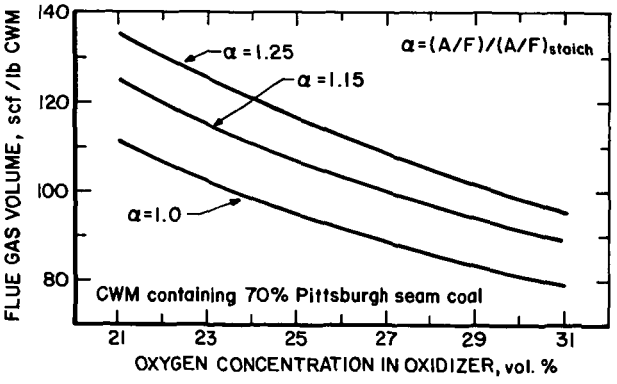

Figure 4. Flue gas volume for CWM combustion with oxygen-enriched air

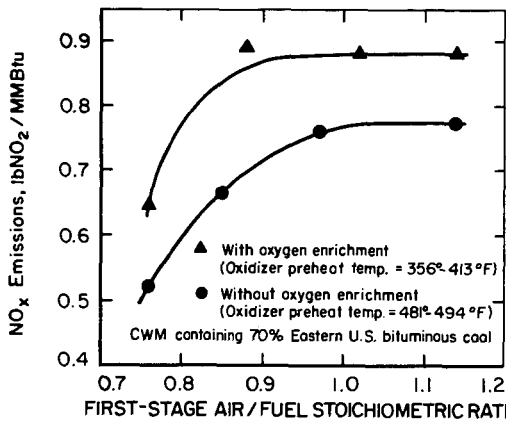

Figure 5. Effect of Staged Firing on NO_x Emissions (Overall oxygen/fuel stoichiometic ratio ≈1.15; full boiler load)

Fluidized Bed Combustion of Petroleum Cokes: Kinetics and Catalytic Effects

Dennis E. Walsh and Gary J. Green

Mobil Research and Development Corporation
Central Research Laboratory, P.O.Box 1025, Princeton, New Jersey 08540

INTRODUCTION

In the fluid coking process, large quantities of coke particles are circulated between a burner vessel and the fluid coking reactor, with the coke-to-fresh feed ratio generally about 7 to 8 pounds of coke per pound of residual feed. During each burning cycle, a portion of coke equivalent to about 5% of the charge is burned off, and the hot coke particles are then returned to the coker supplying process heat. As a result of this type of repeated burning and coke deposition cycle, the coke is deposited in multiple, thin "onion-skin" layers. Product coke is withdrawn from the burner vessel, the temperature of which is maintained between ~595° and 650°C. Because the fluid coking process itself takes place at ~510°C, followed by the coke being first steam stripped and then burned at ~625°C, an essentially "dry" coke product is produced, i.e., one which is free of residual oils.

In the delayed coking process, coke is produced in a batch fashion. Residual oil is fed to a coke drum while a companion drum, used in the previous cycle, is de-coked. Product oil vapors pass upward through the forming coke mass en route to exiting. Coke drum inlet temperatures are maintained at ~485°C-500°C while the outlet is maintained at ~440°C; thus, cooling of the charge takes place during the 24 hour fill cycle. This process, therefore, produces coke at a lower temperature than fluid coking. Hence, the coke product from a delayed coking process is not free of residual oils (~2-10 wt.% on coke).

Although fluid coking is attractive from the viewpoint of higher liquid yield, the coke tends to be higher in sulfur than delayed coke, which could create SO_x pollution problems in any subsequent combustion application. In addition to the sulfur question is that of the intrinsic combustibility of fluid coke vs. delayed coke. Since little information is available in the literature on this point, the present work examined whether process differences have any major impact on the combustion characteristics of the coke products.

A second goal of this study was the investigation of the possibility of catalytically enhancing coke burning rates by employing separate particle catalysis. Though the catalytic oxidation effect of metals impregnated on solid carbonaceous fuel has been recognized for many years, no industrial process using this catalytic technique is in operation due to concerns over the cost of catalyst loss and possible environmental effects of emitted metal particles (1). Fluid bed combustion of solid fuels for steam generation operates at temperatures which may be low enough (~650 to 900°C) for catalytic effects to be operative. Such catalysis would allow increased throughput for a given unit size or permit the use of a smaller unit for a given steam production rate. Catalytically enhanced combustion of solid fuels such as petroleum cokes by active metals on separate particles could obviate the above cited problems associated with direct impregnation of catalysts on a solid fuel.

EXPERIMENTAL

Coke samples were first calcined in nitrogen for ~1 hour at a temperature in excess of the highest anticipated experimental temperature (~650°C) to drive off any residual volatiles which might complicate data interpretation. As noted above, little or no volatiles evolution was observed in the case of fluid coke; delayed coke samples did evolve some volatile constituents. The delayed coke samples included both "needle" and "sponge" cokes, which have different morphologies as reflected by their names. Also, in the case of the delayed coke samples, a brief exposure (~90 sec.) to high temperature air was employed to effect a mild surface area enhancement. Thus, all the samples are compared at "dry" conditions (i.e., free of residual oil volatiles) and at similar initial surface areas. Properties of these materials are given in Table 1. At each temperature, repeat runs with successively smaller coke particle sizes were performed until burning rates remained unchanged, thereby insuring that all burning rate data were uninfluenced by diffusion.

The sample of coke to be burned was diluted to 0.1-1.0 wt.% in a bed of acid washed sand particles. The bed was then fluidized in N_2 and brought to reaction temperature in a three zone furnace. Initiation of the experiment, collection of data and termination of the run were all computer controlled. Essentially, the solenoid valve supplying N_2 to the flow controller closes and the O_2 valve opens to start an experiment. Combustion gases leaving the fluid bed are quenched, dried and filtered. An NDIR monitors the CO and CO_2 concentrations and the computer records the CO_x levels and bed temperature as a function of time. The interval between readings accelerates or decelerates depending upon the CO_x level in the product gases. Bed isothermality was usually $\pm$ 2-3°C and the oxygen supply rate was generally $\geq$10 times the consumption rate. Experiments were conducted over the temperature range from 500-600°C; reactor pressure was atmospheric.

Preparation of candidate catalytic materials was accomplished by impregnation of clean sand using aqueous solutions containing a quantity of metal sufficient to provide the desired loading (generally ~1 wt.%). The dried preparations were then O_2 calcined at ~600°C prior to use. When Pt preparations were made (using H_2PtCl_6), dried samples were H_2 reduced (~2 hours at 425°C) prior to O_2 calcination. A low surface area support (viz. sand) was chosen since solid-solid contacting at the exteriors of the fuel and catalyst particles would be the likely mechanism of any catalytic combustion enhancement; "interior" active sites present in high surface area catalyst formulations would likely be unavailable for catalyzing the primary combustion step ($C+O_2 \rightarrow CO/CO_2$). Metals analyses of catalyst-impregnated sand samples taken from the bed before and after combustion showed that no measurable decrease in catalyst concentration occurred during the course of any of the experiments. In addition, negligibly small amounts of bed material were lost to entrainment.

RESULTS AND DISCUSSIONS

Burning Characteristic of Fluid Coke vs. Delayed Coke

The burning rate data for all coke samples tested were adequately described by first order kinetics over ~85% of the burn off. As illustrated in Figure 1, a plot of the natural log of the fraction of unburned carbon vs. time is well-fit by a straight line, the slope of which is the apparent first order rate constant.

Figure 2 is an Arrhenius plot of the rate constant data obtained for the delayed coker needle coke samples; the activation energy is ~41 kcal/mole. This value is in excellent agreement with that reported recently for the combustion of a sample of petroleum coke used in the preparation of pre-baked anodes for aluminum production (2). This value is also comparable to that observed for uncatalyzed combustion of carbon deposited on solid oxide supports (3). Additionally, 41 kcal/mole is in good agreement with the value calculated (4) based on literature data for a wide variety of carbonaceous materials including some delayed coker petroleum cokes. For comprehensive treatments of carbon combustion/ gasification kinetics, the reader is referred to several excellent reviews (5,6,7).

Figure 3 is an Arrhenius plot of the rate constant data for the fluid coke samples. Again, the data define a straight line, the slope of which yields an activation energy of ~27 kcal/mole. This value is in good agreement with ~30 kcal/mole found over a slightly lower temperature range for carbons doped with vanadium at levels roughly equivalent to that of the fluid coke (8). For comparison, Figure 4 shows Arrhenius plots for both delayed coker needle coke and fluid coke, as well as points obtained for sponge coke, which is a delayed coke with substantially larger metals content than the needle coke samples. The lines in Figure 4 converge at ~550°C, showing behavior very consistent with that found for pure and vanadium-doped carbon oxidation (8). This convergence indicates the increasing influence of the higher activation energy, thermal oxidation relative to the catalyzed oxidation reaction.

Figure 4 shows that fluid coke burns at a somewhat faster rate than delayed coker needle coke at temperatures below ~550°C. However, delayed coker sponge coke behaves in a manner similar to fluid coke. Both of these materials have high metals contents (Table I) relative to delayed coker needle coke, which exhibits lower rates and a higher activation energy. Thus, it is probable that petroleum cokes having higher metals concentration exhibit catalytically influenced combustion. In fact, such catalytic effects were reported (8) for carbons containing as little as 150 ppm vanadium, with little change in activation energy for vanadium concentrations up to 3.5%!

In summary, it appears that process origin does not have a major impact on the burning rates of "dry" petroleum cokes having similar initial surface areas and metals contents. The metals content of the coke can exert a catalytic influence on its burning rate. However, this effect is lessened at higher temperatures. Based upon these observations, it was inferred that any major differences between the combustibility of fluid coke and delayed coke under practical industrial conditions would likely be due to the presence of the heavy residual oils in the delayed coke. Volatilized residual oils would be more readily oxidized than the delayed coke itself and thus would aid in initiating and stabilizing the coke combustion process.

Enhancement of Coke Burning Rates by Separate Particle Catalysis

Effect of temperature Burning rate data for needle coke burned in the presence of clean sand and sand impregnated with metallic catalysts are presented in Figure 5. It is apparent that all the candidate catalytic materials investigated produced a burning rate enhancement. The apparent activation energy for coke burning in a 1% Pt/sand bed was ~17 kcal/mole versus ~41 kcal/mole for the baseline

(clean sand) data. The divergence of the two lines shows that the relative rate enhancement decreases with increasing temperature. When extrapolated, the two lines converge at a point corresponding to ~555°C, virtually identical to the point of convergence observed for the burning rate data presented in Figure 4 which showed the effect of metals intrinsic to the coke. This consistent finding suggests that a significant catalytic benefit of metals (whether intrinsic or present on separate particles) for burning rate enhancements may be realized only at temperatures below ~550°C. Furthermore, the data indicate that this effect is not highly sensitive to the identity of the metal.

Choosing 505°C as a comparison temperature, the data show that both 0.1% Pt and 1% Pt are equally effective, increasing the rate by a factor of 2.2. This behavior might be expected on such a low surface area support since more than enough Pt is present in both cases to cover the available surface. Also, nickel oxide is as effective as Pt in enhancing the burning rate, while cobalt oxide is only slightly inferior. Both Ni and Co have been previously reported as having catalytic activity for carbon gasification when directly impregnated on the solid fuel (9). As shown in Figure 5, sodium oxide is also quite effective as a catalyst. Alkali metal oxides have also been identified previously as effective gasification catalysts when impregnated on the fuel (10,11). However, they are believed to function by a different mechanism than noble or transition metals (12), some evidence of which is given below.

The data in Table II present the CO/CO_2 ratio in the combustion gases at 50% carbon burnoff. In all baseline cases with clean sand as the bed material, both CO and CO_2 were produced over the course of the burn in fairly fixed proportions, while in all Pt and transition metal experiments CO was never observed, indicating more efficient combustion. The similarity between the CO/CO_2 ratios of the baseline data and the sodium oxide data indicates that the alkali metal oxide enhances gasification of carbon to CO but does not effectively improve combustion efficiency by promoting complete conversion of CO to CO_2.

Figure 6 presents baseline and catalytic results obtained using sponge coke. Catalysis was again observed, but the 40% rate enhancements at 500-510°C are more modest than those observed with needle coke. The similar behavior of fresh and used Pt suggest that there is no rapid deterioration in performance. In contrast, fresh nickel oxide, which was initially as effective as Pt, rapidly lost its activity as shown by a decrease in burning rate and the appearance of CO in the combustion gases upon subsequent use. Though this suggests that the catalyst was being poisoned, presumably by coke-derived impurities, it is not clear why, under similar circumstances, the Pt activity remained unaffected. For comparison, Figure 7 shows baseline and 1% Pt/sand catalytic data for fluid coke. At ~505-510°C a moderate rate enhancement of ~50% was observed.

Based on the collective results shown in Figures 5-7, it may be concluded that no significant rate enhancement benefits are to be gained by separate particle catalysis in practical fluid bed combustors, which typically operate at temperatures >650°C. However, the results given in Table II show that separate particle catalysis can be beneficial in completing the conversion of CO to CO_2, resulting in higher combustion efficiencies and minimizing CO emissions from the unit. This benefit of lowered CO emissions, even

at the higher temperatures typical of practical fluid bed combustors, is not unexpected in light of the proven effectiveness of Pt CO combustion promoter additives used in the fluid bed, air regeneration of fluid cracking catalysts at temperatures >650°C (13).

Effect of intrinsic metals The higher rate increases observed with low-metals needle coke vs. sponge and fluid cokes parallel the relative burning rates discussed above in the absence of separate catalytic particles. Moreover, this behavior suggests that the extent to which a rate enhancement can be obtained with separate particle catalysts also depends upon the intrinsic metals content of the coke. To examine this point further, some additional data were obtained by burning toluene-derived soot (96% C, 2% O, 2% H) as a convenient model of a metals-free carbonaceous pyrolysis residue.

Although differing in "process" origin, both coke and soot are carbonaceous pyrolysis products having quite similar elemental analyses. Furthermore, both coke and soot have been shown elsewhere to have very similar reactivities and activation energies (~39 kcal/mole) with respect to combustion (4). In contrast, high purity graphite does not exhibit burning behavior similar to that of low-metals needle coke, as evidenced in related studies where the burning rate constant for ultra-high purity graphite (<5 ppm total impurities) was found to be over two orders of magnitude lower than that of the coke. This result is also consistent with earlier work which showed that high purity graphite has a reactivity ~3 orders of magnitude lower than coke and has a much higher activation energy (~50 to 70 kcal/mole) (4). This evidence shows that soot better models "high purity" petroleum coke burning behavior than do other carbonaceous residues such as ultra-high purity graphite.

Soot experiments were performed over clean sand, over 1% Pt/sand, and over clean sand with the soot directly impregnated with 1% Pt. These results are summarized in Table III. Despite its extremely fine particle size, in the absence of catalyst particles, the soot burning rate constant at 505°C was 6-7 times lower than that of low-metals needle coke. This factor seems reasonable in light of the soot's zero metals content and the discussions in the previous section.

In discussing the impact of added catalyst particles, the use of burning rate enhancements, i.e. relative burning rates with and without a catalyst, will facilitate comparisons among the various carbonaceous materials. Figure 8 shows the relative burning rates ($k_{catalyst}/k_{baseline}$) at ~505°C for soot and all the cokes investigated using 1% Pt on sand. The data point for needle coke is plotted somewhat arbitrarily at 30 ppm since the reported analytical results provided only upper bounds on the Ni and V contents (see Table I). The plot indicates that the extent of rate enhancement obtained by separate particle catalysis is a function of the intrinsic metals content of the solid fuel being burned. Therefore, above a certain threshold concentration of metal ($\sim$ 100 ppm Ni + V) intrinsic to the carbonaceous fuel, the otherwise large influence of external catalysts will be greatly diminished.

Pertinent to the question of intimacy between the metal and the solid fuel, a 17 fold increase in rate was obtained by separate particle catalysis of metals-free soot (Table III). In this case, soot was burned in a bed of Pt impregnated sand where the initial atomic Pt/C ratio was ~0.26/1. A 30 fold increase resulted, however,

when soot impregnated with 1 wt.% Pt was burned in a bed of clean sand where the initial atomic Pt/C ratio was 400 times lower. Clearly, the more intimate the contact between carbon and metal, the more effective the catalysis.

Mechanistic implications The fact that coke burning rate enhancements are observed when the bed material (sand) is impregnated with metals indicates that "solid-solid" catalytic interactions are occurring between the coke particles and bed particles in the presence of oxygen. Regardless of the particular metal or metal oxide particle, intimate contact between it and the carbon surface is required for the oxidation-reduction cycle of the metal particle to occur at the carbon surface, which is the generally accepted mechanism for the catalyzed oxidation of carbon (12). It is highly unlikely that gas phase transport of the metal or metal oxide to the carbon surface is involved under the current experimental conditions due to the low vapor pressures of these species at temperatures below 550°C.

The first step in any heterogeneous catalytic reaction is the transport of reactants from the bulk phase to the external surface of the catalyst. In the present work, only the external mass transfer step can influence and mask the intrinsic kinetics since the catalyst particles employed are non-porous and intraparticle diffusion is not a factor. If the external mass transfer step is rate controlling, then the observed apparent activation energy will be lower than that of the true activation energy of the catalyzed chemical reaction. This results because, compared to the reaction rate constant, the mass transfer coefficient is much less sensitive to changing temperature.

Standard methods exist for estimating the importance of external mass transfer gradients on the observed kinetic parameters (14). However, those procedures were developed for fluid phase reactants and, therefore, are not directly applicable to the case at hand where the reactants are macro-sized carbon particles. Nevertheless, the strong influence of convective transport of coke particles to the active external surface seems reasonable in light of the size of the solid reactants. Such an influence would explain the decline in apparent activation energy from ~27 kcal/mole for carbon particles containing a significant amount of intimate catalytic sites (fluid and sponge cokes) to ~17 kcal/mole where few such sites exist and transport of the carbon particle to external catalytic centers is required (needle coke). External mass transport rate control would also account for the apparent insensitivity of catalyst type on the extent of the rate enhancement observed for needle coke burning in the presence of external catalyst particles versus burning in the absence of an external catalyst.

CONCLUSIONS

The burning rates of "dry" petroleum cokes (i.e., cokes which are free of residual oil volatiles) having similar initial surface areas are not influenced by process origin (delayed vs. fluid coking). Differences in burning rate among the coke samples tested are related to the metals level in the coke which can exert a catalytic influence on the burning rate. This effect diminishes with increasing temperature as higher activation energy thermal reactions begin to dominate.

The addition of separate particles of low surface area catalytic solids can accelerate the combustion of petroleum coke and similar carbonaceous residues. The extent of the rate enhancement from an external catalyst declines with increasing temperature and increasing intrinsic metals content of the solid fuel. Moreover, these findings suggest that the primary benefit from separate particle catalysis in practical fluid bed combustors for steam generation would be enhanced conversion of CO to CO_2. Finally, the low activation energies observed are qualitatively consistent with a rate-limiting step involving transport of coke particles to the surface of the catalyst particles.

ACKNOWLEDGEMENTS

The technical assistance of Messrs. D. B. Steel and L. R. Koenig and Ms. B. A. Paquin are gratefully acknowledged in the construction of the apparatus and execution of the experiments. Helpful discussions with Drs. H. J. Schoennagel and J. Wei are also appreciated.

REFERENCES

1. Juntgen, H. (1983). Application of catalysts to coal gasification processes: incentives and perspectives. Fuel 62, 234.
2. Tyler, R. J. (1986). Intrinsic reactivity of petroleum coke to oxygen. Fuel 65, 235.
3. Weisz, P. B. and Goodwin, R. D. (1966). Combustion of carbonaceous deposits within porous catalyst particles. II. Intrinsic burning rate. J. Cat. 6, 227.
4. Smith, I. W. (1978). The intrinsic reactivity of carbons to oxygen. Fuel 57, 409.
5. Walker, Jr., P. L., Rusinko, Jr., F., and Austin, L. G. (1959). Gas reactions of carbon. Advances in Catalysis 11, 133.
6. Laurendaen, N. M. (1978). Heterogeneous kinetics of coal char gasification and combustion. Progress in Energy and Combustion Science 14 (4), 221.
7. Mulcahy, M. F. R. and Smith, I. W. (1969). Kinetics of combustion of pulverized fuels: a review of theory and experiment. Reviews of Pure and Applied Chemistry 19, 81.
8. Buch, T., Guala, J. A., and Caneiro, A. (1978). Oxyreactivity of doped sucrose carbon. Carbon 16, 377.
9. Marsh, H. and Adair, R. R. (1975). Catalytic gasification of doped carbon - a kinetic study. Carbon 13, 327.
10. McKee, D. W., Spiro, C. L., Kosky, P. G., and Lamby, E. J (1983). Catalysis of coal char gasification by alkali metal salts. Fuel 62, 217.
11. McKee, D. W. (1980). Mechanisms of catalyzed gasification of carbon. General Electric Corporate Research and Development Report No. 80CRD143.
12. McKee, D. W. (1981). The catalyzed gasification reactions of carbon. In Walker, Jr., P. L., and Thrower, P. A. (Ed.), Chemistry and Physics of Carbon, Marcel Dekker, New York, Vol. 16, pp. 1-118.
13. Chester, A. W., Schwartz, A. B., Stover, W. A., and McWilliams, J. P. (1981). Catalyzing the energy balance of "cat" cracking. Chemtech 11, 50.
14. Hougen, O. A. (1961). Engineering aspects of solid catalyst. Industrial and Engineering Chemistry 53 (7), 509.

TABLE I

COKE ANALYSES

	Needle Coke+	Sponge Coke+	Fluid Coke*
C (wt%)	93.8	90.4	87.3
H	2.4	1.7	1.6
O	2.3	1.7	1.6
N	0.48	1.1	1.2
S	0.54	3.68	8.0
Ash	0.53	1.17	.33
Ni (ppm)	<20	145	275
V	<25	390	540
Cu	5	7	5
Fe	200	215	60
Surface Area, m^2/g	8	6	8

+ N_2 Calcined to 650°C, air burned at 650°C, ~90 sec, ~1hr. N_2 calcination at 600°C.

* ~1 hr. N_2 calcination at 600°C.

TABLE II

CO/CO_2 RATIO AT 50% NEEDLE COKE BURN-OFF (505°C)

Catalyst	CO/CO_2
None	0.64
.1% Pt	0
1% Pt	0
1% NiO	0
1% CoO	0
1% NaO	0.67

TABLE III

INFLUENCE OF Pt ON TOLUENE SOOT BURNING RATE AT 505°C

	$k\ (min^{-1})$	k_{Pt}/k_{base}
Base case (no catalyst)	0.015	1.0
1 wt% Pt on Sand	0.260	17.3
1 wt% Pt on Soot	0.452	30.1

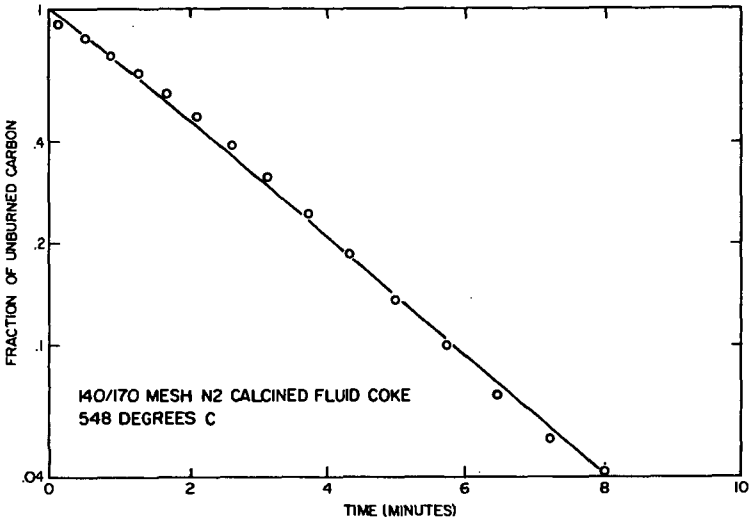

FIGURE 1. FRACTION OF UNBURNED CARBON VS. TIME

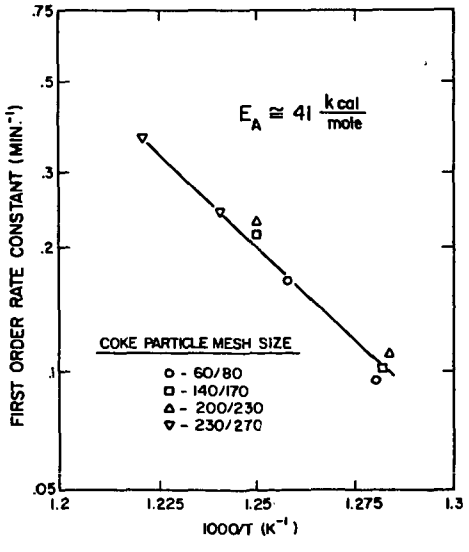

Figure 2. ARRHENIUS PLOT FOR NEEDLE COKE COMBUSTION

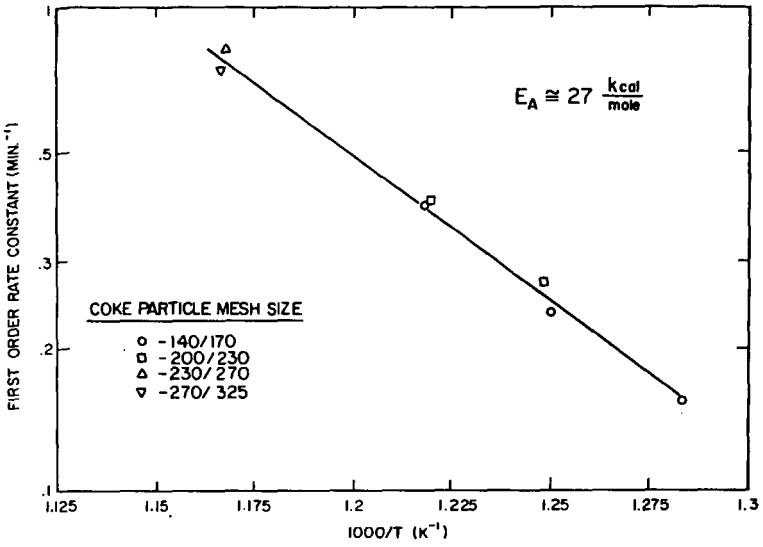

Figure 3. ARRHENIUS PLOT FOR FLUID COKE COMBUSTION

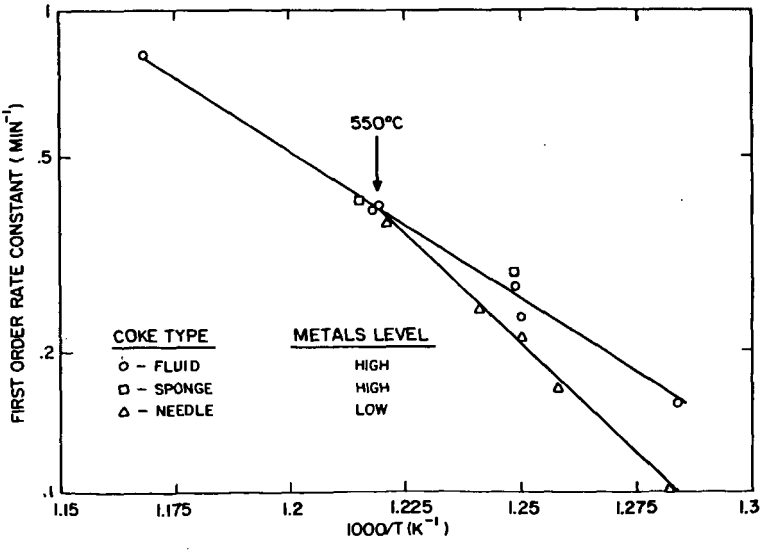

Figure 4. INFLUENCE OF COKE METALS CONTENT ON ARRHENIUS BEHAVIOR

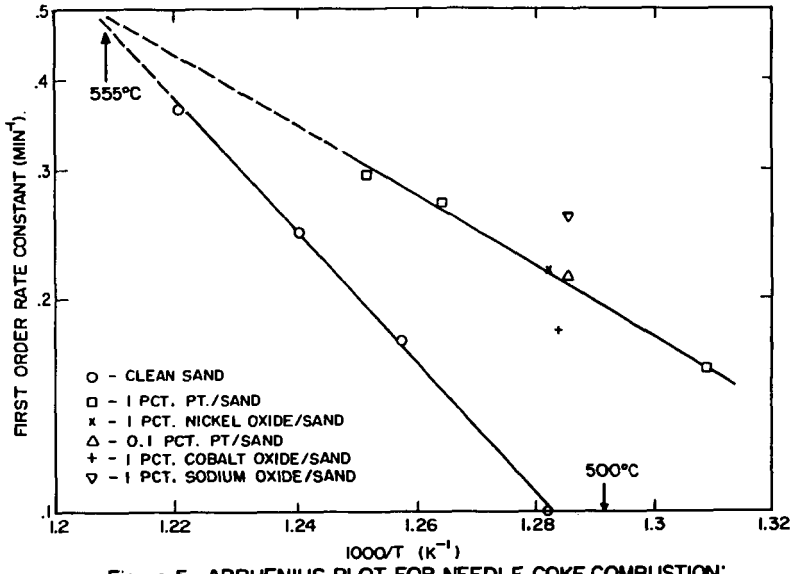

Figure 5. ARRHENIUS PLOT FOR NEEDLE COKE COMBUSTION: EFFECT OF SEPARATE PARTICLE CATALYSIS

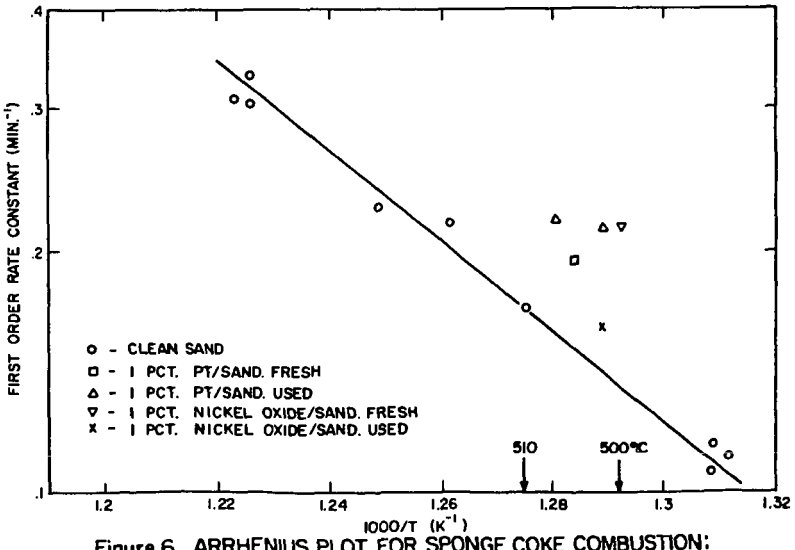

Figure 6. ARRHENIUS PLOT FOR SPONGE COKE COMBUSTION: EFFECT OF SEPARATE PARTICLE CATALYSIS

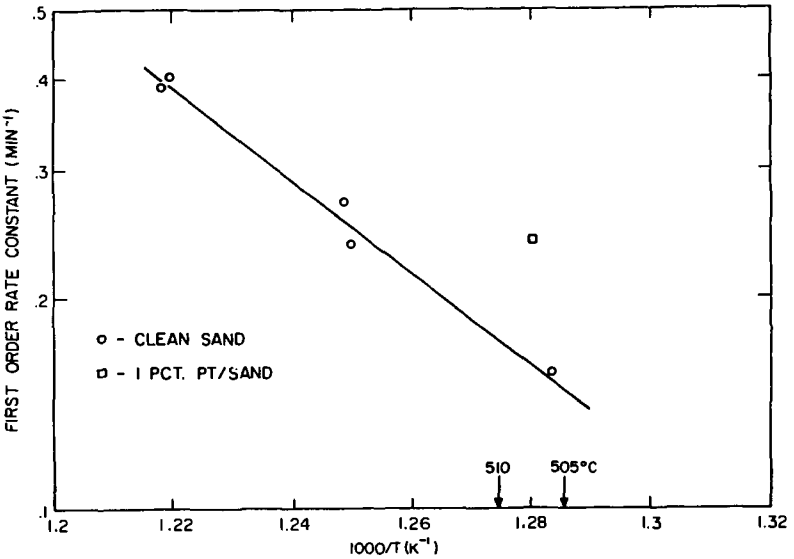

Figure 7. ARRHENIUS PLOT FOR FLUID COKE COMBUSTION: EFFECT OF SEPARATE PARTICLE CATALYSIS

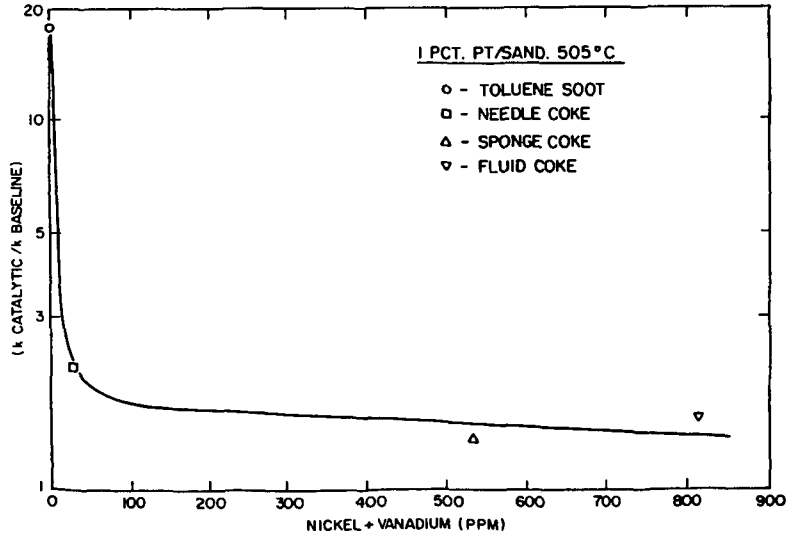

Figure 8. RATE CONSTANT RATIO VS. INTRINSIC METALS CONTENT

THE PREDICTION OF SLAGGING PROBLEMS AS A RESULT OF COAL BLENDING

Edward J. Zecchini and Gary L. Foutch

School of Chemical Engineering
Oklahoma State University
Stillwater, Oklahoma 74078-0537

INTRODUCTION

Power generating facilities which use coal face several problems caused by the nature of the fuel. Of these problems, fireside fouling and deposition is of major importance. Fireside deposition affects boiler availability and operating efficiency. Determination of when a coal or blend of coals will cause significant slagging problems is extremely important. The properties and mechanisms behind fireside deposition due to coal blending is the focus here (1).

Such a problem occurred at the Public Service Company of Oklahoma's (PSO's) northeast generating facility. The problem arose when two Wyoming, subbituminous coals were blended. These two coals, Jacob's Ranch (JR) and Clovis Point (CP) cause only moderate fireside deposition when burned separately. Any blend of the two coals causes more boiler deposition and fouling than either pure coal, based on observations by PSO's engineers (2). The blend which results in the most severe fireside deposition is approximately 75% JR-25% CP. Although avoiding blending eliminates this problem, in some circumstances operating conditions require the use of blended coals.

When blending coals, care must be taken to determine if the two (or more) coals are compatible. Lee and Whaley (3) examined the modification of combustion and fly-ash characteristics due to the blending of coals. They concluded that potential operational problems due to the blending can be minimized or avoided by careful determination of coal and coal ash properties before usage. Dooley and Chacinski (4) agreed on not using empirical slagging correlations to predict blended coal slagging propensities. To further support this, a number of the standard slagging indices (5) have been evaluated with the available data on Jacob's Ranch and Clovis Point coals. As Table I summarizes, none of the standard indices describe the problem as observed by PSO's engineers.

As a result, a new approach seems to be necessary. A possible approach, and the one used in this study, is one analogous to reaction order theory.

EXPERIMENTAL DATA

There is certain data that is necessary in evaluating the predictive method to be employed in this study. A proximate analysis of both coals (Jacob's Ranch and Clovis Point) is given in Table II (6). The data that will be of most interest in the approach used here are the coal ash compositions. There are two different sets of coal ash composition data, one is an independent analysis conducted by Williams Brothers Laboratory (6), the other is the analysis at OSU. This data is presented in Table III. The analysis of the ash from different blends of the two coals is presented in Table IV.

GENERAL APPROACH

The approach selected to predict the observed problem is similar to reaction rate theory. If one coal is rich in component A and the other coal is rich in component B, then a reaction analogy applies. An interaction between two components is modeled as if it were a reaction with a rate equation given by: $aA + bB \rightarrow$ Products (reaction or interaction); Rate $\alpha [A]^n [B]^m$ (rate expression). Where n and m are exponents on the concentrations of reactants A and B, respectively. The order of the interaction is given by n + m. There are certain unknowns here that need to be selected or determined by trial and error.

DISCUSSION

The general description of the deposition problem leads immediately to a conceptual form of the desired slagging correlation (Figure 1). The problem is how to predict such a dramatic change in the slagging properties of the coal burned as the %Jacob's Ranch in the blend changes with the numerous variables that are as of yet undefined. The most pressing problem is the selection of the data to be used as concentrations. Finding actual concentrations in such a situation is impossible, so some means of finding relative or pseudo concentrations is necessary. The weight percents of oxides in the ash represent relative concentrations. Using these values as the concentrations in the rate equation resolves two of the unknowns. The problem of interaction order needs to be addressed, since it has been shown that overall first order involving either sodium or iron (historically the most important elements in slagging) has not been successful. An overall second order has been selected for application in this study. The most reasonable values for n and m in this scheme are one. The final problem is in determining A and B, the coal and coal ash constituents. The selection of A and B is not obvious and will be determined via trial and error with those resulting in the desired profile considered further. The interactions will be plotted as a function of the percent Jacob's Ranch in the blend. Where available the actual blend data points will also be included on the graph to compare the predicted value with the actual data.

There is more than one basis to calculate these interactions. The first and simplest is to assume that the relative amounts of ash contributed by each coal are the same. This means that the interaction is just the product of the values determined for the percentages of the oxides in the ash. A more realistic approach is to employ an ash correction factor to account for the two coals have differing ash contents. This correction factor is based on equal weights of the coals (or blends) being burned. A further correction may be used to account for differing heating values for the coals to produce the same heat output. A linear relationship between the pure coal heating values for the heating values of blends has been used. The actual effect of this correction factor will be to shift the curve towards the Clovis Point axis (0% JR).

Those curves with the desired profile are shown in Figures 2 through 5. Table V summarizes the interactions that showed the desired profile for any one of the above methods. Those interactions that are of most interest involve sodium or iron. These elements have been considered most influential in the formation of fireside deposits. Hence, these interactions support work done with pure coals.

CONCLUSIONS

This work is preliminary and involves only the two coals used at PSO where the blending problem was observed. Further work in this area is clearly necessary. However, the results clearly indicate that an overall second order reaction analogy can show an optimum as a function of coal blend which previous slagging prediction methods could not do. Efforts are continuing to evaluate interaction for other blending problems in hopes of obtaining a correlation which will be predictive for any coal blend.

REFERENCES

1. Zecchini, E. J., Masters Thesis, Oklahoma State University, 1986.

2. Lehman, D., "Slagging Experiences while Blending Wyoming Coal," Internal Report, Public Service Company of Oklahoma, Northeast Station, Oologah, Oklahoma, 1983.

3. Lee, G. K. and H. Whaley, Journal of the Institute of Fuel, 190, 1983.

4. Dooley, R. B. and V. Chacinski, Proceeding of the American Power Conference, 43, 106, 1981.

5. Raask, E., Mineral Impurities in Coal Combustion, Hemisphere Publishing Corp., New York, 1985.

6. Personal Communication from Williams Brothers Laboratory, Analysis of Jacob's Ranch and Clovis Point Coals, 1984.

TABLE I
STANDARD SLAGGING CORRELATION SUMMARY

	Williams Brother Data			This Study HTA Data		
Index	JR	Blends	CP	JR	Blends	CP
Silica Ratio	MS	MS	MS	HS	HS	HS
$\%Na_2O$	MS	MS/HS	HS	MS	MS/HS	HS
$\%Fe_2O_3$	LS	LS	LS	LS	LS	LS
Na Equivalent	LS	LS	LS	LS	LS	LS
R_b/a	LS	LS	LS	SS	SS	SS
Fy	MS	MS	MS	MS	HS	HS
Fs'	LS	LS	LS	LS	LS	LS

ND = Not Determined
LS = Low Slagging
MS = Medium Slagging
HS = High Slagging
SS = Severe Slagging

TABLE II
PROXIMATE ANALYSIS OF PURE COALS

Jacob's Ranch			
Analysis (wt%)	As Received	Moisture Free	Moisture and Ash Free
Moisture	25.44	****	****
Vol Matter	36.55	49.02	53.95
Ash	6.81	9.13	****
Fixed Carbon	31.70	41.85	46.05
H.H.V. Btu/lb	8,863	11,886	13,081
Clovis Point			
Analysis (wt%)	As Received	Moisture Free	Moisture and Ash Free
Moisture	31.32	****	****
Vol. Matter	33.85	49.28	54.11
Ash	6.14	8.94	****
Fixed Carbon	28.69	41.78	45.89
H.H.V. Btu/lb	8,014	11,668	12,813

Data from Williams Brothers Laboratories

TABLE III
JACOB'S RANCH ASH ANALYSIS

Component	Williams Brothers	This Study HTA
Iron as % Fe_2O_3	7.15	5.93
Calcium as % CaO	14.22	19.43
Magnesium as % MgO	3.15	4.75
Sodium as % Na_2O	0.68	0.76
Potassium as % K_2O	1.37	0.33
Silicon as % SiO_2	46.38	45.45†
Aluminum as % Al_2O_3	13.81	15.04
Titanium as % TiO_2	1.15	N.D.
Phosphorus as % P_2O_5	1.11	N.D.
Sulfur as % SO_3	6.05	N.D.
% Ash in the Coal	6.81	6.40

N.D. = Not Determined
† = By Difference

TABLE III
(Continued)

Clovis Point Ash Analysis

Component	Williams Brothers	This Study HTA
Iron as % Fe_2O_3	4.29	3.94
Calcium as % CaO	14.64	21.93
Magnesium as % MgO	3.12	5.58
Sodium as % Na_2O	1.08	1.66
Potassium as % K_2O	1.45	0.10
Silicon as % SiO_2	50.24	44.71†
Aluminum as % Al_2O_3	13.55	15.04
Titanium as % TiO_2	0.95	N.D.
Phosphorus as % P_2O_5	1.56	N.D.
Sulfur as % SO_3	4.53	N.D.
% Ash in the Coal	6.14	7.0

N.D. = Not Determined
* = Negligible
† = By Difference

TABLE IV
ASH COMPOSITION OF SELECTED BLENDS

a) High Temperature Ash (HTA)

Component	100%JR	75%JR-25%CP	50%JR-50%CP	25%JR-75%CP	100%CP
Fe_2O_3	5.93	4.72	4.49	3.94	3.94
CaO	19.43	20.14	20.62	21.15	21.93
MgO	4.75	5.15	5.25	5.35	5.58
Na_2O	0.76	1.04	1.18	1.44	1.66
K_2O	0.33	0.27	0.22	0.16	0.10
SiO_2	45.45†	46.21†	45.52†	45.40†	44.71†
Al_2O_3	15.04	14.76	15.04	15.04	15.04
TiO_2	N.D.	N.D.	N.D.	N.D.	N.D.
P_2O_5	N.D.	N.D.	N.D.	N.D.	N.D.
SO_3	N.D.	N.D.	N.D.	N.D.	N.D.

* = Negligible
† = By Difference

TABLE V
POSSIBLE INTERACTIONS FOR SLAGGING PREDICTION

	Interaction Williams Brothers Data			This Study HTA		
	Uncorr.	Ash Corr.	Heat Corr.	Uncorr.	Ash Corr.	Heat Corr.
Na * Fe	DP	DP	DP	NP	NP	NP
Na * K	NP	NP	NP	DP	DP	DP
Fe * P	NP	NP	NP	DP	UP	UP
Na * S_{coal}	NP	DP	NP	NP	NP	NP
Na * S_{ash}	NP	UP	NP	NP	ND	NP

NP = No Peak
DP = Desired Profile
UP = Undesired Profile

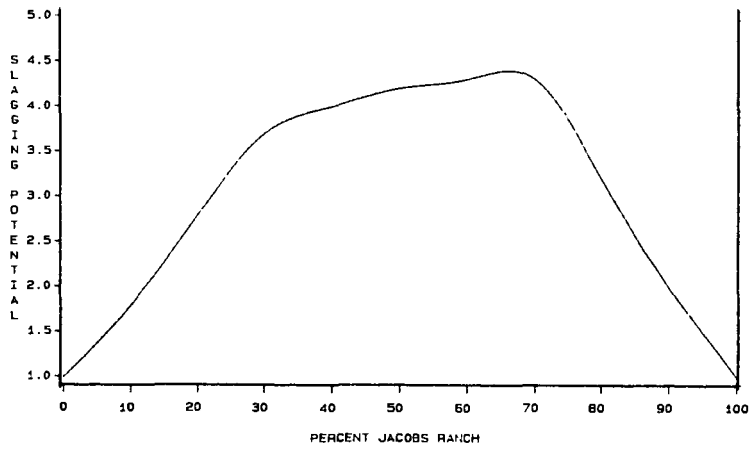

Figure 1. Desired Slagging Index Profile as a Function of Blend

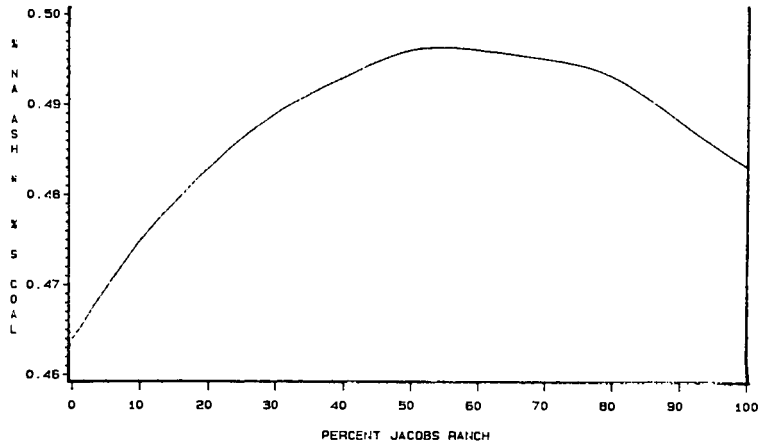

Figure 4. Ash Corr. 2nd Order Interaction of Na and S(coal)
(Williams Brothers Data)

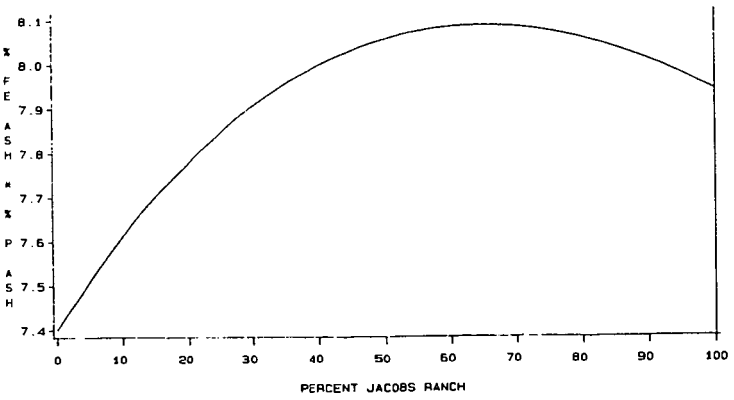

Figure 5. Heat Corrected 2nd Order Interaction of Fe and P
(Williams Brothers Data)

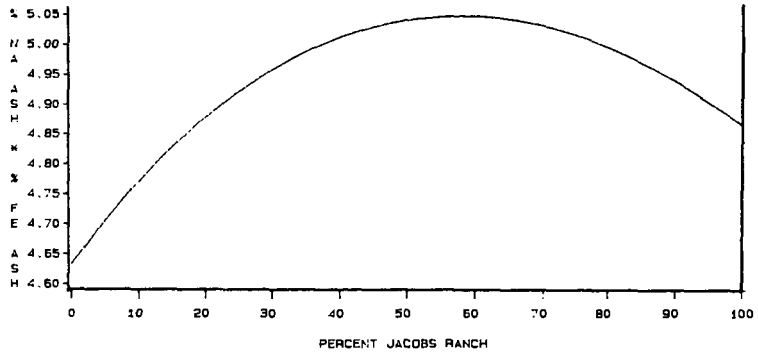

Figure 2. Uncorrected 2nd Order Interaction of Na and Fe
(Williams Brothers Data)

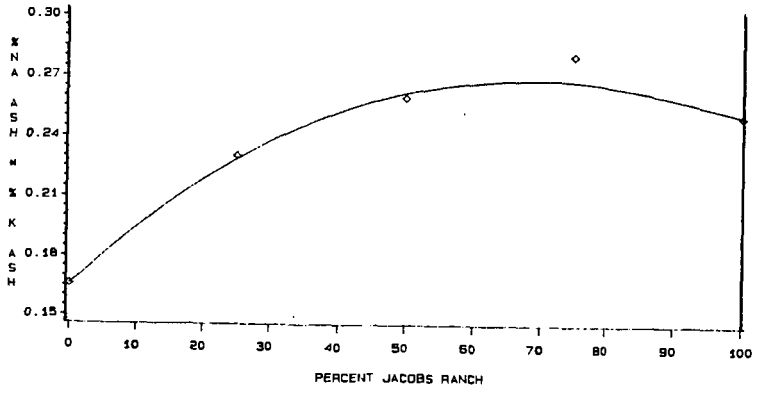

Solid line= This Study Predicted
Diamond= This Study Actual Data

Figure 3. Uncorrected 2nd Order Interaction of Na and K

THE EFFECT OF SODIUM ON DEPOSITION IN A SIMULATED COMBUSTION GAS TURBINE ENVIRONMENT

Jeffrey S. Ross and Rodney J. Anderson
U.S. Department of Energy
Morgantown Energy Technology Center
Morgantown, West Virginia 26505

Ramamurthy Nagarajan
Department of Mechanical Engineering
West Virginia University
Morgantown, West Virginia 26506

ABSTRACT

The effect of gas phase alkali concentration on the adhesion properties of micronized coal has been studied using a laboratory-scale entrained reactor capable of accelerating the combustion products of an injected coal-air mixture to the velocities observed in a combustion gas turbine. Alkali metal sulfates are reputed to act as liquid "glue" binders which promote inorganic deposit formation under these conditions. In this study, the concentration of alkali was varied by utilizing a series of naturally occurring coals (Arkwright Pittsburgh bituminous, Spring Creek Montana subbituminous, and North Dakota lignite), and by doping Arkwright coal samples with sodium benzoate. Measured sticking coefficients (i.e., the mass fraction of incident ash which sticks to a deposition target) obtained from this series exhibited trends consistent with the glue hypothesis and with the amount of liquid phase sodium sulfate predicted by equilibrium thermodynamic and vapor deposition rate calculations. Thus, between the melting point and dew point of sodium sulfate, higher sodium concentrations in the coal feed resulted in enhanced sticking. Below the sulfate melting point, the sodium concentration had no effect. These measurements provide a confirmation of the glue-like behavior of sodium sulfate in enhancing deposition rates and represent the first successful probing of the effect of an individual element upon the properties of fly ash originating from natural and chemically doped fuels under gas turbine combustor temperature and velocity conditions.

INTRODUCTION

One purpose of the U.S. Department of Energy's Fossil Energy Program is the development of technology for use of fossil fuels in the production of energy for domestic consumption. As a part of that program, the Morgantown Energy Technology Center has initiated a program to examine deposition effects in coal-fired heat engines, with the final objective being the development of techniques to mitigate the deposition problem in direct coal-fired gas turbines. This paper reports results from an effort, as a part of that program, to sepa-

rate the deposition problem from erosion and corrosion and to identify the relationship between deposition and the various chemical constituents in coal.

The use of coal and coal-derived fuels in direct-fired gas turbines provides an attractive alternative to other fuel sources such as petroleum or natural gas. Advantages of coal-based direct-fired turbine systems are the increase in efficiency provided when steam vaporization is removed from the energy production cycle, low capital costs for construction of moderate capacity systems, and a readily available inexpensive fuel. Limitations to the use of coal include dry handling costs and the large fraction of non-combustible material occluded within the coal matrix. Impurities can damage turbine components by a combination of erosion, corrosion, and deposition. These three complications can result in increased maintenance costs and/or losses in cycle efficiency due to either deposit buildup on the airfoils or the imposition of filtration equipment to prevent the problems. The effect of dry handling on the use of coal derives from two sources. First, the technology of dry fuel is considerably different from that of liquid feeding processes. Thus, power plants equipped for diesel or petroleum are not equipped to utilize coal, except perhaps as a coal-water mixture (CWM). However, the formulation of a CWM requires significant grinding of the coal and represents an added expense. Also, the problems of erosion, corrosion, and deposition all require grinding and/or beneficiation of the coal in order to meet gas turbine particulate operating specifications. If these problems can be solved, coal-based plants based on gas turbines can have a distinct competitive price relative to alternatives such as oil, natural gas, or petroleum.

The context of the present study derives from the observation that deposit growth may be promoted by the presence or formation of a liquid layer on the surfaces of ash particles (1,2,3,4). The liquid layer may consist of sodium (or other alkali) sulfate(s) which, due to rapid cooling arising from the expansion out of a gas turbine nozzle, can condense on the surface of an ash particle or on a component surface (rotor or stator blade). The condensation mechanism may be either heterogeneous as observed by Liang, et al. (5), in a recent binary nucleation study or homogeneous as suggested by the calculations of Ahluwalia, et al. (6). Regardless of the mechanism of deposition, experimental determinations of the elemental composition of ash particles have confirmed that surface enrichment does occur on the outer surfaces of fly ash particles (7). In fact, such observations have led to the suggestion that the injection of small particles into combustion turbines could have a mitigating effect on liquid-assisted deposition by acting as sodium gettering sorbents (8).

This set of observations has led to our determination of the "sticking coefficients" of a variety of coals under a wide range of conditions. Portions of this work have appeared as preliminary communications in which the qualitative effects of target temperature, reactor temperature, particle velocity, and coal composition have been discussed (9,10,11). We have now merged our previous deposition results with new observations made on sodium-doped coals and, in an effort to rationalize our observations and predict the sticking behavior of other coals, present those observations within the framework of a preliminary theory of molten glue-assisted deposition (12).

EXPERIMENTAL

The deposition tests were performed in a laboratory-scale entrained reactor (LETR) which consisted of a mass flow controlled air flow circuit, a particle injection system, a high-temperature furnace, a deposition target assembly, a filtration assembly, and a set of temperature and pressure diagnostics interfaced to a personal computer (Figure 1). The system attempts to simulate deposition processes at the leading edge of a gas turbine. To accomplish this, coal particles are entrained from a fluidized bed feeder and transported into the combustion zone (muffle tube H [Figure 1]) of the LETR. Combustion of the coal leaves the occluded inorganic material entrained as "ash" particles in the hot gas stream. These particles are, in turn, accelerated through a pinhole nozzle located at the end of the muffle tube to velocities in excess of 100 m/s. The degree of acceleration depends upon the temperature of the gas, the pressure drop across the nozzle, and the nozzle diameter. The high velocity particles then impinge upon a platinum target placed normal to the downflow of the gas-particle mixture. Target temperature is measured by radiation pyrometry. The sticking coefficient of the particular sample is obtained as the fraction of ash impinging on the target that actually adheres to the target. A detailed description of the LETR and the typical operating procedure are given below.

Particle Injection System

The particle injection system consisted of a TSI Model 3400 fluidized-bed aerosol generator (FBAG), a source of dry mass flow controlled compressed air, and a sample splitter, also mass flow controlled, in series with a vacuum pump. Prior to an experiment, the sample compartment of a TSI Model 3400 fluidized-bed aerosol generator was charged with about 10 grams of coal. All coal samples were ground to below -400 mesh (< 40 microns) to facilitate entrainment by the carrier gas. A small motorized conveyor transferred the coal particles into a 1.5-inch diameter bed that was filled with 100 grams of clean copper beads, which served to break up coal agglomerates. A dry air stream was used as both the fluidizing gas and the entrainment gas. The volumetric flow rate of the gas was mass flow controlled at 14 liters per minute, with 80 percent of the flow directed through the bed and the remainder used to purge the particle conveyor. A mass flow controlled aspirator near the entrance of the furnace served to limit the total flow of particle-laden gas to the reactor to below 5.0 liters per minute. The remainder of the gas was exhausted through a filtration system. This throttling was required to hold the nozzle pressure drop within safe limits.

Furnace Assembly

The furnace was an Astro Industries Model 1000 vertical graphite element tube furnace equipped with a helium purge gas system and an alumina muffle tube assembly. An alumina nozzle (25 mm length, 0.127 mm diameter) was cemented into the muffle tube so that the nozzle exit was 2.5 inches from the exit of the muffle tube. The temperature of the muffle tube was estimated with the aid of two thermocouples, one of which was held in contact with the muffle tube, while the other monitored the temperature adjacent to the heating element. Heating of the tube was accomplished by radiation and conduction through the helium purge gas, which also prevented oxidation of the graphite elements. A set of profiles of the temperature at the center line of the muffle tube (Curves a-c [Figure 2]) obtained with no acceleration nozzle in place were consistent with laminar flow through the furnace.

Deposition Target Assembly

The platinum target disks (0.25 mm thick, 5 mm diameter) were supported on an Inconel pedestal (Figure 3) bolted to the bottom of the furnace assembly. Pedestal height was adjusted by a series of stainless steel shims in order to position the target at approximately one nozzle diameter (1.27 mm) from the nozzle exit. The pedestal was hollow and contained a quartz lens which focused infrared light emitted from the target onto the entrance of a bifurcated fiber optic bundle. The two legs of the fiber bundle were directed to optical filters with wavelengths of 902.5 nm (14 nm bandwidth) and 1,039.5 nm (19 nm bandwidth), respectively. The transmitted signals were detected by photodiodes, amplified, and output as millivolt signals to an Apple computer. This permitted determination of the target temperature by radiation pyrometry. The targets were weighed to within +/-3 micrograms before and after a deposition run and the deposit weight determined by difference. Deposit weights were typically in the range of 20 to 100 micrograms.

Filtration Assembly

The arrival rates of ash particles at the target surface were estimated by replacing the target with a filtration assembly fabricated from a combination of a Gelman stainless steel filter holder and a 4-inch porous alumina cylinder. An air flow of 2.0 liters per minute through the porous cylinder provided a radial pressure which prevented deposition of ash vapor and/or particles except on a silver membrane filter (Osmonics, Inc.) held in place by the filter holder. A vacuum pump downstream from the filter was used to balance (via mass flow control) the sampling rate through the filter with the gas input from the furnace exit and the filter inlet. The balance was required in order to prevent escape of particles from the filter and to prevent thermal shock to the muffle tube due to aspiration of room temperature air. In a typical deposition run, three to five filter samples were obtained and used to establish an average ash arrival rate (10 to 80 micrograms per minute, depending on the settings of the particle injection system).

Preparation of Sodium-Doped Coals

A known amount of sodium benzoate (Fischer Scientific) was dissolved in excess (> 150 mL) of HPLC grade methanol (J. C. Baker) and the clear solution added to a round-bottomed flask containing 10 grams of Arkwright Pittsburgh bituminous coal. The methanol was then removed using a rotary evaporator. The ground glass joints of the evaporator were ungreased to avoid contamination of the coal with silicon. The product consisted of a grayish-black powder with some small whitish lumps of (presumably) pure sodium benzoate occluded within the coal matrix. This material was then ground to pass a 400 mesh screen.

Typical Deposition Procedure

The coal sample of interest was loaded into the FBAG and the entrainment gas flow and aspiration rates adjusted such that the pressure drop across the acceleration nozzle in the muffle tube was within safe limits and was providing a gas stream of high velocity. During this process, the coal particles were removed from the gas flowing to the reactor by an absolute filter (close Valve 1, open Valves 2 and 5 [Figure 1]) to prevent contamination of the cold furnace. After the muffle tube (heated at a rate of 200°C per hour) and the

deposition target reached their appropriate test temperatures, the filter was removed from the flow path (open Valve 1, close Valves 2 and 5 [Figure 1]) and the particle-laden flow was directed into the muffle tube. After collection of several samples, the filtration assembly was removed and the absolute filter reinserted into the particle flow stream. The target assembly was then affixed to the furnace and the target allowed to reach thermal equilibrium in the absence of particles. Blank runs were performed and indicated that deposition ceased when the absolute filter was in the flow path. The absolute filter was then removed from the flow path and the deposition process allowed to proceed for about 1 hour, after which the target was isolated from particles, the target assembly removed, and the target weighed.

Data Acquisition

Furnace temperature, target temperature, reactor coolant temperature, and nozzle pressure drop measurements were recorded continually during each test by an appropriate interface to a personal computer. For high-speed measurements of the nozzle pressure drop (which determines the nozzle exit particle/gas velocities) and of the target temperature, an IBM PC-AT was employed as a data acquisition device. The IBM interface hardware included a Data Translation DT2805 12 bit A/D board and a DT2807 interface board. Data was acquired by means of a FORTRAN program which employed subroutines from PCLAB and Wiley's FORTRAN Scientific Subroutines, and Fifty More FORTRAN Scientific Subroutines.

RESULTS AND DISCUSSION

This combined experimental and theoretical report deals only with the effects of deposition in direct-fired coal-burning systems and, therefore, it is appropriate to first outline the justifications for neglecting or removing other effects during the subject experiments (e.g., erosion and corrosion). Also appropriate is a brief discussion of the chosen target design and its relationship to deposition phenomena.

Industrial combustion turbine research has shown that if the gas stream particle size is kept below 10 microns, then deposition and corrosion, not erosion, are the effects responsible for limiting the useful lifetime of a gas turbine (13). This observation was used to decouple erosion from LETR experiments; only micronized coal samples (< 400 mesh) were used. An added benefit of micronized coal is that the particles are easily entrained and when moving through the apparatus, they follow the flow paths of the gas (i.e., they have a negligible inertial slip velocity). This helps to eliminate deposition of slag within the reactor which could develop in a drop tube by overloading of the combustion zone. Some of the detrimental effects of slagging in a test reactor are changing combustion heat transfer properties, a buildup of liquid/glass phase species of unknown vapor pressure that could contaminate future samples, and variation within sample runs of the equilibrium vapor pressures of slag components. By employing the entrainment principle, the combustion zone loading is sufficiently low to avoid slagging.

The decoupling of corrosion from LETR experiments was accomplished by fabricating the targets from platinum metal. This is justified by the inertness of platinum toward oxidation, poor affinity for adsorption of gases such as carbon monoxide and carbon dioxide, and resistance to attack by hot corrosive liquids (14,15,16). An important qualification which has not been

addressed is the utility of deposition data in absence of the competing effects of erosion and corrosion.

Conversely, after combustion of the coal particles, it is desirable to force as much of the ash as possible to impact upon the target. The use of a target placed normal to the gas stream at the nozzle exit satisfies this condition if the target diameter is much larger than the nozzle diameter and if the target is located less than five nozzle diameters from the nozzle exit (17). This design was employed in the LETR and imposed the requirement of zero velocity (both particle and gas) at the target surface. The overall result is that a stagnation point has been created at the intersection of the target and the expanding gas-particle jet. The significance of this is that particle arrival rates and vapor deposition rates are at or near their maximum values under stagnation conditions which should result in the observation of the maximum effect of an additive upon coal ash deposition properties. Finally, the leading edge of a gas turbine blade also has a stagnation line configuration.

Deposition data was obtained for the following coals: Arkwright Pittsburgh bituminous (APB), Spring Creek Montana subbituminous (SCMS), AMAX-II (cleaned) Kentucky bituminous (KB), North Dakota lignite (NDL), and acid-washed North Dakota lignite (AWL). The ultimate analyses for these coals are presented in Table 1. Figure 4 shows a plot of the "sticking coefficient" (mass fraction of material adhering to the target) obtained for these coals at a variety of target temperatures.† These data are reproducible to within about ± 20 percent. Although NDL has the highest ash content and the highest sticking coefficient, the correspondence between ash content and sticking coefficient does not continue for the other coals. Similarly, although increased sodium content may increase the fouling tendencies of coal, a simple (i.e., linear) correspondence between sodium and sticking coefficient does not appear to be operative here. Furthermore, the ordering of the sticking coefficients is not explained by simple parametric indices such as the fouling index (10,18). Thus, although the extreme cases agree with predictions based on coal ash content, alkali level, or fouling index, a more detailed description of coal ash sticking must be employed in any rational analysis of ash deposition.

The approach offered here is to use the ash analysis as an input for chemical equilibrium thermodynamic calculations to determine the amount of liquid glue likely to be present in the deposit at a given deposition temperature. The quantity of liquid phase was, in turn, used as input for the sticking code (vide infra) and directly compared to the observed sticking coefficients (Figure 4). The first step in our predictive procedure is calculation of combustion deposit compositions based on the premise that the condensed solution phases indicated by an equilibrium thermodynamic analysis are the ones likely to appear on the target surface. The NASA CEC free-energy minimization computer program (19) is widely used toward this end in spite of several numerical difficulties associated with its newly acquired ideal solution capability; these are usually singular matrices and convergence problems

† There is no provision in the LETR to vary the target temperature independently of the combustion gas temperature; this makes it difficult to decouple the effects of the two temperatures on the sticking coefficient.

are encountered when condensed phases are added. Significant improvements (i.e., the addition of a phase rule check) have been incorporated in the PACKAGE code (20) which is, thus, essentially a more robust version of the CEC-solution code. Due to its demonstrable efficiency in analyzing the complex phase equilibria in coal conversion gas streams and cleanup devices, the PACKAGE program has been used to perform the equilibrium/thermodynamic computations presented here.

Having obtained the condensed liquid phase fraction and composition by exercising the PACKAGE code at the pressure, surface temperatures, and feed compositions of interest, the steady-state sticking coefficient, $\underline{s}$, of impacting fly ash particles is evaluated in the presence of the deposited liquid glue. This is done by means of a mechanistic theory of deposition (12) which incorporates impaction/diffusion interactions neglected in previous work. Briefly, the principles underlying this theory of "self-regulated" liquid-enhanced capture of supermicron ash may be stated as follows. The inertial impaction deposition rate will depend linearly on $\underline{s}$, but $\underline{s}$ itself will depend on the inventory (and physical properties) of "glue" available to each particle on the deposit surface layer. Therefore, the steady-state values of $\underline{s}$ and particle deposition rate must be obtained by solving a coupled nonlinear equation. This fundamental concept is discussed in more detail by Rosner and Nagarajan (12) and Ross, et al. (21).

In Figure 5, the PACKAGE-generated liquid-condensate mole fraction is plotted as a function of surface temperature for the four coals. The glue-liquid solution (assumed to be ideal) is comprised principally of aluminosilicates, silicates, oxides, and sulfates of calcium, potassium, sodium, aluminum, silicon, and titanium. Solid phases predicted to separate out include Al_2TiO_5, Al_2SiO_5, $CaAl_2Si_2O_8$, $CaSO_4$, Fe_2O_3, K_2SO_4, and SiO_2; these are relatively benign with respect to fouling and corrosion, although they could contribute to the erosion of surface material if they were encapsulated in particles larger than about 10 μm diameter. The plotted results show that a minimum fraction of feed material condenses as liquid for KB, while NDL experiences maximum liquid inundation. However, the Arkwright Pittsburgh and Montana subbituminous coals are inverted with respect to Figure 4. Thus, as with ash content, alkali level, and fouling index, the fraction of condensing material in the combustion product stream gives a reasonable qualitative indication of the sticking propensity of the coal-ash but does not correlate exactly with the sticking coefficient, $\underline{s}$. This demonstrates the inadequacy of a strictly thermodynamic analysis to predict the sticking coefficient and again hints at some unknown but vital piece of information required to provide an accurate gauge of deposition behavior. To address this problem, the thermodynamic analyses have been combined with the effects of mass transfer between the gas mainstream and the deposition surface, with the assumption that $\underline{s}$ depends primarily upon the relative arrival rates of ash particles and glue-liquid to the surface.

Using the thermodynamic data to provide the total condensed phase fraction at a given temperature and providing that data to a modified version of the self-regulated sticking computer code (based on the work of Rosner and Nagarajan [12]), calculated sticking coefficients can be obtained for each of the tested coals (Figure 6). Now the predicted ordering of coals with respect to their sticky nature is in line with experimental observation (i.e, NDL >

SCMS > APB > KB).† There is even good quantitative agreement in certain ranges of surface temperature. Discrepancies between the measured temperature dependence of $\underline{s}$ and the prediction may be accounted for by uncertainties in the experimental data collection procedure or limitations in the accuracy of the admittedly preliminary model for sticking or, most likely, both. For instance, the theory does not model the process of ash softening due to high-energy impact (12) in sufficient detail. Improvements to the present theoretical model will be made as fresh data or insight into the physical processes become available.

Another facet of the LETR deposition tests was to study the effectiveness of metallic additives in mitigating deposition-related problems as well as to identify troublesome coal constituents that need to be selectively removed. There are a few precedents reported in literature for our additive strategy. Nagarajan (22) has investigated the use of trace additives to minimize turbine blade "hot corrosion" due to molten alkali sulfate condensation from jet fuel combustion gases. Rathnamma and Nagarajan (23) have studied high-temperature corrosion control by metal additions to vanadium-contaminated fossil fuels. A recent study conducted by Battelle Columbus Laboratories evaluated the use of chemical additives to reduce gas-side fouling and corrosion in oil- and coal-fired systems (24). Attempts have been made to counteract high-temperature fouling with $CaCO_3$ and with boron-, manganese-, and magnesium-based additives. The Saskatchewan Power Corporation has used limestone to combat ash fouling in boilers fired with lignite (24). Austin (25) has examined the effect of sodium on the strength of sintered ash mixtures. The effects of added alumina and emathalite particles were investigated by Shannon (26) in an effort to reduce alkali concentration by gettering sodium in the combustion process.

However, even when such tactics have proved to be successful, the reasons for the success have not been clearly understood, particularly in coal combustion applications. In order to address this deficiency in our appreciation of the roles played by the individual additives, our research does not merely acquire empirical information regarding the "best" additive, but attempts to gain insight into what makes the "best" additive so effective.

The first round of deposition tests in the LETR were conducted with sodium benzoate as the metal-containing additive. Upon addition of a 30-fold excess of sodium to a sample of APB coal, the sticking coefficient at 1,107 K was raised from about 0.15 to about 0.6, a four-fold magnification. This is consistent with the formation of a larger condensed phase fraction following the addition of a large excess of sodium (Figure 9). Sticking coefficients obtained for lower target temperatures (< 1,000 K) showed no change upon addition of the sodium, which is expected because the liquid phase fraction is not sensitive to sodium level as the temperature decreases significantly below the melting point of sodium sulfate (1,157 K). Future experiments will utilize dopants containing aluminum, magnesium, calcium, and other metals.

---

† The lower ash content of the Spring Creek coal relative to the Arkwright coal implies a larger inventory of glue available per impacting particle and, hence, enhanced sticking coefficients.

An equilibrium thermodynamic analysis of the effect of these additives on condensed liquid formation during the combustion of the APB coal in the LETR has been carried out and the results are displayed in Figures 8 and 9. In these figures, the mole fraction of the molten solution condensate in the combustion product mixture is plotted against additive concentration, the axes being nondimensionalized with respect to corresponding reference Arkwright coal values. From Figure 8, it appears that iron, silicon, calcium, and aluminum are all effective suppressants of glue-liquid formation, with aluminum being the most effective of these. Figure 9 indicates that potassium, sulfur, and titanium are bad additives (i.e., adulterants that should be removed from the coal to reduce its fouling tendency). Sodium and magnesium additions do not result in monotonic trends; 10 times as much sodium in the seeded coal as in the reference coal results in a minimum solution phase fraction, and about 10 times as much magnesium results in maximum. Since, on the basis of the ash deposition theory (12), these phase fractions correlate fairly well with predicted sticking coefficients, an optimum level of each additive that minimizes sticking may be determined on the basis of these plots. However, the added mass loading introduced may increase erosion of machine components even though fouling is alleviated. These considerations, while of secondary importance to this paper, should certainly be included in a more ambitious life prediction venture.

The influence of sodium and aluminum additives on the predicted sticking coefficient at a LETR target temperature of 1,107 K is displayed in Figure 7. With the addition of sodium beyond 10 times its level in the reference Arkwright coal, $\underline{s}$ begins to increase until it reaches a value of about 0.6 at 30 times the reference value of sodium concentration which is in reasonably good quantitative agreement with the experimentally measured sticking coefficient under these conditions. In the aluminum added case, $\underline{s}$ drops to about a third of its value of 0.6 (corresponding to combustion of sodium-enriched coal) with the addition of only about five times as much aluminum as is present in the reference Arkwright coal and remains nearly constant with further increases in the aluminum concentration. The predictions in Figure 7 also suggest the interesting possibility of decreased $\underline{s}$ upon addition of smaller quantities of sodium; a fact which no doubt contributed to the lack of correlation between alkali level and sticking coefficient. These trends will be explored as testing of sodium- and aluminum-doped coals continues. A confirmation, based on such comparisons, of the accuracy of our theory in predicting sticking behavior of coals will imply the availability of a powerful predictive tool that will enable us to evaluate different coals with respect to their fouling characteristics and aid in the development of suitable seeding/cleanup techniques to minimize ash deposition.

To assist in acquisition of the sticking data, a new deposition test facility has been fabricated. It is performance rated at 12 atmospheres as opposed to the previously available atmospheric pressure LETR unit and contains three sets of optical access ports which permit the use of non-intrusive optical diagnostic equipment. The combustion/deposition entrained reactor (CDER) has a higher throughput, a wider range of accessible velocities and temperatures, a temperature-controlled target assembly, and an extensive set of automated control features. In addition, the target assembly may be modified to examine impaction geometries other than 90° and thereby extend our studies beyond the stagnation point to model deposition on the pressure and vacuum sides of a gas turbine blade. Some of the code modifications under way include an improved

description of deposit thermal conductivity (21), incorporation of deposit shape effects and differential sticking coefficients (obtained from high-speed photography of growing deposits), addition of a subroutine to allow glue uptake by particles during their transit across the boundary layer (this may be studied experimentally by methods similar to those of Liang [5]), consideration of simultaneous deposit erosion (i.e., negative instantaneous sticking coefficients), and incorporation of phase change processes and particle-glue diffusion within already formed deposits (possibly accessible by in situ specular reflectance FTIR).

CONCLUSIONS

Predictions of ash fouling behavior have previously been made based on a variety of empirical or thermodynamic factors. Unfortunately, neither the empirical parameters (i.e., sodium level, fouling index) nor the thermodynamics-based liquid phase fraction provided an adequate prediction of the sticking behavior of a given coal. However, by a combination of thermodynamic analysis via the PACKAGE code to obtain liquid phase fractions and the application of that data within the context of the self-regulated sticking concept (12), a fairly good comparison was obtained between predicted sticking values and experimental results. This was especially encouraging because the self-regulation concept is still in its developmental stages.

The overall objective of this research has been to suggest methods of mitigating the deposition process in direct coal-fired gas turbines and, thus, relieve the economic burdens of maintenance and aerodynamic efficiency loss. The good agreement between the simple equilibrium/mass transfer model and the sticking coefficients obtained in the LETR represents a first step toward that objective. Thus, given the ultimate analysis of a particular lot of coal, the propensity of that coal to form deposits in a boiler or gas turbine could be determined. In addition, specific coal cleaning procedures or coal additives could be recommended to mitigate the formation of deposits. A combined experimental and theoretical program has been initiated that extends the work presented here to provide a data base of standard coal, coal additive, and pure mineral sticking coefficients. In the course of these tests, the sticking model will be updated to better reflect conditions within actual gas turbines. Future manuscripts will provide detailed comparisons between the operational characteristics of real-life gas turbines and the deposition and combustion environments in the LETR and the CDER, and the relationships between sticking coefficients, turbine fouling rates, and actual as well as simulated turbine deposit compositions.

ACKNOWLEDGMENTS

This work was funded by the U.S. Department of Energy's Fossil Energy Advanced Research and Technology Development Program. Jeffrey S. Ross acknowledges funding through the Oak Ridge Associated Universities Postdoctoral Training Program. The authors appreciate the assistance of Dale W. Wilson, Jr. in construction of the apparatus, David R. Goff in the design of the two-color optical pyrometer, and Cindy J. Romanowski for the collection of some of the experimental data.

DISCLAIMER

The use of trade names by the authors of this paper does not imply the endorsement of any product, apparatus of configuration by the authors, the U.S. Department of Energy, or by Oak Ridge Associated Universities. Such references are made only for the purpose of clarity.

REFERENCES

1. Cross, N.L., and R.G. Picknett, "Particle Adhesion in the Presence of a Liquid Film," The Mechanism of Corrosion by Fuel Impurities, H.R. Johnson and D.J. Littler, eds., Butterworths, London, pp. 383-390 (1963).

2. Wibberley, L.J., and T.F. Wall, "Alkali-Ash Reactions and Deposit Formation in Pulverized Coal-Fired Boilers: The Thermodynamic Aspects Involving Silica, Sodium, Sulphur, and Chlorine," Fuel, 61, 87-92 (1982).

3. Wibberley, L.J., and T.F. Wall, "Alkali-Ash Reactions and Deposit Formation in Pulverized Coal-Fired Boilers: Experimental Aspects of Sodium Silicate Formation and the Formation of Deposits," Fuel, 61, 93-99 (1982).

4. Wibberley, L.J., and T.F. Wall, "Deposit Formation and Sticky Particles from Alkali-Ash Reactions," Fouling and Slagging Resulting from Impurities in Combustion Gases, R.W. Breyers, ed., Engineering Foundation, New York, New York, pp. 493-513 (1983).

5. Liang, B., A. Gomez, J. Castillo, and D.E. Rosner, "Experimental Studies of Nucleation Phenomena within Thermal Boundary Layers -- Influence on Chemical Vapor Deposition Rate Processes," submitted to AIChE Journal.

6. Aluwalia, R., K. Im, C.F. Chuang, and H.K. Geyer, "Evolution and Deposition of Ash Particles in Coal-Fired Gas Turbines," Proceedings of the First Annual Heat Engines Contractors Meeting, May 1-3, 1986, pp. 317-325, DOE/METC/84-31(CONF-8405138--)(DE85001953).

7. Raask, E., "Creation, Coalescence, and Capture of Mineral Species in Coal Flames," J. Institute of Energy, 231-239 (1984).

8. Scandrett, L.A., and R. Clift, "The Thermodynamics of Alkali Removal from Coal-Derived Gases," Journal of the Institute of Energy, 391 (1984).

9. Anderson, R.J., C.J. Romanowski, and J.E. France, "The Adherence of Ash Particles from the Combustion of Micronized Coal," Research Report, DOE/METC-85/2007 (DE 85008600), October 1984.

10. Anderson, R.J., C.J. Romanowski, R.E. Conn, and R.A. Dennis, "Deposition Effects in the Combustion of Coal-Derived Fuels," Proceedings of the Advanced Research and Technology Development (ARTD) Direct Utilization Contractors Review Meeting, 252-264 (August 1985). DOE/METC-85/6027 (DE85013718).

11. Anderson, R.J., S.D. Woodruff, R.A. Dennis, and J.S. Ross, "Deposition Effects in the Pressurized Combustion of Coal-Derived Fuels," Proceedings of the Advanced Research and Technology Development (ARTD) Direct Utilization Contractors Review Meeting, September 1986, in Press.

12. Rosner, D.E., and R. Nagaranjan, "Toward a Mechanistic Theory of Deposit Growth from Ash-Laden Flowing Combustion Gases: 1. Self-Regulated Sticking of Impacting Particles in the Presence of Vapor- or Submicron Mist Glue," to be presented at the AIChE-ASME-ANS National Heat Transfer Conference, Pittsburgh, Pennsylvania, August 9-12, 1987.

13. Hoy, H.R., A.G. Roberts, and J. Stringer, "Combined-Cycle Power Plant Via Pressurized Fluidized-Bed Combustion," Proceedings of the Second Conference on Advance Materials for Alternative Fuel Capable Heat Engines," U.S. Department of Energy and Advance Fuel Research Institute, 2-115 (1985).

14. Satterfield, C.N., "Heterogeneous Catalysis in Practice," McGraw-Hill, New York (1980).

15. Klabunde, K.J., "The Chemistry of Free Atoms and Molecules," Academic Press, New York (1980).

16. Speight, J.G., "The Chemistry and Technology of Coal," Marcel Dekker, New York (1983).

17. Marple, V.A., and K. Willeke, "Impactor Design," Atmospheric Environment, 10, 891-896 (1976).

18. Ghosh, S.K., "Understanding Thermal Coal Ash Behavior," Mining Engineering, 158-162 (1986).

19. Gordon, S., and B.J. McBride, "Computer Program for Calculation of Complex Chemical Equilibrium Compositions, Rocket Performance, Incident and Reflected Shocks, and Chapman-Jouguet Detonations," NASA Sp-273, Interim Revision, March 1976.

20. Yousefian, V., M.H. Weinberg, and R. Haimes, "PACKAGE (Plasma Analysis, Chemical Kinetics, and Generator Efficiency): A Computer Program for the Calculation of Partial Chemical Equilibrium/Partial Chemical Rate Controlled Composition of Multiphase Mixtures Under One-Dimensional Steady Flow," Aerodyne Research, Inc., Report No. ARI-RR-177 (1980).

21. Ross, J.S., M. Ramezan, R.J. Anderson, and R. Nagarajan, "Prediction and In Situ Measurement of the Thermal Conductivity of Multiphase Fouling Deposits Formed in Direct Coal-Fired Combustors," to be presented at the ASME 1987 Winter Annual Meeting Session on Measurements in Combustion Equipment, Boston, Massachusetts, December 13-18 (1987).

22. Nagarajan, R., "Theory of Multicomponent Chemical Vapor Deposition Boundary Layers and Their Coupled Deposits," Dissertation Thesis, Department of Chemical Engineering, Yale University, May 1986.

23. Rathnamma, D.V., and R. Nagarajan, "High-Temperature Hot Corrosion Control by Fuel Additives," to be presented at the Tenth International Conference on Metallic Corrosion, Madras, India, November 7-11, 1987.

24. Marner, W.J., "Gas-Side Fouling," Mechanical Engineering, pp. 70-77, March 1986.

25. Tangsathitkulchai, M., and L.G. Austin, "Studies of Sintering of Coal and Ash Relevant to Pulverized Coal Utility Boilers," Fuel, 64, 86-92 (1985).

26. Shannon, S., MS Thesis, University of Pittsburgh, 1986.

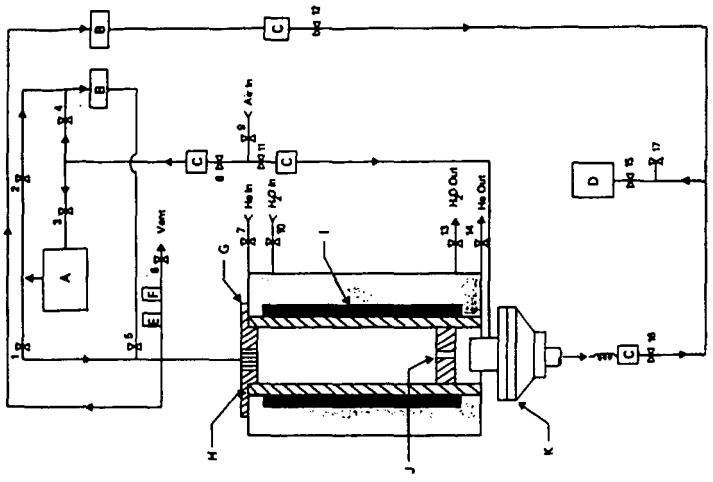

Figure 1. Laboratory Entrained Test Reactor (LETR) Schematic Drawing: A, Fluidized-bed aerosol generator; B, Absolute filters; C, Mass flow controllers; D, Vacuum pump; E, Pressure relief valve; F, Pressure transducer; G, Preheater with flow straightener; H, Alumina muffle tube; I, Graphite heating element; J, Acceleration nozzle; K, Filter holder.

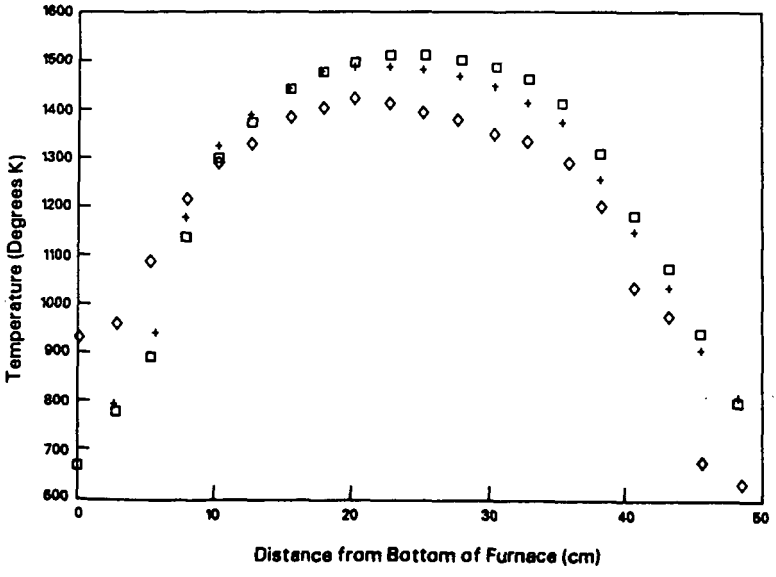

Figure 2. Temperature Profile in the LETR Without a Nozzle: □, 42 m Volts and 0.3 lpm; +, 42 m Volts and 1.0 lpm; ♦, 42 m Volts; and 3.0 lpm.

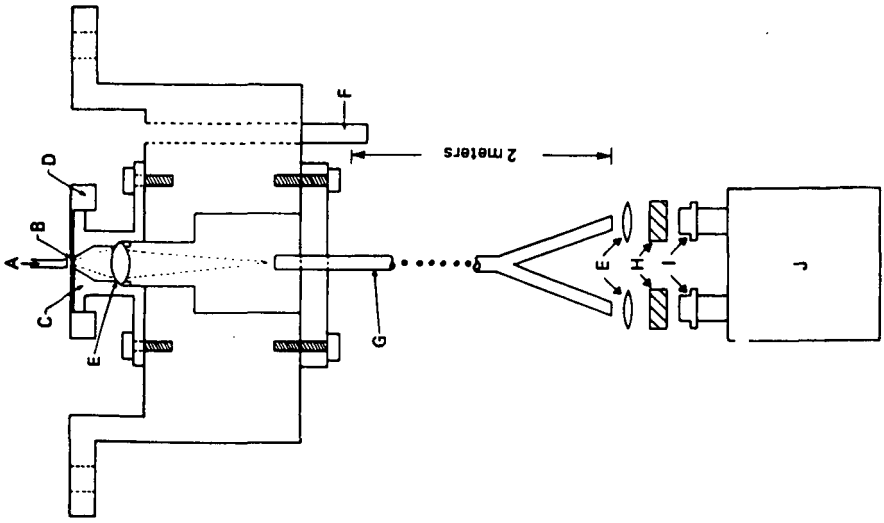

Figure 3. Target Assembly with Fiber Optic Pyrometer: A, Nozzle; B, Target; C, Target Pedestal; D, Target Retaining Ring; E, Lens; F, Exhaust; G, Fiber Optic; H, Optical Filter; I, Detector; J, Signal Amplifier, Electronics and Computer Interface.

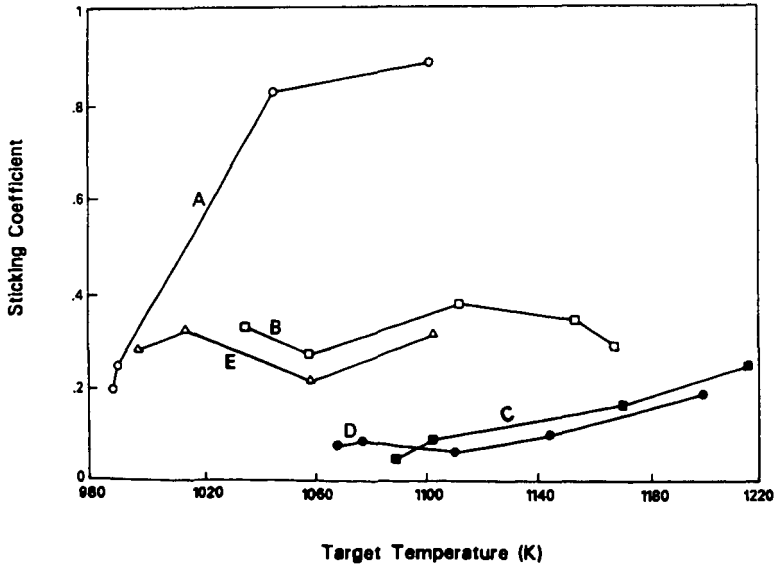

Figure 4. Measured Values of Sticking Coefficient Versus Target Temperature for Tested Coals: A, North Dakota Lignite; B, Spring Creek Montana Subbituminous; C, Arkwright Pittsburgh Bituminous; D, Kentucky (Cleaned AMAX-2) Bituminous; E, Acid Washed Lignite.

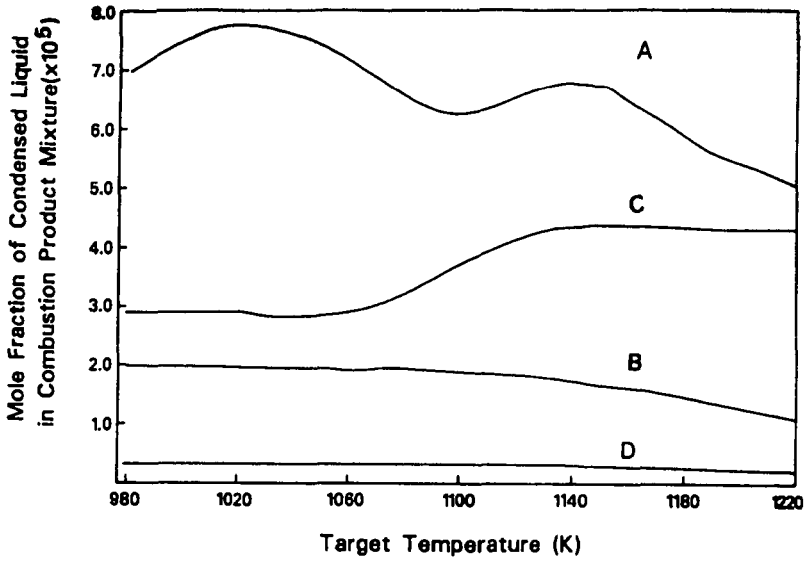

Figure 5. Predicted Values of Condensed Glue Fraction Versus Target Temperature for Tested Coals: A, North Dakota Lignite; B, Spring Creek Montana Subbituminous; C, Arkwright Pittsburgh Bituminous; D, Kentucky (Cleaned AMAX-2) Bituminous.

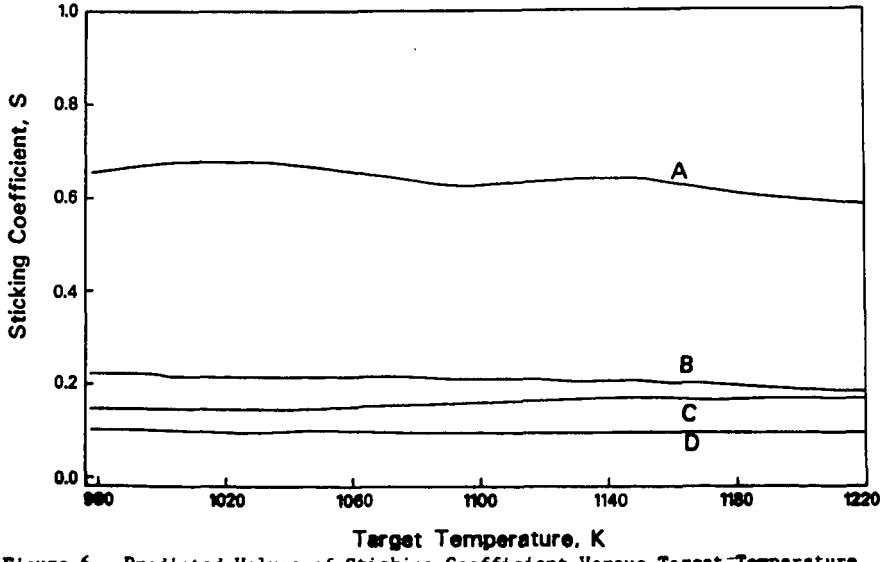

Figure 6. Predicted Values of Sticking Coefficient Versus Target Temperature for Tested Coals: A, North Dakota Lignite; B, Spring Creek Montana Subbituminous; C, Arkwright Pittsburgh Bituminous; D, Kentucky (Cleaned AMAX-2) Bituminous.

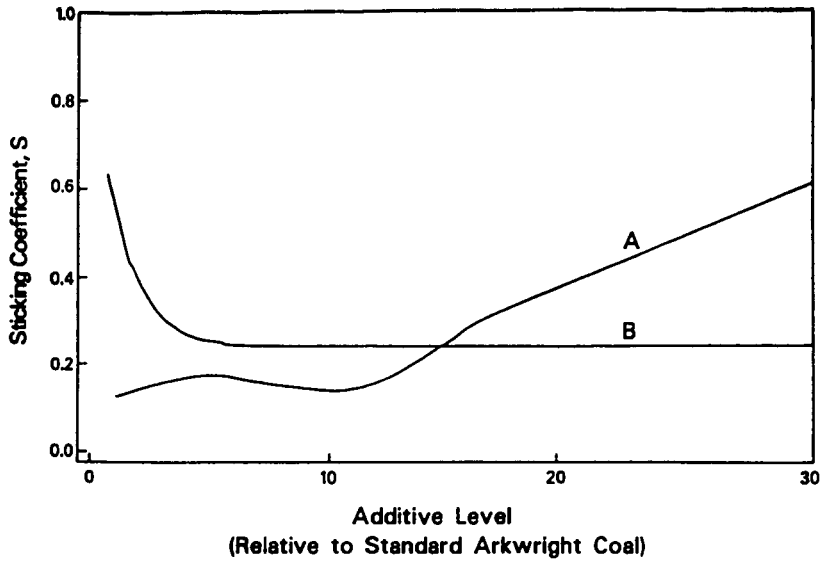

Figure 7. Predicted Effect of Additives on Impacting Ash Particle Sticking Characteristics in the LETR. Target Surface Temperature = 1107 K. A, Sodium; B, Aluminum.

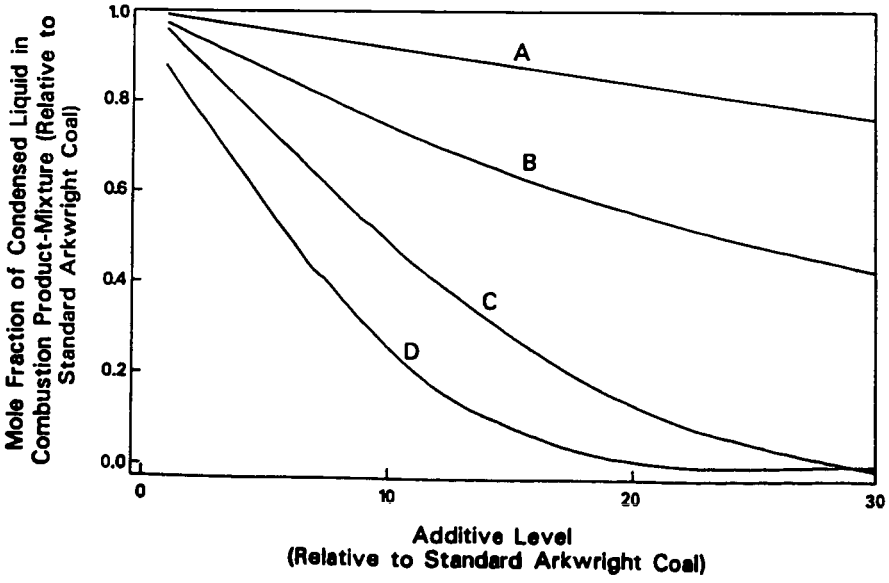

Figure 8. Predicted Effect of Additives in Supressing Condensation of Liquid Glue on the Target Surface in the LETR. Target Surface Temperature = 1107 K. A, Iron; B, Silicon; C, Calcium; D, Aluminum.

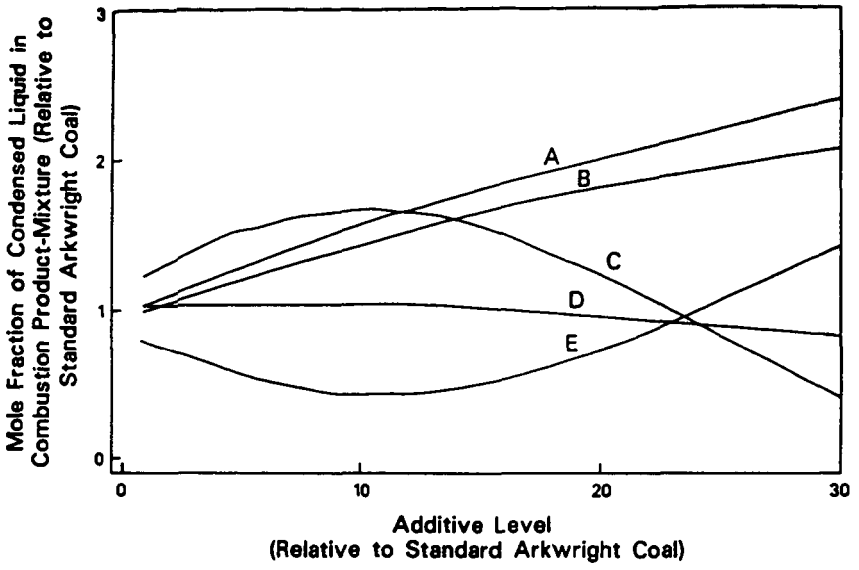

Figure 9. Predicted Effect of Additives on Condensation by Liquid Glue on Target Surfaces in the LETR. Surface Temperature = 1107 K. A, Potassium; B, Titanium; C, Magnesium; D, Sulfur; E, Sodium.

TABLE 1

Ash Composition of Coals Tested in LETR

COAL RANK	Arkwright Pittsburgh Bituminous	Kentucky (Cleaned) Bituminous	Spring Cr. Montana Subbituminous	North Dakota Lignite	North Dakota (Acid Washed) Lignite
% ASTM ash	6.93	0.68	2.30	20.45	16.05
Ash Comp.(Wt%)					
SiO_2	48.09	25.48	18.6	20.08	*
Al_2O_3	25.07	15.92	13.5	11.19	*
Fe_2O_3	10.95	32.35	4.7	13.19	*
TiO_2	1.27	7.77	1.3	0.48	*
P_2O_5	0.18	0.48	0.4	0.28	*
CaO	5.78	1.32	26.5	22.85	*
MgO	1.25	0.62	6.5	6.68	*
K_2O	1,16	0.30	0.1	0.32	*
Na_2O	0.90	9.53	13.1	8.26	*
SO_3	5.34	6.22	15.4	16.07	*

* An insufficient quantity of coal ash was available for quantitative analysis.

DESORPTION TURNOVER NUMBERS FOR THE CARBON-OXYGEN REACTION

Joseph M. Ranish
General Electric Company
Cleveland, OH 44112

Philip L. Walker, Jr.
The Pennsylvania State University
University Park, PA 16802

INTRODUCTION

For graphitic carbons reacting with O_2, it is well established that the C atoms in the gasification products originate from the active surface, the (11*l*) and (10*l*) planes [1,2,3,4,5,6]. Even when the basal plane is gasified, it is gasified at defects which expose C atoms in these planes [7]. The gasified atoms are produced via either or both of the reactions below depending upon the reaction conditions.

$$C_{sd}(O)(s) \xrightarrow{k_1} CO(g) \tag{1}$$

$$2C_{sd}(O)(s) \xrightarrow{k_2} CO_2(g) + C_{sd}(s) \tag{2}$$

The 'sd' subscript (strongly desorbing) in reactions 1 and 2 is used to show that only part of the active surface, the part comprised of C_{sd} surface atoms, is able to form the $C_{sd}(O)$ surface complex which is the precursor to the desorbed products. The rest of the surface oxygen complex is stable [8,9]. The fraction of the active surface which can form unstable surface oxides increases with increasing temperature. Because it is difficult to separate primary product CO or CO_2 from that produced by secondary reactions, a net desorption turnover number for C gasification, TON_C, will be used. It is defined in Equation (3) below as the atoms of C gasified per unit time per O atom of surface complex and incorporates the two more fundamental constants from reactions 1 and 2 above.

$$TON_C = k_1 + k_2[C_{sd}(O)] \tag{3}$$

Square brackets, [ ], denote species activities. Equation (4) shows that TON_C is the slope of the C gasification rate versus $[C_{sd}(O)]$ plot.

$$\text{C gasification rate} = TON_C\,[C_{sd}(O)] \tag{4}$$

To the extent that the steady state primary product CO/CO_2 ratio is large, the gasification rate will be a more linear function of the unstable surface oxide concentration and the TON_C will better approximate k_1.

Although low temperature O_2 chemisorption techniques have been used to measure the active surface [8,10,11], the part of the active surface actually measured and its relationship to the part involved in the gasification, the covered strongly desorbing part, is not always clear. Aside from an in situ spectroscopic examination of the surface which, as yet, is undeveloped, a better way to estimate the surface involved in gasification may be to cool down a gasifying sample in O_2 and then measure the surface O content. At the instant of cooldown, the surface oxides consist

of stable and unstable types. As the temperature decreases, more of the unstable surface oxides become stable. Some of the unstable surface oxides desorb but should be replaced because the activation energies for adsorption and migration of O species are smaller than the activation energy for desorption [12,13,14]. The replacement of recently desorbed surface oxide would be less complete as the kinetics become less dominated by the desorption step. This limits the technique to low temperature, high O_2 pressure gasification. The cooled sample then contains oxygen originating from both the stable and unstable surface oxides. This oxygen can be recovered as CO and CO_2 by heating the surface oxides to about 1240 K [8].

The technique described above was used to study the gasification of a spectroscopic purity graphite powder in various pressures of O_2 at temperatures low enough so that the observed gasification rates were clearly chemically controlled. The results demonstrate a relationship between the gasification rate and the amount of surface oxide collected immediately after gasification. The relationship may be interpreted in terms of stable and unstable surface oxide and yields an estimate for the TON_C. This estimate is compared to global turnover numbers from the literature. The comparisons dramatize the importance of active site coverage in clarifying the role of active surface in gasification.

EXPERIMENTAL

Reactivity and linear programmed thermal desorption (LPTD) runs were performed in the same computer interfaced high pressure flow reactor. Gasification or desorption products were quantified by CO and CO_2 nondispersed infrared detectors and a mass flowmeter. Hydrocarbon free O_2 of >99.99% purity with a reported moisture content < 3 ppm was used for the reactivity studies. Ultra high purity Ar (>99.999%), passed through a Zr alloy gettering furnace to lower H_2O and O_2 levels to < 0.1 ppm, was used for the LPTD runs. The carbon studied was Union Carbide SP-1 spectroscopic purity graphite powder which had a total impurity content of < 0.1 ppm. It was supported unconsolidated in the reactor on high purity alumina or quartz trays or on sapphire disks.

Graphite samples were loaded into the reactor, given a LPTD, then gasified to 20% burn-off at 840±3 K at a fixed O_2 pressure. After cooling in O_2, the surface oxide was collected with another LPTD. Once loaded into the reactor, the sample was not exposed to ambient air until the final LPTD was finished. LPTD's were performed from ca. 300 K to 1234 K at 5 K/min. Full details are given elsewhere [15].

RESULTS AND DISCUSSION

Gasification proceeds through three stages as noted before [16,17]. All samples were burnt-off to 20% to be within the range of steady state gasification. Figure 1 illustrates that, when the reaction conditions are kept constant, the gasification rate exhibits more variability at low sample weights and decreases with increasing sample weight. A mass transfer calculation following the procedure in reference [19] for the case most limited by O_2 transfer yields a value of $\phi^2\eta = 0.0032$ which is safely below the 0.1 upper limit for chemical control. ($\phi^2\eta$ is roughly the ratio of the actual O_2 consumption rate to the mass transfer limited O_2 supply rate.) Therefore, O_2 mass transfer limitation is not causing the decrease in gasification rate with increasing sample weight. For the largest weight samples, CO inhibition can explain the slight gasification rate decreases [18]. For the smaller weight samples, however, the decrease in rate with sample weight appears to be due to the influence of extrinsic catalysis. This view is supported by the higher CO_2/CO

ratio in the product gas for these samples as well as microscopic examinations of the burnt graphite powder which reveal that the smaller weight, higher reactivity samples exhibit a much higher incidence of flakes with roughened edges and channels. The gasification rates were not significantly influenced by changing the sample support materials.

A typical LPTD profile obtained after 20% burn-off in 2.3 MPa O_2 at 837 K is illustrated in Figure 2. All LPTD profiles were similar and differed mainly in the evolution rates and total amounts but little in the rate-temperature profile. Most of the gas recovered during LPTD was CO. It is likely that the similarity in LPTD profiles is due at least partly to very rapid surface oxide migration or rearrangement.

Figure 3 illustrates the relationship between the steady state gasification rate and the surface oxide collected afterwards expressed in terms of total O collected. Because a vertical temperature gradient existed at the highest O_2 pressure, 3.5 MPa, the sample temperature during gasification at this pressure could be as high as 851 K. Regardless of whether the rate differences among the samples are caused by sample size (catalysis) or O_2 pressure differences the data follow the same trend. A least squares linear fit to the data shows that 5.5 μmole O/g of the surface oxide is stable. The excess is unstable and has a TON_C of 0.043 s^{-1}. The absence of significant curvature in Figure 3 implies that the TON_C closely approximates k_1.

This turnover number is compared with other more global turnover numbers from the literature in Figure 4. In Figure 4, the right hand vertical scale is in units appropriate for turnover numbers, the left hand vertical scale is in units appropriate for edge recession rates. Where necessary, reactivities in Figure 4 were extrapolated to 1.3 KPa using an O_2 reaction order of 0.5. The literature global turnover numbers are the gasification rates divided by the total active surface areas, i.e. C atoms gasified per unit time divided by C atoms exposed at edges of basal planes. These global turnover numbers may be obtained directly from microscopic observations of the recession rates of pits in the basal plane [5,20,21,22,25] or of the recession rates of unwet catalyst channels at points far from the catalyst particle [23,24]. They may also be obtained by dividing the gasification rate by the amount of chemisorbed O [8]. The chemisorption conditions must be chosen with care. Low temperature chemisorption may suffer from failure to saturate the entire active surface due to kinetic limitations. At higher temperatures, significant fractions of the active surface will be C_{sd} type and unable to retain surface oxide. Since active surface coverages are not known for the literature global turnover numbers, they cannot be converted into TON_Cs, however they do represent the lower limits to the TON_Cs. The scatter in the data in Figure 4 is probably due to variable coverages of active surface caused by variable degrees of catalysis, since the data were normalized for O_2 pressure. The upper line in Figure 4 is constructed using data having the lowest reported O_2 reaction order of 0.3 [21] and thus the highest active surface coverage. This line should more closely approximate the TON_C.

ACKNOWLEDGEMENTS

This research was performed at The Pennsylvania State University and was supported by the Division of Chemical Sciences, Office of Basic Energy Sciences, U. S. Department of Energy on Contract No. DE-AC02-79ER 10488.

References

[1] J. A. Hedley, Nature, 188, 44 (1960)

[2] I. M. Dawson, E. A. C. Follett, and D. M. Donaldson, Proc. Eur. Reg. Conf. on Electron Microscopy, Delft 1960, Vol. I, p. 337

[3] G. R. Hennig, J. Chim. Phys., 58, 12 (1961)

[4] I. M. Dawson and E. A. C. Follett, Proc. Roy Soc., A274, 386 (1963)

[5] E. L. Evans and J. M. Thomas, Proc. of Third Conference on Carbon and Graphite London 1970, p. 3, Soc. Chem. Ind., London (1971)

[6] J. R. Fryer, Proc. Third Conf. on Industrial Carbon and Graphite, p. 246, Soc. Chem. Ind., London (1971)

[7] C. Wong, R. T. Yang, and B. L. Halpern, J. Chem. Phys., 78(6), 3325 (1983)

[8] N. R. Laine, F. J. Vastola, and P. L. Walker, Jr., J. Phys. Chem., 67, 2030 (1963)

[9] P. L. Walker, Jr., F. J. Vastola, and P. J. Hart in *Fundamentals of Gas-Surface Reactions*, (H. Saltsburg, J. N. Smith, Jr., and M. Rodgers -Eds.), p. 307, Academic Press, NY (1967)

[10] E. M. Suuberg, J. M. Calo, and M. Wojtowicz, ACS Div. Fuel Chem. Prep., 31 (3), 186 (1986)

[11] L. R. Radovic, P. L. Walker, Jr., and R. G. Jenkins, Fuel, 62, 849 (1983)

[12] J. Nagle and R. F. Strickland-Constable, Proc. of the Fifth Conf. on Carbon, Vol 1, p. 154, Pergamon Press, NY (1962)

[13] J. Dollimore, C. M. Freedman, and B. H. Harrison, Carbon, 8, 587 (1970)

[14] P. R. Olander, W. Siekhaus, R. Jones, and J. A. Schwartz, J. Chem. Phys., 57, 408 (1972)

[15] J. M. Ranish, Ph. D. Thesis, The Pennsylvania State University, (1984)

[16] P. Magne and X. Duval, Bull. Soc. Chem., France, 5, 1585 (1971)

[17] D. J. Allardice and P. L. Walker, Jr., Carbon, 8, 375 (1970)

[18] J. M. Ranish and P. L. Walker, Jr., Carbon, 24, 109 (1986)

[19] P. L. Walker, Jr., F. Rusinko, Jr., and L. G. Austin in *Advances in Catalysis*, Vol. XI (D. D. Eley, P. W. Selwood, and P. B. Weisz -Eds.), p. 133, Academic Press, NY (1959)

[20] G. R. Hennig in *Chemistry and Physics of Carbon*, Vol. 2, (P. L. Walker, Jr.-Ed.), p. 1, Marcel Dekker, NY (1966)

[21] J. M. Thomas in *Chemistry and Physics of Carbon*, Vol. 1, (P. L. Walker, Jr.-Ed.), p. 121, Marcel Dekker, NY (1965)

[22] R. T. Yang and C. J. Wong, J. Chem. Phys., 75(9), 4471 (1981)

[23] R. T. K. Baker and P. S. Harris, Carbon, 11, 25 (1973)

[24] R. T. K. Baker and J. J. Chludzinsky, Jr., Carbon, 19, 75 (1981)

[25] J. J. Baker, Ph. D. Thesis, The Pennsylvania State University (1970)

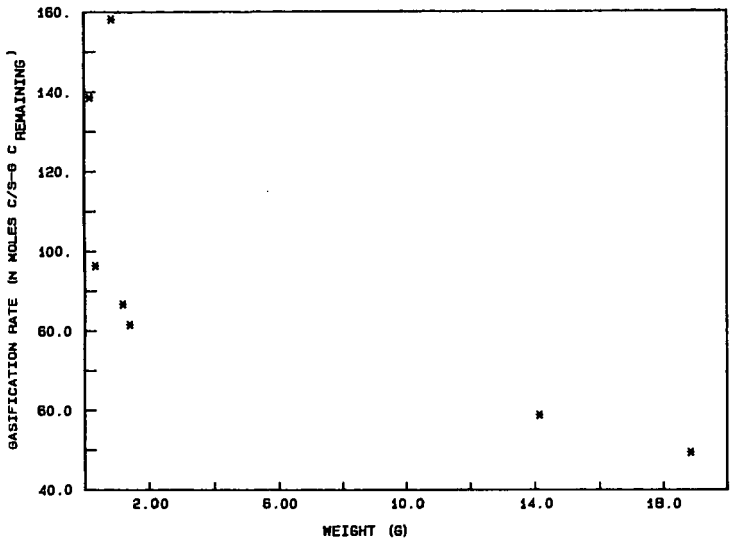

Figure 1: Effect of Initial Sample Weight on Gasification Rate. Gasification at 840±3 K, 0.1 MPa O_2, 20% Burn-Off

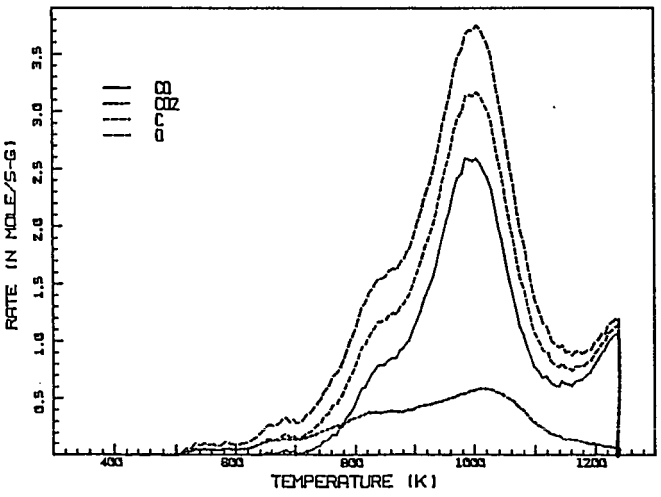

Figure 2: Evolution Rates During LPTD After Gasification. Gasification to 20 % Burn-Off at 837 K in 2.3 MPa O_2

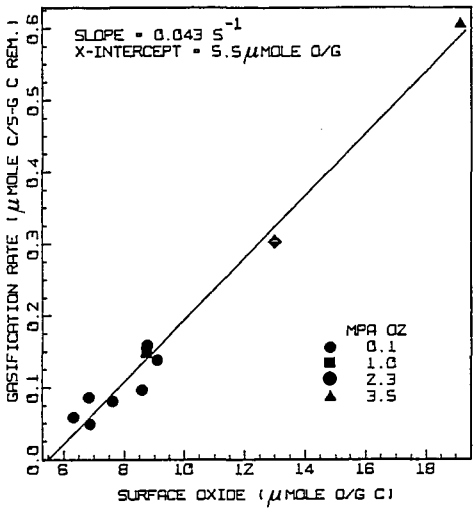

Figure 3: GASIFICATION RATE AT 20 % BURN-OFF, 840±3 K VERSUS SURFACE OXIDE

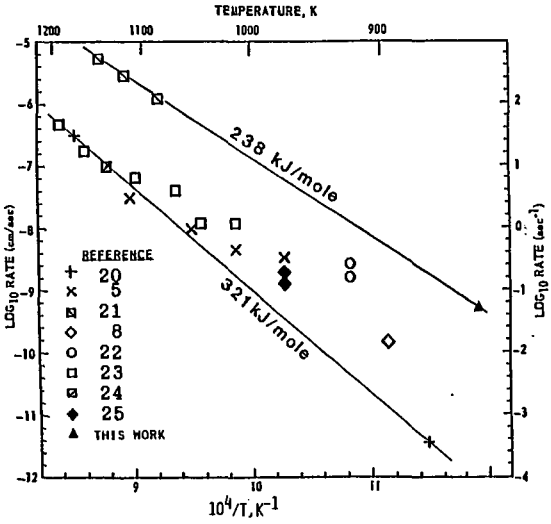

Figure 4: TURNOVER NUMBERS FOR THE CARBON-OXYGEN REACTION AT 1.3 KPA

THE RELATIONSHIP BETWEEN CHAR REACTIVITY AND PHYSICAL AND CHEMICAL STRUCTURAL FEATURES

P.E. Best+, P.R. Solomon, M.A. Serio, E.M. Suuberg*,
W.R. Mott, Jr., and R. Bassilakis
Advanced Fuel Research, Inc., 87 Church Street, East Hartford, CT 06108

INTRODUCTION

This study focuses on correlations observed between char reactivity, on the one hand, and char resistivity and structural properties on the other. It is the continuation of a study reported recently on the relationship between char reactivity and pyrolysis conditions (1). There, it was found, as others have observed before (2-5), that for most coals, reactivity decreases with increasing degree of pyrolysis. As pyrolysis progresses a number of changes occur in the char: hydrogen and oxygen content decrease, a greater degree of order is brought about and changes occur in the sample shape, pore size distribution and surface area.

With so many factors varying, the observation of a correlation between char reactivity and one factor need not imply a cause and effect relationship between the two. The traditional way to deduce cause-and-effect is to vary only one factor at a time, and observe its effect on the measurement. This is not readily done for chars. The result is that the research in char reactivity has established trends, but not a quantitative theory.

A great deal is known about char reactivity, as can be seen from two reviews of the subject (4,5). For the present work, only a subset of this information is needed, which we take from the reviews. Correlation of char reactivity has been made with heteroatom content (oxygen and hydrogen in this instance), with structure and with mineral content. The "structure" generally refers to the number of exposed edge atoms of lamellae (6,7). In pure graphite these sites have been shown to be the most reactive towards oxidation, and it is commonly held that these edge sites are most reactive in chars, also. An exception to this is the location of sites activated by mineral matter. These sites are found in the basal plane of graphite (4). Reactivities have also been correlated with resistivity (8).

In this work, chars have been characterized with respect to reactivity, surface area, heteroatom content, ash content, x-ray diffraction, and resistivity. The char characteristics have been correlated with coal rank, coal mineral content, and the heating rate and final temperature used for char preparations. The paper presents a summary of the observed trends.

EXPERIMENTS

Char Preparation

The experiments described here were carried out on a char formed from phenol formaldehyde resin, as described by Suuberg, et al. (9) and on chars formed from raw and demineralized coals and lignites. Demineralization was carried out by the procedure of Bishop and Ward (10). The chars were formed by heating in an inert gas within an entrained flow reactor (EFR) for a variety of residence times and maximum temperatures, or by heating in a Thermogravimetric Analyzer (TGA) at 30°C/min to 600, 700, 800 or 900°C. The composition of the starting material as well as those of the charred materials, are shown in Table I.

*Div. of Engineering, Brown University, Providence, RI, 02912
+Physics Department, University of Connecticut, Storrs, CT 06268

Reactivity Measurements

Initial char reactivity measurements were made using the isothermal technique developed at Pennsylvania State University (11). In this method, the char is heated in a TGA in nitrogen to the desired temperature, usually 400-500°C. The time for 50% burnoff, $\tau_{0.5}$, is used as the reactivity index. In our char characterization work, we had difficulty applying the isothermal techniques to chars formed over a wide range of conditions. A temperature level selected for one char was inappropriate for another.

In order to overcome this difficulty, a non-isothermal technique was developed using a Perkin-Elmer TGA 2 (1). The sample (about 1.5 mg) is heated in air at a rate of 30 K/min until a temperature of 900°C is reached. The TGA records the sample weight continuously and, at the end of the experiment, the weight and derivative are plotted. The temperature (T_{cr}) at which the derivative of the fractional weight loss with respect to time reaches a value of 0.11 wt. fraction/min was chosen as an index of reactivity. This was compared with the $\tau_{0.5}$ values measured by the isothermal technique and a good correlation was observed (1).

Surface Area Determinations

The surface areas reported in this paper have been obtained at Brown University using a Quantasorb instrument, manufactured by Quantachrome, Inc. The sample cell is immersed in liquid N_2 for N_2 adsorption or a dry ice-acetone bath at -78°C, for CO_2 adsorption. Determinations of surface area from the sorption data have been made using classical BET theory; typically three points have been taken at values of (P/P_o) of 0.1, 0.2, and 0.3.

X-Ray Diffraction Measurement

Powder diffraction patterns were recorded on film with a Debye-Scherrer camera (dia. 57.3 mm), in air. The films were read with a diode-phototransitor pair, feeding a logarithmic amplifier whose output drove the Y-channel of an X-Y recorder. The X-Y chart record, then, is of film darkening (proportional to x-ray intensity) versus distance along the film. Graphite was the reference material. The sample capillary diameter (0.5 mm) and the aperture of the limiting slit in the film reader, were chosen so that the **(100)** and **(101)** lines of graphite were resolved.

Where intensity measurements of more than one sample are compared, the same exposure conditions and times were used to record the data. The background scattering from air and capillary were determined by a "blank" (empty capillary) run, and sample densities were estimated from the sample contribution to the large angle scattering, assumed to be incoherent (12). Heteroatom contribution was not taken into account when estimating the sample density. "Line" intensities were determined by subtracting the interpolated smooth background from the corrected data.

Resistivity Measurements

The apparatus that was used for the sample cell in the electrical resistivity tests is similar in form to that described by Mutso and DuBroff (8), although smaller. In the apparatus used here, a small amount of sample (about 15 mg) is introduced into the cell, and the electrical resistance of the sample, under a constant pressure of 1000 p.s.i. is measured by a digital ohm-meter. Both the exact ($\pm$ 0.1 mg) sample weight and compressed density are determined, and from these measurements and the known cell dimensions, a resistivity is calculated.

It is possible that interparticle resistance, as well as the intrinsic material property, contributed significantly to the measured resistivity. This possibility was investigated for a number of chars by measuring the resistivity for a sieved sample (-200 +325 mesh), and a sample ground to micrometer sized particles. A small effect was seen, although all measurements on one char were within $\pm$ 5%.

Likewise, the effect of char drying on resistivity was investigated. No significant effect was observed between the resistivity of chars that had been in jars for several days, and that of freshly dried material.

RESULTS AND DISCUSSION

Reactivity vs. Extent of Pyrolysis

Figure 1 summarizes the results for chars from the five coals. This figure is based on Fig. 5 of Ref. 1 with additional coals and with measured values rather than calculated values of hydrogen for the Kentucky No. 9 chars. The critical temperature (T_{cr}), which varies inversely with reactivity, is plotted as a function of the (daf) hydrogen content, which is used as a measure of the extent of pyrolysis. For each char type, there is a trend for increasing T_{cr} (decreasing reactivity) with decreasing hydrogen. Most of the change occurs below 2 1/2% hydrogen, after the evolution of aliphatic hydrogen is complete. That is, T_{cr} appears to vary primarily with the concentration of aromatic hydrogen. This variation could be due to a variation in the active site concentration, possibly correlated with the ring condensation accompanying the elimination of aromatic hydrogen. There does not appear to be any drastic effects due to heating rate for low rank coals containing minerals, as chars for a wide range of conditions all fell along the same curve. The preliminary results for bituminous coals and demineralized low rank coals do not exhibit the same degree of reactor independence.

It should be noted that there is also ring oxygen in the char which is removed at about the same rate as the hydrogen and which may be related to the reactivity changes. Similar correlations were observed with oxygen concentration for chars produced from a single coal, i.e., the reactivity decreases with decreasing char oxygen concentration. However, it is thought that the hydrogen is the major indicator of reactivity, since it is present at about five times the level of oxygen on an atomic basis. Our studies indicate that the oxygen content of the parent coal is more important (see below).

The upper solid line in Fig. 1 is a "best fit" line drawn through the data for Kentucky No. 9 and Pittsburgh Seam bituminous chars. The lower solid line is a best fit line drawn through the Zap lignite chars.

Reactivity vs. Mineral Content

It is known that the vertical displacement of the curves in Fig. 1 is at least partly due to the variations in catalytic activity of minerals. This effect has been observed in previous studies which have been reviewed by Mahajan and Walker (13). The most reactive chars are for the Zap lignite which are known to have a high Na and Ca content. The results for T_{cr} versus daf hydrogen content for Zap chars demineralized by two procedures are shown in Fig. 2. In both procedures, the Bishop and Ward technique (10) was used, except that in procedure 1 the HF was used at one-fifth normal strength. It is apparent that this produced a lower extent of demineralization, which was verified by XPES analysis. Both data sets are compared to the "best fit" line drawn through the Zap data in Fig. 1. It is evident that reactivity results for the Zap demineralized by procedure 2 are similar to chars from bituminous coals (see Fig. 1). Samples of Pittsburgh Seam and Illinois No. 6

bituminous coals were also subjected to demineralization but did not exhibit as dramatic an effect.

Reactivity vs. Surface Area

Another area of investigation was the differences in surface area among the chars that were tested for reactivity. N_2 surface areas varied from 1 to over 100 m^2/gram. In general, for any given coal, N_2 surface areas went up with decreasing hydrogen content below 3% hydrogen, where the reactivity was observed to decrease. N_2 surface areas also increase with the extent of burnoff at essentailly constant reactivity. So reactivities do not correlate with N_2 surface areas.

CO_2 surface areas varied from around 10 to over 300 m^2/gram with almost all chars in the range of 100 to 300 m^2/gram. The CO_2 surface area which varies by factors of 3 shows no correlation with reactivity which varies by factors of 100.

The fact that reactivities do not correlate with surface is not surprising. As discussed by Walker and coworkers (3,7,13), it is the active surface area (ASA) as measured by oxygen chemisorbtion which is important. However, Suuberg, et al., (9) have recently called into question the utility of oxygen chemisorbtion as a technique for measuring the ASA of "young" chars. In this work, we have not attempted to measure ASA's.

Reactivity vs. Rank

A systematic study of the variations of reactivity with coal rank has been performed. Figure 3 presents a correlation between the oxygen content in the parent coal and the reactivity of char produced in the TGA by heating in nitrogen at 30°C/min to 900°C. The open squares are results obtained for raw coals, the solid squares show the results for demineralized coals. For raw coals there is a decrease in reactivity with increasing rank. Similar results were summarized by Mahajan and Walker (13). For demineralized coals above 8% oxygen, the reactivity does not vary with oxygen. The results suggest that the decrease in reactivity with increasing rank is a property of the organic matter at high rank (less than 8% oxygen) and mineral matter at lower rank (greater than 8% oxygen).

Reactivity vs. Molecular Order

For a series of chars formed from Eastern and demineralized Western coals and lignites, the reactivity and the x-ray diffraction patterns were measured. With increasing degree of pyrolysis, T_{cr} increases, indicating reduced reactivity (1). This correlation has been observed before (7). Also with increasing degree of pyrolysis, the extent of ordering increases, as indicated by the greater intensity and lower breadth of the **(10)** diffraction line from the chars (Fig. 4). Franklin was amongst the first to describe this particular correlation (14). Combining the two, it is seen that there is a correlation between decreasing reactivity and increasing order, apparently implicating lamellae edges as the active sites.

In looking for a parameter from the x-ray scattering data to characterize "order" in a simple way, it is noted that most workers in the field use crystallite diameter, L_u. For ideal crystallites, the diameter can be found from the breadth of the **(10)** line, or its angular shift$_o$(15). For the chars investigated in this work, lamellae diameters are under 30 A, and do not change dramatically during pyrolysis. On the other hand, the intensity in the **(10)** band, for a fixed density of lamellae, increases as N^2, where N is the number of atoms in the lamellae (15). Under these circumstances, the intensity increases with L_u to the fourth power. The intensity is a very sensitive measure of lamellae growth, and therefore, of order. This is the parameter which Radovic, et al. used in their work (7).

Figure 5 presents the intensity of the (10) band versus the critical temperature, for a number of chars formed by slow heating. These chars were all prepared from demineralized chars to avoid interference from the mineral diffraction lines. It is seen that there is a trend of increasing intensity of the (10) band with increasing T_{cr}. In other words, the chars become less reactive as they become more ordered (7). As mentioned above, other properties of the char change with increasing heat treatment. It has not been demonstrated here that the correlation in Fig. 5 is one of cause and effect; the relationship is as expected, however (5). Chars created at high heating rates (not shown) appeared to fall near the other chars but with higher uncertainty due to their low density.

Reactivity vs. Resistivity

In continuing to seek correlations between char reactivity and other parameters, we were led by the work of Mutso and DuBroff to investigate the relationship between reactivity and resistivity (8).

In the work described in Ref. 8, and other earlier wqrks, the relationship between reactivity and resistivity was performed for cokes, formed from coking coals which come from a relatively narrow range of coal rank. In the present case we plot reactivity, indicated by T_{cr}, versus resistivity, for a wider range of starting coals, including the demineralized lignite, as well as for the resin char (Fig. 6).

Also in Fig. 6 are plotted data points for chars formed from North Dakota lignite without treatment. These are the points on the line far removed from the shaded band which encompasses all other points. For Eastern coals, and for demineralized Western lignite, there is an excellent correlation between char reactivity and electrical resistivity.

The removal of the data points from the shaded band for lignite with minerals, can be traced to the effect of minerals on reactivity (4). The minerals do not have a major effect on resistivity for the samples measured here.

CONCLUSIONS

Results are presented which are used to make, or to restate, the following conclusions:

- A new test has been developed which allows relative reactivity to be determined for chars of widely varying reactivity.
- Reactivity was found to decrease with increasing extent of pyrolysis, as determined by (daf) hydrogen content.
- The effect of heating rate or reactivity appeared to be unimportant for non-demineralized low rank coals.
- The differences in reactivity of chars do not depend strongly on the char surface area measured by N_2 or CO_2.
- For coals with more than 8% oxygen, mineral effects appear to be important in determining reactivity differences between chars from different coals.
- A relationship between extent of order and char reactivity is demonstrated for chars formed by slow heating. This is done by plotting T_{cr} against the intensity of the (10) x-ray diffraction line.

- The work done by others (8) showing a correlation between coke reactivity and electrical resistivity, is extended to chars. Again, a correlation is observed, although only in the absence of mineral effects.

ACKNOWLEDGEMENT

This work was supported under Contracts No. DE-AC21-84MC21004 and DE-AC21-85MC22050 from the Morgan Energy Technology Center of the Department of Energy.

REFERENCES

1. Solomon, P.R., Serio, M.A., and Heninger, S.G. ACS Div. of Fuel Chem. preprints, **31**, (2), 200, (1986).
2. van Krevelen, D.W., Coal, Elsevier, NY, (1961).
3. Laine, N.R., Vastola, F.J., and Walker, P.L., Jr., Proceedings of the 5th Carbon Conference, **2**, 211, Pergamon Press, NY (1963).
4. Essenhigh, R.H., in Chemistry of Coal Utilization, Suppl. Vol., (H.H. Lowry, Ed.), J. Wiley, Chapt. 20, (1962) and references therein.
5. Laurendeau, N.M., Progr. En. Comb. Sci, **4**, 221, (1978) and reference therein.
6. Chang, H.W. Rhee, S.K., Carbon, **16**, 17, (1978).
7. Radovic, L.R., and Walker, P.L., Jr., Fuel, **62**, 849, (1983).
8. Mutso, R. and DuBroff, W., Fuel, **61**, 305, (1982).
9. Suuberg, E.M., Calo, J.M., and Wojtowicz, M., ACS Div. of Fuel Chem. preprints, 31, (3), 186, (1986).
10. Bishop, M. and Ward, D.L., Fuel, **37**, 191, (1958).
11. Mahajan, O.P., Yarzab, R., and Walker, P.L., Jr., Fuel, **57**, 643, (1978).
12. Franklin, R.E., Acta, Cryst. **3**, 107, (1958).
13. Mahajan, O.P. and Walker, P.J., Jr., Chapter 32 in Analytical Methods for Coal and Coal Products, Vol. II, (C. Karr, Ed.), Academic Press, NY, pp 465-492, (1978).
14. Franklin, R.E., Proc. Roy Soc. A. **209**, 196, (1951).
15. Warren, B.E., Phys. Rev. **59**, 693, (1941).

TABLE I

Composition of Starting Demineralized Coals and Chars (wt% DAF)

	Carbon	Hydrogen	Nitrogen	Ash
Zap Lignite	63.54	4.32	0.79	0.18
Lignite Charred in EFA to 0"	78.85	2.55	1.05	0.76
8"	86.31	1.36	0.79	0.60
16"	87.55	0.93	0.91	1.54
24"	88.74	0.51	0.53	0.43
Lignite Charred in TGA at 30°C/min to a final temp. of 600°C				0.38
700°C				0.37
800°C				0.49
900°C				0.29
Pocahontas Coal	91.03	4.71	0.98	1.54
Rosebud Coal	72.10	4.90	1.20	3.68
Pittsburgh Seam Coal	80.90	5.50	1.40	2.31

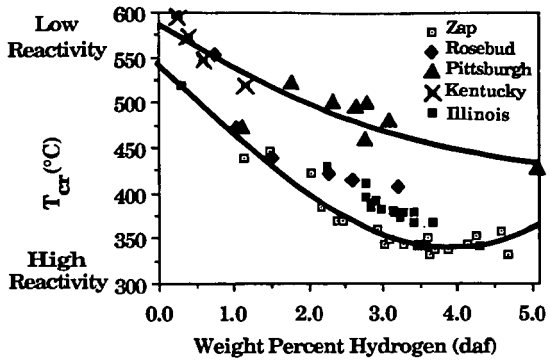

Figure 1. Comparison of Reactivity for Chars from Five Coals of Various Rank as a Function of Hydrogen Concentration. T_{cr} Varies Inversely with Reactivity.

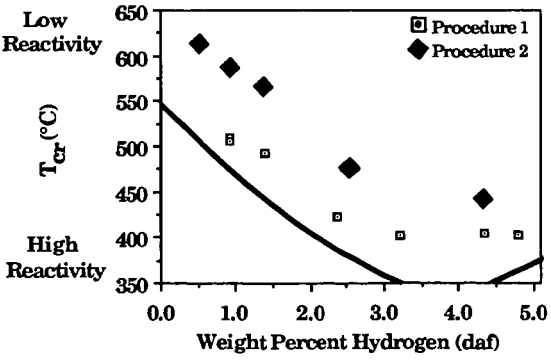

Figure 2. Comparison of Reactivity of Chars from Demineralized Zap Lignite (data) with Chars from Raw Zap Lignite (line from Figure 1). Procedure 1 was a Modification of the Bishop and Ward (ref.10) technique with a Lower HF Strength. Procedure 2 was the Standard Bishop and Ward Technique.

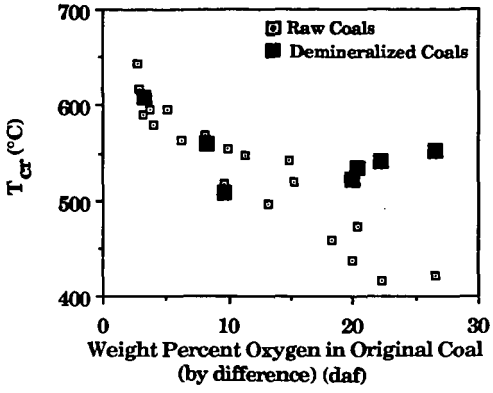

Figure 3. Variation of Reactivity with Coal Oxygen Content for Chars Prepared by Heating in Nitrogen at 30°C/min to 900°C.

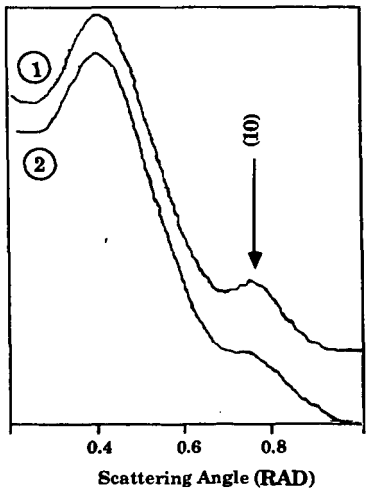

Figure 4. Diffracted X-ray Intensity Versus Angle, for Two Chars Formed from Demineralized North Dakota (Zap) Lignite. The Curves have been Displaced Vertically to Facilitate Comparison. The Char for (1) was Formed by Heating at 0.5°C/sec to 900°C; for (2) to 600°C.

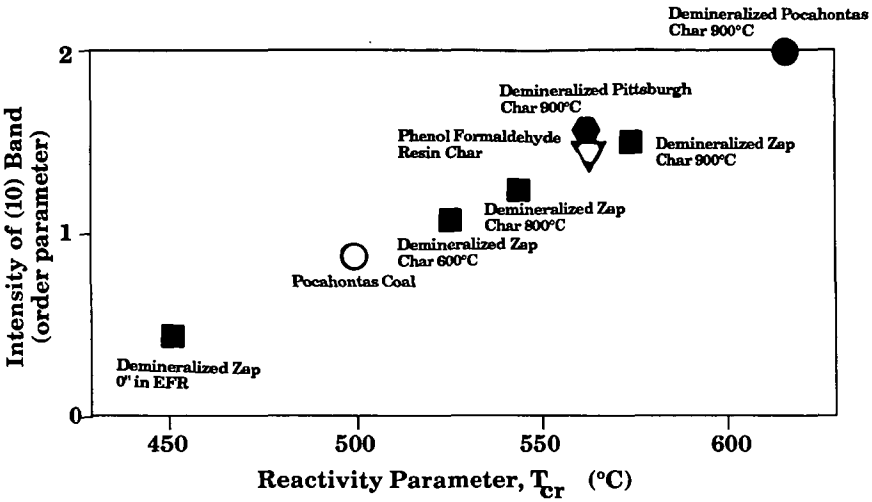

Figure 5. Plot of Order Versus Reactivity for some Eastern and Demineralized Western Chars Formed Under Slow Heating Conditions, and One High Rank Coal.

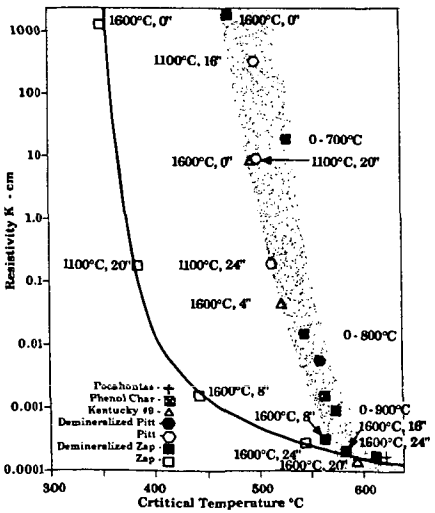

Figure 6. Plot of Resistivity Versus Critical Temperature for a Variety of Chars. The Data for Eastern Coals, or Demineralized Western Coals, Fall Within the Shaded Band.

Role of Carbon Active Sites in the Oxidation of Coal Chars

Robert G. Jenkins and Andrej Piotrowski

Fuel Science Program
The Pennsylvania State University
University Park, PA 16802

INTRODUCTION

Over the last two decades there have been numerous coal char and carbon gasification studies that have determined relative rates of the carbon/gas reactions. It has been demonstrated, quite clearly, that the measured chemical reactivities of chars are functions of coal rank, pyrolysis severity, the presence of catalytically active species, and, of course, the reactant gas and the specific reaction conditions utilized. The goal of this, and other investigations is to attempt to rationalize this range of reactivities in terms of some fundamental parameter/property of the char. The specific aim is to determine if a fundamental rate constant can be obtained for, say, the carbon-oxygen reaction. It is felt that such an approach will lead, eventually, to a better understanding of char gasification in terms of theoretical and practical considerations.

Our approach has been to examine further the role that carbon active sites play in governing the reactivity of a wide range of chars and carbons. This concept was first put forward by Laine et al. (1,2) and has been extended by others (3,4,5). There appear to be relationships between reactivity and active site concentrations (as determined by oxygen chemisorption). The thrust of this study was to extend these types of reactivity studies and to examine, especially, the changes in active site concentration with degree of gasification (burn-off). An attempt has been made to develop a concept of "reactive" sites. That is, to consider sites that are actively participating in gasification reactions. The starting point of this concept is to define an equivalent reactive surface area (RSA) that can be utilized to normalize rates in terms of a pseudo Turn-over Number (TON).

EXPERIMENTAL

i. Materials

Five coals ranging from lignite to anthracite have been used throughout this study. In addition, a relatively "pure" carbon was prepared from Saran polymer (a copolymer of vinyldene and vinyl chloride). The coals are PSOC 833 - a Montana lignite; PSOC 465 - a Wyoming subbituminous A coal; PSOC 1099 - a HVA coal from Pennsylvania; PSOC 1133 - LV, Pennsylvania coal; and PSOC 868 - a Pennsylvania anthracite.

Samples of the raw coals were subjected to a range of pretreatments to alter, in a selective fashion, the inorganic constituents. These modifications were brought about by ion exchange and acid-washing procedures for the lignite (PSOC 833) and by acid-washing procedure for the other coals. Selected samples of all the coals were treated with calcium acetate solutions, varying from 0.001 M to 1.5 M, in order to change the calcium loading in the coals. Chars/cokes from the raw and treated coals were prepared either by slow heating (10^{o}K/min) up to final temperatures of between 975 K and 1275 K, or by rapid pyrolysis (~ 10^{4} K/min) at 1275 K in an entrained flow reactor.

ii. Apparatus and Procedures

Isothermal and nonisothermal reactivities were determined in thermogravimetric analyzers (TGAs). Concentrations of CO and CO_2 in the product gas stream were measured by nondispersive infrared analyzers.

Nonisothermal reactivity measurements were performed using a small sample of coal (< 4 mg) placed in a TGA bucket and heated at a constant heating rate 5 K min^{-1} to an ultimate final temperature in the reactant gas (air). The weight loss, and its first derivative were recorded. The parameter used to represent this reactivity is T_m, the temperature at which the maximum rate of weight loss (maximum of the first derivative) occurs. For isothermal reactivity measurements a sample of char is heated to the desired reaction temperature, in the absence of oxidizing gas, and then the reactant (air) gas was introduced. Weight change and its first derivative with time were determined directly by the thermogravimetric analyzer and also calculated from the composition of the gaseous products of reaction (CO and CO_2). Thus, the TGA reactivity is estimated from the following expression

$$R_{TGA} = 1/w \times \frac{dw}{dt}$$

where R_{TGA} is the reactivity (min^{-1}) at a given temperature and burnoff; w is the mass of the sample and dw/dt the instantaneous slope of the burn-off curve. The reactivity determined from the gas composition is calculated by a similar expression.

Reactive surface area (RSA) at any given level of burn-off is calculated from a knowledge of the quantities of CO and CO_2 evolved. It is assumed that each oxygen atom occupies 0.083 nm^2 (1). Using the values of Reactivity (R) and Reactive Surface Area (RSA), a Turn-over Number (TON) can be calculated (R/RSA). The units of TON are g/m^2 min.

RESULTS AND DISCUSSION

Nonisothermal reactivities for the five coals are listed in Table 1. It can be observed that the reactivity of the coals (T_m-temperature at which maximum weight loss occurs) inversely follows rank. That is, as the rank of coal increases the reactivity decrease (higher value of T_m). Significant differences in the T_m values (630 K to 800 K) are noted over the rank range examined for the raw coals. The values for the demineralized coals exhibit somewhat less variability (701 K to 809 K). It is important to note that the reactivities of the raw subbituminous and lignitic coals are significantly greater than those determined for the respective demineralized samples. However, for the higher rank coals, demineralization can actually produce a slightly more reactive material. Thus, we see that in the lower rank coals, and their chars, the presence of inorganic species does indeed dominate reactivity. In all cases (except raw lignite), heat treatment does reduce "reactivity." As would be anticipated, one also observes that increasing the heat treatment temperature for any given sample produces a less reactive carbonaceous material. These results, of course, show the influence of reduction in active site concentration and possible catalyst deactivation with increasing heat treatment. Overall, perhaps the most important observation to be made is that catalytic effects of inorganic matter in higher rank coals are less important than those found for lower rank coals. In addition, it is possible that during the demineralization process some closed porosity is opened, thus, increasing the overall accessibility to active area. It is also possible that acid treatment reduces the thermoplastic properties of the higher rank coal, which in turn leads to slightly higher reactivity.

It is interesting to note that for lignite the reactivities follow the level of calcium loading. However, loadings above some value of the raw sample (0.09 mmol/g) have relatively little additional influence on reactivity. It should be noted that the biggest changes in reactivity occur at the lower calcium loadings.

Typical isothermal reactivity plots for a char (PSOC 833; Demineralized + 0.3 MCa; rapid pyrolysis at 1275 K, 0.3 s) are given in Figure 1. In this figure one can see that the reactivity profiles, as a function of burn-off, for this sample are very similar for the IR and TGA methods. The major discrepancy occurs at high levels of burn-off. In this case, the instantaneous reactivity appears to be increasing to about 10% burn-off, it then levels off to a relatively constant value up to 40% burn-off, and continues to increase to about 80% conversion. If one uses the gas analysis data to calculate the RSA then one obtains the plot shown in Figure 2. Using these RSA values, a TON as a function of burn-off (at 677 K) can be estimated (Figure 3). The variation of TON with conversion is quite small and appears to remain at a value of about 1.3×10^{-4} g/m^2 min. The only exceptions in this plot are at low levels of gasification (< 5%). We have found that application of this approach yields a relatively narrow range of values for TON for approximately 5 to 85% burn-off from all the chars and carbons studied (prepared at all degrees of pyrolysis severity). As an example, Figure 4 shows the values of TON for all the demineralized, heat treated coals used in this study (reactions for this suite of samples were made at temperatures between 658 to 721 K). It should be noted that TON's for the higher rank coal demineralized chars (anthracite and LV) have values of around 1.45×10^{-4} g/m^2 min, whereas the values for the equivalent chars from the lower rank coals (HVA, Subbit and Lignite) are somewhat lower (~ 1.3×10^{-4} g/m^2 min), and appear to decrease slightly with burn-off. A brief summary of the preliminary data is given in Table 2. These results do show a remarkable degree of constancy for all these materials being gasified in air.

CONCLUSIONS

Nonisothermal reactivity measurements, in air, indicate the influence of the severity of time/temperature history on the subsequent reactivity of chars derived from a wide rank range. Instantaneous reactivities can be normalized by use of a reactive site concept. The calculated TON is quite constant for several chars (and carbons), over a wide degree of conversion and reaction temperature.

ACKNOWLEDGEMENTS

This research was sponsored by the Gas Research Institute, Chicago. Special thanks is given to Dr. Charles Nelson for his continued interest in these studies.

REFERENCES

1. N. R. Laine, F. J. Vastola and P. L. Walker, J. Phys. Chem., 67, 2030 (1963).

2. N. R. Laine, F. J. Vastola and P. L. Walker, 5th Carbon Conf., p. 211, Pergamon Press, Oxford (1963).

3. L. R. Radovic, P. L. Walker, Jr. and R. G. Jenkins, Fuel, 62, 849 (1983).

4. L. R. Radovic, K. Steczko, P. L. Walker, Jr. and R. G. Jenkins, Fuel Processing Technology, 10, 311 (1985).

5. M. R. Khan, ACS (Fuel Chemistry Div.) Preprints, 32(1), 298 (1987).

TABLE 1

VALUES OF TEMPERATURE OF MAXIMUM WEIGHT LOSS (T_m) FOR NONISOTHERMAL REACTIVITIES IN AIR AT 5 K MIN^{-1} FOR ALL COALS AND THEIR RAPID AND SLOWLY PYROLYZED CHARS

Sample	T_m (K) No Pyrolysis	Slow Pyrolysis 975 K (1 h)	Slow Pyrolysis 1275 K (1 h)	Rapid Pyrolysis 1215 K (0.3 s)
Lignite				
Raw	630	630	697	593
Demin	723	755	829	744
Demin + 0.01 Ca	639	660	760	624
Demin + 0.1 Ca	630	613	741	574
Demin + 0.5 Ca	613	622	743	568
Demin + 1.0 Ca	608	619	748	570
Subbit				1275 K (0.3 s)
Raw	648	--	809	--
Demin	701	750	809	709
Demin + 0.1 Ca	--	735	--	588
Demin + 0.5 Ca	--	720	--	541
HVA				
Raw	711	--	846	--
Demin	686	790	811	725
Demin + 0.1 Ca	--	701	--	709
LV				
Raw	735	--	846	--
Demin	704	765	818	730
Demin + 0.1 Ca	--	738	--	728
Anth				
Raw	800	--	853	--
Demin	809	823	851	794
Demin + 0.1 Ca	--	774	--	780

TABLE 2

EXAMPLES OF CALCULATED TON'S AT 50% BO

Sample	Reaction Temp. K	Ton x 10^4 $g/m^2.min$
Saran Char	683	1.52
"	702	1.49
"	710	1.50
"	721	1.53
"	732	1.51
Lignite - Demin (1275, 1 h)	720	1.49
Lignite - Demin + 0.3 Ca (1275, 1 h)	677	1.30
Subbit - Demin (1275 K, 0.3 s)	654	1.38
HVA - Demin (1275, 0.3 s)	635	1.35
LV - Demin (1275, 0.3 s)	638	1.36
Anth. - Demin (1275, 0.3 s)	738	1.50

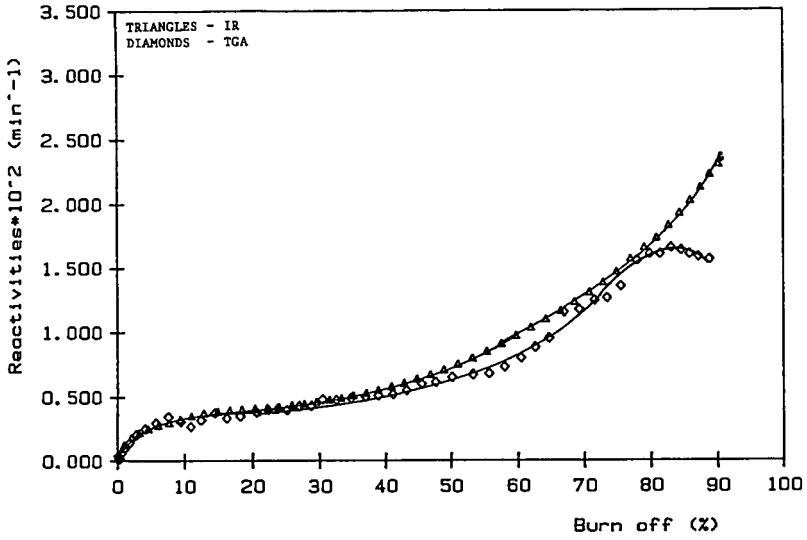

FIGURE 1. TGA and IR Ractivities at 677 K vs. Burn-off for PSOC 833 (DEM + 0.3 Ca) Heated to 1275 K (1 h)

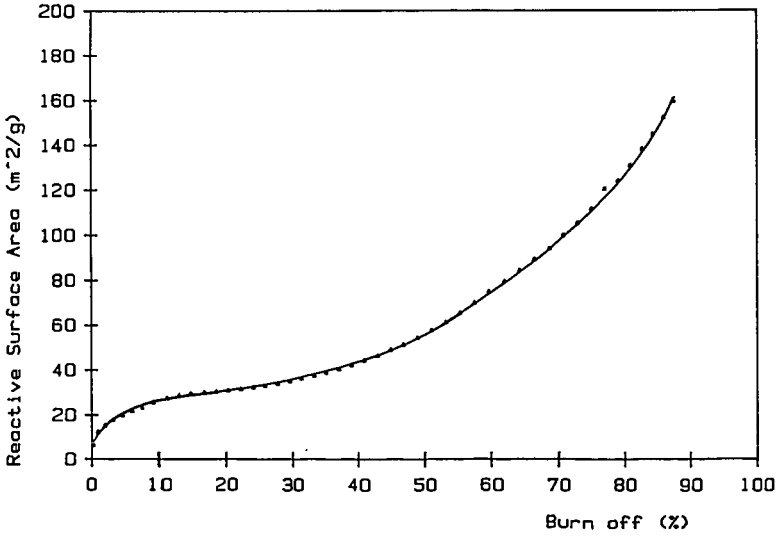

FIGURE 2. RSA vs Burn-off (677 K) for PSOC 833 (Dem + 0.3 Ca), 1275 (1 h)

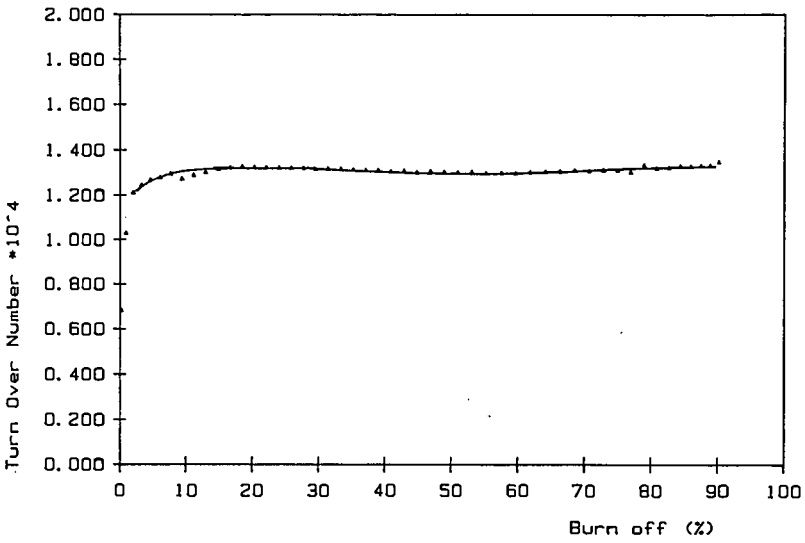

FIGURE 3. TON vs Burn-off (677 K) for PSOC 833 (Dem + 0.3 Ca), 1275 (1 h)

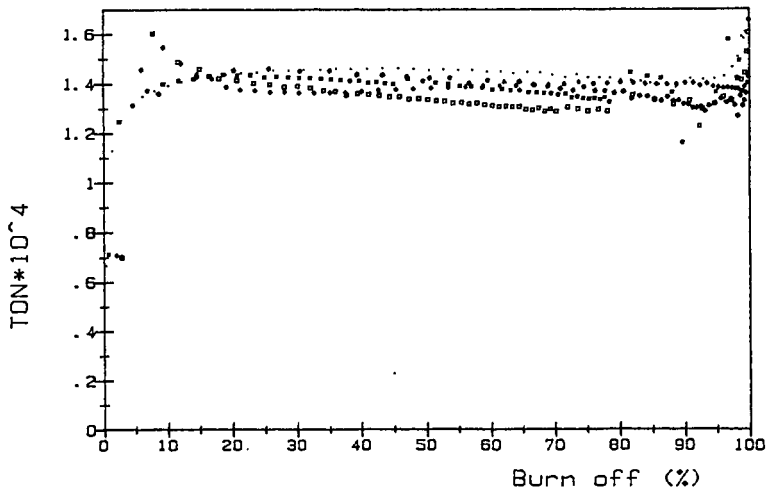

FIGURE 4. TON vs Burn-off for Demineralized Coal Chars (Rapidly Heated)

NON-MAGIC ANGLE SPINNING NMR - AN APPROACH TO DETERMINE THE CHEMICAL SHIFT TENSORS IN CHAR PARTICLES

Naresh K. Sethi,[a] Ronald J. Pugmire,[b]

and David M. Grant[a]

Departments of Chemistry[a] and Fuels Engineering,[b]
University of Utah
Salt Lake City, Utah 84112

INTRODUCTION

Carbon-13 NMR spectroscopy has been widely accepted as a major analytical technique for studying fossil fuels. Axelson[1] and Davidson[2] have reviewed the various solid state NMR spectroscopic techniques for coal studies. Cross polarization/magic angle spinning (CP/MAS)[3] provides information on aromaticity while the dipolar dephasing technique (DD/MAS)[4] provides additional definition of the structure of coal by using the ^{13}C-^{1}H dipolar coupling to separate the carbons into sub-classes; i.e., those that are strongly coupled to protons from those that are weakly coupled in both the aliphatic and aromatic regions of the spectrum. The combination of these two experimental procedures permits one to derive a carbon skeletal structure of coal samples.[5,6]

MAS experiments produce narrow lines in solids but valuable structural information is lost; i.e., the chemical shift anisotropy (CSA) which is a manifestation of the three-dimensional shielding of the nucleus by the surrounding electrons.[7] The CSA is a second rank tensor having three principal elements σ_{11}, σ_{22}, and σ_{33} characterized by unique resonance frequencies. These three tensor components taken together with the isotropic shielding value (the MAS value which is the average of the three tensor components) provide valuable data regarding the local electronic environment. The tensor can be obtained from the ^{13}C NMR spectrum of a finely powdered sample and the tensor elements are extracted by analysis of the line shape. This technique provides not only tensor components but population values as well. However, the spectral analysis is complicated if more than one tensor is present and unique results are not always achievable. Evenso, Pines, et al.[8] used the technique to analyze the static spectra of several coals. These workers succeeded in differentiating the contributions from aromatic and condensed aromatic carbons. Furthermore, they pointed out that there is little difference in the isotropic chemical shifts between these types of carbons and these shift differences cannot be resolved in a CP/MAS experiment. The DD/MAS experiment has been shown to differentiate between benzene-like (i.e., C-H) and non-protonated aromatic carbons[5] (substituted plus inner, or bridgehead) but the resolution of substituted and inner carbons is not readily attainable with standard MAS experiments. The shielding anisotropies of the three general types of aromatic carbons are quite different and, in principal, should be resolvable in the "non-spinning" experiment.

Only for isolated carbons, or for simple compounds where breakpoints in the powder pattern are discernible, is it possible to obtain unique fits of the line shape. Tensor information can be extracted by other techniques such as analysis of the spinning side bands from slow spinning MAS experiments[9] and variable angle sample spinning[10-13] (VASS). In this study we have used the static and VASS methods to study pertinent model compounds and have used these data as a guide to analyze line shapes and extract CSA tensor values and population factors in coals. The experimental techniques are applicable to chars as well as coals. The data permit us to estimate the size of the polycondensed aromatic structure that is the main structural component in chars. The aromatic structure of coal chars should provide valuable information regarding their reactivity.

EXPERIMENTAL

1. NMR Spectroscopy

The NMR spectra were obtained on a Bruker CXP-100 as described previously.[6] The VASS method has been described by Sethi, et al.[13]

2. Spectral Fitting Procedure

The NMR powder pattern analyses were carried out by means of recently developed fitting methods[14]. The technique is briefly described as follows. It is assummed that spins are only experiencing orientation dependent chemical shift interactions. This is usually the case when employing high power proton decoupling. Single spectral simulation requires an initial estimate of these parameters: 1) the principal values of the different CSA's or a linear combination of elements in an irreducible form; 2) the relative intensities; and 3) a broadening factor. One or more of these parameters can be locked to some predetermined or known value, which is then held constant throughout the fitting process. For example, in model organic compounds, the relative intensity is usually locked to the atomic ratios given by the molecular structure. In coals, however, these population parameters are allowed to vary freely so as to provide quantitative data on individual carbon types. Theoretical spectra are calculated using the "POWDER" method[14]. The parameters are adjusted with a simplex optimization routine to minimize the sum of squares deviation between the theoretical and experimental spectra. In cases which necessitate obtaining spinning spectra at different angles, all spectra are fit simultaneously with the same set of CSA values. The total sum of squares from all spectra is used as the minimization criteria. Using this technique, the redundant data provide refinements in fitting parameters which, for a single spectrum, may exhibit ill-conditioned behavior.

RESULTS AND DISCUSSION

Aromatic CSA bands can be calssified into four different subgroups which have tensor components that exhibit variations of ca. 10-20%. These groups are: 1) benzene-like (sp^2 C-H); 2) substituted (e.g. alkylated); 3) condensed (inner and bridgehead); 4) carbons

bonded to heteroatoms (nitrogen, oxygen, etc.).[15] The spectrum of an isolated carbon in a static sample presents a characteristic powder pattern which exhibits break points corresponding to the tensor elements of the individual carbons of each sub-class. Examples of the isotropic peak superimposed with their first three sub-classes, together with their isotropic peaks, are given in Figure 1. These three sub-classes represent the predominant types of aromatic carbons present in chars and high rank coals. An unambiguous tensor analysis usually cannot be performed on static lineshapes due to the overlap of several different CSA bands. This problem is especially accute for aromatic carbons since the upfield components of these bands are usually buried under the much narrower aliphatic resonances. The static spectrum of 1,2,3,6,7,8-hexahydropyrene provides a convenient representation of this problem. In addition, this molecule contains the types of carbons of interest in chars and high rank coals. The components of the individual aromatic carbon tensors have been simulated together with their composite pattern. This composite pattern is compared with the experimental data (Figure 2). The low field components are resolved but the high field (σ_{33} components) are obscured by the aliphatic carbons.

The VASS method scales the individual carbon tensors with respect to their isotropic frequencies by a factor of $1/2(\cos 3\theta^2-1)$ where θ is the spinning angle relative to the external magnetic field.[13] The break points from different bands change as θ is changed. The high field component of the aromatic carbon shielding tensors can be inverted through the isotropic value by proper selection of θ. Hence, overlapping tensor components can be unscrambled by this technique. In addition, a change in θ produces pronounced changes in all of the aromatic tensors so that the line shape is no longer a scaled replica of the static powder pattern. Such intensity and shape changes are readily recognized in our fitting routines which are sensitive to small changes in the line shape. In Figure 3, one observes the line shape changes of an alkylated aromatic carbon as the spinning angle is changed. In Figure 4 the VASS data on hexahydropyrene has been simulated and the tensor components are given in Table 1.

The ability to fit experimental data with high precision is vital to the analysis of complex materials. The hexahydropyrene model is of sufficient complexity to demonstrate the feasibility of unscrambling overlapping tensor components. The availability of multiple angle data decreases the chance of encountering a given spectrum which is insensitive to one or more of the adjustable parameters and therefore reduces ill-conditioned fits of the data.

Using the fitting procedure described above, we have fit the anthracite data (Figure 5). With an aromaticity value $f_a = 1.0$, no alkylated carbons are present and, hence, a multiple angle fit of the data was not deemed necessary. A two tensor fit of the static spectrum produced the results presented in Table 1. The population factor of 0.13 for the C-H tensor is essentially the same as the atomic ratio H/C = 0.123 for this coal. Hence, we are able to independently verify that the method gives valid results.

The anthracite provides a useful model for a char that has been subjected to extensive pyrolysis or to a high temperature environment and thus may be thought of as one extrema of a char model. On the other hand, coals that undergo pyrolysis for relatively short periods of time or at moderate temperatures are not composed entirely of polycondensed aromatic rings. Aromaticity values in the range 0.8 - 1.0 are observed in chars.[16] The inertinite macerals semi-fusinite and fusinite found in coals provide a useful model for char. Natural processes of heat and pressure have produced a char-like material. Such is the case for the Aldwarke Silkstone inertinite (86% inertinite) consisting chiefly of charcoal-like fusinite with an f_a value of 0.88.[6] The tensor components (see Figure 6) and population factors contained in Table 1 provide a distribution of the three major types of aromatic carbons present and one is not required to calculate the atomic ratio for hypothetical unsubstituted nuclei (H_{aru}/C_{ar}) as has been done in the past.[16] One can now directly measure this parameter together with the fraction of substituted carbons without resorting to calculated approximations.

The experimental value of H_{aru}/C_{ar} = 0.39 has been reported previously by means of dipolar dephasing data[6] and, hence, this value was used in fitting the spectra. The fit of the VASS data provided the other two tensors. The population of inner carbons (0.54) and substituted carbons (0.07) provide the remainder of the aromatic structural types. The substituted carbon population is of the order of 0.10, or less, and the total aliphatic carbon content is 0.12. Using the elemental analysis, i.e., the H/C ratio, it is clear that the alkyl substituents, on average, consist of 1-2 carbon fragments and that the non-methyl carbons are highly substituted.

The VASS technique provides a very useful means for supplementing other types of NMR data and is particularly useful in assessing the structure of polycondensed aromatic materials such as chars. As char reactivity is an important consideration in combustion studies, NMR data may be able to play a significant role in structure/reactivity correlation.

ACKNOWLEDGMENTS

This work was supported by the Office of Basic Energy Sciences, Department of Energy under Grant No. DE-FG02-86ER13510 and the National Science Foundation Advanced Combustion Engineering Research Center, Contract No. CDR-8522618.

REFERENCES

1. David E. Axelson, Multiscience Publications Ltd.; CANMET, Energy, Mines, and Resources Canada and the Canadian Government Publishing Centre, Supply and Services Canada, 1985.

2. R.M. Davidson, Nuclear Magnetic Resonance Studies of Coal, IEA Coal Research, Report Number ECTis/TR32, London, 1986.

3. J. Schaefer and E.O. Stejskal, J. Amer. Chem. Soc., 1976, 98, 1031.

4. S.J. Opella and M. A. Frey, J. Amer. Chem. Soc., 1979, 101, 5854.

5. L.B. Alemany, D.M. Grant, R.J. Pugmire, and L.M. Stock, Fuel, 1984, 63, 513.

6. A. Soderquist, D.J. Burton, R.J. Pugmire, A.J. Beeler, D.M. Grant, B. Durrand, and A.Y. Huk, Energy and Fuels, 1987, 1, 50.

7. A helpful review of chemical shift anisotropy can be found in C.A. Fyfe, Solid State NMR for Chemists, C.F.C. Press, Guelph, Ontario, 1983, Chapter 5.

8. D.B. Wemmer, A. Pines, and D.D. Whitehurst, Phil. Trans. Roy. Soc. Lond. A300, 1981, 15.

9. J. Herzfeld and A.E. Burger, J. Chem. Phys. 1980, 73, 6021.

10. E.O. Stejskal, J. Schaefer, and J. McKay, J. Magn. Reson., 1977, 25, 569.

11. J.S. Frye and G.E. Maciel, J. Magn. Reson., 1982, 48, 125.

12. P.D. Murphy, T. Taki, and B.C. Gerstein, J. Magn. Reson., 1982, 49, 99.

13. N.K. Sethi, D.M. Grant, and R.J. Pugmire, J. Magn. Reson. 1987, 71, 476.

14. D.W. Alderman, M.S. Solum, and D.M. Grant, J. Chem. Phys., 1986, 84, 3717.

15. T.M. Duncan, J. Phys, Chem. Ref. Data, 1987, 10(No. 1), 125.

16. E. Furimsky and J. Ripmeester, Fuel Proc. Technal., 1983, 7, 191.

TABLE 1

Tensor Components[a] for Aromatic Carbons

Sample/Carbon Type	σ_{11}	σ_{22}	σ_{33}	Population[b] Factor
1,2,3,6,7,8 hexahydropyrene				
Benzene-like	225	128	22	0.40
Substituted	231	168	9	0.40
Inner	203	197	-6	0.20
Anthracite (PSOC-867)				
Benzene-like	217	137	20	0.13
Inner	194	180	-8	0.87
Inertinite[c]				
Benzene-like	223	149	17	0.39
Substituted	231	161	46	0.07
Inner	204	192	-30	0.54

a. ppm from TMS.

b. Based on total aromatic carbon present.

c. Semi-fusinite from Aldwarke Silkstone coal (Great Britain). The sample is described in reference 6.

FIGURE CAPTIONS

FIGURE 1. Chemical shielding tensors of aromatic carbons. The characteristic shapes are used to fit overlapping tensor elements. The narrow isotropic line obtained by magic angle spinning is also shown for purposes of clarity.

FIGURE 2. The static spectrum (top) of 1,2,3,6,7,8 hexahydropyrene. The individual tensors for the three different types of carbons are shown (bottom) together with the composite pattern. This theoretical fit of the data is superimposed in the top of the figure. Only the simulated aromatic carbon tensors are shown.

FIGURE 3. The tensor for a substituted aromatic carbon is simulated as a function of θ, the spinning axis relative to the magnetic field. The VASS experiment can be used to scale the position of the tensor components σ_{11}, σ_{22}, and σ_{33}. At the magic angle, $\theta = 54.7°$, the components converge to the isotropic value.

FIGURE 4. VASS spectra of 1,2,3,6,7,8 hexahydropyrene together with the simulated spectra arising from the aromatic carbons.

FIGURE 5. Experimental and simulated spectra of an anthracite coal. The two tensor fit gives near ideal correlation and the population factor for the benzene like tensor is within experimental error of the H/C value.

FIGURE 6. VASS spectra of Aldwarke Silkstone inertinite maceral (fusinite). The simulated spectrum of the aromatic carbons (bottom) is used to portray the population factors. The simulated aromatic carbon spectra at 43° and 72° are overlaid on the experimental data.

CSA
(aromatic carbons)

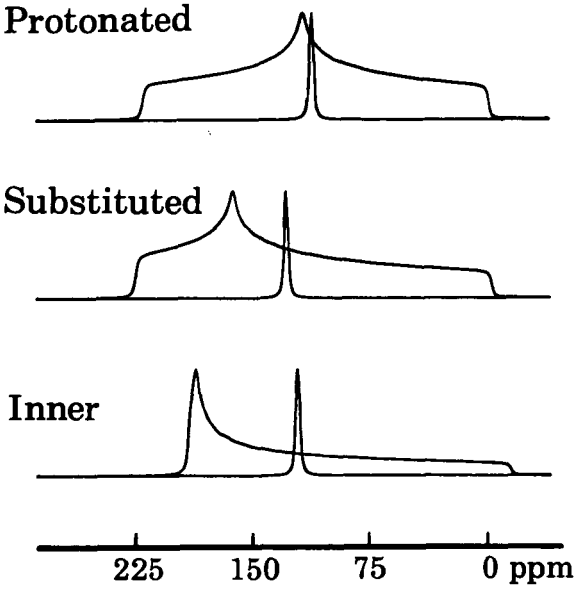

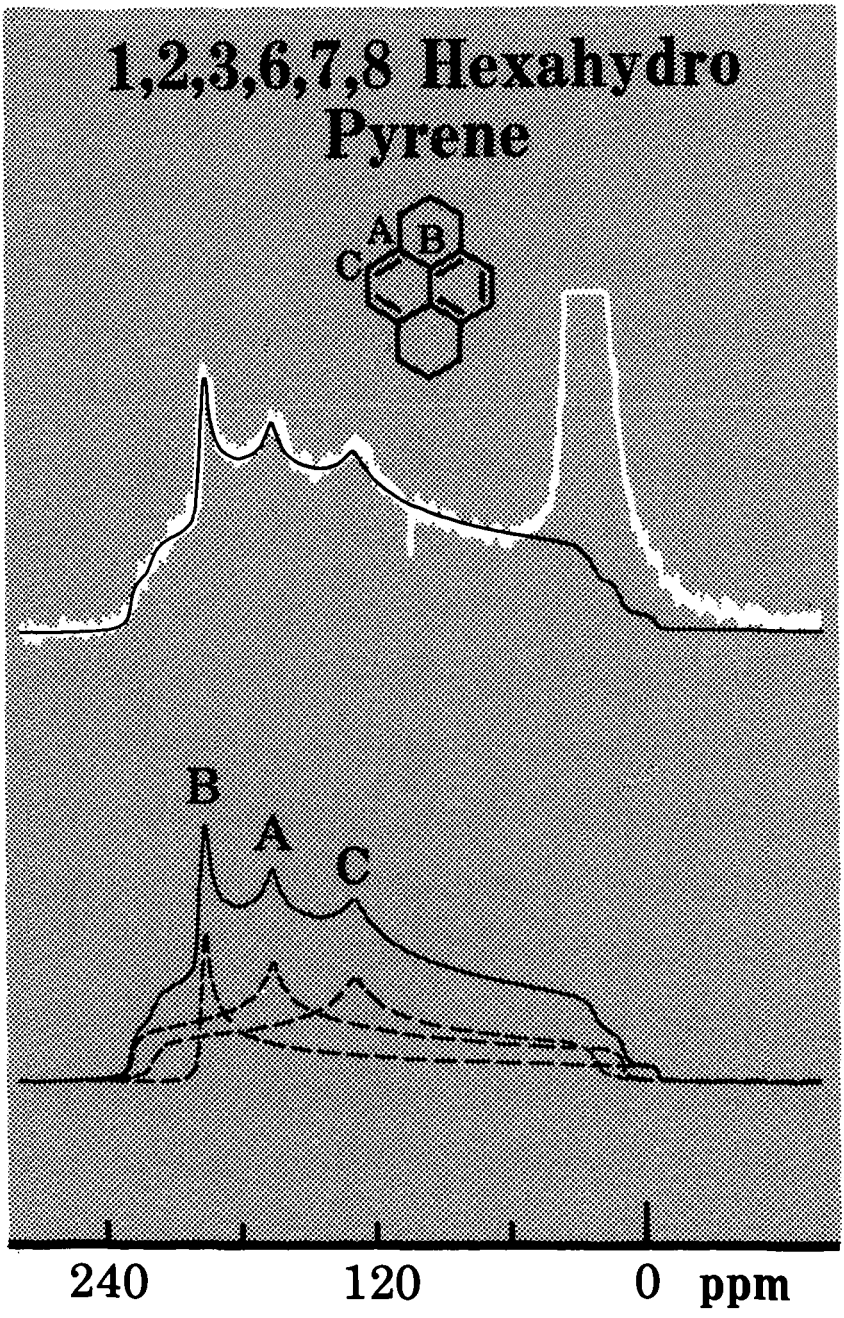
1,2,3,6,7,8 Hexahydro Pyrene
A
B
C
B
A
C
240
120
0 ppm

VASS

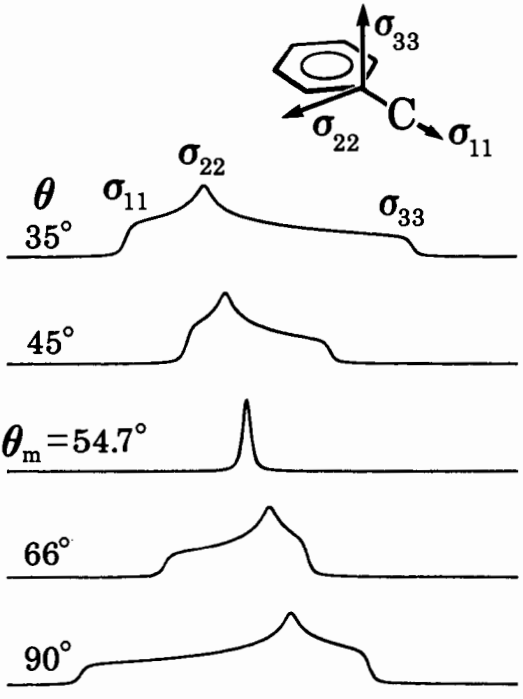

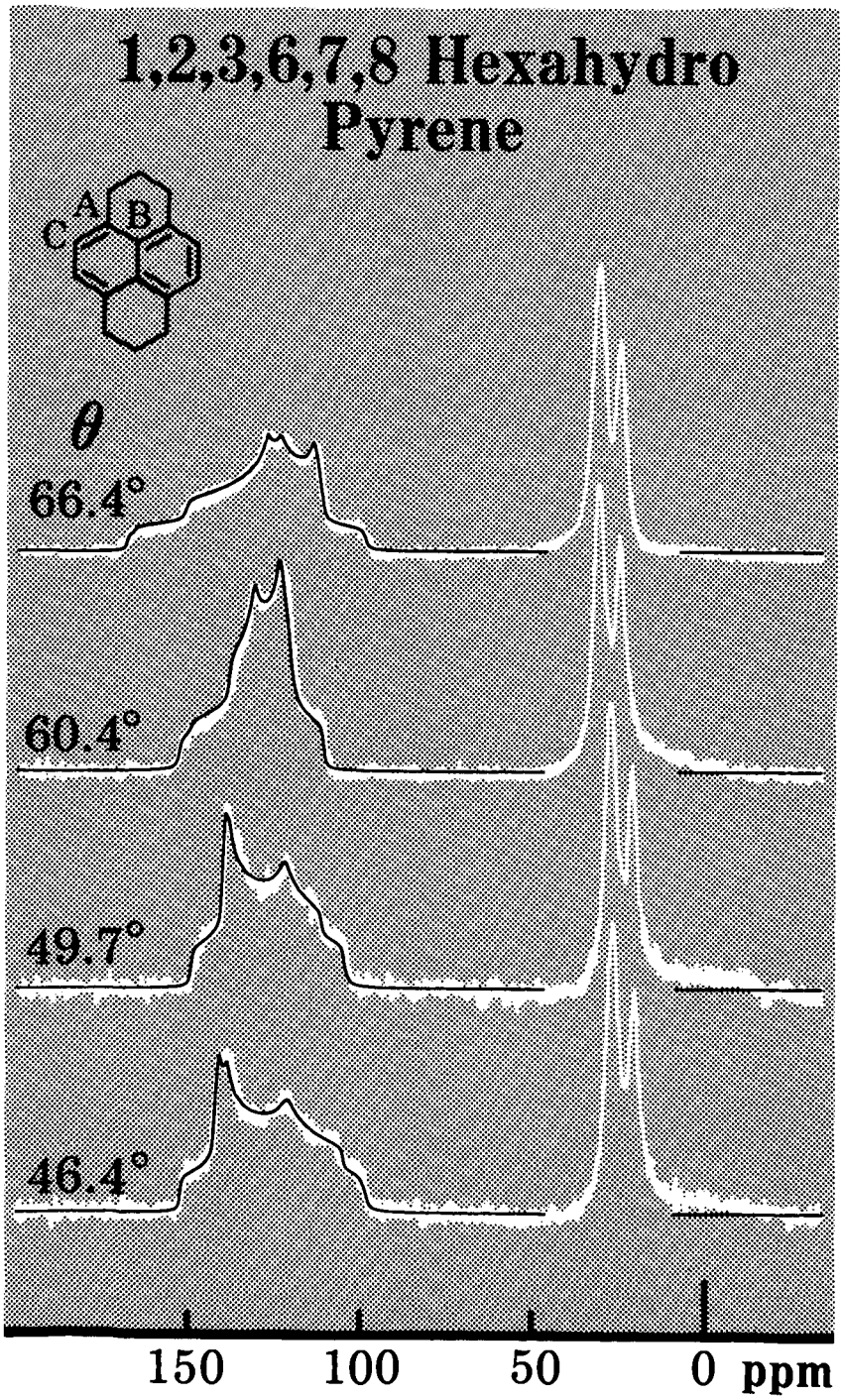
1,2,3,6,7,8 Hexahydro Pyrene
A
B
C
θ
66.4°
60.4°
49.7°
46.4°
150
100
50
0 ppm

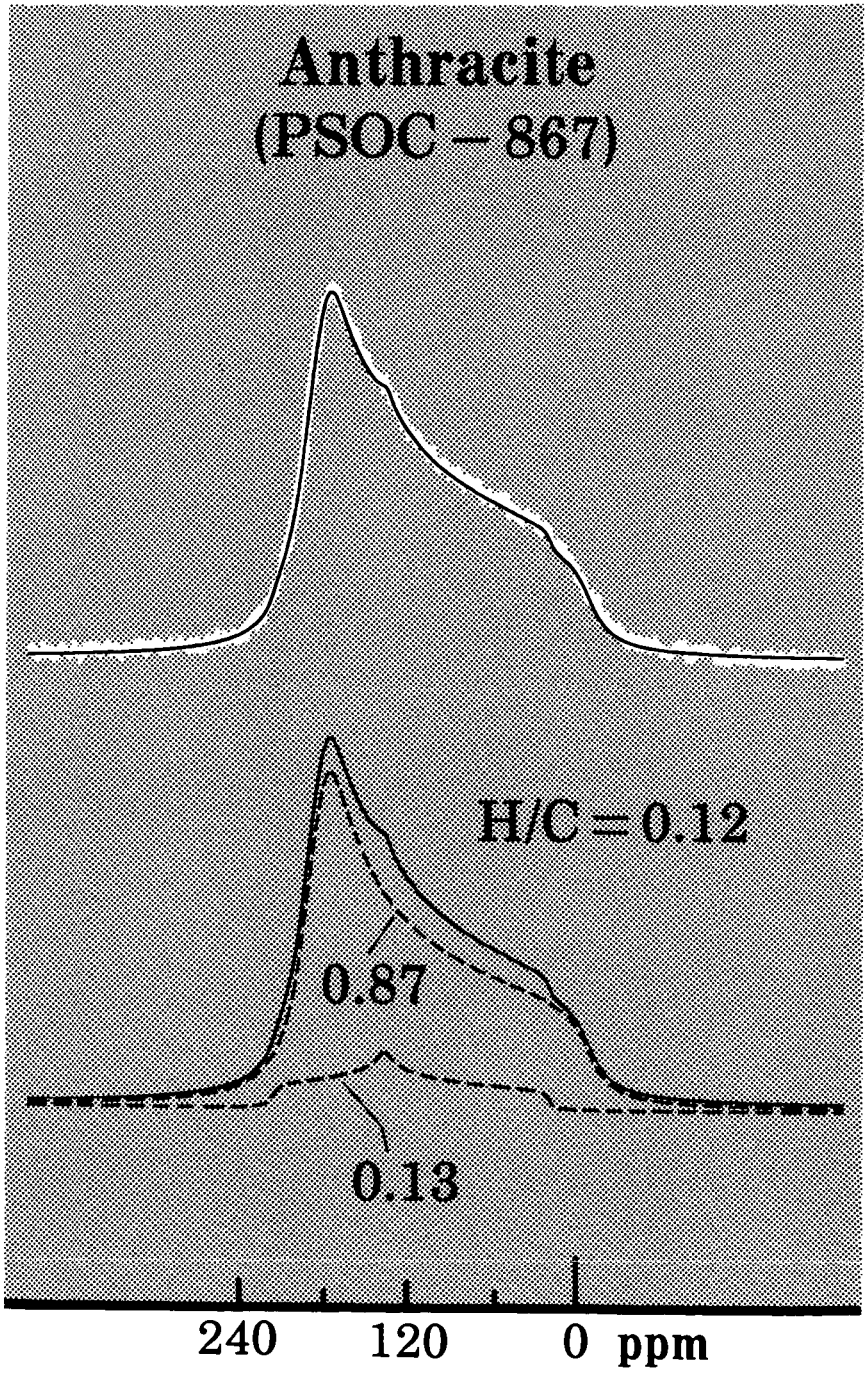
Anthracite
(PSOC – 867)
H/C = 0.12
0.87
0.13
240
120
0 ppm

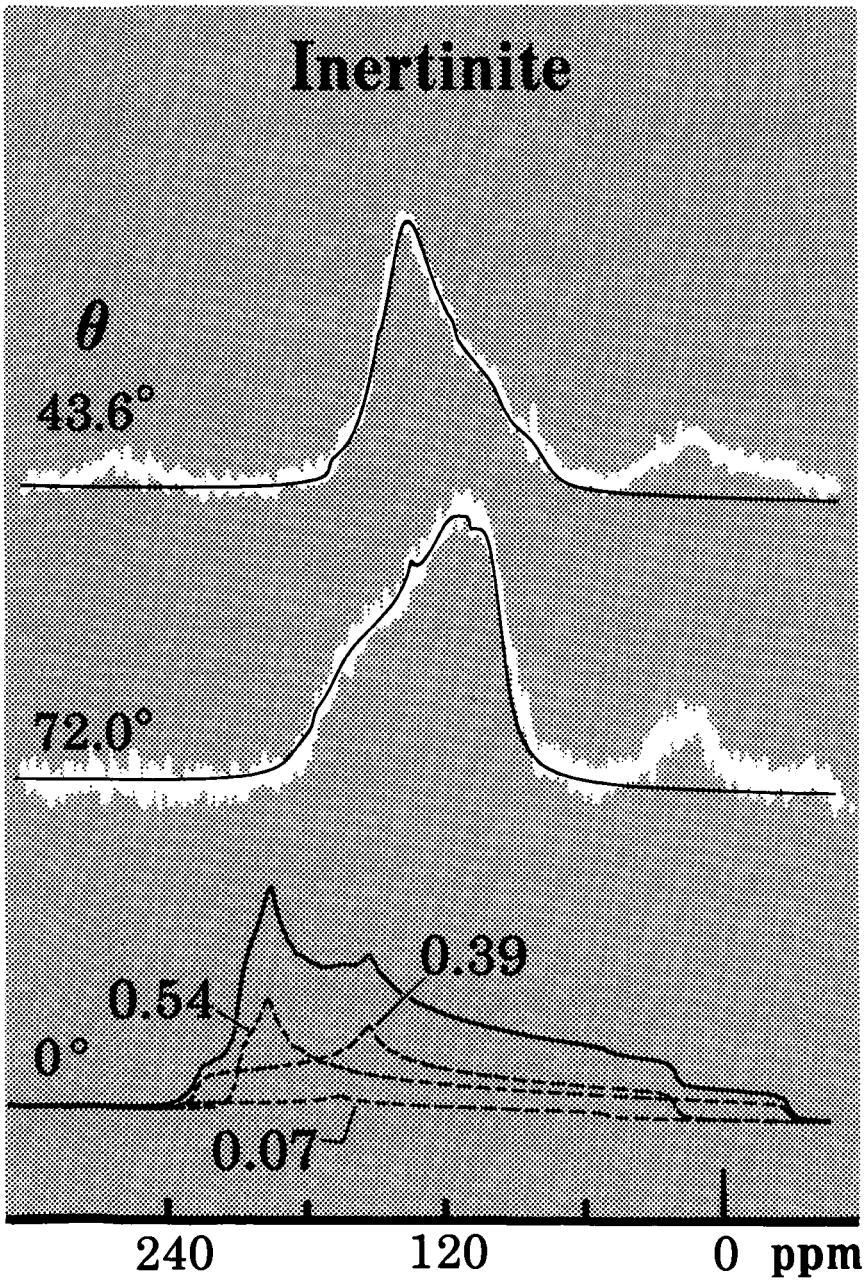
Inertinite
θ
43.6°
72.0°
0°
0.54
0.39
0.07
240
120
0 ppm

AN EXPERIMENTAL SIMULATION OF CROSSFLOW COAL GASIFICATION

M. Gallagher, J. Zondlo, E. Johnson, and E. Monazam
College of Engineering
West Virginia University
Morgantown, WV 26506-6101

ABSTRACT

A novel combustion test-pot facility was constructed and operated so as to simulate crossflow coal gasification with steam at ambient pressure. The test pot was fully instrumented to allow transient measurements of pressure drop, weight change of the bed, and product gas composition. In addition, the temperature front within the bed was tracked as a function of both time and position. Experiments were conducted at different air and steam flow rates in a packed particle bed of coke. The weight of an average coke charge was approximately 35 pounds and the fuel utilization rate ranged between 7.8 and 22 lb/ft^2-hr. Based on the experimental results, energy and mass balances were performed and closed to about 90%. Data obtained were used to verify a computer simulation of the process.

1. INTRODUCTION

The most common commercial coal gasification system in use today is the counter-flow moving bed system. In this system, the coal feestock moves downward and passes through four idealized zones in the gasification process. These zones in order from the top to the bottom of the bed are drying, pyrolysis, gasification and combustion. However, most moving-bed units are size-limited and several must be operated in parallel for larger throughputs.

An alternate approach to the design of a large-scale coal gasification system would be to borrow established technology from a similar process. One such process has long been utilized to sinter iron ore and produce a "strong clinker" suited for feed stock in a blast furnace. The sintering machine most commonly used today is a modification of the Dwight-Lloyd continuous sintering machine, formerly used only in the lead and zinc industry [1]. Originally developed in the early 1900's, the machine consists of a strong structural steel frame supporting two large gears and steel tracks. A system of pallets, or trays, with perforated bottoms is driven by these gears at a speed of 1 to 3 feet per minute. The sintering machine for iron ore may be 6 to 12 feet wide by 90 to 168 feet in length with pallets to hold the charge. Underneath the pallet train is a series of suction boxes which are connected with a fan to induce a downdraft through the perforated bottom and ore charge. Located at the input of the machine is a burner which serves to initiate the sintering process by igniting the top layer of charge. The charge is typically a mixture of ore particles up to 1/4-inch in diameter, flux, to aid in the agglomeration, and fuel, such as coke. The charge layer may be 6 to 12 inches deep. The largest machines will treat as much as 4500 tons of ore per day.

The possible application to coal gasification would be the replacement of the ore charge with coal [2]. The coal particles up to 1/4-inch in diameter would be placed on another layer of inert material, such as limestone, roughly 1/2-inch in diameter. This inert material would serve to protect the grate thermally, support the smaller coal particles, trap out particulates and possibly aid in sulfur removal from the product gas stream.

The main objectives of the work presented here were the design, construction and start-up of an experimental appratus that would effectively simulate the crossflow process. The independent variables such as air temperature and flow rate, and relative humidity of the air feed were selectively examined to determine their effect on the exit gas composition and fuel utilization rate. These data will assist in determining the reliability of the experimental test-pot system and its potential for use in future experimental and modelling efforts.

II. EXPERIMENTAL APPARATUS

A flowsheet of the proposed test-pot facility is shown in Figure 1. Ambient air, fed from a ring compressor, was preheated and humidifed before it entered the combustion pot. An orifice plate served as an air flowmeter, while the air was preheated using a steam heater. Supply steam at 30 psig was regulated, using a Kaye MacDonald regulator, to the pressure required to obtain the desired heater temperature. The air was humidifed by direct injection of saturated steam. The temperature and relative humidity (RH) of the feed air were measured as the air entered the combustion pot using an Omega RH-20F hygrometer. This instrument is capable of reading temperatures to 175°F ± 0.5°F and relative humidity to 95% ± 2%. The humidity measurement was backed with a Hygrodynamics L4-4822W sensor and L15-3050 Universal Indicator capable of reading to 98% RH ± 1.5%. After the product gas exited the test pot, a sample was taken for analysis and the remainder combusted in an afterburner.

The test pot itself is shown in Figure 2. It consists of a 24-inch o.d. steel pipe, 1/2-inch thick wall, with a 1/8-inch thick stainless steel plate welded to the bottom. The plate is perforated with 3/8-inch diameter holes located on 1/2-inch triangular centers. The pipe is lined with 5 inches of insulation brick refractory, resulting in an inside bed diameter of 13 inches. Pt vs. Pt 10% Rh thermocouples (TC) are placed at 2-inch intervals above a 6-inch layer of non-combustible material. The thermocouples are rated to 3000°F and can be used in oxidizing or reducing atmospheres. The temperature in the coal bed is monitored automatically as a function of time as well as position by means of a Doric Digitrend 220 data logger.

Operating at near atmospheric pressure, the test pot is free-hanging while the transient weight change of the coal is recorded utilizing a load cell. The load cell is a Sensotec model RM-1K, hermetically sealed to withstand humid and corrosive environments and temperature compensated to 160°F. It has a range of 0 to 1000 pounds mass and its stated accuracy is ± 0.2% of full scale or ± 2 pounds. A Sensotec 450D digital readout with a 0-5 volt recorder output is used in conjunction with the load cell. The separation between the inlet and outlet of the pot is maintained by a water seal which allows the test pot to hange freely and still maintain the division between the inlet and outlet of the bed.

a) Experimental Procedure

The bed was charged with 35 pounds of coke, resulting in a coke bed density of 38 lb/ft^3. Coke, the devolitalized product of coal, was selected as the feedstock for the initial tests as it would produce a less complex gasification product, free of tars and volatile material. For a typical experimental run, the procedure is as follows. The air, fed at 25 CFM and 77°F, is heated to 140°F and humidifed to near 100% RH before entering the combustion pot. The air feed is started first and allowed to reach steady state at which point the fuel charge is ignited with charcoal placed at the top of the charge. Ignition of the fuel occurs within 5 to 10 minutes. The data logger is used to record the temepratures at specific time intervals, initially every

minute. The weight change with time as monitored by the load cell is also recorded continuously with a strip-chart recorder. Finally, gas samples from the outlet of the test pot are taken at specific time intervals, every 10 minutes, and analyzed with a gas chromatograph (GC). The GC is a Gow-Mac Series 550 thermal conductivity-type gas chromatograph equipped with a gas sampling valve, series/by-pass column switching valve, one 5A molecular sieve column and one Porapak Q column. The run is considered finished when the combustion front reaches the bottom of the bed. This is tracked via the thermocouples placed at intervals within the depth of the bed, and is also indicated by abrupt changes in the gas composition and the pressure drop across the bed.

III. RESULTS

a) Product Gas Composition

Samples of the product gas were withdrawn from the bottom of the combustion pot at approximately 10 minute intervals. The GC was configured for the detection of N_2, CO_2, H_2, CH_4, CO and O_2. A representative composition/time profile is shown in Figure 3. After an initial transient period (around 20 minutes for the run in Figure 3), the product gas composition remains essentially constant for the duration of the test. The onset of breakthrough is signalled by an abrupt increase in the N_2 composition late in the run. A typical product gas contained roughly 20% CO_2, 10% CO, 10% H_2, 2% CH_4 and 60% N_2. The GC was checked before and after each run with a standard calibration gas obtained from Supelco, Inc.

b) Weight Change

The transient weight of the bed provided the data necessary to calculate the fuel utilization rate and the rate of progression of the combustion front. Representative data for a typical run are shown in Figure 4. This data, used in conjunction with the transient pressure drop across the bed, permitted the actual weight change with time to be determined.

In all cases, the weight change profiles showed an initial period in which the weight of the bed remained relatively constant, followed by a uniform decrease in weight until the end of the run. The slope of this line when divided by the cross-sectional area of the bed yielded the fuel utilization rate at the conditions of the experiment. This was found to vary from 7.8 lb/ft^2-hr at the lowest air flow rate to 22.1 lb/ft^2-hr at the highest air flow rate. These values are well within the range of those reported for the Wellman-Galusha gasifier with a coke fuel [3]. Comparable results were also found by Essenhigh who reported fuel utilization rates of 5 to 25 lb/ft^2-hr under similar experimental conditions [4].

The fuel utilization rate when multiplied by the density of the packed bed yielded the rate of progression of the combustion front which ranged from 0.06 to 0.13 inches per minute.

c) Temperature Profiles

The temperature profiles of a typical experimental run are shown in Figure 5. Such data are useful in determining the progression of the combustion and gasification zones through the bed. A sharp increase in temperature in the early stages followed by a peak as the combustion zone passed, and finally a decrease in slope as the gasification zone passed, are characteristics of all the profiles.

The temperature profiles were used as an alternate method for calculating the

progression of the combustion front through the bed by measuring the time between the temperature maxima at each thermocouple location. The progression of the combustion front determined in this manner was compared with the progression as determined from the weight change data as a check of the load cell instrumentation and as a check on the evenness of the burn. Good agreement was seen in the progression of the combustion front as determined by each method. This would indicate that the combustion front of the fuel bed is burning in a relatively uniform, plug-flow manner.

d) Mass and Energy Balances

The calculation of the mass and energy balances was done as a check of the overall performance of the instrumentation.

The mass balance focused primarily on the carbon present in the charge. In order to calculate the carbon balance, it was necessary to obtain the inlet gas flow rate and composition, the outlet gas flow rate and composition, and the length of time the run was in progress. From this information the mass of carbon present in the exit gas could be determined and compared to the mass of carbon that was consumed as calculated from the weight change. Such a balance resulted in closure to over 90% in most cases, indicating that the instrumentation was functioning adequately for the intended purpose.

The energy balances also showed good results, usually accounting for over 90% of the energy released from the coke fuel. Approximately 50% to 55% of the energy leaves the bed in the form of combustables in the product gas. The heat losses to the system were 20% of the energy available, while the energy carried as sensible heat in the product gas accounted for approximately 20% as well. These results are encouraging in showing that the instrumentation and the experimental system are operating reliably.

IV. DISCUSSION

For the Wellman-Galusha gasifier with a coke fuel the CO and H_2 concentrations observed in the product gas are 29 mol% and 15 mol% respectively [3]. The data collected from the test pot came to only 50% to 60% of those for the Wellman-Galusha gasifier. Moreover, the heating value reported for the Wellman-Galusha was 130 BTU/ft^3; the crossflow product gas was only 80 BTU/ft^3. Also, Essenhigh reports CO concentrations of 23 mol% for his similar test-pot studies using a coke fuel [4]. He does not report a value for hydrogen. In an associated modelling effort, both the results of the test pot and the other workers could be predicted by including a reactivity factor in the rate equations to account for variations in feedstock characteristics [5]. Thus differences in product gas composition may reflect variations in the physical and chemical characteristics and hence reactivity of the feedstock.

The test pot responded to changes in air feed to the bed as expected. Under the same steam feed conditions, higher air flow rate resulted in higher combustion temperature and a shorter run time. The test-pot also responded as expected to changes in the steam feed to the bed. High steam rates resulted in lower temperatures in both the combustion and gasification zones. This in turn affected the product gas compositions by suppressing CO production and increasing H_2 production. The lower combustion and gasification temperatures also allowed for more uniform heating of the bed and a more defined and stable gasification zone. Conversely, low steam flows yielded higher combustion and gasification temperatures, with CO production favored and H_2 suppressed.

It should also be noted that CO_2 generated in the combustion zone is not being completely converted to CO as it passes through the gasification zone. Low temperature, short residence time, gas channeling, clinker formation or low fuel reactivity are possible factors affecting conversion.

V. CONCLUSIONS

The fuel utilization rates for this system were comparable to those for the Wellman-Galusha gasifier [3]. The carbon mass balance resulted in over 90% closure in most cases, a result which is consistent with that reported by other researchers in the gasification area [3,4]. The energy balances show approximately 50% of the energy leaves the gasifier in the form of combustables. Another 20% of the energy leaves in the form of sensible heat and roughly 20% is lost to the system.

Based upon the data collected and the mass and energy balances performed, the experimental test pot system operated reliably and produced good data.

REFERENCES

1. Kirk-Othmer Encylopedia of Chemical Technology, Third Edition, John Wiley & Sons, New York, Volume 24, p. 816, 1980.

2. Gallagher, M. A., M. S. Thesis, Department of Chemical Engineering, West Virginia University, Morgantown, WV, 1986.

3. Probstein, R. F. and Hicks, R. E., Synthetic Fuels, McGraw-Hill, New York, pp. 95-107, 1982.

4. Eapen, T., Blackader, R., and Essenhigh, R. H., "Kinetics of Gasification in a Combustion Pot: A Comparison of Theory and Experiment," Proceedings of the 16th Symposium on Combustion, Pittsburgh, PA p. 515-522, 1977.

5. Monazam, E. R., Ph.D. Dissertation, Department of Mechanical & Aerospace Engineering, West Virginia University, Morgantown, WV 1986.

This work was funded in part by the State of West Virginia through the Energy Research Center at West Virginia University.

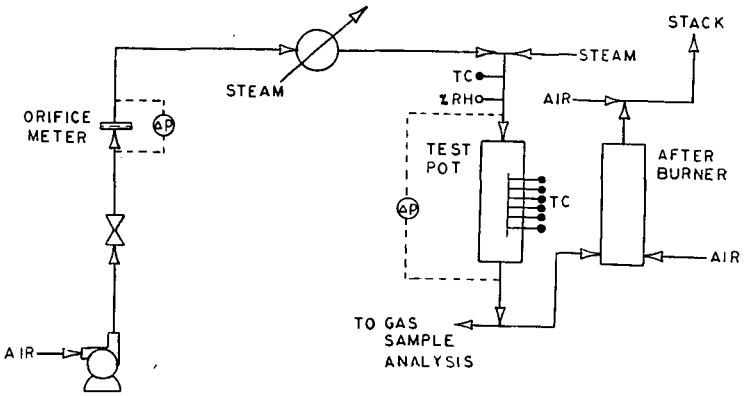

Figure 1. Overall flowsheet of crossflow coal gasification test pot facility.

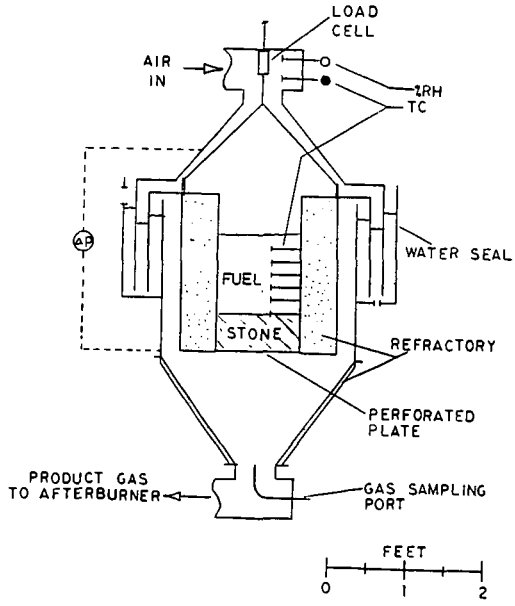

Figure 2. Cross-sectional view showing details of experimental test pot.

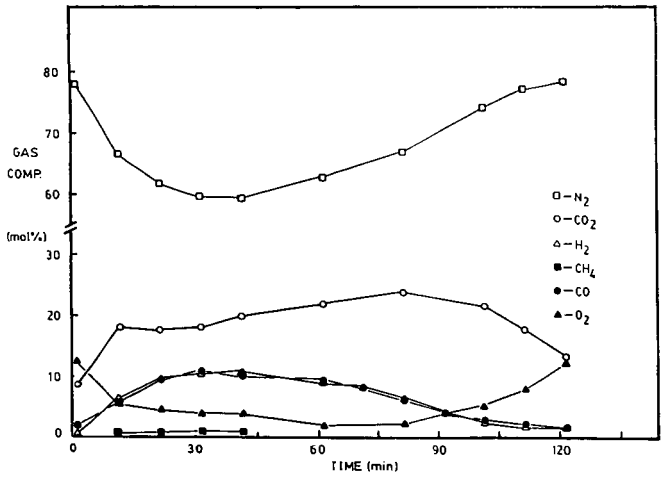

Figure 3. Representative composition/time profiles for major components in product gas stream.

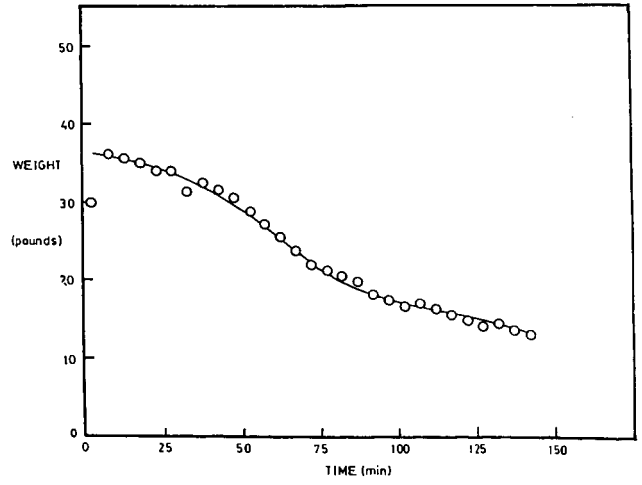

Figure 4. Transient weight change of coke charge for a typical gasification test.

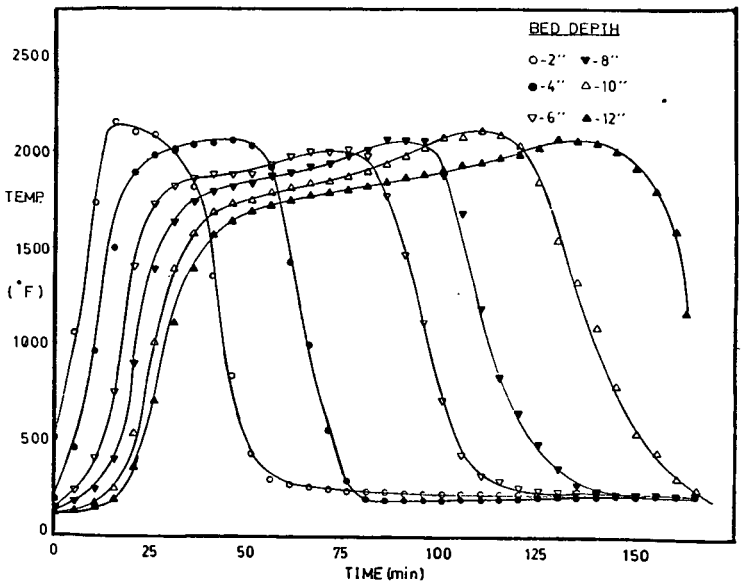

Figure 5. Transient temperature profiles at varous bed depths as measured from the top of the bed.

MODELING OF HYDROGASIFICATION OF A SINGLE LIGNITE CHAR PARTICLE

G.P.Sakellaropoulos, G.Skodras, S.P.Kaldis,
G.G.Stavropoulos and P.S.Kokorotsikos

Department of Chemical Engineering and
Chemical Process Engineering Research Institute
Aristotle University of Thessaloniki
Thessaloniki, Greece 54006

INTRODUCTION

Gasification, devolatilization, combustion and other coal conversion processes are quite complex, involving numerous, not well defined reactions, and simultaneous physical structure transformations. In order to describe these phenomena, several efforts have been reported, based either on empirical kinetic expressions (1-5) or on theoretical models (6-12). In the former, rate expressions are given in terms of volatile species, residual and active carbon, and reactant gas concentration or pressure. Theoretical models attempt to couple reaction rates with mass and heat transfer processes. The various models, however, differ significantly from each other, because of the diversity of the chemical and physical phenomena which they describe (e.g. pyrolysis, combustion, steam gasification etc) and the differences in assumptions and simplifications involved in each one.

Fast coal processes, such as oxygen combustion, rapid pyrolysis and devolatilization are usually considered to proceed via a shrinking core model, either isothermally or non-isothermally (6-11). Mass transport limitations are often assumed to occur within a reacted shell, surrounding a coal particle (6-7). The pore structure of the reacting particles is considered unchanged, in most of these models (6-9), although the effect of pore size distribution has been examined (8).

Structural variations of coal with reaction time have been included in few models, such as in hydropyrolysis of softening coals (10), in coal-oxygen reactions (11) and in char gasification (12). In a comprehensive analysis of coal combustion models, Sotirchos and Amundson (11) considered only the macropores of coal. Thus, local conversion and pore structure depended only on the thermal gradients at various total conversions. Lee at al. (12) developed a char gasification model, in which Knudsen diffusion (in the micropores), as well as pore structure variations due to carbon consumption, were included. However, only one reaction was considered to take place, with CO_2 as a gasifying medium. This model simplifies the reaction network, ignoring the participation of an active carbon species and also the product mass transfer and the reactant accumulation. These simplifications yield an analytical solution, at pseudosteady state conditions.

The model proposed here considers the physical and chemical processes occuring in a gasifying single particle and correlates the predicted results with experimental macroscopic data. An active carbon species is assumed (13) to react in two parallel steps to form a gaseous product or stabilized char (coke). Reactant and product diffuse in and out of the particle while the local micropore structure can vary due to carbon reaction and consumption. The model permits estimation of the local radial distribution of reactant and product concentrations, reaction rates, surface areas and porosities with time. Global properties, such as product yields, surface area and porosity are also calculated, for comparison with the corresponding experimental quantities. The model is applied here to coal hydrogasification, a process which has received less attention compared with steam or CO_2 gasification.

FORMULATION OF THE MODEL

A single spherical lignite or coal particle, of radius r_o, is considered to undergo hydrogasification, after initial rapid devolatilization. During this initial stage, a measurable, uniform pore structure, and an assumed hydrogen profile have developed within the particle. The following assumptions apply to the model formulation:
- Isothermal reaction in a uniform, constant hydrogen atmosphere.

- Constant particle size, with uniform radial pore structure distribution initially (t=0).
- Negligible film diffusion resistance around the particle.
- Predominantly micropore structure for the particle.

Char hydrogasification involves an active carbon species, which, with hydrogen yields methane, or by crosslinking results in coke formation and carbon stabilization:

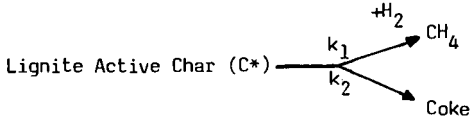

1a)

1b)

From available rate expressions for CH_4 and coke formation (13), the instantaneous, local reaction rates within the particle are given by Equations 2 and 3.

$$R_{CH_4}(r,t) = k_1^o \exp(-\frac{E_1}{RT})\ \rho_p S_g\ C_{C^*} C_{H_2} \qquad 2)$$

$$R_{Coke}(r,t) = k_2^o \exp(-\frac{E_2}{RT})\ \rho_p S_g\ C_{C^*} = \frac{dC_{coke}}{dt} \qquad 3)$$

Reactant (H_2) and product (CH_4) counter diffuse through the porous particle matrix which varies with time and location due to reaction. Thus, the continuity equation for the two gaseous species gives:

$$\frac{\partial C_{H_2}}{\partial t} = \frac{1}{r^2}\frac{\partial}{\partial r}(r^2 D_{e,H_2}\frac{\partial C_{H_2}}{\partial r}) - 2R_{CH_4}(r,t) \qquad 4)$$

$$\frac{\partial C_{CH_4}}{\partial t} = \frac{1}{r^2}\frac{\partial}{\partial r}(r^2 D_{e,CH_4}\frac{\partial C_{CH_4}}{\partial r}) + R_{CH_4}(r,t) \qquad 5)$$

The effective diffusivities ($D_{e,j}$) can be related to the Chapman-Enskog diffusivity (D_{H_2/CH_4}) and the Knudsen diffusivity into the micropores (D_k), (14), by

$$D_{e,j} = (\frac{I}{D_{12}} + \frac{1}{D_k})^{-1}\ \varepsilon^2 \qquad 6)$$

Weight (m) loss and increase of surface area (S_g) and porosity (ε) of the particle occur because of the first reaction, 1a, and, thus, they can be correlated with the conversion to methane (X_{CH_4})

$$\varepsilon = 1 - (1 - X_{CH_4})\ (1 - \varepsilon_o) \qquad 7)$$

$$m = m_o + \frac{4}{3}\pi r^2\ \rho_t(\varepsilon_o - \varepsilon) \qquad 8)$$

$$\rho_p = \rho_t\ (1 - \varepsilon) \qquad 9)$$

Relation 6, between bulk (ρ_p) and true (ρ_t) particle density, is valid for non-swelling or -shrinking particles of constant size. For moderate conversions, the surface area may be assumed to vary linearly with porosity (15)

$$S_g = S_o\ \varepsilon \qquad 10)$$

This system of non-linear partial differential equations was converted to a system of dimensionless non-linear algebraic equations by the explicit finite difference method. Equation 2-4 and 6-10 were solved iteratively, using the Brown technique (16) and the appropriate boundary conditions for C_{C*}, ϵ, C_{H_2} below. Solution of Eq. 5, with the pertinent B.C. for C_{CH_4} below, gives the methane distribution in the particle.

$$\text{At } t = 0 \text{ and } 0 \leq r \leq r_o \qquad \begin{cases} C_{C*} = C_{C_o^*} \\ \epsilon = \epsilon_o \\ X_{CH_4} = 0 \\ X_{coke} = 0 \end{cases}$$

$$t > 0 \text{ and } r = r_o \qquad \begin{cases} C_{H_2} = C_{H_2,S} \\ C_{CH_4} = 0 \end{cases} \qquad 11)$$

$$t > 0 \text{ and } r = 0 \qquad \begin{cases} \frac{\partial C_{H_2}}{\partial r} = 0, \quad \frac{\partial C_{CH_4}}{\partial r} = 0 \end{cases}$$

All char carbon ($C_{C_o^*}$) is considered reactive, as indicated by its complete conversion in high pressure experiments. Since hydrogasification occurs after initial rapid hydropyrolysis (17), some hydrogen profile is expected within the particle matrix. Thus, instead of the conventional boundary conditions for hydrogen, a simple linear initial profile has been assumed and tested

$$\text{At } t = 0 \text{ and } 0 \leq r \leq r_o \qquad C_{H_2} = \frac{r}{r_o} C_{H_2,S} \qquad 12)$$

A linear, or perhaps a parabolic, hydrogen profile should be more realistic, since hydrogen has penetrated into the pores during the first stage. Alternatively, a uniform zero hydrogen concentration may be assumed ($C_{H_2} = 0$ at $t = 0$, $r \leq r_o$), or even a uniform concentration equal to the bulk one ($C_{H_2} = C_{H_2,S}$ at $t = 0$, $r \leq r_o$).

Parameter values were obtained either experimentally or from the literature. Values of k_1^o, E_1, S_o, ϵ_o and ρ_t were measured at 800 - 950°C, while k_2^o and E_2 are experimental values reported in reference (18). The following values were used

E_1 = 35600 cal/mol
E_2 = 28600 cal/mol
k_1^o = 1.7x10^{-6} m^4/mol·min
k_2^o = 3.77x10^{-7} m/min
ρ_t = 1.42 gr/cm^3

S_o^{800} = 355 m^2/g
S_o^{850} = 388 m^2/g
S_o^{900} = 395 m^2/g
S_o^{950} = 410 m^2/g

ϵ_o^{800} = 0.17
ϵ_o^{850} = 0.175
ϵ_o^{900} = 0.18
ϵ_o^{950} = 0.19

EXPERIMENTAL

Lignite hydrogasification experiments, to obtain kinetic parameters and macroscopic, global properties, were performed in a TGA (DuPont 99) system and in an isothermal, tubular reactor (17, 19). Products were continuously analyzed by GC and IR. Pore structure, porosity, density and surface area of lignite chars, at various times and temperatures, were characterized by multipoint BET, helium pycnometry, CO_2 and N_2 adsorption (20).

RESULTS AND DISCUSSION

The model formulated above has been solved using a simple, linear profile for the initial concentration of hydrogen within the particle. Solution has been obtained at eleven radial positions for a time period of 30 min using a time increment of one minute. The results permit estimation of non-measurable quantities, such as the temporal-radial distribution of (a) hydrogen, methane and coke concentration; (b) porosity and surface area; and (c) local rates of methane and coke formation, under various reaction conditions. Integration of predicted results over the whole particle yields global properties, such as particle weight loss, methane yield and rate of formation, total porosity and surface area.

Comparison of predicted and measured macroscopic properties should establish first the adequacy of the model to describe the chemical and physical processes. Figure 1 shows calculated and experimental values of carbon conversion to methane at various times and temperatures. In most cases, agreement is good. Some deviation of experimental data, especially at high temperatures, may arise from a number of reasons, e.g. different initial hydrogen profile, slightly higher order in H_2 for reaction 1a, or higher k_2 and E_2 values than those obtained from the literature for the crosslinking and carbon stabilization reaction.

Similarly, the predicted development of total particle surface area and porosity is in good agreement with the measured physical properties up to 30-40 min, Figures 2 and 3. One should note, here, that Equations 7 - 10 of the model assume a linear growth of surface area and porosity, directly proportional to carbon conversion to methane. Pore blockage, because of carbon stabilization and crosslinking, is not currently considered in the model. This phenomenon may explain the decline of S_g and ε at prolonged times.

After the above macroscopic comparison of model and experimental results, a microscopic examination should unravel the transformations that a lignite particle undergoes during hydrogasification. Figure 4 shows the anticipated hydrogen concentration profile in the particle, at various times. If the initial (t=0) hydrogen concentration is assumed to vary linearly with radius, C_{H_2} in the pores increases with time; however, it always remains less than the bulk one, because of partial consumption of H_2 to form methane and counter-diffusion of the product. The hydrogen concentration in the pores is also expected to increase (albeit somewhat slower) in the case of uniform, zero C_{H_2} initially. If at t=0, $C_{H_2}=C_{H_2,S}$, hydrogen diffuses into the pores faster than it reacts and its concentration remains constant with time.

Methane is produced by reaction of active carbon with H_2 and diffuses out of the gasifying particle. Its concentration distribution radially can be predicted by this model, as shown in Figure 5. At the outer layers of the particle, the high local C_{H_2} results in high carbon-to-CH_4 conversion and, thus, methane concentration increases. The decline of CH_4 at the surface ($r=r_o$) is caused by the assumption that methane is so diluted in the bulk stream that its bulk and surface concentration is virtually zero. Methane concentration in the particle increases with time because of C_{H_2} increase, cf. Fig. 4.

Carbon consumption to form gaseous methane should increase the number and size of pores within the particle, dependent on rate. If the "specific surface area", S_g, is used as an approximate, lumped measure of pore structure development, a surface area radial distribution can be predicted, Figure 6. This area increases, from the center of the particle outwards, because of the higher H_2 concentration and rate in the outer shells. Since C_{H_2} increases with time within the particle, S_g also increases, to a substantial difference of ~ 50 m^2/g between surface and center at 30 min reaction time. A similar trend is predicted for the local "porosity", ε, radially with time.

The calculated local values of C_{H_2}, S_g, ε permit estimation of the local reaction rate for methane formation at any time, Figure 7. Rate increases outwards, following a trend analogous to C_{H_2} and S_g. Around the center of the particle, C_{H_2} increase with time results in significant increase of R_{CH_4} after 30 min. Near the surface, R_{CH_4} is affected by the surface area increase (cf. Fig. 6), since C_{H_2} there changes little (Fig. 4).

Figure 7 and Equation 2 indicate that hydrogasification is sensitive to H_2

partial pressure. Thus, recycle of the reactant stream without prior separation of product could affect rates in the pores significantly. Figure 8 shows a drastic decrease of methane formation rate within a gasifying particle, at 5 min. With $P_{CH_4} : P_{H_2} = 1 : 1$ in the bulk stream, rates drop to almost zero for $r < 0.5\ r_o$, and to less than 15 % of that for pure H_2, at r_o. Integration of these curves with location and time show that carbon conversion to methane at 900°C should drop from ~6% in pure H_2 to ~1% at $P_{H_2} = 0.5$ atm.

The model described here takes into account a realistic, two path reaction scheme for hydrogasification, with simultaneous variation of the pore structure properties of the gasifying char particle. Porosity and surface area do not develop uniformly, within the particle, with time and this affects hydrogen penetration, methane counter-diffusion and, thus, the microscopic and global rate of gasification. The model predicts succesfully experimental macroscopic quantities, up to 30-40 min of gasification. Beyond this time, carbon stabilization and pore blockage may cause some deviation. The use of the model can be easily extended to noncaking coals other than lignite and to other gasification media such as CO_2 or steam.

ACNOWLEDGEMENT

The authors wish to thank the European Coal and Steel Community and the Chemical Process Engineering Research Institute of Thessaloniki for financial support of this work.

LIST OF SYMBOLS

C^*	Active carbon concentration (mol/m^3).
C_{CH_4}	Intraparticle methane concentration (mol/m^3).
C_{H_2}	Intraparticle hydrogen concentration (mol/m^3).
$C_{H_2,S}$	Bulk hydrogen concentration (mol/m^3).
$D_{e,j}$	Effective diffusivity of species j (H_2 or CH_4) (m^2/s).
D_{12}	Chapman-Enskog diffusivity (m^2/s).
D_k	Knudsen diffusivity (m^2/s).
E_1, E_2	Activation energies of methane and coke formation (cal/mol).
ϵ	Porosity of particle.
I	Binary diffusivity coefficient (0.25 for D_{e,H_2} and -0.5 for D_{e,CH_4}).
k_1^o, k_2^o	Rate constants of methane and coke formation.
m	Particle mass (g).
ρ_p	Bulk density of particle (g/cm^3).
ρ_t	True density (g/cm^3).
r	Particle radial coordinate (μ).
r_o	Particle radius (μ).
R	Universal gas constant (1.987 cal/mol K).
R_{CH_4} (r,t)	Rate of methane formation (mol/m^3 min).
R_{coke} (r,t)	Rate of coking reaction (mol/m^3 min).
S_g	Specific surface area (m^2/g).
T	Temperature (K).
t	Time (min).
X_{CH_4}	Methane conversion.

Subscripts

o	Initial values at t = 0.
s	Bulk stream and particle surface property.

REFERENCES

1. Moseley F. and Paterson D., J. Inst. Fuel., 38, 13, (1965).
2. Johnson J.L., Adv. Chem. Ser., 131, 145, (1974).
3. Wen C.Y. and Huebler J., Ind. Eng. Chem. Process Des. Dev. 4, 142, (1965).
4. Schmal M., Monterlo J.L.F. and Castellan J.L., Ind. Eng. Chem. Process Des. Dev. 21, 256, (1982).

5. Anthony D.B. and Howard J.B., AIChE J., 22, 625, (1976).
6. Arri L.E. and Amundson N.R., AIChE J., 24, 72, (1978).
7. Russel W.B., Savill D.A. and Greene M.I., AIChE J., 25, 65, (1979).
8. Gavalas R.G. and Wilks K.A., AIChE J., 26, 201, (1980).
9. Bliek A., Poelje W.M., Swaalj W.P.M. and van Beckum F.P.H., AIChE J., 31, 1666 (1985).
10. Shaub G., Peters W.A. and Howard J.B., AIChE J., 31, 903, (1985).
11. Sotirchos S.V. and Amundson N.R., AIChE J., 30, 537, (1984).
12. Lee S., Angus J.C., Edwards R.V. and Gardner N.C., AIChE J., 30, 583, (1984).
13. Zahradnik R.L. and Glenn R.A., Fuel, 50, 77, (1971).
14. Walker Jr., P.L., Rusinko Jr., F. and Austin L.G., Adv. Catal., 11, 133, (1959).
15. Hill, Jr., C.G., "An Introduction to Chemical Engineering Kinetics and Reactor Design" J.Wiley, N.Y. (1977), pp 434.
16. Brown K.M., Comm. ACM, 10, 728, (1967).
17. Kokorotsikos P.S., Stavropoulos G.G. and Sakellaropoulos G.P., Fuel, 65, 1462, (1986).
18. Banerjee D.K., Laidler K.J., Nandi B.N. and Patmore D.J., Fuel, 65, 480, (1986).
19. Kokorotsikos P.S., Stavropoulos G.G. and Sakellaropoulos G.P., Proc. Int. Conf. Coal Sci., 253, Sydney, Oct. 1985.
20. Stavropoulos G.G., Kokorotsikos P.S., Sakellaropoulos G.P., Carbon 86, 4th Int. Carbon Conf., 579, Baden-Baden, July 1986.

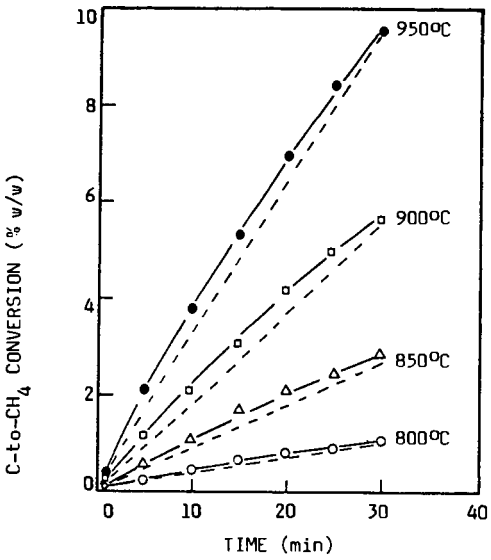

Figure 1. Comparison of model-predicted (dashed) and experimental values for the conversion of char carbon to methane. Points and solid lines are experimental data for hydrogasification.

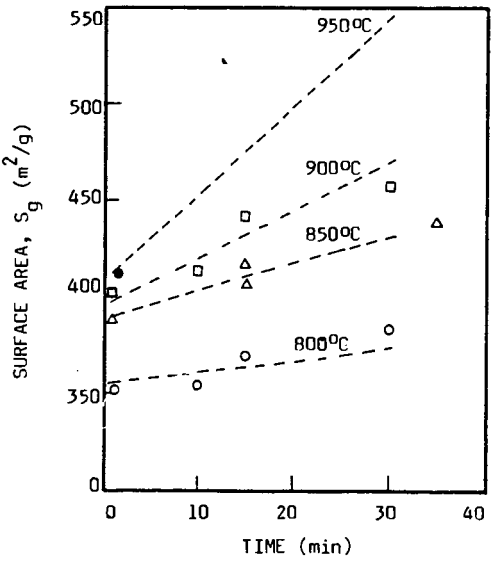

Figure 2. Calculated total surface area (dashed lines) and experimental data (points), compared at various conditions.

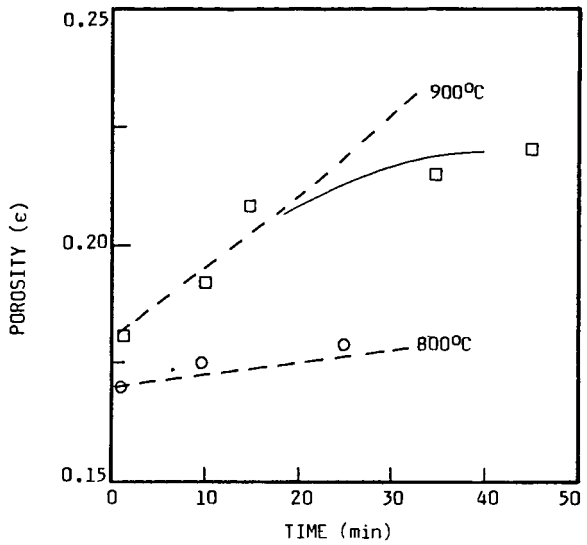

Figure 3. Porosity development of a lignite particle as measured experimentally (points) and predicted by the model (dashed lines).

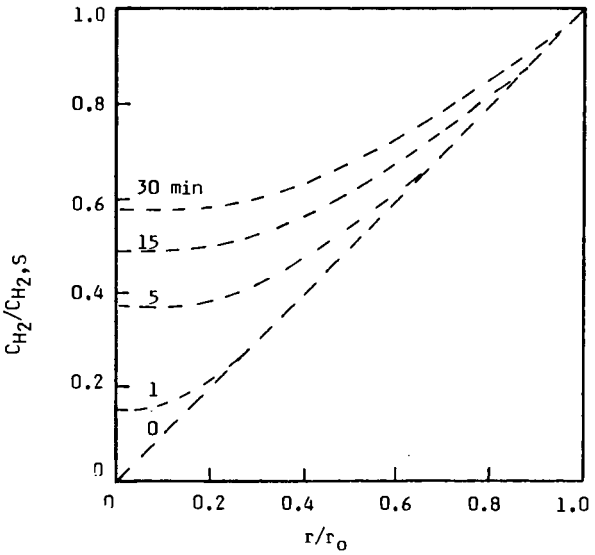

Figure 4. Hydrogen concentration profile with time in a gasifying lignite particle at 900°C (r_o=100μ).

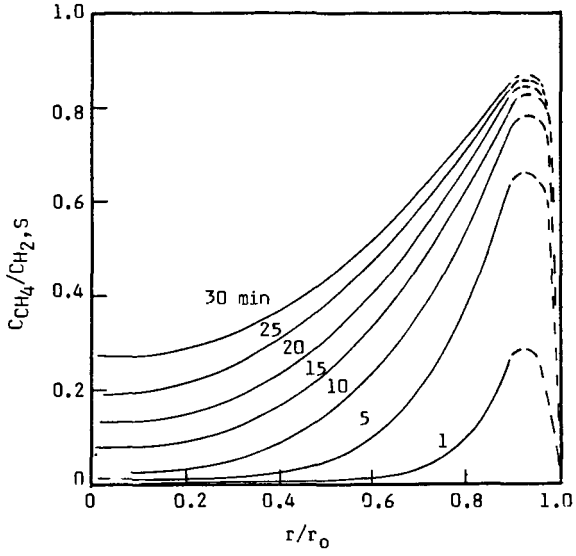

Figure 5. Methane concentration profile with time in a lignite particle at 900°C (r_o≈100μ).

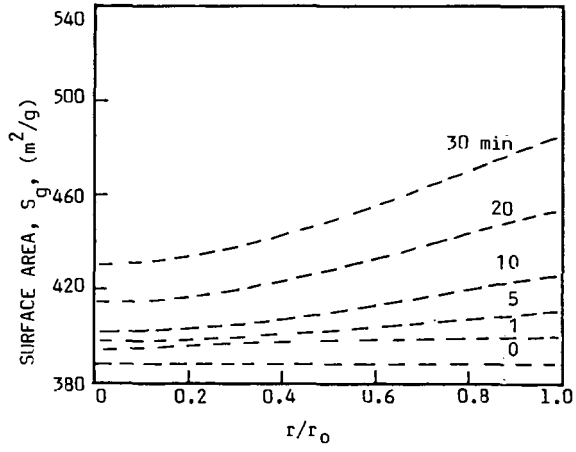

Figure 6. Surface area distribution with time, within a gasifying lignite particle at 900° C (r_o = 100 μ).

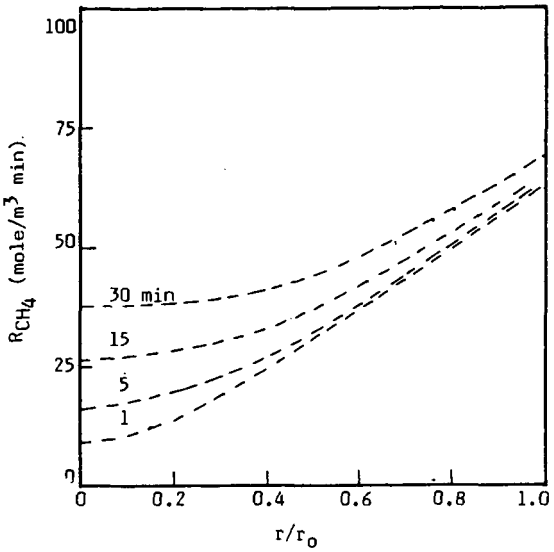

Figure 7. Radial distribution of methane formation with time in a lignite particle at 900°C (r_o = 100μ).

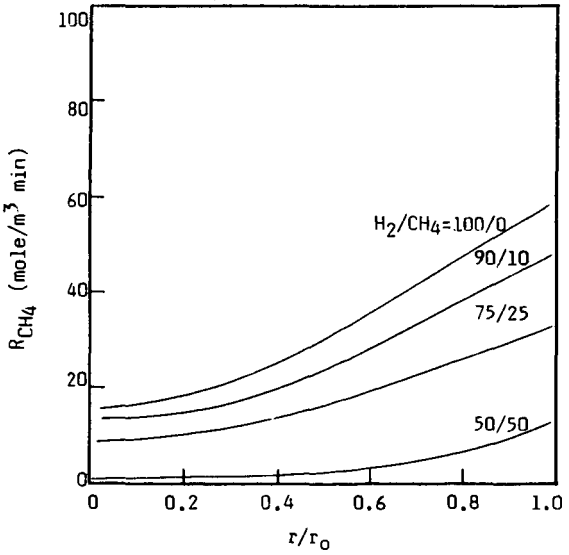

Figure 8. Effect of H_2 partial pressure on the radial distribution of methane formation, at 900°C and 5 min, (r_o = 100 μ).

DETERMINATION OF ATOMIC SODIUM IN COAL COMBUSTION USING LASER-INDUCED FLUORESCENCE

Philip G. Sweeny, Harmon B. Abrahamson, Lewis J. Radonovich, and Thomas A. Ballintine

Department of Chemistry, University of North Dakota, Box 7185 University Station, Grand Forks, North Dakota 58202

ABSTRACT

A laser-induced fluorescence spectrometer (LIFS) was assembled and sodium atom densities produced from the aspiration of solutions and direct introduction of a lignite into a flame were determined from fluorescence measurements. The average flame volume observed was 0.4 mm^3. This small volume allowed the measurement of sodium concentrations as a function of vertical and horizontal flame position. Temperature profiles of the flames employed were also obtained and compared with the sodium atom densities. The sodium atom densities calculated from the fluorescence measurements (N_{tf}) are compared with the sodium atom densities calculated from thermodynamic considerations (N_{tt}) and sodium concentrations derived from aspiration/introduction rates (N_{ta}).

INTRODUCTION

Many western low-rank coals contain significant quantities of alkali, primarily sodium, that is associated as salts of organic groups (1,2). Sodium content has been correlated with serious operational problems in combustion systems such as convective pass fouling (3,4). The flame-volatilized alkali can condense on surfaces of entrained fly ash particles forming low-melting-point layers which enhance adhesion of ash particles to heat transfer surfaces (5,6). Other studies relating flame composition and temperature to sodium volatilization have been published (7,8). These studies are all similar in that only the initial and final forms of sodium were analyzed. A few attempts have been made using mass spectrometry to directly measure amounts of alkali in coal-fed flames (8,9), with some difficulty. In order to accurately measure the density of volatilized sodium atoms in the flame region, an alternative approach is necessary.

Laser-induced fluorescence spectroscopy (LIFS) is well suited for probing various locations in flames to examine alkali release. This technique permits the quantitation of atomic species and has a small spatial resolution. The goal of this study was to determine if LIFS could be used to quantitate sodium atom densities in flames into which coal had been directly introduced, and to determine the effect of temperature and flame position on the sodium atom densities so measured.

EXPERIMENTAL

A laser-induced fluorescence spectrometer (LIFS) was used to measure the sodium atom densities produced from the aspiration of solutions and direct introduction of solids into a methane/argon/oxygen flame (2.9, 3.2, and 3.2 L/min, respectively). Argon (3.9 L/min) was used for the flame sheath. The excitation beam was generated by a flashlamp-pumped dye laser, focused and passed through a polarizing beam splitter. The horizontally polarized

beam was directed through the flame and the intensity of the vertically polarized rejected beam was monitored with a photomultplier tube (PMT). The bandwidth of the laser beam was 2-3 Å, the maximum energy available was 1 J, and the pulse length was 500-1000 ns. The diameter of the laser beam in the sample region was 2.0 mm.

The fluorescence detector was mounted perpendicular to the excitation beam in the horizontal plane, and two convex lenses were used to collect the Na fluorescence and focus it on the monochromator entrance slit. A polarizing filter set to pass only horizontally polarized light was placed directly in front of the monochromator. A PMT was positioned at the monochromator exit slit. The monochromator settings used for the Beulah lignite studies produced a bandpass of 1.2 nm and measured a sample volume of 0.4 mm^3. Various monochromator settings were used in the solution studies. Stanford Research Systems gated integrator/boxcar averagers were used to collect the signals from both PMTs. The first 300 ns of the fluorescence pulse was used to quantitate the sodium atom density. The boxcars were triggered by the laser flash via a photodiode.

The reported flame temperatures are those directly measured with a Pt/Pt-10%Rh thermocouple. The burner head was similar to that used by Daily and Chan (10). The radius of the burner head was 0.25 inch and the horizontal positions reported are those measured from the burner center with positive values indicating positions closest to the detector.

Solutions were aspirated into the flame via a Perkin Elmer nebulizer. The coal samples were introduced through a spouting bed coal feeder at a rate of 38.6 mg/min. The coal selected for the initial studies was a Beulah lignite. The proximate, ultimate, and ash analyses of this coal are shown in Table 1. A sized fraction between 200 and 325 mesh dried at 50 °C and 1 torr was used in this study.

The fluorescence intensity of the sodium solutions was defined as the difference between the intensity measured upon the aspiration of the analyte-containing solution less the intensity measured when plain deionized water was employed. The background signal for the coal studies was measured by tuning the laser and the monochromator to a wavelength 3 nm lower than the sodium doublet and introducing the coal sample. The fluorescence signal was taken as the difference between the intensity measured at the sodium doublet and the background measured at the lower wavelength.

The fluorescence data were obtained by taking ten points and averaging the results and calculating the standard deviation. The data among the original ten points not within a standard deviation were discarded leaving six to nine values to average for the reported data point.

The sodium atom densities were calculated in two different ways: from fluorescence intensities in the manner of Daily (11) to obtain N_{tf} values, and from a thermodynamic model described by Benson (12) to generate N_{tt} values. The total sodium concentrations in the flame were derived from sample aspiration/introduction rates following the procedure suggested by Wineforder and Vickers (13) to obtain N_{ta} values.

RESULTS

The LIFS was assembled and tested by aspirating sodium-containing solutions into the burner. The fluorescence signal was found to be linear over three orders of magnitude of Na concentration (N_{ta} = 7.6 x 10^7 atoms/mm^3 to N_{ta} = 7.6 x 10^{10} atoms/mm^3). The N_{tf} values for these solutions varied from 1.0 x 10^7 atoms/mm^3 to 1.0 x 10^{10} atoms/mm^3 respectively. The fluorescence measurements were taken at the flame edge closest to the detector. Five different sodium salts (NaCl, Na_2CO_3, $Na_2S_2O_3$, $NaCO_2C_6H_5$ and NaOH) were analyzed in the solution studies. The fluorescence intensity was independent of the sodium source.

In order to correlate the fluorescence measurements to actual sodium atom densities in the flame, it was necessary to establish saturation of the fluorescence signal (11). Plots of fluorescence intensity vs. laser power were obtained for both the solution studies and the Beulah lignite profiles. The laser intensity necessary to achieve saturation in the solution studies was 1.5 x 10^6 W/cm^2 nm and 1.2 x 10^7 W/cm^2 nm for the coal studies.

A horizontal fluorescence profile produced by the introduction of Beulah lignite into the methane/argon/oxygen flame was obtained (Figure 1). These results show that significantly higher fluorescence is observed upon viewing the side of the flame closest to the detector. The maximum fluorescence was observed at 0.28 inch from the flame center, producing the corresponding maximum in calculated sodium atom density.

A vertical fluorescence profile taken at the flame center is shown in Figure 2. The fluorescence signal was highest directly above the burner head, and decreased to a constant value at positions between 0.115 to 1.115 inches above the burner. A vertical temperature profile taken at a position of 0.175 inch is shown in Figure 3. The temperature was greatest at a distance of 0.056 inch above the burner. The temperature decreased from 1710 °C to 1600 °C upon travelling from 0.056 to 1.525 inches.

A vertical fluorescence profile was taken at the horizontal position of 0.35 inch (Figure 4). This graph shows that the fluorescence initially increases with vertical position and then levels off at an intensity corresponding to 1.6 x 10^9 atoms/mm^3. A vertical temperature profile was taken at the horizontal position of 0.35 inch (Figure 5). The temperature at this position increased rapidly with vertical position and leveled at a maximum near 1600 °C.

DISCUSSION

LIFS can measure changes in the density of sodium atoms generated by the introduction of solutions and solids into a flame. The linearity of the sodium concentration profile established this fact for solutions. The horizontal profile of Beulah lignite (Figure 1) establishes this fact for solids by showing increased fluorescence readings upon moving from outside to inside the flame zone.

The initial solution studies show that the LIFS can be used to quantitate sodium atom density in the flame, in addition to merely measuring differences in concentration. The

uniform increase in fluorescence signal with increased sample concentration demonstrates a range of concentration where quantitation is possible. The observation that the N_{tf} value is independent of the composition of the initial sodium salt indicates that equilibration of the sodium atoms with the other flame species is complete, and that this equilibrium is not significantly affected by the identity of the counter ion. It is significant that the N_{tf} values are only 14% of the N_{ta} values, while the thermodynamic calculations (N_{tf}) predict that 83 % of the sodium should be in the atomic form. The discrepancy between N_{ta} and N_{tf} values is of a magnitude similar to that reported by Smith et al. (14). These workers attributed this discrepancy to the estimates which contribute to N_{ta}, most significant in our case is the uncertainty in the degree of flame expansion. This explanation is realistic and therefore the difference between the percentages of sodium present in the atomic form calculated from the N_{tf}/N_{ta} ratio (14%) and that from thermodynamics (83%) is most likely due to the inaccuracy of N_{ta}.

The seemingly low N_{tf} values could also be due to decreased fluorescence intensity because of chemical reactions of the excited state sodium atoms (quenching). These types of reactions have been detailed by Muller et al. (15). In order to avoid this complication in our measurements only the initial 300 ns of the fluorescence was used for quantitation.

The calculation of the sodium atom densities depends on operation in the saturated state. Saturation was confirmed in both the solution and coal studies. The intensities needed for saturation are comparable to those reported by Smith et al. (14) for sodium solutions. Our observation that the saturation threshold is higher for solids than for solutions may be due to differences in the optical densities of the flames.

The horizontal profile of Beulah lignite (Figure 1) shows a maximum N_{tf} value at the flame edge closest to the detector. This asymmetry is a result of self absorption and/or the optical density of the coal entraining flame. A similar result was observed by Daily and Chan (10) when solutions of high sodium concentration were measured. This result points to the necessity of making measurements near the flame edge if accurate quantitation is desired.

The vertical fluorescence profile taken at the center of the flame (Figure 2) shows the fluorescence signal to be constant above 0.1 inch. Comparison of this result to the profile taken at the flame edge shows that the self absorption effect occurs up to flame positions of 1.115 inch. Comparison of Figure 2 with Figure 3 shows the fluorescence to be unaffected by small temperature changes. Comparison of Figure 4 to Figure 5 shows that the fluorescence apparently increases with flame temperature. The large variation in flame temperature at this latter horizontal position (0.35 inch) is because this is outside the burner radius and increasing vertical position moves the sample volume from outside to inside the expanded flame zone. Thus the fluorescence signal should increase as the observation point is moved into the active flame. (This latter fact leads to the conclusion that the data points taken at vertical positions of 0.015 inch are artifacts due to reflection of the laser off the burner head and do not represent actual sodium atom fluorescence.)

The vertical fluorescence profile taken at the flame edge (Figure 4) shows that N_{tf} reaches a maximum value of 2.1×10^9 atoms/mm^3; this corresponds to 1.8% of the N_{ta} value

(1.2×10^{11} atoms/mm^3). The thermodynamic calculations predict 83% of the sodium to be released at equilibrium. The N_{tf}/N_{ta} ratio for the coal (1.8%) is approximately 7.8 times smaller than that observed for solutions (14%). If we assume that equilibrium was reached in the solution studies, and that the N_{tf} values are correct, then the N_{ta} values are 5.9 times larger than the actual sodium densities. Incorporating this factor into N_{ta} for coal produces the conclusion that the maximum amount of sodium present as atomic vapor in the flame containing Beulah lignite is 11%.

SUMMARY AND CONCLUSIONS

LIFS can be used to measure differences in sodium atom concentrations in both solution- and solid-containing flames. Quantitation of the sodium atom density is possible at the flame edge. The sodium atom densities produced from the introduction of Beulah lignite are not affected by small changes in temperature. The maximum percentage of sodium present as atomic vapor in the Beulah lignite flame was 11% of the total sodium in the coal.

ACKNOWLEDGMENT

We are grateful for the support of the United States Department of Energy (through James Hickerson and Philip Goldberg at PETC), and the cooperation and assistance of the UND Energy Research Center.

REFERENCES

1. Benson, S. A.; Holm, P. L. *Ind. Eng. Chem. Prod. Res. Dev.* **1985**, *24*, 145.
2. Miller, R. N.; Given, P. H. U. S. Dept. of Eng. Report **1978**, FE-2494-TR1.
3. Raask, E. *Mineral Impurities in Coal Combustion* , Hemisphere Publishing Company: New York, 1985.
4. Sondreal, E. A.; Tufte, P. H.; Beckering, W. *Comb. Sci. .Tech.* **1977**, *16*, 95.
5. Wibberly, L J.; Wall, T. F. *Fuel* **1982**, *61*,87.
6. Boow, J. *Fuel* **1972**, *51*, 170.
7. Neville, M.; Sarofim, A. F. *Fuel* **1985**, *64*, 384.
8. Stewart, G. W.; Stinespring, C. D.; Davidovits, P. *Prepr., Div. Fuel Chem., Am. Chem. Soc.* **1982**, *27(1)*, 138.
9. Daily, J. W.; Chan, C. *Combustion and Flame* **1978**, *33*, 47.
10. Milne, T. A.; Beachey, J. E.; Greene, F. T. in *Ash Deposits and Corrosion Due to Impurities in Combustion Gases* , Bryers, R. W., Ed.; Hemisphere Publishing Corp.: Washington, 1978, p 217.
11. Daily, J. W. *Appl. Opt.* **1977**, *16*, 568.
12. Benson, S. A. Ph. D. Dissertation, Pennsylvania State University, 1987.
13. Winefordner, J. D.; Vickers, T. J. *Anal. Chem.* **1964**, *36*, 1939.
14. Smith, B.; Winefordner, J. D.; Omnetto, N. J. *Appl. Phys.* **1977**, *48*, 2676.
15. Muller, C. H.; Schofield, K.; Steinberg, M. J. *Chem. Phys.* **1980**, *72*, 6620.

TABLE I.
Analysis of Beulah High-Sodium Lignite.

Ultimate Analysis (wt% moisture-free)	
C	62.8
H	3.9
N	1.5
S	1.7
O	16.8
ash	13.3

Proximate Analysis (wt% as received)	
H_2O	34.9
ash	8.7

Ash Analysis (wt% ASTM)	
SiO_2	20.4
Al_2O_3	12.6
Fe_2O_3	10.8
TiO_2	1.2
P_2O_5	0.9
CaO	18.9
MgO	5.9
Na_2O	6.3
K_2O	0.0
SO_3	22.8

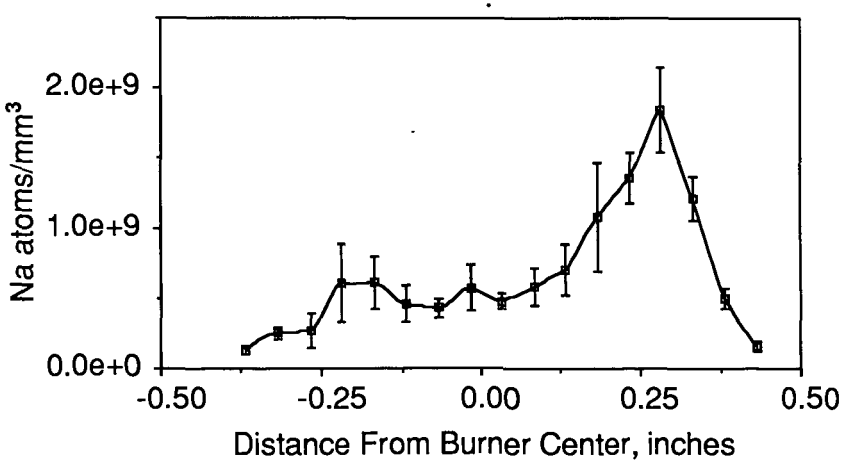

Figure 1. Horizontal fluorescence profile of Beulah lignite at a vertical position of 0.415 inch.

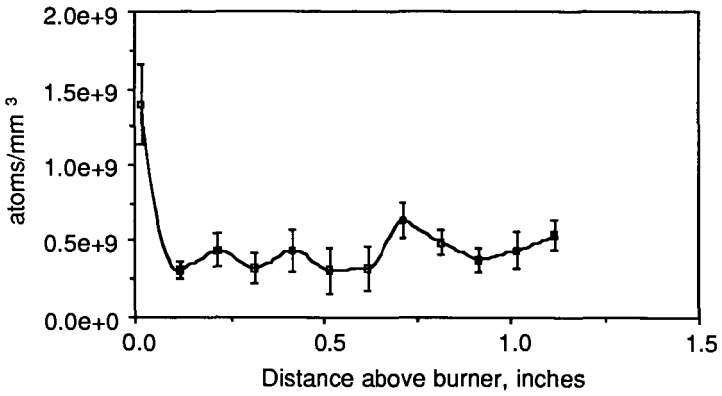

Figure 2. Vertical fluorescence profile of Beulah lignite at the flame center.

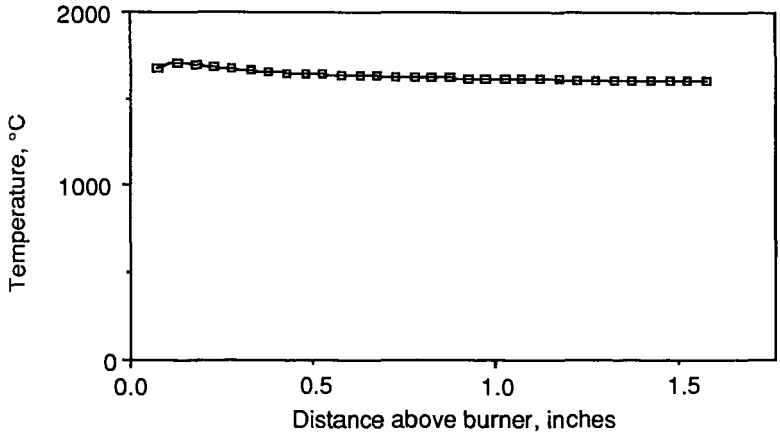

Figure 3. Vertical temperature profile of Beulah lignite at a horizontal position of 0.175 inch.

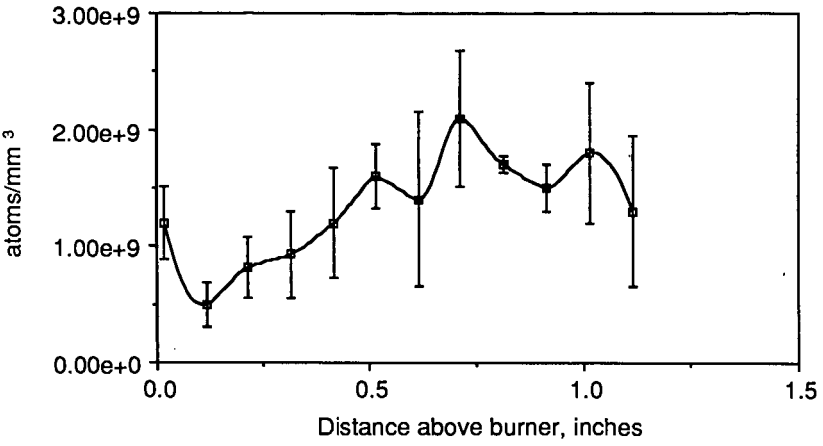

Figure 4. Vertical fluorescence profile of Beulah lignite at a horizontal position of 0.35 inch..

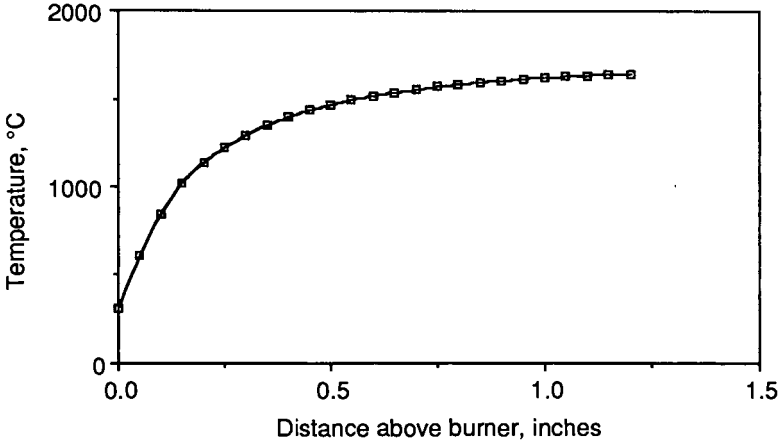

Figure 5. Vertical temperature profile of Beulah lignite at a horizontal position of 0.35 inch.

The Effects of Ion-exchanged Cobalt Catalysts on the Gasification of Wood Chars in Carbon Dioxide

William F. DeGroot and G.N. Richards

Wood Chemistry Laboratory, University of Montana, Missoula, Montana 59812 USA

Wood is composed primarily of cellulose, hemicelluloses, and lignin, with lesser quantities of extractives (material extractible in organic solvents) and mineral matter. The cottonwood species used in this study has been analyzed previously in this laboratory and it was found to contain 44% cellulose and 32% hemicelluloses on an extractive-free basis (1). The major component of the hemicelluloses is O-acetyl-4-O-methylglucuronoxylan, a polymer comprised of repeating units of xylose with acetyl and 4-O-methylglucuronic acid substituents substituted along the polymer chain. Figure 1 shows a representative chemical structure of this polymer, but does not correctly represent the frequency of substituents; approximately half of the xylose residues contain an acetyl group and there is one 4-O-methylglucuronic acid group per 10-20 xylose residues (1,2). These acid groups provide a means of incorporating catalysts into wood in a reproducible, highly-dispersed manner by ion exchange. Similar methods are used in catalysis of low-rank coals, but the ion exchange capacity of wood is much lower than that of coals. Our wood sample was found to contain 8-10 meq of carboxylic acid groups per 100 grams of wood (2), while low-rank coals typically contain 10-50 times higher concentrations of carboxylic acid groups (3,4).

The effects of several ion-exchanged catalysts on gasification of wood chars in carbon dioxide were described in an earlier paper (5). Ion-exchanged cobalt and calcium were found to be very effective catalysts of gasification of wood chars (HTT 800°C). In this paper we focus on the activity of cobalt catalysts for gasification of wood chars prepared at different heat treatment temperatures.

The gases formed by pyrolysis of low-temperature chars have also been determined by temperature-programmed desorption (TPD) using mass spectrometry. This analysis is indicative of structural features of the char and helps to elucidate the chemical transformations occurring in low-temperature chars (HTT 400°C) as they are heated to high temperatures.

EXPERIMENTAL

The wood sample used in this study was sapwood from black cottonwood (Populus trichocarpa). The wood was ground in a Wiley mill, sieved, and the 20/30 mesh fraction was retained for analysis. Chars were prepared in a tube furnace purged with flowing nitrogen, as described previously (1), and they were stored in nitrogen- or argon-purged containers between analyses.

Acid washing and cobalt ion exchange treatments were carried out by column percolation. For cobalt ion exchange the ground, acid-washed wood (2.5 g) was degassed in a small quantity of 0.01 M cobalt acetate solution and transferred to a glass chromatography column. The wood was then washed slowly with 500 ml of the 0.01 M cobalt acetate solution, followed by a thorough wash with distilled, deionized water to remove any unbound salt. Acid washing was carried out by essentially the same procedure except that 0.01 M HCl was used.

Reactivity measurements were carried out in a gasification reactor/detector system described previously (1). Briefly, the system consists of a small-scale temperature-programmed alumina reactor coupled to a combustible gas detector. The reactor can be maintained under either an inert or a reactive atmosphere. For inert conditions it is swept with nitrogen or helium (40 cc/min) and an equivalent flow of carbon dioxide is valved into the reactor for gasification.

The detector consists of a ZrO_2 solid electrolyte oxygen sensor which is maintained at a temperature of 650-700°C. Combustible gases formed in the reactor combine with an air stream after they leave the reactor and they undergo combustion in the hot detector. The detector monitors the depletion of oxygen content in the combined gas streams. The rate of carbon gasification is calculated from the combined gas flow rates and the oxygen depletion, assuming that one mole of carbon is gasified for each mole of oxygen consumed.

The rate of gasification of a char (HTT 800°C) prepared from untreated cottonwood is shown in Figure 2. The detector output can be integrated over the entire run to give the total extent of gasification, or it can be integrated above the baseline defined by the rate of pyrolytic gasification (dotted line) to give the extent of gasification due to reaction with CO_2. The extents of gasification reported in this paper are those due to gasification alone, i.e. excluding pyrolysis. Extents of conversion determined in this way compare well with measured weight losses, generally amounting to 100-110% of the weight loss. This system is preferred to gravimetric systems for our purposes because of its greater sensitivity and better control of temperature and gas flows.

The gasification system was modified to include a unit resolution mass spectrometer (Hewlett-Packard Model 5970B) for qualitative analysis of gas mixtures formed during pyrolysis of the sample prior to gasification. When the mass spectrometer was in use helium was used as the reactor purge gas. A splitter was placed in the gas line between the reactor outlet and the combustion air inlet. One meter of uncoated vitreous silica capillary tubing (0.20 mm ID) connected the splitter to the mass spectrometer. The capillary tubing was contained in a transfer line heated to 100°C. This arrangement diverted approximately 0.1 ml/min (0.3%) of the reactor gas flow to the mass spectrometer. On the basis of preliminary runs which revealed no high molecular weight pyrolysis products, the mass range of 10 to 110 amu was scanned and approximately fifteen mass spectra were accumulated per minute.

X-ray diffraction patterns were obtained using a Phillips diffractometer (CuKα, 35kV, 20mA) at a scan rate of 1 degree per minute. The sample was mounted on a glass slide using a vaseline smear.

RESULTS

Gasification Rate Determination

Table 1 shows the yields and reactivities of chars prepared at different HTT's from wood treated by ion exchange with cobalt, calcium, and potassium. The char prepared from one of the cobalt-exchanged samples was initially so reactive that the rate of gasification exceeded the detection limits of the detector, i.e., all of the oxygen in the combustion air supply was consumed by combustion of product gases. In this case the maximum rate of gasification was not observable, and the extent of gasification was therefore indicated as being "greater than" the value of the integrated detector response. The change in sample weight is indicated to show the total extent of reaction.

The reactivities of the chars containing cobalt catalyst are clearly less dependent on HTT than are those of the chars containing calcium and potassium. The reactivities of the latter chars toward gasification at 800°C increase by at least a factor of two as the HTT is reduced from 1000° to 800°C. This behavior is typical of trends shown by other investigators who have studied the effects of HTT on catalyzed gasification of lignite chars (6-8). By contrast, chars prepared from cobalt-exchanged wood at 800° and 1000°C are gasified to a similar extent at 800°C. When HTT and gasification temperature are reduced to 600°C, the char prepared from cobalt-treated wood is completely gasified, whereas the chars prepared from calcuim and potassium-exchange wood are completely unreactive at this temperature. When

cobalt-exchanged wood was charred and gasified at 400°C, no gasification occurred.

Table 1. Effect of HTT on extent of CO_2 gasification of chars from ion-exchanged wood. Gasification was for 30 min in 90.9 kPa of CO_2.

Treatement	HTT (°C)	Char Yield[b] (%, d.a.f.)	Gasification Temperature (°C)	Percent Gasified
Co-exchanged	1000	7.4	800	>69[a]
	800	9.2	800	73
			600	46
	600	12.9	600	96
	400	21.3	400	0
K-exchanged	1000	9.9	800	6%
	800	13.4	800	13
	600	17.5	600	0
Ca-exchanged	1000	8.1	800	36
	800	9.3	800	102[c]
	600	12.7	600	0

[a]Measured weight loss was 73%.

[b]Char yields are reported on a dry, ash-free basis assuming that the weight of the ash in the original wood remains in the char.

[c]Sample gasified completely. Percent of conversion determined by integration of combustible gas detector signal was consistently 100-110% of measured weight loss.

In order to better assess the dependence of reactivity on HTT in more detail, chars prepared from cobalt-exchanged wood at 100°C increments of HTT were gasified at 500°C. The results are shown in Table 2. The maximum reactivity is attained at the HTT 600°C. The reactivity decreases slightly when the HTT is raised to 700°C and more dramatically when the HTT is raised to 800°C. There is very little reaction for the sample of HTT 500°C. These results suggest that there is a threshold temperature for activation of the catalyst at about 600°C.

Table 2. Effect of heat treatment temperature (HTT) on the yield and reactivity of chars prepared from cobalt-exchanged wood. Gasification was carried out for 30 min at 500°C in 90.9 kPa of CO_2.

Sample	HTT	Char Yield (%, d.a.f.)	Percent Gasified
Co-exchanged wood	800	9.2	16
(0.23% Co, 0.34% ash)	700	10.9	66
	600	12.9	70
	500	17.2	3

To obtain a more detailed description of the nature of catalysis by cobalt it is helpful to consider the changes in reaction rate with extent of gasification or "gasification rate profiles", as shown in Figure 3. The gasification rate profile for the HTT 800°C char prepared from cobalt-exchanged wood undergoes two phases of reaction when gasified at 800°C. The first stage is very rapid but decreases as the

reaction proceeds. The second phase is characterized by a lower, more constant rate of reaction.

Figure 4 shows the gasification rate profile of a low-temperature char (HTT 600°C) gasified at 600°C. This char was much more reactive than the char prepared at 800°C and the maximum rate exceeded the detector capacity. As shown by the extents of gasification in Table 1, the low-temperature char was completely gasified in this case, and there was no evidence of the second, slower phase of gasification which was observed in gasification of higher temperature chars (HTT 800°C) at 800°C.

Pyrolytic Gasification of Low-Temperature Chars

We investigated the pyrolytic transformations that occur in chars (HTT 400°C) prepared from untreated and cobalt-exchanged cottonwood upon heating to 800°C in order to determine the existence and nature of any significant catalyst/substrate interactions which occur during pyrolysis. Figure 5 shows the gasification rate profile and the total ion profile for a char (HTT 400°C) prepared from untreated cottonwood heated in flowing helium to 800°C; both curves are from the same experiment. The shape of the gasification rate profile is distinctly different from that of the total ion profile. The former peaks at 10.5 min, corresponding to the end of the temperature ramp, while the total ion profile peaks at 8.5 minutes (600°C). The difference in the two profiles is apparently due to evolution of molecular hydrogen in the higher temperature range. Hydrogen is not detected by the mass spectrometer, but the combustible gas detector is very sensitive to the evolution of hydrogen, since its combustion requires three times more oxygen per unit weight than does combustion of carbon. Comparison of these curves therefore suggests that evolution of molecular hydrogen from the char predominates at high temperatures (T>650°C), while carbonaceous compounds are evolved at lower temperatures.

Analysis of individual mass spectra acquired during these experiments indicates that the most prominent species evolved are CO (m/z 28) and CO_2 (m/z 44), with CO_2 evolution decreasing at higher temperatures. There is also a smaller, but significant quantity of water (m/z 18) evolved throughout the pyrolysis process. Mass peaks indicative of methanol, low molecular weight aldehydes and hydrocarbons are also present in very low abundances.

The gasification rate profile shown in Figure 5 has been demonstrated to be representative of untreated wood as well as wood treated with alkali and alkaline earth metals (9). However, as shown in Figure 6, the gasification rate profile of low-temperature chars containing the cobalt catalyst differs from this pattern. The profile for the char (HTT 400°C) prepared from cobalt-exchanged wood peaks much earlier than that of the char from untreated wood, and this appears to be due to a peak (5.8 min, 630°C) superimposed on the profile of the untreated wood. The same peak is evident on the total ion profile, which suggests that this additional transition involves evolution of carbonaceous species. However, analysis of the mass spectra corresponding to this peak does not indicate that this peak in the gasification rate profile corresponds to the enhanced evolution of any single product. The data do not, therefore suggest a specific solid phase reaction involving interaction of the cobalt catalyst with carbon. However, we believe that this transition, which is unique among the catalysts studied and corresponds to the HTT at which the catalyst became active (see Tables 1 and 2), corresponds to the reduction of the catalyst to the elemental state which has been shown to be the active state of transition metal catalysts for gasification of graphite (10), wood chars (11), and coal chars (12).

X-Ray Diffraction

X-ray diffraction (XRD) patterns for chars prepared at 800° and 1000°C from cobalt-exchanged wood are shown in Figure 7. The diffraction patterns show evidence

of different crystalline phases in the two chars. Two of the peaks in the diffraction pattern of the higher temperature char, correspond to d-spacings characteristic of elemental cobalt (2θ=44.2° and 51.5°) (13). The large, broad peak in the XRD pattern for this char is not identified and probably corresponds to ordered regions in the carbon lattice. The peaks in the diffraction pattern of the char of HTT 800°C could not be correlated with a crystalline cobalt compound or with compounds of the small quantity of calcium remaining in this sample. No XRD peaks were observed in chars (HTT 800°C) from potassium- or calcium-exchanged samples.

DISCUSSION

The results obtained in this study demonstrate the exceptionally high activity of cobalt in catalyzing the gasification of wood chars in carbon dioxide. A pyrolysis temperature of about 600°C appears to be required to activate the catalyst. At higher heat treatment temperatures the maximum catalytic activity declines.

Figueiredo et al. studied the gasification of chars (HTT 850°C) prepared from pine wood doped with higher levels of cobalt nitrate (1.6% metal) (14). These authors report gasification behavior in pure CO_2 similar to that reported here, i.e., an initial period of rapid gasification lasting a few minutes followed by slow gasification of the remaining char. They measured gasification rates in the temperature range of 740-910°C and report an initial (presumably maximum) rate at 805°C of 0.18 min^{-1} which is very comparable to the initial rate of 18 mMoles $C \cdot min^{-1} \cdot g^{-1}$ (0.22 $g \cdot g^{-1} \cdot min^{-1}$) found in this study for a char (HTT 800°C) gasified at 800°C (see Figure 3). Their data extrapolate to much lower rates at 600° and 500°C than those found in this study for gasification of a char prepared at 600°C (see Figure 4). The effect of the higher concentration of cobalt in their wood is presumably offset by lower dispersion of the catalyst due to the mode of addition, higher HTT, and larger heat treatment time used in preparation of chars (1 hr vs 10 min in this study). These authors suggest that the decline in activity is due to oxidation of the active reduced form to CoO during gasification, and they cite XRD evidence for CoO in chars after gasification. However, the results of this study show that the rapid, catalyzed stage of gasification can be maintained throughout the reaction to give complete gasification of chars prepared and gasified at lower temperatures (600°C, see Figure 4). We therefore believe that the slower stage of gasification is due to gasification of carbon which is no longer in contact with the catalyst due to its agglomeration at high temperatures.

The combined data from this study suggest a picture of catalysis by cobalt involving (1) reduction to an active catalytic state, probably elemental cobalt, near 600°C followed by (2) agglomeration of the catalyst particles to form crystalline cobalt. The latter process, which is much more important at temperatures greater than 800°C, gives rise to two distinct phases of gasification. The first, corresponding to gasification of carbon in contact with cobalt crystallites is fast, while the second, slower rate corresponds to gasification of char which is not in contact with catalyst (see Figure 1). On the basis of the XRD evidence for crystalline elemental cobalt in chars of HTT 1000°C, we believe that elemental cobalt is the active phase of the catalyst throughout the reaction, but it is detectable by XRD only when crystallite growth is at an advanced stage.

The presence of reduced cobalt in wood chars also suggests that the relative activities of transition metal catalysts in gasification by carbon dioxide might be associated with the rate of dissociation of the reactant gas on the metal surface. Grabke has reported rate constants for dissociation of CO_2 on cobalt, nickel and copper at 1000°C (15), which are pertinent to the non-equilibrium conditions used in our studies. The rate constants decrease in the order: $k_{Co} > k_{Ni} >> k_{Cu}$, which is the same order of relative activities reported for transition metal catalysts in the earlier paper (5). The results of these studies are therefore consistent with an oxygen transfer mechanism, as described by Walker et al. in the iron-catalyzed

gasification of graphite by CO_2 (10) or possibly an oxygen 'spillover' mechanism (16), depending on whether the adsorbed atomic oxygen reacts with the metal to form the metal oxide before reacting with carbon in contact with the catalyst particle.

ACKNOWLEDGEMENT

This work was supported by the Gas Research Institute under Grant No. 5082-260-0683. We are grateful to Dr. John Wehrenberg of the University of Montana Department of Geology for providing the XRD data and to Dr. R.K. Osterheld of the University of Montana Department of Chemistry for helpful discussions.

REFERENCES

1. Shafizadeh, F. and McGinnis, G.D., Carbohydr. Res., 16, 273 (1971).

2. DeGroot, W.F., Carbohydr. Res., 142, 172 (1985).

3. Kube, W.R., Schobert, H.H., Benson, S.A., and Karner, F.R., in The Chemistry of Low-Rank Coals, H.H. Schobert, ed., American Chemical Society, Washington, D.C., 1984, pp. 39-52.

4. Shafer, H.N.S., Fuel, 49, 197 (1970).

5. DeGroot, W.F. and Richards, G.N., Prepr. Pap., 191st ACS National Meeting, Division of Fuel Chemistry, 31(2), 28 (1986).

6. Radovic, L.R., Walker, P.L., Jr., and Jenkins, R.G., Fuel, 62, 209 (1983).

7. Jenkins, R.G., Nandi, S.P., and Walker, P.L., Jr., Fuel, 52, 288 (1973).

8. Hippo, E.J., Jenkins, R.G., and Walker, P.L., Jr., Fuel, 58, 388 (1979).

9. DeGroot, W.F. and Richards, G.N., "Chemistry of Carbon Gasification Reactions," Final Report, Gas Research Institute, Chicago, 1986.

10. Walker, P.L., Jr., Shelef, M., and Anderson, R.A., "Chemistry and Physics of Carbon," P.L. Walker, Jr., ed., Marcel Dekker, New York, 1968, Vol 4, p. 287.

11. DeGroot, W.F. and Shafizadeh, F., Fuel, 63, 210 (1984).

12. Kasaoka, S., Sakata, Y., Yamashita, H., and Nishino, T., Int. Chem. Eng., 21, 419 (1981).

13. ASTM Publication No. PDIS-17i, "Index (Inorganic) to the Powder Diffraction File," Amer. Soc. for Testing and Materials, Philadelphia, 1967.

14. Figueiredo, J.L., Orfao, J.J.M., and Ferraz, M.C.A., Fuel, 63, 1059 (1984).

15. Grabke, H.J., Ber. Bunsenges Phys. Chem., 71, 1067 (1967).

16. Baker, R.T.K. and Chludzinski, J.J., Carbon, 19, 75 (1981).

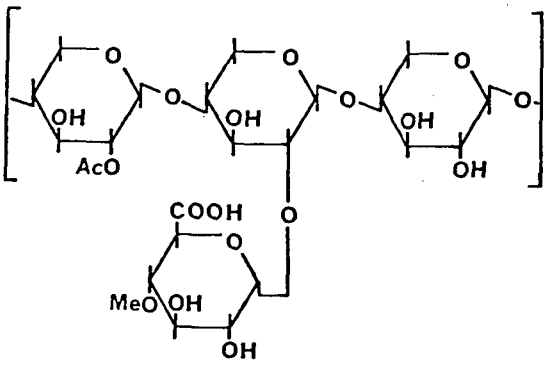

Figure 1. Representative structural elements of acetyl 4-O-methylglucuronoxylan.

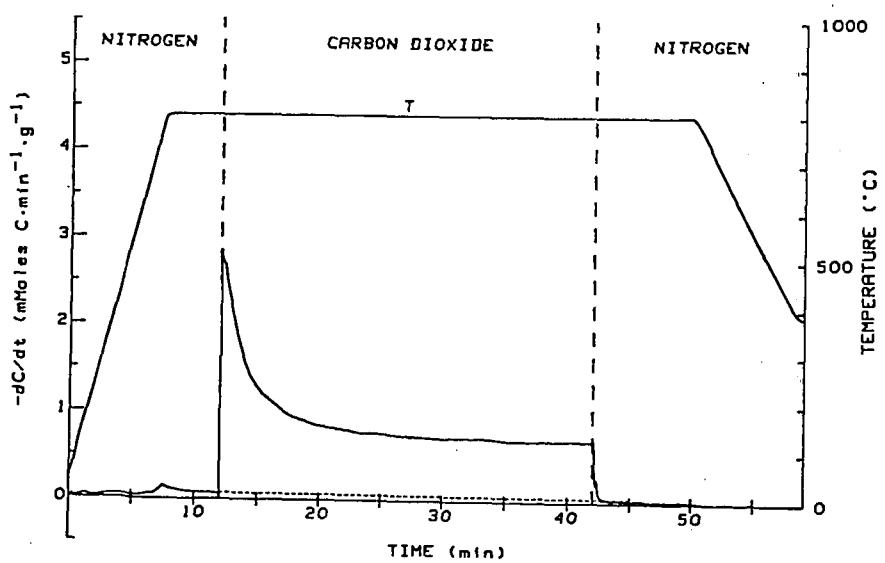

Figure 2. Gasification rate profile for gasification at 800°C of char (HTT 800°C) prepared from untreated cottonwood.

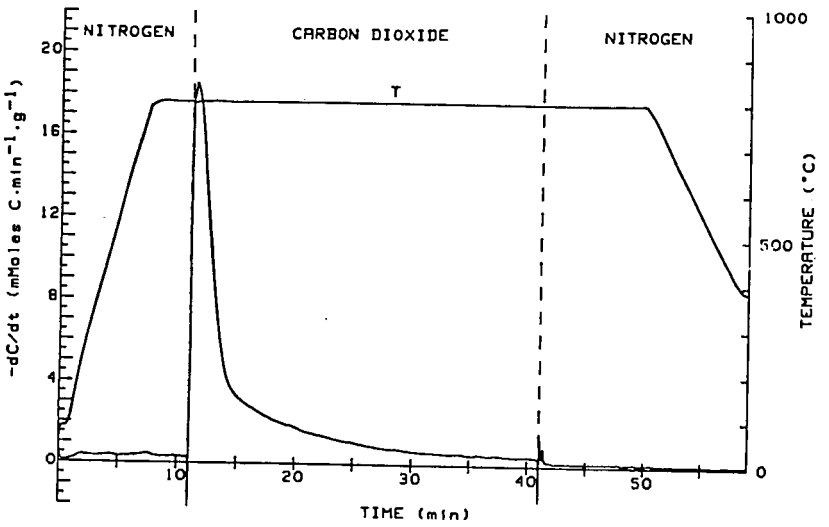

Figure 3. Gasification rate profile for gasification at 800°C of char (HTT 800°C) prepared from cobalt-exchanged cottonwood.

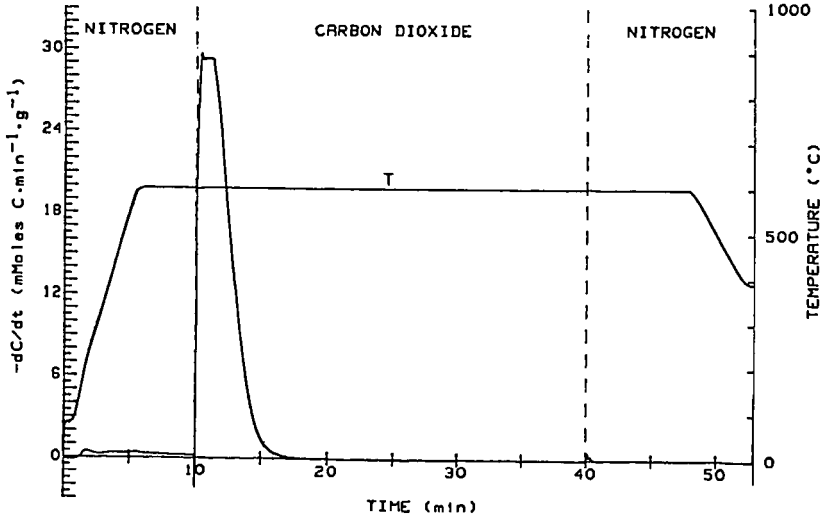

Figure 4. Gasification rate profile for gasification at 600°C of char (HTT 600°C) prepared from cobalt-exchanged cottonwood.

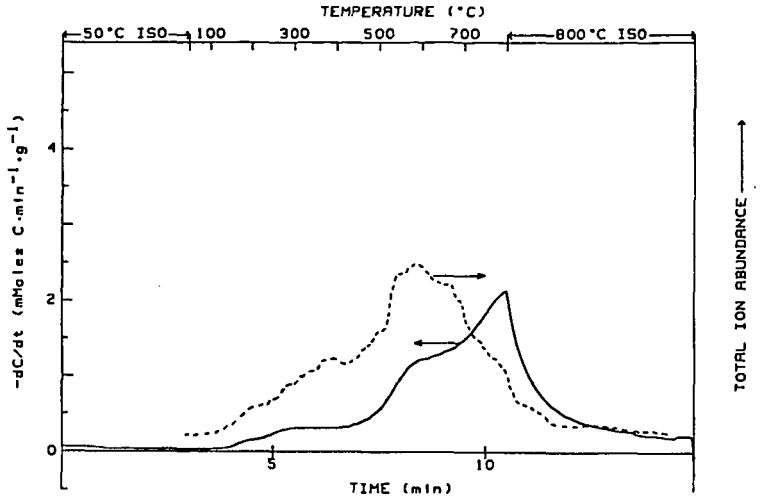

Figure 5. Gasification rate profile and total ion profile for pyrolytic gasification in helium of char (HTT 400°C) prepared from untreated cottonwood.

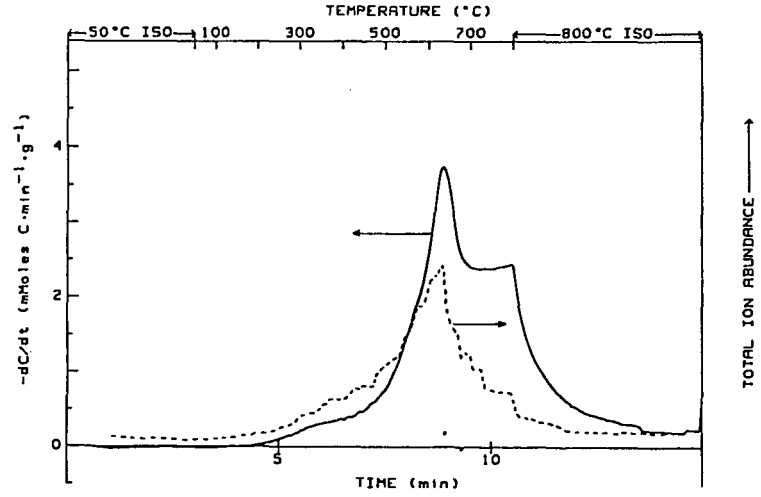

Figure 6. Gasification rate profile and total ion profile for pyrolytic gasification in helium of char (HTT 400°C) prepared from cobalt-exchanged cottonwood.

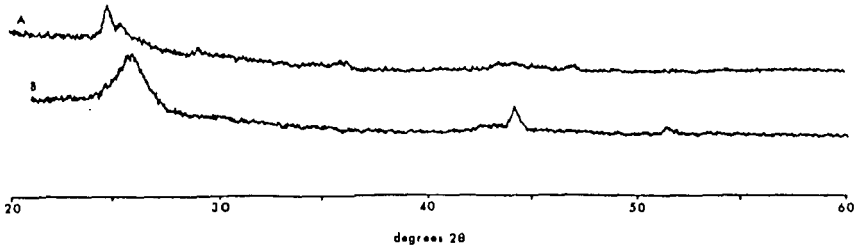

Figure 7. XRD patterns obtained from chars prepared from cobalt-exchanged cottonwood at HTT's of (A) 800°C and (B) 1000°C.

Determination of the Distribution of Ash, Pyrite and Basic Constituents in Coal Particles

D. M. Mason and S. S. Chao

Institute of Gas Technology
3424 South State Street
Chicago, Illinois 60616

INTRODUCTION

In fluidized-bed gasification of high-sulfur coals, such as the KRW and U-GAS processes, relatively low melting ash is produced by reaction of iron from pyrite with the siliceous components produced from clays and quartz.(1,2) To prevent catastrophic growth of ash clinkers and defluidization of the bed, ash in the bed must be limited to 40 to 50 weight percent. As a result of this low ash content of the bed, the ash must be agglomerated to facilitate its removal from the bed without unacceptable loss of char carbon and decrease of gasification efficiency. To obtain a detailed understanding of the behavior of mineral matter and ash in fluidized-bed gasification, a fundamental research investigation is in progress at IGT under a program supported by the U.S. Department of Energy.(2,3)

In our approach to the problem, we note that pyrite quickly decomposes to ferrous sulfide when the coal is introduced into the hot fluidized bed of a gasifier; also that sufficient hydrogen sulfide is produced from high sulfur coal to stabilize the ferrous sulfide in the back-mixed fluidized bed away from the oxygen inlet region; also that in the back-mixed bed the gasification reactions with steam and carbon dioxide occur relatively slowly and thus tend to occur throughout char particles. Complete removal of the carbon in char particles must occur before the oxidized iron can contact the siliceous components in the ash. Both this carbon removal and the oxidation of the ferrous sulfide occur only in the oxygen inlet region. Elevated temperatures in this region also facilitates the reaction of oxidized iron with the siliceous components to form relatively low-melting iron aluminosilicates. In both the KRW and U-GAS processes, oxygen is introduced through a central jet, forming an oxygen reaction region resembling a burner flame. Thickness, shape, and temperature of this reaction region is known only within wide limits.

We envision that the initial formation of ash reaction products occurs by reaction of the minerals present in single particles of char formed from single particles of coal. The oxide composition of the ash of single particles determines their melting point, viscosity and potential for agglomeration. In this paper we report the results of the application of some methods of investigation of ash composition in single particles of coal.

Selection of Coals

As part of the research on the behavior of ash in fluidized-bed gasification, several coals were selected for test in a 2-inch reactor. These were five eastern U.S., one western (New Mexico) bituminous, and one subbituminous coal. All had been washed except the subbituminous coal. Four of the eastern U.S. coals were selected to cover a range of iron oxide content of the ash from about 10 to 30 weight percent Fe_2O_3 along with a calcium oxide content of 2.5 weight percent or less; the other, an Illinois No. 6 seam coal, was selected to show the effect of high calcium oxide content with low iron oxide. Analytical data pertaining to minerals and ash of the coals, including iron distribution by Mossbauer spectroscopy and mineralogy by computer-assisted scanning electron microscopy (SEM), are presented in Table 1.

Table 1. ANALYSES OF MINERALS AND ASH OF COALS USED IN GASIFICATION TESTS

Seam Mine	KY No. 9 Providence	OH Pitt No. 8 Franklin 125	KY No. 13 Ken No. 13	IL No. 6 Burn. Star 4	IN VI Universal	York York Canyon	Rosebud Rosebud
Ash Composition, wt %							
SiO_2	54.5	41.6	58.5	54.1	51.1	44.4	48.8
Al_2O_3	17.8	20.9	26.9	16.9	21.9	24.3	23.5
Fe_2O_3	19.9	31.7	8.1	10.7	15.7	9.0	7.02
TiO_2	0.80	1.02	0.87	0.70	0.85	1.02	0.12
P_2O_5	0.07	0.07	0.16	0.13	0.12	2.11	0.25
CaO	2.29	1.14	0.90	8.34	2.48	8.15	7.16
MgO	0.67	0.36	1.21	0.95	1.18	2.15	2.57
Na_2O	0.54	0.35	0.24	0.75	0.65	0.90	0.09
K_2O	2.20	0.98	2.94	1.96	2.85	0.44	0.36
SO_3	2.10	1.00	0.80	7.00	1.30	5.50	9.91
Total	100.9	99.2	100.6	101.5	98.1	98.0	99.78
Ash Content (as ashed for analysis of ash, dry basis)	7.9	7.7	8.2	13.4	13.5	8.0	
Iron Distribution (by Mossbauer Spectrocopy)*							
Pyrite	92.1	95.8	71.4	91.6	80.5	9.7	--
Clay	--	--	11.2	--	6.9	70.6	--
Siderite	--	--	--	--	--	15.5	--
Ferrous Sulfate[a]	7.9	4.2	--	4.6	tr?	--	--
Ferric Sulfate[b]	--	--	17.4	3.8	12.7	4.2	--
Mineral Distribution (by SEM)*							
	wt % of total minerals						
Quartz	20	11	17	20	23	6	--
Kaolinite	5	10	7	3	3	14	--
Illite	7	11	20	7	18	2	--
Chamosite[c]	--	--	1	<1	<1	8	--
Montmorillonite	<1	1	1	2	1	5	--
Mixed Silicates[d]	22	20	28	23	25	31	--
Pyrite	33	36	17	23	18	1	--
Iron Sulfates	3	2	2	<1	1	--	--
Siderite	<1	<1	<1	--	<1	2	--
Calcite	5	--	<1	16	4	10	--
Ankerite	--	--	--	--	--	1	--
Rutile	<1	1	<1	<1	<1	--	--
Apatite	--	--	--	--	--	2	--
Misc. Mixed	>4	>8	>6	>5	>5	18[e]	--

*By G. F. Hoffman and Associates at Macro-Arom, Inc.

[a] $FeSO_4 \cdot H_2O$ and $FeSO_4 \cdot 7H_2O$.

[b] $KFe_3(SO_4)_2(OH)_6$.

[c] Hydrated magnesium-iron aluminosilicate.

[d] Mostly mixed layer clays.

[e] Includes many Ca(Sr)-Al(Si)-P particles, possibly crandallite.

Distribution of Ash Composition Among Particles

Moza and Austin have described the analysis of individual pulverized coal particles by computer-assisted SEM.(4) The objective of this work was the evaluation of coals for slag deposition in electric utility boilers fired with pulverized coal. Sieve fractions of particles from 10 to 106 μm in diameter were mounted separately, sectioned and polished; those particle cross-sections falling within the size range of the sieve fraction were selected for x-ray emission analysis; about 280 particles of the coarsest fraction and 800 to 900 of the finest were analyzed.

Moza and Austin's method seems admirable for pulverized fuel, but of doubtful applicability to the 1/4-inch top size feed to fluidized-bed gasifiers. One difficulty is that sections oriented parallel to the coal bedding are not representative of the minerals of the whole particle.

For this investigation, we adopted a chemical method in which the ash compositions of 32 single particles were determined. Particles from the -10+12 mesh fraction of the 1/4 inch top size coal were taken for analysis; this size furnishes enough ash for the chemical analysis and is about the average size, by weight, of the coal feed to a pilot plant or commercial fluidized-bed gasifier. Particle weight, ash content, and iron oxide and calcium oxide in the ash were determined. In addition to determined contents of iron and calcium oxide in the ash, the content of basic constituents was estimated by adding the average amount of other basic oxides (MgO, K_2O and Na_2O), as determined by a conventional major and minor oxides analysis, to the determined iron and calcium oxides. A correction for sulfur trioxide in the particle ash was made, based on the average ratio of SO_3 to CaO in the conventional analysis of the ash of the eastern U.S. coals that we investigated. This method of correction was not satisfactory when the content of calcium oxide in the single particle ash was higher than about 20%.

Analysis of the single particles are reported in detail elsewhere.(3) Averages for the first 16, the second 16, the odd-numbered particles, the even-numbered particles, and for all particles are also listed; the subsets were calculated to obtain a measure of the effect of number of analyzed particles. For eastern bituminous coals, the most important distribution is that of the iron oxide content of the ash. For the Kentucky No. 9 coal, the average iron oxide contents of the four groups of 16 particles ranges from 21.72 to 26.35 weight percent, and the average for all particles is 22.27 weight percent compared to 19.9 weight percent obtained by the conventional analysis for major and minor oxides. We conclude from this and similar data on the other coals that analysis of 32 particles is necessary and may be sufficient for characterizing the distribution.

A comparison of the averages of the particles with the values of the conventional major and minor oxides is presented in Table 2. While the average iron oxide in the ash of the 32 particles of Kentucky No. 9 coal agrees well with the conventional analysis, less than half as much calcium oxide was present in the -10+12 mesh particles as in the conventional analysis. We think that the missing calcium oxide occurs as calcite in the cleat of the coal, along which fracture occurs in crushing and sieving, resulting in its concentration in the finer sieve fractions. Presence of plates of calcite, about 10 μm thick, in the cleat fractures of the Kentucky No. 9 coal is shown in a photomicrograph (Figure 1) of a polished section of coal etched by low temperature oxidation to expose the minerals. In the photomicrograph, only the crack normal to the bedding is a cleat fracture; the curved cracks are artifacts produced in the preparation and etching.

Similar loss of calcium oxide from the -10+12 mesh particles is also evident with the Indiana VI coal (Table 2), while 90% of the average 8.34 weight percent of calcium oxide in the ash of the Illinois No. 6 coal has been lost. No loss, or

Table 2. SUMMARY OF SINGLE PARTICLE ANALYSES

	Ash Content (moist basis)		Fe_2O_3 in Ash		CaO in Ash	
	Avg. of Particles	Conventional	Avg. of Particles	Conventional	Avg. of Particles	Conventional
	wt %					
KY No. 9	6.3	7.6	22.3	19.9	1.10	2.29
Pittsburgh	10.9	7.5	34.2	31.7	1.14	0.90
KY No. 13	8.2	7.3	8.6	8.1	0.69	0.90
IL No. 6	10.3	11.9	12.1	10.7	0.83	8.34
IN VI	16.4	13.4	6.9	15.7	0.36	2.48
Rosebud	10.3	11.3	0.55	7.0	9.4	7.2

only a marginal one, is evident from the Pittsburgh No. 8 or Kentucky No. 13 coals. Neither did it occur with the subbituminous B Rosebud coal in which the calcium occurs dispersed in the organic matter, partly as carboxylate and (probably) partly as calcite from decomposition of calcium carboxylates. However, about 90% of the average amount of iron oxide is absent from the -10+12 mesh particles of this coal. This is in accord with observations on coal from this seam by other investigators; Kuhn et al. examined pyrite grains in coal ground to pass a 20-mesh sieve and found that all were unattached to coal.(5) The mean diameter of the pyrite grains was 80 μm. Chadwick et al. reported that "pyrite in the coal occurs principally as sheets or film on vertical fracture, or cleat, surfaces."(6)

The distributions in the Kentucky No. 9 particles are shown in Figure 2. To prepare a plot, the particle analyses were arranged in the order of increasing amount of the component, such as iron oxide and the cumulative amount of ash for that order was calculated. Note that a different order of the particles is obtained for each component in the ash of a coal. The plots for iron oxide and basic constituents indicate the presence of two different populations, one with iron oxide content up to about 30 weight percent and the other from 20 to 100 weight percent. It appears likely that the first is from attrital coal and mixtures of attrital coal and vitrain, and the second mainly from vitrain only. Vitrain is recognized as shiny black layers or lenses in the coal thicker than 0.5 mm, and is attributed to the coalification of relatively large fragments of wood and bark. Thus it is almost entirely free of particles of minerals except those, such as pyrite, that are deposited from infiltrating solutions or are present in the woody plant. Alternatively, it is possible that the iron-rich particles contain pyrite of a bedding layer adjacent to vitrain; however, this appears unlikely, as the ash in these particles ranges only from 2.3 to 10.0 weight percent.

The distributions in larger and smaller particles than the -10+20 mesh also should be considered. In general, the distribution is expected to become wider (greater deviation from the average) as particle size decreases; and, for example, the number of particles with a single layer, whether attrital coal or vitrain, increases. The opposite may be true of larger particles, but not if the size of particles is less than that of the predominant width of layers. Ashes of individual -4+5 mesh particles of the Kentucky No. 9 coal are shown in the photograph of Figure 3. Large differences in the iron content of the ash is indicated by the white or gray appearance of some, which have little or no iron, in contrast to others that are very dark because of the presence of hematite from pyrite. This suggests that the distribution of iron in -4+5 mesh particles does not differ much from that of the -10+12 mesh particles.

Distributions in the particles of the Pittsburgh No. 8, Kentucky NO. 13, and Rosebud coal (except for basic constituents) are shown in Figures 4, 5, and 6. Distributions in the particles of the Illinois No. 6 and Indiana VI coals were similar to those of the Kentucky No. 13.

When a knowledge of jet temperatures and a correlation between composition, temperature, and agglomerating tendency becomes available in the future, the distributions will indicate how much of the ash, after burnoff of the char, is immediately available for agglomeration — that is, without need for combination with the ash of a different particle. At present, it is estimated that, in the absence of more than about 2 weight percent of calcium oxide, ash with iron oxide contents from about 20 to 80 weight percent may fall in this category. This upper limit is expected to decrease with decreasing silica-to-alumina ratio and increasing magnesia content, according to phase diagram considerations.(2)

A summary of the distribution of iron oxide in the ash of the -10+12 mesh particles is presented in Table 3 for the eastern bituminous coals, together with

the average iron oxide content. Ash of Kentucky No. 9 coal, from the same mine as that used here, agglomerated without difficulty in U-GAS pilot plant tests with bed temperatures at about 1870°F. (Temperaturea in the jet are substantially higher.) The particle analyses of this coal show 59% of the ash to have 0 to 20 weight percent Fe_2O_3 and 38% to have 20 to 80 weight percent Fe_2O_3. Although the ash of the Pittsburgh No. 8 coal has an average Fe_2O_3 content of 31.7 weight percent, much higher than that of the ash of the Kentucky No. 9, its fraction of ash in the 20 to 80 weight percent Fe_2O_3 range is much lower, only 10%. This suggests that the ash of the Pittsburgh coal should agglomerate more slowly, but its real significance has not been determined as yet. The same is true of the Indiana VI coal, whose total ash has sufficient iron, 15.7 weight percent Fe_2O_3, for agglomeration although very little falls in the 20% to 80% range. The Kentucky No. 13 and Illinois No. 6 coals probably have insufficient iron for agglomeration of their ash, but in this case the ash content of the bed in a gasifier can be allowed to rise to such an extent that very little carbon is ungasified.

Table 3. SUMMARY OF DISTRIBUTION OF Fe_2O_3 IN -10+12 MESH PARTICLES OF EASTERN BITUMINOUS COALS

Coal	Avg. Fe_2O_3 Content, wt %	0-20% Fe_2O_3	20-80% Fe_2O_3	80-100% Fe_2O_3
		% of ash		
Kentucky No. 9	19.9	59	38	3
Pittsburgh No. 8	31.7	61	10	29
Kentucky No. 13	8.1	95	5	0
Illinois No. 6	10.7	93	5	2
Indiana VI	15.7	96	4	0

CONCLUSIONS

The distribution of ash compositions in single particles of coal fed to fluidized bed gasifiers governs the amount and particle size of low-melting ash immediately available as agglomerating medium after burnoff of char from the particles. We have investigated the distribution in the 1/4-inch top size coal from several sources by chemical analysis, for ash content and calcium and iron oxides content of the ash, of 32 particles of the -10+12 mesh fractions of the coals. The distributions, though probably not very accurate, show substantial differences among the coals that were investigated. For example, much of the calcium oxide of the coal, as shown by the conventional analysis for major and minor oxides, was missing from a Kentucky No. 9 seam coal and from an Illinois No. 6 seam coal; the loss was attributed to the presence of calcite in the cleat of the coals, resulting in its attrition from the particles in crushing and other handling. Pyrite in the cleat was similarly lost from particles of some of the coals. Other differences in distribution were also evident; the Kentucky No. 9 coal had a substantial amount of ash with ferric oxide content between 20 and 80 weight percent whereas a Pittsburgh No. 8 coal from Ohio had little of this, although its average iron oxide content was much higher.

Etching by oxygen plasma of 1-1/2-inch pieces of the Kentucky No. 9 coal, sectioned normal to the bedding and lightly polished, furnished a striking display of the prevalence of minerals in the attrital layers of coal and its virtual absence in vitrain, except that the presence of thin plates of calcite in the cleat of the vitrain was clearly evident.

ACKNOWLEDGEMENT

The funds for this research investigation were provided by the Morgantown Energy Technology Center, United States Department of Energy under Contract No.: DE-AC21-84MC21313

REFERENCES CITED

1. Mason, D. M. and Patel, J. G., "Chemistry of Ash Agglomeration in the U-GAS® Process," Fuel Processing Technology 3, 181-206 (1980).

2. Institute of Gas Technology, "Coal Gasification Research Studies," Washington: U.S. Department of Energy, DOE/MC-19301-10, November 1985.

3. Carty, R. H., Mason, D. M. and Babu, S. P., "Reaction Kinetics and Physical Mechanisms of Ash Agglomeration," Washington: U.S. Department of Energy, DOE/MC/61075. To be published in 1987.

4. Moza, A. K. and Austin, L. G., "Analysis of Pulverized Coal Particles (10-100 μm) for Fe, S, Ca, Si and Al on a Particle-by-Particle Basis," Fuel 62, 1468-73 (1983).

5. Kuhn, J. K., Fiene, F. and Harvey, R., "Geochemical Evaluation and Characterization of a Pittsburgh No. 8 and a Rosebud Seam Coal," Report METC/CR-78/8, 1978.

6. Chadwick, R. A., Rice, R. C., Bennett, C. M. and Woodriff, R. A., "Sulfur and Trace Elements in the Rosebud and McKay Coal Seams, Colstrip Field, Montana," Mont. Geol. Soc. Ann. Field Conf. Guide. 22, 167-75 (1975).

APPENDIX

Method of Analysis of Single Particles

Thirty-two coal particles were randomly selected, and individually ashed overnight (16 to 20 hours) in small Pt-5% Au boats. The boats were specially fabricated for this experiment by cutting a 0.006-inch thick Pt-5% Au crucible into 10 X 10 mm squares and folding up all sides to form boxes in the shape of cubes. A Cahn automatic electrobalance Model 25 was employed to obtain the particle and ash weights. The crucible plus ash was dropped into an acid-cleaned 10 ml volumetric flask to which 5 ml of 6N HCl was then added. The flasks were heated on a hot plate to the boiling point until the reddish color of the oxidized iron from the ashed particle solids had disappeared. Cesium chloride and lanthanum chloride solutions were added to the volumetric flask to obtain a final concentration of 1000 mg/l and 2500 mg/l, respectively, as the metal. The volumetric flask was then diluted to volume using double-distilled water. The volume of the Pt-Au crucible did not contribute any significant volume to the solution. The standards were diluted from commercially obtained stock solutions of iron and calcium, and were made to contain Cs, La and HCl matrices the same as those of the samples. Both iron and calcium were determined by atomic absorption spectrophotometry using a Perkin-Elmer 305B double beam instrument.

An observation was made that the coal particles were not completely destroyed by the ashing and acid treatment. Subsequently, the residual solids of the first coal analyzed were collected and analyzed by X-ray fluoresence spectrophotometry utilizing a Phillips 3100 X-ray generator and a PW1410 X-ray spectrometer. Silica was found to be the major constituent. Iron and calcium were found in trace quantities, however their quantities were negligible in comparison with those determined by HCl leaching.

LTA Etching

Pieces of coal about 1-1/2-inch in size were cut across the bedding, and the resulting section was lightly polished and cemented to a 1 X 2-inch glass slide. A parallel cut was made to obtain a section 1/8- to 1/4-inch thick; the top surface was polished by thin section techniques to a final polish with 1000 grit diamond impregnated on a metal disc.

After drying in a vacuum oven the section was exposed for periods of 15 minutes to an hour in an oxygen-plasma LTA asher.

PAP/mason-pap

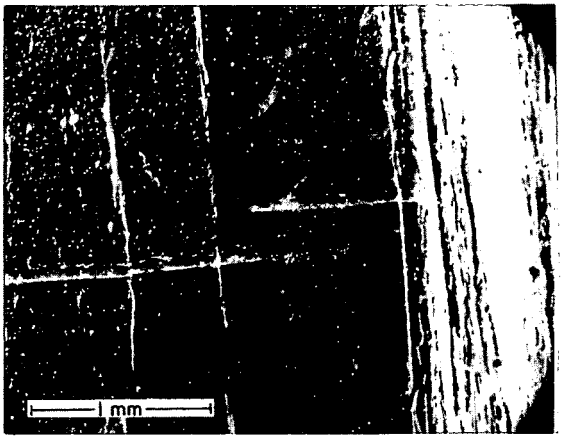

Figure 1. PHOTOMICROGRAPH OF LTA ETCHED KENTUCKY NO. 9 COAL

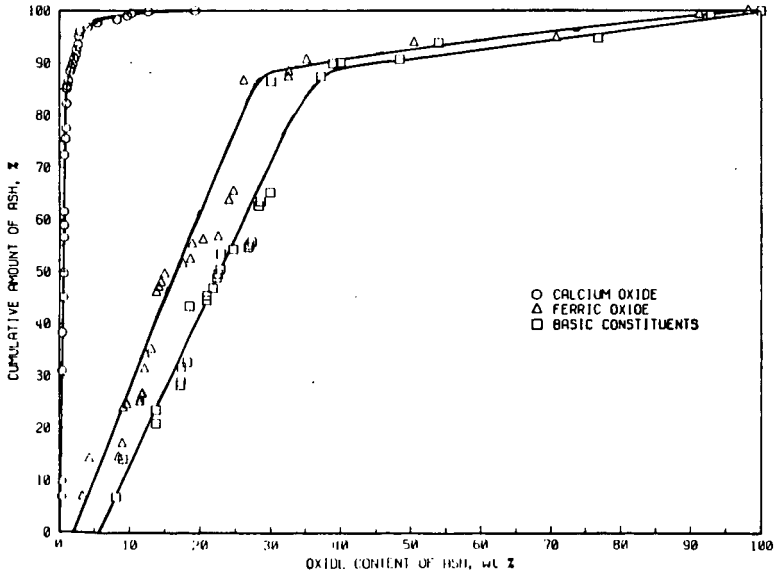

Figure 2. DISTRIBUTION OF BASIC OXIDES IN PARTICLES OF KENTUCKY NO. 9 COAL

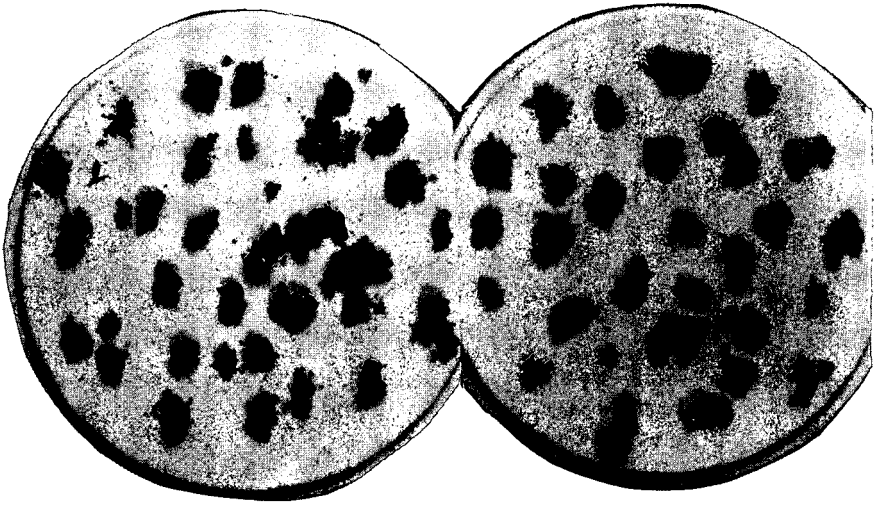

Figure 3. ASH FROM -4+5 MESH PARTICLES OF KENTUCKY NO. 9 COAL

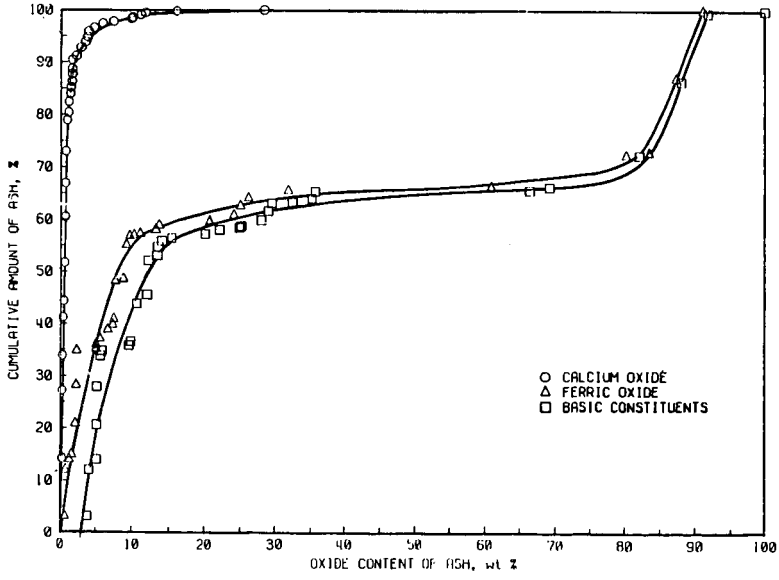

Figure 4. DISTRIBUTION OF BASIC OXIDES IN PARTICLES OF PITTSBURGH NO. 8 COAL

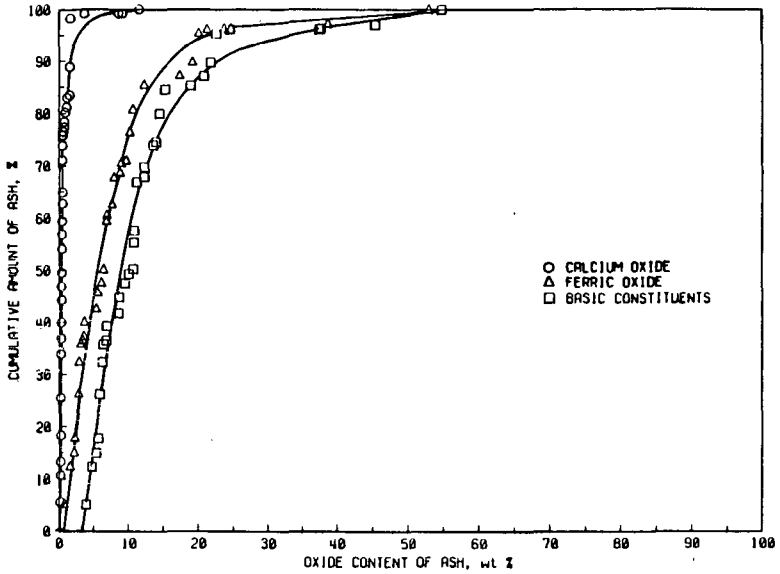

Figure 5. DISTRIBUTION OF BASIC OXIDES IN PARTICLES OF KENTUCKY NO. 13 COAL

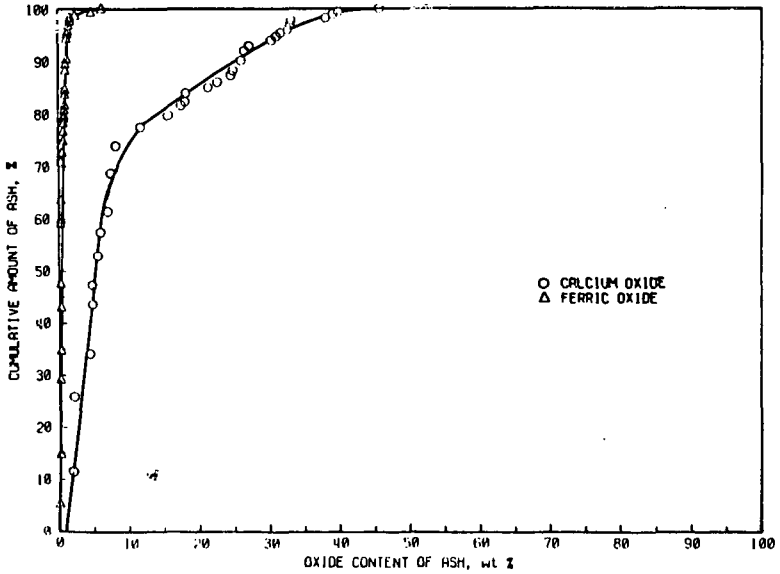

Figure 6. DISTRIBUTION OF FERRIC OXIDE AND CALCIUM OXIDE IN PARTICLES OF ROSEBUD COAL

IMPROVED METHODS FOR DETERMINATION OF FERROUS SULFIDES IN COAL CHARS

S. S. Chao, D. M. Mason, and A. Attari

Institute of Gas Technology, 3424 S. State St., Chicago, IL 60616

INTRODUCTION

A fundamental research investigation of the behavior of mineral matter in fluidized bed gasification of coal is in progress at IGT under a program largely supported by the U.S. Department of Energy. Special attention has been focused on the gasification of high sulfur and high iron containing coals, and the mechanism of ash agglomeration which facilitates the selective removal of ash from a reactor bed without loss of unacceptable amounts of char carbon.

Sulfur occurs in coal mineral mostly as iron disulfides, mainly pyrite with some marcasite. The disulfides quickly decompose to pyrrhotites ($Fe_{(1-x)}S$) and hydrogen sulfide in the charring process with an inert atmosphere or in the absence of air (1-3). The same transformation was also observed when the coal, especially bituminous coal, is fed into the fluidized bed of a gasifier typically at about 1850°F (4). The resulting pyrrhotites may partly transform to troilite (FeS) on cooling to room temperature.

It has been noted that ferrous sulfides, especially pyrrhotite, play a variety of important roles in coal conversion processes. Their possible catalytical activity in coal liquefaction (5) and coal gasification (6,7) was reported recently. In our pilot plant studies we have occasionally found that ferrous sulfide may play an independent role in agglomeration, acting as a binding medium between shale particles in the bed when run-of-mine coal is fed (Fig.1) (4). Under some circumstances, ferrous sulfide has formed deposits in the hot cyclone, which returns entrained char particles to the bed. In order to better understand their functions in coal conversion, an accurate quantitative method for ferrous sulfides determination is needed.

Mossbauer spectroscopy has been employed as a useful method for the semi-quantitative determinations of various iron-containing species including ferrous sulfides in coal chars and gasification residues (8,9). It's accuracy highly depends upon the complexity of the Mossbauer spectra and the concentration level of ferrous sulfides.(10) The major disadvantage of this method is that it can not detect non-iron containing sulfide species, such as calcium sulfide.

X-ray diffraction spectroscopy has also been used to analyze the mineral contents of chars and residues. But, it's utility in the analysis of non-stoichiometric ferrous sulfides is often limited to the qualitative determination, because these sulfides may or may not be present in crystalline forms and their x-ray spectra is often complicated and obscured by the spectra of other major minerals.

In the past IGT has developed a wet chemical method, involving determination of hydrogen sulfide evolved by treating a sample with 6N hydrochloric acid. Although this method was successfully employed to determine the sulfide sulfur contents of chars prepared at 1700°F and gasification residues that had been subjected to higher temperature, it was found to be unsatisfactory when applied to ferrous sulfide-rich coal chars prepared at 1400°F for use as feed for gasification. In most of cases only a fraction of sulfur from ferrous sulfide (sulfide sulfur) could be recovered as hydrogen sulfide. The calculated total sulfur of these chars from sulfide sulfur, pyritic sulfur and organic sulfur is usually 5 to 20% lower than the total sulfur determined by the Eschka method, depending on the types of ferrous sulfides present and their concentration.

In the search of a more accurate method, we have re-evaluated a number of potential existing methods and developed a few new methods for ferrous sulfides analysis. The most successful method uses a reducing agent to enhance the recovery of ferrous sulfide as hydrogen sulfide in a hydrochloric acid evolution procedure. Results from the analyses of six 1400°F coal chars using different methods are presented and discussed.

EXPERIMENTAL

Two model coal char compounds synthesized from high purity carbon plus a composite 1400°F coal char sample were prepared for the initial study of the recovery of sulfide sulfur during hydrochloric acid digestion. The first model consists of troilite and the second a natural pyrrhotite. Using an acid-evolution train, the efficiencies of hydrogen sulfide evolution were examined for these three samples at four hydrochloric acid concentrations (1,2,4 and 6 normal) with and without the addition of the reducing agent, stannous chloride. The hydrogen sulfide evolved was collected in an alkaline trap composed of 10% cadmium chloride in water and subsequently determined by an iodometric method with thiosulfate back titration. The hydrochloric acid extract was then filtered and analyzed by atomic absorption method for the HCl-soluble iron. The residue collected was examined by an x-ray diffraction spectroscopic (XRD) method for the amount of ferrous sulfide left intact.

For the composite coal char, a complete sulfur-by-types analysis was also carried out to check the sulfur mass balance. A modified method of ASTM D-2492 procedure for forms of sulfur in coal was employed to analyze the sulfate, pyritic, organic, and total sulfur. The sulfate sulfur was determined by a gravimetric method as barium sulfate. The pyritic sulfur was calculated from the concentration of pyritic iron found in the dilute nitric acid extract of the residues, which was determined by an atomic absorption method. The organic sulfur was determined by digesting the residue from the dilute nitric acid digestion with concentrated nitric acid and analyzing the resulting sulfate as barium sulfate gravimetrically. The total sulfur was determined by the Eschka method.

In the course of a gasification investigation, five coal chars were prepared at 1400°F in a 4-inch diameter devolatilizer purged with nitrogen from washed bituminous coals with 1/4-inch top size. The residence time of the feed coal at 1400°F was approximately 30 minutes. A -200 mesh fraction of Kentucky No. 9 coal was used to prepare the sixth coal char. All samples were ground to about 325 mesh and analyzed for their contents of sulfide sulfur, residual sulfur, 6N HCl-soluble iron and total iron. Both the residual sulfur and total sulfur were determined by the Eschka method. The 1N, 1.6N (5%) and 2N HCl-soluble iron were also determined separately and used to calculate the sulfide sulfur content.

A Philips vertical goniometer and a copper x-ray source were employed for the x-ray diffraction analysis of all coal char samples. The total concentration of iron sulfides was determined using potassium chloride as an internal standard. The diffraction peak at a 2 theta angle of about 43.3 degree was used for the quantitation. The same peak was also profile-fitted in an attempt to deconvolute the complex peaks, measuring their precise d-spacings at the 102 crystal plane and consequently estimating the iron content of various hexagonal pyrrhotites (11).

A Ranger Scientific MS-900 Mossbauer spectrometer with a 5 mCl Co-57 source was used to acquire Mossbauer spectra of all char samples. The relative percentage of sulfide iron in total iron as ferrous sulfides was measured by a spectral subtraction technique. The concentration of sulfide sulfur in each coal char was calculated by multiplying the total iron percentage of coal char by the relative percentage of sulfide iron and a S/Fe conversion factor of 0.574.

RESULTS AND DISCUSSION

Figure 2 represent the effects of hydrochloric acid and the reducing agent, stannous chloride, on the recovery of sulfide sulfur by the described evolution method. By comparison of the mole ratios of sulfide sulfur to HCl-soluble iron, we found that the troilite (FeS) could be easily decomposed to hyrogen sulfide and determined quantitatively. However, pyrrhotite was not completely converted to hydrogen sulfide even though all ferrous sulfides would be completely decomposed in hydrochloric acid with a concentration higher than 2 normal as indicated by XRD analysis of the digested residue, unless a suitable reducing agent, such as stannous chloride, was present. We believe that pyrrhotite is partially degraded to elemental sulfur in the hydrochloric acid medium as the following equation. The stannous chloride and possible other reducing agents may inhibit this competitive degradation mechanism, converting all sulfide sulfur to hydrogen sulfide.

$$Fe_{(1-x)}S + 2\,(1-x)\,HCl \xrightarrow{\Delta} (1-x)\,FeCl_2 + (1-x)\,H_2S + S^0$$

The results in Table 1 indicate that a good sulfur mass balance was obtained when 10% or more stannous chloride was used. The insignificant difference between the calculated total sulfur of 2.02% and 2.05% while using 4N and 6N HCl respectively suggests that either concentration is adequate for effective hydrogen sulfide evolution. The variation of the mole ratios of sulfide sulfur to HCl soluble iron in the same table further confirms that stannous chloride definitely promotes the hydrogen sulfide evolution. The sulfide sulfur calculated from 2N HCl-soluble iron provides good agreement with the determined sulfide sulfur using stannous chloride. This method could be used as a quick method to determine the sulfide sulfur in coal char, provided that there are little other types of HCl-soluble iron, such as iron oxides, iron sulfates, illites and chlorites, present in the sample.

Table 1. Sulfur-by-types analysis of a composite 1400°F Coal Char

Digestion Acid Promoting Agent	4N HCl	4N HCl 10% $SnCl_2$	4N HCl 20% $SnCl_2$	6N HCl	6N HCl 10% $SnCl_2$
Sulfate Sulfur %	<0.01	<0.01		<0.01	<0.01
Sulfide Sulfur %	.66	1.04	1.07	.74	1.04
Pyritic Sulfur %	.06	.05		.06	.04
Organic Sulfur %	1.06	.93		1.05	.97
Total S % (calc.)	1.78	2.02		1.85	2.05
Total S % (detn.)	2.09	2.09		2.09	2.09
HCl Soluble Fe %	1.81	1.84	1.86	1.92	1.88
S/Fe Mole Ratio	.64	.98	1.00	.67	.96
2N HCl-Soluble Fe	1.81	1.84	1.86	1.92	1.88
Sulfide S % (calc. from Fe)	1.05	1.07	1.08	1.11	1.09

We found also that the organic sulfur contents determined in the procedure without stannous chloride are higher than those found in the procedure with stannous chloride. This is probably because the elemental sulfur, formed during the hydrochloric acid digestion, may be partially associated with the solid residue and recovered as organic sulfur in the subsequent concentrated nitric acid digestion. This indicates that the acid evolution method without stannous chloride is likely to give a high estimation of organic sulfur in char in addition to a low quantitation of sulfide sulfur.

Table 2 presents the concentrations of sulfide sulfur, residual sulfur and total sulfur of six coal chars. The total sulfur calculated from the sulfide and residual sulfur was again found to agree well with the determined total sulfur in all analyses when stannous chloride was used in the evolution procedure. The mole ratios of sulfide sulfur to the HCl-soluble iron deviate significantly from unity in four analyses, indicating the presence of other 6N HCl-soluble iron species in those char samples. However, the quick method to determine the sulfide sulfur using the percentage of iron soluble in 1N, 1.6N (5%) and 2N HCl seems to be quite satisfactory in most of the cases (Table 3). Further studies should be conducted to select an optimum hydrochloric acid concentration for this method.

Another method, using the relative percentage content of the sulfide iron determined by Mossbauer spectroscopy and the total iron percentage in char to calculate the sulfide sulfur, was successfully employed. However, only the results of two coal char samples with high ferrous sulfide content were reported in Table 3. They agree quite well with the data reported by the evolution method. Greater difficulties were encountered in analyzing the rest of the samples because of their relatively low iron concentration and the presence of various other iron species. During this study, we found that pyrrhotites ($Fe_{(1-x)}S$) with varying stoichiometric quantity of sulfur may give different Mossbauer spectra, rendering the Mossbauer spectral subtraction technique inaccurate, especially when no suitable pyrrhotite standards were available.

Table 2. Determination of sulfide sulfur of 1400°F coal chars using HCl evolution method

1400 °F Coal Char	Sulfide S %	Residual S %	Total S % (Calc)	Total S % (Detn.)	HCl-Soluble Fe %	S/Fe (Mole)
Kentucky No. 9						
(with $SnCl_2$)	.90	1.38	2.28	2.50	2.00	.78
(w/o $SnCl_2$)	.57	1.53	2.10		1.97	
Kentucky No. 9 (prepared from -200 mesh coal fines)						
(with $SnCl_2$)	.74	1.30	2.04	2.14	1.65	.78
(w/o $SnCl_2$)	.24	1.35	1.59		1.64	
Pittsburgh No. 8						
(with $SnCl_2$)	2.11	.90	3.01	2.96	3.76	.98
(w/o $SnCl_2$)	1.70	1.12	2.82		3.70	
Kentucky No. 13						
(with $SnCl_2$)	.30	.68	.98	1.02	.60	.87
(w/o $SnCl_2$)	.04	.85	.89		.60	
Illinois No. 6						
(with $SnCl_2$)	1.44	1.35	2.79	2.79	2.46	1.02
(w/o $SnCl_2$)	.87	1.61	2.48		2.40	
Rosebud						
(with $SnCl_2$)	.56	.74	1.30	1.33	1.20	.81
(w/o $SnCl_2$)	.30	.93	1.23		1.18	

Table 3. Comparison of methods for sulfide sulfur analysis of 1400°F Coal Chars

1400 °F Coal Char	Sulfide S % (determined) w/o $SnCl_2$	Sulfide S % (determined) with $SnCl_2$	Sulfide S % (calculated) From Mossbauer	From HCl-soluble Fe (1N)	(1.6N	(2N)	(6N)
Kentucky No. 9	.57	.90	ND	.87	.80	.88	1.13
Kentucky No. 9 (-200 mesh coal)	.24	.74	ND	.76	.81	.84	.94
Pittsburgh No. 8	1.70	2.11	2.07	2.08	2.05	1.98	2.12
Kentucky No. 13	.04	.30	ND	.30	.30	.30	.34
Illinois No. 6	.87	1.44	1.41	1.35	1.37	1.33	1.38
Rosebud	.30	.56	ND	.61	.60	.57	.68

NOTE: ND = not determined.

No results from XRD analysis were reported at this time. The quantitative method using potassium chloride as an internal standard gave erroneous results because no effective method was developed yet to resolve and quantitate the broad and deformed x-ray peak corresponding to diffractions at the crystal 102 planes of various ferrous sulfides. The even broader XRD background induced by the char itself further complicates the XRD spectra. In order to achieve better accuracy in the quantitative measurement of total ferrous sulfide, the sensitivity of diffraction from each of the different ferrous sulfides must also be determined.

CONCLUSION

A hydrochloric acid evolution method using stannous chloride as a promoting agent was developed and employed successfully for ferrous sulfides determination in 1400°F coal char. This method not only provides an accurate analysis of ferrous sulfides, but also improves the accuracy of the organic sulfur analysis of coal char. We believe this method could be and should be employed in the sulfur-by-types analysis of all coal derivatives containing ferrous sulfides.

Among other methods studied, the methods using 1N, 1.6N (5%) and 2N HCl-soluble iron to calculate the ferrous sulfides content could be employed to determine the ferrous sulfides content in coal char, provided that little other HCl-soluble iron species are present. The method using Mossbauer spectroscopy to determine the sulfide iron concentration and atomic absorption spectroscopy to determine the total iron would be a good technique, if pyrrhotite standards as well as other iron standards resembling the iron species in coal char were found. Further Mossbauer apectroscopic studies with temperature control may provide more information and may simplify the current procedure. X-ray diffraction spectroscopy also encounters a similar problem caused by various ferrous sulfides with discrete composition and structures. However, the latter problem is even more significant and tends to be too complex to resolve.

ACKNOWLEDGMENT

The funds for this research investigation were provided by the Morgantown Energy Technology Center, United States Department of Energy under Contract No. DE-AC21-84MC21313 and The Institute of Gas Technology under IR&D Project 20317.

The authors would like to thank Ms. K. L. Crippen for her technical assistance in analyzing the samples.

REFERENCE

(1) M. Saporoschenko, et.al., "Mossbauer spectroscopic studies of the mineralogical changes in coal as a function of cleaning, pyrolysis, combustion and coal conversion processes," FUEL 59, 567 (1980).

(2) I. Stewart, S. G. Whiteway, P. J. Cleyle, and W. F. Caley, "Decomposition of pyrite in a coal matrix during the pyrolysis of coal." Mineral Matter and Ash in Coal, K. S. Vorres, ed. ACS Symposium Series No. 301, 485 (1985).

(3) P. A. Montano, V. Shah, S. Reddy and A. S. Bommannavar, "Mossbauer study of the transformation of iron minerals during coal conversion," New Approaches in Coal Chemistry, ACS Symposium Series 169, 377 (1981).

(4) R. H. Carty, D. M. Mason and S. P. Babu, "Reaction kinetics and physical mechanisms of ash agglomeration," Final Report to U.S. Department of Energy, March 1987 (DE-AC21-84MC21313).

(5) M. G. Thomas, T. D. Padrick, F. V. Stohl and H. P. Stephens, "Decomposition of pyrite under coal liquefaction conditions: a kinetic study," FUEL 61, 761 (1982).

(6) K. J. Huttinger and W. Krauss, "Catalytic activity of coal minerals in hydrogasification of coal," FUEL 60, 93 (1981).

(7) O. P. Mahajan, A. Tomita, J. R. Nelson and P. L. Walker, Jr., "Differential scanning calorimetry studies on coal. 2. Hydrogenation of coals," FUEL 56, 33 (1977).

(8) A. S., Bommannavar and P. A. Montano, "Mossbauer study of the thermal decomposition of FeS_2 in coal," FUEL 61, 523 (1982).

(9) Pedro A. Montano, "Characterization of iron-bearing minerals in coal," Coal Structure, M. L. Goorgbatz and K. Ouchi, ed. ACS Advances in Chemistry Series 192, 337 (1981).

(10) R. H. Carty, D. M. Mason and S. Babu, "Coal gasification research studies," Report to U.S. Department of Energy for Aug. 1983 through Nov. 1983 (DOEMC/19301-5).

(11) J. R. Craig and S. D. Scott, "Sulfide phase equilibria," Sulfide Mineralogy, P. H. Ribbe, Volume 1, s-21, November 1974.

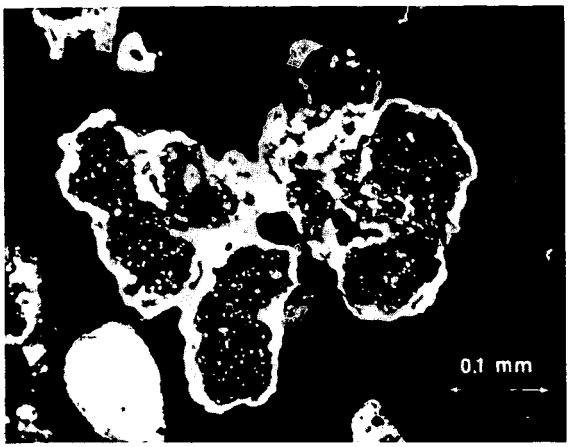

Figure 1. FeS (white) Joining Shale Particles in Bed Material From a Pilot-Plant Run on Run-of-Mine Coal

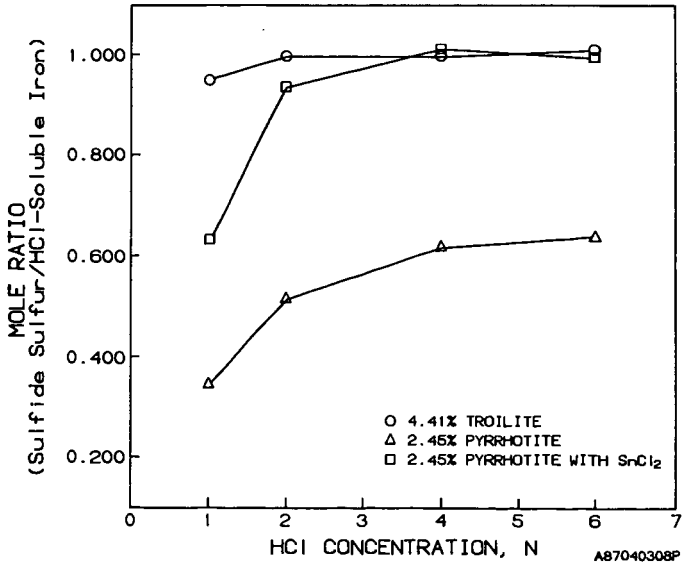

Figure 2. Recovery of Ferrous Sulfide as Hydrogen Sulfide in a Hydrochloric Acic Evolution Procedure With and Without Stannous Chloride

THE PREPARATION AND DISTRIBUTION OF

ARGONNE PREMIUM COAL SAMPLES*

Karl S. Vorres
Chemistry Division, Bldg. 211
Argonne National Laboratory
Argonne, IL 60439

* Work performed under the auspices of the Office of Basic Energy Sciences, Division of Chemical Sciences, U. S. Department of Energy, under contract number W-31-109-ENG-38.

ABSTRACT

The eight Argonne Premium Coal Samples were each collected in about 1 1/2 ton quantities, placed in steel drums, purged with argon and taken to ANL for processing. After transfer to a nitrogen filled enclosure, they were crushed, pulverized, mixed and packaged in sealed amber borosilicate ampoules containing 10 grams of -20 mesh or 5 grams of -100 mesh sample. Five gallon carboys hold about 80% of the batch in reserve for filling more ampoules after the original about 5,000 of -20 mesh or 10,000 of -100 mesh samples are depleted. More than 70 laboratories are participating in the analysis. Over 90 shipments have been made to more than 45 different organizations for a range of programs which will be the subject of later papers in the symposium.

INTRODUCTION

The Premium Coal Sample Program is intended to provide the basic coal research community with the best quality samples of a limited number (8) of coals for basic research. The availability of the ampoules is the result of the cooperation of many individuals within a number of organizations whose efforts made the high quality of the samples possible.

The premium coal samples produced from each coal and distributed through this program are chemically and physically as identical as possible, have well characterized chemical and physical properties, and will be stable over long periods of time. Coals have been mined, transported, processed into the desired particle and sample sizes and packaged in humid nitrogen environments as free of oxygen as possible. The need for a Premium Coal Sample Program was expressed on a number of occasions, culminating in the Coal Sample Bank Workshop held March 27 and 28, 1981 in Atlanta, Georgia.

SELECTION OF THE COALS

Support has been provided by the Office of Basic Energy Sciences

to make eight carefully selected coals available. The selection of these coals was based on those parameters which would represent significant differences among the available coals and maximize our understanding of the fundamental properties of coal. A cluster analysis was carried out to establish desirable samples in terms of the significant compositional parameters, C, H, O and S. This was augmented by considerations of maceral content, paleobotanic origins, age and coking properties.

IDENTITY OF SAMPLES AND CHARACTERISTICS

The coals are listed in the order collected. Preliminary data describing the samples are given below. The moisture and ash-free values are given in %, except for sulfur and ash which are in dry %.

#	Seam	State	Rank	C	H	O	S	Ash
1	Upper Freeport	PA	Med. Vol. Bit.	87	5.5	4	2.8	13
2	Wyodak-Anderson	WY	Subbituminous	74	5.1	19	0.5	8
3	Illinois #6	IL	High Vol. Bit.	77	5.7	10	5.4	16
4	Pittsburgh (#8)	PA	High Vol. Bit.	83	5.8	8	1.6	9
5	Pocahontas #3	VA	Low Vol. Bit.	91	4.7	3	0.9	5
6	Blind Canyon	UT	High Vol. Bit.	79	6.0	13	0.5	5
7	Lewiston-Stockton	WV	High Vol. Bit.	81	5.5	11	0.6	20
8	Beulah-Zap	ND	Lignite	73	5.3	21	0.8	6

COLLECTION AND TRANSPORTATION OF SAMPLES

The samples were collected from sites selected in cooperation with the U. S. Geological Survey. The USGS provided technical supervision while a special collection crew from the Pittsburgh Testing Laboratory removed the channel-type sample from each of the underground sites. Usually a fresh block of coal about 18" wide, the thickness of the seam and several feet deep was isolated, removed and placed into stainless steel 55 gallon drums. Surface samples were placed directly into the drums. The drums of coal were placed in a semi-trailer within 1-4 hours from the initiation of the sample collection. The drums were then purged with enough argon gas to reduce the oxygen content to 100 ppm by the same truck driver. The drums were pressurized to 5 psi and taken to Argonne National Laboratory at 42°F, usually within 24 hours.

PREPARATION OF SAMPLES

The drums were unloaded from the truck, weighed and placed into an airlock in a nitrogen-filled processing facility. The oxygen content of the facility was maintained below 100 ppm of oxygen, and typically was about 30 ppm. After the airlock was purged, the drums were opened, and the contents were transferred to a crusher, where the sample was reduced to pieces that would pass between bars with openings 1/2" apart. The crushed coal was

elevated to the pulverizer where it was ground to pass a 20 mesh screen. The entire one-ton batch used for processing was ground and accumulated in a 2000 liter mixer-blender. After thorough mixing the sample was transferred by a tubular conveyer to a second enclosure. About half the batch was transferred to special 5 gallon leverlock pails for transfer back to the initial airlock for later repulverizing to -100 mesh. The balance was mostly placed into 5 gallon borosilicate glass carboys for long-term storage. About 5,000 ampoules containing 10 grams of -20 samples were sealed with a hydrogen-oxygen torch. The flame was kept at the stoichiometric composition with a mass flow controller. The half batch that was transferred to the initial airlock was pulverized to pass a 100 mesh screen and accumulated again in the mixer-blender. After mixing the -100 mesh material was transferred to the second enclosure for placing into 5 gallon borosilicate carboys and into 10,000 ampoules of 5 grams of -100 mesh material. The ANL glassblower sealed the carboys for long term storage. Samples were taken during the processing for homogeneity analyses to establish the uniformity of the samples during the processing and sealing.

One of the samples, the Illinois #6, was taken from the same block of coal which was also collected for the Illinois State Geological Survey. That sample is known as the Illinois Basin Coal Sample Program #5. Larger quantities (1 lb to 50 lbs) of that sample may be obtained from the ISGS.

ANALYSIS OF SAMPLES

The homogeneity samples were irradiated and the induced radioactivity of several isotopes was counted to indicate the content of each species in the samples. A high degree of uniformity was found.

Additional samples have been submitted for a range of analyses including: proximate, ultimate, major and minor elements in the ash, heat content, forms of sulfur, maceral analysis, and reflectance measurements. A large number of laboratories is participating in the analytical studies.

In order to establish the long term stability of the samples, additional analytical work is done including the evaluation of the gas atmosphere inside of the ampoules at two month intervals. For the bituminous samples, Gieseler plasticity measurements are being made to establish the fluidity at various intervals. To date, no indications of oxidation or loss of fluidity have been found.

DISTRIBUTION OF SAMPLES

Samples are distributed as 5 gram ampoules of -100 mesh or 10 gram ampoules of -20 mesh material. Shipments typically involve multiples of 6 or 12 ampoules in special cardboard cartons, with

added foam padding to increase the probability of safe arrival. Orders are sent to the Assistant Controller at ANL, and after processing, are filled and shipped by UPS or international air courier. Order forms may be obtained from the author. A nominal charge of $8 (US) is made for the 5 gram ampoules and $16 for the 10 gram ampoules. International shipments involve an additional charge of $20 for a set of six ampoules.

To date over 89 orders have been filled for more than 3,000 ampoules.

Two types of ampoules have become available during processing. Initially the ampoules were of a standard type with a gradually sloping shoulder to the tip. The "easy-break" ampoules became available later and have been used for the latter coal samples. Instructions for opening the ampoules are included with each shipment. Appropriate care must be exercised in the opening to avoid mixing glass fragments in the coal and to protect the hands of the experimenter.

The importance of mixing must be stressed. All coal samples are subject to segregation on standing. It is necessary to remix the sample before opening the ampoule. The recommended method is to turn the ampoule so that the coal alternately falls into the top and then the body of the ampoule. This should be repeated a number of times (at least 10). Rolling the ampoule on its side is not as effective and should not be relied upon for thorough mixing.

The samples are intended to be used immediately after opening. Any unused portion should be discarded, as the original properties may change on further storage.

RESEARCH BEING DONE WITH THE SAMPLES

The types of research being done with the premium samples includes a cross section of the areas of basic and applied coal research. Some major areas include:

Analytical Studies

A number of analytical studies are being carried out. A direct measurement of organic sulfur by examination of a number of individual coal particles by reflected radiation is being developed. The initial results indicate that the sulfur content of a given maceral may be different than the parent coal but is similar from one maceral particle to another particle of the same maceral. A direct measurement of oxygen is being developed by the use of fast neutron activation, and direct counting of the induced oxygen activity. Corrections are made for oxygen present in the moisture and mineral matter. Several groups are working to establish the relative amounts of the different macerals in

the coal and to separate these macerals. Another group is studying the occurrence of sodium and chloride in the coal to establish the forms in which it may be bound. Still others are using some of the newer instruments, such photoacoustic FTIR to understand the functional groups present in the coal and near the surface. Plasma excitation is being studied to establish the species produced by this technique. Trace element geochemistry is being used to evaluate the relative amounts of the trace elements and to correlate the occurrence of these elements with other factors. One researcher is comparing the carbon found in coal with that found in meteorites.

Physical Properties

The heat capacities of the samples over a range of temperatures are being studied with fresh and aged samples. Interesting differences have been found. The pore characteristics are being studied by a variety of techniques. Solvent swelling studies have also been initiated.

Structure Studies

At least six laboratories are using nuclear magnetic resonance techniques to carry out a variety of structural studies. Several of these will be reported later in the symposium. Chemical techniques are being used by at least three different laboratories. Solvent extraction is being used to evaluate the classes of materials which are present and to determine the effects of aging on the relative amounts of these species. Supercritical extraction is being used at three or more laboratories for similar purposes. The nature and amount of acidic sites is the subject of study at two laboratories. Other workers are using alkylation of sites to establish the effects of altering certain classes of functional groups. Two groups are examining the nature of the water in the coal. Other workers are studying the different forms of sulfur present in the samples to establish the organic and inorganic species which are present. In a number of cases the researchers are using a variety of techniques to probe more deeply into the structural features of the coal material.

Coal Conversion

Pyrolysis is being used at seven or more laboratories to release different species and understand the factors involved in the thermally induced changes. Coal desulfurization by a variety of techniques is another popular area of research. Liquefaction is also being studied at three laboratories with these samples. The catalytic effects on coal conversion is also being evaluated.

The Program Manager is also following the progress of small changes in gas composition of the atmosphere in the ampoules as time passes.

ACKNOWLEDGMENTS

The sponsorship of the U. S. Department of Energy, Office of Basic Energy Sciences, Chemical Sciences Division is gratefully appreciated. The efforts of many who made the program work as effectively as it has must also be mentioned. These include the original planners: Phil Horwitz, John Unik, Randall Winans, Gary Dyrkacz and John Young; the staff of the U. S. Geological Survey who supervised the sample collection: C. Blaine Cecil, Ron Stanton and Peter Warwick; the coal companies who generously made samples available including: Rochester and Pittsburgh Mining Company, Peabody Coal Company, Coteau Properties, Inc.; many involved in the design and construction of the processing facility: Herbert Brown, K. Michael Myles, Gale Teats, Kurt Schultz, Ed Lewandowski, Mike Slawecki, Rich Graczyk, Pat Doolin; the sample collection crew from the Pittsburgh Testing Laboratory: David Allen, Tim Graham, Ron Lowman; the truck driver: Randy Engelhart: those who assisted with the coal processing: Gale Teats, Kurt Schultz, Don Piatak, Wally Czyz, Stuart Janikowski, Freddie Morris, Dmitry Silversteyn, Bart Beals, David Clow, James Krizek, and Mark Kopciewski; the glassblower: Joe Gregar; homogeneity analyses: Bob Heinrich; chemical analyses: Peter Lindahl and Toni Engelkemeir; computer programming by Paul Day and Miriam Bretscher; purchasing by Joe Forzley and Ronette Stachelski.

SMALL ANGLE NEUTRON SCATTERING STUDIES OF SWELLED COAL

Randall E. Winans and P. Thiyagarajan

Chemistry Division, Argonne National Laboratory,
9700 South Cass Avenue, Argonne, Illinois 60439

INTRODUCTION

The objective of this study is to determine changes that occur in the physical structure of coals upon swelling in an organic solvent. It is known that bituminous coals will swell in solvents such as pyridine (1). The phenomenon of coal solvent swelling is being used to characterize coal structure especially in the determination of molecular sizes between cross-links. Swelling can affect coal reactivity in thermolysis reactions. Also, it is important to note that swelling increases reagent accessibility in chemical modification of coals (2). Small angle neutron scattering (SANS) is the approach used in this study to examine the changes in pore structure in a Pittsburgh #8 seam hvA bituminous coal, Argonne Premium Coal Sample #4 (3). Two perdeuterated solvents are used, benzene for non-swollen and pyridine for swelling conditions. The deuterated solvent provides a large contrast between the solvent and the solid coal for neutron scattering.

Coal porosity has been studied by SANS in the dry state (4,5,6) and in non-swelling deuterated solvents (4,6). These studies suggested that this technique can be useful for examining pore structure. Our current results show that the pore structure of a coal swollen in pyridine is dramatically altered from its original state.

EXPERIMENTAL

The SANS measurements were made at Argonne National Laboratory's Intense Pulsed Neutron Source (IPNS) using the Small Angle Diffractometer (SAD). Neutrons were produced in pulses by spallation from 450 MeV protons followed by moderation by solid methane (18°K) to produce wavelengths of 0.5 to 14 Å. The sample saw a 0.9 cm diameter beam. A 64x64 array position sensitive multidetector was used to detect neutrons scattered by the sample while the wavelength of the neutrons (λ) was determined by time-of-flight. The data were corrected for scattering from the cell and incoherent scattering. Finally, the intensity (I) was expressed as a function of the scattering vector, Q:

$$Q = (4\pi/\lambda) \sin\theta \qquad (1)$$

where θ was half the scattering angle and:

$$I(Q) = K\langle\int_v(\rho_s-\rho_m)\exp(iQr)d^3r\rangle^2 \qquad (2)$$

where K included all the experimental constants and ρ_s and ρ_m were the scattering length densities of the solvent and the matrix. A Q range of 0.005 to 0.35 $Å^{-1}$ was accessible on the SAD instrument at IPNS.

The preparation of the Argonne Premium Coal Sample has been described (3). A -100 mesh APCS #4 sample was used. (Preliminary analytical data, on a maf basis: C 83%, H 5.8%, N 1.6%, O 8% S(dry) 1.6% and ash(dry) 9%.) A sealed glass ampoule containing the coal was broken open in a nitrogen atmosphere glove box. The coal was well mixed and a portion transferred to a 2 cm diameter x 1.85 mm thick quartz cell leaving enough room for swelling. Perdeuterosolvent was added to the coal and then the cell was sealed. The sample was allowed to sit for several days before doing the SANS experiment to insure complete swelling in the case of d_5-pyridine.

RESULTS AND DISCUSSION

A Guinier plot (7), based on the relationship shown in Equation 2, for both solvents is shown in Figure 1. Even though d_6-benzene and d_5-pyridine have similar scattering length densities, 5.35 and 5.69 x $10^{+10}/cm^2$ respectively, there is a striking difference between the scattering data from the two solvents. The scattering data for both solvents exhibit a steep slope at low Q. These results are indicative of large pores with sizes up to 1000 A. The largest pores that have been reported previously had a 500 A limit which was constrained by the instrumentation (1). Further analysis of the d_6-benzene data shows a distribution of pore sizes from 12 A up to the 1000 A limit. The difference of the porosity between the coal and swollen coal may be in the shape of the pores.

In low angle scattering it is possible to determine the shape of the pore or particle using a modified Guinier analysis (7). There are three types of pore shapes: spherical, elongated (tubular) and lamellar. From the Guinier analysis one can determine the radius for spherical, cross sectional radius and length (1/Q) for elongated, and thickness and area ($1/Q^2$) for the lamellar shapes due to the following scattering laws:

$$\text{Elongated:} \quad I = I_c \cdot 1/Q$$

$$\text{Lamellar:} \quad I = I_t \cdot 1/Q^2$$

To investigate the possibility of elongated pores $\ln(I \cdot Q)$ is plotted versus Q^2 in Figure 2. For d_6-benzene there is no correlation, but for the d_5-pyridine a negative slope is found. At low Q tubular pores with a radius of 9-11 A are found. Figure 3 shows that lamellar pores are not seen in either sample since positive slopes are observed for both samples.

From these preliminary results we conclude that in a good swelling solvent the tertiary structure of this bituminous coal undergoes major rearrangement. Whereas the original coal contains a broad size range of roughly spherical pores, the swollen coal contains elongated pores with several distinct sizes. The pyridine appears to be determining the new pore dimension. Exactly five pyridines can be fitted into a 9 A radius circle as shown in Figure 4. Table 1 lists the dependence of pore radius on the number of pyridines packed into a cross-section of the elongated pore. The size of the pyridine molecule has been estimated from space-filling computer models based on the van der Waals radii of the individual atoms. Even at high Q, up to the instrument limit, a negative slope for the modified Guinier analysis is

TABLE 1. Possible Packing Arrangements of Pyridine Molecules in Tubular Pores

Number of Pyridines	Radius of Pore (Å)
1	3.37
2	6.74
3	7.26
4	8.14
5	9.10
6	10.11
7	11.14

observed giving a radius of approximately 6 Å. This size of tubular pore could accommodate stacks of two or three pyridine rings. It is important to note that we are observing relative narrow elongated pores. These results could be explained by invoking hydrogen bonding between the pyridines and the phenols or other acidic hydroxyls on the surface of the tubular pores. In addition, it is thought from the NMR and ESR experiments that the motion of pyridine in a coal is restricted (8). Our SANS data argues against a layered, polycyclic aromatic structure for this coal. Possibly hydrogen bonding is more important in determining the tertiary structure.

ACKNOWLEDGMENTS

This work was performed under the auspices of the Office of Basic Energy Sciences, Division of Chemical Sciences, and Material Sciences (IPNS), U.S. Department of Energy, under contract number W-31-109-ENG-38.

REFERENCES

1. T. Green, J. Kovac, D. Brenner and J.W. Larsen, in "Coal Structure", R.A. Meyers Ed., Academic Press, p. 199 (1982).
2. R. Liotta, Fuel 58, 724, (1979).
3. K.S. Vorres and S.K. Janikowski, Preprints, Div. Fuel Chem., ACS., 32 (1), 492, (1987).
4. H. Kaiser and G.S. Gethner, Proceedings, Inf. Conf. Coal Science, 300, (1983).
5. M.J. Tricker, A. Grint, G.J. Audley, S.M. Church, V.S. Rainey and C.J. Wright, Fuel 62, 1092, (1983).
6. G.S. Gethner, J. Appl. Phys. 59, 1068, (1986).
7. A. Guinier and G. Fournet, "Small Angle Neutron Scattering" trans. by C.B. Walker and K.L. Kudowitch, Wiley, NY p. 19, (1955).
8. B.G. Silbernagel, L.B. Ebert, R.H. Schlosberg and R.B. Long, in "Coal Structure", M.L. Gorbaty and K. Ouchi Eds., ACS Adv. Chem. Series 192, 23, (1981).

Figure 1. Guinier plot for SANS of the Pittsburgh #8 Bituminous coal, APCS #4

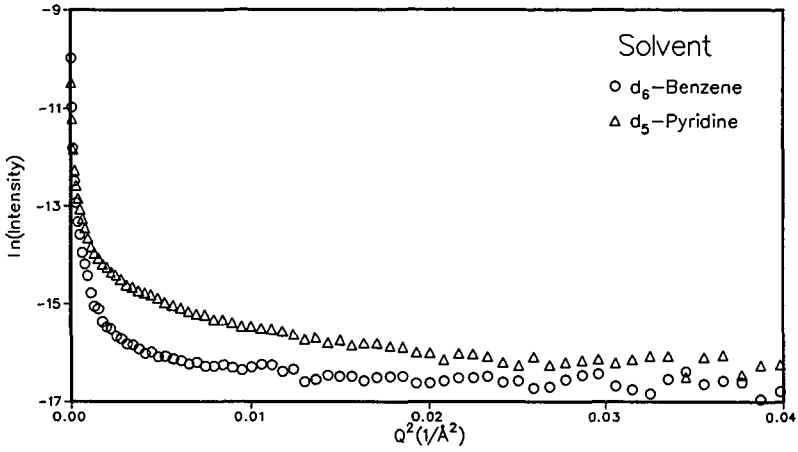

Figure 2. A modified Guinier plot of SANS data for APCS #4 to evaluate the possiblity of tubular pores

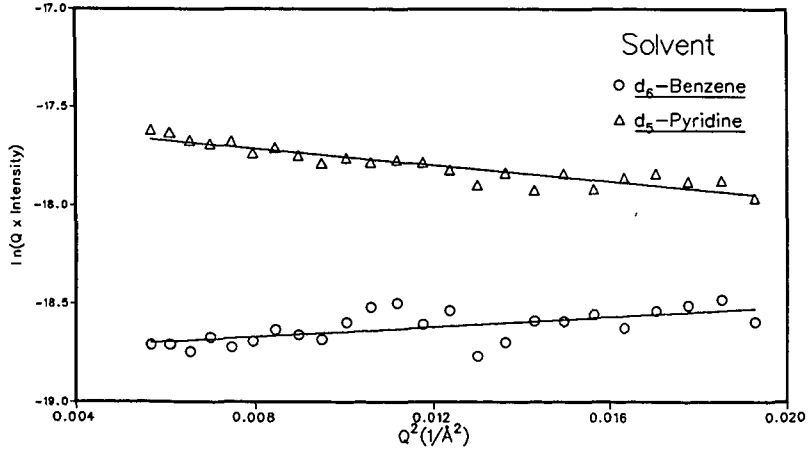

Figure 3. A modified Guinier plot of SANS data for APCS #4 ta evaluate the possiblity of sheet–shaped pores

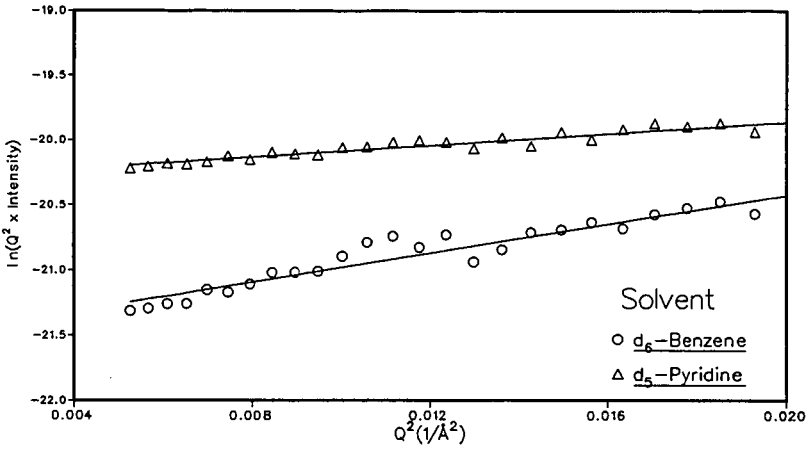

Figure 4. Possible arrangement of five pyridine molecules in a 9Å radius elongated pore.

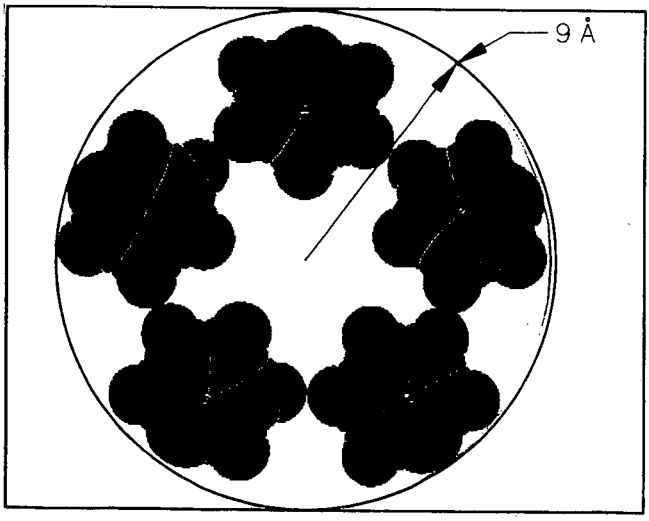

A Possible Connection Between Gas Solubility in Coals and BET Surface Areas

J. W. Larsen and P. C. Wernett

Department of Chemistry
Lehigh University
Bethlehem, Pa. 18015

INTRODUCTION

Gas adsorption techniques have been widely used in determining surface areas of porous and nonporous solids. The surface areas of coals, calculated from nitrogen isotherms at 77.8°K. are considerably less than those obtained using CO_2 at 195°K.[1-4] It is generally believed that N_2 yields low surface areas because the micropores in the coals are not completely accessible to N_2 at 77.8°K. Limitations are imposed by an activated diffusion process for N_2 and/or shrinkage of the coal pores at 77.8°K.[1,4] Carbon dioxide has a lower activation energy for adsorption than N_2.[1,5,6] It has been suggested that CO_2 interacts with oxygen functionalities in coals resulting in swelling which may contribute to the large surface areas for coals.[7]

As part of another investigation, we have measured BET surface areas of a high volatile bituminous coal with small hydrocarbon gases expected to be insoluble in the coal. We report here a comparison of these surface areas with those obtained using CO_2 and Ar. We tentatively conclude that the solubility of CO_2 in coals is important in that it gives CO_2 access to closed pores which are otherwise ignored in surface area measurements by gas adsorption. It may be that the majority of the coal surface area lies in closed pores.

EXPERIMENTAL

A high volatile Ill. No. 6 coal sample (100 mesh, 75.2% C, 4.5% H, 1.4% N, 3.3% O, 2.4% S all dmmf) was obtained from the Premium Coal Sample Bank at Argonne National Laboratory. 100 mg samples of this coal were transferred into a preweighed sample container in a nitrogen filled glovebox for each experiment. The samples were outgassed on a glass BET isothermal apparatus under a vacuum of approximately 10^{-3} torr for no less than 8 hrs. A Datametrics Barocel pressure sensor was used to measure the pressure drop from a known volume to the sample container. The dead volume of the sample container was determined by the pressure difference of He from the known volume to the sample container at 77.8°K. This instrument has given correct surface areas for standard materials.

RESULTS AND DISCUSSION

The surface areas we obtained using Ar and CO_2 (Table I) are consistent with those reported for Ill. No. 6 coal[2] by others.[2,4] The astounding feature of the data in Table I is the very low surface area obtained with cyclopropane. It is considerably less than the surface area given by CO_2. Cyclopropane and CO_2 have the same cross-sectional area when they are determined by the method of Emmett and Brunauer.[8] The cross-sectional area of cyclopropane, calculated from its structure and standard bond lengths is 23.2 A^2 if it lies flat and 20.3 A^2 if it lies on a side. These are close enough to the calculated value and to each other to have no effect on our conclusions. Since the molecules are of similar size, it is difficult to rationalize the very large surface area differences using arguments based on molecular sieving by the pore system. When an adsorbate molecule is soluble in the coal, the surface area increases with solubility (Fig.I, work by Reucroft and Patel, ref. 2). On this basis, it is possible that the low surface areas observed with nitrogen (Table II), CCl_4, and n-hexane (Fig. I) are all correct and the surface area obtained from CO_2 is in error due to its solubility in the coal. We disagree with this. The solubility of CO_2 in coals is not great enough to explain the large surface areas observed and CO_2 surface areas agree well with those obtained using X-ray scattering.[1,9] It seems likely that the CO_2 surface areas are approximately correct for coals and we must seek an explanation for the anomalously low surface area obtained with cyclopropane.

If the CO_2 surface areas are approximately correct, then CO_2 must be able to reach coal surface which is inaccessible to cyclopropane. This brings us to consider the solubility of the two gases in coals. The solubility of CO_2 in coals has been experimentally demonstrated (see however ref. 10).[7] Cyclopropane is probably insoluble in the coal. It has been established that alkanes do not swell coals to any appreciable extent and the heats of wetting of coals by alkanes is zero.[11,12] We conclude that cyclopropane is probably insoluble in the coal.

This solubility difference is the basis of an explanation of the different surface areas obtained with these two gases. If a large portion of the pores in coals are closed, they will remain inaccessible to molecules unable to dissolve in coals. The pores are not directly connected to the external surface so a molecule must dissolve in and diffuse through solid coal to reach the closed pores. Adsorbate gases capable of dissolving the coal have accessibility to pores that are closed to insoluble molecules. Thus, soluble CO_2 gains access to all of the pores in this coal while insoluble cyclopropane can only reach those connected to the exterior by the pore network. If this is correct, most of the coal pore system is closed.

It can be argued that the coal is shape selective and that the rod-like CO_2 molecule can penetrate the pores while the flat

cyclopropane cannot. Work with amines has shown that planar molecules easily penetrate coals while branched molecules do not.[13] It has been shown that both n-butane and CF_2Cl_2 also give low coal surface areas.[14,15] If coals are shape selective, they are extraordinarily discriminating. Molecules such as methanol which interact specifically with coals and dissolve in them report very large surface areas which are incorrect.[15] What is being measured is solubility in the coal, not surface area. It seems to us most reasonable to conclude that coal pores are mostly closed and inaccessible to molecules not soluble in the coal.

With this model there are three classes of sorbed molecules. Molecules which interact specifically and strongly with coals or which are soluble in coals report very large and meaningless surface areas. The experiment measures their solubility in the coal. Molecules which are insoluble in coals can be used to measure that part of the surface area which is open to the surface and accessible to the probe molecule. This accessibility is governed by the pore size, the molecule size, and the temperature since diffusion may be activated. Finally, there are those molecules whose solubility in coal is low, but which can penetrate all of coal by virtue of that solubility. These molecules will have access to all of the pores, even those not connected directly to the surface, and can be used to determine an approximately correct total surface areas.

ACKNOWLEDGMENTS

We are grateful to the U. S. Department of Energy for financial support of this work.

REFERENCES

1) Mahajan, O. P. in "Coal Structure", R. A. Meyer, ed., Academic Press:New York, 1982.

2) Reucroft, P. J.; Patel, K. B. Fuel 1983, 62, 279.

3) Kini, K. A. Fuel 1964, 43, 173.

4) Gan, H.; Nandi, S. P.; Walker, P. L. Fuel 1972, 51, 270.

5) Mahajan, O. P.; Walker, P. L.,Jr. in "Analytical Methods for Coal and Coal Products, Vol. I.", C. Karr Jr., ed., Academic Press:New York, 1978.

6) Klotzkin, M. P. Fuel 1985, 64, 1092.

7) Reucroft, P. J.; Patel, H. Fuel 1986, 65, 816.

8) Emmett, P. H.; Brunauer, S. J. Am. Chem. Soc. 1937, 59, 1553.

9) Spitzer, Z.; Ulicky, L. Fuel 1977, 55, 212.

10) Stacy, W. O.; Jones, J. C. Fuel 1986, 65, 1171.

11) Larsen, J. W.; Green, T. K.; and Kovac, J. J. Org. Chem. 1985, 50, 4729.

12) Kennard, L.; Larsen, J. W. unpublished data.

13) Larsen, J. W.; Lee, D. Fuel 1985, 64, 981.

14) Malherbe, P. le R.; Carman, P. C. Fuel 1952, 31, 210.

15) Anderson, R. B.; Hall, W. K.; Lecky, J. A.; Stein, K. C. J. Phys. Chem. 1956, 60, 1548.

Table I. Surface Areas of Ill. #6 Coal

Adsorbate	Adsorption Temperature (°K)	Cross-Sectional Area (A^2)	BET Surface Area (m^2/g)
Argon	77	16.2	14
			15
Carbon Dioxide	178	25.3	132
			132
Cyclopropane	203	25.2	36
			31

Table II. Surface Areas of Kentucky #12 (from ref.2)

Adsorbate	Cross-Sectional Area (A^2)	BET Surface Area (m^2/g)
Nitrogen (77.8°K)	16.27	4
Carbon Dioxide	25.30	101

FIGURE I.

Dependence of Surface Area for Kentucky #12 Coal on Solvent Swelling (data from ref.2)

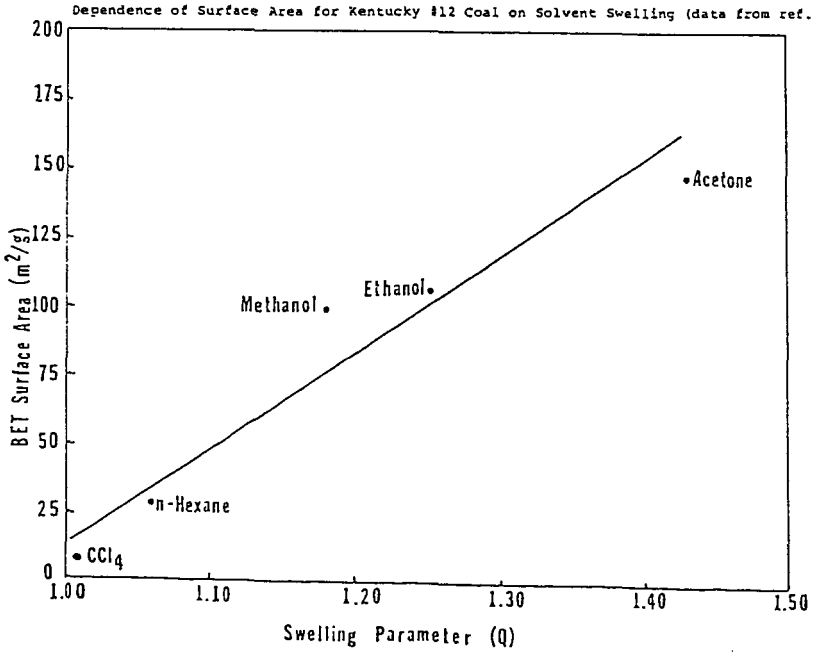

SPECIFIC HEAT MEASUREMENTS OF TWO PREMIUM COALS

Jane E. Callanan and Kathleen M. McDermott

Center for Chemical Engineering, National Bureau of Standards[1]
Boulder, Colorado 80303

Introduction

Our purpose in initiating the study of the premium coal was threefold. Our first aim was to observe the behavior of the premium coal. Second, we wished to obtain reliable heat capacity data to add to the pool of available information on the premium coals and thus extend the data base available for the development of useful correlations. Third, we wished to compare the results obtained for premium coals with those obtained on a nonpremium coal during our development of transferable measurement techniques. The heat capacity measurements made on the nonpremium coals had shown the development of a deep exotherm on initial heating as the coal became more oxidized. We surmised that the difference between the initial and repeat measurements on the oxidized coal could be ascribed in some way to the increased oxidation level of the nonpremium coal. However, the contributions to that effect were not clear.

The heat capacity measurements have been made in sealed cells with no significant mass loss. Water has been shown to be released from the coal as it is heated above the temperature at which it was dried in the course of specimen preparation.(1,2) Three possible sources of this water have been identified. First, it may be water physically trapped in the coal structure that is released as the coal is heated above its drying temperature. Second, the water could be produced by mineral reactions that occur as the coal is heated. Carling has applied a thermodynamic predictive program, which identifies the most likely mineral reactions at various temperatures, to the nonpremium coal used in our studies.(3) Reactions that produce significant amounts of water are predicted to occur between 400 and 450 K, which is within the range of our measurements. Third, the water may be generated by condensation reactions occurring within the organic component of the coal. These would increase as the coal becomes more oxidized.(4)

One possible contribution to the deepening of the exotherm with increased oxidation was the increased exothermicity expected on readsorption of water on a more oxidized surface. Barton has evaluated the effects of increased oxidation on the enthalpy of adsorption of water on coal surfaces.(5)

Two investigations in our laboratory have shed light on the causes of the observed exotherm: The heat capacity of both premium coals and

---

1 Contribution of the National Bureau of Standards. Not subject to copyright.

macerals have been measured. Measurements on the macerals will allow separation of the mineral contributions from those of the organic moieties of coal. The studies on the premium coal aid in the evaluation of the effects of oxidation. It is the studies of the premium coals which are discussed in this contribution.

Experimental

(i) Materials

The premium coals used in this study were the medium volatile bituminous coal from the Upper Freeport Seam and the high volatile bituminous coal from the Pittsburgh #8 Seam.(6) The Upper Freeport Seam coal was the first of the premium coals available and was obtained at the very beginning of this study. During the analysis of the results of these measurements it became evident that measurements on a high volatile premium coal would be most helpful and the Pittsburgh Seam coal was obtained. Comparisons are made with measurements on a high volatile Colorado coal, PSOC-854, that was obtained from the Coal Sample Bank at Pennsylvania State University. The as-received oxygen content of the premium coal was less than two percent; for the nonpremium coal, it was 11 percent.

(ii) Sample preparation

The premium coals were opened in a controlled-atmosphere chamber with low oxygen and moisture levels.(7) They were dried to constant weight at 383 K in a stream of dry nitrogen; the premium coals reach constant weight within 24 hours. The sample is then riffled to ensure representative sampling. The coal is pelletized and sealed in an inert atmosphere within the controlled-atmosphere chamber. Specimen masses ranged from 11-25 mg. Forty specimens of each coal were prepared. Some were used in the initial studies reported here; other, sealed at the same time under the same conditions, are available for further work.

(iii) Measurements

Heat capacity measurements were made in sealed cells with a power-compensated differential scanning calorimeter (DSC) over the temperature range 300-520 K at a heating rate of 5 K/min. Calorimetry Conference sapphire was used as a standard.(8) The heat capacity of the sapphire standard, determined before beginning the measurements reported here with the instrument settings to be used, was accurate to ±1.5 percent. Heat capacity measurements were made on 20 specimens of the Upper Freeport Seam coal; 10 specimens of the Pittsburgh Seam coal were used.

The standard operating procedures and data acquisition and reduction methods used for heat capacity measurements in our laboratory have been described.(9) Modifications have been made to these procedures for a material that undergoes an irreversible reaction on the first heating.(10)

The moisture content of the specimens as used was determined by means of a thermogravimetric balance (TGA).

Results and Discussion

In Figure 1 the heat capacities of the Upper Freeport Seam coal, for both initial and repeat runs, are shown. For purposes of comparison, similar measurements on an oxidized coal, PSOC-854, are shown in Figures 2 and 3. Though this coal, not a premium coal, had an as-received oxygen content of 11 percent, it was ground to -100 mesh in our laboratory before we had the capability of protecting it from the atmosphere. Because it was already well-oxidized when our protective facility was ready, no attempts were made to prevent further oxidation. The moisture content of the specimens actually measured, as determined by TGA, was less than 0.3 percent.

A significant difference between the premium and the nonpremium coals is evident on comparison of Figures 1, 2 and 3. The premium coal does not exhibit the deep exotherm on initial heating that is observed for the nonpremium coal. Both coals manifest expected, or normal, heat capacity behavior on the repeat runs. Differences between initial and repeat runs similar to those for the oxidized coal have also been reported by Singer and Tye(11) and by Richardson.(12) The differences noted strengthen our supposition that the exotherm is associated with the increased oxidation level of the coal.

The exotherm is now believed to result from exothermic condensation reactions which occur on the oxidized coal surface.(4) In the course of development of measuring techniques which will give valid results universally (transferable measuring techniques) we have made heat capacity measurements during several years on the PSOC-854 coal. As the coal has become more severely oxidized, the exotherm has deepened. A quantitative evaluation of the exotherm for coal specimens sealed in an inert atmosphere shows an increase from 6 J/g for a coal containing minimal amounts of oxygen to 38 J/g for a severely oxidized coal. For coals sealed in air, the enthalpy difference between initial and repeat runs is 60 J/g. The small energies stated here, when translated to tons, of coal are on the order of 5-34 MJ.

As our measurements were made in sealed specimen cells, the possibility of a contribution from readsorption of water exists. The water that was released during the heating of the coal to a temperature above that at which it was dried has the potential to react with the altered coal surface. Barton has shown that the exothermicity of the enthalpy of adsorption of water on a coal surface increases significantly as the coal becomes more oxidized.(5)

Another contribution to the differences observed between initial and repeat runs on premium and nonpremium coals arises from the difference in the volatile matter content of the two coals studied. Proximate analysis of the medium volatile premium coal gives a volatile matter content of 32 percent; for the high volatile coal, it gives 43 percent. In analyzing the results of measurements on the Upper Freeport seam (a

medium volatile coal) and comparison with the PSOC-854 coal (a high volatile coal) the effects of the difference in volatile matter content of the two coals were of concern.(4) These effects, however, could not be evaluated until measurements on a premium high volatile coal were completed. The Upper Freeport Seam coal was the first of the premium coals to be distributed and was the only one available at the time this study was initiated. A sample of a high volatile premium coal (Pittsburgh #8 Seam) has since been obtained; measurements in progress on this coal will permit the effects of volatile matter content to be assessed.

References

1. MacDonald, R. A., Callanan, J. E., and Sullivan, S. A., High Temperatures-High Pressures, 17, 387 (1985)

2. Callanan, J. E., Sullivan, S. A., and MacDonald, R. A., Int. J. Thermophys. 8, 133 (1987)

3. Carling, R. W., Mar, R. W., and Nagelberg, A. S., ACS Fuel Division Preprints, 28, 223 (1983)

4. MacDonald, R. A., Callanan, J. E., and McDermott, K. M., Energy and Fuels, to be submitted.

5. Barton, S.S., Evans, M. J. B., Holland, J., and Koresh, J. E., Carbon, 22, 265 (1984)

6. Vorres, K. V. and Janikowski, S. K., ACS Fuel Division Preprints, 32 (1), 492 (1987)

7. Filla, B. J. and Callanan, J. E., Rev. Sci. Instrum., 56, 592 (1985)

8. Ditmars, D. A., Ishihara, S, Chang, S. S., Birnstein, G., and West, E. D., J. Research NBS, 87,159 (1982)

9. Callanan, J. E. and Sullivan, S. A., Rev. Sci. Instrum., 57, 2584 (1986)

10. Hust, J. G., Callanan, J. E., and Sullivan, S. A., Specific Heat of Insulations, in Thermal Conductivity, Vol. 19, New York, Plenum Press (in press)

11. Singer, J. M. and Tye, R. P., Bur. Mines RI 8364 (1979)

12. Richardson, M. J., Anal. Proc., 22, 46 (1985)

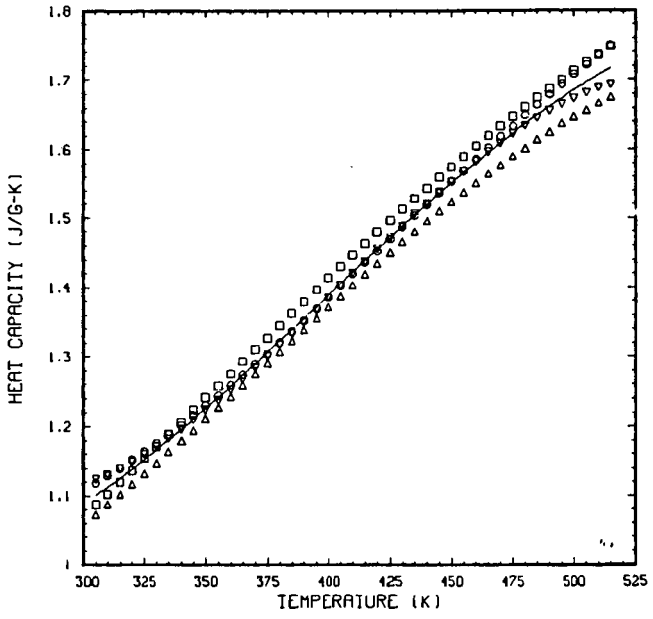

Figure 1. Initial and repeat measurements of premium coal. Fitted value for all measurements, —; fitted values for sets of five replicates, symbols; repeat measurements, Δ; initial measurements, other symbols.

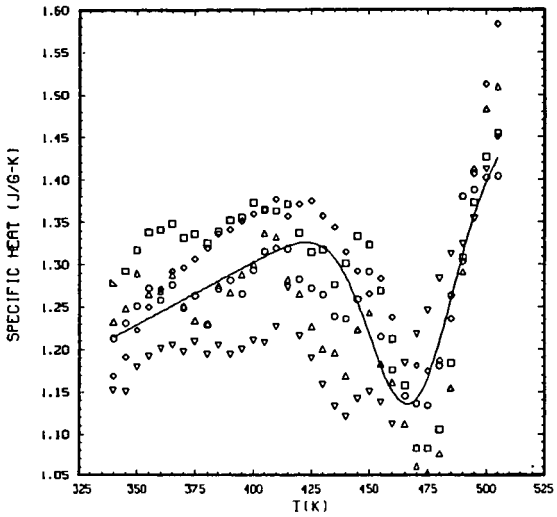

Figure 2. Initial measurements on nonpremium coal. Fitted value for five replicates, ; individual measurements, symbols.

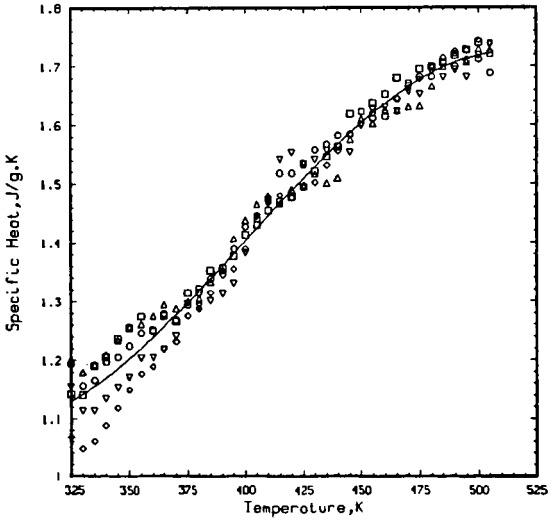

Figure 3. Repeat measurements on nonpremium coal. Fitted value for five replicates, ; individual measurements, symbols.

HEAT CAPACITIES OF ARGONNE PREMIUM COAL SAMPLES

L.L. Isaacs and E. Tsafantakis

The City College of the City University of New York
New York, New York 10031

INTRODUCTION

The thermal effects on coal have been the subject of numerous investigations dating back to the 1890's. (1) Many techniques have been used to study thermal effects, including differential scanning calorimetry (DSC), differential thermal analysis (DTA) and thermogravimetric analysis. DTA and DSC studies of coals by different researchers yield conflicting information (2-5). Numerous heat capacity determination (6-11) have been done on coals over the years. However in these investigations no particular care was taken to check the effects of "weathering" on the measured parameters. A number of the coals investigated were the same as those which are part of the Argonne Premium Coal sample series.

In this communication we report the results of recent DSC investigations on the Argonne Premium Coal Sample series. In these experiments care was taken to correlate the heat capacity with the thermal history of the specimens.

EXPERIMENTAL PROCEDURE

Differential scanning calorimetry was used to determine the response of coal samples to heating. Heating rates of 10K/min. were used. Sample sizes were of the order of 10 to 15 milligrams. Temperatures for the measurements ranged from 100K to 700K. All experiments were done under flowing nitrogen (1 stp l/min.), and the exposure of the samples to the ambient environment was limited to less than two minutes. The heat flow curves were obtained while maintaining constant experimental conditions. The uncertainity in the reproducibility of the data is estimated at one percent. Heat capacities were calculated from the heat flow curves, using sapphire as a standard for comparison. The error in the derived heat capacities is estimated at two percent.

RESULTS AND DISCUSSION

Coal is a complex mixture of organic matter, inorganic matter and water. The usual way of correlating the coal heat capacity data as a function of temperature is to follow Kirov's (6) procedure of expressing the total heat capacity as a weighted sum of the heat capacities of fixed carbon, volatile organic matter, ash and water. Implicit in Kirov's method are the assumptions that these components do not interact, and up to the pyrolysis temperature, the coal does not undergo either a chemical reaction or a structural rearrangement. However, there are a numoer of experimental findings which bring these assumptions into question.

Mraw (12) has measured the heat capacities of coals as a function of water content and found that one must consider the water associated with a

coal to be composed of two types: freezable water, which forms a liquid layer adsorbed on the coal and nonfreezable water which resides in the form of molecular clusters in the pore structure of the coal. The nonfreezable water contributes an excess low temperature heat capacity to the coal due to the onset of rotational and vibrational motions of the clusters inside the pores.

Measurement of coal char heat capacities (13) and of coal ashes (14) indicate that the heat capacity of the char is not a weight-average sum of the ash free char heat capacity and of the ash heat capacity. Thus, there is additional evidence that Kirov's correlation method must be reconsidered. Furthermore, as noted in the introduction, many coals undergo both endothermic and exothermic reactions at temperatures prior to the onset of pyrolysis breakdown. Therefore, it is even questionable that a meaningful heat capacity can be assigned to a coal at temperatures past the onset of reactions accompanied by thermal effects.

In Figure 1, the heat absorption rate (kJ $kg^{-1}sec^{-1}$), $\dot{Q}$, for the Wyoming Sub-bituminous coal is shown as a function of temperature. These data are derived from the heat flow curves for a given sample by dividing the heat flow (milliwatts) versus temperature curves by the weight of the residual sample at the maximum temperature of a given run. The particular features of the figure to be noted are:

* An endothermic peak at low temperatures due to the "pore" water present;

* Melting and evaporation of the "freezable" water extending over a wide temperature range. This endotherm would mask any other endotherm occurring in the same temperature range;

* Start of an exotherm around 400K;

* An endothermic reaction between 575K and 675K.

In the above context endothermic and exothermic are defined as heat absorption relative to that which would be calculated from the heat capacity versus temperature curve for a non-reactive sample. Such an absorption curve is indicated on the figure.

By repeating the heating curve for the same sample we note the disappearance of the endothermic peaks associated with water desorption and the reduction and eventual disappearance of the high temperature endotherm. The exotherm also decreases in magnitude, at a given temperature with recycling. The sample loses weight on heating. The total weight loss is 55% of the starting weight. The major portion (40-48% of starting weight) of the weight loss is due to the removal of water.

In Figure 2 we show the heat absorption rate versus temperature data for a sample of the Pittsburgh #8 High Volatile-bituminous coal. This coal has much less water. The total weight loss of 3% is almost totally due to water loss. Inspection of Figure 2 shows the existence of a low temperature endotherm starting at 300K. This endotherm persists after the removal of the water and blends smoothly into the exotherm starting about 400K.

Even stronger evidence for the existence of a low temperature, nonwater-related endotherm preceding the exotherm is seen in Figure 3 for the Pocahontas #3 Low Volatile-bituminous coal. For this coal there is no weight loss observed, but a well defined endotherm is seen starting at 300K.

It is our belief that the low-temperature endotherm followed by exothermic behavior is associated with a free-radical polymerization reaction in the coal. Petrakis and Grandy (15) have reported that a substantial number of free radicals are present in coal heated between 375 and 700K. We feel that the 300K to 400K endotherm is associated with free-radical formation. The recombination of the free radicals is sufficiently exothermic that the overall behavior is exothermic above 400K. The overall reaction is rather slow and does not approach completion in the time span of the experiment.

The high temperature endotherm could be due to either the softening of the partially reacted coal and/or to bond-breaking reactions in the unreacted coal. Previous studies (16) have shown that the reaction is reversible as long as the material is kept below 630K. Hydrogen bond-breakage has been postulated (4) as a source of this endotherm. However, additional free-radical formation can not be ruled out. If the coal is pretreated in flowing steam at around 610K it yields more volatile products during steam pyrolysis at high temperatures (17). But if the pretreated coal is exposed to air (O_2) even for a few minutes the steam pyrolysis yield of the coal reduces to levels below that of untreated coal.

The heat absorption curves of the other coals are qualitatively similar to those shown. The major differences between the coals, are due to the difference in water content, the progressive reduction in the magnitude of the exotherm at a given temperature as the rank (carbon content) of the coal increases.

Heat capacity data can be extracted from the heat absorption rate curves using the relation:

$$C_p(T) = \dot{Q}(T)/\dot{T}(T) \qquad 1)$$

where $C_p(T)$ is the heat capacity in $kJkg^{-1}K^{-1}$ at a given temperature and $\dot{T}(T)$ is the actual (determined) heating rate at the same temperature.
In our experiments $\dot{T}(T)$ is nominally 0.1667 K/sec. However, for each experiment the actual heating rate was determined by running the heat absorption rate curve for a sapphire standard under the same exact experimental conditions as those for the sample runs.

The heat capacities were calculated based on the assumption that up to 270K there is no weight loss on heating. The heat capacities above 300K were calculated by extrapolating the heat absorption rate curves which would have been obtained in the absence of heat absorbing or heat releasing reactions. The calculated heat capacities are shown in Figure 4 and are also tabulated in Table 1.

There was no general trend with coal rank observable in the heat capacities. This was not, surprising since the heat capacity was not

separated into contributions due to the organic, inorganic and water components.

At the present time (May 1987) work is still in progress to complete the data for the rest of the Argonne Premium Coal Sample series, to prepare and measure ash heat capacities, and to investigate the effect of accelerated weathering on the heat absorption rates and on the heat capacities.

Table 1. Heat Capacity ($kJkg^{-1}K^{-1}$) of Argonne Premium Coals

Temp(K)	Wyoming Sub-bit	Illinois #6 HV-bit	Blind Canyon HV-bit	Pittsburgh #8 HV-bit	PA-Up.Freeport MV-bit	Pocah. #3 LV-bit
100	0.179	0.325	0.485	0.410	0.396	0.256
125	0.307	0.466	0.660	0.574	0.605	0.762
150	0.503	0.584	.815	0.683	0.667	0.969
175	0.727	0.760	0.902	0.800	0.698	1.137
200	0.973	0.958	1.001	0.956	0.799	1.241
225	1.312	1.251	1.121	1.103	0.882	1.270
250	1.841	1.515	1.159	1.169	0.970	1.333
275	1.771	1.481	1.206	1.228	1.075	1.348
300	1.415	1.277	1.252	1.281	1.156	1.355
325	1.244	1.167	1.219	1.364	1.070	1.390
350	1.307	1.237	1.267	1.409	1.205	1.411
375	1.355	1.270	1.332	1.459	1.265	1.432
400	1.389	1.317	1.351	1.500	1.315	1.453
450	1.463	1.363	1.423	1.573	1.385	1.480
500	1.507	1.422	1.494	1.646	1.450	1.508
550	1.559	1.443	1.538	1.701	1.486	1.522
600	1.576	1.467	1.577	1.756	1.534	1.536
650	1.608	1.511	1.618	1.792	1.548	1.543
700	1.609	1.514	1.650	1.828	1.586	1.550

ACKNOWLEDGEMENT

The coal samples were obtained courtesy of Dr. K.S. Vorres of the Argonne National Laboratory.

REFERENCES

1. W.C. Anderson and J. Roberts., J. Soc. Chem. Ind. Lond. XV11, 1013 (1898).

2. H.D. Glass, Fuel, 39, 253 (1955).

3. N. Berkowitz, Fuel 36, 355 (1957).

4. N.Y. Kirov, and J.N. Stevens, in "Physical Aspects of Coal Carbonization", Univ. of N.S. Wales, Sidney, Australia (1967).

5. O. Mahajan, A. Tomita, P.L. Walker, Jr., Fuel, 55, 63 (1976).

6. N.Y. Kirov, Br. Coal Util. Research Assoc., Mon. Bull., 29, 33 (1965).

7. Internal Report of the Thermodynamics Research Group, Bartlesville, Energy Research Center, DOE, "Thermal Data on Gasifier Streams from Synthane Test" (1973).

8. V.I. Kasatochkin, K. Usenbaev, V.M. Zhadanov, K. Sabyraliev, M. Rasalbaev, and K. Zhumalieva, Dokl. Akad., Nauk, S.S.S.R., 216, 93 (1974).

9. R.P. Tye, A.O. Desjarlais and J.M. Singer, High Temperature - High Pressures, 13, 57 (1981).

10. L.L. Isaacs and W.Y. Wang, "The Specific Heats of Coals and Chars" in the Proceedings of The Governor's Conference on Expanding the Use of Coal in in New York State (M.M. Tress, J.C.Dawson eds.), 379 (1981); W.Y. Wang, Ph.D. Thesis submitted to the Graduate Faculty of Engineering,The City University of New York (1981).

11. E. Melchoir and H. Luther, Fuel 61, 1071 (1983).

12. S.C. Mraw and D.F. Naas-O'Rourke, Science 205,901 (1973).

13. L.L. Isaacs, Preprint of Papers, A.C.S. Div. of Fuel Chem., 29, 234 (1981).

14. R. Ledesma, P. Compo and L.L. Isaacs, in Materials Research Society Symposia Proceedings, Vol. 86, "Fly Ash and Coal Conversion By-Products; Characterization, Utilization and Disposal III," (G.J. McCarty, F.P. Glasser, D.M. Roy, Eds.) (1987).

15. L. Petrakis and D.W. Grandy, Analytical Chem., 50, 303 1978.

16. Wei-Chong Li, Undergraduate Honors Research Report to the Dept. of Chem. Engrg., The City College of CUNY (1984), unpublished.

17. R. Graff and S. Brandes, Journal of Energy and Fuels, 1, 84 (1987).

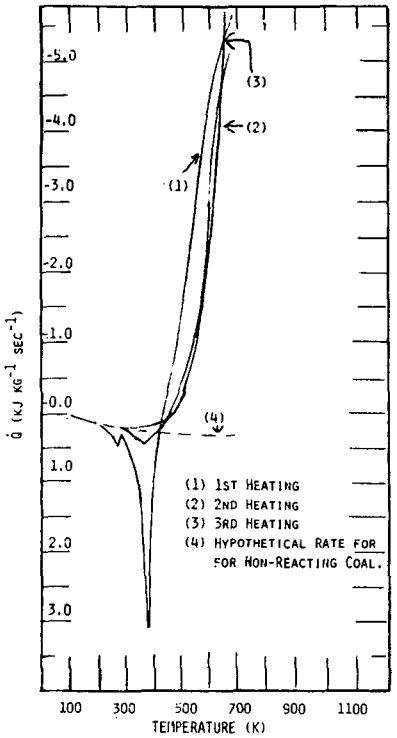

FIGURE 1. WYOMING SUB-BITUMINOUS COAL; HEAT ABSORPTION RATE.

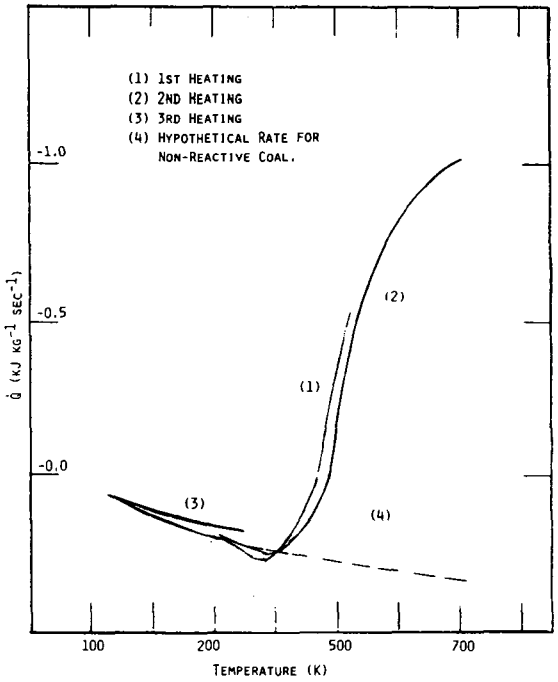

FIGURE 2. PITTSBURGH #8 COAL; HEAT ABSORPTION RATE.

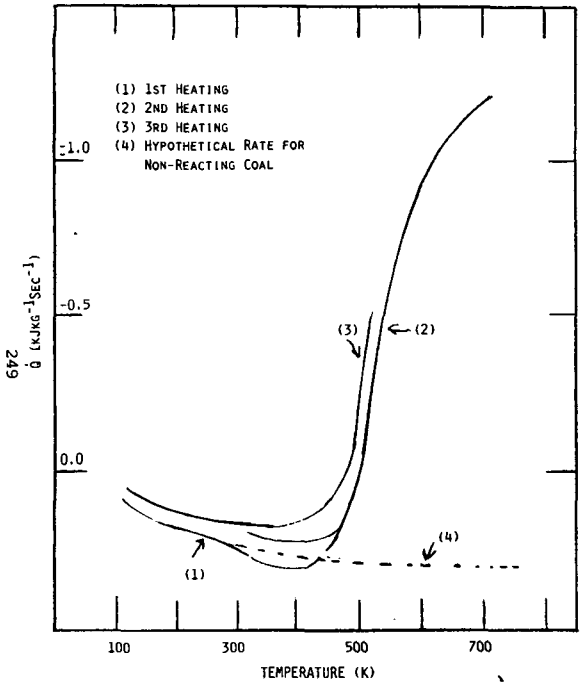

FIGURE 3. POCAHONTAS #3 COAL; HEAT ABSORPTION RATE.

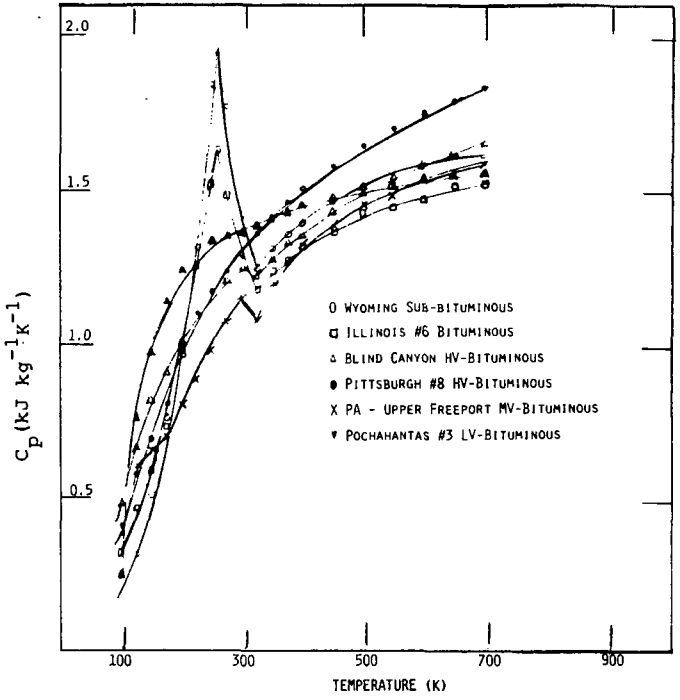

FIGURE 4. HEAT CAPACITY OF ARGONNE PREMIUM COALS.

Spatial Variation of Organic Sulfur in Coal

C. A. Wert, B. H. Tseng, K. C. Hsieh, M. Buckentin and Y. P. Ge
Department of Materials Science and Engineering
and Materials Research Laboratory
University of Illinois at Urbana-Champaign
1304 W. Green Street
Urbana, Illinois 61801

INTRODUCTION

Spatial variation of organic sulfur concentration in coals has been generally known for years. The high resolution of the transmission electron microscope permits that variation to be measured more precisely than is possible by bulk techniques; variations may be measured over distances less than 1 μm.

Measurement of organic sulfur content using the transmission electron microscope requires use of ultra thin films or very fine powders. We typically use foils less than 1 μm thickness or powders ground to a few μm. The organic sulfur content is proportional to the ratio of the count rate for the sulfur Kα line to the count rate for the background radiation measured over some convenient energy interval. The proportionality constant is determined using sulfur standards. The technique is highly reliable for sulfur, as is shown in earlier publications (1-3). The PIXE method for heavier elements also utilizes the background radiation to permit absolute numerical concentrations to be derived.

This paper reports a particular application of the TEM method to determination of the spatial variation of organic sulfur, both within a given maceral and among maceral types. Some of the observations report measurements on powdered specimens, others on foil specimens prepared from bulk coal.

SPATIAL VARIATION

We have reported several measurements of the spatial variation of organic sulfur in coal. We cite two new measurements here. The variation in organic sulfur content of a sporinite maceral embedded in a larger vitrinite maceral in an Illinois #5 coal is shown in Fig. 1. Several features are evident. A considerable variation exists across a maceral, but an even larger variation exists between the two macerals. The sporinite maceral has a much higher concentration of organic sulfur than of the vitrinite. In contrast, resinite commonly has a lower organic sulfur content than vitrinite in a particular coal. This is evident from the data in Fig. 2 for a resinite maceral embedded in vitrinite in a block of Illinois #6.

MEASUREMENTS ON WHOLE COALS

Many measurements have been made of the organic sulfur content of whole coals, both to find the spread in sulfur content and to determine the average organic sulfur content. A number of these coals have been from the Argonne Premium Coal Bank. We show in Fig. 3 the sulfur distribution obtained for seven of these coals. The concentration varies widely for each of the coals. We have not separated these coal into maceral types, so we do not know

the variation by maceral type. We have reported measurements on other bituminous coals separated into maceral fractions, though, and report such an observation in the next section.

Measurements on individual particles of a coal have considerable variation as the data of Fig. 3 show, but the average over a number of independent measurements has been found to be very close to the average organic sulfur content of that coal determined by bulk methods. A comparison made between eight coals measured in the TEM and the reported organic sulfur content measured by ASTM methods independently shows good agreement, Fig. 4.

ORGANIC SULFUR CONCENTRATION FOR SEPARATED MACERALS

Variation in organic sulfur concentration can easily be made for maceral fractions separated by density. We have measured several such fractions separated by Dyrkacz (4,5). Results for an Indiana block coal, a high volatile bituminous (PSOC 106) are shown in Fig. 5. There the organic sulfur concentration is plotted as a function of the density of the separated macerals. Approximate boundaries between exinite, vitrinite and inertinite for this coal are shown in the figure. One sees a smooth variation of organic sulfur concentration with density, rising from the inertinites through the vitrinite, peaking at a density near 1.20 g/cc and falling off toward the lighter fractions. The peak at 1.20 corresponds to the maceral-type sporinite.

We have repeated this measurement for four other coals and find the same pattern, the curve being shifted up or down in accordance with the average organic sulfur content (2). We find, as did Raymond earlier (6), that the average sulfur content of the whole coal is about that of vitrinite.

The purpose of this paper is not to emphasize the average organic sulfur concentration of coal or of separated macerals, but to examine the variation of organic sulfur from particle to particle within a particular maceral type. We show this in two steps.

First, measurement of the organic sulfur concentration of the major maceral groups of the Indiana Block Coal (PSOC 106) shows wide variation. The measurements are shown in Fig. 6. One sees wide variation, especially for the exinite.

Second, measurement has been made of the variation of organic sulfur concentration for each of the separated density fractions plotted in Fig. 3. Three of the measurements are shown in Fig. 7 one for each of the major maceral groups. The range of sulfur concentration for the inertinite and vitrinite macerals of density 1.42 g/cc and 1.30 g/cc is again small. But for the fraction at 1.18 g/cc (sporinite) the range is still enormous. Is this a result of maceral impurity, or do pure macerals of the exinites have an intrinsic variation of sulfur content which is very broad?

To make sure that this pattern was not peculiar to coals separated by this gravity-centrifuge process, we have made measurements in situ for 4 macerals of an Illinois #5 coal (7). Those measurements are plotted in Fig. 8, where they are compared to measurements on separated macerals of an Illinois #5 coal. The agreement is satisfactory.

DISTRIBUTION OF ORGANIC SULFUR IN FINELY SEPARATED MACERALS

A laboratory for separating coals into submaceral types by the density gradient method has been established by Professor Crelling at SIU. By pushing the techniques of Dyrkacz to the extreme, he can prepare powdered macerals of even higher purity. He has supplied us with specimens from a bituminous coal #SIU 647 J, an Indiana paper coal. We have measured the organic sulfur content of four of those specimens and show the distributions in Fig. 9.

The organic sulfur content of specimen #1, a cutinite, is a narrow distribution with an average value of about 0.45 wt%, Fig. 9a. The distribution is a single mode. That of specimen #2, also a cutinite with a somewhat lower density, is also a single mode except for 4 isolated points at a much higher organic sulfur concentration, Fig. 9b. Including all points, the average organic sulfur concentration is 0.57 wt%, neglecting the 4 highest points it is about 0.49. It is possible that specimen #1 has a few macerals of another subtype with a higher organic sulfur concentration.

That same trend continues for maceral type #3, a sporinite with a specific gravity about 1.16. One hundred measurements were made for this coal, yielding a bimodal distribution shown in Fig. 9c. It would appear that two maceral subtypes may be present, one with an organic sulfur content near 0.4 wt%, the other near 1.3 wt%. This same biomodal distribution is shown for the density fraction near 1.21, near the edge of the vitrinites, Fig. 9d. A maceral type with organic sulfur content near 0.40 must again be mixed with a maceral with organic sulfur content slightly above 1.0.

These measurements seem to show that macerals separated on a density basis may not be "pure". Thus the broad ranges of data in Figs. 4 and 5 may demonstrate that macerals separated by density techniques may contain two or more submaceral fractions. If one considers the data of Figs. 9c and 9d, the values for the individual modes among this bimodal distribution show a variation of not more than ±20%, a value not much different from the variations seen in Fig. 1 for the in-situ macerals, which are assuredly a more pure type, at least locally.

Chlorine Distribution in Coal

The Indiana bituminous coal, PSOC 106, also contains chlorine. We have measured the spatial variation of chlorine in the separated macerals; measurements are shown in Fig. 10. The average chlorine content of this coal is relatively small, about 0.35 wt%. In vitrinite and inertinite the range is relatively small, from about 0.15 to about 0.55 wt%. For the exinites again, the chlorine content is much larger on the average and the spread is much higher, nearly a factor of 10. We have not measured the chlorine distribution in the macerals separated on a finer scale, but it would be easily feasible.

Organic Iron in Coal

We occasionally observe x-ray lines for iron in regions of the foil in which these are not observable precipitates, nor x-ray lines of any other element. We have concluded that these x-rays must show the presence of organic iron. An example is shown for Illinois #5 coal in Fig. 11. The quantity is quite small, less than 0.1 wt%. No variation among the three

major maceral groups was observed. Of course, one always worries that fine oxide particles may be present; but they must be less than perhaps 3 nm in size or we could detect their presence.

SUMMARY

The TEM method for measuring organic sulfur concentration is most valuable when its fine scale spatial resolution can be utilized. We have demonstrated that the variation of organic sulfur is about ±10% of the average when measured over distances separated by 1 m. The technique also has value in showing the organic sulfur variation in minute particles of separated macerals. Apparently, it is very difficult using density techniques to obtain pure maceral types.

Acknowledgement: We acknowledge support of the Division of Materials Research, DOE, under contract DE-AC02-76-ER1198. We thank Professor Crelling, SIU, for specimen materials. Support for one of us (M. Buckentin) also came from the State of Illinois through the Center for Research on Sulfur in Coal.

REFERENCES

1. Hsieh, K. C. and Wert, C. A., Fuel, 64, 255-262 (1985).
2. Tseng, B. H., Buckentin, M., Hsieh, K. C., Wert, C. A. and Dyrkacz, G. R., Fuel, 65, 385-390 (1986).
3. Hsieh, K. C. and Wert, C. A., Paper in "Mineralogy-Applications to the Minerals Industry", Ed. D. M. Hausen and O. C. Kopp, The Metallurgical Society, New York, NY, 21-30 (1985).
4. Dyrkacz, G. R. and Horowitz, E. P., Fuel, 61, 3 (1982).
5. Dyrkacz, G. R., Bloomquist, C.A.A. and Ruscic, L., Fuel, 63, 1166 (1984).
6. Raymond, R. Jr., Am. Chem. Soc. Symp. Series, 205, 19 (1982).
7. Buckentin, M., M.S. Thesis, University of Illinois at U.C. (1985).

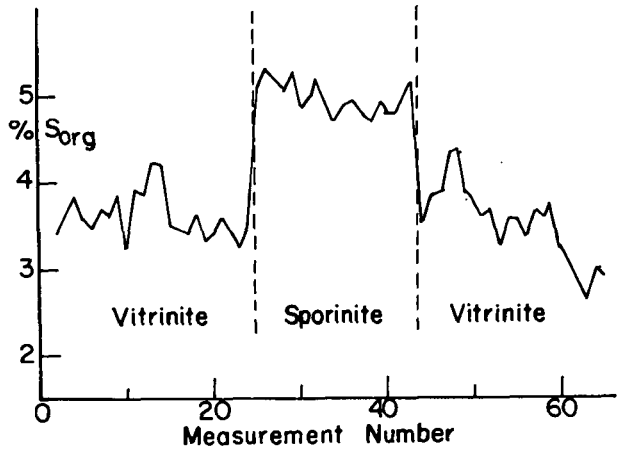

Fig. 1. Organic sulfur trace across a sporinite maceral embedded in vitrinite. Illinois #5.

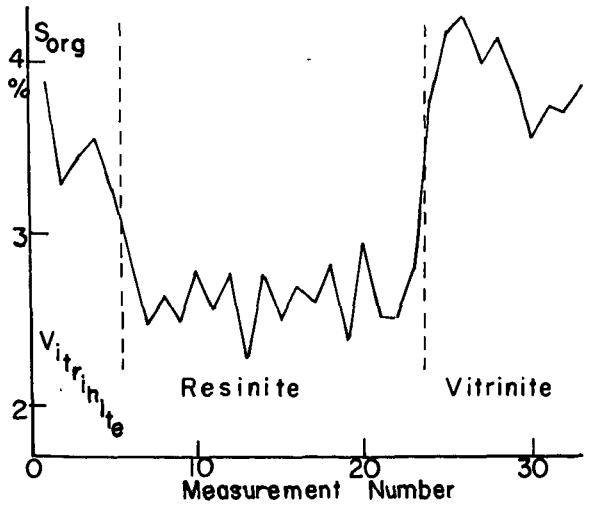

Fig. 2. Organic sulfur trace across a resinite maceral embedded in vitrinite. Illinois #6.

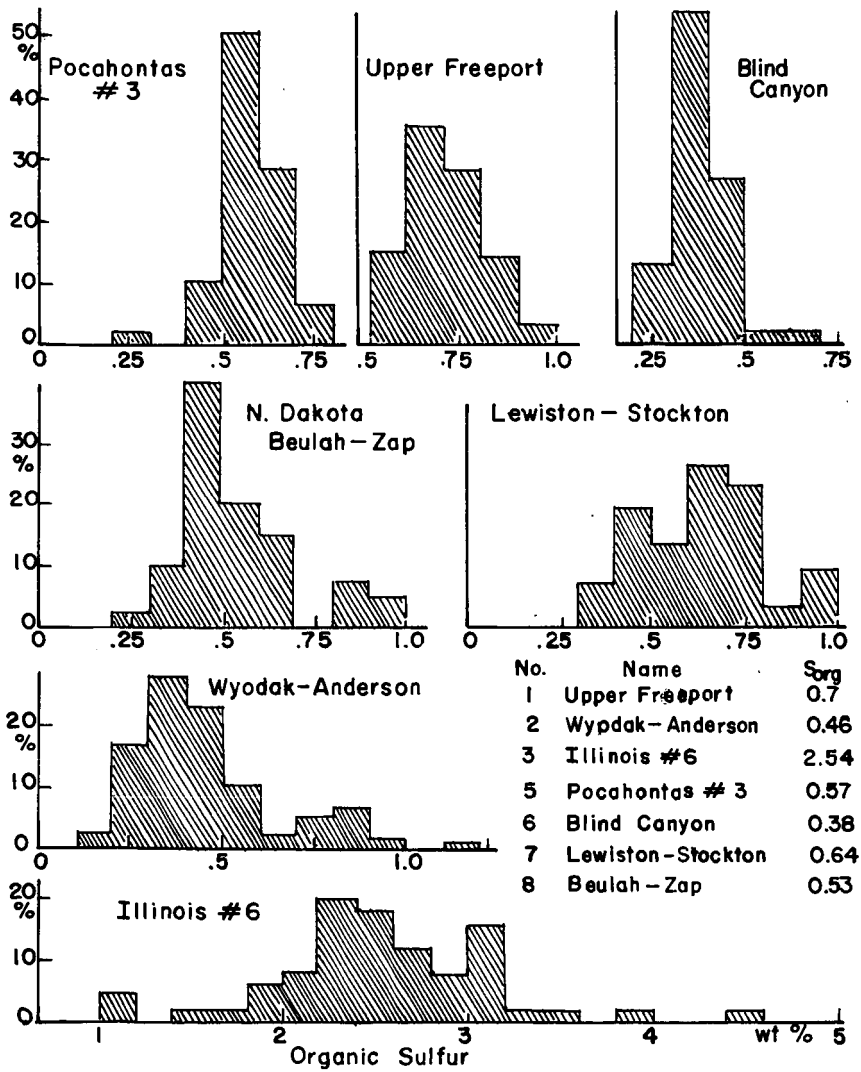

Fig. 3. Distribution of organic sulfur in seven whole coals from the Premium Coal Bank. The inset Table gives the average organic sulfur concentration for each coal.

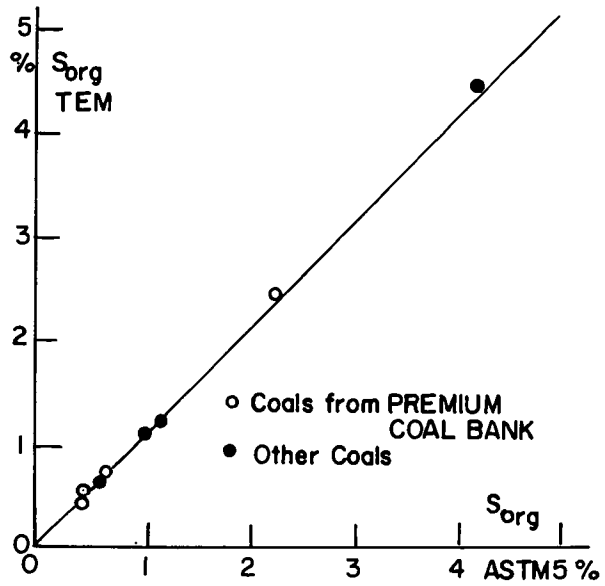

Fig. 4. Comparison of organic sulfur concentration measured by the TEM method and by the ASTM method.

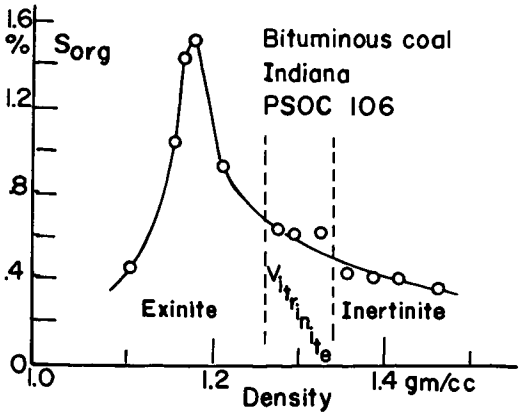

Fig. 5. Variation of organic sulfur for macerals separated by density. Indiana Block coal.

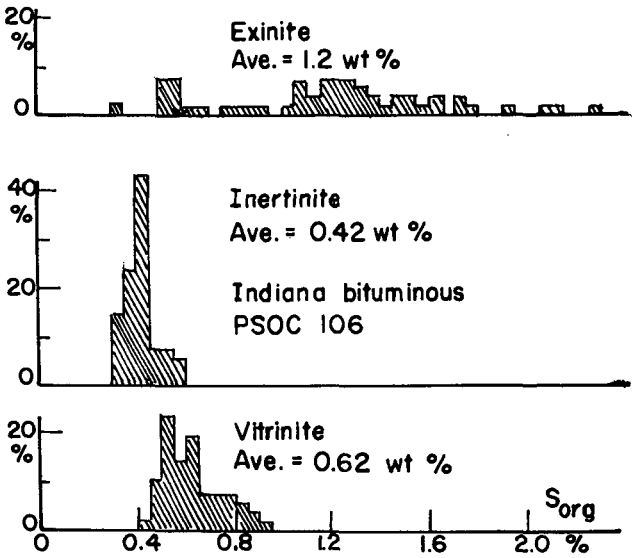

Fig. 6. Distribution of organic sulfur for the major maceral types.

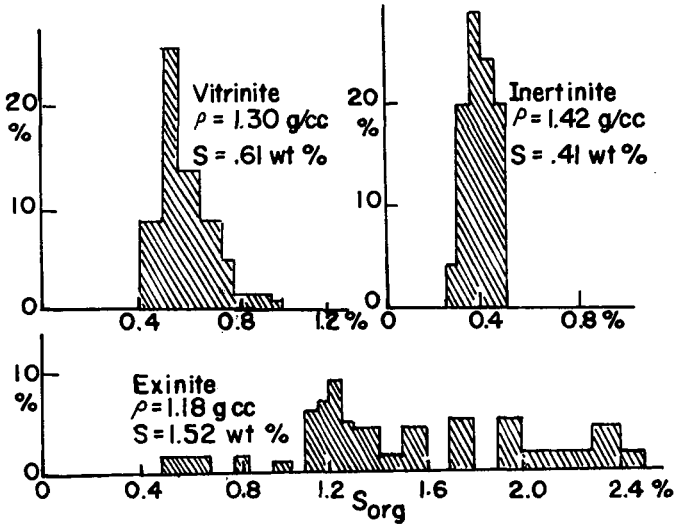

Fig. 7. Distribution of organic sulfur for 3 specific density splits, see Ref. 2 for distribution of other splits.

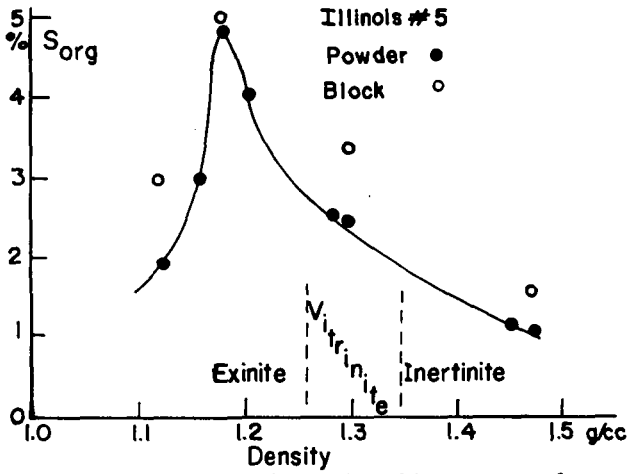

Fig. 8. Comparison of organic sulfur content of separated and in situ macerals.

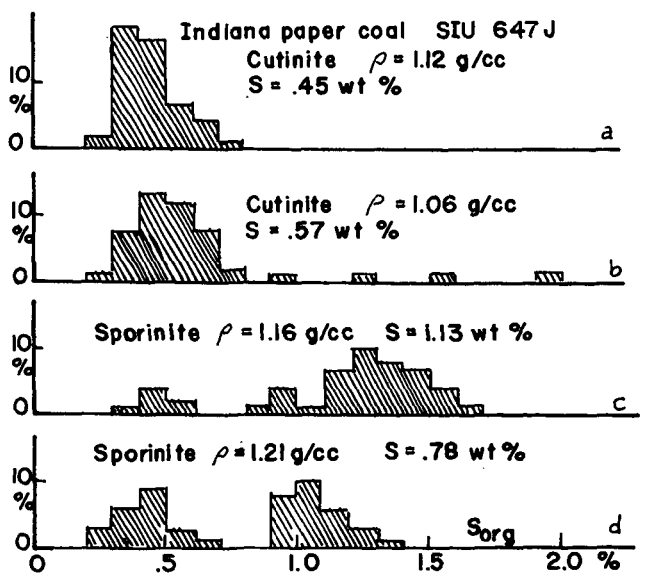

Fig. 9. Distribution of organic sulfur in fine density splits of an exinite.

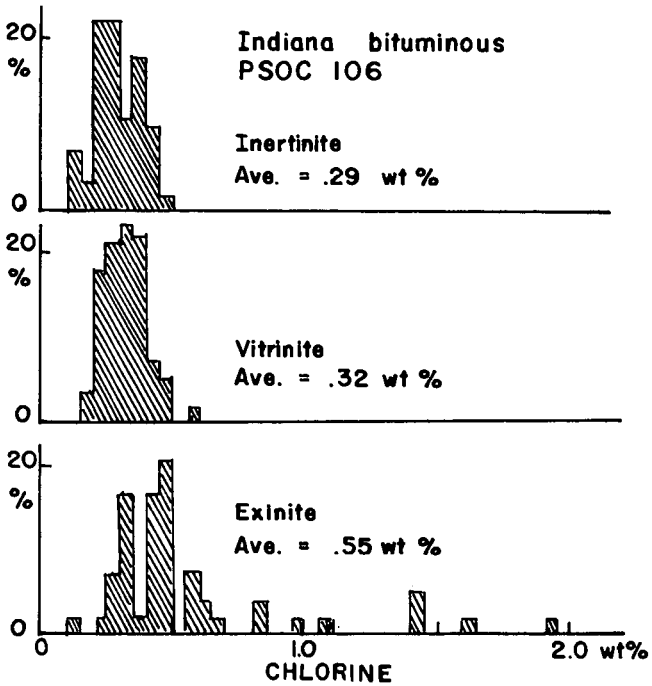

Fig. 10. Distribution of chlorine content of a bituminous coal as a function of maceral type.

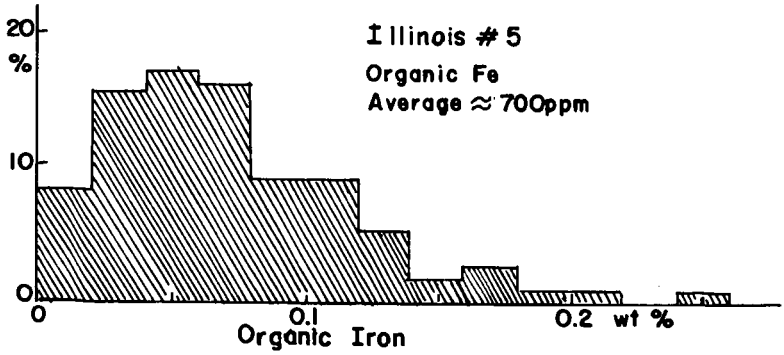

Fig. 11. Distribution of organic iron in a specimen of Illinois #5.

AN ISOTOPE DILUTION STUDY OF EXCHANGEABLE OXYGEN IN PREMIUM COAL SAMPLES

Dennis Finseth
Pittsburgh Energy Technology Center
P.O. Box 10940
Pittsburgh, PA 15236

The analysis of the moisture content of coals has been the subject of a number of extensive discussions (1-3). Interest in the determination of water in coal is a result of both its importance in commerce and its influence on the elemental analysis of the organic portion of the coal. Although simple weight loss methods, such as ASTM 3173, are the accepted methods for the analysis of moisture in coal, it is well documented that these methods are not without error, especially in low-rank coals. A question of importance is, How much of the water of combustion determined by classical combustion analysis of the coal was present in the "dry" coal as water and is not a combustion product? This water, if present in "dry" coal, can introduce a significant error into the organic elemental analysis. For example, 1% water present in a dry Illinois #6 coal and mistakenly identified as a product of combustion would introduce an error of ~3% in the hydrogen analysis and ~10% in the oxygen analysis. The 3% error in the hydrogen analysis translates into an error of 3 H/100 C for the Illinois No. 6 coal.

Our particular concern regarding the accurate determination of water stems from an interest in the chemistry of hydrogen during direct coal liquefaction. In such systems the change in organic hydrogen across a reactor will often be in the range of 5 H/100 C. If errors due to the unknown amount of moisture in coal are $\pm$3 H/100 C, a problem exists. If we cannot have confidence in our ability to determine the change in organic elemental composition across a reactor, we cannot, with confidence, discuss the chemistry occurring in that reactor.

The investigation of coal structure can also be complicated by inadequate analysis of the water in the coal. Drying procedures for moisture determination may cause substantial structural changes and, if done in the presence of oxygen, may also induce significant oxidation. The problem of structural collapse on drying is more acute for studies of lower rank coals. Study of the dependence of coal structure on moisture content would be aided by improved methods to measure the nature and amount of water in whole coals.

A difficulty with improving the ability to quantitate water in coal is that truly independent methods do not always exist. The "true" value of any analytical parameter is always easier to determine if totally independent

---

Reference in this report to any specific commercial product, process, or service is to facilitate understanding and does not necessarily imply its endorsement or favoring by the United States Department of Energy.

methods exist to determine that parameter. This paper describes the possibility of using a simple isotope dilution technique to determine the water content of coal and presents a comparison of these isotope dilution measurements with classical results for the set of Argonne coals from the premium coal sample program (4).

Isotope dilution is a widely used analytical method and has been applied to the analysis of water in matrices as diverse as chicken fat (4), living humans (5), and coal (6). Virtually all of these applications involved the use of deuterium as the diluted isotope. This poses some problems if the sample contains a significant amount of exchangeable organic hydrogen and one is interested in discriminating exchangeable organic hydrogen from water. This is a potential problem in the coal system. To avoid this potential problem ^{18}O was used as the diluted isotope in this work.

Experimental

The isotope dilution experiment, as applied in this study, involves equilibration of a fixed amount of labeled water with a known amount of coal. If it can be established that complete equilibration has been achieved and if proper allowance is made for isotopic impurities and contributions from the apparatus, the isotope ratio of the final equilibrated system directly measures the exchangeable isotope reservoir in the coal. Further work can then be directed to determining what species compose the exchangeable oxygen reservoir.

The equilibration of the coal with labeled water is accomplished by placing a weighed amount of coal (20-300 mg) in a thin-walled Pyrex tube, adding 5 μL of $H_2{}^{18}O$, and using a torch to seal the equilibration tube. The premium coals used were the 100-mesh samples, and all equilibration tubes were filled and sealed within 15 minutes of opening the ampoule. The $H_2{}^{18}O$ was 90% enriched and was obtained from Mound Laboratories. Before sealing, a small amount of dry CO_2(g) is added to each equilibration tube as a probe molecule to facilitate mass spectrometric analysis of the isotope ratio. Before analysis, the sealed tubes are equilibrated at 100°C for 16 hours. Measurement of the equilibration rate of coal samples using this experimental approach established that at 100°C, 16 hours was sufficient to guarantee complete equilibration. The isotope ratio measurement on the final system was done by measuring the relative abundances of the isotopic CO_2 species ($C^{16}O_2$, $C^{16}O^{18}O$, and $C^{18}O_2$) using a CEC 103 mass spectrometer. Stable isotope geochemists routinely use CO_2 to measure the oxygen isotopic composition of water samples (7). Distilled water was used for calibration.

Results and Discussion

Determination of the size of the exchangeable oxygen reservoir in the premium coals was accomplished by plotting the observed $^{16}O/^{18}O$ isotope ratio against the sample size. Since the amounts of labeled water, CO_2, and any exchangeable oxygen associated with the sample vessel are held constant, the change in isotope ratio with sample size should be a function of only the size of the exchangeable oxygen reservoir in the coal. The isotope dilution data obtained for the eight currently available premium coals are

presented in Figure 1. The slopes of the plots shown in Figure 1 are simply proportional to the size of the exchangeable oxygen reservoir in each of the premium coals.

Conversion of the raw data to "water" content and comparison of these results with the best currently available moisture analyses on the premium coals is shown in Table 1. The assumption that is made is that the exchangeable oxygen reservoir is all present as water. These results indicate good agreement between the isotope dilution measurement and the classical moisture measurements on this set of samples. There appears to be a small systematic positive difference between the isotope dilution and the weight loss results. This difference is believed to be outside our experimental error. Before the set of premium coals was analyzed, a number of ground coals being used in process-related studies had been analyzed by this method. For these samples, which had not been handled with the care lavished on the premium samples, discrepancies between the isotope dilution measurements and the classical weight loss analyses were significantly greater. This is illustrated by the last two entries in Table 1. At this point in the development of the isotope dilution technique, a definitive explanation of the larger discrepancies between isotope dilution and weight loss results for the non-premium samples would be premature. A potential source of these differences could be mild oxidation and structural changes in the non-premium samples, resulting in water being more strongly bound and thus incompletely measured in the weight loss analyses. Further work is needed to clarify the reasons for these differences.

The data presented indicate that an isotope dilution approach is capable of reproducibly measuring the size of an exchangeable oxygen reservoir in coal. To determine what oxygen is included in the exchangeable oxygen reservoir, the size of the reservoir was determined for a variety of model systems, including clay minerals, calcite, gypsum, inorganic hydrates, phenolics, carboxylic acids, carboxylate salts, carboxylate salt hydrates, and accepted geochemical standards. The discussion of all these results exceeds the scope of this preprint; however, the preliminary conclusion is that under the conditions described in this work, the exchangeable oxygen reservoir includes most strongly bound hydrate water in both organic and inorganic systems and does not include any organic oxygen in compounds that are stable under the equilibration conditions.

Conclusions

Equilibrium isotope exchange for the investigation of oxygen in coal appears to have promise as a tool for determination of the "true" water content of coals. Its applicability appears to extend across the rank scale. The technique measures the size of the exchangeable oxygen reservoir under very mild conditions without removing the water from the coal, thus avoiding structural changes that could complicate the analysis. A more comprehensive discussion of the results on a variety of systems is currently being prepared. Preliminary results indicate that it may provide a simple, reliable, and totally independent method for the measurement of coal water content. Comparison of this method with classical weight loss methods may provide a significant improvement in our ability to measure the "true" water content of coal and thus the "true" organic hydrogen and oxygen contents as well.

Acknowledgments

The author is indebted to Anthony Logar and Joseph Malli for their valuable assistance in obtaining the mass spectrometric results.

References

1. Hoeppner, J.J., Fowkes, W.W., and McMurtrie, R., Bureau of Mines RI, No. 5215, 1956.

2. Selvig, W.A., and Ode, W.H., Bureau of Mines RI, No. 4968, 1953.

3. Stansfield, E., and Gilbart, K.C., American Institute of Mining and Metallurgical Engineers, Preprint, 19 pp., Feb. 1932.

4. Vorres, K.S., and Janikowski, S.K., Am. Chem. Soc. Fuel Div. Preprints, 1987, 32(1), 492.

5. Ouhayoun, J., and Penard, R., Ann. Biol. Anim. Biochemie Biophys., 1970, 10(4), 621-630.

6. Benesath, F.A., Bradlon, H.L., and Field, F.H., Biomedical Mass Spectrometry, 1983, 10(11), 596-600.

7. Bornhop, D.J., Manahan, S.E., and Farrier, D.S., Anal. Lett. 1980, 13(A12), 1041-1061.

8. Epstein, S., and Mayeda, T., Geochim. Cosmochim. Acta, 1953, 4, 213-224.

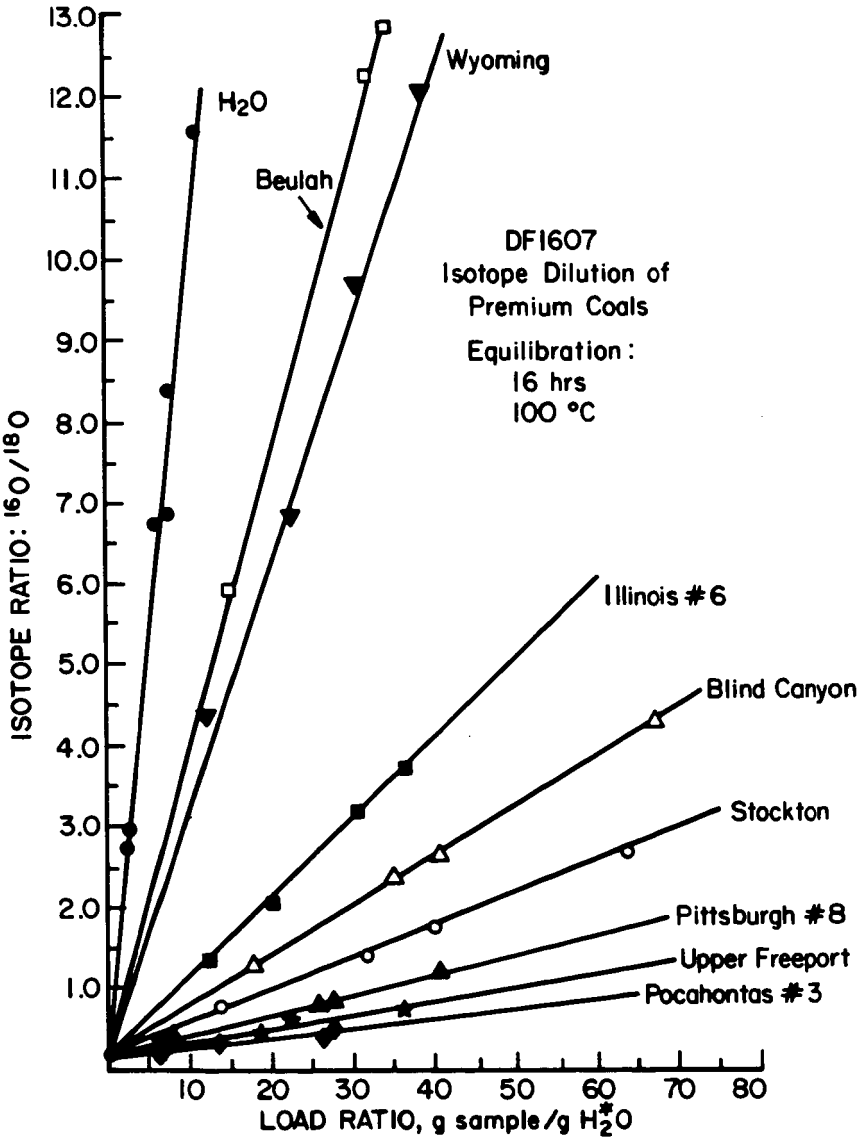

Figure 1. Isotope Dilution Analysis of Premium Coals.

NO./13,806

TABLE 1.
"MOISTURE" IN COALS
(Exchangeable Oxygen Reservoir)

Coal	Isotope Dilution Analysis (Wt%)	Standard Method (Wt%)*	
Beulah-Zap	34.4	32.8	*"Premium" Samples*
Wyodak	30.0	28.84	
Illinois #6	9.6	8.8	
Blind Canyon	5.9	4.7	
Stockton	3.9	2.6	
Pittsburgh #8	2.5	1.8	
Upper Freeport	1.5	0.83	
Pocahontas	1.0	0.66	
Clovis Point	27.6	20.4	*"Non-Premium" Samples*
River King	9.8	7.7	

*For Premium Samples, Data Obtained from Argonne National Lab.
Non-Premium Samples Were Analyzed by ASTM 3173.

NO./14,292

THE APPLICATION OF INVERSE GAS CHROMATOGRAPHY TO COALS AND OXIDIZED COALS

P. H. Neill and R. E. Winans

Chemistry Division, Argonne National Laboratory,
9700 South Cass Avenue, Argonne Illinois 60439

INTRODUCTION

In two previous papers (1,2) we reported preliminary results concerning the application of Inverse Gas Chromatography (IGC) to coals and air oxidized coals. In this paper we will report on the reproducibility of the IGC technique, its application to other Argonne Premium Coals, and compare the results with those obtained with pyrolysis mass spectroscopy. The objective of this study is to provide detailed information concerning the possible non-oxidative changes in the chemical and physical structures of the Argonne Premium Coal Samples (APCS) during long term storage. Inverse gas chromatography is just one of the techniques being utilized in meeting this objective. It is known that subtle changes in coal structure can effect changes in plasticity when a coal is heated. However, the techniques traditionally used to measure plasticity do not yield information which can be used to understand the underlying chemical and physical changes in the coal structure.

Inverse gas chromatography, a technique widely used for studying polymers, is being used to study the transitions that the APCS undergo upon heating. Inverse gas chromatography has been applied to polymers to measure the glass transition temperature, the degree of crystallinity, melting point, thermodynamics of solution, and chemical composition (3-5). Inverse gas chromatography has also been applied to coals in the temperature region less than 85°C to determine the enthalpy of sorption of methane and oxygen on dried coals (6). For methane the enthalpies of sorption ranged from 4.4 to 0.9 Kcal/mole for Czechoslovakian coals between 90.7 and 83.3 percent carbon on a dry ash free basis.

In contrast to classical gas chromatography, inverse chromatography probes the stationary phase, a coal, by determining the retention time of known compounds on it. This transposition of known and unknown in the gas chromatography experiment gives rise to the term "inverse chromatography". Two types of information are provided by the IGC experiment. The slope of a plot of the log of the retention time versus the inverse of the temperature is proportional to the enthalpy of retention for the probe molecule on the coal. This is a thermodynamic measure of strength of the interaction between the probe molecule and the coal. The temperatures at which major changes in slope are observed represent the points where the mechanism of retention has changed significantly, indicating that a significant change in the chemical or physical structure of the coal has occurred.

EXPERIMENTAL

The elemental compositions of the coals used in this study are shown in Table 1. The preparation of the Argonne Premium Coal Samples has been

described by K. Vorres and S. Janikowski (7). The -100 mesh samples were thoroughly mixed with non-porous glass beads (-400 to -60 mesh) to give a mixture approximately 10% coal on a weight basis. A blank experiment utilizing only glass beads yielded an effective slope of 0, indicating that adsorption of methane on the non-porous glass beads was minimal. The six foot by 1/4 inch glass columns were packed with ca. 30 grams of the mixture. All transfers and weighings were performed in a glove box under nitrogen atmosphere.

A diagram of the experimental apparatus is provided in Figure 1. The gas chromatography equipped with a single flame ionization detector could be controlled from an external computer. The injector was a computer controlled Carle gas sampling valve in a thermostated box. Flow control was provided by two flow controllers one with a 0-5 ml/min. element and the second with a 0-60 ml/min. element. The second controller was connected to the injector through a computer controlled solenoid. The experiment was controlled and the data analyzed by an IBM PC computer.

A flow diagram of the IGC experiment is shown in Figure 2. The experiment begins with an initial equilibration period of at least 24 hours, during which the flow rate of the helium carrier gas was cycled between it's chromatographic rate of 1 ml/min. and the higher rate (30 ml/min.). The higher flow rate was used to speed the removal of volatile matter from the column after each temperature increment. The probe, 10% methane in argon, was injected onto the column and it's retention time at the specific temperature determined. In the experiment duplicate chromatograms were obtained in four degree increments between 50 and 450°C. After each temperature increment the baseline signal was determined and compared to the baseline at the previous temperature. If it had increased more than 10% the solenoid isolating the second flow controller was opened increasing the rate at which the coal volatile matter was purged from the column. Even with increasing the flow rate, an IGC experiment could take up to a month to perform. The injector was held at 100°C and the detector at 400°C.

The Pyrolysis Mass Spectrometry (PyMS) technique has been described previously (8). Briefly the coal sample was placed on a platinum 5% rhodium mesh on the end of a probe as a slurry. After the solvent had evaporated the probe was inserted into the mass spectrometer and positioned within 5 mm. of the source. The probe which had been previously calibrated with an infrared thermometer was computer controlled to give a temperature profile beginning at 100°C and increasing at 50°C/min. to 800°C. This technique results in the relatively slow vacuum pyrolysis of the coal sample.

RESULTS AND DISCUSSION

The results from the IGC experiment on Upper Freeport Coal (APCS #1) are presented in Figure 3. The plot of the Log of the retention time versus the inverse of the temperature in degrees Kelvin is divided into three general regions based on the slope of the curve. The first major transition is bounded by the significant change in slope normally found between 100 and 120°C. We believe that this transition is caused by the loss of water from the pore structure of the coal. This change in slope indicates that the way the methane probe molecule interacts with the wet coal, or the mechanism of

retention, is different enough from that of the dry coal to produce the observed deviation in curve. The intermediate temperature region (ca. 115°C to ca. 350°C) is a long region in which a relatively constant slope is observed. This indicates that the mechanism of retention for the methane probe molecule does not change significantly. However, above 200°C a large number of small transitions are encountered which do not result in a major deviation from the prevailing slope. We believe that these are due to the loss of volatile matter occluded within the coal structure. The loss of relatively minor amounts of material should result in small deviations in retention time, which are observed but would not be expected to modify the overall mechanism of retention significantly. In region 3 (>350°C) there is a marked change in the slope indicating a major change in the mechanism by which the methane probe is retained by the coal in the IGC experiment. This corresponds to the temperature region in which Giesler Plastimeter results indicate that the coal is in the fluid state.

The reproducibility of the IGC technique is shown in Figure 4, where the results from duplicate experiments on Illinois No. 6 (APCS #3) are presented. As can easily be seen, the results from the two experiments are very similar. Not only do the major transitions occur at the same temperatures, but many of the minor transitions are reproduced as well. The two curves appear to be most dissimilar in the low temperature region. This is where we believe that changes in retention are dominated by water in the coal. Thus the results should be most sensitive to variation in sample handling. The minor transitions in the intermediate temperature region (120-300°C) are reproduced very accurately. Both curves show minor transitions around 190, 230 and 285°C. The temperature of the major transition appears to be similar for the two experiments. An exact assignment of the temperature of this transition in experiment two is impossible due to a problem with the data system, which resulted in the loss of data between 300 and 326°C. In the higher temperature region (>326) reproducible transitions occurred near 380 and 420°C. The enthalpies of sorption were very similar and well within the calculated precision of the data as can be seen in Table 2.

The variation in the temperature at which the major transition peak occurs for each of the coals studied are plotted versus percent carbon in Figure 5. This peak marks the start of the high temperature region in each of the experiments. This transition can be seen in Figure 3 just above 350°C for Upper Freeport coal, in Figure 4, just below 326°C for Illinois No. 6, and at 370°C in Pocahontas coal in Figure 7. The limited number of samples studied precludes stating that a correlation exists, however one is safe in assuming that a trend is indicated.

The enthalpy of sorption for each of the coals studied plotted versus carbon content is presented in Figure 6. The data was derived from the regression of the IGC data above the temperature of the major transition. As with the temperature of the major transition a trend is definitely indicated. However, several of the enthalpies are unrealistically high. This is probably due to changes in column void volume in this region which would significantly affect the calculated values.

Figure 7 compares the results from the IGC experiment with those obtained from PyMS for Pocahontas coal. Although the pyrolysis was started at 100°C, the total ion current signal below 208°C was dominated by an internal standard

added to the coal. Other experiments indicate that very little material of molecular mass >31 is released below this temperature. Above this temperature minor transitions in the IGC curve become more numerous. This indicates that these minor transitions in the IGC are indicative of the loss of volatile material. The maximum in the Total Ion Current (TIC) is observed at a temperature very close to that of the major transition in the IGC experiment. At temperatures above the major transition the TIC curve indicates that the release of volatile material begins to decrease significantly.

Overall, IGC appears to be a very reproducible method for following the chemical and physical changes that occur when coals are heated in an inert atmosphere. Differences in both the temperature of the transitions and enthalpies of sorption can be observed for coals of various rank. Pyrolysis Mass Spectrometry results indicate that the minor transitions observed in the intermediate temperature region are due to the loss of volatile matter from the coal.

ACKNOWLEDGMENTS

The coal analyses were provided by I. Fox and P. C. Lindahl of the Argonne Analytical Chemistry Laboratory. The Bruceton coal was provided by J. W. Larsen of the Dept. of Chemistry, Lehigh University. Reference 6 was translated from Czechoslovakian by Petr Vanysek of the Dept. of Chemistry, Northern Illinois University.

This work was performed under the auspices of the Office of Basic Energy Sciences, Division of Chemical Sciences, U. S. Department of Energy, under contract number W-31-109-ENG-38.

REFERENCES

1. R. E. Winans, J. P. Goodman, P. H. Neill, and R. L. McBeth, ACS Fuel Chemistry Division Preprints, 30(4), 427, (1985).

2. P. H. Neill and R. E. Winans, ACS Fuel Chemistry Division Preprints, 31(1), 25, (1986).

3. S. G. Gilbert, in "Advances in Chromatography", Vol. 23, J. C. Giddings, E. Grushka, J. Cazas, and P. R. Brown, Eds., Marcel Dekker, New York, (1984).

4. V. G. Berezkin, V. R. Alishoyev, and I. B. Nemirovskaya, J. Chromatography Library, 10, 197, (1977).

5. J. E. Guillet, in "New Developments in Gas Chromatography", J. H. Purnel, Ed., Wiley, New York, (1973).

6. B. Taraba and K. Cap, Uhli, 33(7-8), 278, (1985).

7. K. Vorres and S. Janikowski, ACS Fuel Chemistry Division Preprints, 32(1), 492, (1987).

8. R. E. Winans, R. G. Scott, P. H. Neill, G. R. Dyrkacz, and R. Hayatsu, Fuel Processing Technology, 12, 77, (1986).

TABLE 1. Composition of Coals Studied.

Coal	% C (dmmf)	Empirical Formula
Upper Freeport mv Bituminous (APCS #1)	87.1	$C_{100}H_{75}N_{1.5}S_{0.3}O_{2.6}$
Illinois No. 6 hvC Bituminous (APCS #3)	77.8	$C_{100}H_{88}N_{0.6}S_{0.5}O_{3.7}$
Pocahontas lv Bituminous (APCS #5)	89.6	$C_{100}H_{63}N_{1.2}S_{0.2}O_{3.3}$
Bruceton hvA Bituminous	82.3	$C_{100}H_{78}N_{1.6}S_{0.3}O_{9.3}$

TABLE 2. Enthalpies of Sorption in the Three Temperature Regions.

Coal	50-100°C Very Low Temperature Region†	100-300°C Low Temperature Region†	350-400°C High Temperature Region†
Upper Freeport mv	2.9 ± 0.5	1.93 ± .07	12.5 ± 0.4
Pocahontas lv	--- *	2.01 ± .04	14.8 ± 0.4
Bruceton hvA	1.6 ± 0.2	1.96 ± .04	7.7 ± 0.4
Illinois No. 6 (1)	4.0 ± 0.3	2.00 ± .16	4.9 ± 0.5
Illinois No. 6 (2)	4.3 ± 0.3	1.90 ± .15	5.1 ± 0.5

†Temperatures indicated are approximate, the actual boundaries were determined by the temperature of the actual transitions in the specific experiment.

*Pocahontas coal exhibited a negative slope in this region for some unknown reason.

Figure 1. Experimental apparatus for inverse gas chromatography experiment.

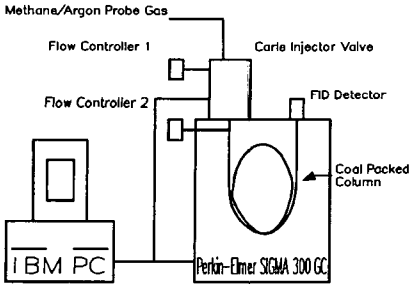

Figure 2. Flow Diagram of inverse gas chromatography Experiment.

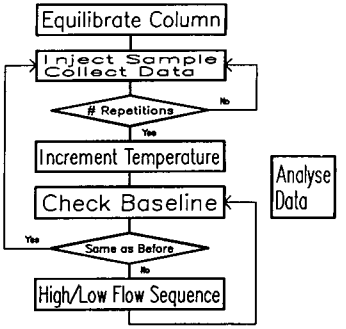

Figure 3. Plot of the log of the retention volume versus the inverse of temperature for Upper Freeport coal (APCS No. 1).

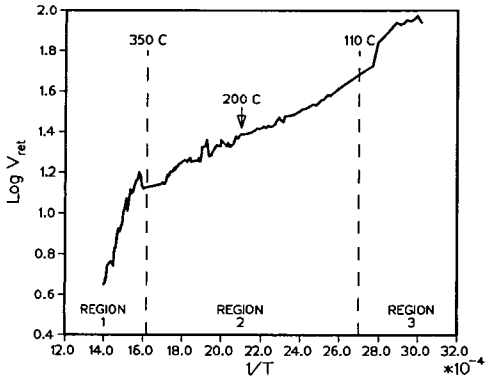

Figure 4. Comparison of IGC experiments on Illinois No. 6 coal (APCS No. 3).

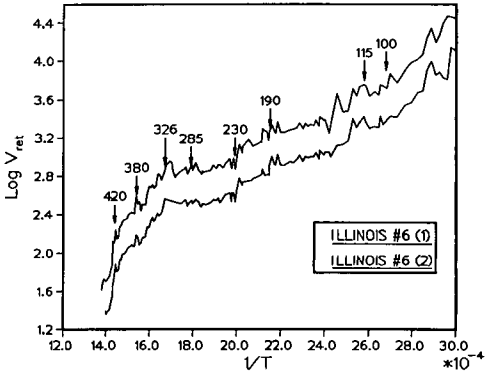

Figure 5. Variation in the temperature for the start of the major transition versus carbon content (dmmf) for APCS#3, Bruceton, APCS#1, and APCS#5 coals.

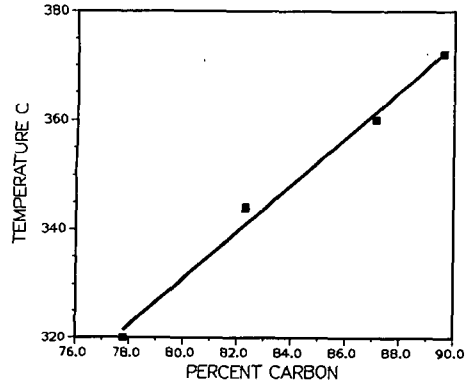

Figure 6. Variation in the enthalpy for the high temperature region (350--450 C) versus carbon content (dmmf) for APCS#3, Bruceton, APCS#1, and APCS#5 coals.

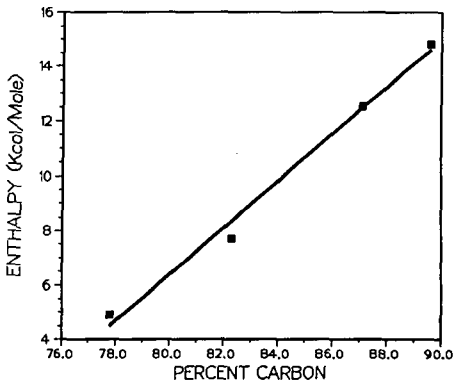

Figure 7. Comparison of IGC and pyrolysis high resolution mass spectrometry data for Pocahontas lv bituminous coal (APCS No. 5).

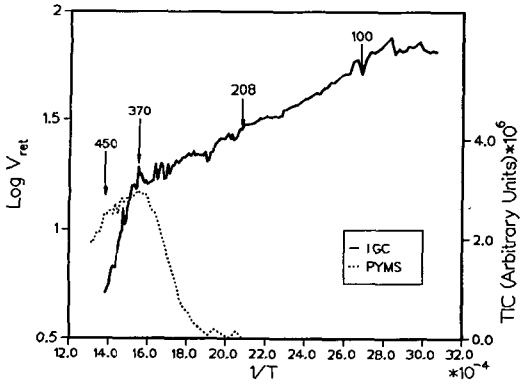

^{13}C NMR Structural Determination of the Coals in the Premium Coal Sample Bank

M. S. Solum[a], R. J. Pugmire[b], and D. M. Grant[a]

Departments of Chemistry[a] and Fuels Engineering[b]
University of Utah
Salt Lake City, UT 84112

Introduction

Solid state ^{13}C cross polarization (CP) magic angle spinning (MAS) NMR experiments have become very useful for the study of the structure of coal and other fossil fuels (1, 2). Solid state NMR techniques have the advantage over liquid NMR methods because the whole solid coal can be analyzed in a nondestructive manner and no assumption need be made that the soluble portion represents the whole organic portion of the coal. From CP/MAS experiments twelve NMR structural parameters may be determined including the aromaticity, f_a, that give information on the carbon skeletal backbone. The variation of the NMR structural parameters for coals of different rank from lignite to anthracite has been demonstrated (3). The coals in the Premium Coal Sample Bank (PCSB) have been included in the set of coals studied at the Advanced Combustion Engineering Research Center. The NMR data obtained on these coals will be used to provide chemical structural parameters for refinement of the devolatization sub-model of the PCGC-2 combustion model.

This paper reports the twelve structural parameters for two of the PCSB coals, Pittsburgh #8 (HVB) and Blind Canyon (HVB). These data were derived from integrated intensities in a normal CP/MAS experiment along with a complete set of dipolar dephasing experiments. In addition, the proton spin lattice relaxation times for these coals have been determined. From relaxation experiments on the Pittsburgh #8 coal there is some evidence of heterogeneity between different sample vials of the same standard coal.

Experimental

The coal samples studied were Argonne Premium Coal Bank samples of: Pittsburgh #8, high volitle bituminous, COAL_ID: 401, vials 137,140,157,159 and Blind Canyon Seam, high volitle bituminous, COAL_ID: 601, vial 90. All spectra were taken on a Bruker CXP-100. A single contact of 2.5 ms was employed for all T_1 and dipolar dephasing experiments together with a pulse delay time of 1.0 ms which is greater than $5T_1$'s for both coals. The samples were opened in a nitrogen glove bag, placed in a capped boron nitride rotor, and spun under nitrogen gas except for vials 137 and 159 of the Pittsburgh #8 which were opened in air and then placed immediately in the rotor. All

chemical shielding values are given in ppm with respect to external TMS. The pulse sequence used to measure the proton T_1 indirectly by observing the carbon resonance is described in detail by Axelson (1) and the dipolar dephasing sequence which includes refocusing pulses in both carbon and proton channels has been described by Alemany et. al. (4).

Results and Discussion

Proton Spin Lattice Relaxation

The proton T_1's are given in Table I for both the aromatic and aliphatic regions of one Blind Canyon vial and for four different vials of the same Pittsburgh #8 coal.

Table I: T_1^H(ms) Values for Two Argonne Coals.

Coal and Vial #	Aliphatic	Aromatic
Pittsburgh #8		
137	192 ± 7	193 ± 6
140	206 ± 9	194 ± 5
157	152 ± 5	140 ± 2
159	151 ± 10	138 ± 5
Blind Canyon		
90	60 ± 3	43 ± 2

± = one marginal standard deviation from three parameter fit.

The four different vials of Pittsburgh #8 have T_1^H values that fall into two groups, two with T_1's of approximately 195 ms and two with values in the 140-150 ms range. To check the reproducibility of the T_1 data, two different experiments were performed on a sample without removing it from the spectrometer. The measured T_1's were well within one marginal standard deviation (MSD) of each other, implying that the difference in the Pittsburgh #8 is greater than the experimental error. It is postulated that during the physical mixing and grinding of this coal, paramagnetic centers may not have been randomly distributed. The T_1^H's measured for both aliphatic and aromatic regions give the same value within two MSD for the Pittsburgh #8 samples demonstrating that spin diffusion is an efficient relaxation mechanism in this sample. For the Blind Canyon sample T_1^H is much shorter than Pittsburgh #8. The T_1's for the aliphatic and aromatic regions of the spectrum differ by more than three MSD indicating that spin diffusion does not occur throughout the whole sample.

Dipolar Dephasing and Structural Parameters

Under the conditions of the dipolar dephasing experiment the carbon magnetization can be characterized by a decay constant, T_2, which depends on the strength of the ^1H-^{13}C dipolar coupling. Characteristic values of T_2 for CH, CH_2, and CH_3 groups in model compounds and coals have been reported (3, 4, 5, 6). The T_2 decay curve is usually characterized by two time constants: a Gaussian component characterized with a time constant, T_G, for rapidly decaying components (CH and CH_2 groups) and a Lorentzian component with a time constant, T_L, for slowly decaying components (rapidly rotating methyl groups and nonprotonated carbons). An example of the decay curve for the magnetization, M(t), for the aromatic region of Pittsburgh #8 is shown in Figure 1 and was fit to the following equation:

$$M(t) = M_{0L}e^{-t/T_L} + M_{0G}e^{-0.5(t/T_G)^2} \qquad 1)$$

where M_{0L} and M_{0G} are the relative amounts of slow and fast decaying carbon magnetization at t = 0.

The above equation is applied separately to the decay of the aromatic and aliphatic regions of the spectrum and four parameters (M_{0L}, T_L , M_{0G}, T_G) are determined for each region and are used with integrated intensities, I, over various regions of the spectrum to determine the 12 structural parameters as follows:

$$f_a = (I_{>90} + 2I_{ss})/I_{total}$$
$$f_a^C = I_{>165}/I_{total}$$
$$f_{a'} = f_a - f_a^C$$
$$f_a^H = (M_{G0}^{ar}/M_{total}^{ar})\times f_{a'}$$
$$f_a^N = f_{a'} - f_a^H$$
$$f_a^P = I_{150-165}/I_{total}$$
$$f_a^S = I_{135-150}/I_{total}$$
$$f_a^B = f_a^N - f_a^S$$
$$f_{al} = 1 - f_a$$
$$f_{al}^H = (M_{G0}^{al}/M_{total}^{al})\times f_{al}$$
$$f_{al}^* = f_{al} - f_{al}^H$$
$$f_{al}^O = I_{50-90}/I_{total}. \qquad 2)$$

where I_{total} is the total integrated intensity of the whole spectrum, I_{ss} is the ingetrated intensity of the down field spinning sideband and I_{ppm}'s are the integrated intensities over

selected chemical shift ranges in ppm. These structural parameters are listed in Table II for the two coals and the normal CP/MAS spectrum is shown in Figure 2 for Pittsburgh #8 (bottom) and Blind Canyon (top).

Although both of these coals are of the same rank and nearly identical carbon content there are variations in some of the structural parameters. The $f_{a'}$ value for the Pittsburgh #8 is 0.75 while a lower value of 0.64 is found for the Blind Canyon coal indicating that more of the carbon is sp^2-hybridized in the Pittsburgh #8. From the elemental analysis data (7) the atomic H/C ratio is 0.79 for the Pittsburgh #8 and 0.91 for the Blind Canyon samples. The higher H/C ratio for the Blind Canyon coal is not surprising since this coal contains approximately 15% liptinite which is highly aliphatic and thus hydrogen rich. Using H/C data together with the f_{al}^{H} and f_{a}^{H} values for the two coals one notes that the H/C ratios for the aromatic and aliphatic regions are 0.37 and 2.0 for Pittsburgh #8 and 0.34 and 1.97 for Blind Canyon. This would seem to indicate that both the aliphatic and aromatic regions are quite similar but, as can be seen from the spectra, the aliphatic regions of the two coals appear to be significantly different. If it is assumed that the parameter f_{al}^{*} represents only methyl groups and the H/C ratio of the aliphatic region appropriately corrected, then the H/C ratio of the remaining aliphatic region for the two coals is 1.3 for Pittsburgh #8 and 1.7 for Blind Canyon. These differences can now be used to rationalize the marked spectral differences observed in the aliphatic regions of the two coals. The aliphatic structure of the Pittsburgh #8 is probably more highly branched, having more CH groups and a lower H/C ratio than the Blind Canyon coal which probably has more straight chains with CH_2 groups or nonsubstituted tetrilin-type structures contributing to the higher aliphatic H/C ratio.

This work demonstrates that solid state NMR techniques can be used to distingush structural differences in coals that are of the same rank as well as determining structural differences in coals of varying ranks. Similar data will be taken on all of the PCSB coals. This data will be used to assess those structural features that make major contributions to devolatization behavior of the coals in the combustion processes.

ACKNOWLEDGEMENTS

This work was supported by the National Science Foundation's Advanced Combustion Engineering Research Center, Contract No. CDR-8522618.

Table II: Structural Distribution of Argonne Coals.

COAL	f_a	$f_{a'}$	f_a^C	f_a^H	f_a^N	f_a^P	f_a^S	f_a^B	f_{al}	f_{al}^H	f_{al}^*	f_{al}^O
PITTSBURGH #8 (HVB)	.75	.75	.00	.28	.47	.06	.17	.30	.25	.14	.11	.03
BLIND CANYON (HVB)	.65	.64	.01	.22	.42	.07	.15	.27	.35	.27	.08	.04

f_a = Fraction of total carbon that is sp^2-hybridized.

$f_{a'}$ = Fraction of total carbon that is sp^2-hybridized and in an aromatic ring.

f_a^C = Fraction of total carbon that is carbonyl - $\delta > 165$ ppm.

f_a^H = Fraction of total carbon that is sp^2-hybridized and protonated.

f_a^N = Fraction of total carbon that is sp^2-hybridized and nonprotonated.

f_a^P = Fraction of total carbon that is phenolic or phenolic ether - $\delta = 150 - 165$ ppm.

f_a^S = Fraction of total carbon that is sp^2-hybridized and alkylated - $\delta = 135 - 150$ ppm.

f_a^B = Fraction of total carbon that is sp^2-hybridized and at a bridgehead position.

f_{al} = Fraction of total carbon that is sp^3-hybridized.

f_{al}^H = Fraction of total carbon that is sp^3-hybridized and CH or CH_2.

f_{al}^* = Fraction of total carbon that is sp^3-hybridized and CH_3 or nonprotonated.

f_{al}^O = Fraction of total carbon that is sp^3-hybridized and bonded to oxygen - $\delta = 50$-90 ppm.

References

1. Axelson, D. E. *Solid State Nuclear Magnetic Resonance of Fossil Fuels*; Multi Science: Canada, 1985.
2. Davidson, R. M. *Nuclear Magnetic Resonance Studies of Coal*; IEA Coal Research: London, 1986.
3. Wilson, M. A.; Pugmire, R. J.; Karas, J.; Alemany, L. B.; Woolfenden, W. R.; Grant, D. M.; Given, P. H. *Anal. Chem.*, **1984**, *56*, 933.
4. Alemany, L. B.; Grant, D. M.; Alger, T. D.; Pugmire, R. J. *J. Am. Chem. Soc.*, **1983**, *105*, 6697.
5. Alemany, L. B.; Grant, D. M.; Pugmire, R. J.; Stock, L. M. *Fuel*, **1984**, *63*, 513.
6. Soderquist, A.; Burton, D. J.; Pugmire, R. J.; Beeler, A. J.; Grant, D. M.; Durand, B.; Huk, A. Y. *Energy & Fuels*, **1987**, *1*, 50.
7. Private communication Karl Vorres

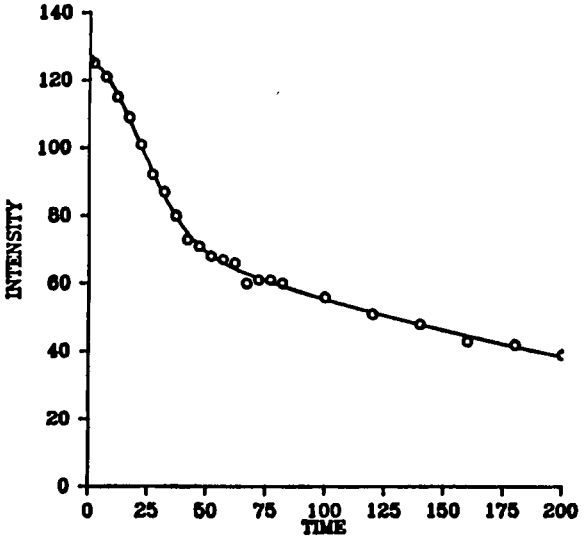

Figure 1. Dipolar dephasing decay curve for the aromatic carbons of Pittsburgh #8. Times are in μs.

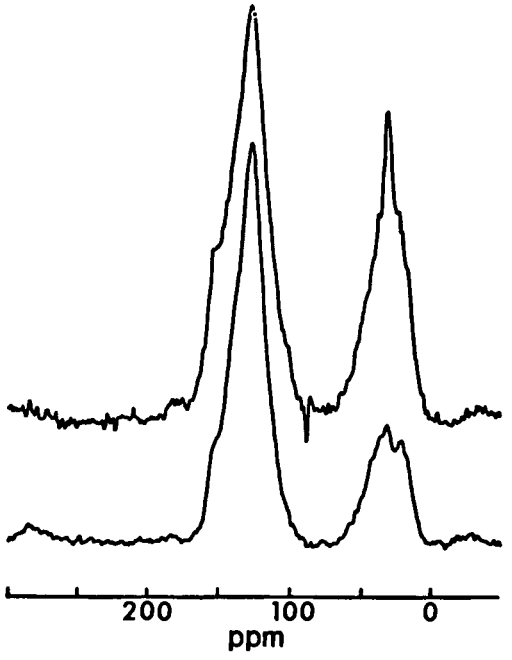

Figure 2. CP/MAS spectra of Blind Canyon (top) and Pittsburgh #8 (bottom).

MULTINUCLEAR NMR CHARACTERIZATION OF THE LAYER SILICATES IN ARGONNE PREMIUM COALS AND MODEL SYSTEMS

Arthur R. Thompson and Robert E. Botto

Chemistry Division, Argonne National Laboratory,
9700 South Cass Avenue, Argonne, Illinois 60439

INTRODUCTION

A variety of pulse sequences have been used to obtain solid-state aluminum-27 and silicon-29 nuclear magnetic resonance (NMR) spectra on the mineral matter in Argonne Premium Coals. The aim of this research investigation is two-fold; to improve our knowledge of minerals found in coals and to elucidate the possible roles of layer silicates in coal formation. To facilitate the latter objective, layer silicates that are intimate with the carbonaceous portion and present during coalification must be identified. Nuclear magnetic resonance should provide valuable information because it is sensitive to all mineral particles independent of their size and it is a direct characterization method, thus does not require any modification of the coals.

In the present study, NMR has been applied to the entire suite of Argonne Premium Coals before and after separation of the detrital mineral particles by sink-float separation (1). Preliminary results are presented for the direct characterization of the minerals more intimately associated with the organic portion of these coals.

EXPERIMENTAL

NMR Spectroscopy. The silicon-29 cross-polarization (CP) (2) and spin-echo (3) spectra employing magic-angle sample-spinning (MAS) (4) were recorded at 19.89 MHz on a Bruker Instruments spectrometer, model CXP-100. The CP/MAS spectra were recorded with contact times varying from .1 to 20 ms, a 2-second repetition time and with proton-decoupling during acquisition. The Hartman-Hahn matching condition was set with pure kaolinite spinning at about 3.5 kHz; all CP/MAS spectra were recorded at the same speed as the standard. The spin-echo spectra were recorded with and without proton decoupling during acquisition and with a repetition time of .2 to 2 seconds depending on T_1. The total time required to obtain the silicon-29 spectra varied from an hour to 15 hours for CP/MAS spectra and 2 to 50 hours for spin-echo spectra. The aluminum-27 MAS, variable angle sample spinning (VAS) (5) and static spectra were recorded with a 45° pulse (2.5 μs pulse width) at 52.2 MHz on a Nicolet Magnetics spectrometer, model NTC-200. The aluminum-27 spectra required an hour to 15 hours for data acquisition. Chemical shifts are referenced to TMS for silicon-29 and a 1 M aqueous solution of $AlCl_3$ for aluminum-27.

Preparation of Mineral Concentrates by Sink-Float Separation. A typical procedure to obtain concentrates of minerals was to suspend -100 mesh Argonne Premium Coal in a 1.42 g/cm solution (1 g coal/10 mLs) by ultrasonification. The coal slurries were centrifuged for 30 to 90 minutes to allow for the density separation. The raw coal was clearly separated into a black,

carbonaceous upper portion (low density) and a grayish mineral portion on the bottom. These two portions could be readily separated with minimal mixing by decantation. The two portions were separately washed with water and ethanol to remove the CsCl and Brij-35 and were subsequently dried in a vacuum oven at room temperature.

RESULTS AND DISCUSSION

Several commercially available layer silicates and their chemically modified variants were analyzed to determine the optimum spectral parameters required for their observation. Methods were also developed to distinguish between the layer silicates present and to find ways to overcome the problems of poor sensitivity. In silicon-29 NMR experiments, cross-polarization can be used to take advantage of the dipolar coupling to protons thereby enhancing the signal of the dilute nuclear spin system. The appropriate mix time depends on the rate of polarization transfer, or the effective silicon-proton internuclear distance, and the lifetime of the proton magnetization. The results of these experiments on all Argonne Premium coals showed that using a mix time of approximately 5 ms selectively enhances the sharp kaolinite resonance at -92.5 ppm (compare Figs 1a and 1b). This was a surprising result since other silicates are expected to have structures with silicon-proton distances similar to kaolinite. However, it allowed the unambiguous identification of kaolinite in all of the Argonne Premium Coals even when a small amount of kaolinite was found in the presence of a large number of other minerals. The silicon-29 spin-echo NMR spectrum, in addition to having a resonance from kaolinite (see Fig. 1a) also exhibits a resonance at -108 ppm from quartz, as well as resonances from several other silicon sites (some minerals may have several resonances due to crystallographic inequivalence) in the region from -75 to -95 ppm. Silicon-29 resonances in the latter region are typical of montmorillonite or illite clays having SiO_4 structures with two or three of their next nearest neighbors as silicon and the remaining next nearest neighbors as aluminum and/or hydrogen. The kaolinite resonance at -92.5 ppm was narrowed from 3 ppm to 1 ppm when proton decoupling was employed. However, no significant change in linewidth was observed for the other resonances which prevented further identification of other layer silicates. A proton decoupling field of 48 kHz was employed and should have been of sufficient magnitude to decouple all protons from silicon. Thus, other line-broadening mechanisms, for example, bulk susceptibility anisotropy effects arising from noncrystallinity, must dominate the resonances of the other minerals. It should be pointed out that the silicon-29 NMR spectral parameters were selected to discriminate against quartz-like minerals (although quartz resonances do appear in some spectra at -108 ppm, Figs. 1a and 1c) in order to maximize conditions for observation of the layer silicates.

The solid-state aluminum-27 NMR spectra of the Argonne Premium Coals show that a greater proportion of their aluminum is found in octahedral environments (Table 1), some of which is due to kaolinite, and differing amounts of tetrahedral aluminum. The aluminum-27 spectrum of Illinois #6 bituminous coal (APCS #3) shown in Fig. 2a exhibits tetrahedral resonances in the region centered at 65 ppm and octahedral resonances in the region at 0 ppm. The Utah bituminous coal (APCS #6) was found to have the most tetrahedral aluminum, about one-third the area of the total aluminum signal (see Table 1 and

Fig. 2c). The values in Table 1 were determined from the MAS spectra. Static and VAS spectra were also run to confirm that the octahedral resonances were devoid of spinning sidebands that would influence the relative intensities of the tetrahedral and octahedral aluminum centerbands.

In addition to the spectra of the raw coals, NMR measurements were performed on density separated materials. The predominantly carbonaceous portion of the Argonne Premium Coals was separated from the heavier, mineral-rich material to provide information on the distribution of the different layer silicates closely associated with the organic matter. Minerals that are finely dispersed within the organic matrix were found to float in a solution of density 1.42 g/cm^3 (aqueous solution of CsCl and Brij-35), while the larger, mineral-rich material sank after centrifugation. We chose APCS #6 as one of the first coals to separate because it had the most favorable tetrahedral to octahedral aluminum ratio. The aluminum-27 NMR spectrum (Fig. 2d) of the mineral concentrate obtained from density separated APCS #6 shows at least a two-fold increase in intensity of the tetrahedral resonance over that observed for the raw coal (Fig. 2c). Moreover, this treatment apparently does not alter the structure of the minerals. The aluminum-27 or silicon-29 NMR spectra of raw APCS #3 (Illinois #6) are essentially the same as the corresponding spectra of its mineral concentrate obtained by sink-float, Figs. 1a and 1c, 2a and 2b. The effect of concentrating the mineral matter is apparent from the reduction in time needed to acquire the spectra; the raw coal required approximately 15 hours of total acquisition (Fig. 2c) while the mineral concentrate required less than 2 hours (Fig. 2d). In addition, the silicon-29 spectrum of the carbonaceous upper portion of the same coal (Fig. 1d) (50 hours total accumulation time) shows substantial differences in mineral composition compared with spectra of the raw coal or mineral concentrate.

These spectra of the density separated fractions clearly demonstrate that a different mix of minerals is intimately dispersed in the organic matrix compared to that found for the detrital material. We are currently pursuing additional density separations in order to see whether spectral differences can be observed with mesh size or whether other Argonne Premium Coals show interesting behavior. We feel these initial results demonstrate that NMR can yield valuable information about the type of mineral matter present in coal and that the technique has the potential to resolve mineral matter intimately associated with the organic portion of coals from epigenetic minerals that are present.

ACKNOWLEDGMENT

The authors would like to thank C.-Y. Choi for his advice and the many helpful discussions on density separation.

This work was performed under the auspices of the Office of Basic Energy Sciences, Division of Chemical Sciences, U.S. Department of Energy, under contract number W-31-109-ENG-38.

REFERENCES

1. G. R. Dyrkacz and E. P. Horwitz, Fuel, 1982, 61, 3.
2. A. Pines, M.G. Gibby, and J.S. Waugh, J. Chem. Phys. 1973, 59, 569.
3. A.C. Kunwar, G.L. Turner, and E. Oldfield, J. Magn. Reson., 1986, 69, 124.
4. J. Schaefer and E.O. Stejskal, J. Amer. Chem. Soc., 1976, 98, 1031.
5. S. Schramm and E. Oldfield, J. Amer. Chem. Soc., 1984, 106, 2502.

TABLE 1. Distribution of Tetrahedral and Octahedral Aluminum Found in the Argonne Premium Coal Samples (APCS) by Solid-State Aluminum-27 NMR.[a]

Coal	Number	% Tetrahedral	% Octahedral
Upper Freeport mv bituminous	(APCS #1)	25	75
Wyodak subbituminous	(APCS #2)	8	92
Illinois No. 6 hvC bituminous	(APCS #3)	10	90
Pittsburgh No. 8 hvA bituminous	(APCS #4)	13	87
Pocahontas lv bituminous	(APCS #5)	32	68
Utah bituminous	(APCS #6)	33	67
Stockton hvA bituminous	(APCS #7)	10	90
North Dakota lignite	(APCS #8)	5	95

[a]Estimated error is ±5%.

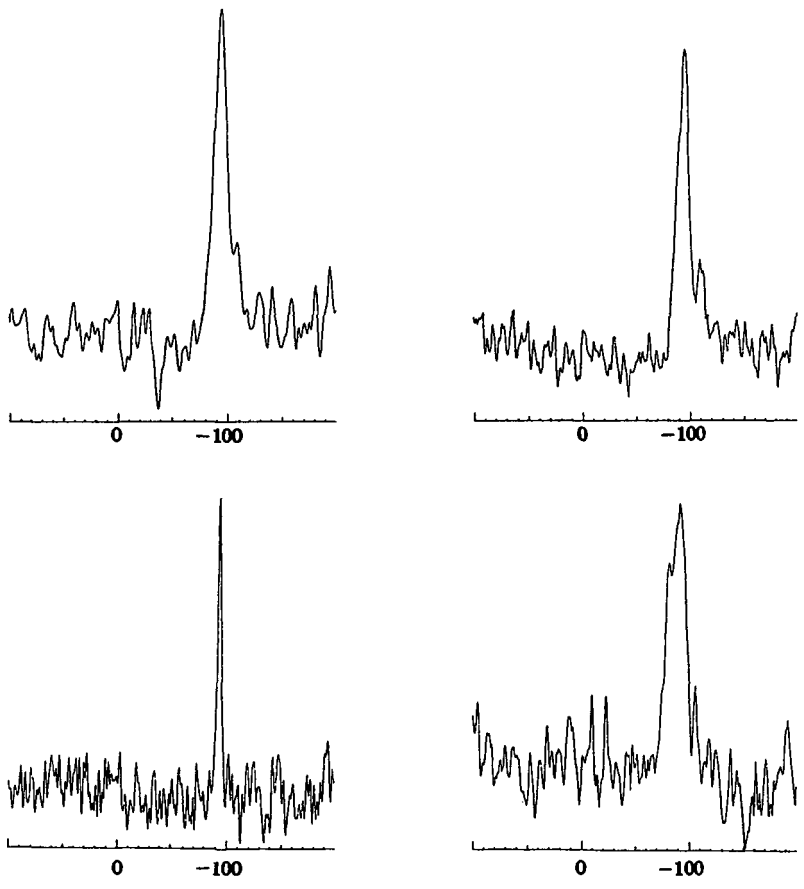

Figure 1. Silicon-29 MAS NMR spectra of raw APCS #3: (a) spin-echo and (b) CP; and spin-echo spectra of its density separated (c) sink (mineral-rich) and (d) float (organic-rich) material.

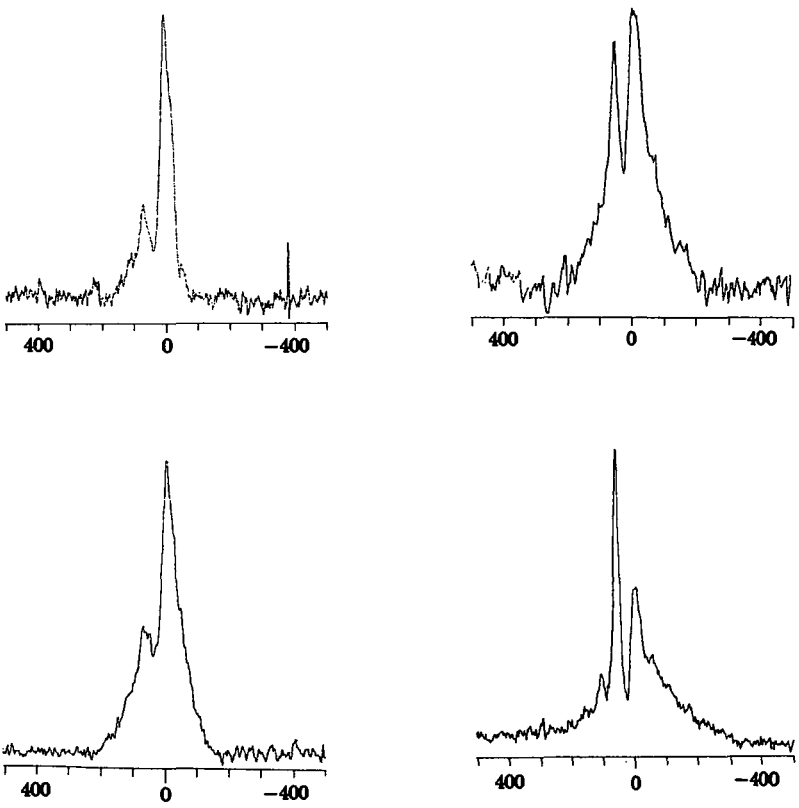

Figure 2. Aluminum-27 MAS NMR spectra of (a) raw APCS #3 (b) sink of APCS #3 (c) raw APCS #6 and (d) sink of APCS #6.

An EPR Study of Nitroxide Spin Probe Doped Illinois no. 6 Coal From the Premium Coal Sample Program: Reactive Site Distribution

Lowell D. Kispert, Lalith S. Cooray, and Shing K. Wuu

Chemistry Department, The University of Alabama,
Tuscaloosa, Alabama 35487

INTRODUCTION

The conversion of coal by an economically feasible catalytic method is an important area of research for our future energy requirements. However, knowledge of the coal structure is necessary before optimum use can be made of the catalyst. For instance, the catalyst must be able to diffuse into the coal sample so that hydrogenation catalysis can occur from within as well as the normal surface catalysis. This requires an estimation of the size, number, and shape of the pores in the coal before and after swelling with different solvents and the number distribution of different reactive sites within a coal sample. In the past, efforts have been made to estimate the total void volume (porosity) and distribution of pores by measuring the moisture content of coal and penetration by mercury as a function of pressure (1). It was concluded that the internal surface of coal is associated with a capillary system of < 4 nm pores connected by 0.5 - 0.8 nm passages. Liquid and vapor sorption studies (2) of porosity and internal surface of coal suggest that a definable pore structure may not exist and that accessibility is a better term to use.

Recently, we reported (3) a method to determine the relative pore (accessibility) size and number distribution in selected high-volatile bituminous coal samples by diffusing nitroxide spin probes of different shapes, varying in diameter or length from 0.47 nm to 3.5 nm, into the swellable pores of the coal samples. The relative spin probe concentration was measured by Electron Paramagnetic Resonance (EPR) methods for each sized spin probe. From these measurements, a relative number and size distribution was estimated for the swellable pores of Mary Lee (MRI, PSOC-271) and Black Creek (MRI) coal seams of Alabama and the Illinois no. 5 (PSOC-699) seam. The coal samples were obtained from the Mineral Resources Institute (MRI) at the University of Alabama and the Penn State Coal Sample Bank (PSOC) at Penn State University. The pore sizes deduced from these studies were consistent with those deduced by mercury penetration studies carried out as a function of pressure. It was found (3) that the size and number distribution of pores deduced from the spin probe concentration is different for each coal seam. For instance, there are 5 times as many swellable pores of the shape of a long chain stearamide (length 3.4 nm) in Mary Lee coal as there are in Black Creek coal, while there are 18 times as many short chain (1.2 nm length) cylindrical pores and only 0.3 times as many medium length cylindrical pores. Further details of the size and number

distribution reported earlier, can be found in Table 2 of reference 3.

It was also observed (3) that the nitrogen coupling in the principal z direction of the incorporated spin probe (those with a diameter or length greater than 1 nm) exhibited a temperature dependence above 250 K that is largely a result of librational motion of the nitroxide moiety about the N-C bond. Below 250 K, the temperature dependence of the nitrogen coupling is like that found for spin probes in solids that exhibit an equilibrium between a nonbonded and a hydrogen bonded state; the hydrogen bonded state exhibiting the larger coupling. The possibility of hydrogen bonding may suggest a mechanism whereby the spin probes are incorporated in the porous structure of the coal samples.

While the earlier study (3) dealt largely with determining the number distribution for swellable pores with diameters between 0.46 nm and 3.5 nm, no attempt was made to study reactive site distributions and whether a hydrogen bonding mechanism is an important mechanism for spin probe incorporation in pores of the coal samples.

Thus this study reports the results of a series of similar but small sized spin probes (~ 0.6 nm in diameter), each containing a different reactive substitutent, to determine the number distribution of reactive sites containing acid, phenol and amine substituents. The smaller size of the spin probes with reactive sites, will permit a measure of all accessible sites with diameters greater than approximately 0.6 nm.

In addition, a study was made to differentiate hydrogen-bonding to the nitroxyl group from that of a substitutent group in swellable pores with diameters of approximately 0.4-0.6 nm.

EXPERIMENTAL

Samples of Mary Lee (MRI), Black Creek (MRI) and Illinois no. 5 (PSOC-669) high-volatile bituminous coal from the stock samples previously studied (3) and samples of Illinois no. 6 obtained from the Premium Coal Sample Program at the Argonne National Laboratory were selected for study. The proximate and ultimate analyses for all coals except Illinois no.6 have been previously given (3) while the ash free percentage by weight values of the Illinois no. 6 sample equal C (79%), H (5.6%), O (9.7%), and S (5.4%). All coal samples were stored under a blanket of N_2 except Illinois no. 6 which arrived in sealed ampoules under humid nitrogen. Upon opening, the samples were stored under N_2 or argon.

A 30 mg sized, dried and unmodified sample of each coal was added to a 10^{-3} M solution of nitroxide spin probe in toluene. Six different spin probes (I-VI), obtained from Molecular Probes, Inc. Junction City, Oregon, were used. These probes were selected because they are all of similar size and because spin probes I and III react with amines, spin probes II and IV react with acids and phenols and spin probes V and VI can be used to distinguish between hydrogen bonding to a ketone and to a nitroxyl group.

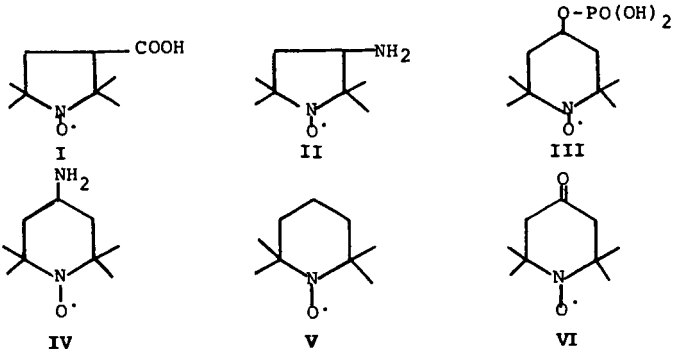

Each coal and spin probe mixture was stirred vigorously at 50-60°C in a sealed flask. After 16-18 hours, the excess toluene was suction-filtered off and the remaining solid material evacuated to dryness to collapse the coal around the spin probe. The dried material was washed with ethanol (a nonswelling solvent) to remove any spin probe attached to the exterior of the coal, suction filtered, packed into an EPR sample tube, evacuated and sealed. The prepared spin-probe-doped coal sample was stored under liquid nitrogen.

EPR powder specta were recorded on a Varian E-12 EPR spectrometer interfaced to an IBM-XT for each sample as a function of temperature (77-335 K) using the standard Varian variable-temperature and liquid nitrogen accessory. The magnetic field was calibrated using a Bruker ER 035 M NMR Gaussmeter and the microwave frequency was measured with a model H/P 5246 L frequency counter. EPR spectra were recorded on disk with an IBM-XT using the EPRDAS software program from Adaptable Laboratory Software. For spectra recorded only on graph paper, input to disk was achieved by use of a Kurta Tablet Digitizer using Sigma-Scan software. A computer program has been developed using the ASYST language (MacMillan Software) to calculate the relative concentration of spin probes in different coal samples in the presence of the severe spectral overlap by the EPR spectrum of the undoped coal. The computer program has also been expanded to analyze temperature dependent coupling constants in terms of hydrogen-bond equilibrium or/and small amplitude librational motion. Output is to a H/P 7440 A Plotter.

RESULTS:

EPR spectra obtained from coal samples containing spin probes gave rise to a spectrum similar to that shown in Figure 1, consisting of an intense central line due to undoped coal (curve B) and, at high gain (curve A), resolved powder EPR lines at high and low magnetic fields due to the z tensor component of the nitrogen hyperfine coupling (A_{zz}) arising from the nitroxide spin probe dopant. The separation between the high and low field component equals $2A_{zz}$. The relative spin concentrations were determined by integrating the low field peak. The relative spin probe concentration is given in table I for probe I (reacts with amines), probe IV (reacts with acids and phenols), probe V (hydrogen bonding only to the nitroxyl group) and

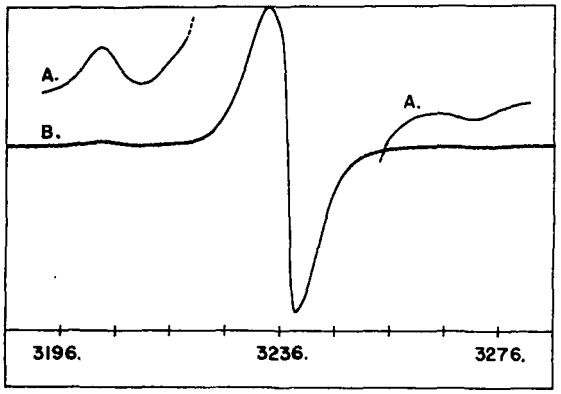

Figure 1. EPR spectrum of a spin probe in a sample of Black Creek coal at (A) high gain (X10) and (B) at low gain (X1) at 300 K.

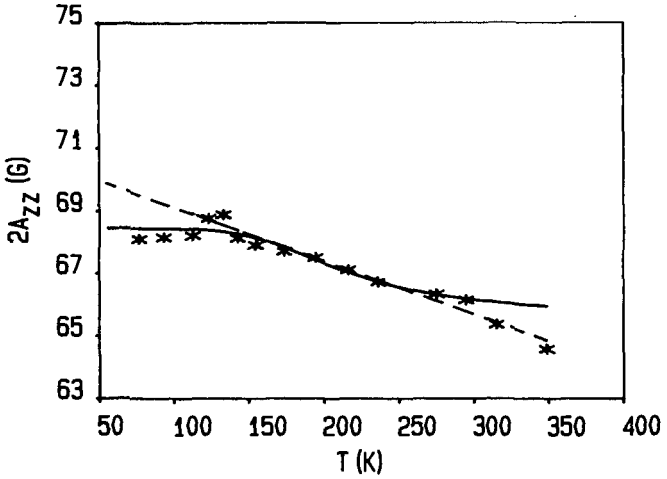

Figure 2. $2A_{zz}$ against temperature for spin probe VIII (DCT-Tempamine) incorporated in a sample of Illinois no. 6 (premium coal): *, experimental data; -----, librational model; _____, hydrogen-bond equilibrium.

probe VI (hydrogen-bonding to ketone and nitroxyl groups). The results for spin probes II and III are not reported here.

Table I. Relative Site Distribution for Spin Probes I, IV, V and VI.

	Spin Probes*			
Coal Sample	I (COOH) Base/acid	IV ($-NH_2$) reaction	V (sub.) No hydrogen	VI (=O) bonding
Mary Lee	220	67	24.0	1.0
Black Creek	230	1550	5.3	5.0
Illinois no. 5	100	53	4.1	17.0
Illinois no. 6	14	164	4.9	11.0

*Relative spin probe concentration normalized to probe VI in Mary Lee coal.

Notably, the ratio of pores containing acid or phenolic groups to those containing amine groups is 1/3; 6.7/1; 0.5/1; and 12/1 for Mary Lee, Black Creek, Illinois #5 and Illinois #6 respectively. In addition, Black Creek coal has approximately 25 more sites containing acid or phenol groups than either Mary Lee or Illinois no. 5 coal samples, and nearly an order of magnitude greater than that found in the Illinois no. 6 sample. The sites containing amine functions are similar except for the Illinois no. 6 sample for which the amine concentration decreases by nearly an order of magnitude. It is interesting to note that more spin probe V (factor of 23) can be incorporated into Mary Lee (only one site available for hydrogen-bonding), than spin probe VI (2 sites for spin probe hydrogen-bonding), while the presence of hydrogen-bonding sites does not seem to matter for spin probe incorporation in Black Creek coal, but is a factor of 4 greater for VI in Illinois no. 5 and a factor of 2 greater for incorporation of VI in Illinois no. 6. It is apparent from these measurements that the presence of an additional site for hydrogen bonding is of little importance in determining the amount of spin probe incorporated in small (0.4 to 0.6 nm) pores in samples of Mary Lee and Black Creek coal.

The separation between the high and low field EPR lines ($2A_{zz}$) for each spin probe exhibits a temperature dependence between 350 and 77 K. It was previously shown for bulky or long chain spin probes (3) that at high temperature, the temperature dependence of A_{zz} is due to librational motion of the NO group of the spin probe with respect to the CNC plane of the nitroxide ring and is given by Equation 1

$$2A_{zz}(t) = A^{o}_{zz}[1+\cos(kt/E_a)^{0.5}] \qquad 1)$$

where E_a = the barrier to librational motion and A^o_{zz} is a temperature independent hyperfine coupling. At temperatures below 270 K, the temperature dependence can be fit to an equation derived from the assumption that the spin probe exists in an hydrogen-bond equilibrium between two states, one with a larger coupling due to hydrogen-bonding and the second to a non-bonding state. This type of dependence follows the solid line in Figure 2 and is noted by the near temperature independence at low temperature (3). Similar behavior is observed for spin labels tightly bound within hemoglobin (4).

Temperature dependent studies of 4-aminotempo-(IV) in Illinois no. 6 coal, Mary Lee, Black Creek, and Illinois no. 5, showed a very interesting dependence. A near perfect fit to the librational model (dashed line in Figure 2) occurred for the $A_{zz}(t)$ value observed for IV in the Illinois no. 6, Mary Lee and Black Creek and a small dependence of a hydrogen-bond model was observed for IV in Illinois no. 5 coal. In addition when the smaller spin probe tempo, (VII),

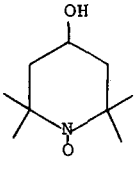

VII

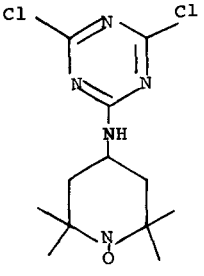

VIII

(the OH substituted for NH_2 in IV) was incorporated in Illinois no. 6 it gave a temperature dependence of A_{zz} that was clearly due only to a librational motion as the temperature dependence follows a straight line relationship. However the temperature dependence of DCT-tempamine, (VIII) incorporated in Illinois no. 6 exhibits a behavior like that found for other large spin probes - librational behavior at high temperature and evidence of hydrogen-bond equilibrium below 200 K (See Figure 2).

In Table II are given the energy barriers to librational motion of the spin probes deduced from the temperature dependent hyperfine coupling parameter A_{zz}. Although the variation is not large, the large sized spin probe VIII does have a higher barrier to rotation than IV, as would be expected for a large size probe trapped in the swellable coal pores.

Table II: Energy Barrier to Librational Motion of Spin Probes in Four Coal Samples.

Coal	Spin Probe	E_a(kJ/Mole)
Illinois no. 6	IV	6.69 (±.04)
Illinois no. 6	VII	7.57 (±.04)
Illinois no. 6	VIII	8.59 (±.04)
Mary Lee	IV	8.61 (±.03)
Black Creek	IV	7.88 (±.02)
Illinois no. 5	IV	7.26 (±.04)

CONCLUSION

The reactive site distribution detected by spin probes approximately 0.6 nm in diameter, varies from coal seam to coal seam. The detected acid and phenolic sites in Black Creek Coal and the Illinois No. 6 coal (Premium Coal Sample Program) exceed the detected amine sites by approximately an order of magnitude while slightly more amine than acid or phenolic sites are detected in samples of Mary Lee and Illinois no. 5. On the other hand, the greatest number of reactive acid and phenolic sites were detected in Black Creek coal. The ability for the coal pore to hydrogen bond to a spin probe was shown not to be an important process for incorporating spin probes in Mary Lee and Black Creek coal and only a slight factor in samples of Illinois no. 6, and Illinois no. 5. Because of this the number of swellable pores containing spin probes V and VI was at least an order of magnitude lower than the reactive sites containing I and IV. Spin probes V and VI exhibited large librational motion in the swellable pores.

ACKNOWLEDGMENTS

The authors gratefully acknowledge the U. S. Department of Energy, Pittsburgh Energy Technology Center, University Coal Research Program for support of this research under Grant no. DE-FG22-86PC90502. We wish to thank Professor William Spackman and Mr. C. Phillip Dolsen from the Penn State Coal Sample Bank at the Pennsylvania State University, Dr. Hanna in the Mineral Resources Institutes at the University and the Premium Coal Sample Program at Argonne National Lab for providing coal samples of known composition.

REFERENCES

1. Berkowitz, N. "An Introduction to Coal Technology"; Academic: New York, 1979; ch. 4 and references therein.

2. Fuller, E. L. Jr., Adv. Chem. Ser. 1981, 192, ch 19.

3. Wuu S-K.; L. D. Kispert, Fuel, 1985, 64, 1681.

4. Johnson, M. E. Biochemistry 1981, 20, 3319.

THE EFFECT OF AIR OXIDATION ON SEQUENTIAL SOLVENT EXTRACTION OF THE ARGONNE PREMIUM COAL SAMPLES

David H. Buchanan and Wanping Mai

Chemistry Department
Eastern Illinois University
Charleston, IL 61920

INTRODUCTION

Sequential solvent extraction of coal with a series of increasingly better solvents (Toluene, THF, DMF, Pyridine) has been used to examine the effect of artificial weathering on several Illinois coals.(1) A similar method with a different set of solvents was recently employed by Kister, et al. on a low-rank French coal.(2) In both cases, each extract is soluble in all later solvents and analysis of the entire set of extracts produces more information than extraction with a single solvent. Because extracts so isolated have experienced some fractionation and concentration, FT-IR and GPC analyses of the extracts often reveal subtle changes due to chemical treatment, such as weathering, not obvious from analysis of the whole coals.

The availability of premium coals is an opportunity for many laboratories to study the effects of both coal rank and coal weathering on a variety of properties of the same coals. Changes in sequential solvent extraction, FT-IR spectra of extracts and residues, GPC analyses of extracts, and solvent swelling of residues brought about by weathering of five Argonne Premium Coals are the subject of this paper.

EXPERIMENTAL PROCEDURES

Argonne Premium coal samples were dried to constant weight in an Abderhalden apparatus at 100°C and 0.05 Torr (standard conditions) immediately prior to extraction or oxidation. Samples were oxidized as thin layers, in recrystallizing dishes covered to exclude dust, but permit free circulation of air, at ambient temperature and humidity for at least four months. Weathering coals were stirred once a week to promote uniform air exposure and redried to constant weight before extraction. Sequential solvent extraction of coals in the order: toluene, THF, DMF, pyridine followed the method described previously.(1) Samples of coal and oxidized coal (7-10 g) were exhaustively extracted with purified, Argon purged, solvents in a Soxhlet apparatus, under an Argon atmosphere. Extraction with each solvent was continued until no color was visible in the siphoning solvent for at least ten hours. All extracts and washing solvents were filtered through 0.45 um Nylon membrane filters before vacuum evaporation and standard drying to constant weight. Residues plus DMF and pyridine extracts were washed several times with 80% methanol/water to remove those solvents.

Gel Permeation Chromatography (GPC) analyses of all extracts were determined on pyridine solutions (6mg/mL) using a train of three Ultragel columns with pyridine mobile phase.(1) KBr pellets (3.0 mg sample/300 mg KBr) were prepared in an nitrogen flushed glove bag and dried under standard conditions to reduce surface moisture. FT-IR spectra were collected at 2 cm^{-1} resolution on a Nicolet 20-DXB spectrometer. Phenol contents were determined by the Blom acetylation procedure(3) with N,N-dimethylaminopyridine (DMAP) as a catalyst. Volumetric solvent swelling of residues with dry, distilled solvents followed standard methods.(4)

RESULTS AND DISCUSSION

Analytical data for coals, oxidized coals, and two residues are presented in Table 1. Preliminary elemental analyses of the coals are based on many analyses by

several labs, the values for the oxidized coals are from single samples. The well-known problems of comparing such data sets are illustrated by the %C values for fresh and oxidized samples of coals 1, 3, and 4. The expected decrease in carbon content with oxidation is not shown. Additional analyses of both sample sets are needed. Volumetric solvent swelling ratios of extraction residues are listed with the coals they were derived from in Table 1. The effect of oxidation on solvent swelling is both rank and solvent dependent. A decrease in swelling correlates with an increase in cross-linking, either from covalent or hydrogen bonds. Swelling of fresh coals increases and then decreases with rank, as does the extractability reported in Table 2. Total extract yield does not correlate directly with swelling in any single solvent, but swelling ability of the solvent is clearly important in determining extract yield. Differences in swelling between toluene and anhydrous ethanol correlate with oxygen contents of the original coals, showing that ethanol is an hydrogen bond donor in swelling experiments. Except for coal #1, changes in toluene and ethanol swelling caused by oxidation correlate with the change in total extractability and show that room temperature oxidation can cause either a net increase or decrease in cross-linking depending on the rank of the coal.

Phenol contents of fresh coals generally increased with weathering. Liotta(5), using alkylation with NMR and FT-IR spectroscopy to measure phenols, found the phenol content of a Monterey Illinois 6 coal to be close to our result for Argonne #3, but observed no change upon weathering for several months, in contrast to the increases we measured for the coals in Table 1. This may reflect differences between coals or oxidation procedures or it may indicate that the Blom acetylation procedure is counting as phenol other reactive groups in coals through transesterification or anhydride formation. This would cause oxidized coals, which contain esters or acids, to give high phenol analyses. Residues of our oxidized coals usually have fewer phenols than residues of fresh coals.

Sequential solvent extractions are tabulated in Table 2 and summarized in Figure 1. Variations in total yield with rank are consistent with early work by Dryden.(6) In this and previous studies(1), we have shown that total extract yields are reproducible to within $\pm$ 0.5%; that changing the order of extraction to pyridine, toluene, THF, DMF does not change the total extract yield; and that pyridine removes over 97% of all soluble material when it is the first solvent in the sequence. In single solvent extractions with THF or DMF on several Illinois coals, yields equal the sum of the sequential extraction yields for all solvents up through that solvent in the sequence. We believe that each solvent in the sequence can dissolve everything removed by previous solvents plus additional material made soluble by the increased swelling and solvating power of that solvent.

Extracts and residues which have been in contact with DMF or pyridine were washed with 80% methanol/water to remove these solvents. Only for the sub-bituminous coal did the methanol washes extract highly colored material and leave a significant residue (> 0.1%) after evaporation. Small amounts of colloidal material were isolated from the membrane filtration of extracts from oxidized #2 and #3 coals. For material balance purposes, methanol solubles were counted as part of total (but not individual) extracts and colloids as part of residues.

On Figure 1, total extract yields for oxidized coals have been plotted at the carbon values of the fresh coals for comparison. Individual solvent extract yields for fresh coals have been plotted on the same graph to illustrate the variation with rank for each solvent in the sequence. Studies which use single solvent extractability with 'early' solvents such as THF to measure the extent of some reaction within coal risk missing production or loss of material which may be of a size and polarity to dissolve in that solvent but which remains trapped in the coal pores because of the poor swelling characteristics of the solvent.

Of particular note is the unusual pattern of individual solvent extract yields

of coal #1 in contrast to the 'normal'(6) total extract yield for a coal of this rank. This may be due to the low swelling of this coal in the early solvents. Only with the effective swelling solvents, DMF and pyridine, can the potentially soluble material diffuse out of the coal network. FT-IR spectra of extracts (below) support this view. DMF extraction of coal #1 took nearly a month to reach completion because of slow diffusion of extracts from the coal. In general, extraction time correlated with extract yield and solvent viscosity. DMF extractions were always the slowest.

Only the two lowest rank coals showed significant changes in total extract yield after artificial weathering. Previous results with a variety of Illinois coals(1,5) and Bruceton (hvAb) coal(7) led us to expect reduction in extract yield to be more general than observed. Larsen(7) found a significant decrease in pyridine extractability when Bruceton coal was heated at 80°C, in contrast to our results for coal #4. If the different results are due to oxidation temperature, the reactions leading to a decrease in extractability apparently have large free energies of activation. Larsen's values for pyridine solvent swelling of the Bruceton coal showed little change upon oxidation and fall between our values for fresh and oxidized coal #4 (Table 1).

Changes in FT-IR spectra of sequential extracts upon oxidation were much more striking than changes in the spectra of whole coals or insoluble residues, consistent with the idea that sequential solvent extraction fractionates and concentrates mobile material from coal. Smaller, mobile molecules are more reactive and change more upon weathering than the insoluble network. Figures 2 and 3 present FT-IR spectra of the toluene and pyridine sequential extracts from coal #1 (B), oxidized coal #1 (A), and the difference (A-B). The new carbonyl peak at 1722 cm^{-1} is barely visible in the difference spectrum of #1-OX - #1 coal. This new band has been observed previously in oxidized coals and is suggested to be due esters.(8) It is observed in several sequential extracts of coals 1-OX, 2-OX, 3-OX, 4-OX, and 5-OX in this study and is always accompanied by bands near 1260 and 1102 cm^{-1}, consistent with ester formation. The 1722, 1260, and 1102 cm^{-1} bands are more prominent in extracts of higher rank coals. They are small, but visible, in the THF and pyridine extracts of coals 2-OX and 3-OX. That they occur at all in pyridine extracts, produced from coal exhaustively extracted by toluene, THF, and DMF, is consistent with the idea that the superior swelling ability of pyridine is allowing material similar to the toluene extracts to escape.

The difference spectrum of 3-OX (Figure 4) is dominated by a band at 1666 cm^{-1}, which is also present at low intensity in polar extracts of 1-OX, 2-OX, and 5-OX, and possibly as a shoulder in 1-OX, Figure 3. This band was ascribed by previous workers to quinone or related aryl carbonyl functional groups.(8a,9) Many spectra of oxidized coals and their extracts show a single, sharp band at 750 - 725 cm^{-1}. Aromatic C-H bending and mineral matter both produce sharp bands in this region, however these extracts contain less than 2% ash. The source of this band is currently under investigation and, if not an artifact, could serve as a simple marker for weathering.

GPC analyses of the extracts are consistent with Dryden's early observation that molecular size generally correlates with extract yield.(6) Figures 5 - 7 present Molecular Size Profiles of coals #1, #1-OX, and #2. In each profile, GPC traces of all sequential extracts from a coal are plotted together. Profiles for several Illinois coals similar to #3 and #3-OX have been published previously.(1) Comparison of Figure 5 with 6 shows that even though total extract yield was little changed by weathering, a larger fraction is being removed by DMF and this material came from the pyridine extract. Changes in the shapes of the GPC curves indicate that toluene is extracting a broader range of molecular sizes after weathering and that the THF extract of #1-OX contains more oxygenated molecules than the other fractions. GPC curve height is very sensitive to the presence of hydroxyl and carbonyl functional groups.(10) Comparison of Figure 5 with 7 illustrates changes due to rank in both average molecular size and distribution of extracts.

ACKNOWLEDGMENT

We thank Linda Warfel and Daniel Cleaveland for technical assistance, Dr. Karl Vorres for samples, and the Illinois Coal Development Board for financial support through the Center for Research on Sulfur in Coal.

REFERENCES

1 Buchanan, D.H.; Warfel, L.C.; Mai, W.; Lucas, D.; ACS, Div. Fuel Chem., Preprints, 1987 32(1), 146.
2 Kister, J.; Guiliano, M.; Mille, G.; Dou, H.; ACS, Div. Fuel Chem., Preprints, 1987 32(1), 21.
3 Blom, L.; Edelhausen, L.; van Krevelen, D.W.; Fuel 1957 36, 135.
4 a) Hombach, H.P. Fuel 1980, 59, 465. b) Green, T.K.; Kovac, J.; Larsen, J.W. ibid. 1984, 64, 935. c) Larsen, J.W.; Green, T.K.; Kovacs, J.; J. Org. Chem. 1985 50, 4729. d) Matturro, M.G.; Liotta, R.; Isaacs, J.J. ibid. 1985, 50, 5560.
5 Liotta, R.; Brons, G.; Issacs, J.; Fuel, 1983 62, 781.
6 a) Dryden, I.G.C.; Fuel 1951 30, 217. b) Dryden, I.G.C.; in Lowry, H.H., ed.; "Chemistry of Coal Utilization", Suppl. Vol., John Wiley & Sons, New York, 1963, 232.
7 Larsen, J.W.; Lee, D.; Schmidt, T.; Grint, A.; Fuel 1986 65, 595.
8 a) Rhoads, C.A.; Senftle, J.T.; Coleman, M.M.; Davis, A.; Painter, P.C.; Fuel 1983 62, 1387. b) Liotta, R.; ibid 1979 58, 724.
9 a) Solomon, P.R.; Carangelo, R.M.; Fuel 1982 61, 663. b) Painter, P. C.; Starsinic, M.; Squires, E.; Davis, A.; ibid 1983 62, 742.
10 Warfel, L.C.; Bailey, S.; unpublished observations.

Table 1 Analyses of Samples (DAF)

Argonne Sample	%C	%H	%N	%S	%O	% Ash	Solvent Swelling in Toluene	Ethanol	Pyridine
#2[a]	74	5.1	-	0.5	19	8	1.31	1.43	1.68
2-OX[b]	70.68	5.77	0.75	0.28	22.60	10.16	1.61	1.52	1.82
#3	77	5.7	-	5.4	10	16	1.64	1.82	2.31
3-OX	78.09	5.99	1.39	5.52	9.01	16.90	1.51	1.53	2.51
3-Res[c]	76.71	5.84	1.68	6.85	8.92	19.91			
3-OX-Res[c]	76.89	5.55	2.32	6.24	9.00	18.85			
#4	83	5.8	-	1.6	8	9	1.54	1.74	2.76
4-OX	83.31	5.91	1.39	2.26	7.13	10.06	1.56	1.63	2.23
#1	87	5.5	-	2.8	4	13	1.17	1.05	1.31
1-OX	87.29	5.37	1.53	3.00	2.81	11.23	1.59	1.37	1.75
#5	91	4.7	-	0.9	3	5	1.06	1.11	1.10
5-OX	89.72	4.95	1.17	0.21	3.95	4.22	1.02	1.05	1.06

a Preliminary elemental analyses, Dr. Karl Vorres, A N L.
b Air oxidation, ambient temperature and humidity, four months. Elemental analyses for oxidized coals and residues by Galbraith Laboratories, Knoxville, TN. Ash determined by L.C. Warfel, ASTM D 3174.
c Insoluble residue from sequential extraction (Table 2).

Table 2 Sequential Solvent Extraction Yields
Weight %

Argonne Sample	Toluene Extract	THF Extract	DMF Extract	Py Extract	Total Extract	Insoluble Residue	Material Balance
#2	2.16	1.38	1.76	0.34	6.1[a]	91.8	97.9
2-OX	2.35	0.97	3.52[b]	0.54	9.0[c]	86.9	95.9
#3[d]	7.08	7.76	11.40	0.86	27.1	75.5	102.6
3-OX	5.18	5.08	7.38	0.54	18.2	84.8	103.0
#4	5.80	8.18	10.35	0.64	25.0	76.0	101.0
4-OX	5.72	7.78	10.97	1.18	25.6	73.7	99.3
#1[d]	0.58	0.16	12.63	7.56	20.9	77.9	98.8
1-OX	1.12	0.19	17.37	1.45	20.1	76.3	96.4
#5	0.40	0.24	0.25	0.30	1.2	100.2	101.4
5-OX	0.37	0.37	0.48	0.28	1.5	96.3	97.8

a Includes 0.44% material recovered from the MeOH/H_2O wash of the residue.
b An additional 1.20% was recovered from the MeOH/H_2O wash of the extract.
c Includes 0.37% material recovered from the MeOH/H_2O wash of the residue.
d Average of duplicate extractions.

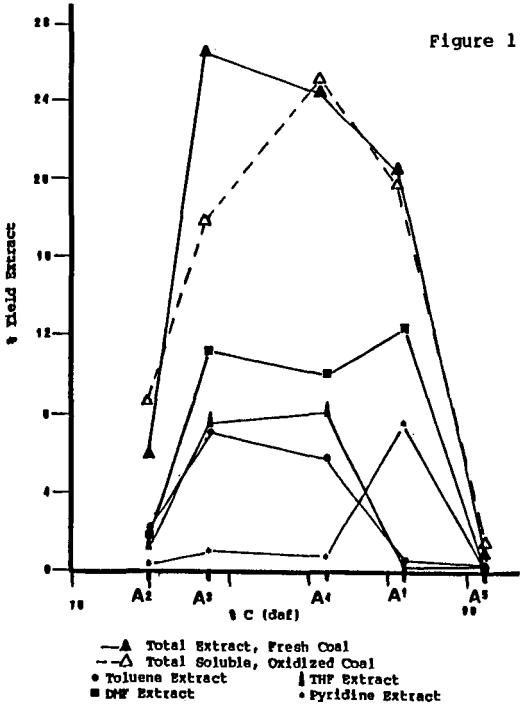

Figure 1 Extraction yield as a function of rank (% C) for Argonne Premium Coals A_1-A_5.

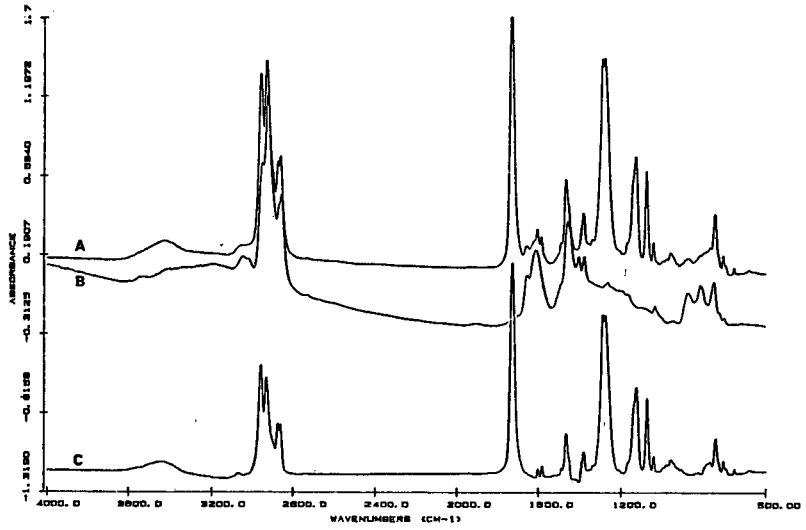

Figure 2 FT-IR spectra of toluene extracts from Argonne #1.
A) Oxidized coal, B) Fresh coal, C) Difference A-B.

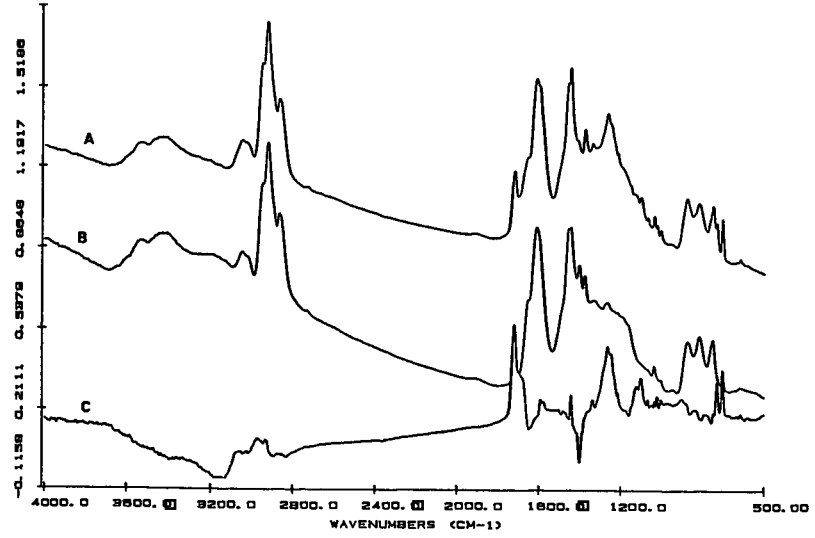

Figure 3 FT-IR spectra of pyridine extracts from Argonne #1.
A) Oxidized coal, B) Fresh coal, C) Difference A-B.

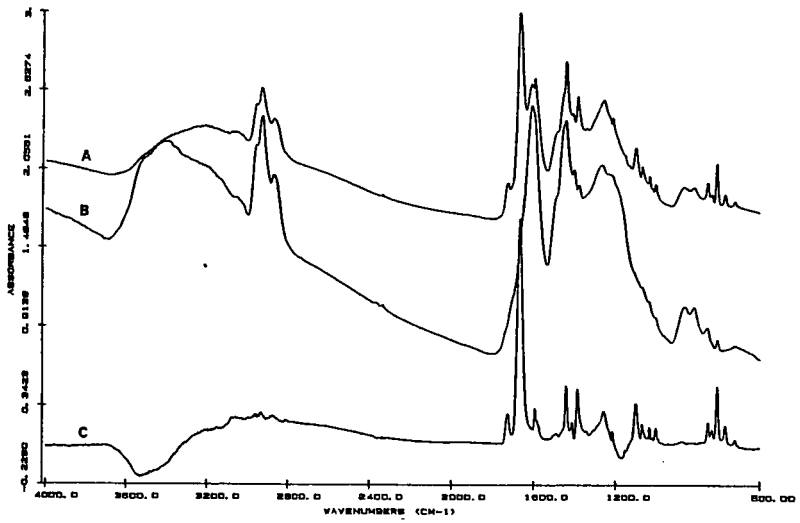

Figure 4 FT-IR spectra of pyridine extracts from Argonne #3. A) Oxidized coal, B) Fresh coal, C) Difference A-B.

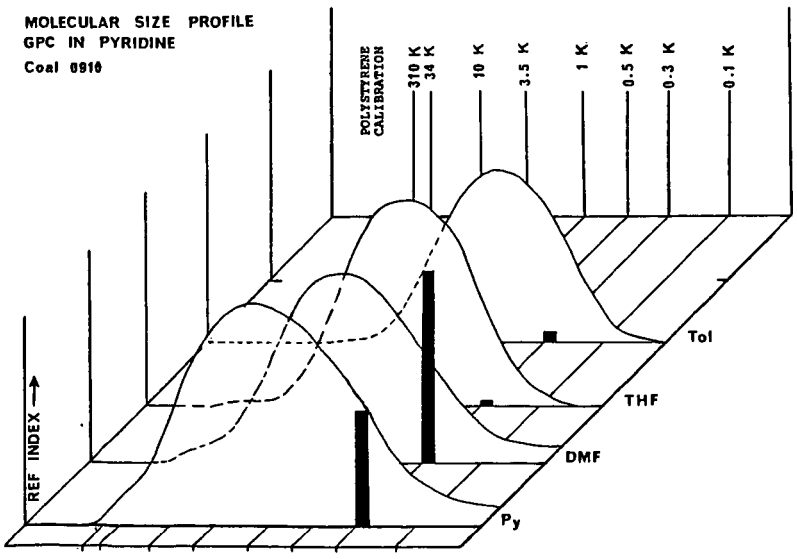

Figure 5 GPC traces from Argonne #1. Vertical bars indicate fraction of total extract removed by indicated solvent.

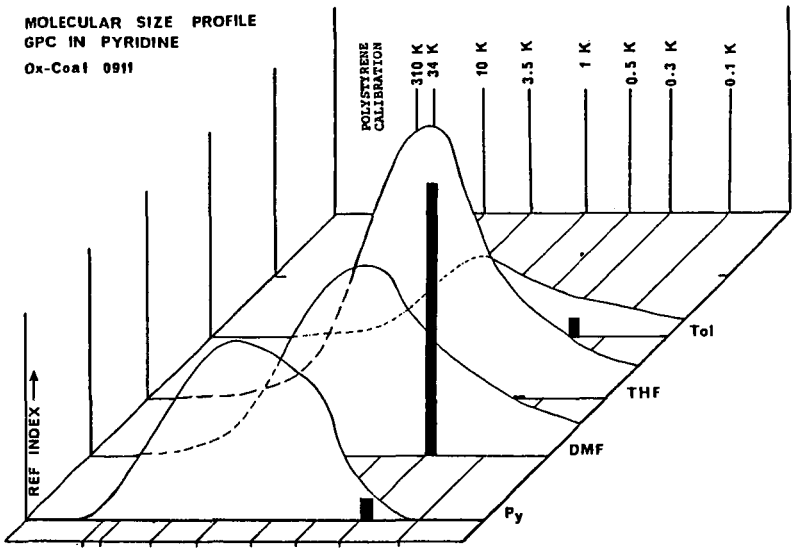

Figure 6 GPC traces from Argonne #1-OX. Vertical bars indicate fraction of total extract removed by indicated solvent.

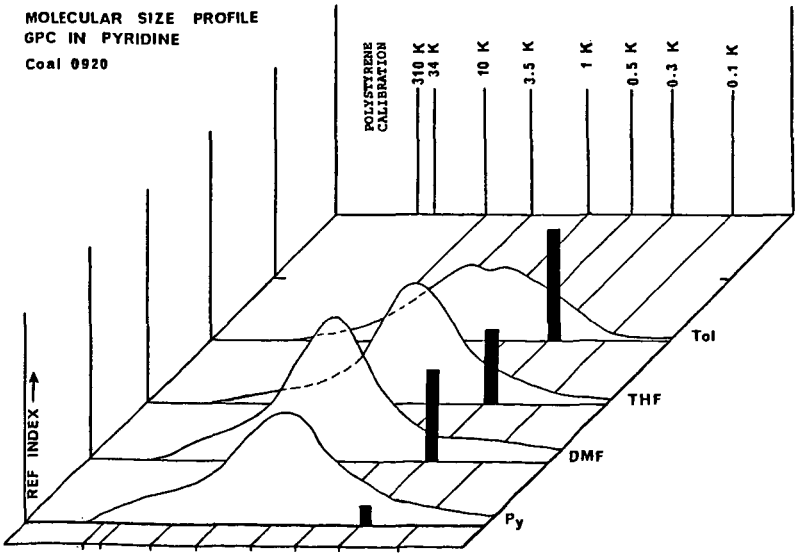

Figure 7 GPC traces from Argonne #2. Vertical bars indicate fraction of total extract removed by indicated solvent.

ATTEMPTED DEVELOPMENT OF A "WEATHERING INDEX" FOR ARGONNE PCSP COALS

Yongseung Yun, Barbara L. Hoesterey, Henk L.C. Meuzelaar and George R. Hill

Biomterials Profiling Center, University of Utah
391 S. Chipeta Way, Suite F, Research Park
Salt Lake City, Utah 84108

INTRODUCTION

It is well known that weathering has a profound effect on many important coal properties such as coking characteristics, slurry pH, flotability, tar yield, extractability, etc., as well as on coal utilization processes such as combustion, pyrolysis, gasification and liquefaction. However, since coal is a very heterogeneous material and its properties differ according to rank and seam, it is very difficult to define reliable standard values for the degree of weathering. Therefore, most methods for determining the degree of weathering provide relative values and have practical usefulness only if measured values can be calibrated against coal samples weathered under carefully standardized conditions. Since fresh samples from several standard coals are now available from the Argonne Premium Coal Sample Program (PCSP) systematic studies of the weathering behavior of these coals have become practical as well as timely.

In the past, many different attempts have been made to measure the degree of weathering of a given coal sample. One of the more obvious approaches is perhaps to determine the oxygen content by oxidative (1,2), reductive (3,4), or pyrolytic methods (5). Alternatively, oxygen content can be measured directly by neutron activation analysis (6). However, the uptake of oxygen by a given coal can be offset to a significant degree by the concomittant loss of CO_2, CO and H_2O (7), thus making the net increase in oxygen content far from easily predictable. Moreover, most oxygen measurement techniques are notoriously time-consuming and unreliable.

Workers in the coke producing industry have known for a long time that caking properties of coal change dramatically upon weathering. Consequently, they have tried to develop simple and practical methods for determining the degree of weathering. Gray et al. (8) suggested an alkali-extraction method as one of several candidates. Lowenhaupt and Gray (9) applied this alkali-extraction method using light transmittance as an index of weathering for high to low volatile bituminous coals. The fact that coal swelling properties change dramatically when a caking coal is weathered presents many potential opportunities for determining the weathering status. Swelling properties of coal can be measured by means of Free Swelling Index (FSI), dilatation, Gieseler fluidity or gas flow resistance tests (10,11). For strongly caking coals FSI is not as sensitive as dilatation or Gieseler fluidity (12,13). In the early stage of weathering, Gieseler fluidity appears to be the most sensitive of the three methods. However, Gieseler values tend to drop to zero after some oxidation time. Under moderate and severe weathering conditions, however, FSI is a good index of weathering, especially in the FSI range between 1 and 4 (14).

Fourier Transform Infrared Spectroscopy is known to show an increase in carbonylic, carboxylic and phenolic groups as well as a decrease of aromatic and aliphatic moieties. Huggins et al. (15) proposed the ratio of reflectance in the carbonyl band region to that in the region of the aromatic and aliphatic C-H stretch bands as a possible weathering index.

Thermal analysis methods, e.g., thermogravimetry (TG), as well as analytical pyrolysis techniques (e.g., pyrolysis MS (Py-MS)) also show a strong response to weathering. Izuhara et al. (16) used the change of maximum weight loss rate in TG

as a weathering parameter, whereas Jakab et al. (17) used time-resolved Py-MS to show that the evolution profiles of several components (carboxylic acids, naphthalenes, methanol, water, etc.) were quite different when coal was weathered.

The Zeta potential of coal particle suspensions in H_2O can also be a good indicator of weathering. Since weathered coal shows poor flotation characteristics, several studies were undertaken to understand this phenomenon in more detail (18-20). In general, weathered coal shows lower Zeta potential values than fresh coal.

Another important feature of weathered coal is its acidic character. Thus, Gray et al. (8) suggested coal slurry pH measurement method as one of several candidate techniques for determinating weathering status. They reported slurry pH changes from 7.1 to 5.5 for fresh and severely weathered Pocahontas #3 coal, respectively. Hill et al. (21) applied this idea to subbituminous (Adaville #6) coal, but added 0.01 wt% surfactant to the slurry in order to enhance the wetting of coal with water. For fresh and moderately weathered (1 to 6 days at 100° C)coals, they reported pH changes from 7.2 to 5.0 and applied this result to coal samples obtained from coal storage piles in order to estimate concomittant btu losses. When coal is exposed to air, oxygen, hydrogen peroxide, nitric acid, potassium permanganate, and other oxidizing agents, mixtures of water soluble acids are formed. For bituminous coal, chromatographic and mass spectrometric studies show that these acids consist mainly of benzoic, phthalic, mellitic and trimellitic acids and their isomers (22). Py-MS results also show an increase of short chain carboxylic acids, e.g., acetic acid, during weathering (23). Moreover, in some cases phthalic anhydrides can be detected by FTIR (24,25) as well as by time-resolved Py-MS (26). If these phthalic anhydrides formed due to weathering can be hydrated to the free acid form, then simple slurry pH measurements can be used as a method of detecting the degree of weathering, as will be shown in this presentation.

Even though some success was reported with the use of slurry pH as an index of weathering, its practical use appeared to be limited to severely weathered coals and some low rank coals. Here we report a modified and improved sample preparation titration method which overcomes these limitations.

EXPERIMENTAL

One to two pound aliquots of 2-4" sized PCSP coals were obtained submersed under water in sealed metal cans. Coals were dried with Drierite in a nitrogen atmosphere overnight and then ground to -60 mesh in a ball mill under nitrogen. Ground coals were transferred to 25 ml polyethylene vials in a glove box filled with nitrogen and stored at -90°C.

Twenty gram aliquots (-60 mesh) of all eight PCSP coals were exposed to a dry air flow (10 ml/min) in a 100 ml glass reactor, at 100°C for 8 days. The Blind Canyon seam coal was weathered for 2, 4, 6 and 8 days in separate glass reactors at 100°C and the Pittsburgh #8 seam coal was weathered at 150°C for 1 and 3 days in order to determine the effects of weathering time and temperature, respectively.

Weathered coal samples were then transferred to a Parr 4745 general purpose digestion bomb. 2.0 g of coal were mixed with 20 ml deionized water and was put in a 23 ml Teflon container and heated to 150°C for 2 hours. Subsequently, the bomb was cooled under tap water for 10 minutes. Next the coal slurry was transferred to a polystyrene beaker for pH measurements. 20 ml of deionized water were used to rinse remaining coal from the teflon container. Resistivity of the deionized water used was more than 16 Meg ohms-cm. pH titrations were performed with a Mettler DL40RC titrator using a 20 ml burette with 0.01 ml titrant (0.01N NaOH) increments.

RESULTS AND DISCUSSION

In earlier weathering studies involving a subbituminous Adaville coal (21), direct pH titration at ambient temperature showed a marked increase in acidity by more than 2 pH units after exposure of the coal sample to air at 100°C for 6 days. However, subsequent pH titration experiments with coals of different rank, including Wyodak (subbit/lignite), Hiawatha (hvBb) and Freeport (mvb) coals gave negative or ambiguous results under the same weathering conditions. Nevertheless, Py-MS analyses of the same coals showed a distinct increase in carboxylic and carbonylic functional groups (23). In subsequent Py-MS studies of the weathering behavior of individual macerals (26), strong signals were noted which appeared attributable to anhydrides of phthalic acid and/or other aromatic acids. This provided us with a possible clue to the observed lack of strong pH changes since anhydride formation would effectively remove the acidic protons. Therefore, an attempt was made to re-hydrate the weathered coal samples before carrying out pH titrations. As described under Experimental, rehydration was carried out at 150°C in teflon-lined Parr bombs. As shown in Figure 1 and subsequent figures this procedure was found to be very simple as well as effective in "restoring" the acidity of all weathered coals investigated thus far. Py-MS analysis of the solution extracted during the rehydration procedure, however, indicated that CO_2^+ fragment from acids and acetic acid were the main products, not phthalic acid. Thus more detailed studies are needed to clarify the chemistry behind this method. Figure 1 further suggests that the initial pH can also be a good weathering index for Utah Blind Canyon coal.

Figure 2 shows the effect of weathering duration on pH and repeatability of the method. Clearly, as coal is weathered, more acidic products are dissolved out and therefore lower pH values are obtained. The small differences between repeat analyses on the same weathered coal may be due to temperature variations of the solution. More precise standardization of the method is planned to overcome this problem.

Figure 3 shows the effect of different coal rank, viz. low volatile bituminous (lvb) to lignite. As expected, lower rank coals produce more acidic products during weathering. The difference in the amount of titrant needed to reach pH 8 between fresh and weathered coals reveals even more clearly the effect of rank. Difference spectra obtained by Py-MS analysis of coals of different rank confirmed this observation by showing that structural changes in mvb Upper Freeport coal were only about 30% of those observed in subbituminous Wyodak coal when weathered at 100°C (23).

Possible depositional effects for four coals of similar rank (hvb) are shown in Figure 4. Profound differences in terms of the initial pH as well as the slope of the titration curve are found. Lewiston - Stockton coal has the highest initial pH. This is thought to be due to major differences in depositional environments. Although Lewiston-Stockton coal and Pittsburgh #8 coal show very similar titration curves the difference of the initial pH is most noticeable. In contrast to these coals, Illinois #6 coal produces the most acidic solution. This may be due to its higher sulfur content (and/or higher surface area) than other coals.

The effect of weathering temperature is shown in Figure 5. Note the dramatic pH difference after only 1 day at 150°C as contrasted to up to 8 days weathering at 100°C. This suggests that the weathering temperature may be the most important variable in weathering.

In conclusion, a simple pH titration method based on rehydrating coal slurries with water at 150°C was proved to be a successful way of monitoring weathering effects in all 8 ANL-PCSP coals. For LVB and higher rank coals, however, slurry concentrations should perhaps be increased to compensate for the decreased

susceptibility to low temperature weathering. Further work is underway to elucidate the structural moieties responsible for the observed differences in the shape of the titration curves. Moreover, detailed characterization of the low MW components extracted by the rehydration procedure is expected to yield important information on the underlying mechanisms of the weathering process.

ACKNOWLEDGEMENTS

The authors thank Dr. Karl Vorres (Argonne National Laboratory) for eight PCSP coals. Dale Urban and John Oestreich are thanked for their help on weathering and titration experiments. The work reported here was supported by DOE contract DE-FG22-84PC70798.

REFERENCES

1. Dolch, M., Will, H, Brennstoff-Chem. 12, 141 (1931).
2. Kimer, W.R., Ind. Eng. Chem., Anal. Ed., 8, 57 (1936).
3. Macara, M.S., Swaine, D.J., Fuel 43 (5), 349 (1964).
4. Spooner, C.E., Fuel 26, 15 (1947).
5. Ignasiak, B.S., Nandi, B.N., Montgomery, D.S., Anal. Chem. 41 (12), 1676 (1969).
6. Berkowitz, N., An Introduction to Coal Technology, Academic Press, 1979, 34-35.
7. Meuzelaar, H.L.C., Hill, G.R., Yun, Y., Windig, W., "Weathering Effects on Structure and Reactivity of U.S. Coals", Third Quarterly Report to DOE, contract no. DE-FG22-84PC70798 (1986).
8. Gray, R.J., Rhoades, A.H., King, D.T., AIME Trans. 260, 334 (1976).
9. Lowenhaupt, D.E., Gray, R.J., Int. J. of Coal Geology, 1, 63 (1980).
10. Kam, A.Y., Hixson, A.N., Perlmutter, D.D., Ind. Eng. Chem., Process Des. Dev. 15 (3), 416 (1976).
11. Boyapati, E., Oates, W.A., Moxon, N.T., Day, J.C., Baker, C.K., Fuel 63, 551 (1984).
12. Cagigas, A., Escudero, J.B., Low, M.J. D., Pis, J.J., Tascon, J.M.D., in J.A. Moulijn and Kapteijn (eds.) Coal Characterization for Conversion Processes, Elsevier, 1987, 245-256.
13. Huffman, G.P., Huggins, F.E., Dunmyre, G.R., Pignocco, A.J., Lin, M.C., Fuel 64, 849 (1985).
14. Hill, G.R., Meuzelaar, H.L.C., Kithany, S. "Free Swelling Index of Utah High Volatile Bituminous Coals" Final Report to Utah Power & Light, UP&L R&D-1003-83 (1983).
15. Huggins, F.E., G.P. Huffman, Dunmyre, G.R., Nardozzi, M.J., Lin, M.C. in J.A. Moulijn and F. Kapteijn (eds.) Coal Characterization for Conversion Processes, Elsevier, 1986, 233-244.
16. Izuhara, H., Tanibata, R., Nishida, S., "Determination of Coal Weathering by Thermogravimetric Analysis", Proc. 1985 International Conf. on Coal Science, Oct. 1985, Sidney, Australia, Pergamon Press, 1985, 491-494.
17. Jakab, E., Windig, W., Meuzelaar, H.L.C., "Time-Resolved Curie-point Pyrolysis Mass Spectrometry of Fresh and Weathered Hiawatha Coal", submitted to J. of Energy and Fuel Research (1986).
18. Kelek, S., Salman, T., Smith, G.W., Canadian Metallurgical Quarterly, 21(2). 205 (1982).
19. Wen, W.W., Sun, S.C., AIME Trans. 262, 174 (1977).
20. Wen, W.W., "Electrokinetic Behavior and Flotation of Oxidized Coal", Ph.D. Thesis, Penn State Univ., Univ. Microfilms ADG77-23287 (1977).
21. Hill, G.R., Meuzelaar, H.L.C., Hoesterey, B.L., "Weathering Losses in Coal Storage Piles", Final Report to Utah Power & Light Co., UP&L-R&D-1011-84 (1984).
22. Volborth, A., Analytical Methods for Coal and Coal Products, Vol. III, Chap. 55, Academic Press, 1979, 543-583.

23. Yun, Y., Jakab, E., McClennen, W.H., Hill, G.R., Meuzelaar, H.L.C., "The Role of Aliphatic and Aromatic Coal Structures and Macerals in Low Temperature Oxidation Processes" ACS Preprints (Div. of Fuel Chem.), 32(1), 1987, 129-137.
24. Painter, P.C., Snyder, R.W., Starsinic, M., Coleman, M.M., Kuehn, D.W., Davis, A., Appl. Spectrosc., 35, 475 (1981).
25. Pandolfo, A.G., Johns, R.B., Nichols, P.D., White, D.C., "Aerial Oxidation of Maceral Isolates from an Australian Bituminous Coal", ACS Preprints (Div. of Fuel Chem.) 32(1), 1987, 171-178.
26. Chakravarty, T., Yun, Y., Meuzelaar, H.L.C., unpublished results.

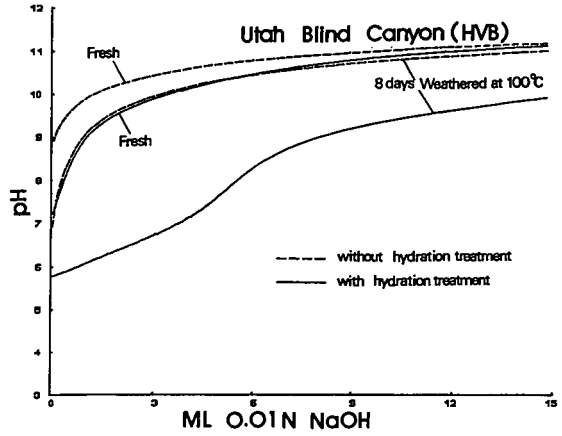

Figure 1. Effect of hydration treatment at 150°C on titration curve.

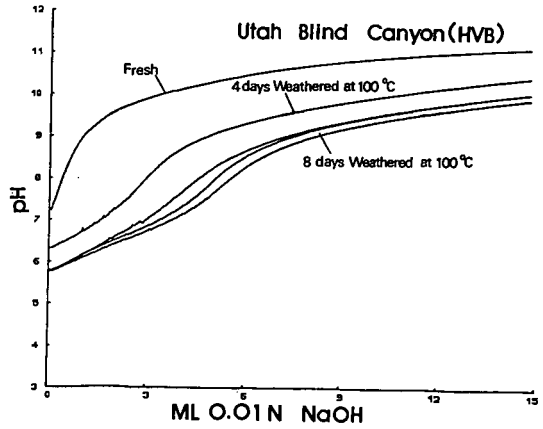

Figure 2. Effect of weathering duration on titration curves. Lower three curves show repeatibility for 8 days weathered coal at 100°C.

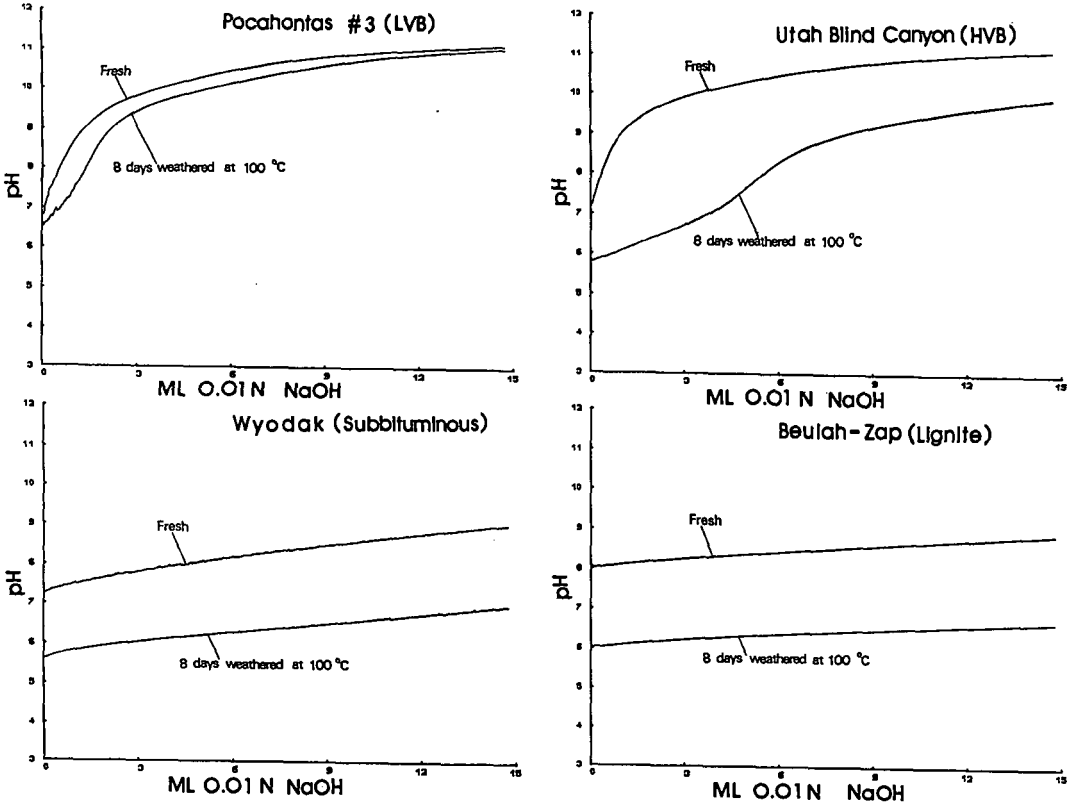

Figure 3. Effect of rank on titration curves.

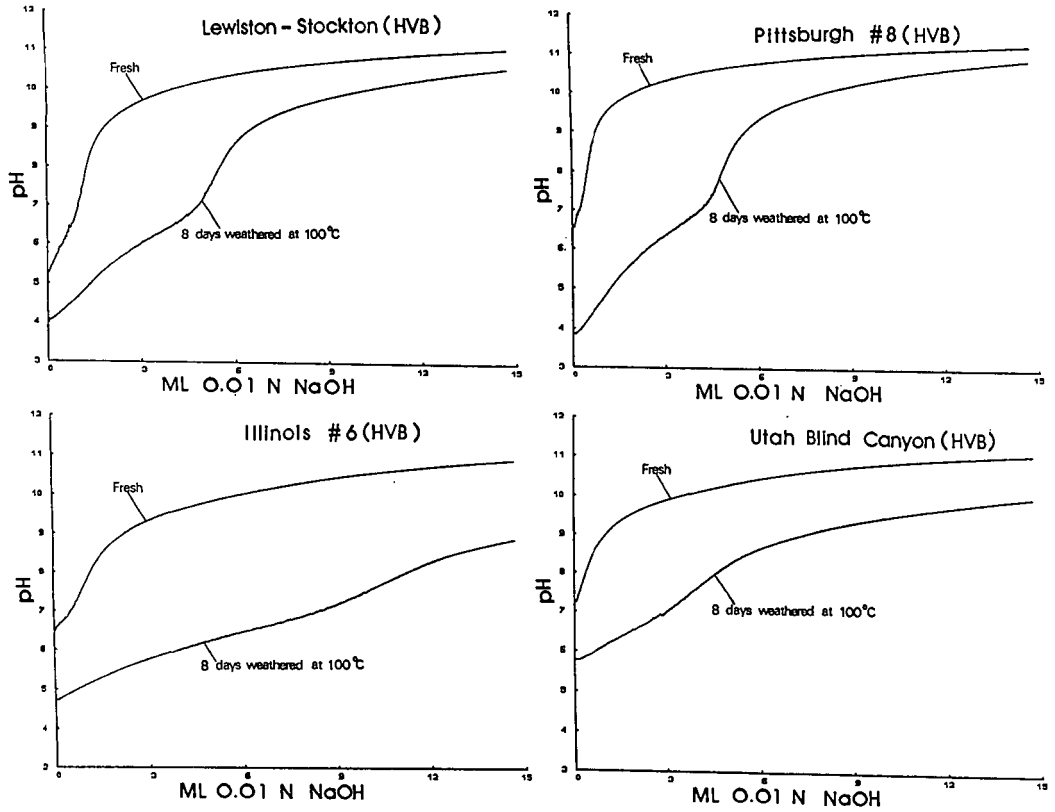

Figure 4. Effect of deposition on titration curves.

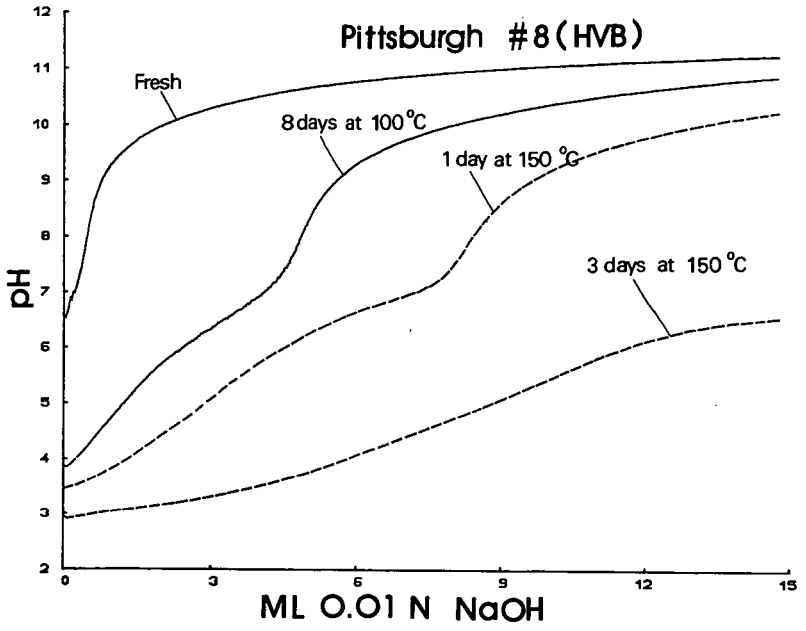

Figure 5. Effect of weathering temperature on titration curves for Pittsburgh #8 coal.

STRUCTURAL INFORMATION FROM THE SELECTIVE METHYLATION OF ACIDIC O-H AND C-H SITES IN AN ARGONNE PREMIUM COAL SAMPLE*

R. Rife Chambers, Jr., E. W. Hagaman and M. C. Woody

Chemistry Division
Oak Ridge National Laboratory
Oak Ridge, Tennessee 37831-6197

INTRODUCTION

With the establishment of the Argonne Premium Coal Sample Program (1), a long-term supply of a limited number of coal samples for basic research has become available to the coal research community. These coals offer the advantage of having been processed and stored under the controlled conditions of relative humidity, temperature, minimum oxygen exposure, etc. Since special care has been taken to insure sample homogeneity, direct inter-laboratory comparisons of experimental results will now be possible. Furthermore, it will now be possible to evaluate the chemical and physical changes which accompany the long-term storage of coal.

RESULTS AND DISCUSSION

Initially, it will be necessary to fully characterize the physical and chemical properties of these samples by a variety of chemical and spectroscopic means. It has been demonstrated that important coal structural information can be established by the application of selective chemical modification reactions to derivatize independently the acidic O-H and C-H sites in coal. For example, it is possible to O-alkylate the phenols and carboxylic acids in bituminous and subbituminous coals by reaction with hydroxide and methyl iodide (2) or methyl tosylate (3). Solid (2c,4) and solution (2b) ^{13}C NMR of coal derivatives prepared with C-13 enriched methylating agents have established that indeed O-methylation of phenols and carboxylic acids does occur. On the other hand, it is apparent that significant C-alkylation also occurs under the phase-transfer O-alkylation procedure developed by Liotta (2). For example, as much as 30% of the chemistry is C-alkylation when Illinois No. 6 hvCb is the coal and the alkylation conditions are tetrabutylammonium hydroxide (TBAH) and methyl iodide in aqueous THF (4). The reasons for this phenomenon have never been established. It could derive from ionization and methylation of highly acidic C-H sites or it may indicate competitive O- and C-methylation of phenoxide salts (5). Whatever the reason(s), the results clearly demonstrate that a 'fine tuning' of the reaction conditions towards exclusive O-alkylation is desirable.

We have found that it is possible to 'fine tune' this O-methylation reaction in favor of carboxyl vs phenolic O-methylation by limiting the amount of hydroxide base and replacing the methyl iodide or methyl tosylate with dimethyl sulfate (6). Specifically, the coal is treated with an excess of TBAH. After a specified time

*Research sponsored by the Division of Chemical Sciences/Office of Basic Energy Sciences, U.S. Department of Energy under contract DE-AC05-840R21400 with the Martin Marietta Energy Systems, Inc.

period (16 h), the excess base is neutralized with HCl. This 'back titration' with acid is monitored, a glass electrode being used to evaluate the pH of the solution. After equilibration, the resulting coal anions are quenched with C-13, C-14 double labelled dimethyl sulfate. The pH dependency of the reaction is evaluated by measuring the total number of introduced methyl groups using C-14 combustion analysis (7). The number of methyl esters in the alkylated coals is defined as the number of hydroxide labile methyl groups measured by hydrolysis (8). Typical results are shown in Table 1 for a nonpremium sample of Illinois No. 6 hvCb. As expected, the degree of methylation is a sensitive function of the solution pH. Over the pH region 2-12, the total number of added methyls increases with an increase in solution pH. More importantly, however, is the observation that the formation of methyl esters is preferred at the lower pH values (pH < 7). This useful property of coal means that the reaction selectivity can be optimized by careful control of the reaction pH. The 'site specificity' of the reaction can be evaluated quantitatively by measuring the ratio, base labile methyls to total methyls. For this particular coal sample, site specificities approaching 70% can be realized when the methylation is carried out at pH 2-7.

An important step in the selective methylation of the acidic C-H sites in coal is the conversion of the phenols and carboxylic acids to their methyl ether and methyl ester derivatives (6,8b,9). This is accomplished by the preparation of a pH 12 O-methyl coal using natural abundance dimethyl sulfate as the methylating agent.

To examine the distribution of acidic C-H sites in coal by selective C-methylation chemistry, the pH 12 O-methyl coal is treated in separate experiments with an excess of the conjugate bases of 9-phenylfluorene (pK_a = 19 in THF (10)), fluorene (pK_a = 22 in THF (10)) and triphenylmethane (pK_a = 31 in THF (10)) as their lithium salts (solvent:THF, T:0°C). After a predetermined neutralization time (68 h, typically), the reaction mixtures are quenched with C-13, C-14 double labelled methyl iodide and the products isolated by a series of organic and aqueous extractions. ^{14}C combustion analysis is used to establish the number of $^{14}CH_3$ groups introduced under each set of reaction conditions. The isolated derivatives are treated sequentially with base and $^{13,14}CH_3I$ a total of three times. Previous work (6,9) has established that repetitive treatments are necessary to achieve exhaustive C-methylation. This observation along with the CP/MAS ^{13}C NMR of serially alkylated coal derivatives suggest the chemistry includes the reaction of structural units containing the $-CH_2-$ group (11).

To facilitate the discussion of the results, we define the number of acidic C-H sites with $pK_a < 19$ as equal to the number of $^{14}CH_3$ groups introduced when 9-phenylfluorenyllithium is the base. The number of acidic C-H sites with $19 < pK_a < 22$ is taken as the difference: number of $^{14}CH_3$ added with fluorenyllithium minus the number of $^{14}CH_3$ added with 9-phenylfluorenyllithium. And finally, the number of acidic C-H sites with $22 < pK_a < 31$ is set equivalent to the difference: number of $^{14}CH_3$ added with trityllithium minus the number of $^{14}CH_3$ added with fluorenyllithium.

The structural information available from the application of this chemical approach is illustrated in Table 2 for an O-methyl low volatile bituminous coal, PSOC 1197 (6). Specifically, we can evaluate the distribution of acidic C-H sites in coal as a function of pK_a. In terms of coal structure analysis, this type of information is particularly useful. Since the pK_a values for C-H groups in a variety of organic compounds have been evaluated (10), we can begin to assign a structure to the reactive structural units. For this particular coal, namely

PSOC 1197, we note that the majority of the C-H sites have pK_a values $19 < pK_a < 22$. This observation suggests that structural types such as indenes and fluorenes as well as those containing C-H bonds adjacent to election withdrawing substituents (e.g., carbonyl) are important structural features in this bituminous coal, while 9,10-dihydroanthracene structural types are absent. The results from the application of these structural probes to one of the coals from the Argonne Premium Coal Sample Program will be presented during the talk.

REFERENCES

1. K. S. Vorres and S. K. Janikowski, Prepr. Pap. Am. Chem. Soc., Div. Fuel Chem., 32(1), 492 (1987).

2. (a) R. Liotta, Fuel, 58, 724 (1979). (b) R. Liotta, K. Rose, and E. Hippo, J. Org. Chem., 46, 277 (1981). (c) R. Liotta and G. Brons, J. Am. Chem. Soc., 103, 1735 (1981).

3. M. Ettinger, R. Nardin, S. R. Mahasay, and L. M. Stock, J. Org. Chem., 51, 2840 (1986).

4. E. W. Hagaman, R. R. Chambers, Jr., and M. C. Woody, Anal. Chem., 58, 387 (1986).

5. H. O. House, Modern Synthetic Reactions, 2nd Edition, W. A. Benjamin: USA, 1972, Chapter 9.

6. R. R. Chambers, Jr., E. W. Hagaman, and M. C. Woody, ACS Advances in Chemistry Series No. 217, 'Chemistry of Polynuclear Aromatics', in press.

7. V. F. Raaen, G. A. Ropp, and H. P. Raaen, Carbon-14, McGraw-Hill: New York, 1968, Chapter 11.

8. (a) L. M. Stock and R. S. Willis, Prepr. Pap. Am. Chem. Soc., Div. Fuel Chem., 30(1), 21 (1985). (b) L. M. Stock and R. S. Willis, J. Org. Chem., 50, 3566 (1985).

9. R. R. Chambers, Jr., E. W. Hagaman, M. C. Woody, K. E. Smith, and D. R. McKamey, Fuel, 64, 1349 (1985).

10. D. A. Bors, M. J. Kaufman, and A. Streitwieser, Jr., J. Am. Chem. Soc., 107, 6975 (1985).

11. E. W. Hagaman, R. R. Chambers, Jr., and M. C. Woody, Energy and Fuels, 4, 000 (1987).

Table 1. Selective O-Methylation of Illinois No. 6 using nBu_4NOH and $^{13,14}(CH_3)_2SO_4$

pH	No. $^{14}CH_3$/100 Coal C		Site Specificity
	Total	Base Labile	
12	4.0 ± 0.4	1.1 ± 0.1	28 ± 5%
7	1.37 ± 0.01	0.90 ± 0.01	66 ± 1%
5	0.90 ± 0.08	0.68 ± 0.05	76 ± 13%
2	0.18 ± 0.02	0.12 ± 0.01	66 ± 14%

Table 2. Selective C-Methylation of O-Methyl PSOC 1197: The Distribution of Acidic C-H Sites as a Function of pK_a

pK_a Range	No. C-H Sites/100 Coal C
$pK_a < 19$	0.06
$19 < pK_a < 22$	1.8
$22 < pK_a < 31$	0

COAL DESULFURIZATION BY PHOTOOXIDATION

Virendra K. Mathur and Usha Govindarajan
Department of Chemical Engineering
University of Nev Hampshire
Durham, NH 03824

ABSTRACT

Oxidative desulfurization of coal has been studied by several workers. These methods primarily involve selective oxidation of organic sulfur to sulfoxide and sulfones, followed by thermal decomposition of the oxidation product.

In this investigation, photooxidation of sulfur functionalities in coal is studied. Finely divided coal, suspended in a solvent, is exposed to radiations of wavelength 300-600 nm using a xenon mercury lamp. The coal sample, is next subjected to hydrolysis to remove the oxidized sulfur from the coal matrix. It is observed that coal desulfurization increased by 7.4%, 3.4%, and 23.7% when coal was photooxidized prior to hydrolysis by water, hydrochloric acid and sodium hydroxide, respectively. Sulfur removed by this technique as sulfonic, sulfurous or sulfuric acid or their salts would be mostly organic in nature.

Introduction

Coal is unquestionably the fuel of the future for the generation of electrical energy but its use gives rise to a number of ecological problems, such as acid mine drainage and air pollution from particulate, sulfur dioxide, and NO_x emissions. Man-made sulfur dioxide and nitrogen oxides emissions in the U.S. are estimated to be over 40 million ton/year. Coal-fired utility power plants account for 55% and 27% of all the man-made sulfur dioxide and nitrogen oxides emissions, respectively in the United States. Sulfur dioxide emissions appear to acidify fresh-water lakes located in acidic soil areas whereas nitrogen oxides emissions appear to kill trees. As U.S. environmental groups become more aware of the tree losses in the Appalachian Mountains, reduction of nitrogen oxides emissions in existing coal-fired utility boilers is expected to be a critical issue.

There are many acid rain control technology options for existing large coal-fired electric utility boilers, namely

(i) switch to low sulfur coal or natural gas,
(ii) coal cleaning,
(iii) flue gas treating,
(iv) limestone injection multistaged burning,
(v) fluidized bed combustion, and
(vi) coal gasification.

The first three options are commercially proven techniques. Coal cleaning reduces only small percent of sulfur as it removes only pyritic sulfur. Sulfur and nitrogen reduction potentials using the flue gas treatment technique are high but the capital and operating retrofit costs are exorbitant. Consequently, there is still a need for an efficient and inexpensive coal desulfurization technique which utility companies could readily use.

In this paper, desulfurization of coal using a photooxidation technique is discussed. Coal samples exposed to radiation of wavelength 300-600 nm using a xenon mercury lamp are subsequently analyzed for sulfur content.

Scientific Rationale for Photo Desulfurization of Coal

Coal is a highly heterogeneous solid originating from plant remains. It contains, in varying amounts, essentially all elements of the periodic table combined into nearly all of the minerals normally present in the earth's crust. In other words, coal is a complex mixture of organic and inorganic compounds in which the organic matrix comprises most of the coal weight. Organic coal matrix can be viewed as a complex macromolecular structure containing the classical organic functional groups such as carbonyl and hydroxyl, aromatic and heterocyclic ring units, and aliphatic bridges.

Coal structure and processing have been the subject of intense research for several years. The exact chemical structure of organic coal matrix varies and is not completely understood. However, enough information is available on the nature of sulfur containing functional groups in organic coal matrix. The organic sulfur in coal can be categorized into one of the functionalities such as thiol, sulfide, disulfide, thiophene, benzothiophene, and dibenzothiophene.

Desulfurization of coal has been investigated by several workers (1,2). They have used techniques such as oxidation (3-6), chlorinolysis (7-8), electrolysis (9), etc. All these methods essentially oxidize sulfur in coal. There are other methods reported in the literature involving hydrogenolysis, hydrolysis, etc. It is observed that among the organic sulfur functionalities, removal becomes increasingly difficult in the order thiolic < sulfide < disulfide < thiophenic < benzothiophenic < dibenzothiophenic. As the complexity of the sulfur containing functionality increases the selectivity of desulfurization, without affecting the rest of the coal matrix, becomes difficult. For example, the selectivity of hydrodesulfurization is reduced whenever the n-electrons of sulfur are in resonance with π-electrons as in the cases of thiophene, benzothiophene, etc. This leads to competing hydrogenolysis of the carbon-carbon bonds since the energies of carbon-sulfur and carbon-carbon bonds become practically identical due to resonance (10). It has been reported that atmospheric weathering leads to desulfurization of coal which can be due to the combined effect of air oxidation and photo-oxidation. However, the authors have not presented any mechanism or photonic role for this process (6).

It has been suggested that accompanying the oxidation of the sulfur to sulfone, the bond energy between the carbon and the sulfur is reduced on the average by 5.2 kcal/mole for aliphatic sulfides and by 11.8 kcal/mole for aromatic sulfides and thiophenes. Thus, the selectivity of decomposition at the sulfur-carbon bond is increased (3).

Oxidative desulfurization of coal has been studied by several workers (1-8). These methods primarily involve two steps: (1) selective oxidation of organic sulfur to sulfoxide and sulfones as shown below and (2) thermal decomposition of the oxidation product expelling sulfur dioxide.

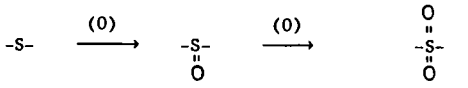

Sulfoxide Sulfone

Photo-oxidation of Sulfur in Coal

No work is reported on the photochemical oxidation of coal. It is important to understand how the coal molecule would react in the presence of light and air. Coal due to its strong absorption of the entire visible spectrum has black color. It is also well known that coal has a complex aromatic structure with polyaromatic nuclei capable of absorbing light in the visible region. Attached to these are the sulfur atoms. The n-electrons on sulfur can resonate with the aromatic π-cloud. Hence, in the presence of light the n,π* transition is also feasible which would affect the bonding properties of sulfur. This might lead to either electron deficient sulfur linkage or formation of diradical or free radicals. Due to the complexity of coal structure it is difficult to theoretically predict the exact course of reaction from the excited state.

There is enough literature evidence that oxygen in air attacks the organic sulfur compounds photochemically (11). Extending the mechanism of photo-oxidation of sulfur compounds to coal, two courses of reaction can be predicted. One of them could be the formation of free radical/diradical center at sulfur from the excited coal molecule and subsequent oxidation and hydrogen abstraction leading to oxidized sulfur functionalities such as sulfonic acid. The second one would be the attack of sulfur center by excited molecular oxygen, namely, singlet oxygen, if the reaction conditions are conducive to the production of singlet oxygen. Either of these mechanisms would cause the formation of sulfoxides, sulfones or sulfonic acids depending upon the reaction conditions. Hence, it is safe to predict that the organic sulfur functionalities in coal could be oxidized in the presence of oxygen and visible light.

By this photo-oxidation treatment the sulfur in coal would remain in an oxidized form. The next step would then be to eliminate the oxidized sulfur from the coal matrix. This can be achieved by subjecting the photo-oxidized coal to hydrolysis. This procedure is reported to be used in other chemical desulfurization techniques also. It is envisaged that most sulfur removed by this technique as sulfonic, sulfurous or sulfuric acid or their derivatives would be organic in nature.

Experimental Set-up and Procedure

Finely crushed coal was suspended in 95% ethanol and kept agitated by bubbling oxygen at such a rate that the coal particles were not allowed to settle down. Also, oxygen bubbling would facilitate the removal of sulfur by oxidation. The coal slurry was subjected to photolysis in an internally lighted reaction vessel. Methylene blue was used as a sensitizer for the production of singlet oxygen. The photo-oxidized coal was washed thoroughly with ethanol to remove the dye and the ethanol was separated by centrifugation. Next, the coal was dried at 110°C for 8 hours. A portion of the photo-oxidized coal was subjected to hydrolysis either in boiling water or by refluxing with solutions of HCl or NaOH. Reference coal was also hydrolyzed with water, acid or base under the same conditions employed for photolysed coal in order to study the effect of photolysis. The samples were analyzed for their sulfur contents. The experimental conditions are summarized in the following Table 1.

Table 1: Experimental Conditions

Coal	Illinois No. 6, Bituminous		
Slurry Concentration	2% in coal and 0.1% in methylene blue		
Hydrolysis Conditions	2% in coal; reflux; 6 h.		
Parameters	Set I	Set II	Set III
Particle Size	74 micron	44 micron	44 micron
Solvent	95% Ethanol	95% Ethanol	95% Ethanol
Reactor	Internal	Internal	Internal
Sensitizer	Methylene Blue	Methylene Blue	Methylene Blue
Radiation	350-550 nm	300-600 nm	300-660 nm
Light Intensity	45 Watts	450 Watts	450 Watts
Reaction Time	10 h.	16 h.	16 h.
Hydrolysis Medium	Water	1 N HCl	1 N NaOH

Results and Discussion

The sulfur contents of the coal samples are presented in Table 2.

Table 2: Sulfur Contents of Coal Samples

Sample	Set I			Set II			Set III		
	Run 1	Run 2	Mean	Run 3	Run 4	Mean	Run 5	Run 6	Mean
Reference	3.92	3.86	3.89	4.56	4.51	4.54	4.56	4.51	4.54
Light Unhydrolysed	3.83	3.80	3.82	4.65	4.45	4.55	4.65	4.45	4.55
Dark Hydrolysed	3.66	3.77	3.72	3.88	3.94	3.91	4.18	4.50	4.34
Light Hydrolysed	3.45	3.42	3.44	3.88	3.60	3.74	3.32	3.22	3.27

Table 3: Percent Sulfur Reduction

Reaction	Set I	Set II	Set III
Dark Hydrolysis	4.5	14.9	4.2
Light Hydrolysis	12.0	17.4	27.8
Photonic Advantage	7.4	3.4	23.7

The desulfurization based on total sulfur is on the average higher by 7.4% (Set I, Table 3) when hydrolysis is conducted by refluxing with water if coal is subjected to photolysis prior to hydrolysis. In other words, the desulfurization increased by about 7.4% as a consequence of photooxidation. It is also seen from Table 3 that photonic advantage increased on the average by 23.7% (Set II) if hydrolysis is conducted in boiling sodium hydroxide solution. However, with acid hydrolysis the photonic advantage is very low (3.4%; Set II, Table 3).

The probable mechanism of desulfurization is the oxidation of some of the organic sulfur functionalities such as sulfide and thiol to sulfoxides, sulfones and sulfonic acids and subsequent hydrolysis of these functional groups. A strong base such as sodium hydroxide would eliminate sulfinic acid from the sulfones and with some difficulty from the sulfoxides while hydrochloric acid would convert the sulfoxide to the original sulfide. It is to be noted that pyritic sulfur would also be affected by hydrolysis though the photolysis might not have significant influence on the removal of pyritic sulfur.

Conclusions

These results show a definite photonic advantage in desulfurization of coal. However, the understanding of the mechanism of desulfurization, nature of functional groups that are affected by photolysis, role of pyrite in modifying the excited state reactivities, influence of reaction medium and optimization of desulfurization conditions need further study.

Acknowledgment

This study was funded by the Solar Energy Research Institute, U.S. Department of Energy, Golden, Colorado 80401.

References

1. R.A. Meyers, "Coal Desulfurization", Marcel Dekker, Inc., NY, 1977.

2. R.C. Eliot (Ed.), "Coal Desulfurization Prior to Combustion", Noyes Data Corporation, 1978.

3. A. Attar, and W.H. Corcoran, Ind. Eng. Chem. Prod. Res. Dev., 17(2), 103 (1978).

4. D.J. Boron, and S.R. Taylor, Fuel, 64, 210 (1985).

5. L. Lompa-Krzymien, Fuel, 61, 871 (1982).

6. D. Chandra, J.N. Chakrabarti, and Y.V. Swamy, Fuel, 61, 204 (1982).

7. N.P. Vasilakos, and W.H. Corcoran, Fuel, 62, 1112 (1983).

8. N.P. Vasilakos, and C. Gage, Fuel, 65, 593 (1986).

9. S. Lalvani, M. Pata, and R.W. Coughlin, Fuel, 65, 122 (1986).

10. A. Attar, and W.H. Corcoran, Ind. Eng. Chem. Prod. Res. Dev., 16, 168 (1977).

11. K. Gollnick, "Advances in Photochemistry", ed. W.A. Noyes, Jr., G.S. Hammond, and J.N. Pitts, Jr., Interscience Publisher, NY, 1968, Vol. 6, pp. 109-111.

THE EFFECT OF HEATING RATE AND HOLD TIME ON PRIMARY COAL PYROLYSIS PRODUCT DISTRIBUTION

Jon Gibbins-Matham and Rafael Kandiyoti

Department of Chemical Engineering and Chemical Technology,
Imperial College of Science and Technology, London SW7 2AZ, England

Introduction

The study of primary pyrolysis reactions in coals is complicated by the number of secondary effects that must be considered. In particular, secondary volatile-cracking reactions are likely to occur with most pyrolysis techniques for low heating rates (eg. Fischer Assay, Gray-King, thermobalance), which use a relatively large coal sample and allow the volatiles to remain in the heated zone for extended periods. A well-dispersed sample of fine coal must, however, be used to achieve high heating rates (eg. as in a fluidised bed or wire-mesh reactor). This has made it impossible to determine whether the increases in volatile yields noted in many fast heating rate studies (probably the best-known of which is the work by Howard and associates at MIT using a wire-mesh apparatus (1)) were due entirely to a reduction in secondary char-forming reactions, or were at least in part an effect of the heating rate itself. The MIT apparatus used a pulse of direct current to heat the sample holder and the lowest heating rate that could be obtained was about 100 K/s; in any case slow heating experiments might also have been affected by secondary reactions, because volatile products were allowed to circulate freely in the same vessel as the hot wire-mesh. Both of these problems have been addressed, though not always together, in subsequent studies (eg. 2,3,4,5,6), but a systematic examination of the effect of time/temperature history under conditions where secondary reactions would be at a minimum appears to be lacking. It was therefore proposed to construct a wire-mesh apparatus which could cover virtually any time/temperature history and provide for rapid removal of volatile products as part of a study on fundamentals of coal pyrolysis and hydropyrolysis funded by the UK Science and Engineering Research Council (GR/D/06582). Although work has concentrated on British coals, the wealth of published data available for US coals made it essential to test some of these for comparison. These trials, with samples from the Argonne Premium Coal (APC) Sample programme, have shown a general increase in volatile yield with heating rate that does not appear to be due to secondary effects. This suggests that more complex interactions occur in pyrolysis than has sometimes been considered.

Sample preparation

To avoid loss of particles through the wire-mesh sample holder all coals were screened to 100-150 microns. The Pittsburgh#8, Illinois#6 and Pocahontas#3 samples were all obtained as -100 mesh and were screened without further treatment. The Wyoming subbituminous sample was originally -20 mesh and was ground gently by hand in air to all pass through a 150 micron sieve. After screening, coals were dried overnight at 105°C in a nitrogen-purged oven and stored under nitrogen until required. A large amount of fines had to be rejected from all the original samples; this would seem to be a general problem for any experiment requiring sieved coal as it may result in selective enrichment with certain petrographic constituents. An agreement to establish standard sub-fractions of sized coal would be welcome.

Apparatus and experimental procedure

Principal features of the apparatus, shown in Fig.1, are a sweep gas flow through the wire-mesh sample holder and a feedback temperature control system using alternating current. The sweep gas, helium flowing at 0.1 m/s, gives a mean volatile residence time within the sample holder of less than 2 ms. Five to ten milligrams of coal are spread in a 12 mm diameter circle at the centre of the sample holder, less than monolayer loading. The sample temperature is defined as the average from two chromel/alumel thermocouples, at the centre and approximately 1mm from the edge of the coal sample, formed from wires inserted through the mesh. Typically, temperatures across the sample are within 20 K of the average and the average is less than 10 K (or 20ms in time at high heating rates) from the target control value. Tar can be caught in a pre-weighed sinter trap cooled with liquid nitrogen which is then heated to 50°C for 30 minutes in air and re-weighed. More details of the apparatus will be available elsewhere (7).

Results and discussion

Fig.2 shows variations with peak temperature in total volatile yields from Pittsburgh#8 coal at 1000 K/s and 1 K/s with zero hold time, and at 1000 K/s with 30 seconds hold time. The reactor geometry, gas flow rate etc. are identical for all runs. With zero hold time, volatile yields for the two heating rates follow different trends, and the higher heating rate yield is below that for slow heating up to about 700°C, after which the 1 K/s yield reaches a plateau at about 42% while the 1000 K/s yield continues to rise to about 48% at 950°C. It could thus be concluded that increasing the heating rate would give either lower or higher yields depending on the peak temperature. At 30 seconds' hold, however, the volatile yields for the two heating rates follow similar trends, and the higher heating rate gives greater weight losses at all temperatures above 400°C. This suggests that provided pyrolysis reactions are allowed to run to completion higher heating rates give higher primary volatile yields.

Runs with Pittsburgh#8 at 1,10,100 and 1000 K/s to 700°C with 30 seconds' hold using tar trapping, plotted in Fig.3, confirm the trend of higher volatile yields with faster heating and indicate that the rise in total volatile yields is due mainly to an increase in tar production. Such differences might be caused by more rapid removal of tar by gas entrainment at the higher heating rates, leaving less time for char-forming reactions. Experiments under vacuum at 1 K/s and 1000 K/s to 700°C were therefore made, with the expectation that if evaporation was a limiting step at low heating rates the 1 K/s yield would increase by more than the 1000 K/s yield. In fact the opposite was observed: the 1 K/s volatile yield increased by about 2% while the 1000 K/s yield went up by about 4%. Under vacuum the 1000 K/s samples swelled much less, suggesting that some plasticising/swelling agent was being removed. The 1 K/s samples never swelled, but were fused. It was also considered that slow heating might be allowing time for slight oxidation of the sample by adsorbed gases, or even the trace of oxygen (less than 2 vpm) in the helium gas supply, and that this enhances subsequent tar-precursor polymerisation reactions. Trials on a UK coal indicate, however, that pyrolysis yields at both high and low heating rates are not sensitive to the level of trace oxygen in the sweep gas.

Comparison with published data for Pittsburgh#8 coal (1,4,8), mostly for 1000 K/s and zero hold, showed that while the maximum volatile yields above 800°C were comparable, reported variations in yield with

temperature fell both above and below the zero hold line in Fig.2. Since the cooling rate in these previous experiments varied from about 10^2 to 10^4 K/s its effect was examined but, as Fig.4 shows, at 600°C yields are not sensitive to cooling rate above 100 K/s. Subsequent experiments demonstrated that the hold time at 600°C is an important factor, however, and the results in Fig.5 show that one second suffices for almost complete devolatilisation. This, together with the steepness of the Fig.2 1000 K/s zero hold curve around 600°C, suggests that experimental variations in the time that the coal is held at 600°C or above are more important than the length of time spent at lower temperatures during cooling. Uncertainties in temperature measurement are possible in cases where, to avoid interference from the heating current, the thermocouple had to be electrically isolated from the sample holder (1) or the junction placed away from the surface (4). The local effect of the thermal inertia of the coal sample itself, reported by Freihaut and Seery (8), could also lead to the temperature being overestimated by perhaps as much as 100°C if the loading near the thermocouple was not representative. As far as possible these errors have been minimised in this apparatus since the sample holder is part of the thermocouple circuits and the coal sample is held around the thermocouples. The temperature of the coal is not, and cannot, be measured directly, however, nor can variations in temperature away from the thermocouples be detected, so experimental scatter can still be significant in regions where yield is a sensitive function of temperature. This is not the case for the conditions used to establish the effect of heating rate as Fig.2 shows, and it is therefore unlikely that errors in temperature measurement could be responsible.

Volatile yields from Illinois#6 and Wyoming subbituminous coals were also found to increase with heating rate, but the yield from the Pocahontas#3 sample showed little or no variation. Results for heating rates between 1 and 1000 K/s are shown in Fig.6.

Conclusions

When secondary effects are minimised, an increase in heating rate from 1 to 10^3 K/s will increase pyrolysis yields from a number of coal types provided that sufficient time is allowed at peak temperatures. The extra volatiles are mainly tars, suggesting either a reduction in polymerisation reactions among tar precursors and/or an increase in tar precursor production due to a greater concentration of reactive species within the coal mass. One coal tested showed little or no effect of heating rate, however, and this, together with the absence of more abrupt variations in volatile yields with heating rate for the other coals, probably means that only a portion of the potential volatile-forming pathways in coals are being affected.

References

1. Howard, J.B., in Chemistry of Coal Utilization, 2nd supplement, (Ed. Elliot, M.A.), Wiley, NY, 1981
2. Freihaut J. D. & Seery, D. J., ACS DFC Prepr. 28(4), 1983, 265-277.
3. Hamilton L. H., Fuel 60, 1981, 909-913.
4. Niksa S. J., Ph.D thesis, Princeton, NJ, 1982.
5. Arendt, P. & van Heek, K., Fuel 60, 1981, 779-787.
6. Stangeby P. C. & Sears P. L., Fuel 60, 1981, 131-135.
7. Gibbins-Matham J. R., Ph.D thesis, Imperial College, London, 1987 (in preparation).
8. Suuberg, E. M., Unger P. E. & Lilly, W. D., Fuel 64, 1985, 956-962.
9. Freihaut J. D., Zabielski M. F. & Seery D. J., ACS DFC Prepr. 28(5), 1983, 89-98.

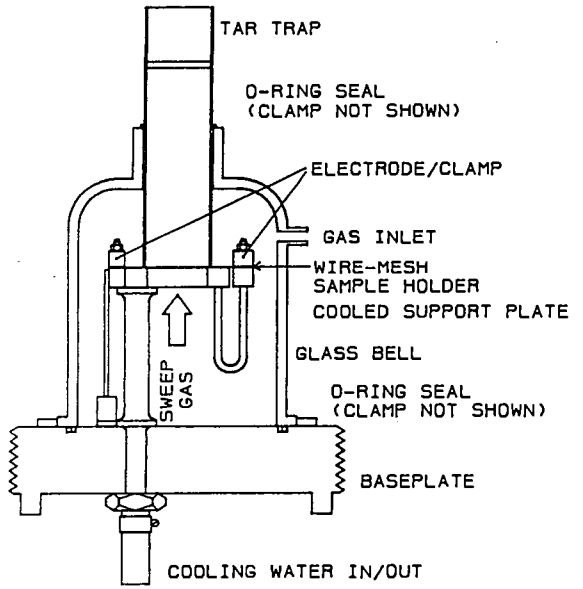

FIG.1 WIRE-MESH APPARATUS

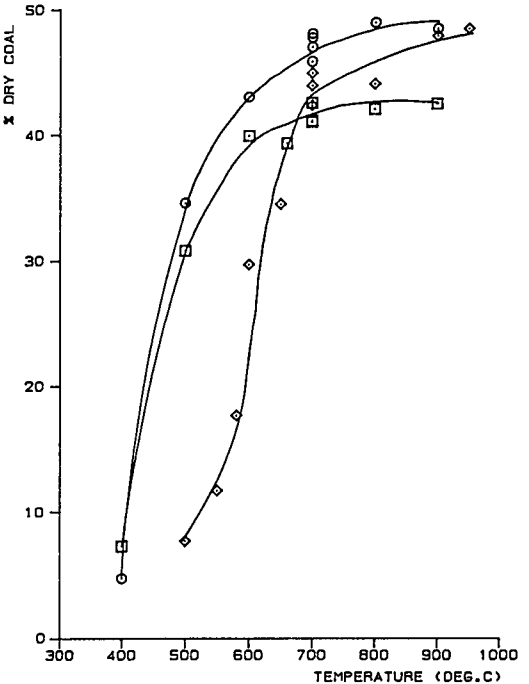

FIG.2 PYROLYSIS YIELDS FROM PITTSBURGH#8
EFFECT OF TIME/TEMPERATURE HISTORY

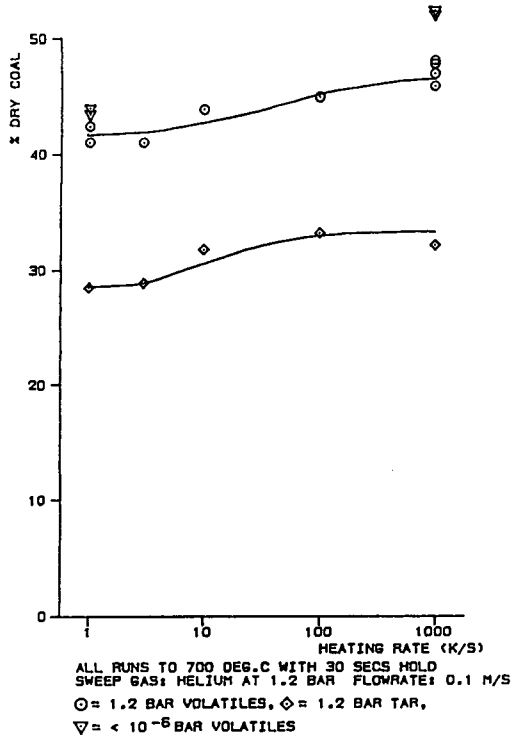

FIG.3 PYROLYSIS YIELDS FROM PITTSBURGH#8
EFFECT OF HEATING RATE AND PRESSURE

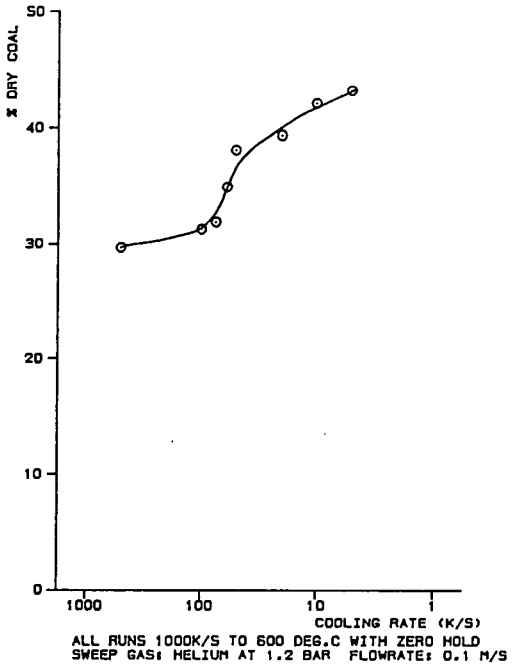

FIG.4 PYROLYSIS YIELDS FROM PITTSBURGH#8
EFFECT OF COOLING RATE FROM 600 °C

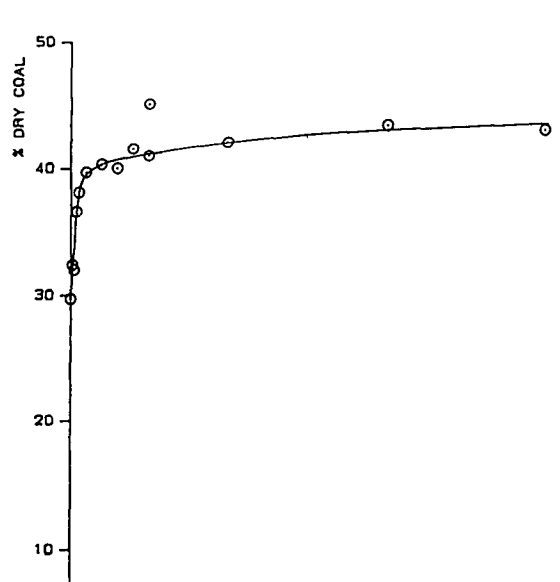

FIG.5 PYROLYSIS YIELDS FROM PITTSBURGH#8
EFFECT OF HOLD TIME AT 600 DEG.C

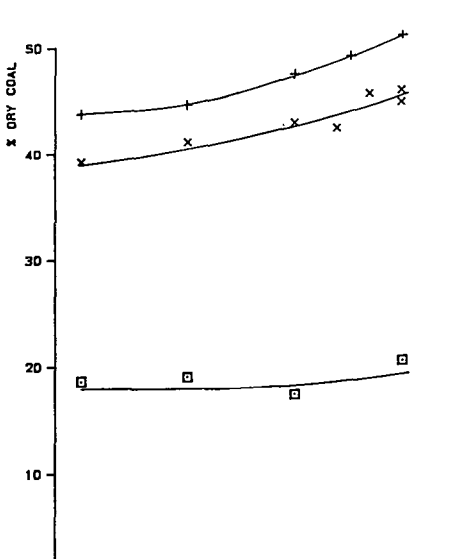

FIG.6 EFFECT OF HEATING RATE ON VOLATILE YIELDS
FROM ARGONNE PREMIUM COAL SAMPLES

SPECTROSCOPIC CHARACTERIZATION OF ARGONNE PREMIUM COALS AND SHORT RESIDENCE TIME LIQUEFACTION PRODUCTS

James A. Franz, Mikhail S. Alnajjar, and John C. Linehan

Pacific Northwest Laboratory
P. O. Box 999
Richland, Washington 99337

ABSTRACT

Illinois No. 6 (high volatile bituminous) , Pittsburgh No. 8 (bituminous), Wyoming Subbituminous, Pennsylvania Upper Freeport (medium volatile bituminous) and Pocahontas #3 (low volatile bituminous) coals from the Argonne Premium Coal Sample Program were heated in tetralin for 10 minutes at 430 ±5° C. The products were examined by gel permeation chromatography and ^{13}C NMR spectroscopy. Yields for conversion of the coals to THF-soluble products were determined. Yields and GPC characteristics of products from direct extraction of the coals with THF were determined. The most reactive coal in this group, based on conversion to products below MW 600, appears to be Wyoming subbituminous.

INTRODUCTION

The availability of pristine coal samples from the Argonne Premium Coal Program now makes possible the meaningful comparison of experimental results of spectroscopic studies and reactions between laboratories. In previous work with medium-rank coals, we have examined the structural evolution of thermal degradation products by NMR and gel permeation chromatography (GPC) techniques, and we have characterized the processes of hydrogen transfer and exchange under liquefaction conditions using deuterium labeling techniques(1-3). In this paper we present results of a study of the molecular weight distributions of products liberated from a short (10 minute) exposure of five of the premium coals to thermal decomposition in tetralin at 430 °C, and results of ^{13}C NMR characterization of the fractionated products.

EXPERIMENTAL

Coals. The five coals examined in this study were Pennsylvania Upper Freeport medium volatile bituminous coal (Penn UF), coal ID 101; Wyoming subbituminous coal (WYO), coal ID 201; Illinois No. 6 high volatile bituminous (Ill #6), coal ID 301; Pittsburgh #8 bituminous coal (Pitt #8), coal ID 401; and Pocahontas

*This work was supported by the Office of Basic Energy Sciences, U. S. Department of Energy, under Contract DE-AC06-76RLO 1830.

#3 low volatile bituminous coal (Poc #3), Coal ID 501.

Extraction of Coals with THF. The five coals (4-5 g each) were washed with three 100 mL portions of tetrahydrofuran (THF). The THF solution was filtered through a 0.45 micron Millipore type FH filter, concentrated, weighed, and examined by GPC and NMR.

Reactions of Coals with Tetralin. The reactions of the coals with tetralin were carried out in 3-mL stainless steel vessels described previously.[1] Tetralin (2 mL) and coal (1 g) were added, and the tube was heated for 10 minutes at 430±5 °C in a Tecam SBS-4 fluidized sand bath. The tubes were opened and washed out with THF. The THF solution and solids were filtered with a 0.45-micron type FH Millipore filter. The residue was air dried and weighed. The THF solution containing the coal products and reaction solvent (tetralin and naphthalene) were concentrated on a rotary evaporator to ca. 20 mL and pipetted into ca. 400 mL of hexane, resulting in the precipitation of brown flakes of the coal product. The THF-soluble, hexane-insoluble product (preasphaltenes and asphaltenes (P+A)) was weighed and examined by GPC and NMR spectroscopy. Occasionally, incomplete removal of tetralin and naphthalene occured. In these cases, the P+A fraction was redissolved in THF and reprecipitated from hexane. THF oxidation products were occasionally encountered, and were removed by precipitation of a THF solution of the P+A fraction by adding ca. 5-ml of the THF solution to about 100 mL water, which removes the water-soluble THF-associated impurities. For examination of the whole coal reaction mixtures by GPC, reaction tubes were washed out with THF, filtered, and examined directly by GPC.

Gel Permeation Chromatography of P+A, Whole Reaction Mixtures and THF Extracts. Gel permeation chromatography was carried out using one 500Å and one 100Å Waters Associates μStyragel® column in series, eluting with THF at a flow rate of 1.0 mL/min. The system was calibrated with polystyrene standards from 600-17500 MW and with a variety of low molecular weight compounds below MW 400.

^{13}C NMR Spectroscopy of Preasphaltenes + Asphaltenes (P+A). ^{13}C NMR spectra of the THF-soluble P+A fractions were determined with a Varian VXR-300 operating at 75 MHz. Approximately 250 mg of P+A fraction was dissolved in 3.0 mL THF-d_8 containing 0.1 M $Cr(acac)_3$. Spectra were acquired using a 90° pulse, 0.8-s acquisition time and a 3-s pulse delay with inverse gated decoupling. The use of 3% $Cr(acac)_3$ with inverse gated decoupling has been reported(4) to produce quantitative results for SRC-II liquids with negligible change in aromaticity (f_a) for pulse delays beyond 4 seconds, and an increase in measured f_a of less than 2% between pulse delays of 2 and 5 seconds. To obtain aromatic/aliphatic ratios, the integral of the 50-10 ppm region obscured by the upfield THF-d_8 multiplet was corrected using the integral of the downfield 67.4 ppm THF peak and a carefully determined integral ratio of the two multiplets of the spectrum of a solution of $Cr(acac)_3$ in THF-d_8. The values of f_a must be considered qualitative since the error for this procedure is probably 5-7%, while the error in the distribution in aromatic structure is lower.

RESULTS AND DISCUSSION

Direct extraction of the coals (Table I) produced 2-12% of THF-soluble product. Ill #6 is unique in its high solubility, whereas the other coals are

normal, exhibiting 2-4% solubility. The bulk of the directly extractable material clearly is of low molecular weight, with 60-90% below MW 600. Ill #6 and Pitt #8 give noticeably greater amounts of material above MW 600 than the other coals (Figure 1).

Reaction of the coals with tetralin for 10 minutes at 430° C produced yields varying from 3% for Pocahontas #3 to 56% for Pittsburgh #8. The yields from the 10-minute reactions are qualitatively in agreement with rank for the various coals. Total conversions are higher for Wyoming subbituminous, Pittsburgh #8, and Illinois #6. Notice in Table II that while Wyoming subbituminous exhibits the highest conversion, it produces only 25% preasphaltenes and asphaltenes. This means that up to 50% of Wyoming subbituminous is converted to hexane solubles (transfer loss and loss of volatiles is included in this upper estimate), making the Wyoming subbituminous by far the most readily converted coal in this group. The difference between conversion and P+A (%) in Table II is the yield of hexane solubles plus transfer loss and water loss, etc. Thus, hexane solubles may be produced in up to 8% (Penn UF), 17%(Poc #3), 19%(Pitt #8), 15%(IL #6) and 50%(Wyo Sub).

GPC data of Table III show that the bulk of THF-soluble products from all coals at short reaction times consists of material below 600 nominal molecular weight. The effectively inert Poc #3 produced primarily low molecular weight materials at both 10 and 40-minute reaction times. The P+A fractions all exhibit significant amounts of higher molecular weight material (Table IV), consistent with the expected characteristics of THF-solubility. Among the high yielding coals, Pitt 8, Wyo Sub, and Ill #6, the P+A fraction of Wyo sub (Table IV) shows the greatest amount of product below MW 600, consistent with the much greater apparent yield of hexane-solubles discussed above for Wyoming subbituminous. GPC data for extracts of raw coals, total reaction mixtures, and preasphaltene + asphaltene subfractions are depicted in Figure 1.

^{13}C FTNMR spectra of P+A fractions determined for the five coal extracts are presented numerically in Table V. THF solubility and hexane solubility tends to produce material of high polarity and rather similar NMR characteristics in the preasphaltene + asphaltene subfraction. The ranges of Table V correspond roughly to phenolic and aryl ether CO (168-148 ppm), substituted aryl C (148-129.5 ppm) and protonated aryl carbon (129.5-110 ppm), the latter group including protonated aryl carbon adjacent to aryl CO structure(5). Within the range of probable error, Table V results indicate higher aryl oxygen content for IL #6, Wyo Sub, and Pitt #8 than for Penn UF and Poc #3, and higher ring substitution for Poc #3.

The results of this paper provide quantitative data for estimation of the amount and structural distribution of products from short residence time liquefaction of the Argonne Premium Coals. A more detailed spectroscopic study of the organic structure of the Argonne coals is presently underway.

REFERENCES

(1) Franz, J. A. and Camaioni, D. M. Fuel, 1984, 63, 990-1002.
(2) Franz, J. A., Camaioni, D. M., and Skiens, W. E. in "Coal Structure" (Eds. M. L. Gorbaty and K. Ouchi), Adv. Chem. Ser. Am. Chem. Soc. Washington, D. C., 1981, 192, 75-94.
(3) Franz, J. A. Fuel, 1979, 58, 405.

(4) Wilson, M. A., Collin, P. J., Pugmire, R. J., and Grant, D. M. Fuel, 1982, 61, 959-967.
(5) Davidson, R. M., "Nuclear Magnetic Resonance Studies of Coal," Report No. ICTIS/TR32, IEA Coal Research, 14-15 Lower Grosvenor Place, London SW1W OEX, United Kingdom (ISBN 92-9029-126-5), January 1986.

Table I. Direct Extraction of Coals with THF

Coal	Wt. Coal Extd.	Wt. Extract	Wt. %
Ill #6	4.11 g	0.50 g	12%
Penn UF	4.36 g	0.07 g	2%
Wyo Sub	3.97 g	0.12 g	3%
Pitt #8	3.07 g	0.13 g	4%
Poc #3	4.77 g	0.10 g	2%

Table II. Asphaltene + Preasphaltene Yields from Coals[a]

Coal	Wt. Coal	Wt. Residue	Wt. P+A	%P+A	Conversion[b]
Penn UF	5 g	3.1 g	1.5 g	30%	38%
Poc #3	1 g	0.8 g	0.03 g	3%	20%
Poc #3[c]	3.5 g	2.0 g	0.6 g	17%	43%[c]
Pitt #8	4 g	1.0 g	2.24 g	56%	75%
Wyo Sub	4 g	1.0 g	1.0 g	25%	75%
Ill #6	4 g	1.7 g	1.0 g	43%	58%

[a] 10 minutes, 430 ± 5 °C.
[b] based on recovered coal ((Wt. Coal-Wt. Residue)/Wt. Coal), includes transfer losses, hexane-soluble products not included in P+A, and water losses.
[c] 40 minutes, 430 ± 5° C

Table III. GPC Data For THF-Soluble Products of Coal-Tetralin Unfractionated Reaction Mixtures

Coal	Area % MW Above 8500	Area % MW 8500-600	Area % MW Below 600
Ill #6[a]	3.9	17.3	78.8
Ill #6[a]	0.3	13.2	86.5
Pitt#8	5.9	35.0	59.1
Penn UF	1.0	28.1	70.9
Wyo Sub	0.6	25.3	74.1
Poc #3[b]	0.5	7.8	91.7
Poc #3[b]	0.6	11.0	88.4

[a] Coal was pre-extracted with THF before reaction
[b] 40-minute reaction time

Table IV. GPC Data for P+A Fractions from Premium Coals

Coal	Area % MW above 8500	Area % 8500-600	Area % Below 600
Ill #6	3.4	38.6	58
Pitt #8	5.6	52.8	41.5
Penn UF	7.2	44.0	48.7
Wyom Sub	3.1	31.3	65.6
Poc #3	3.2	40.3	56.4
Poc #3[a]	0.7	13.7	85.7

[a]40-minute reaction time

Table V. ^{13}C Spectroscopic results from P+A fractions

Coal	Distribution of Aromatic C %, ppm range			Aromaticity[a],%
	168-148	148-129.5	129.5-110	
Ill #6	10	44	46	81
Wyo Sub	12	41	47	76
Poc #3	7	55	38	ND
Pitt #8	10	43	47	80
Penn UF	7	34	59	70

[a]Estimated error ±5%

Table VI. GPC Data of THF Extracts of Premium Coals

Coal	Area % MW Above 8500	Area % MW 8500-600	Area % MW Below 600
Ill #6	1.6	30.6	67.9
Pitt #8	5.1	31.9	63.1
Penn UF	0.2	10.9	89.0
Wyo Sub	0.4	7.7	92.0
Poc #3	0.1	9.6	90.0

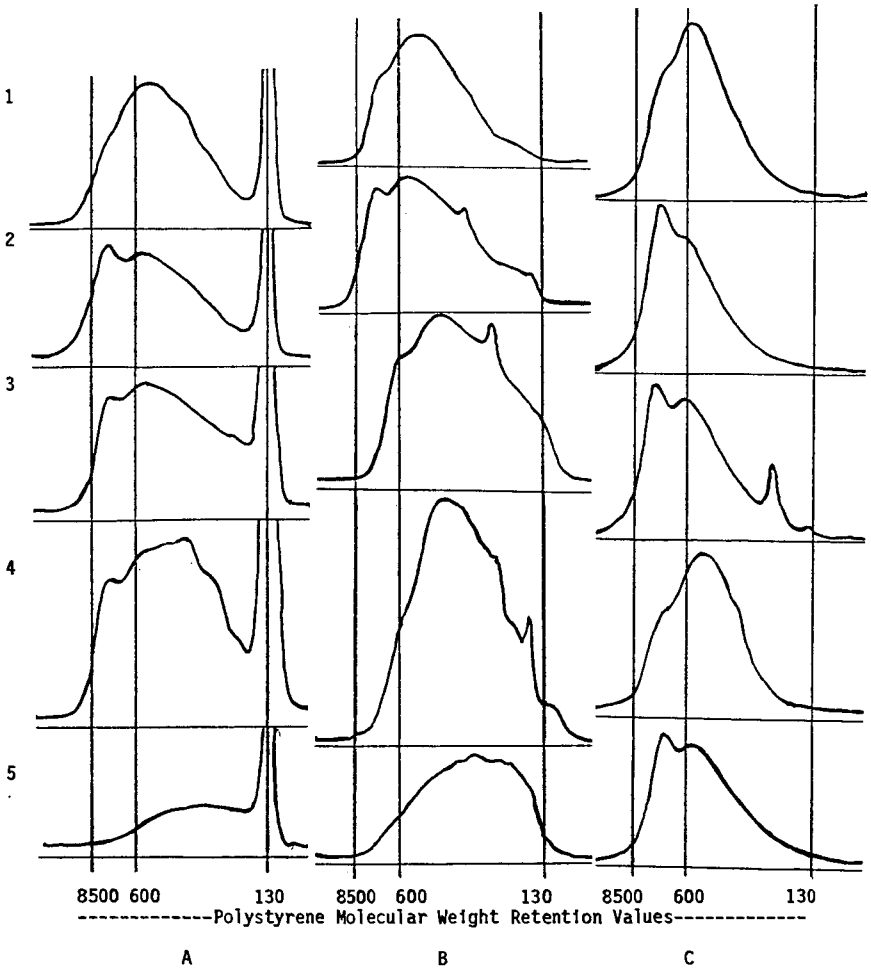

Figure I. Gel Permeation Chromatography Traces for A) Unfractionated Coal/Tetralin Reaction Mixtures; B) Products of THF extraction of the raw coals, and C) THF-Soluble, Hexane-insoluble Products (Preasphaltenes and Asphaltenes). The coals are Row 1, Illinois #6; Row 2, Pittsburgh #8; Row 3, Pennsylvania Upper Freeport; Row 4, Wyoming Subbituminous; Row 5, Pocahontas #3

REACTION OF PREMIUM WYODAK SUBBITUMINOUS COAL WITH POTASSIUM-CROWN ETHER REAGENT

Shuyen L. Huang and Ramani Narayan

Laboratory of Renewable Resources Engineering
and
Coal Research Center
A. A. Potter Engineering Center
Purdue University
West Lafayette, IN 47907

INTRODUCTION

Coal conversions typically involve reacting coal under severe conditions of temperature and pressure. As a result, bond cleavage is nonselective and often accompanied by retrogressive (bond forming) reactions. This has resulted in less than satisfactory results in deducing coal structure, coal behavior, and reactivity. Incorrect model of the basic structural units of the coal, and the nature of the linkages joining these units have been postulated. In our laboratory, we are studying the solubilization of coal at ambient temperatures and pressures using a site-specific reagent potassium-crown ether (K-CE), and the characterization of the soluble coal oligomer fragments (1,2). The small size and high reactivity of the solvated electrons generated by the K-CE reagent, promotes cleavage reactions at ether (3-5), ester (9), and diarylethane linkages (6,7), resulting in depolymerization and solubilization of coal. Reduction of aromatic rings to dihydro and tetrahydro analogs also occur (2,8). In this paper we report on the solubilization of a Wyodak premium subbituminous coal using K-CE reagent. The characterization of the solubilized coal fragments by IR, NMR, GPC, and microanalysis, is described.

EXPERIMENTAL

Material

Premium Wyodak subbituminous coal (-20 mesh, C=74%, H=5.1%, O=20%, S=0.5%) was obtained from the Argonne Premium Coal Sample Bank, Argonne National Laboratory, IL. Coal samples were used immediately upon opening the glass ampoule. -100 mesh coal used in our study was prepared by grinding the -20 mesh coal in a glove box under liquid nitrogen. The coal was then dried under vacuum for three hours and used immediately for the K-CE reactions.

Reaction of Wyodak Coal With K-CE Reagent

The stoichiometry of the reagents, and the experimental conditions for the coal-K-CE reaction followed established procedure as reported earlier (1,2). The work-up procedure for the reaction is shown in Figure 1.

NMR Spectroscopic Analysis

Proton NMR spectra was obtained from a Nicolet NTC-470 spectrometer (470 MHz) at ambient temperature. Coal samples (20 mg) were dissolved in 0.5 ml of chloroform-d (THF-1

fraction), or DMSO-d6 (THF-2 and alkali-soluble fractions). Proton decoupled ^{13}C NMR spectra were obtained from NTC-200 (50 MHz) at 45°C (22°C for THF-1 fraction). The sample concentration was 50 to 75 mg of sample per 1 ml of NMR solvent. For alkali-soluble fraction $NaOD/D_2O$ was used in the ^{13}C NMR experiment.

Gel Permeation Chromatography

Gel Permeation Chromatography (GPC) experiments were carried out on a Waters M-6000A pump with two ultrastyragel columns (500 A and 1,000 A) in tandem using THF eluent and a differential refractometer detector. Polystyrene standards were used to obtain a calibration plot. The molecular weight distribution of the THF-soluble coal samples were based on the elution time and the standard calibration plot.

RESULTS AND DISCUSSION

Solubility Studies

The work-up of the coal/K-CE reaction mixture and the extraction of coal into different soluble fractions (THF-1 fraction, alkali-soluble fraction, and THF-2 fraction) are shown in Figure 1. The percent coal solubilized in the various fractions is summarized in Table 1.

Our previous report (2) suggests that the solubility of K-CE treated coal is related to the stoichiometries of the reactants. We found that when the ratio of potassium to coal was decreased, the solubility of coal decreased significantly. We also found that successive K-CE reactions with coal solubilized additional coal. A total solubility of up to 70% was obtained after a coal sample was consecutively treated with K-CE reagent for three to four times. These results suggest that the diffusion of the solvated electrons into the coal matrix is an important factor in determining the solubility of coal, (the amount of soluble coal oligomer fragments formed) after the K-CE reaction.

The present results showed that the diffusion of the solvated electrons is, indeed, an important factor in determining the solubility of the coal, especially the alkali-soluble fraction, in the coal/K-CE reactions. As shown in Table 1, when the coal particle size was changed from -20 mesh to -100 mesh, the alkali-soluble fraction increased from 25% to 47%, whereas the THF-1 and THF-2 fractions did not change significantly. A smaller particle size of coal provides more surface area which allows more of the solvated electrons to react with the aryl ether, ester, and aryl ethane linkages of the coal macromolecule. The alkali-soluble fraction increased two fold on going from a -20 mesh coal particle size to -100 mesh, while the THF-1 and THF-2 fractions were not affected as much. These results suggested that the cleavage of the aryl ether and ester linkages was a predominant reaction during the coal/K-CE reaction.

The alkali-soluble fraction was also subjected to THF extraction. The results are summarized in Table 2. It was interesting to note that the THF extractability of the alkali-soluble fraction from the second K-CE reaction (72%) was higher than that of the first K-CE reaction (55%). During the second K-CE treatment, greater reduction of the polar groups of the coal structure, such as aromatic hydroxyl group to a corresponding less polar dihydro-ketone group, would account for the observed higher solubility in THF.

Elemental Analysis

Elemental compositions of the soluble fractions, the insoluble fractions, and the original premium Wyodak coal are shown in Table 3. The results show that there was an overall increase of the hydrogen content. This hydrogen uptake suggested that Birch-Huckel type

reductions, and cleavage of aryl methylene linkages and ether linkages occurred during the K-CE reaction (7).

THF-1 and THF-2 fractions show relatively high H:C ratios indicating that these fractions are rich in aliphatic material. The THF-1 extraction step (Figure 1) extracted the non-polar hydrocarbon material, that arose from the cleavage of the macromolecular network or was present as trapped molecules. THF-2 step extracted hydrocarbon material containing some polar functionality like OH, or COOH groups (confirmed by high field proton NMR spectroscopy) discussed in the next section. Under alkaline conditions, they are present in salt form (i.e., $-O^-M^+$), and therefore, not extracted during the THF-1 extraction. However, these compounds were not acidic enough (contained more hydrocarbon groups, to make it alkali-soluble). Acidification of the residue converted the salts into the free acid form (O^-M^+ to -OH) and this rendered the hydrocarbon material THF extractable.

An oxygen balance of the K-CE reaction is shown in Table 3. The result showed that there was no significant increase or uptake of oxygen during the reaction. This was important to establish because of the distinct presence of a number of oxygen functionalities like carboxylic groups, phenolic -OH groups, and carbonyls in all the extracts. Therefore, the appearance of these oxygen functionalities arose by chemical transformations (cleavage reactions, reductions) of the original oxygen functionalities.

Gel Permeation Chromatography Analysis

GPC was carried out on all the THF-soluble fractions including THF-1 fraction, THF-2 fraction, and THF extract of the alkali-soluble fraction. GPC experiments were expected to yield information on the size (molecular weights and molecular weight distribution) of the various clusters being held together by K-CE cleavable linkages. The absolute molecular weights of the coal extracts were not determined. The results of the GPC analysis are summarized in Table 4.

The results show that K-CE reagent is dismantling the coal macromolecule into low molecular weight, non-polar, hydrocarbon material (THF-1), large (34,000-42,000 and 900-1400) polar oligomer fragments (THF extract of the alkali-soluble fraction), and a second hydrocarbon fraction (MW 1300-2200) containing few polar (-OH) functionalities. The results also suggested that upon second consecutive treatment of the coal sample, the size of the resulting coal oligomer fragments are slightly larger than that of the first K-CE reaction. A definite confirmation of these results would require the determination of the absolute molecular weight of the coal extracts.

Infrared Spectroscopy

Infrared spectra of the soluble fractions were obtained and compared to that of the original untreated coal. IR spectra of THF-1 and THF-2 fraction both showed strong absorption at the aliphatic C-H stretching regions, which corresponds well with the finding of the microanalysis. The carbonyl absorption bands (1725 and 1700 cm^{-1}) are found in the IR spectra of all the soluble fractions. These carbonyl absorptions are attributed to the functional groups such as ketone and carboxyl which arose from the reduction of the phenolic OH and the cleavage of the ester groups (2,9).

NMR Spectroscopy Analysis

Proton NMR spectra of the soluble fractions are shown in Figure 2. The spectra of THF-1 and THF-2 fractions (Figure 2A and Figure 2C) confirmed that hydrocarbon material is more abundantly in the THF fractions than in the alkali-soluble fraction. Strong signals at 1.3

ppm and at 1.0 ppm correspond to the methylene protons of long chain polymethylenes and the parafinic methyl protons respectively. Broad signals at 9-10 ppm and 11-13 ppm corresponding to the phenolic protons and carboxylic protons respectively are found in the spectra of the alkali-soluble fraction and the THF-2 fraction. The broad signals disappeared from the spectra upon the addition of D_2O to the NMR samples thus confirming the presence of these acidic protons. The disappearance of the 4.0 ppm strong broad signal on addition of D_2O to the NMR sample, suggested the presence of aliphatic alcohols. These aliphatic alcohols could arise from the cleavage of the ester linkage of the coal macromolecule.

^{13}C NMR spectra of the alkali-soluble fractions from first and second K-CE reactions are shown in Figure 3. It is interesting to note an increase in the intensity of the peak centered around 110 ppm (corresponding to olefinic carbons) in the spectrum of the alkali-soluble fraction from the second K-CE reaction. The results suggest that during the second K-CE treatment, more of the aromatic ring of the coal oligomer fragments were reduced to the corresponding dihydroaromatics. The spectrum of the alkali-soluble fraction from second K-CE reaction also showed a sharp decrease in the intensity of the alkane carbons resonances.

The proton and ^{13}C spectra of the soluble fractions obtained from the K-CE treated premium Wyodak coal were compared with the proton and ^{13}C spectra of similar fractions of the K-CE treated regular Wyodak coal obtained from Electric Power and Research Institute (EPRI), and stored under water. The spectra are compatible, i.e., the same distinct structural characteristics are observed in the soluble fractions from both the premium Wyodak and regular Wyodak coals.

SUMMARY

In this paper we have shown that a total of 53% premium Wyodak coal was solubilized into THF- and alkali-soluble fractions after the first K-CE reaction. The alkali-soluble fraction accounted for 89% of the total solubles. This result is consistent with our previous findings using the regular Wyodak coal obtained from EPRI. The results showed that a decrease in the coal particle size increased the amount of alkali-soluble coal formed. The oxygen balance, based upon the results of the elemental analysis, showed that the oxygen functionalities (phenolic and carboxylic OH groups and carbonyl groups) found in all the soluble fractions arise by chemical transformations (cleavage reactions, reductions) of the original functionalities.

ACKNOWLEDGMENTS

Funding for this work was provided by the Electric Power Research Institute under Contract No. RP8003-1. We are grateful to the Purdue University Biomagnetic Resonance Laboratory supported by NIH Grant No. RR01077 for the NMR spectra reported here. Mr. James Jones is also acknowledged for doing the solubility studies.

REFERENCES

1. S. L. Huang, K. Wood, and R. Narayan, Amer. Chem. Soc., Div. Fuel Preprints, *31*(4), 85 (1986).

2. S. L. Huang, and R. Narayan, Amer. Chem. Soc., Div. Fuel Preprints, *32*(1), 32 (1987).

3. B. Weinstein and A. H. Fenselan, J. Org. Chem., *34*,126 (1969).

4. J. A. Marshall, and N. H. Anderson, J. Org. Chem., *30*, 1291 (1965).

5. D. H. Eargle, Jr., J. Org. Chem., *12*, 1918 (1967).

6. L. Schanne and M. W. Haenel, Tet. Letter, *44*, 4245 (1979).

7. C. J. Collins, H. P. Hombach, B. E. Maxwell, N. C. Woody, and B. M. Benjamin, J. Amer. Chem. Soc., *102*, 851 (1980).

8. R. A. Benkeser, M. L. Burrows, J. J. Hazdra, and E. M. Kaiser, J. Amer. Chem. Soc., *28*, 1094 (1963).

9. S. L. Huang, and R. Narayan, "Reduction of Benzyl Benzoate by K-CE Reagent," to be submitted to J. of Amer. Chem. Soc.

Table 1. Solubility of Premium Wyodak Subbituminous

	THF-1 Fraction (%)	Alkali-Soluble Fraction (%)	THF-2 Fraction (%)	Total
One K-CE Reaction[a]	7	25	2	34
Total of Two K-CE Reaction[a]	9	29	6	44
One K-CE Reaction[b]	4	47	2	53

a. Particle size of coal was -20 mesh.

b. Particle size of coal was -100 mesh.

Table 2. THF Solubility of Alkali-Soluble Fractions and Total Solubility in THF for Wyodak Subbituminous[a]

	% THF Solubility of Alkali-Soluble Fraction	Total % THF Solubility for Wyodak
First K-CE Reaction (20 mesh)	55 (out of 21%)	24
Second K-CE Reaction (20 mesh)	72 (out of 14%)	15
First K-CE Reaction (100 mesh)	53 (out of 47%)	31

a. THF extraction of untreated Wyodak coal was negligible.

b. This includes THF-1 and THF-2 fractions, and THF fraction of alkali-soluble.

Table 3. Elemental Analysis of Premium Wyodak Subbituminous and Soluble Fractions[a] (Moisture and ash-free values)

Coal Samples	C	H	O	N	S	H/C	Yield %[c]	Empirical Formula
Wyodak[b] Subbituminous	74	5.1	20	0.40	0.50	0.83		$C_{100}H_{83}O_{20}$
THF-1 Fraction	77.9	8.9	12.9	0.20	0.36	1.37	7.38	$C_{100}H_{137}O_{12}$
Alkali-Soluble Fraction	71.2	4.9	22.3	0.98	0.59	0.82	25.01	$C_{100}H_{82}O_{23}$
THF-2 Fraction	74.6	7.4	16.8	0.54	0.63	1.19	2.45	$C_{100}H_{119}O_{17}$
Insoluble Fraction	72.1	5.4	21.1	0.89	0.52	0.90	57.82	$C_{100}H_{90}O_{22}$
Total Yield	--	--	--	--	--	--	92.66	$C_{92.7}H_{85.6}O_{19.8}$
Normalized to C_{100}	--	--	--	--	--	--	--	$C_{100}H_{92}O_{21}$

a. The results reported here are from first K-CE reaction.

b. These values are from the Argonne National Laboratory reported data.

c. The solubility % yield from first K-CE reaction.

Table 4. GPC Results of THF Soluble Fractions

	Molecular Weight Distribution		
	Number Average $\bar{M}_n$	Weight Average $\bar{M}_w$	Peak Mol. Wt.
First K-CE Reaction[a]			
THF-1 Fraction	414	1441	1117
THF-2 Fraction	986	4029	2244
Alk-THF Fraction	23,990	27,170	33,880
	532	1457	930
Second K-CE Reaction[a]			
THF-1	641	1981	906
THF-2	1079	4059	1319
Alk-THF Fraction	32,345	35,030	42,204
One K-CE Reaction[b]			
THF-1 Fraction	522	1606	956
THF-2 Fraction	1310	4070	1784
Alk-THF Fraction	20,080	24,860	35,714
	1062	2553	1395

a. The coal particle size was -20 mesh.

b. The coal particle size was -100 mesh.

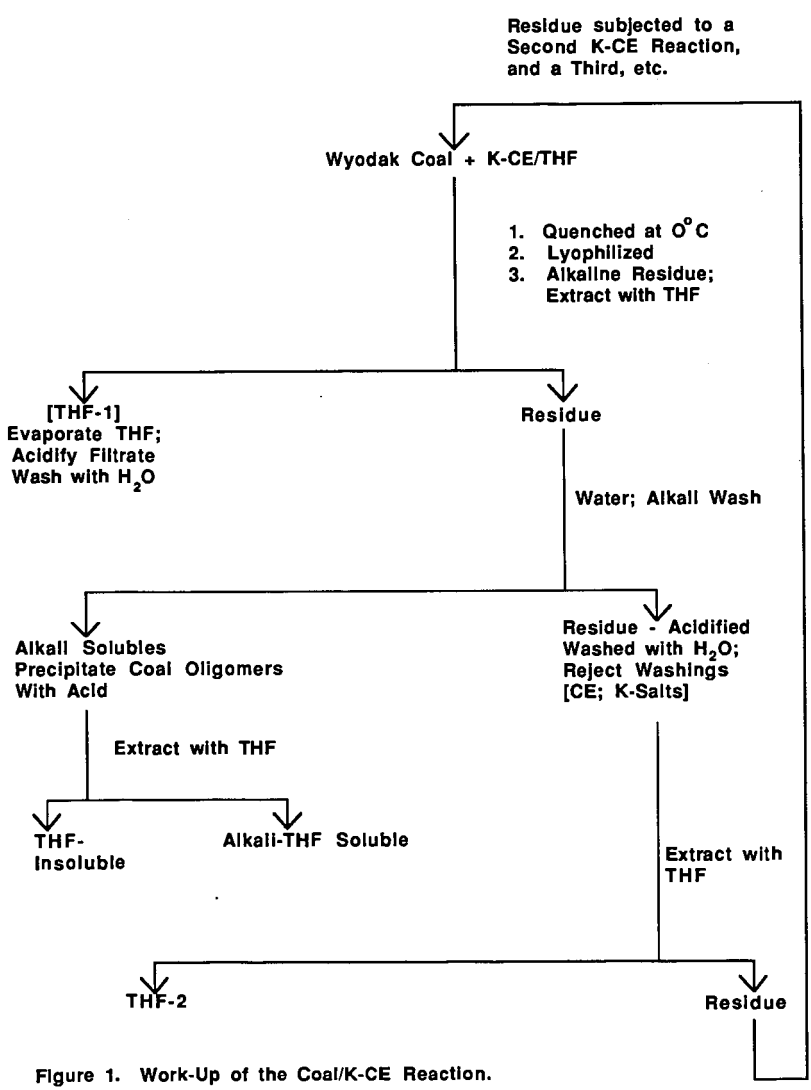

Figure 1. Work-Up of the Coal/K-CE Reaction.

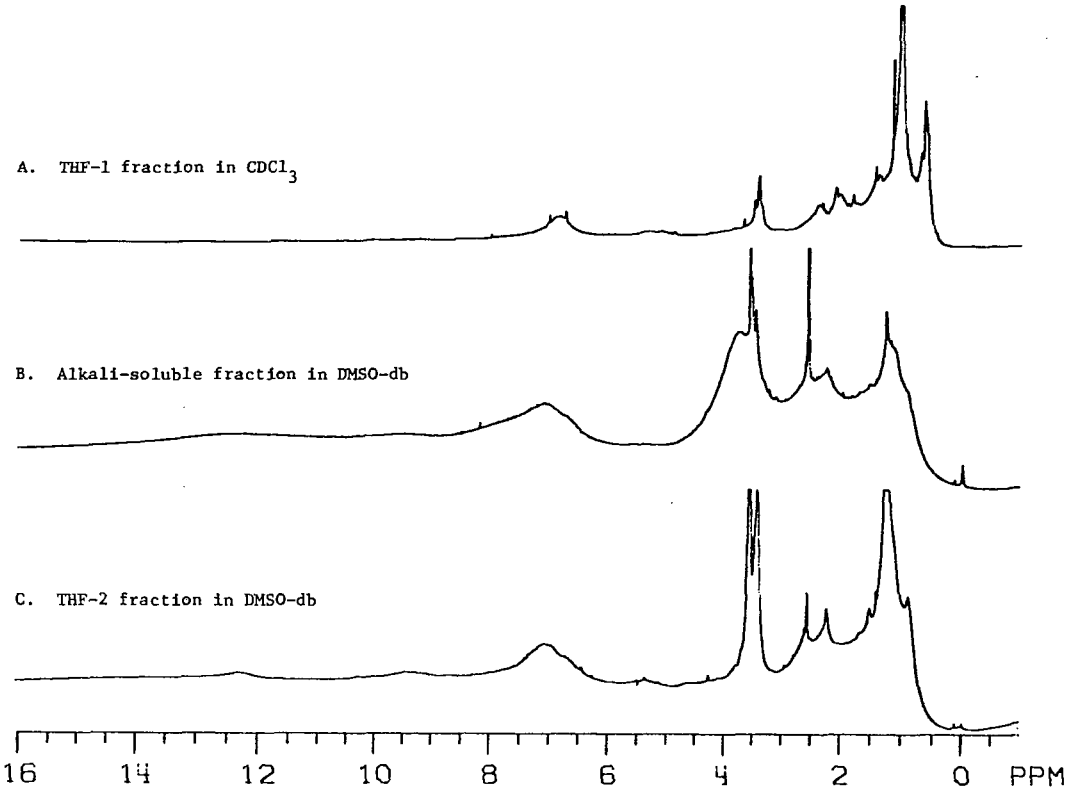

Figure 2. 470 MHz ^1H NMR spectra of soluble fractions of K-CE treated premium Wyodak coal.

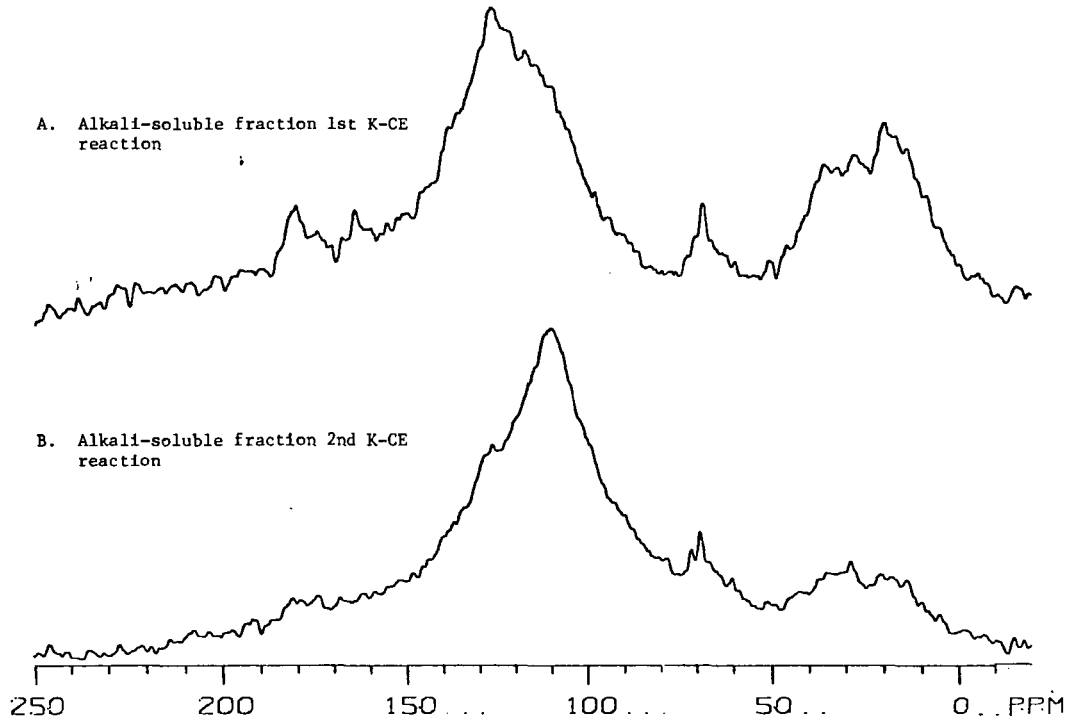

Figure 3. Proton decoupled ^{13}C NMR spectra (50 mHz) of alkali-soluble fractions in $NaOD/D_2O$

CHARACTERIZATION OF THE BENZENE METHANOL EXTRACTS FROM THE ARGONNE PREMIUM COAL SAMPLES

Y. J. Xia, P. H. Neill and R. E. Winans

Chemistry Division, Argonne National Laboratory,
9700 South Cass Avenue, Argonne, Illinois 60439

INTRODUCTION

The Argonne Premium Coal Samples represent a unique opportunity to study a set of pristine samples selected to represent the vast diversity of chemical structures exhibited by U.S. coals. In order to determine if there will be any non-oxidative changes in these coals during long term storage a project has been initiated utilizing a wide rage of chemical and physical techniques. One of these techniques meant to focus on any changes which may occur in the volatiles and extractables is described in this paper.

We believe that the material that can be extracted from the coal will provide important information concerning any changes which may occur during long term storage. These materials are easily studied by well established techniques (1-5) and the suggestion has been made that they may be representative of the chemical structures found in the bulk coal (1-3).

EXPERIMENTAL

An overview of the experimental procedures is presented in Figure 1. In order to reduce exposure to atmospheric oxygen all transfers and weighings were performed in a glove box under nitrogen. The Argonne Premium Coal Samples (APCS) used in this study and their elemental analysis are given in Table 1. The preparation of the Argonne Premium Coal Samples has been described by Vorres and Janikowski (6). All of the samples were - 100 mesh except for APCS #2 and #6 which were not available in the smaller mesh size when the work was performed. The coals, excluding the low rank APCS #2 were dried before extraction at 100°C for 16 hours under vacuum then brought to constant weight. APCS #2 was extracted without drying due to possibility that drying would irreversibly modify its physical and chemical structure. The water content of this coal was determined in a separate experiment.

Each coal was extracted in 250 ml. of boiling benzene/methanol (31/69 w/w percent) for 48 hours under nitrogen. The extract was removed by vacuum filtration. The residue was washed with ca. 50 ml. of the benzene/methanol, dried at 100°C under vacuum to constant weight. The benzene/methanol was stripped from the extract at 70°C under vacuum in a rotary evaporator and the extract brought to constant weight.

The extract was then separated into nine fractions using the desorption column chromatographic technique developed by Farcasiu (7). In our application of this technique the extract was dissolved in 7 ml. of the benzene/methanol and coated on 6.65 grams of dried silica gel by evaporating the solvent. The coated silica gel was placed on the top of the column containing 26.8 grams of Aldrich Grade 12 silica gel. This silica gel had

been dried for 8 hours at 120°C and then rehydrated to 4 percent water. The sequential elution solvents in order of use and the classes of compounds reported finding in each fraction are presented in Table 2. A standard volume of 500 ml was used for each elution. In order to correct for silica gel dissolved in each of the fractions, blank elutions were performed under the same conditions as used for the actual separation. The solvent was striped form each fraction by rotary evaporation under vacuum, and the extract brought to constant weight.

Analysis of each fraction was by Gel Permeation Chromatography (GPC) and Gas Chromatography Mass Spectroscopy. The GPC separation in utilized three Ultra Styragel columns with exclusion limits of 1000, 500 and 100 angstroms connected in series to an refractive index and ultraviolet detector. The tetrahydrofuran mobil phase was pumped through the columns at a flow rate of 1 ml/min. Calibration for the conversion of retention times to molecular weight utilized a series of aromatic compounds ranging from naphthalene (128 g/mole) to erythromycin (734 g/mole). The GCMS separations were performed on a Kratos MS25 instrument with a OV-1701 column.

Solvent swellings of the residues from the extractions were performed using the gravimetric technique utilized by Green et al. (8). Briefly ca. 1.1 grams of the residue from the extraction was placed in a desiccator with the benzene methanol swelling mixture in the base. The solvent mixture was frozen and the desiccator evacuated to remove the air. After thawing the freeze thaw cycle was repeated two more times. The swelling coefficients (weight of swollen coal/weight of unswollen coal) were determined after 36 hours.

RESULTS AND DISCUSSION

The yields of benzene/methanol extractables are plotted versus carbon content in Figure 2. Excluding Wyodak subbituminous coal (APCS #2), the yields decreased with rank in a non-linear manner. The low extractability of Wyodak, relative to the trend defined by the higher rank coals, may be attributable to two factors. This coal contains a much higher oxygen content. Thus, the extractables from this coal should be more polar and exhibit a greater propensity towards intramolecular hydrogen bonding than extractables from coals of higher rank. The relatively non-polar benzene/methanol may be incapable of solvating the potentially extractible material. The solvent swelling coefficient (Figure 6) for this coal indicates that benzene/methanol does not show a disparity in its ability to gain access to the macromolecular structure. The Wyodak coal contained 30.4 ± 0.4 percent water which was the highest water content of all the coals studied. It was also the only coal which was not dried prior to extraction. The water from this coal could have modified the extraction potential of the benzene methanol enough to account for the observed yield. Reproducibilities of the extractions were quite good with standard deviations as indicated by the error bars on Figure 2. ranging from 0.0 to 0.22 percent of the mean extraction yield.

The percentage of the benzene/methanol extract in each of the LC fractions corrected for dissolved silica gel is presented in Figure 3. The solvent or mixture used to elute each of the fractions can be found in

Table 2. Only fractions 2, 5 and 6 appeared to show any rank dependence. Fraction 2 which Farcasiu (7) attributed to small non-polar aromatics was found to contain a homologous series of linear alkenes of even number dominance, having a maximum in their distribution near 20 carbons. This distribution is probably not inherent to the coal, but an artifact of the severe conditions used in removing the solvents from the extracts and LC fractions. Figure 4 presents the total extract in this fraction plotted with respect to carbon content for each of the coals studied. The opposite trend may occur, with a higher percentage of the extract from the higher heteroatom content lower ranked coals eluting in fractions 5 and 6. This trend of a higher percentage of the extractables eluting at higher eluent polarity for lower rank coal is illustrated in Figure 5 where yields are plotted versus fraction number for Upper Freeport and Wyodak coals. Although the trends can easily be seen the errors associated with the measurements are so large that no statistically valid conclusion can be drawn.

The average molecular weight from GPC for LC fractions 2-9 is presented in Figure 6. All of the retention times were within the linear portion of the calibration curve (128-734 grams/mole). One must be careful in assigning molecular weights for GPC retention times for compounds dissimilar to the calibration standards due to the basis of the GPC technique on molecular size rather than molecular weight (9). However, comparisons of intrafraction variation in molecular weight should be valid if similar material is eluted for each sample. The maximum in the molecular weight distribution increased up to fraction 7. Indicating a possible dependence of the LC fractionation technique on molecular size as well as functionality. Above fraction 6 the molecular weight appeared to decrease. Only a small amount of the total extract (<10%) was eluted in these two fractions. No valid intrafraction differences could be observed, due to the similarities in the mean molecular weight values and the relatively large errors associated with the measurements.

The swelling coefficient in benzene/methanol is plotted versus carbon content in Figure 7. It decreases with rank in a non-linear manner up to Upper Freeport coal (APCS #1) at 87.1 percent carbon. The Pocahontas lv bituminous coal (APCS #5) at 89.6 percent carbon exhibited a statistically significant increase in its swelling coefficient. This break in the swelling trend corresponds to the break in the coalification pattern around 87 percent carbon attributed to a maximum in the macromolecular cross-link density by Larsen and Kovac (10). Standard deviations were found to be less than 0.4 percent of the swelling coefficient indicating a valid difference between the mean values for each of the coals studied.

CONCLUSIONS

Significant differences have been observed in the total amount of material extracted from the Argonne Premium coal samples and the swelling coefficients of the resulting residues. Each generally decreased with increasing carbon content as would be expected. Differences were observed in the amount of the extract proportionating into each of the LC fraction. A higher percentage of the extract from coals of lower rank appeared to elute in the more polar fractions, although the experimental procedure will have to be refined before one can be sure that this conclusion is valid. There did not

appear to be any significant differences between the intrafraction maximum in the molecular weight profile for any of the samples. The data reported in this paper represents baseline values for the benzene/methanol extractables from the Argonne Premium Coals. The next phase of the project will involve the repetition of these experiments in order to determine if any changes are occurring during storage.

ACKNOWLEDGMENTS

The coal analyses were provided by I. Fox and P. C. Lindahl of the Argonne Analytical Chemistry Laboratory.

This work was performed under the auspices of the Office of Basic Energy Sciences, Division of Chemical Sciences, U.S. Department of Energy, under contract number W-31-109-ENG-38.

REFERENCES

1. R. Hayatsu, R. E. Winans, R. G. Scott, L. P. Moore and M. H. Studier, Nature (London), 275, 116 (1987).
2. R. Hayatsu, R. E. Winans, R. G. Scott, L. P. Moore and M. H. Studier, Fuel, 57, 541 (1978).
3. M. H. Studier, R. Hayatsu, and R. E. Winans, in "Analytical Methods for Coal and Coal Products", Karr C., ed., Vol. 2, pp. 43-74, Academic Press, NY (1978).
4. T. J. Palmer and M. Vahrman, Fuel, 51, 22 (1972).
5. Z. Mudamburi and P. H. Given, Org. Geochem., 8, 441 (1985).
6. K. Vorres and S. Janikowski, ACS Fuel Division Preprints, 32(1), 492 (1987).
7. M. Farcasiu, Fuel, 56, 9 (1977).
8. T. Green, J. Kovac, D. Brenner, and J. W. Larsen, in "Coal Structure", R. A. Meyers, ed., pp. 199-282, Academic Press, NY (1982).
9. B. Brule, ACS Fuel Chemistry Division Preprints, 26(2), 28 (1981).
10. J. W. Larsen and J. Kovac, ACS Symp. Series, 71, 36 (1978).

TABLE 1. Composition of the Coals used in this Study.

APCS No.	Coal	% Carbon (dmmf)	Composition
1	Upper Freeport mv bituminous	87.1	$C_{100}H_{75.8}N_{1.48}S_{.26}O_{2.58}$
2	Wyodak subbituminous	72.0	$C_{100}H_{95.0}N_{1.19}S_{.26}O_{21.3}$
3	Illinois #6 hvC bituminous	77.8	$C_{100}H_{87.9}N_{1.54}S_{1.30}O_{8.8}$
4	Pittsburgh No. 8 hvA bituminous	83.4	$C_{100}H_{84.9}N_{1.69}S_{0.40}O_{6.03}$
5	Pocahontas lv bituminous	89.6	$C_{100}H_{62.9}N_{1.15}S_{0.17}O_{3.26}$
6	Utah Blind Canyon bituminous	75.7	$C_{100}H_{111.0}N_{1.59}S_{0.2}O_{15.16}$

TABLE 2. The sequence of solvents used for the elutions of the various LC fractions, and classes of compounds eluted as reported by Farcasiu (7).

Fraction No.	Solvent	Major Components
1	Hexane	Saturates
2	Hexane/15% benzene	Aromatics
3	Chloroform	Polar aromatics, Non-basic N,O,S-heterocyclics
4	Chloroform/10°C diethyl ether	Monophenols
5	Diethyl ether/3% ethanol	Basic nitrogen heterocyclics
6	Methanol	Highly functional molecules (>10 wt% heteroatoms)
7	Chloroform/3% ethanol	Polyphenols
8	Tetrahydrofuran	Increasing O content and increasing basicity of nitrogen
9	Pyridine/3% ethanol	Increasing O content and increasing basicity of nitrogen
10		Non-eluted, unidentified materials

Figure 1. Overview of the experimental procedure.

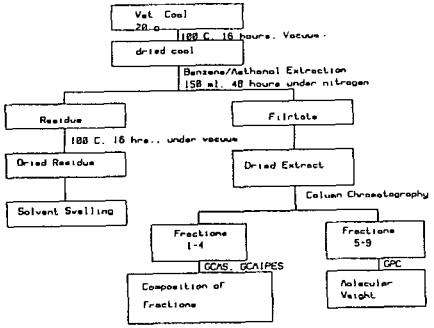

Figure 2. Variation of benzene/methanol extractables with carbon content, APCS No. in brackets.

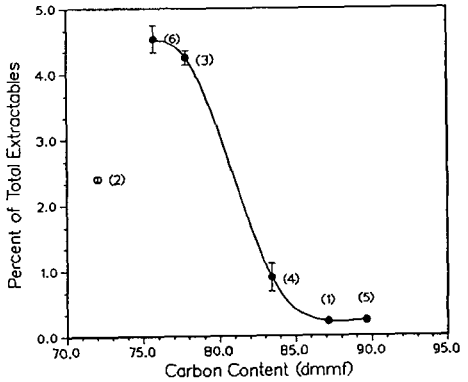

Figure 3. Average percentage of total extractables in LC fractions for APCS #1 – #4.

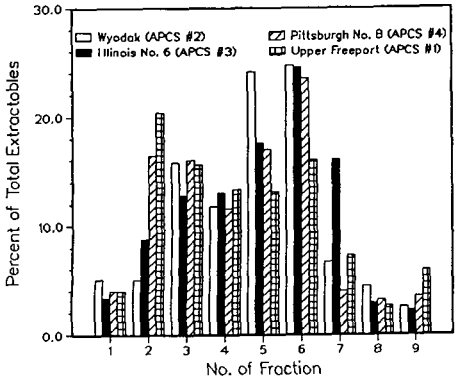

Figure 4. Variation in the percentage of the total extractables in liquid chromatographic fraction with respect to carbon content, the APCS no. is in brackets.

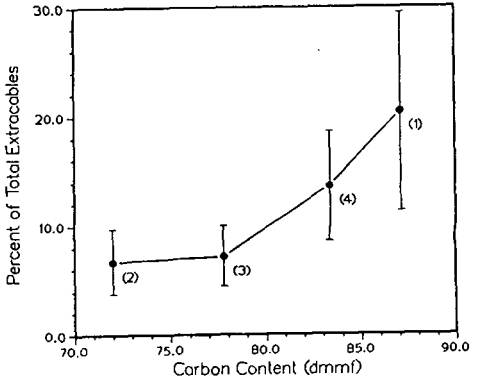

Figure 5. Percentage of total extractables in LC fractions 1–9 for APCS #1 and #2.

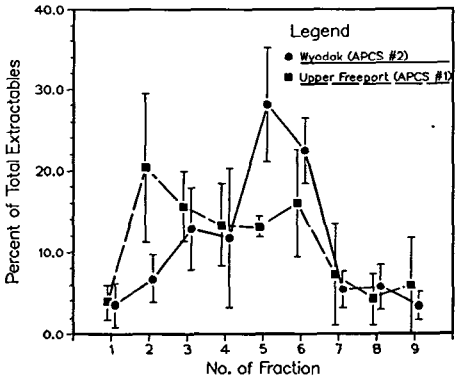

Figure 6. The variation in molecular weight (GPC) with fraction number for APCS 1–4.

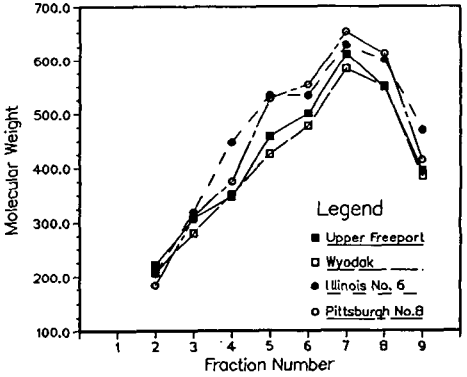

Figure 7. Variation of swelling coefficient in benzene/methanol with carbon content, APCS No. in brackets.

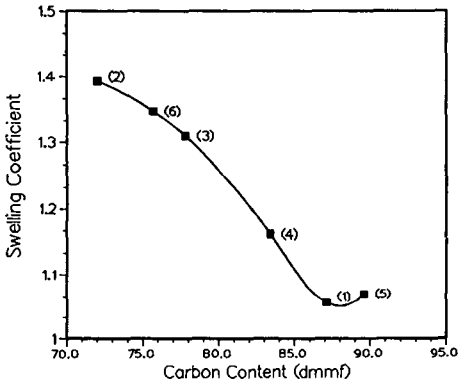

Cobalt Stearate-Aluminum Alkyl Catalyzed Hydrogenation of Illinois no. 6 High Volatile Bituminous Coal and Model Compounds

Lowell D. Kispert and Abbas Alvanipour

Department of Chemistry, The University of Alabama, Tuscaloosa, AL 35487

INTRODUCTION

In a previous study, some preliminary results (1) showed that a particular cobalt stearate-aluminum alkyl ($Co(stearate)_2Et_3Al$), [I], homogeneous transition metal complex related to Ziegler catalysts was a very effective hydrogenation promoter under mild temperature conditions (50-100°C) and hydrogen pressures of from 500-1000 psi. Initial results indicated significant yields of gasoline-light oil products from solvent refined coal at 90°C and hydrogen pressures of 700 psi. Ziegler catalysts are not often used for hydrogenation and are rarely employed for coal hydrocracking. However since they have been shown to hydrogenate olefins (2) and aromatic compounds and are Lewis acids, it seems possible to use them in some instances as hydrocracking catalysts. Besides our earlier findings for [I], Dinh et al. (3) have also described selective hydrogenation of naphthalene by Ziegler type catalysts consisting of metal stearates, acetylacetonates and aluminum alkyls. For example hydrogenation of naphthalene using a nickel stearate - $AlEt_3$ catalyst (5:20 mole equivalent ratio of Ni/Et_3Al) yielded 93% tetralin at 150°C and 44 psi, while the use of cobalt acetylacetonate - $AlEt_3$ (5:25) yielded 99% tetralin at 150°C and 145 psi in an eight hour reaction period. Other Ziegler hydrogenation catalysts have been reported to promote the hydrogenation of aromatic compounds but under more drastic conditions. The complexes of triethylaluminum with Co(2-ethylhexanoate)$_2$ and Ni(2-ethylhexanoate)$_2$ have been used to produce 100% conversion (2) of naphthalene [II] to decalin and tetralin at 210°C and 1000 psi. Both catalysts have also been used with benzene, a particularly difficult compound to hydrogenate (2, 4).

Studies (2, 4-5) have shown that the reactivity of the catalyst varies with the transition metal and anionic ligand in the order Ni>Co>Fe>Cr>Cu and 2-ethylhexanoate>benzoate>acetoacetate>acetate>chloride respectively. This roughly follows the order of solubility of the transition metal salts in the hydrocarbon solvents used in the reactions.

Since most of the aromatic structures studied consisted of one, two and three ring units, the Ziegler catalysts used as hydrogenation catalysts should successfully add hydrogen to the aromatic rings in coal. Significantly, aromatic compounds such as naphthalene [II] and polynuclear nitrogen heteroaromatic compounds such as quinoline [III] are found to occur in coal and oil shale. The selective hydrogenation of these materials to form additional useful compounds i.e., naphthalene [II] to form 1,2,3,4-tetrahydronaphthalene [IV] would provide an alternate use of a rather abundant natural resource. Recently, it has been reported (6) that quinolines and isoquinoline can be selectively hydrogenated in the nitrogen-containing ring to form 1,2,3,4-tetrahydroquinoline [V] and N-formyl-1,2,3,4-tetrahydro-

isoquinoline by means of a carbon monoxide and water mixture in the presence of a catalytic amount of rhodium carbonyl cluster at 150°C, 800 psi hydrogen and with stirring for 24 hr. We wish to report that similar hydrogenation of naphthalene [II], quinoline [III], 2-methylquinoline, and isoquinoline can be carried out using catalyst [I] under somewhat milder conditions but no hydrogenation occurs for nitro- or chloro substituted quinolines. We will also discuss the results of using catalyst [I] to hydrogenate Illinois no. 6 coal from the premium coal sample program.

EXPERIMENTAL

The catalyst system [I] for the hydrogenation of the model compounds, was prepared by the addition of 2.2 mmol of triethylaluminum in a dry N_2 atmosphere to a suspension of 1.9 mmole cobalt stearate in hexane. The black catalyst mixture was transferred under dry N_2 to a bomb reactor and 31 mmol of substrate was added. The reactor was pressurized to the desired pressure and heated to the value given in Tables I and II. The products were

Table 1. Hydrogenation of naphthalene (II) with the $Co(stearate)_2$-Et_3Al Catalyst

Conditions			% Yield*		
Time/h	Temp °C	Pressure Psi	Tetrahydro-naphthalene (IV)	Cis-Decalin	Trans-Decalin
16	90	700	95	-	-
7	90	700	95	3	1
16	90	300	5	-	-
16	22	700	94	3	1
16	45	700	90	6	2

*based on GC analysis.

Table II. Hydrogenation of nitrogen heteroaromatic by $Co(stearate)_2$-Et_3Al Catalyst.

Substrate	Conditions* Temp	% Yield A	B	C
quinoline (III)	90	66	21	0
	RT	73	--	27
isoquinoline	90	70	--	
	RT	--	--	100
2-methylquinoline	90	76	--	
	RT	44	--	52
8-nitro-2-methylquinoline	90	--	--	100
4-chloro-2-methylquinoline	90	--	--	100
5-nitroquinoline	90	--	--	100

A) 1,2,3,4-tetrahydro product.
B) 5,6,7,8-tetrahydro product.
C) remaining starting material.

*all reactions were carried out at 700 psi pressure for 16 hrs.

purified by either distillation under reduced pressure or by running the crude products through a silica gel column (chloroform). NMR spectra of the products were recorded on a 60 MHz Varian EM 360L spectrometer. Gas chromatography analyses of products were performed on a Hewlett-Packard 5790 A Series chromatograph using ultra cross-linked methyl Silicon gum column (25 m x 0.2 mm x 0.33 μm film thickness).

The hexane solvent was stored and distilled from Na/benzophenone. Naphthalene was used as purchased, however quinolines were dried over $MgSO_4$, filtered, and vacuum distilled. All reactions were carried out in a 150 cm^3 capacity stainless steel high pressure bomb reactor that could be varied in temperature. The preparation of the catalyst, the assembly of the bomb reactor, and the preparation of the reactants were all carried out under nitrogen in a dry box. The yield of hydrogenated product from naphthalene and quinolines is given in Table I and II for some typical runs.

Hydrogenation of Illinois no. 6 premium coal was also carried out using catalyst [I]. In a typical experiment, 5 g. of coal was added to the catalyst, prepared as described before, in hexane (35 cm^3) in a bomb reactor. The bomb reactor was heated at 90°C under hydrogen pressure of 800 psi and shaken for 24 hrs. The bomb reactor was cooled to room temperature and gas samples collected for analysis. Mass spectrometer-GC analysis of the gaseous products was carried out on a Hewlett Packard 5890 GC/MS system using a J&W DBS thick film column (5 μm) (12 m x 0.32 mm I.D.). The bomb reactor was then depressurized and a sample of the crude product was filtered through cotton wool or Celite. NMR analysis of the filtrate was carried out in hexane or after removal of hexane.

RESULTS AND DISCUSSION

A. Model Compounds

The NMR spectrum for the hydrogenation of II was in agreement with the spectrum previously recorded for IV. GC analysis of the crude products in Table I shows that naphthalene was hydrogenated selectively at room temperature and at 90°C with only negligible amount of decalin produced. It is important to note that if the hydrogen pressure is dropped to 300 psi from 700 psi, only a 5% yield of IV occurs, with the other 95% being the starting material. Reducing the temperature from 90°C to room temperature (22°C) does not significantly change the 95% yield of IV. Thus the value of the hydrogen pressure is critical to the hydrogenation of II. Lowering the temperature and changing the length of the reaction has almost no effect on the hydrogenation yield. From Table II, it is seen that III is hydrogenated selectively at room temperature to give 73% yield of V and 27% of III remained intact. However, when the temperature is raised to 90°, MS/GC analysis revealed 66% yield of V along with 21% yield of 5,6,7,8-tetrahydronaphthalene with no sign of the starting material. 2-Methylquinoline was also hydrogenated to 2-methyl-1,2,3,4-tetrahydroquinoline at room temperature and 90°C with 45 and 76% yield respectively. Isoquinoline on the other hand, can only be hydrogenated at 90° to 1,2,3,4-tetrahydroisoquinoline (70%); at room temperature no hydrogenation took place and the starting material was recovered completely. Hydrogenation of isoquinoline under water-gas

shift condition (6) produced N-formyl-1,2,3,4-tetrahydoisoquinoline whereas under our catalyic conditions, 1,2,3,4-tetrahydroisoquinoline can be prepared in good yield.

Catalyst [I] failed to hydrogenate compounds such as 5-nitroquinoline, 8-nitro-2-methylquinoline, and 4-chloro-2-methylquinoline. In each case the starting material was recovered. It is thought that functional groups such as nitro and chlorine interact with the aluminum alkyl, a Lewis base, and deactivate the catalyst. It has been reported that nitrobenzene and p-nitrophenol could not be hydrogenated in the presence of a catalyst system made of Ni(2-ethylhexanoate)$_2$-AlEt$_3$ whereas benzene was successfully hydrogenated to cyclohexane at 150-190^{o}C (2).

B. Hydrogenation of Illinois no.6 premium coal

The successful results obtained from hydrogenation of the model compounds suggested the possibility of hydrogenating coal under almost similar conditions. Comparison of the NMR spectrum of the coal hydrogenation product with that of a control experiment (heating the same sample of coal in hexane under similar conditions but in the absence of the catalyst), revealed that more signals appeared in the aliphatic region (3.5-1 ppm) when hydrogenation was carried out in the presence of the catalyst, indicating that some aromatic material was converted to saturated products. However, due to the small quantity of the coal sample, it has been difficult to identity the liquefied mixture. Mass spectrum-GC analysis of the gaseous products on the other hand, showed that methane, ethane, propane, cyclohexane, methylpentane and butane, and a few fragments assigned to unsaturated material had been produced. We regard this attempt at this stage, as a primary study and are planning further investigations under different conditions and more suitable media for coal liquefaction.

SUMMARY

Naphthalene (II), quinoline (III), isoquinoline and 2-methylquinoline can be hydrogenated selectively to form 1,2,3,4-tetrahydronaphthalene (IV) (94% yield) at room temperature, 1,2,3,4-tetrahydroquinoline (V) (73% yield at 22^{o}C), 1,2,3,4-tetrahydroisoquinoline (70% yield at 90^{o}C), and 2-methyl-1,2,3,4-tetrahydroquinoline (76% at 90^{o}C) by use of the Ziegler catalyst Co(stearate)$_2$-AlEt$_3$ in a hexane solvent at a hydrogen pressure of 700 psi. Hydrogenation of Illinois no. 6 coal using catalyst [I] has produced a liquefied product and identifiable gaseous components.

ACKNOWLEDGMENT

This study was supported by a grant from the School of Mines and Energy Department at The University of Alabama.

REFERENCES

1. Thorstad, C.; Kispert, L. D. Final Report for the 1975 SOS project, NSF no EPP 75-08992, the University of Alabama.

2. Lapporte, S. J.; Schuett, W. R. J. Org. Chem. 1963, 28, 1947.

3. Dinh, C. T.; Martino, G.; Lassau, C. French Patent 2161524, 12 June 1973.

4. James, B. R. "Homogeneous Hydrogenation"; Wiley Sons: New York, 1973: pp. 363-370.

5. Kroll, W. R. J. Catal. 1969, 15, 281.

6. Murahashi, S. I.; Imada, Y.; Hirai, Y. Tetrahedron Letters 1987, 28, 77.

LIQUEFACTION REACTIVITY MEASUREMENTS ON ARGONNE PREMIUM COAL SAMPLES

R.M. Baldwin, S-C. Shin, and R.L. Miller

Chemical Engineering Department, Colorado School of Mines
Golden, CO 80401

ABSTRACT

Liquefaction reactivities for a suite of 4 coals from the Argonne Premium Coal collection have been measured in tubing bomb batch reactors. The coals span a rank range from low volatile through medium and high volatile bituminous to subbituminous. The coals were liquefied in 4 different vehicles (solvents) namely naphthalene, phenanthrene, tetralin, and 1-methylnaphthalene at 698 K (425 C), 6.2 MPa (900 psi) initial hydrogen pressure, and at 5 and 40 minutes residence times. The rate and extent of conversion to THF- and toluene-solubles was measured, and gas make and hydrogen consumption quantified directly. The data show that, for purposes of reactivity comparisons, conversion to toluene-solubles provides the most appropriate data for relative reactivity ranking purposes. The Wyodak subbituminous coal was found to have the highest rate of reaction of the four coals investigated, while the Illinois #6 high volatile bituminous coal exhibited the greatest extent of reaction (conversion to THF- and toluene-solubles).

BACKGROUND

Measurement and correlation of coal reactivity under coal liquefaction conditions has been investigated for many years. Most studies in this area have attempted to find a single parameter or group of parameters capable of correlating fundamental physical, chemical, and geochemical coal properties with the degree of conversion to solvent soluble products under some set of standard reaction conditions (1-6). The relationship between coal organic and inorganic composition and hydrogenation reactivity has been extensively researched by several groups of investigators, most notably by Fischer et al., Given et al., and more recently by Baldwin et al. (7-21).

The purpose of this study was to examine the reactivity of 4 different coals in four different liquefaction vehicles so that the effect of solvent type on coal reactivity could be elucidated. The goal of this portion of the study was to determine the effect of liquefaction vehicle on the absolute and relative reactivities of four coals representing a broad rank range.

EXPERIMENTAL

Four coals from the Argonne Premium Coal collection were liquefied in four different vehicles. The coals employed for this study were:

Wyodak subbituminous
Illinois #6 high volatile bituminous
Upper Freeport medium volatile bituminous
Pocahontas low volatile bituminous

Properties of these coals are available from Argonne National Laboratory. The vehicles (solvents) employed consisted of both donor and non-donor species:

tetralin
1-methylnaphthalene
phenanthrene
naphthalene

Experimental runs were carried out in a tubing bomb microautoclave reactor system at 698 K (425 C), 6.2 MPa (900 psi) initial hydrogen pressure, and for reaction times of 5 and 40 minutes. Data on the conversion of each coal in each solvent to gas, THF-, and toluene-solubles was collected. Details on the procedures utilized have been described elsewhere (22).

DISCUSSION OF RESULTS

Effect of Vehicle on Liquefaction Reactivity

The objective of this study was to determine the reactivity of these four coals under identical reaction conditions, but in different pure solvents. Conversion to both THF- and toluene-solubles was measured. Our previous work has indicated that THF-soluble data provides a poor measure for liquefaction reactivity while toluene solubility data gives excellent correlation between coal properties and coal reactivity (23).

Data from the liquefaction of these four Argonne Premium coal samples in each of the four solvents are shown graphically in Figures 1 through 4. Figures 1 and 2 present the results for conversion of the coals to toluene-solubles at 5 and 40 minutes reaction time, while the data for THF-solubles is presented in Figures 3 and 4. As indicated in Figures 1 and 2, the absolute magnitude of conversion to toluene-solubles is not a strong function of the choice of liquefaction vehicle as long as the type of vehicle (donor vs. non-donor) remains unchanged. Hence the absolute value of the conversions to toluene-solubles are remarkably similar in phenanthrene, naphthalene, and 1-methylnaphthalene. Switching from a non-donor to a hydrogen donor solvent brings about an increase of 20 to 30% in the absolute value of the conversion to toluene-solubles at both 5 and 40 minute reaction times. This observation simply reflects the difference in rate that exists due to the difference in hydrogenation mechanisms in the two solvent systems. In the one case (the donor solvent tetralin) hydrogen needed to stabilize free radicals or to directly attack and cleave strong bonds in the coal matrix can be supplied directly from a hydroaromatic. When a non-donor is used however, the mechanisms of hydrogen transfer are less direct, and involve hydrogen shuttling and/or formation of radical species by reaction of solvent molecules with molecular hydrogen which then can serve as radical cappers and active bond fission promoter as illustrated by McMillen et al. (24).

While the absolute magnitudes of the conversions are functions of solvent, the relative reactivity rankings are <u>not</u> affected by the nature of the solvent if care is exercised in selecting an appropriate data set for purposes of making reactivity comparisons. Different defininitions can be used for reactivity depending on the nature of the processing property of

interest. From a rate processes perspective, the coal with the highest reaction rate would be judged to be the most reactive, while from a static point of view the ultimate extent of conversion to either THF- or toluene-solubles would be the appropriate measure of reactivity. In all cases regardless of vehicle type, the Wyodak subbituminous coal was the most reactive from a kinetic standpoint (based on the rate of conversion to toluene-solubles). In terms of ultimate conversion (extent of conversion to toluene-solubles), the Illinois #6 high volatile bituminous coal was the most reactive, followed by the Wyodak subbituminous coal and the medium and low volatile bituminous coals. These data show clearly that, over a broad range of coal types and reaction times, the nature of the liquefaction vehicle is not a major factor in determining the inherent reactivity of the coal. Figures 3 and 4 display the problems encountered when attempting to utilize data on conversion to THF-solubles as the measure of liquefaction reactivity. As shown, the reactivity rankings are not the same as for the toluene-soluble data set. Further, the relative reactivities of the four coals in terms of both rate and extent of reaction now are a function of the type of liquefaction vehicle employed. The indicated solvent effects and reactivity reversals exhibited by the THF-solubles data make it extremely difficult to draw any concrete conclusions regarding the effect of coal properties on reactivity.

ACKNOWLEDGEMENTS

This work was performed under sponsorship of the United States Department of Energy, Grant no. DE-FG22-85PC80907.

REFERENCES CITED
1. Bergius, F., JOUR. GASBELEUCHT., 54, 1912
2. Francis, W., FUEL, 11, 1932
3. Petrick, A.J., Gaigher, B., and Groenewoud, P., Jour. Chem., Met. Min. Soc. South Africa, 38, 1937
4. Wright, C.C. and Sprunk, G.C., Penn State Coll. Min. Ind. Exp. Sta. Bull. 28, 1939
5. Fisher, C.H., Sprunk, G.C., Eisner, A., Clarke, L., Fein, M.L., and Storch, H.H., FUEL,19, no. 6, 1940
6. Neavel, R.C., FUEL, 55, 1976
7. Shatwell, H.G., and Graham, J.L., FUEL, 4, 1925
8. Horton, L., Williams, F.A., and King, J.G., Dept. Sci. and Ind. Res., Fuel Research Tech Paper 42, 1936
9. Fisher, C.H., Sprunk, G.C., Eisner, A., O'Donnell, H.J., Clarke, L., and Storch, H.H., U.S. Bureau of Mines Tech. Paper 642, 1942
10. Given, P.H., Cronauer, D.C., Spackman, W., Lovell, H.L., Davis. A., and Biswas, B., FUEL, 54, Jan., 1975
11. _____, FUEL, 54, Jan., 1975
12. Abdel-Baset, M.B., Yarzab, R.F., and Given, P.H., FUEL, 57, Feb., 1978
13. Yarzab, R.F., Given, P.H., Spackman, W., and Davis, A., FUEL, 59, Feb., 1980
14. Mori, K., Taniuchi, M., Kawashima, A., Okuma, O., and Takahashi, T., A.C.S. Div. Fuel Chem. Preprints, 24, no.2, 1979
15. Durie, R.A., A.C.S. Div. Fuel Chem. Preprints, 24, no. 2, 1979
16. Gray, D., Barrass, G., Jezko, J., and Kershaw, J.R., FUEL, 59, 1980
17. Mukherjee, D.K., and Chowdhury, P.B., FUEL, 55, 1976
18. Guin, J.A., Tarrer, A.R., Prather, J.W., Johnson, D.R., and Lee, J.M., Ind. Eng. Chem. Proc. Des. and Devel., 17, no. 2, 1978
19. Gray, D., FUEL, 57, 1978
20. Furlong, M.W., Baldwin, R.M., and Bain, R.L., FUEL, 61, Feb., 1982
21. Baldwin, R.M., Durfee, S.L., and Voorhees, K.J., Fuel Proc. Tech., 15, 1987
22. Shin, S-C., M.S. Thesis no. T-3267, Colorado School of Mines, Arthur Lakes Library, 1986
23. Baldwin, R.M., Shin, S-C., and Miller, R.L., Energy and Fuels (in press), 1987
24. McMillen, D.F., Malhotra, R., Hum, G.P., and Chang, S-J., Energy and Fuels, 1, no. 2, 1987

REFERENCES CITED
1. Bergius, F., JOUR. GASBELEUCHT., 54, 1912
2. Francis, W., FUEL, 11, 1932
3. Petrick, A.J., Gaigher, B., and Groenewoud, P., Jour. Chem., Met. Min. Soc. South Africa, 38, 1937
4. Wright, C.C. and Sprunk, G.C., Penn State Coll. Min. Ind. Exp. Sta. Bull. 28, 1939
5. Fisher, C.H., Sprunk, G.C., Eisner, A., Clarke, L., Fein, M.L., and Storch, H.H., FUEL,19, no. 6, 1940
6. Neavel, R.C., FUEL, 55, 1976
7. Shatwell, H.G., and Graham, J.L., FUEL, 4, 1925
8. Horton, L., Williams, F.A., and King, J.G., Dept. Sci. and Ind. Res., Fuel Research Tech Paper 42, 1936
9. Fisher, C.H., Sprunk, G.C., Eisner, A., O'Donnell, H.J., Clarke, L., and Storch, H.H., U.S. Bureau of Mines Tech. Paper 642, 1942
10. Given, P.H., Cronauer, D.C., Spackman, W., Lovell, H.L., Davis. A., and Biswas, B., FUEL, 54, Jan., 1975
11. _____, FUEL, 54, Jan., 1975
12. Abdel-Baset, M.B., Yarzab, R.F., and Given, P.H., FUEL, 57, Feb., 1978
13. Yarzab, R.F., Given, P.H., Spackman, W., and Davis, A., FUEL, 59, Feb., 1980
14. Mori, K., Taniuchi, M., Kawashima, A., Okuma, O., and Takahashi, T., A.C.S. Div. Fuel Chem. Preprints, 24, no.2, 1979
15. Durie, R.A., A.C.S. Div. Fuel Chem. Preprints, 24, no. 2, 1979
16. Gray, D., Barrass, G., Jezko, J., and Kershaw, J.R., FUEL, 59, 1980
17. Mukherjee, D.K., and Chowdhury, P.B., FUEL, 55, 1976
18. Guin, J.A., Tarrer, A.R., Prather, J.W., Johnson, D.R., and Lee, J.M., Ind. Eng. Chem. Proc. Des. and Devel., 17, no. 2, 1978
19. Gray, D., FUEL, 57, 1978
20. Furlong, M.W., Baldwin, R.M., and Bain, R.L., FUEL, 61, Feb., 1982
21. Baldwin, R.M., Durfee, S.L., and Voorhees, K.J., Fuel Proc. Tech., 15, 1987
22. Shin, S-C., M.S. Thesis no. T-3267, Colorado School of Mines, Arthur Lakes Library, 1986
23. Baldwin, R.M., Shin, S-C., and Miller, R.L., Energy and Fuels (in press), 1987
24. McMillen, D.F., Malhotra, R., Hum, G.P., and Chang, S-J., Energy and Fuels, 1, no. 2, 1987

FIGURE 1

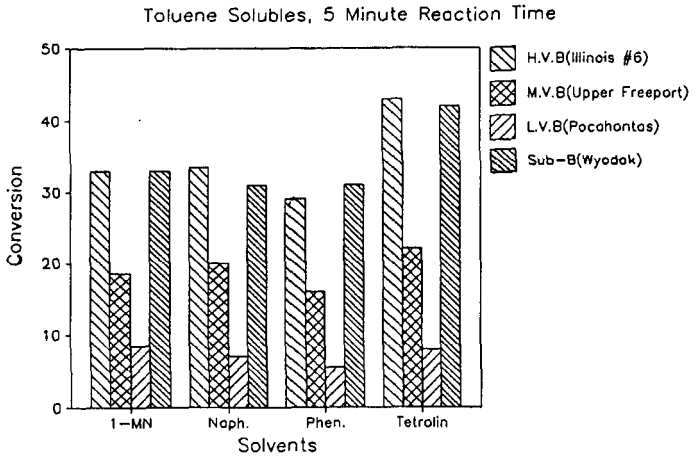

FIGURE 2

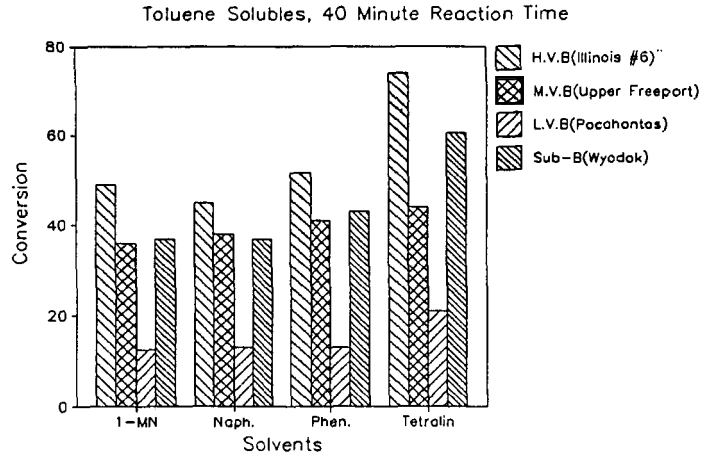

FIGURE 3

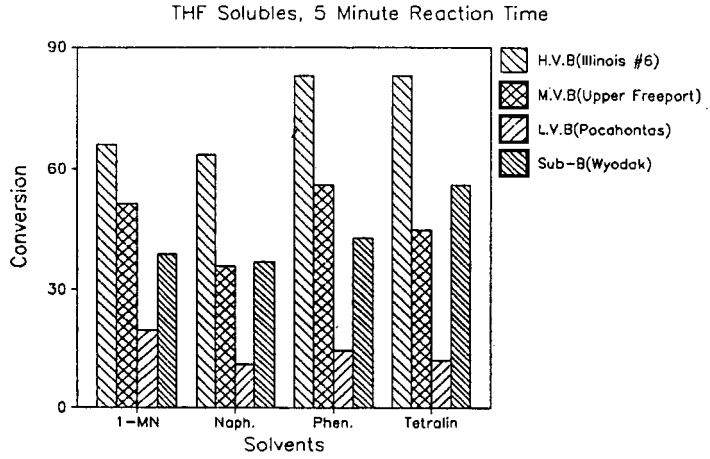

FIGURE 4

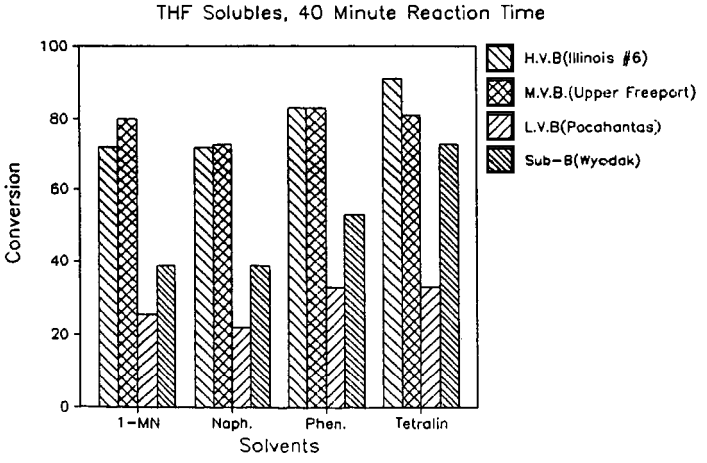

ILLINOIS BASIN COAL SAMPLE PROGRAM AND ACCESS TO INFORMATION ON ILLINOIS BASIN COALS

Carl W. Kruse, Richard D. Harvey and David M. Rapp

Illinois State Geological Survey,
615 E. Peabody Drive
Champaign, IL 61820.

ABSTRACT

The Illinois Basin Coal Sample Program (IBCSP), was established in 1983 at the Illinois State Geological Survey (ISGS) to facilitate comparisons of results among laboratories conducting basic and applied research on Illinois Basin coal. The sizes of samples available to the individual user and the focus on Illinois Basin coals are distinguishing characteristics of this program. The unit sizes provided to most requesters have been 1/256th of a 55-gallon barrel of coal (nominally 1.5-pound), 1/16th of a barrel (nominally 20-pounds) or one barrel (approximately 400 pounds). The Illinois Coal Development Board (ICDB) and the State of Indiana fund the IBCSP through the Center for Research on Sulfur in Coal (CRSC). The program makes samples available not only to CRSC contractors, but other research groups as well. Additionally, the CRSC supports a computerized information system through which on-line access to data bases on compositions of the IBCSP samples at the ISGS and on research being conducted on these samples is available.

Six Illinois Basin coals, designated IBCSP-1 through IBCSP-6, are available. Three mine-washed Illinois coals became available in 1983: IBCSP-1, a Herrin (Illinois No. 6); IBCSP-2, a Colchester (Illinois No. 2); and IBCSP-3, a mixture of a Springfield (Illinois No. 5) and a Herrin (No. 6). A fourth coal, IBCSP-4, a tipple (run-of-mine) Herrin (No. 6) coal, was added to the program in 1984. The fifth sample (IBCSP-5), a 3-ton channel sample of a Herrin (No. 6), was collected in 1985 and processed into 1-pint cans, 1-gallon cans and 5-gallon cans by Argonne National Laboratory (ANL). This sample is of higher quality than the other five; it was maintained under argon from the mine to the processing facility and all processing was carried out in ANL's inert atmosphere facility designed for the Premium Coal Sample Program (PCSP). IBCSP-5 matches the Illinois coal in the PCSP (PCSP-3). Because the replacement cost for this sample will be very high, charges are made depending on the quantity requested. The sixth sample, provided by the State of Indiana in December 1986, is a mine-washed sample of Springfield (No. 5) Coal from Southwestern Indiana. Multi-ton quantities of the five samples (3/8" x 0) are being maintained in 55-gallon barrels under a low pressure of nitrogen gas at the Applied Research Laboratory of the ISGS in Champaign, Illinois.

Characteristic properties -- maceral composition, reflectance of vitrinite, size and maceral association of pyrite grains, mineral matter composition, and minor and trace element compositions -- were determined on the samples. The informational data base comprising these and other data was established on a mainframe computer at the University of Illinois. The name, address, sample numbers, project title, and project objectives for each project using one or more of the IBCSP samples are included in this data base. To date more than 156 uniform splits of the first four samples in the program have been provided to 67 researchers, 34 located in Illinois. The remainder are in other states and Canada. Telephone requests for information on the IBCSP are received at 217-333-5161.

INTRODUCTION

Coal sample programs, frequently called sample banks, facilitate coal research not only by providing a source of samples but also by simplifying comparisons of results among laboratories that use representative fractions of the same coal. A number of sample programs are in operation in the United States -- the most widely known is the Penn State Coal Bank -- but few provide multi-pound quantities to their users. Additionally, few programs concentrate their efforts on coals from one basin.

In Illinois, the Gas Research Institute, Argonne National Laboratory, Southern Illinois University and the Illinois State Geological Survey are leaders in the development of coal sample programs. The Gas Research Institute (GRI) and the U. S. Department of Energy (U.S.DOE) sponsored a Coal Sample Bank Workshop in March of 1981 to resolve some of the technical problems of establishing a premium coal sample program [1]. The goal was the collection and storage of coal under conditions calculated to preserve as many of the physical and chemical properties as possible. With GRI funding, R. R. Dutcher at Southern Illinois University (SIU) began a study in 1981 on techniques for field acquisition, transporting, processing and storage of premium coal samples. The results are available in the final report [2]. The ANL initiated the Premium Coal Sample Program (PCSP) in late 1982 to meet nation-wide, small-scale, basic-research needs of the research community. A rigid-wall facility was constructed for processing barrel quantities of coal in a nitrogen environment with remote-control equipment [3]. Exceptional care was taken in collection, transport, processing, and storage of the channel samples stored in this program. The relative humidity of the nitrogen atmosphere was controlled to avoid changes in the moisture level. The samples are now available in 5 and 10 gram quantities, hermetically sealed in glass ampules [4].

The Illinois Coal Development Board (ICDB) funds a variety of coal research projects in the State of Illinois. To provide continuity in succeeding years, the ICDB at its first meeting in 1982 expressed interest in funding a project to collect and store reasonably large samples of coal. The board desired to assure the availability of a few of the same coals used by the first year's ICDB contractors for research in subsequent years. The Minerals Engineering Section of the ISGS agreed to collect additional coal and store it at room temperature in a nitrogen atmosphere. The maintenance of samples together with the distribution of samples has become the Illinois Basin Coal Sample Program (IBCSP). The State of Indiana joined the effort in December 1986 by supplying a sample and becoming a partner in sharing the maintenance and distribution costs.

Five of the six coals in this program have undergone some oxidation before leaving the mine site, during transport to Champaign by truck, and during the time required to crush, riffle and package the samples. For the five coals in question, homogeneity from barrel to barrel was assured by a series of rifflings. For the three-ton lots, the coal was passed through two riffles in succession to produce four sets of four barrels each, each set being equivalent in composition to the other sets. The composition of barrels within a set was not equivalent. In the next stage of riffling, each set was riffled through two riffles in succession to homogenize the four barrels within the set. Added exposure to air was the offsetting cost for this assurance of sample uniformity. For many types of tests, applied bench-scale process testing in particular, the degree of oxidation which occurred is acceptable because all coals entering a commercial process have undergone some degree of oxidation during mining and cleaning. The units delivered to users have been approximately 0.7 kilogram and 11 kilograms (1.5 and 20 pounds). They are produced by riffling a barrel of coal to produce representative fractions. The particle size distribution of the smallest units (1/256th of a barrel) is minus 8 mesh by zero and that of remaining units (1/16th of a barrel or larger) are minus 3/8" by zero. Larger quantities have been supplied to a few projects.

THE SIX COALS AVAILABLE

The six coals now available are described in Table 1. The results of most of the standard ASTM tests are shown in Table 2. The minor and trace elements were also determined (Table 3).

Chemical analyses

Barrel to barrel variations in the initial composition are small based on the analyses of fractions taken during a pilot testing of the homogenization procedure and by the analyses shown in Table 4 (column 1) from riffled fractions of four barrels of IBCSP-4 at the time of the initial packaging. Variations are not more than expected for the analysis of a given sample by different analysts or by different laboratories. Periodic proximate and ultimate analyses show excellent uniformity. Analyses over a two year period for IBCSP-4 in Table 4 are typical. All samples except IBCSP-5, which was specially prepared and prepackaged under nitrogen, can be expected to contain the trace amounts of elemental sulfur shown to accompany oxidation [5].

Minor and trace element analyses

Comparison of the results of minor and trace element analyses with the average of concentrations found in channel samples collected by the ISGS from the Herrin and Springfield seams in Illinois for many years [6], (see Table 3) indicates IBCSP-4 is notably rich in SiO_2, MgO, Na_2O, F, and Rb. The reason for these high values is the relatively high abundance of mineral matter in this run-of-mine sample. It should also be noted that IBCSP-2 contains a relatively high amount of As, Ge, and Pb compared to the average. Germanium is probably associated with the organic matter in the sample, while As and Pb are probably in pyrite.

Petrographic Analyses

On a mineral matter free basis, all six samples are rich in vitrinite (85 to 90 vol %). On this basis, IBCSP-5 contains the most inertinite group macerals (10 vol %). The reflectance of vitrinite (maceral telocollinite) is highest for IBCSP-3 (0.74 %, mean-maximum) and the other samples range between 0.46 to 0.67 percent. Complete analyses were reported by Harvey, et al. [7].

Mineral matter analyses

The total amount of mineral matter is most abundant in IBCSP-4 because this sample is a run-of-mine product and it contains some shale from the mine roof. A trace of marcasite, an orthorhombic form of FeS_2, was detected in all samples except IBCSP-4. Two different carbonates, calcite ($CaCO_3$) and dolomite ($CaMg(CO_3)_2$), occur in IBCSP-5. The differences in the mineral phases in the samples may affect the outcome of desulfurization or cleaning processes applied to these coals. Complete analyses are given in Harvey, et al. [7].

Pyrite size and maceral association

The mean diameters for pyrite grains in the six IBCSP samples range from 4 μm (IBCSP-3) to 9 μm (IBCSP-4). The distribution of particle sizes in each sample is much wider than one might project from these mean values and significant differences exist in the way pyrite is distributed among the particles. These differences determine the effectiveness of physical methods for removing pyrite. Approximately 25 percent of the pyrite in IBCSP-5 occurs within macerals-rich particles versus 80 percent in IBCSP-3 [4].

Table 1. Samples available (ash and sulfur on a moisture-free basis)

Sample no.	Product	Seam	Location	Rank	Ash[1] %	Sulfur[1] %
1	Prep plant	Illinois No. 6	W. Central IL	HVCB	10.3	4.3
2	Prep plant	Illinois No. 2	Western IL	HVCB	6.7	3.2
3	Prep plant	80% Illinois No. 5 20% Illinois No. 6	Southern IL	HVBB	8.4	2.3
4	Run-of-mine	Illinois No. 6	Southwestern IL	HVCB	38.1	4.2
5	Channel	Illinois No. 6	Southwestern IL	HVCB	18.0	4.6
6	Prep plant	Indiana V[2]	Southwestern IN	HVCB[3]	9.0	3.8

[1] Analyses in February 1987

[2] The Springfield (Illinois No. 5) Coal is called Indiana V in Indiana

[3] Borderline between HVBB AND HVCB

Table 2. Average[1] analyses[2] of the six coals in the IBCSP (values reported on a moisture-free basis except for moisture)

/Sample number	1	2	3	4	5	6
Moisture	14.14	13.62	5.36	10.21	9.47	10.42
Volatile matter	44.12	43.34	39.20	30.56	40.38	39.56
Fixed carbon	45.62	49.92	52.48	31.36	41.61	51.44
H-T ash	10.28	6.66	8.36	38.10	18.00	9.00
Carbon	67.66	73.31	73.82	45.97	63.26	71.64
Hydrogen	4.86	5.21	4.94	3.46	4.40	4.73
Nitrogen	1.18	1.47	1.68	0.80	1.23	1.78
Oxygen (by difference)	11.63	10.09	8.75	7.43	8.39	9.05
Sulfatic sulfur	0.06	0.10	0.09	0.10	0.00	0.0
Pyritic sulfur	1.20	2.34	1.03	2.33	2.55	1.83
Organic sulfur	3.00	0.92	1.16	1.76	2.08	1.94
Pyritic/organic S ratio	0.40	2.53	0.89	1.32	1.23	0.92
Total sulfur	4.26	3.23	2.27	4.19	4.63	3.77
Chlorine	0.13	0.03	0.18	0.05	0.09	0.03
Calorific value (Btu/lb)	12606	13526	13437	8492	11522	13248
Free swelling index[3]	4.5	4.3	5.2	2.1	3.8	4.7

[1] Average of all analyses through December 1986 for IBCSP-1 through IBCSP-5. Average of 10 analyses in February 1987 for IBCSP-6

[2] All values are percent except for pyritic/organic sulfur ratio, calorific values and FSIs

[3] FSIs are normally reported to the nearest 0.5 unit

Table 3. Minor and trace elements

Oxide/element	IBCSP sample number 1	2	3	4	5	Average IL coal*
Minors (%)						
SiO_2	4.6	1.8	4.1	22.1	8.2	5.5
Al_2O_3	1.6	0.9	1.8	6.5	2.9	2.5
Fe_2O_3	1.7	2.8	1.5	3.8	3.4	2.7
MgO	0.09	0.038	0.073	0.529	0.185	0.046
CaO	0.5	0.2	0.1	1.4	1.2	1.0
Na_2O	0.139	0.0182	0.0297	0.337	0.168	0.0987
K_2O	0.21	0.11	0.2	0.99	0.33	0.22
P_2O_5	0.02	0.01	0.03	0.09	0.02	0.02
TiO_2	0.08	0.03	0.09	0.31	0.15	0.11
Traces (ppm)						
Ag	<1	<1	<1	<1	<0.2	0.06
As	2	32	16	5	2.6	11
Ba	32	14	28	135	73	140
Be	1.4	3.3	1.2	2.7	1.0	1.5
B	193	109	71	317	179	118
Br	6	3	12	3	6.5	12
Cd	1.1	0.8	0.1	<0.4	-	1.5
Ce	6	2	10	21	19	14.7
Co	3	6	5	9	3.8	5
Cr	31	7	16	44	19	18
Cs	1.1	0.8	1.2	4	1.9	1.0
Cu	9.7	21.9	8.0	14.4	9.5	12.5
Dy	0.6	1.5	0.9	1.7	-	1.1
Eu	0.2	0.2	0.2	0.5	0.2	0.3
F	63	26	56	460	-	68
Ga	3	3	3	10	3.4	3.9
Ge	<5	30	<5	<5	5	5
Hf	0.4	0.2	0.5	1.7	1.0	0.6
La	4	2	7	16	5.9	7
Li	11.3	18.1	29.9	38.9	8.2	16.3
Lu	0.1	0.1	0.1	0.3	0.08	0.1
Mn	31	16	13	112	71	55
Mo	15	4	13	6	9	9
Ni	11	22	14	23	15	18
Pb	8	149	57	28	6	28
Rb	9	5	11	63	20	16
Sb	0.2	3.4	1.1	0.3	0.3	1.0
Sc	2.1	2.1	2.6	6.4	2.4	2.7
Se	1.5	1.3	2.2	2.2	2.4	2.4
Sm	0.9	0.9	1.4	2.9	1.2	1.4
Sn	<1	<1	<1	1.7	<5	-
Sr	25	12	33	58	29	34
Ta	0.1	0.1	0.1	0.4	0.25	0.2
Tb	0.1	0.2	0.2	0.2	0.13	0.2
Th	1.2	0.7	1.3	3.9	3.2	2.2
Tl	<2	<2	<2	<2	1.0	1.0
U	<2	<1.5	<4	<3	1.2	1.5
V	25	22	26	50	23	31
W	<0.5	<0.5	<0.7	0.9	1.5	0.6
Yb	0.4	0.6	0.5	1.0	0.5	0.6
Zn	172	99.8	45.1	175	77	248
Zr	16	13	23	51	28	35

* Calculated from data on channel samples from the Herrin (No.6) and Springfield (No. 5) Coals (Harvey, et al., 1983).

Table 4. Analyses of IBCSP-4[1]
(values reported on a moisture-free basis except for moisture)

Analysis[2]	C22538-41 July 84 Av. (Std. Dev.)[3]	C23924 Sept 85	C24450-51 March 86	C24893 July 86
Moisture	10.2 (0.05)	10.2	10.2	10.3
Volatile matter	30.3 (0.17)	30.4	31.2	31.1
Fixed carbon	31.6 (0.27)	31.3	30.8	31.0
Ash	38.1 (0.29)	38.3	38.0	38.0
Carbon	46.92 (0.42)	46.09	48.04	48.00
Hydrogen	3.28 (0.054)	3.44	3.27	3.37
Nitrogen	0.68 (0.045)	1.09	0.80	0.98
Oxygen	6.95 (0.40)	6.82	5.24	5.30
Sulfatic sulfur	0.10 (0)	0.26	0.01	0.0
Pyritic sulfur	2.17 (0.059)	2.36	2.77	2.51
Organic sulfur	1.80 (0.036)	1.61	1.78	1.76
Total sulfur	4.07 (0.071)	4.23	4.55	4.27
Chlorine	0.04 (0.007)	0.03	0.10	0.08
Calorific Value (Btu/lb)	8527 (26)	8407	8462	8469
Free Swelling Index	2.5	2.5	1.5	1.0

[1] Herrin (No. 6) coal (run-of-mine) from a southwestern Illinois underground mine collected December 15, 1983

[2] All values are percent except the calorific values and the FSIs

[3] Analyses on riffled fractions from four of the eight barrels

INFORMATION SYSTEM

A computerized information system (data base) is available on a mainframe computer (Control Data, Cyber-175) at the University of Illinois in Urbana. This system operates in parallel with a larger existing data base on the same computer covering the Chemistry of Illinois coals [8]. Both systems can be accessed by an investigator at a remote facility through a modem during a single computer session.

Two types of data files were installed for the IBCSP. The first contains the name, address, project title, and results or objectives of the researchers using the samples; the second contains the chemical and other characteristic properties of the samples:

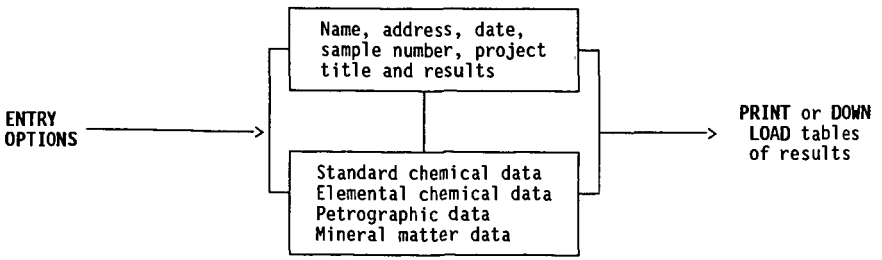

Names of researchers using these samples and the analytical data can be retrieved. Users of the data base may read about the past and current research on the samples directly at their monitor. Users may also select and obtain hard copy for any type of analytical data or other types of data on a single sample or all six of them. Menu options facilitate downloading retrieved files to the user's own microcomputer. Those who have only a terminal and modem can print retrieved data at the ISGS for mailing to the user. Access to the data base can be obtained by contacting R. Harvey (217-244-0836). A small fee is required to cover the direct computer charges. Persons without terminals can obtain information by contacting either the Coal Section or the Minerals Engineering Section of the Illinois State Geological Survey (217/333-4747) or the Center for Research on Sulfur in Coal (217/333-9241), both located in Champaign, Illinois.

ACKNOWLEDGEMENT

This work was funded in part by the Illinois Coal Development Board through the Center for Research on Sulfur in Coal and by the State of Indiana. Many ISGS staff persons have contributed to this program. The authors wish to acknowledge recent assistance and helpful suggestions by Karl Vorees of Argonne National Laboratory and Rodney Ruch, Henry Ehrlinger III and Jimmie Cooper of the ISGS.

REFERENCES

1. Coal Sample Bank Workshop, sponsored by Gas Research Institute and U.S. Department of Energy, Atlanta, GA, March 27 & 28, (1981).

2. Dutcher, R. R., M. E. Gunter, J. C. Crelling, and W. E. Brower, Development of techniques for obtaining and storing premium coal samples: final report (March 1981 - April 1984), for Gas Research Institute, Contract No. 5080-361-0419, GRI-85/0008, (1985).

3. Vorres, K. S. and K. Janikowski, Coal samples available from the premium coal sample program: Preprints of Papers Presented at Anaheim California American Chemical Society Division of Fuel Chemistry, September 7-12, 1986, Volume 31, No. 3, pp 304-309, (1986).

4. Vorres, K. S. and S. K. Janikowski, The eight coals in the Argonne Premium Coal Sample Program; Preprints of Papers Presented at Denver Colorado American Chemical Society Division of Fuel Chemistry, April 5-10, 1987, Volume 32, No. 1, pp 492-499, (1987).

5. Duran, J. D., S. R. Mahasay and L. M. Stock, The occurrence of elemental sulfur in coals, Fuel, volume 65, pp 1167-8, (1986).

6. Harvey, R. D., R. A. Cahill, C.-L. Chou, J. D. Steele, Mineral matter and trace elements in the Herrin and Springfield Coals, Illinois Basin coal field: Final Report, EPA-CR806654 (EPA-600/7-84-036), Illinois State Geological Survey Contract/grant report 1983-4, 162p. (1983).

7. Harvey, R. D., A. Kar, J. D. Steele, Information system on Illinois coal II: Characterization of samples in the Illinois Basin Coal Sample Program, Illinois State Geological Survey, Contract/Grant Report 1986-1, 33p. (1986).

8. Harvey, R. D., A. Kar, M. H. Bargh, and L. B. Kohlenberger, Information system on chemistry of Illinois coal: Final Report, Ill. Coal Research Board, Illinois State Geological Survey Contract/grant Report 1985-5, 20p., (1985).

NO_x EMISSION CONTROL BY PARTICLE QUENCHING IN AN ADVANCED GLASS MAKING PROCESS

K.M. Jeong, R. Tiwary, A. Chatwani, L. Westra, J. Woodroffe, F. Hals, and D. Stickler

Avco Research Laboratory, Inc.
A Subsidiary of Textron, Inc.
2385 Revere Beach Parkway
Everett, MA 02149

and

L. Donaldson

Gas Research Institute
8600 West Bryn Avenue
Chicago, IL 60631

ABSTRACT

The formation of NO_x in an advanced glass melting (AGM) process has been studied. In this system, methane is combusted with preheated air at near stoichiometric conditions resulting in a potential for production of a high NO_x concentration in the exhaust. The minerals required for glass synthesis are entrained as a high loading concentration of fine particles in the preheated air supply. The particles are heated up in suspension by the combustion products. The thermal time scale for gas-particle heat transfer is chosen to be comparable to or less than NO_x formation kinetic time. This was projected to prevent formation of NO_x at a concentration corresponding to the adiabatic gas phase combustion temperature. The measured NO_x concentration in the glass melter exhaust is found to be significantly below anticipated NSPS requirements. A model is proposed for the processes in the AGM based on a kinetics/transport code. The decreased amount of NO_x formation is attributed to gas/particle thermal quenching effects and, possibly heterogeneous catalytic reduction.

INTRODUCTION

The development of an advanced gas-fired glass melting process (AGM) is being investigated as an alternative to the conventional glass melting furnace which is of the open-hearth type. The advanced glass melter is a technical derivative of a slagging coal combustor developed for magnetohydrodynamic power generation applications [1-3]. A primary goal is to transfer heat very efficiently at high temperatures to entrained glass batch particles. The high particulate loading required for this application presents a unique mechanism for limiting the formation of NO_x.

High temperature reaction of air feed nitrogen and oxygen to primarily form nitric oxide, NO, is a source of potentially high NO_x concentrations in the melt furnace exhaust. NO_x control is achieved in the AGM by using the entrained particulate material as a dispersed heat sink with a very short thermal transient time. Thus, the combustion products are rapidly quenched from the adiabatic temperature at which high NO_x concentrations would normally result to a much lower temperature. For the size particles considered, the thermal quenching is accomplished on a time scale much shorter than the NO_x chemical kinetic formation time.

AGM CONCEPT AND EXPERIMENTAL SYSTEM

In the glass melter design concept, premixed batch materials are injected as fine particles into a high temperature combustion air line and transported in suspension to a high intensity gas burner. The materials are heated very rapidly in suspension in the turbulent flow field in the burner. A converging nozzle at the exit of the burner accelerates the flow and directs it into a melt separation and homogenizing chamber. The hot materials are separated inertially from the combustion gas and deposited on a collecting surface where initial homogenization occurs. The thin liquid layer flows from the collecting surface to a melt reservoir at the bottom of the chamber where additional homogenization can occur. The combustion products exit the melt separation chamber and are ducted to downstream heat recovery equipment for heating the incoming combustion air.

The experimental system used for development testing of the burner configuration and the separation centerbody is schematically shown in Figure 1. The unit consists of a pre-burner, a main combustor, and a glass receiver. The purpose of the gas-fired pre-burner is to simulate the high temperature preheat since there was no source of high temperature preheated air with which the system would normally operate. The fine glass feed particles are introduced downstream of the pre-burner through three injectors to promote thorough mixing with the gas. Initial tests used cullet as the feed material.

Gaseous oxygen is added to the combustion products of the pre-burner for combustion of the fuel added in the main or glass melting burner. Natural gas is introduced through eight radial injectors just upstream of the main burner. A sudden enlargement at the burner entrance creates a strong vortex flow region to promote mixing of the fuel and oxidizer. Combustion takes place with the particles still entrained in the gas. Rapid quenching of the combusted gas by these particles acts to keep the peak temperature down, thus reducing the NO_x formation. A convergent nozzle at the exit of the burner accelerates the flow to the velocity required to accomplish the inertial separation of the particulate material from the combustion products, leading to homogenization and glass formation.

NO_X TEST RESULTS

The NO_X concentration in the burner exhaust gas is strongly influenced by the temperature-time history and the oxygen concentration of the gas. The latter is determined by the gas stoichiometry or the air-fuel equivalence ratio used. The process constraint is to maintain a low oxygen concentration as well as a minimal residence time at the peak temperature, yet provide for rapid heat transfer to the entrained batch material. For these conditions, NO_X concentrations significantly below the equilibrium flame adiabatic stoichiometric level are predicted.

Figure 2 shows the equilibrium concentrations of NO which would be expected in the absence of particle quenching effects. For stoichiometric and fuel rich combustion, the NO equilibrium concentration for various calculated adiabatic flame temperatures reached by combustion with preheated air are indicated. If an emission limit of 4 lbs NO_X/ton glass produced is assumed, then the maximum allowed NO concentration in the exhaust gas is 970 ppm for stoichiometric conditions.

Tests were conducted over a wide range of gas mass flows and feed loadings to determine system performance. While tests without batch material demonstrated that fuel-rich combustion offers the lowest NO_X emission due to lower peak flame temperatures, it leads to a lower thermal efficiency because a portion of the combustion energy of the fuel is not released and made available for melting of the glass in the furnace. As a result, the main furnace is typically operated with excess oxygen, $\phi \sim 1.4$. The temperature of the melt chamber is approximately 2500F. For these conditions, NO_X formation is approximately 1200 ppm prior to particle injection. Since the residence time at peak temperature is short, several milliseconds, the NO_X concentration is less than the equilibrium level shown in Figure 2.

Tests with a four component batch comprising 52% silica, 20% soda ash, 13% calcium carbonate, and 15% cullet demonstrated the AGM's ability to capture, homogenize and fine the molten batch material on the centerbody, producing a fully reacted glass product. As predicted, the NO_X production of the melter is considerably reduced by the quenching of the combustion gas by the batch particles. Batch injection is found to reduce the exhaust gas NO_X level to approximately 250 ppm, corresponding to an NO_X loading of 1 lb/ton glass without flue gas treatment.

KINETICS/TRANSPORT MODEL

The chemical kinetic reaction mechanism used to model AGM combustion consists of 31 chemical species and 146 elementary chemical reactions. The principal reactions for formation and decomposition of thermal NO are:

$$O_2 + M \rightarrow O + O + M$$

$$N_2 + O \rightarrow NO + N$$

$$N + O_2 \rightarrow NO + O$$

$$N + OH \rightarrow NO + H$$

The first three reactions, where M is a third body (usually N_2), represent the important and well known Zeldovich mechanism of atomic exchange reactions. The code utilizes experimentally measured reaction rate parameters or the results of thermodynamic calculations if experimental data are not available. The numerical technique used in these calculations is described by Reference 4.

A thermodynamic equilibrium code is initially used to determine the composition of vitiated air from the combustion of air/CH_4 at T ~ 2500K in the pre-burner. These species account for approximately 40% of the total concentration of initial molecular constituents in the main combustor. Given these values and the concentration of added O_2 and CH_4 necessary to obtain the desired air/fuel ratio, the kinetic model is used to obtain the temporal dependence of key reaction species as a function of initial temperature. Figure 3 shows calculated temporal profiles for T = 1500K and a stoichiometric air/fuel ratio. Following an ignition delay of about 1.6 ms, a peak flame temperature of approximately 2350K is attained. The e-fold NO formation time is ~ 3.0 ms. The corresponding NO mass fraction, 0.003, is in good agreement with thermodynamic equilibrium calculations shown in Figure 4. This value is somewhat higher than the AGM test results, but this is attributed to a lower gas temperature in the glass melter.

The kinetic code is modified to include the effects of solid particles and the calculations are repeated. As Figure 3 indicates, the addition of solid particles reduces the NO_x concentration from approximately 2000 ppm to 750 ppm, a factor of ~2.5. The AGM test results show still lower NO_x concentrations in the furnace exhaust, but the general conclusion remains that NO_x control is achieved by using entrained particulates as a dispersed heat sink with a short thermal transient time. Some errors are introduced in the kinetic calculations due to the difficulty of simulating the process which causes ignition, namely, the expansion of gases into a dump combustor, as well as the use of a flameholder, creating recirculation zones which result in bulk flow and mixing of combusted and uncombusted gases. This is analogous to the experimental situation where ignition would also not take place if methane was to be injected into the gas stream without provisions for flameholding.

A numerical simulation model treating transport processes in the AGM is used to describe NO_x formation and decomposition during rapid gas cool down by suspended batch material. The code is 1-D and calculates the temperatures and velocities of gas and particles along the length of the combustor. It assumes that all the particles are entrained in the gas and do not come into contact with each other in the combustor. Gas properties are calculated based on its chemical composition. The batch composition and the gas flow rates were selected to simulate the performance of the AGM. The program starts calculations at the location where particles are injected into the gas and it follows the temperature and velocity of gas and particles as they move along the combustor till the particles separate on the target.

Figure 5 shows the temperature profiles in the combustor section. Cold batch particles (sand, cullet, soda, and lime; batch flow rate=0.12 kg/s) were injected into hot gas coming from the vitiation burner (0.11 kg/s). The particle temperature rises at a rate dependent on the particle size. The flow rates of oxygen and natural gas were 0.037 and 0.0083 kg/s, respectively. The hot combustion gas is initially quenched very rapidly due to the high heat transfer rate from the gas to small particles. The gas temperature exhibits two subsequent sharp drops when oxygen and secondary methane are added to the gas stream. The calculation indicates that the gas cools from its peak temperature to 800-900K in about 12 ms.

At a distance of 1.2 meters from the particle injection location combustion takes place and the gas temperature sharply increases. The particle temperature also rises, but the rate is slower due to particle inertia. By the time the gas exits the combustor, 40 ms after particle injection, the temperature of the gas and the majority of the particles is almost equal, about 1800K. The only exception are the soda particles which due to their large size (150 micron diameter) and, thus, their large thermal inertia, are unable to follow the gas temperature as closely.

A question not presently addressed by the model is the suggestion of NO_x control by heterogeneous catalytic reduction. Evidence for such processes is provided by studies of the reduction of NO by H_2 over a Rh/SiO_2 catalyst [5] and of the decomposition of nitrous oxide on magnesium oxide and cupric oxide [6]. In addition, specific gas-surface interactions have been reported for NO and SO_2 with constituents typically found in entrained fly ash from coal combustion [7]. The effect of batch particle surface absorption sites for catalytic reduction and enhanced NO_x control in the AGM process requires additional analysis.

SUMMARY

The measured NO_x concentration in the advanced glass melter exhaust gas is significantly below anticipated NSPS requirements. This is attributed to gas/particle thermal quenching effects. NO_x formation in the high temperature post-flame gases is chosen to occur over a time scale of several milliseconds, whereas heat transfer takes place on a shorter time scale resulting in significantly lower NO_x emissions than the equilibrium level for adiabatic gas combustion.

ACKNOWLEDGEMENTS

The authors gratefully acknowledge the support of this work by the Gas Research Institute under contract GRI 5086-232-1274.

REFERENCES

1. "Coal-Fired Combustor Development Project," Final Technical Report, Prepared by the Avco Everett Research Laboratory for the U.S. Department of Energy, Report No. ET-10787-3, October 1980.

2. D. B. Stickler and R. DeSaro, "Controlled Utilization of Coal Slag in the MHD Topping Cycle," presented at the Engineering Foundation Conference on Ash Deposits and Corrosion Due to Impurities in Combustion Gases, held at New England College, Henniker, NH, June 26-July 1, 1977.

3. J. G. Hnat, "A Direct Glass Melting System with Integrated Heat Recovery - Pressurized System Design," U. S. Patent, Disclosure Document No. 106632, March 8, 1982.

4. A. K. Varma, A. U. Chatwani, and F. V. Bracco, "Studies of Premixed Laminar Hydrogen - Air Flames Using Elementary and Global Kinetics Models," Combust. Flame 64: 233-236 (1986).

5. B. J. Savatsky and A. T. Bell, "Nitric Oxide Reduction by Hydrogen Over Rhodium Using Transient Response Techniques," in Catalysis Under Transient Conditions, Eds. A. T. Bell and L. L. Hegedus, ACS Symposium Series 178, American Chemical Society, Washington, D. C., 1982, p. 105.

6. H. Kobayashi and K. Hara, "Decomposition of Nitrous Oxide on Magnesium Oxide Compared to that on Cupric Oxide," in Catalysis Under Transient Conditions, Eds. A. T. Bell and L. L. Hegedus, ACS Symposium Series 178, American Chemical Society, Washington, D. C., 1982, p. 103.

7. R. V. Siriwardane and J. M. Cook, J. Coll. Int. Sci. 104, 250 (1985); 110, 504 (1986).

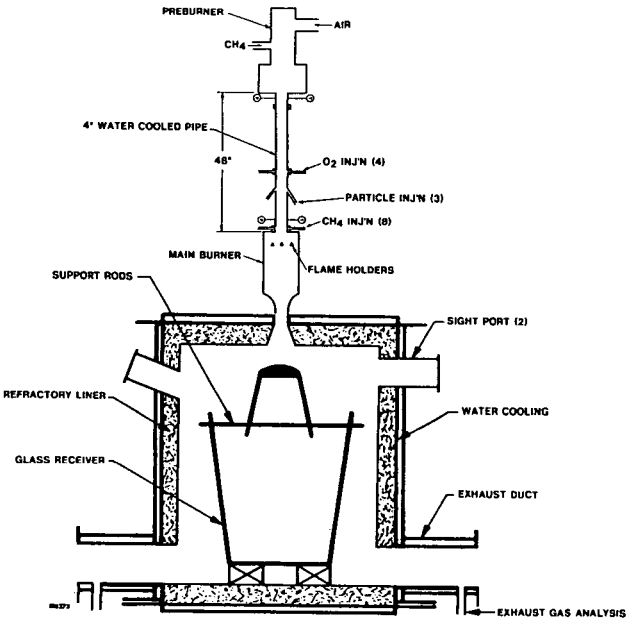

Figure 1 Schematic of AGM Experimental Set-up

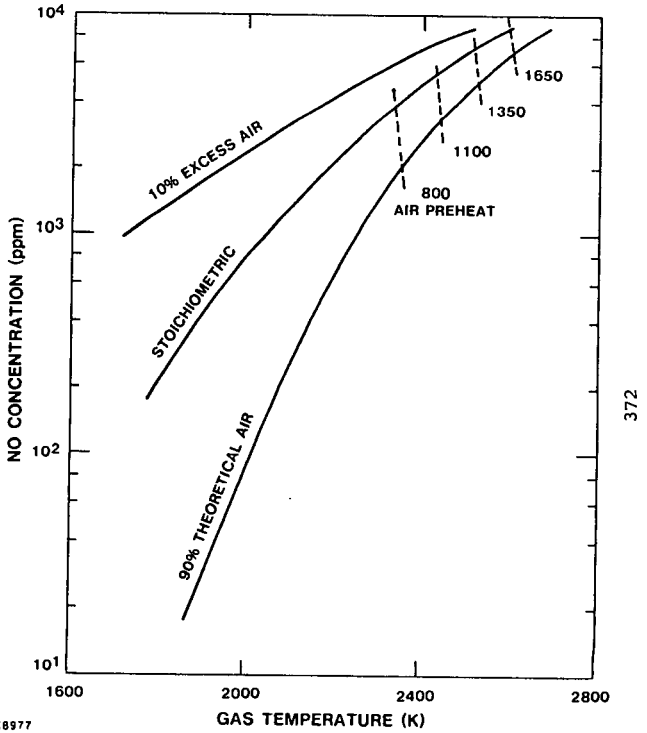

Figure 2 Calculated Equilibrium NO Concentrations for Various Stoichiometries and Gas Temperatures

(a)

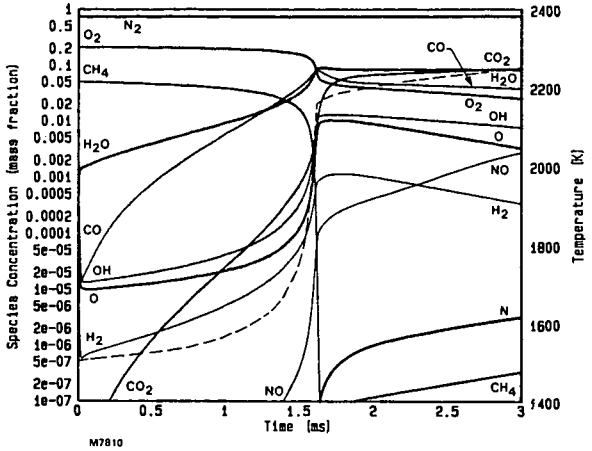

(b)

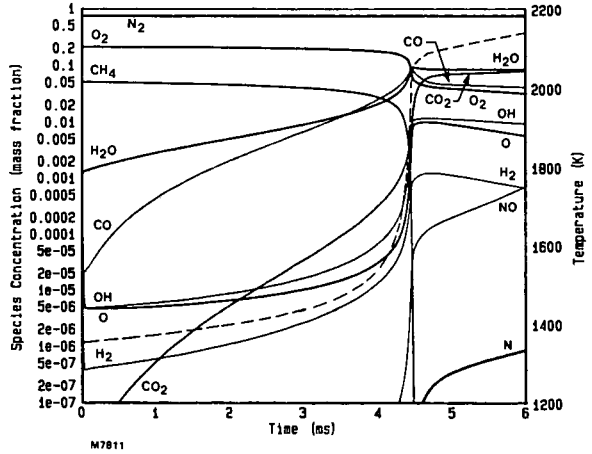

Figure 3 Combustion Species Temporal Profiles
(Dashed Line Shows Temperature Profile)
(a) Without Solid Particles
(b) With Solid Particles

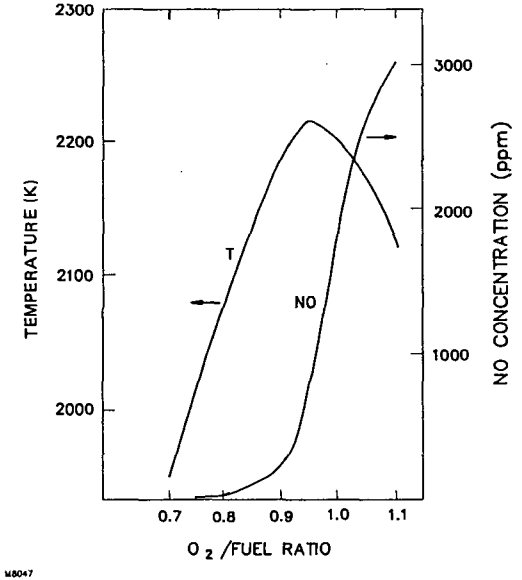

Figure 4 Equilibrium Calculation of Temperature and [NO] as a Function of the Oxygen/Fuel Ratio

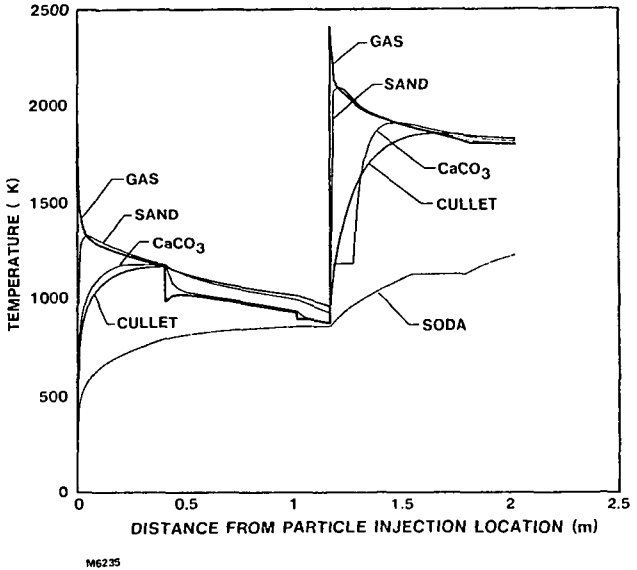

Figure 5 Temperature Profiles in Glass Melter

SO_x-NO_x CONTROL IN A STAGED CYCLONE COAL COMBUSTOR WITH LIMESTONE INJECTION

B. Zauderer,[1] E. Fleming[1] and W. M. Swift[2]

Coal Tech Corporation
P. O. Box 154
Merion Station, PA 19006[1]

Argonne National Laboratory
9700 South Cass Avenue
Argonne, Illinois 60439[2]

ABSTRACT

The results of a preliminary experimental study of SO_x-NO_x control in a two-stage cyclone coal combustor (2 MW_t) with limestone injection are presented. The tests were carried out using a finely pulverized West Virginia low-sulfur bituminous coal (0.8% S), an Illinois No. 6 medium-sulfur coal (1.6% S), and an Illinois No. 6 high-sulfur coal (2.7% S). With limestone injection in either the first or second stage of the combustor, SO_2 reductions in excess of 80% were obtained. The sorbent injection tests indicated that the first-stage combustion temperature as influenced by the air/fuel ratio was a major factor in sulfur capture. NO_x emissions measured at the exit of the second-stage combustor were reduced by up to 55 % over those from single-stage combustion. In addition, the benefits of a staged cyclone combustor for NO_x control were enhanced when the second-stage gas temperature was minimized, either through increasing second-stage air dilution or by maximizing first-stage carbon conversion.

BACKGROUND AND OBJECTIVES

Recent developments in coal cleaning technology and in the preparation of coal-water slurries have prompted renewed interest in the direct firing of gas turbines with coal-derived fuels, such as partially cleaned fuel gas and coal-water mixtures. Several recent studies have identified the potential economic advantages of these systems over conventional coal-fired power generation (1-3).

An alternative approach to the concept of a coal-fired gas turbine is the direct combustion of the coal in a staged slagging combustor. The slag rejecting combustor has been developed primarily in support of magnetohydrodynamics (MHD) technology. More recently, however, development of the slagging combustor for the control of SO_x and NO_x emissions has been considered for application to both the coal-fired gas turbine option and to the retrofit of existing gas and oil-fired boilers.

The concept of the staged slagging combustor for SO_x/NO_x control is similar to the LIMB (limestone injection into multi-stage burners) concept being developed for conventional boilers by the U. S. Environmental Protection Agency and the Electric Power Research Institute: namely, staged combustion (fuel-rich first stage) for the control of NO_x emissions and limestone injection for the control of SO_x emissions. The added advantage of slag rejection during combustion makes the slagging combustor ideally suited to a wide range of utility and industrial applications, including the coal-fired gas turbine system and gas/oil-to-coal conversions.

Although the amount of data available in the literature is fairly limited, the application of advanced slagging combustors to the control of SO_x/NO_x emissions has shown promising results (4,5). In pilot-scale testing of a low NO_x/SO_x burner developed by Rockwell International, better than 70% SO_2 reduction, NO_x emissions below 100 ppm (at 3% O_2), slag/fly ash removal over 70%, and carbon burnout greater than 99% have been demonstrated in tests with low-sulfur western coals (4). In a few cases, better than 95% SO_x reduction and zero NO_x emissions were reported, even when the only calcium used was the calcium inherent in the coal ash.

Equally encouraging results have been reported for the TRW slagging combustor developed in part for MHD applications (5). SO_2 removals of between 50 and 90% are claimed in limestone injection tests at a Ca/S ratio of 3 for coals with sulfur contents ranging from 0.6 to 2.1%. NO_x emissions have ranged from 330 to 450 ppm (at 3% O_2) and carbon conversions were in excess of 99%.

Because of the proprietary aspects of the staged slagging combustor tests just described, details concerning them and the operational parameters that influence the control of SO_2 and NO_x emissions have not been reported. Hence, a series of combustion tests with limestone injection was undertaken in a nominal 2 MW staged slagging combustor at Argonne National Laboratory (ANL). The objective of the tests was to investigate the control of SO_x and NO_x emissions at conditions simulating direct coal firing into a gas turbine.

EXPERIMENTAL

Facility

The test program was conducted in the ANL Fossil Energy Users Laboratory (FEUL), which is a DOE-owned facility constructed to accommodate a wide range of experiments related to coal and oil combustion. The facility has two test legs: one with a combustor capable of burning a variety of liquid fuels (including slurry mixtures) and the other equipped with the two-stage slagging coal combustor used in performing the present work. Each test leg has the necessary independent fuel-feed, support, and control systems. The air compressors, combustion air preheater, effluent control equipment, coolant system, and data acquisition system are shared.

The coal combustor, designed and fabricated by ANL, is illustrated in Fig. 1. The combustor consists of three flanged sections with a fourth section (not shown) downstream of the combustor for instrumentation and gas sampling. The primary combustor consists of two sections: the first section accommodates the combustion air inlet header, coal feed injection nozzle, and a limestone feed port; the second section accommodates a slag tap. Constructed from 24-in. (0.64-m) schedule 20 carbon steel pipe, the primary combustor is refractory lined to a nominal inside diameter of 0.55 m. The overall length is 1.37 m.

As illustrated in Fig. 1, part of the primary combustion air enters axially along the combustor centerline and the remainder enters either tangentially (louvers installed) or radially (louvers removed). The coal to the first stage also enters along the combustor centerline axis. A pintle with an angle of 45° is located at the end of the coal injection line to radially disperse the incoming coal. First-stage limestone injection was accomplished through a port on the front face of the combustor and at an angle that intersected the centerline of the combustor at a point approximately 0.4 m downstream of the coal injector nozzle.

The second stage of the combustor is constructed from 18-in. (0.46-m) schedule standard pipe and is refractory lined to a nominal inside diameter of 0.38 m. The secondary combustion air enters radially through three ports located around the combustor wall. During certain tests, the limestone sorbent was injected through a port just upstream of the secondary air inlet nozzles. The second stage of the combustor is separated from the first stage by a slag baffle with a centerline opening of 0.25 m.

The coal combustor has a nominal thermal input rating of 2 MW, including the sensible heat of the combustion air, which can be preheated up to 1090 K. For the tests that form the subject of this paper, the thermal input to the combustor was in the range 1.1 to 2.4 MW, with most of the tests in the lower end of this range. The split between the primary and secondary combustion air and the ratio of primary axial to swirl air can be independently controlled. For all but one of the tests described herein, the louvers in the primary combustor were not installed; hence, the nonaxial primary combustion air was injected with little or no swirl component.

Test Coals and Limestone

Three different coals were used in the test program: a West Virginia Alma C seam coal and two Illinois No. 6 seam coals. The results from nominal analyses of the three coals are given in Table 1. The West Virginia coal was primarily selected because nearly 70% of the total sulfur in the coal (0.85 wt %) is organic. It was speculated that this might ensure rapid release of the sulfur from the coal during fuel-rich combustion in the first stage, possibly enhancing the capture of the sulfur by the limestone sorbent. The two Illinois coals were selected because of their higher total sulfur (1.6 and 2.7 wt %) and ash content. A limitation on the limestone hopper capacity and injection rate made testing with a very high sulfur coal (>3 wt %) impractical.

All three coals were delivered to a commercial grinding service where the coals were pulverized and loaded into metal bins with a nominal capacity of 900 kg. The first two coals were pulverized to approximately 98% -200 mesh. The third coal was slightly coarser at 92% -200 mesh. The bins of coal were delivered to ANL and, as needed, automatically loaded into a coal feed storage hopper capable of holding approximately 11,400 kg, a quantity sufficient for combustion tests of 6 to 8 hours.

The limestone used in this work was obtained from Grove Lime Co. in Stephens City, Virginia. This limestone, which contains 95.3 wt % $CaCO_3$ and 1.3 wt % $MgCO_3$, was used extensively in the early development of fluidized-bed combustion technology. For this study, the limestone was pulverized to 80% -200 mesh.

Test Procedure and Conditions

The general procedure adopted for each test was to bring the combustor to the desired initial set of operating conditions over a period of one to two hours. Baseline gas analysis data were then recorded without limestone injection. Limestone would then be injected into the first and/or second stage of the combustor and the composition of the gas exiting the second stage of the combustor would be monitored for changing SO_2 concentration until a new "steady-state" value of SO_2 was achieved. The limestone feed would then be discontinued and the SO_2 level in the combustion gas allowed to return to the baseline value. A change in operating

Table 1. Nominal Analyses of Test Coals (Dry Basis)

Analysis	Coal		
	West Virginia Alma C Seam	Illinois No. 6 (Orient #4 Mine)	Illinois No. 6 (Fidelity #11 Mine)
Test Coal Designation	1	2	3
Moisture, As Received	1.2	4.7	7.0
Proximate Analysis, wt %			
Ash	6.0	9.2	12.3
Volatile Matter	33.8	39.5	35.4
Fixed Carbon	60.2	51.3	52.2
Sulfur	0.85	1.6	2.7
Ultimate Analysis, wt %			
Carbon	81.5	73.9	70.7
Hydrogen	5.2	5.7	4.9
Nitrogen	1.4	1.5	1.4
Sulfur	0.85	1.6	2.7
Ash	6.0	9.2	12.3
Oxygen	5.1	8.2	8.0

parameters would then be made and the above procedure repeated at the new set of conditions. This procedure would generally be repeated three or four times during each combustor test period to obtain data over a range of conditions.

Gas analysis probes were located in the first and second stages of the combustor and also downstream of the second stage. The gas samples were cooled as they were withdrawn from the sampling ports and passed through a gas conditioning system where the sample was filtered free of particulates and dried using a membrane-type dryer. The samples then passed to on-line gas analyzers for CO, O_2, SO_2, CO_2, and NO/NO_x analysis. The analyzers were calibrated using standard calibration gases at the beginning of each test and at frequent intervals during each test period.

The nominal test conditions and the measured reductions in SO_2 leaving the second stage of the combustion system are listed in Table 2. The parameters varied in the course of this study were the primary and overall air/fuel ratios (stoichiometry), first- and/or second-stage limestone injection, Ca/S molar ratio, and sulfur content of the coal.

RESULTS

Combustor Operation

Although the ANL combustor performed very well during the limestone injection tests, the combustor did have a number of performance characteristics that influenced the test program. The ANL combustor, for example, is limited to atmospheric pressure operation, whereas gas turbine applications would require

Table 2. Nominal Test Conditions and Experimental Results

Test Condition	Coal[a]	Coal Feed Rate (kg/h)	Stoichiometry Primary	Stoichiometry Overall	Limestone Injection Ca/S	Limestone Injection Stage	Sulfur Retention (%)
2.3-2	1	225	0.5	1.2	3.2	1	23
3.1-2	1	145	0.6	1.7	2.3	1	36
3.1-3	1	145	0.6	1.7	4.4	2	97
4.1-2	1	150	0.7	1.7	2.5	1	49
4.1-3	1	150	0.7	1.7	2.5	2	26
4.2-2	1	150	0.6	1.7	1.0	1	33
5.1-2	2	165	0.9	1.5	3.1	2	49
5.2-2	2	200	0.4	1.2	2.5	1	24
5.3-2	2	140	0.6	1.7	3.6	2	55
5.4-2	2	110	0.9	2.2	4.9	2	31
6.1-2	2	145	1.1	1.7	3.5	2	62
6.2-2	2	135	1.2	1.8	3.6	2	51
6.4-2	2	155	0.6	1.6	2.6	2	72
6.5-2	2	145	0.6	1.7	3.1	2	84
7.1-2	3	170	1.2	1.6	2.6	1	50
7.2-2	3	155	1.2	1.7	2.7	1	44
7.4-2	3	155	0.8	1.7	2.8	2	58
7.5-2	3	155	0.8	1.8	2.9	1	48
8.1-2	3	185	0.6	1.6	2.3	1	55
8.2-2	3	155	0.6	1.7	2.6	1	46

[a] Refer to Table 1 for coal designations

operation at elevated pressure. This was not considered a serious limitation, however, because the identification of parameters affecting SO_x/NO_x control at atmospheric pressure would generally be useful in any application of the concept.

Also, the available supply of combustion air was insufficient to operate the combustor at high thermal inputs and maintain the high excess air conditions of 180 to 200% required to simulate gas turbine applications. As a result, heat losses to the combustor walls were as high as 15 to 20% of the thermal input. This, together with occasional flameouts of the combustor, resulted in slag solidifying and blocking the slag drain in the first stage of the combustor. As a result, the slag rejection capabilities of the ANL combustor could not be evaluated. Further, it was not possible to determine the quantity of slag and limestone that accumulated in the combustor over the duration of a test. Hence, accurate carbon and sulfur material balances at the individual test conditions could not be determined.

A third factor in the tests, which was not a limitation of the equipment, was the decision to operate the combustor without the swirl louvers in the primary combustor. As a result, the combustor performed essentially as a plug flow unit with respect to both gases and particles. In this respect, the ANL combustor more nearly resembled the Rockwell low NO_x/SO_x burner cited above.

The high particle loadings and slagging conditions in the primary combustor also made sampling of the first-stage combustion gases very unreliable. Sampling ports would quickly slag over and/or sampling lines plug, making further sampling impossible. While gas sampling lines at the exit of the second stage of the combustor were also prone to plugging, the availability of multiple sampling ports and the ability to periodically clean lines not in use made second-stage gas sampling highly reliable. Hence, the evaluation of combustor performance was largely based on the results of the second-stage gas analysis.

Evaluation of Limestone Injection for Sulfur Control

As shown in Table 2, measured reductions in SO_2 emissions ranged from a low of 23% to a high of 97% over the full range of test conditions investigated, including both first- and second-stage sorbent injection. The test results indicate that sulfur capture via limestone injection is a complex phenomenon. Since, however, the air/fuel ratio in the primary combustor has a significant influence on both (1) the rate of sulfur release from the coal and the ratio of H_2S to SO_2 formed during fuel-rich combustion, and (2) the resulting first- and second-stage gas temperatures, it was found that the SO_2 reduction during sorbent injection exhibited a noticeable dependency on the first-stage air/fuel ratio.

Figure 2 is a plot of the effect of first-stage combustion stoichiometry on reducing SO_2 during first-stage limestone injection. In producing the plot, the sulfur reduction data in Table 2 were normalized to a Ca/S ratio of 3.0 assuming a linear dependency. Figure 2 also includes some data from injection tests with a hydrated limestone in a related series of tests. The results indicate the optimum reduction in SO_2 occurred at an air/fuel stoichiometric ratio in the range 0.5 to 0.7. This is considered to be largely a thermal effect in that higher first-stage air/fuel ratios resulted in excessively high first-stage gas temperatures (>1900 K, calculated). The apparent low reduction in SO_2 during first-stage injection at an air/fuel ratio of 0.4 is not fully understood.

Figure 3 is a similar plot of SO_2 reduction as a function of first-stage air/fuel stoichiometry for second-stage sorbent injection. The observed dependency is generally the same as for first-stage sorbent injection. This may have resulted from the selection of the second-stage sorbent injection location, which was slightly upstream of the secondary air injection. Hence, the first-stage gas temperatures may also have influenced sorbent performance during second-stage injection.

Although the data are fairly limited and exhibit a high degree of scatter, the general results are encouraging in that the overall measured sulfur reductions in excess of 80% at Ca/S ratios on the order of three are consistent with the results reported for the Rockwell and TRW combustors. Considerably more data are needed, however, to fully understand the complex effects of operating parameters on combustor performance.

NO_x Control

Independent of coal type, the staged combustion for NO_x control exhibited two different dependencies on the first-stage air/fuel ratio, as shown in Fig. 4. The upper curve, which corresponds to less reduction in NO_x emissions, is representative of tests where the second-stage bulk gas temperature was too high (>1750 K) and/or where carbon conversion in the first stage was relatively low (<70%), leading to excess carryover of fuel-bound nitrogen in the char to the oxidizing second stage of the combustor. Greater NO_x reductions occurred when either the second-stage temperatures were lower than 1650 K and where carbon conversion in the fuel-rich first stage was high enough (>70%) to allow release and conversion of the fuel bound nitrogen to N_2.

In both cases, however, measured second-stage NO_x was reducible to less than 100 ppmv at 15% O_2 by controlling the first-stage stoichiometry. This corresponds to 300 ppmv at 3% O_2, a value that is again consistent with the results reported by TRW and Rockwell for their combustors.

CONCLUSIONS

The results of the preliminary investigation of limestone injection in a staged slagging combustor for the control of SO_x and NO_x emissions are very encouraging. Sulfur retentions were in excess of 80% and NO_x emissions were as low as 100 ppmv (at 15% O_2). Considerably more testing is required, however, to fully understand the complex mechanisms controlling the sulfur retention process. The results are consistent with those reported for the TRW and Rockwell slagging combustors.

ACKNOWLEDGMENTS

We gratefully acknowledge the funding of this work by the U. S. Department of Energy Morgantown Energy Technology Center. We would also like to acknowledge F. G. Teats, H. A. Myers, L. N. Ruppert, and R. A. Molson of Argonne National Laboratory who participated in the operation of the slagging combustor.

REFERENCES

1. C. A. Cincotta, "Gas Turbine Systems Research and Development Program," U. S. Department of Energy Report No. DOE/MC/20315-1767 (Sept. 1984).

2. D. A. Horazak et al., "Gas Turbine Systems, Research and Development Program, Final Report," U. S. Department of Energy Report DOE/MC/20324-2033 (Feb. 1986).

3. A. J. Giramonti, "Gas Turbine Systems for Operation on Coal-Derived Fuels, Final Technical Report," U. S. Department of Energy Report No. DOE/MC/20241-T12 (July 1985).

4. O. W. Dykema, "Development of a Low NO_x/SO_x Burner," paper presented at the 35th Canadian Chemical Engineering Conference, Calgary, Canada (Oct. 1985).

5. TRW, "Design and Application of TRW's Entrained Coal Combustor," TRW promotional literature, TRW Inc., Redondo Beach, CA (May 1986).

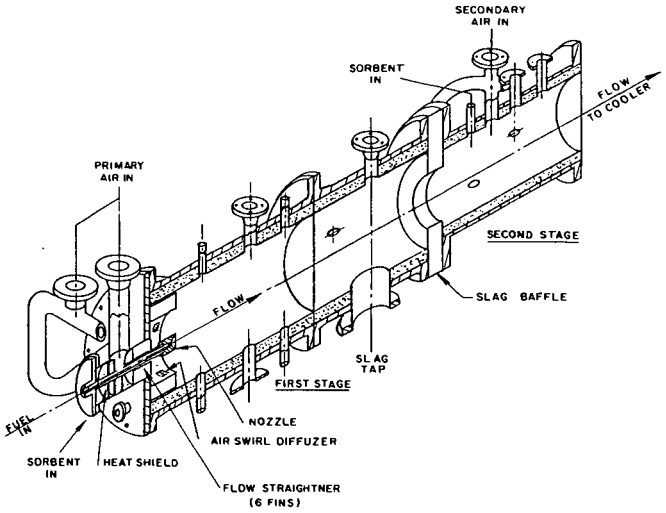

Fig. 1. Schematic of the ANL 2-Stage Slagging Combustor

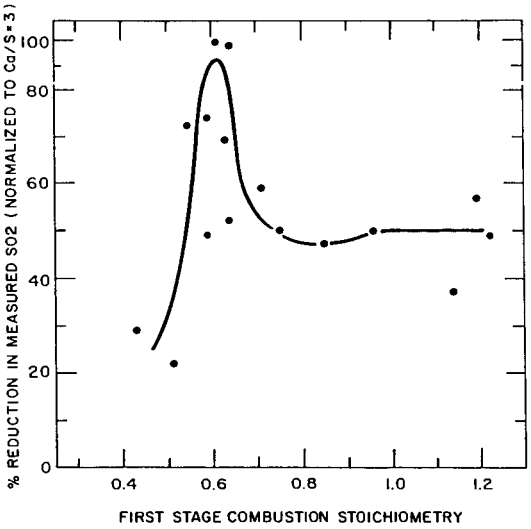

Fig. 2. Measured Reduction in SO_2 with First Stage Limestone Injection

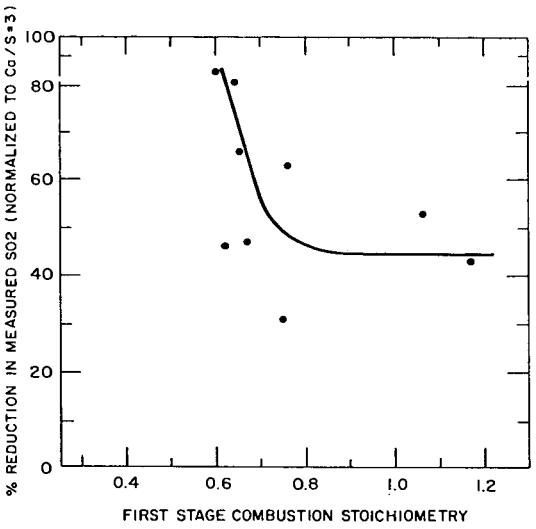

Fig. 3. Measured Reduction in SO_2 with Second Stage Limestone Injection

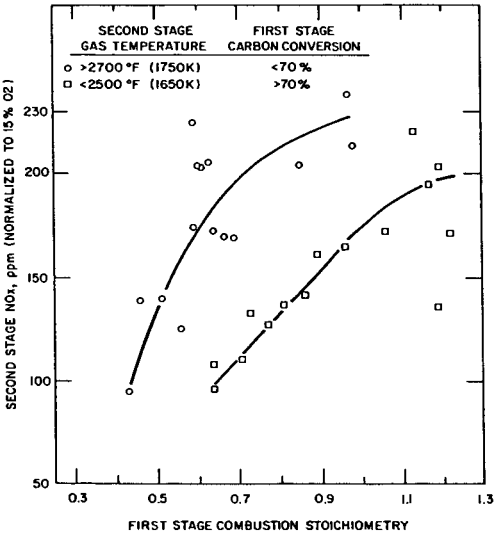

Fig. 4. Measured NO_x Emissions during Limestone Injection Tests

SULFUR IMPACT ON COAL-FIRED GAS TURBINES

C. S. Wen and L. H. Cowell

Solar Turbines Incorporated
P.O. Box 85376
San Diego, CA 92138-5376

ABSTRACT

Solar Turbines Incorporated is conducting a DOE-sponsored program to develop coal-fired cogeneration gas turbines. Solar's approach emphasizes the direct combustion of coal in both dry pulverized form, as well as a coal-water slurry, using a rich-lean, two-stage slagging combustor (TSSC). Under TSSC conditions, H_2S is formed in the atmosphere surrounding burning particles, and may persist in the rich zone, but the dominant sulfur species in the exhaust gas of the lean secondary zone is SO_2. A sulfur distribution based on TSSC combustion of eastern Kentucky bituminous coal showed that up to 90% of the sulfur was converted to oxides while the remainder combined largely with the ash. The studies made to date have also indicated that over 50% of the alkalis introduced with this coal have been retained with the slag in the primary combustion zone.

INTRODUCTION

Sulfur is one of the key elements in coal fuel specifications which requires particular attention. Emissions of sulfur oxides as well as the condensation and/or deposition of corrosive sulfates on blades are major problems in the development of coal-fired gas turbines. Substantial sulfur removal will be needed in order to meet environmental standards and to reduce the interaction between sulfur and alkali compounds. Several processes exist so that clean-up of sulfur is feasible, but they are expensive. Economic considerations will continue to force greater usage of minimally cleaned coal (i.e., coal with high ash and/or sulfur content). An understanding of the role of sulfur during coal combustion and its impact on gas turbines will benefit control of sulfur emissions and corrosion. This paper reviews the role of sulfur in two-stage slagging coal combustion and discusses its impact on coal-fired gas turbines.

EXPERIMENTAL

Combustion tests were performed using a two-stage slagging combustor show in Figure 1. The following test procedure has been used for all combustor tests conducted in this study. The combustor was started using #2 diesel to light off and establish the desired test conditions. When the wall temperatures were stabilized, a gentle transition to the coal-water mixture was accomplished by turning on the coal fuel and turning off the diesel until the combustor was operating on coal-water mixture only.

In Solar's two-stage slagging combustor, the coal fuel is injected via a series of angled injectors with air into the primary zone where the fuel-rich coal combustion takes place rapidly. The reacting jet flow impinges on the primary centerline and is then constrained by the impact dome and the refractory-lined walls to reverse and exit between the incoming flows. A strong toroidal vortex is formed surrounding the main jet and this acts primarily

as a particle retaining system. Particles smaller than some critical size follow the flow streamlines and escape. Other particles, which are larger than some upper limit, are deposited and form slag on the dome and walls. The molten slag is then collected in a slag pit.

The exhaust raw gases from the primary zone which are relatively free of particles pass into the secondary zone where remaining, unburned chars are then mixed with secondary air where combustion is completed to form desirable combustion products. The hot gas leaving the combustor enters a separator to separate particulate fly ash. Reaction temperature at the primary zone is above 2700°F with estimated temperature in secondary zone of 1600 to 1800°F.

Two coal-water fuels were formulated with high volatile bituminous, eastern Kentucky coals (Kentucky #5 and Elkhorn #2 mines) from AMAX Extractive R & D. Fuels were obtained in the form of aqueous slurries and prepared by physical beneficiation. Coals were cleaned in a static-bath dense-medium separator for refusing sinks and collecting clean coal floats. The float coals typically contained less than 3.9% ash and had calorific heating-values above 14,400 Btu/lb on a dry basis. Stable, pumpable slurries of coal and water were prepared by grinding the dense-medium float coal further in a ball mill to achieve a desired particle size. The finish-ground slurry was blended to with 1.2 to 1.4% of dispersant. A list of fuel properties appears in Table 1.

TABLE 1

Coal-Water Slurry Fuel Characteristics

CWM Batch	A	C
Coal Content of Fuel (wt%)	59.98	54.1
Ash Content of Fuel (st%)	1.85	2.1
Coal Particle Top Size (micron)	44	100
Gross Heating Value (But/lb)	14,518	14,397
Viscosity of Fuel @ 100 sec^{-1} (Cp)	400	300
Mean Size, micrometers	----	14.1
Dispersant (wt%)	1.2	1.4
Promimate Analysis of Coal (wt%)		
Ash	3.08	3.88
Volatiles	38.49	36.10
Fixed Carbon	58.43	60.02
Ultimate Analysis of Coal (wt%)		
Carbon	84.00	77.14
Oxygen (by difference)	7.81	14.34
Hydrogen	5.63	5.80
Nitrogen	1.64	1.82
Sulfur	0.92	0.90
Forms of Sulfur (Dry Coal Basis)		
Total Sulfur (wt%)	0.92	0.90
Sulfate	0.05	0.04
Pyritic	0.06	0.01
Organic	0.81	0.85

Sulfur content in all three CWM Fuels are approximately 1 wt% on a dry coal, ash free basis. Physical cleaning removed most of the inorganic sulfur, but left behind organic sulfur. A detailed analysis of sulfur forms (Table 1) further indicated that only trace amounts of sulfate (0.05 wt%) and pyritic sulfur (0.01-0.06%) remained in the sample, the majority was organic sulfur (0.80%). The ash contents in the samples range from 1.9 to 2.1 wt% on a fuel basis. The ash composition analysis (Table 2) indicates the acidic mineral properties in the coal fuels. The base-to-acid ratio is 0.28 for A and 0.18 for C, respectively. The relative amount of the basic and acidic constituents in the ash can be used as a means of predicting the ash fusion temperatures and the slag properties.

TABLE 2

Ash Slagging Properties

CWM Batch	A	C
Ash Composition		
SiO_2	43.40	53.0
Al_2O_3	27.80	28.1
Fe_2O_3	14.10	11.6
CaO	3.33	1.86
MgO	0.816	0.61
Na_2O	1.37	0.91
K_2O	0.723	1.03
TiO_2	2.10	2.07
MnO_2	0.066	0.065
P_2O_5	0.406	0.314
V_2O_5	0.078	0.06
PbO	0.072	0.04
Ash Fusion Temperatures (°F) Oxidizing/Reducing		
Initial Deformation	2375/2308	2670/2460
Softening	2700/2543	+2700/2605
Hemispherical	+2700/2565	+2740/2650
Fluid	+2700/2698	+2700/2700
Base/Acid Ratio	0.28	0.18
Silica Ratio	79.6	70.4
Viscosity From Equivalent Silica @ 2600°F (poise)	169	575
T_{250} Temperature (°F)	2527	2790
Fouling Index	0.38	0.18
Slagging Index	0.26	0.17

RESULTS AND DISCUSSION

The Fate of Sulfur in Slagging Coal Combustion

Upon injecting a coal-water slurry into the primary zone, the coal slurries are atomized and undergo a rapid devolatization followed by a burnout of the char (Refs. 1,2). Figure 2 illustrates a simplified scheme involved in the combustion of a coal particle. The volatile organic and inorganic sulfur species are vaporized from the burning coal particles and are transported to the surface by molecular diffusion. The reducing atmosphere surrounding a burning particle allows the reduction to take place on volatile species, but as soon as the vapors diffuse away from the burning particle, the oxidizing nature of the bulk gas stream would oxidize sulfur species to their highest oxidation state. The rate of sulfur release from coal is very fast from both sulfur bound in the organic matrix and sulfur in discrete minerals even under the local reducing conditions. Recent thermal analysis (Ref. 3) indicated that catalysis or acceleration of coal combustion occurs by its pyrite impurities due to the fact that FeS_2 promotes self-heating and spontaneous combustion of coal.

Under rich zone reducing conditions, pyritic sulfur (pyrite or marcasite, FeS_2) decomposes to sulfur (S_2), hydrogen sulfide (H_2S), and carbonyl sulfide (COS) (Ref. 4). Elemental sulfur is given off at 475°C (887°F) from iron disulfide (pyritic sulfur) with accompanying reduction to FeS (Ref. 5):

$$FeS_2 \longrightarrow FeS + 1/2\ S_2 \qquad <1>$$

The rate of this reaction becomes large above 1000°F. In addition, the decomposition of carbon-hydrogen bonds in coal will occur at relatively low temperatures and yield hydrogen for reduction of FeS_2. Mineral matter such as silicates or basic minerals in coal may catalyze the reduction of FeS_2 (Ref. 6).

$$FeS_2 + H_2 \longrightarrow FeS + H_2S \qquad <2>$$

and

$$FeS + H_2 \longrightarrow Fe + H_2S \qquad <3>$$

Reaction <2> becomes important above 930°F but reaction <3> is slow even at 1470°F (Ref. 7). The combustion product such as CO can also react with FeS_2 according to:

$$FeS_2 + CO \longrightarrow FeS + COS \qquad <4>$$

but the reaction is slow below 1470°F (Ref. 7).

The rich zone devolatilization of organic sulfur is not well documented, however, it is believed that hydrogen sulfide (H_2S) is the principal product, accounting for typically 90% of the evolved sulfur, with contributions of COS, CS_2, and S_2 (Ref. 4). However, these species will turn to higher oxidized states, SOx, as they are exposed to the primary air stream. Thiophenes represent the dominant organic-sulfur in the coal. Thiophene itself is stable

up to 840°F and dibenzothiophene is stable to at least 1020°F (Ref. 7). Reduction of thiophene proceeds according to:

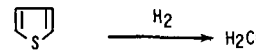

<5>

and dibenzothiophene reacts according to:

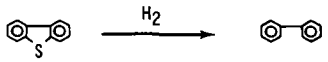

<6>

Sulfur release during coal devolatilization can be inhibited by inherent capture by coal-bound mineral matter, particularly calcium oxides and sodium oxides (Refs. 4,8):

$$CaO + H_2S \longrightarrow CaS + H_2O \qquad <7>$$

In fuel lean flames and oxidizing atmospheres, over 90% of the sulfur is converted to SO_2 while the remaining several percent exist as SO_3 (Ref. 4). Hydrogen sulfide (H_2S) which is originally released from pyritic and organic sulfur in the primary zone is rapidly converted to SO_2 in the lean secondary via the sequence (Ref. 9):

$$H_2S \longrightarrow HS \longrightarrow SO \longrightarrow SO_2 \qquad <8>$$

The capture of sulfur dioxide with the calcium-based coal minerals could also occur as

$$CaO + SO_2 + 1/2\ O_2 \longrightarrow CaSO_4 \qquad <9>$$

but, calcium sulfate is stable only at temperatures below 2200°F (Ref. 10).

Total sulfur conversion to the oxide is generally high in pulverized coal combustion, the remainder largely combining with the ash. Table 3 compares major compositions between a piece of slag retained in the slag pit of primary zone and ash particulates collected from the exhaust gas. A significant amount of sulfur associated with ash particulates was observed, compared to a trace retained in the slag. A sulfur distribution in coal combustion based on TSSC combustion tests of eastern Kentucky bituminous coal is shown, in Table 4 which up to 91% of sulfur was converted to oxides.

TABLE 3

Composition Analysis (a)

Composition, wt.%	Slag (Primary Zone)	Ash (b) Particulates
SiO_2	43.7	44.4
Al_2O_3	32.6	22.6
TiO_2	2.04	2.16
Fe_2O_3	11.6	9.34
CaO	1.72	1.25
MgO	0.70	0.56
SrO	0.22	0.12
K_2O	1.07	1.04
Na_2O	0.75	1.18
P_2O_5	0.12	0.39
Cr_2O_3	0.08	0.39
CuO	0.02	0.08
MnO_2	0.10	0.09
NiO	0.09	0.45
PbO	0.03	2.90
V_2O_5	0.05	0.06
SO_3	0.07	11.3

(a) Using batch 'C' CWM as feed
(b) Carbon-free basis

TABLE 4

Sulfur Distribution in Coal Combustion (a)

	Sulfur Out		
Total Sulfur in Fuel	S Adsorbed as Sulfates in Ash Particulates	(b) S Retained in Slag	S Exhausted as SOx
0.63 lb S/10^6 Btu	0.06 - 0.23	0.001	0.40 - 0.57
100%	9.2 - 36.8%	0.2%	63.0 - 90.6%

(a) Based on an Eastern Kentucky coal having 0.92% wt. S dry coal basis and 8708 Btu/lb CWM where CWM has 60% wt. coal loading (Batch A feed)
(b) Slag based on an average 70% wt. of slag retention.

The Effect of Sulfur on Corrosion and Deposition

In combustion, sodium and potassium are likely to be released from coal as the most volatile species, i.e. chloride or hydroxide. However, in a combustion environment at temperatures below about 1800°F, a significant proportion of the vapor alkali will be converted to condensed phase sulfate (Ref. 11).

$$2\ NaCl(g) + H_2O(g) + SO_2(g) + 1/2\ O_2(g) \rightleftharpoons Na_2SO_4(c) + 2HCl(g) \qquad <10>$$

The estimated residence time required for evaporation of sodium chloride and its conversion to sulfate is about 2 sec. (Ref. 12). Depending on conditions of temperature, pressure, and gas composition, the sulfate could condense onto entrained particulates or nucleate to form an aerosol.

Corrosion could be initiated when the alkali sulfates condense on the metal due to the temperature drop through the turbine and due to the contact with the cooled turbine blades resulting in an increase in alkali sulfate flux to attack the protective oxide (Ref. 13).

$$Na_2SO_4(l) + Al_2O_3(s) + 3SO_2(g) + 3/2\ O_2(g) \longrightarrow 2\ NaAl\ (SO_4)_2 \qquad <11>$$

The protective oxide scale (e.g. Al_2O_3) is destroyed and the subsequent reformation is inhibited.

Corrosion may also occur through an increase in the acidic component (SO_3) to react with protective Al_2O_3 scale on steel without the presence of alkali (Ref. 13).

$$3SO_3(g) + Al_2O_3(s) \longrightarrow Al_2(SO_4)_3(s) \qquad <12>$$

Increased transport of S through the oxide scale will occur and sulfate phase will be formed below the Al_2O_3 scale.

The actual mechanism of corrosion in coal-fired gas turbines is not completely understood. Alkali sulfate vapor released during combustion could partially be adsorbed by the aluminosilicates, inherent coal minerals, which are efficient "getters" for alkali metal sulfates (Refs. 11, 14).

$$K_2SO_4(g) + Al_2O_3.6SiO_2(s) \longrightarrow K_2O.Al_2O_3.6SiO_2(s) + SO_2(g) + 1/2O_2(g) \qquad <13>$$

The slag removal feature of a slagging combustor can also greatly reduce the impact of coal corrosive materials. Over 50% of the alkali introduced in coal feed can be expected to be removed as slag in the primary combustion zone (Table 5). The short residence times in gas turbine combustor, and particularly in the hot end zone could further reduce alkali metal vaporization. Thus, a precombustion cleaning of coal in conjunction with unique operating features of the slagging combustor may greatly reduce the corrosion severity potential of coal.

The formation mechanism of deposited matter on turbine blades or vanes is believed to start with molten ash or fly slag sticking to the metal surface. Chemical analyses of the exhaust deposit and the slag (Table 6) indicated that the deposited matter has almost identical chamical compositions as the slag collected in the slag pit. Neither contained any significant amount of sulfur or water-soluble alkali sulfate salts. Petrographically, the two materials were similar except that the exhaust deposit contained gas bubbles. X-ray diffractionn and electron microprobe studies showed that the two samples consisted basically of a glass phase containing bladed mullite. A spinel-like phase was seen in the deposit material. The mullite and spinel both probably crystallized during solidification of the melt. It has been speculated recently that alkalis may never escape from the coal aluminosilicate coordination environment (Ref. 4). Based on the decomposition mechanisms of coal alkali minerals (Illite) as illustrated in Figure 3, surface moisture and mineral water are desorbed at approximately 300°F (150°C), dehydration

takes place between 890-1100°F at which temperature two water molecules are split off from the four hydroxide units, and somewhere between 1560-1832°F decomposition of the anhydride take place to form spinel ($Al_2FeMg_{1.5}O_6$) and glass ($K_{1.5}Si_{6.5}Al_{1.5}O_6$). However, at higher temperatures (3000°F), such as slagging conditions, the spinel can redissolve into the melt, and glass phases (e.g. mullite and cristobalite) may be reformed while gaseous alkali species can be released.

CONCLUSIONS

The sulfur content of the coal introduced into the gas turbine combustion system dictates the degree to which sulfur capture compounds or hot-gas cleanup must be utilized. The coal desulfurization to a level acceptable for emissions and corrosion control is a key issue in the development of direct coal-fired gas turbines. Uncontrolled sulfur emissions is a direct function of the sulfur level in the coal and will exceed current NSPS levels. Sulfur compounds in the combustor exhaust also have the potential to cause deposition and corrosion on turbine blades. The availability of naturally occurring low-sulfur coal is limited as is the applicability of coal beneficiation. Physical cleaning will remove most of the inorganic sulfur, but will leave behind organic sulfur. Hot aqueous caustic leaching and molten alkali desulfuization can remove part of the organic sulfur, but appear to be expensive. There is also a potential risk of losing volatile and increasing alkali levels in the feed.

Therefore, in the near-term, sulfur control via sulfur retained in rejected slag and sorbent capture during coal combustion represent important routes for development. Coal beneficiation and post combustion gas clean-up upstream of the turbine are alternatives to in-situ sulfur control in the combustor, although the cost effectiveness of these options is questionable. Introduction of lime or dolomite sorbent for sulfur capture will also impact on ash fusion and deposition as well as on inherent coal mineral "getters" for alkali.

TABLE 5

Slag Retention Properties

	CWM Batch					
	A			C		
Ash or Slag Composition	CWM Feed	Slag	% Removal[a] in Slag	CWM Feed	Slag	% Removal[b] in Slag
SiO_2	43.40	46.52	75	53.0	48.7	60
Al_2O_3	27.80	28.38	71	28.1	32.6	75
TiO_2	2.10	1.39	45	2.07	2.04	64
Fe_2O_3	14.10	13.71	68	11.6	11.6	65
CaO	3.33	3.54	76	1.86	1.72	60
MgO	0.82	0.47	41	0.61	0.70	74
Na_2O	1.37	1.09	54	0.91	0.75	53
K_2O	0.72	0.54	56	1.03	1.07	67
P_2O_5	0.41	0.27	50	0.31	0.12	25
	94.05	95.91		99.49	99.30	

(a) Based on 70% slag retention from Batch 'A' CWM
(b) Based on 65% slag retention from Batch 'C' CWM

TABLE 6

Comparison of Compositions between Deposited Material and Slag (a)

Composition, wt.%	Deposited Material	Slag
SiO_2	51.4	52.3
Al_2O_3	29.5	29.2
TiO_2	1.61	1.53
Fe_2O_3	12.0	11.7
CaO	1.95	1.79
MgO	0.66	0.62
SrO	0.23	0.22
K_2O	0.98	0.99
Na_2O	0.98	0.96
P_2O_5	0.31	0.13
Cr_2O_3	0.06	0.07
CuO	0.04	0.01
MnO_2	0.07	0.07
NiO	0.13	0.09
PbO	0.01	0.01
V_2O_5	0.05	0.05
SO_3	0.07	0.19
Soluble Salts, wt%		
Na_2O	0.014	0.010
K_2O	0.004	0.003
SO_3	0.012	0.012

(a) Deposition run using Batch 'C' CWM feed

ACKNOWLEDGEMENTS

The work described in this paper was performed by Solar Turbines Incorporated under a program sponsored by DOE-Morgantown Energy Technology Center with Mr. Nelson F. Rekos, Jr. as Project Manager.

REFERENCES

1. L.K. Carpenter, F.W. Crouse, Jr., and J.S. Halow, "Coal-Fueled Turbines: Desposition Research", ASME Paper No. 85-GT-213, 1985.

2. R.W. Bryers, "The Impact of Segregated Mineral Matter on Fireside Deposits", Proceedings of 2nd Annual Pittsburgh Coal Conference, Sept. 16-20, 1985, p. 695.

3. E.J. Badin, "Coal Combustion Chemistry - Correlation Aspects", Elsevier, New York, 1984, p. 184.

4. A.R. Garman, G.A. Simons, and A.A. Boni, "Surrogate Fuel Exploratory Tests", DOE/MC/20486-1711, 1984.

5. P.C. Malte, "Mechanisms and Kinetics of Pollutant Formation During Combustion", Washington State University, Thermal Energy Laboratory, Report No. 77-24, 1983.

6. L. Robinson, "Doal Minerals Affect Sulfur in Processing", Hydrocatbon Processing, Nov. 1978, p. 213.

7. A. Attar, "Chemistry, Thermodynamics, and Kinetics of Reactions of Sulfur in Coal-Gas Reactions: A Review", Fuel, 57, 201, 1978.

8. H.S. Muralidhara and J.T. Sears, "Effect of Calcium on Gasification", Coal Processing Technology, Vol. 2, 1976, p. 22.

9. J.C. Kramlich, P.C. Malte, and W.L. Grosshandler, "The Reaction of Fuel-Sulfur in Hydrocarbon Combustion", 18th International Symposium on Combustion, Comb. Institute, 151, 1981.

10. J. Bettelheim and B.H.M. Billenge, "Industrial Air Pollution Handbook," (A.A. Parker, ed.), McGraw-Hill, London, 1978.

11. L.A. Scandrett and R. Clift, "The Thermodynamics of Alkali Removal from Coal-Derived Gases", J Inst. of Energ, 57, 391, 1984.

12. E. Raask, "Mineral Impurities in Coal Combustion", Hemisphere Pub. Corp., New York, 1986, p. 202.

13. E.J. Badin, "Coal Combustion Chemistry - Correlation Aspects", Elsevier, NY, 1984, p. 46 and p. 112.

14. S.G. Kimura, "Alkali Species Characterization for Coal-Fueled Gas Turbine", Final Report, DE-AC21-85MC22164, 1986.

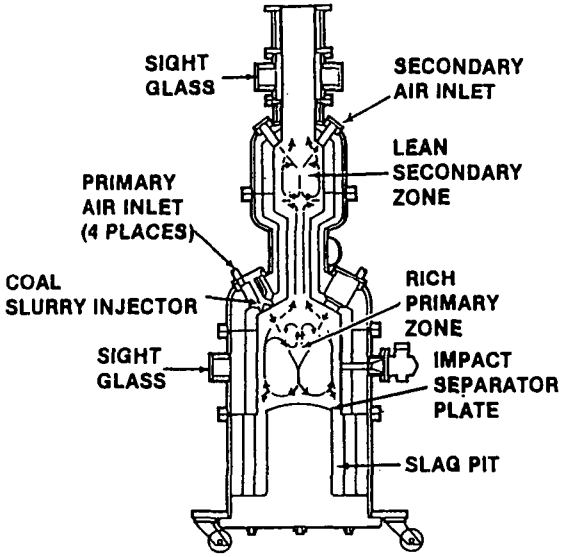

Figure 1. Solar's Two Stage Slagging Combustor

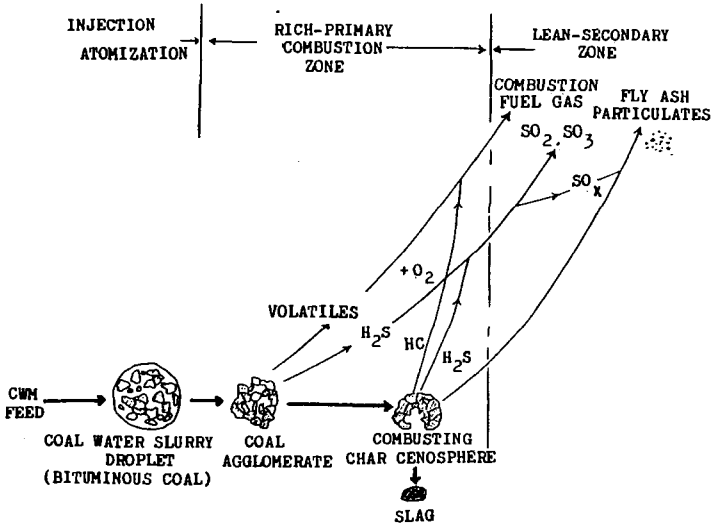

Figure 2. CWM Burnout and Sulfur Routes in Combustion

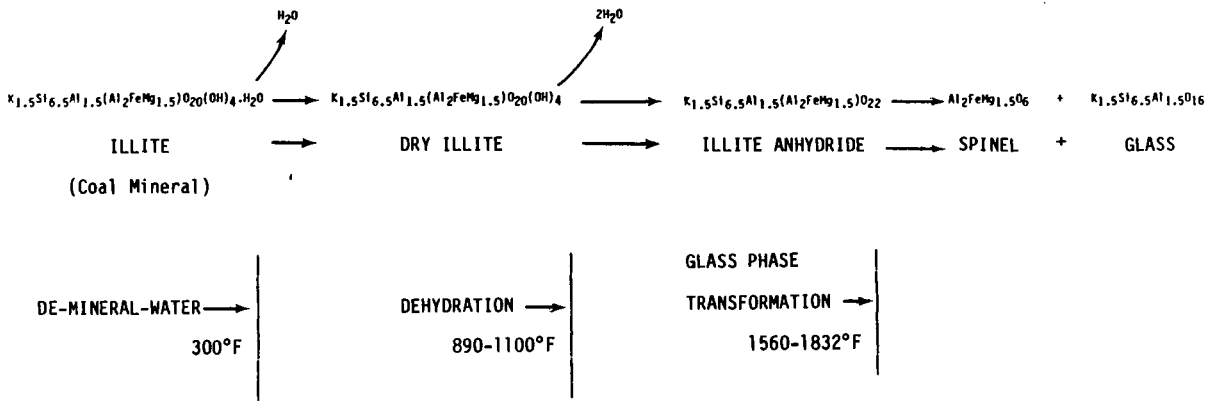

Figure 3. Decomposition Mechanisms of Coal Alkali Mineral

SOX Control In Fluid Catalytic Cracking

Z. C. Mester, E. J. Aitken and P. G. Ritz

Unocal, Division of Science and Technology, Brea, CA 92621

Introduction

Refineries today face a growing challenge to stay in compliance with the increasingly stringent environmental regulations. In fluid catalytic cracking (FCC), which is the largest volume gasoline producing process, the main air pollutants are carbon monoxide, sulfur oxides (SOX), nitrogen oxides (NOX), hydrocarbons and particulates.

At high regenerator temperature operation SOX emissions represent the greatest problem, therefore SOX emission control is of primary importance. As an example, in California the current standard is 60kg SO_2 per 1000bbl feed which is less than half of the previous 130kg SO_2 per 1000bbl feed limit. The EPA also proposed a 90% SOX reduction for FCC operations, but this regulation is still pending (1). The following options are available to the refinery to control SOX emissions: selection of low sulfur feed, flue gas scrubbing, feed hydrotreating and catalytic SOX reduction. The first method is of limited use because low sulfur feeds are not easily available. Flue gas scrubbing is effective but also capital intensive and may pose liquid or solid waste disposal problems. Hydrotreating has the advantage of not only reducing SOX but improving liquid yields too. In the long run this process offers economic advantages, however the high initial investment is a major drawback for many refineries. During the last few years catalytic SOX control emerged as an effective and economically attractive alternative to the above methods (2, 3, 4, 5).

SOX catalysts convert sulfur oxides, formed during coke burn-off in the regenerator, to solid sulfur containing species and release them as hydrogen sulfide in the reactor. This step rejuvenates the catalyst which is then recirculated to the regenerator and the cycle is repeated. In the following we present results of our investigation on the effectiveness of some SOX catalysts using TGA, fluidized bed reactor and in-situ infrared spectroscopy.

Results

The following materials were investigated for SOX performance: alumina, rare earth oxide/alumina, and rare earth oxide/alumina/cobalt oxide. The materials were first evaluated by TGA analysis. The samples were exposed to a gas mixture containing 2000 ppm SO_2, 4% O_2 and nitrogen. The weight gain of the samples were monitored as a function of the temperature with a 10°C/min ramp between 25 - 750°C. The materials were then cooled down to 25°C under nitrogen; hydrogen was introduced and the temperature was ramped as above. This adsorption-reduction cycle was repeated several times to assure good reproducibility. Each sample started to adsorb SOX appreciably around 300°C. Percent weight gains at 750°C were as follows: 2% for alumina, and 5% for the other two samples. The adsorption curves for the rare earth containing samples passed over a maximum around 650-700°C indicating decomposition beyond this temperature range. In the reduction step the cobalt containing sample started to reduce at the lowest temperature (500°C), followed by rare earth oxide/alumina and alumina (540°C).

The next stage in evaluating SOX materials involved the use of a bench scale fluid bed reactor. In a typical experiment the sample (< 5g) was fluidized by a mixture of SO_2 (2000 ppm) / O_2 (3%) / N_2 (balance) at a temperature which corresponded to FCC regenerator temperatures (650-750°C). After a fixed length of reaction time

(2 hrs), the samples were analyzed for sulfur. The unit can be used to simulate the entire catalytic cycle where the gettering step is followed by hydrogen reduction and steam injection at temperatures corresponding to those of typical FCC operations. The SOX gettering experiments at 730°C showed that alumina was the weakest adsorber. The rare earth/alumina and the cobalt impregnated samples had about the same gettering capacity, each adsorbed 2.5 times more sulfur than alumina alone. When the SOX loaded materials were reduced in a flow of hydrogen at 540°C for 0.5 hrs, the cobalt containing sample regained 62% of its original gettering capacity, followed by alumina (55%) and rare earth/alumina (40%).

In order to assess the relative rates of SOX uptake and H_2 reduction, in-situ infrared experiments were conducted. In these experiments the formation of surface sulfates - by exposure of the material to an SO_2 (1500 ppm) / O_2 (3%) / N_2 (balance) gas mixture - and the elimination of the surface sulfates - by exposure to H_2 - were followed by monitoring the appropriate band as a function of time. The SOX adsorption step took place at 600°C and the H_2 reduction was carried out at 525°C. The surface sulfur oxide species formed on the materials were predominantly sulfates. For the rare earth containing samples rare earth sulfates were detected as indicated by the appearance of two broad bands centered at 1125 cm^{-1} and 1050 cm^{-1}. However, a sulfite species also formed on alumina, as evidenced by a band at 1040 cm^{-1}, in addition to a sulfate like species (1370 cm^{-1}). The SOX gettering rate, measured by the increase in intensity of the surface S-O stretching vibrational bands, was dependent upon the composition of the materials. For alumina the adsorption rate decreased drastically after approximately 8 min of SO_2 exposure indicating that maximum gettering capacity was being reached. The gettering rates (normalized adsorption intensity per minute) in the first 8 min of exposure were: 0.0035 for the sulfate band and 0.0045 for the sulfite band of alumina; 0.016 for the rare earth oxide/alumina and rare earth oxide/alumina/cobalt oxide samples. During the hydrogen reduction step the time required to reduce the band intensity to 50% of the intensity prior to hydrogen exposure decreased in the order: 12 min (sulfate band for alumina), 9 min (sulfite band for alumina), 9 min (sulfate band for rare earth oxide/alumina) and 2 min (sulfate band for rare earth oxide/alumina/cobalt oxide).

Conclusions

TGA proved to be a useful method to reveal the SOX gettering potential and regenerability of the materials in a wide temperature range. The fluid bed experiments were useful in evaluating the materials under more realistic conditions related to FCC operations. The infrared study helped to establish the relative rates of SOX gettering and reductions by hydrogen. The results showed that the rare earth containing materials were superior to alumina in SOX gettering. It was also shown that cobalt had an accelerating effect in restoring catalyst activity.

References

(1) Federal Register, Vol 49, No. 11, January 17, 1984, pp 2058 - 2074.
(2) Wall, J. D., Hydrocarbon Processing, October 1984, p 45.
(3) Magnabosco, L. M., Powell, J. W., Katalistiks Fourth Annual Symposium, 1983 Amsterdam.
(4) Habib, E. T., Oil and Gas Journal, Augustus 8, 1983, p 111.
(5) Aitken, E. J., Baron, K., McArthur, D. P., Mester, Z. C., Katalistiks Sixth Annual Symposium, 1985 Munich.

CATALYTIC SOX ABATEMENT OF FCC FLUE GASES

Alak A. Bhattacharyya, Gerald M. Woltermann, Jin S. Yoo(1),
John A. Karch, and William E. Cormier

Katalistiks International Inc., 4810 Seton Drive,
Baltimore, Maryland 21215

ABSTRACT

A cerium containing magnesium aluminate spinel catalyst is used as a SOx emission reducing catalyst in the hydrocarbon cracking catalyst regeneration zone. In the regeneration zone this catalyst oxidizes the SO_2 to SO_3 and chemisorbs it as sulfate and releases it as H_2S when it enters the reactor zone. All FCC units are equipped to handle the H_2S that comes out of the reactor. This paper will discuss some of the materials, such as the cerium containing spinels, that were examined as potential SOx catalysts for FCC units and how they were tested for their ability to remove SOx under conditions prevalent in modern FCC units.

INTRODUCTION

Sulfur oxide emissions (SOx = SO_2 + SO_3) from fluid catalytic cracking units (FCCU) are increasingly becoming the target of EPA and local regulations (2). The removal of such pollutants from FCC units has been the subject of a considerable amount of attention over the past few years. The amount of SOx emitted from a FCC unit regenerator is a function of the quantity of sulfur in the feed, coke yield, and conversion. Generally, 45% to 55% of feed sulfur is converted to H_2S in the FCC reactor, 35% to 45% remains in the liquid products, and about 5 - 10% is deposited on the catalyst in the coke (3). It is this sulfur in the coke which is oxidized to SO_2 (90%) and SO_3 (10%) in the FCC regenerator.

$$S \text{ (in coke)} + O_2 \rightarrow SO_2 + SO_3 \qquad 1)$$

Flue gas scrubbing and feedstock hydrodesulfurization are effective means of SOx control but are laborious and cost intensive. The least costly alternative is the use of a SOx reduction catalyst as an additive to the FCCU catalyst inventory. Designing a catalyst for removal of SOx in a fluid catalyst cracking unit is a challenging problem. One must come up with a particle that will: 1) oxidize SO_2 to SO_3, 2) chemisorb the SO_3, and 3) be able to release it as H_2S as it enters the reactor side of the unit. Another obstacle is the fact that most metals that are in the chemists' repertoire for oxidation or reduction reactions are poisons in the catalytic cracking regime. This paper will discuss some

of the materials that were examined as potential SOx catalysts to remove SOx under conditions prevalent in FCC units.

EXPERIMENTAL

Pseudo boehmite alumina (Condea Chemie), high surface area magnesium oxide (C.E. Basic) and $Ce(NO_3)_3.6H_2O$ (Molycorp) were used as received.

Preparation of CeO_2/Al_2O_3: A pseudo boehmite alumina (87.7 g) was impregnated with a solution containing 42.9 g of 70% $Ce(NO_3)_3.6H_2O$ (CeO_2 content 28.7%) and 40 g water. This material was dried at 120°C for 3h and calcined at 700°C for 1h. Surface area of the catalyst was measured to be 180 m^2/g.

Preparation of CeO_2/MgO: A high surface area Magnesium oxide (87.7 g) was impregnated with a solution containing 42.9 g of 70% $Ce(NO_3)_3.6H_2O$ (CeO_2 content 28.7%) and 35 g water. This material was dried at 120°F for 3h and calcined at 700°C for 1h. Surface area of the catalyst was measured to be 75 m^2/g.

Preparation of $CeO_2/Mg_2Al_2O_5$: A solid solution spinel $Mg_2Al_2O_5$ was prepared by using required amounts of $Mg(NO_3)_2$ and $NaAlO_2$ as per literature procedure (4-6). A portion (87.7 g) of this material was impregnated with a solution containing 42.9 g of 70% $Ce(NO_3)_3.6H_2O$ (CeO_2 content 28.7%) and 40 g water. This material was dried at 120°C for 3h and calcined at 700°C for 1h. The surface area of the catalyst was measured to be 140 m^2/g.

Thermal studies: Thermogravimetric studies were used for the testing of the materials. This was accomplished by placing a small amount (5 - 25 mg) of virgin sample on a quartz pan and passing a desired gas. The experiment was divided into four zones:

Zone A: Under N_2, the sample was slowly (20°C/min.) heated to 700°C. This takes about 35 min.

Zone B: Nitrogen was replaced by a gas containing 0.32% SO_2, 2.0% O_2, and balance N_2. The flow rate was 200 mL/min. The temperature was kept constant at 700°C. This condition was maintained for 30 min.

Zone C: Passage of SO_2 containing gas was ceased and replaced by N_2. Temperature was reduced to 650°C. This is a 15 min. time zone.

Zone D. Nitrogen was replaced by pure H_2. This condition was maintained for 20 min.

Fluidized bed test: A one inch diameter quartz reactor heated by a tube furnace was connected to a gas manifold. Reactor temperature was controlled by a temperature controller with a thermocouple in the middle of the fluidized catalyst bed. A schematic diagram is shown in Figure 5. A blend of DeSOx catalyst in equilibrium FCC catalyst was made such that the concentration of DeSOx catalyst was 1.5 weight per cent.

15 grams of this blend was charged into a quartz reactor. The blend was cycled as described below.

SOx Pickup Side of Cycle

a. The blend was heated to 732°C in flowing N_2.
b. At 732°C N_2 was discontinued, and 5.9% O_2 was allowed to pass through the bed for 4 minutes.
c. Then 1.5% SO_2 was introduced along with the air for a 15 minute period at 732°C. Approximately 105-115 mg SO_2 was delivered during the test. The reactor effluent was trapped in a peroxide trap.
d. After 15 minutes of test with SO_2, the SO_2 flow was stopped, but the oxygen remains on for an additional 4 minutes.
e. Oxygen was replaced with nitrogen for ten minutes at 732°C.
f. The catalyst bed was cooled under flowing nitrogen for about 30 minutes.
g. The peroxide trap was disconnected and worked up as per EPA test no. 6.

H_2 Reduction Side of Cycle

a. The blend was flushed with N_2 and brought to a temperature of 732°C.
b. At 732°C the N_2 was shut off, and the catalyst subjected to 100% H_2 for 5 minutes. The reactor effluent was captured in a 1M NaOH trap.
c. The system was flushed with N_2 at 732°C for 10 minutes, then cooled under flowing N_2.
d. Sulfur analysis of the trap determined the amount of sulfur removed with each H_2 treatment.

RESULTS AND DISCUSSION:

The sulfur in the coke is mainly oxidized (7) to SO_2 (equation 1). Sulfur dioxide should be further oxidized to SO_3 (equation 2) so that it can be reactive (8) towards metal oxides to form sulfate (equation 3).

$$2SO_2 + O_2 = 2SO_3 \qquad 2)$$

$$SO_3 + MO = MSO_4 \qquad 3)$$

As the operational temperature of the regenerator is increased the formation of SO_3 is less favored (7). The free energy of formation of SO_3 (equation 2) is -9.5 KJ/g-mole at 675 C and -4.4 KJ/g-mole at 730°C. The regenerator temperature of an FCC unit is between 650 to 775°C. Catalyzing reaction 2 is one of the major functions of a SOx catalyst. Equation 3 represents the capture of SO_3 in the regenerator by the catalyst. The catalyst then moves to the FCCU reactor where the sulfate is reduced by hydrogen and other reducing gases to metal oxide and H_2S (equation 4) or metal sulfide (equation 5).

$$MSO_4 + 4H_2 = MO + H_2S + 3H_2O \quad 4)$$

$$MSO_4 + 4H_2 = MS + 4H_2O \quad 5)$$

Metal sulfide can be hydrolyzed in the stripper to form the original metal oxide (equation 6).

$$MS + H_2O = MO + H_2S \quad 6)$$

This generally accepted mechanism (3,9-12) and a schematic diagram of an FCCU is shown in Figure 1. A SOx reduction catalyst, thus, has three functions: oxidation, chemisorption, and reductive decomposition. Vanadium pentoxide (13) is an excellent oxidation catalyst and is specially useful for the oxidation of SO_2 to SO_3. However, V_2O_5 cannot be used in an FCC unit because it reacts with zeolites present in an FCC catalyst. Our laboratory experiments indicate that platinum can be used for this purpose (4), but it is expensive and is not very effective under actual FCC regenerator conditions (14). Iron oxides are also very effective oxidation catalysts but iron enhances the formation of coke and unfavorably changes the product distribution. Our tests with iron containing catalysts clearly indicate that more coke is formed causing more than normal SO_2 generation in the regenerator. Cerium dioxide can be used for the oxidation of SO_2. We have found that under FCC conditions CeO_2 is an excellent oxidation catalyst (equation 7) and it regenerates quickly under oxygen (equation 8). An FCC regenerator contains 1 to 3% oxygen.

$$2CeO_2 + SO_2 = SO_3 + Ce_2O_3 \quad 7)$$

$$Ce_2O_3 + 1/2O_2 = 2CeO_2 \quad 8)$$

Once the SO_3 is formed, it has to be chemisorbed by the catalyst. Alumina can be used for this purpose to form $Al_2(SO_4)_3$ (equation 9).

$$Al_2O_3 + 3SO_3 = Al_2(SO_4)_3 \quad 9)$$

One of the catalysts that was tested by us and others (15) is CeO_2 on gamma alumina. This can be conveniently prepared by impregnating gamma alumina with $Ce(NO_3)_3.6H_2O$ solution followed by drying and calcining at 730°C for 3h. The amount of CeO_2 was 12.3%. Aluminum sulfate starts to decompose at 580°C (16). Hence one disadvantage of using this catalyst is the fact that any FCC regenerator operating at a temperature higher than 600°C should have some decomposition of $Al_2(SO_4)_3$ (backward reaction of equation 9). A thermogravimetric analysis (TGA) of this catalyst is reported in Figure 2. The catalyst was first preheated to 700°C under N_2 (zone A). Then it was exposed to a gas containing 0.32% of SO_2, 2.0 % O_2 and balance N_2 at a flow rate of 200 mL/min.(zone B). The weight gain of 5.5% indicated in figure 2 is the amount of SO_3 formed (reaction 7) and absorbed (reaction 9) to form the $Al_2(SO_4)_3$. The TGA indicates that only 2.5% of all the available Al_2O_3 is involved in picking up SO_3 during the first 15 min. period. This number is called SO_2 oxidation and absorption index (SOAI)(17). The SOAI of 2.5 for this catalyst is very low when compared to other catalysts described in this paper. The activity decreases considerably during the second 15 min. period. Zone C is when the passage of SO_2 containing gas was ceased and replaced by pure N_2. At this point the temperature was dropped to 650°C to mimic the FCC conditions. TGA clearly shows that at this temperature the $Al_2(SO_4)_3$ is thermally unstable and releases some of the SO_3 it absorbed in zone 2. However, once the sulfate is formed alumina is regenerated under H_2 fairly easily because aluminum sulfate reduces at 400 to 700°C, which is in the FCC reactor temperature range (equation 10). Figure 2, zone D, is indicative of an efficient reduction of $Al_2(SO_4)_3$ to Al_2O_3 (equation 10). Alumina is regenerated in about 2 min.

$$Al_2(SO_4)_3 + 12H_2 = Al_2O_3 + 3H_2S + 9H_2O \quad 10)$$

The low SOAI and the thermal instability of the sulfate under FCC conditions clearly indicate that CeO_2 in gamma alumina is not a very effective DeSOx catalyst.

A catalyst was prepared by impregnating MgO with cerium nitrate solution. The composition of the final calcined catalyst was 12.3% CeO_2 on MgO. Since MgO is much more basic than Al_2O_3 it was hoped that it would be more reactive towards SO_3. A TGA analysis is shown in Figure 3. The catalyst gains 28.5% weight in 30 min. due to SO_3 absorption (zone B). This is 5.2 times more than the CeO_2/Al_2O_3 catalyst. The SOAI of this catalyst is 8.7 which indicates that the SO_3 absorptivity of CeO_2/MgO catalyst is 3.5 times higher than the corresponding alumina catalyst during the first 15 min. Linearity of the absorption plot (zone B) indicates that the absorption during the second 15 min. is as efficient as the first 15 min. When the passage of the SO_2 containing

gas was ceased and replaced by dry N_2 (zone C), unlike CeO_2/Al_2O_3 catalyst, this material did not lose any weight indicating the thermal stability of the $MgSO_4$. Magnesium sulfate is not expected to decompose below 780°C (16). Under H_2, the sulfate formed reduces at 650°C (zone D), however, the MgO can not be regenerated as efficiently as the alumina catalyst. About 7.7% of the absorbed material still remains with the catalyst even after 20 min. of H_2 reduction, possibly as MgS or unreduced $MgSO_4$. Fast deactivation of this catalyst is one of the major reasons why CeO_2/MgO was not considered as a potential DeSOx catalyst for FCC units.

The higher reactivity of MgO prompted us to look for a compound that was more thermally stable. Magnesium aluminate spinels such as $MgAl_2O_4$ or $Mg_2Al_2O_5$ were the ones we selected. The latter is a solid solution of pure spinel ($MgAl_2O_4$) and MgO. Such a solid solution does not destroy the spinel framework. These spinels can be prepared by the calcination of Mg,Al double hydroxides, formed by the reaction of $Mg(NO_3)_2$ and $NaAlO_2$ at pH 8.5 to 9.5. (4-6). The spinel structure is based on a cubic close packed array of oxide ions. Typically, the crystallographic unit cell contains 32 oxygen atoms; one eighth of the tetrahedral holes (of which there are two per anion) are occupied by the divalent metal ion (Mg^{2+}), and one-half of the octahedral holes (of which there is one per anion) are occupied by the trivalent metal ion (Al^{3+}).

A catalyst prepared by the impregnation of $Mg_2Al_2O_5$ with $Ce(NO_3)_3$ was tested for SOx removal activity. The final composition was 12.3% CeO_2 on $Mg_2Al_2O_5$. A TGA analysis of this material is reported in Figure 4. During preheating (zone A) the material desorbed 7.6% moisture. This material gains 23.3% weight by the absorption of SO_3 which is about the same as the CeO_2/MgO catalyst. The SOAI of this material is 17 indicating that this catalyst is 6.8 times more active than the CeO_2/Al_2O_3 catalyst. We have previously seen that SO_3 absorption by alumina is negligible and MgO is an extremely efficient SO_3 absorbing agent. This indicates that in a spinel it is the MgO structural fragment that is reacting with the SO_3 and our SOAI calculations for spinel catalysts are based on this concept. The SOAI of the spinel containing catalyst is about twice that of the CeO_2/ MgO catalyst. This indicates that the absorption activity of MgO in spinel is much higher than that of pure MgO, possibly due to the dispersion of MgO in the spinel. Linearity of the absorption plot (zone B) indicates that the absorption in the second 15 min. period is as efficient as the first 15 min. period. When the passage of SO_2 containing gas was ceased and replaced by pure N_2 (zone C) no weight loss was observed. This indicates that in zone B only $MgSO_4$ is formed although this catalyst has nearly 50% alumina. Unlike the CeO_2/MgO catalyst this catalyst regenerates efficiently under H_2 (zone D). The catalyst completely regenerates

in twenty minutes of H_2 reduction. Although this reduction time is much longer than that experienced in an actual FCC unit, it can be used to compare potential catalysts. It is clear, if we compare Figures 3 and 4, that $MgSO_4$ reduces much more efficiently in a spinel catalyst compared to pure MgO. This may be due to the fact that MgO in a spinel matrix is more sterically hindered than in a magnesia unit cell. Therefore, any sulfate formed whose decomposition would relieve the steric strain is favored, i.e. the decomposition of a sulfated spinel is thermodynamically more favorable than the decomposition of a sulfated magnesia sample.

Since we realized that a cerium containing magnesium aluminate spinel is the most efficient DeSOx catalyst that we have tested, a laboratory scale fixed fluidized bed reactor system was set-up (figure 5). Absorption and reduction half-cycles are repeated as described in figure 6 to mimic FCC units. Our system used a one inch diameter quartz reactor that was connected to a gas manifold so that the catalyst could be subjected to different gas mixtures. Reactor temperature was controlled by a controller with a thermocouple in the middle of the fluidized catalyst bed. In most cases a blend of DeSOx catalyst in equilibrium catalyst was made, then subjected to a 760°C, 6 hour steaming treatment, and finally tested for SOx pickup. The gas stream was analyzed by absorbing the exit gas in a H_2O_2 trap over a period of time, and then using the EPA 6 method for determining SO_2. The gas stream could also be analyzed instantaneously by an IR analyzer as long as care was taken to remove any SO_3 from the gas stream. In most cases, the sulfated sample was subjected to a reduction with either hydrogen or propane and followed by another SOx pickup. This cycle could be repeated several times to see the effect of adding and removing sulfur to a potential DeSOX catalyst. By adding solenoid controls to the gas lines and a microprocessor the whole system was eventually computerized so that constant monitoring by an individual was not necessary and runs could be made overnight.

Results obtained from fluidized bed tests are reported in Tables 1 and 2. Tables 1 and 2 represent the results obtained from virgin catalyst and a steam deactivated (760°C, 6h, 100% steam) catalyst, respectively. The amount of sulfur picked up was calculated by difference between the amount delivered and the amount found in the trap. The amount of sulfur removed was determined by gravimetric analysis of the contents of the NaOH traps. The concentration of DeSOx catalyst was 1.5 wt% in FCC catalyst. The Tables 1 and 2 indicate that steaming only causes a very minor deactivation. Nearly 90% of the fresh activity is retained even after steaming. Moreover, this catalyst picks up sulfur nearly half of its theoretical maximum in 15 min. indicating very high

activity. A mechanism of SOx reduction showing the catalytic cycle is illustrated in Figure 7. This cycle is given to describe the catalytic nature of the DeSOx components. In the figure, the catalyst $CeO_2/Mg_2Al_2O_5$ is represented by its active cites, namely $\underline{CeO_2}$ and $\underline{MgO}$.

CONCLUSION

A cerium containing magnesium aluminate spinel material was found to be the most effective DeSOx catalyst that we have studied. This spinel based catalyst was commercialized and is recognized as the leading DeSOx catalyst for FCC units.

ACKNOWLEDGEMENTS

The authors would like to thank Emmett Burk, John Magee and Joseph Powell for valuable suggestions.

REFERENCES AND NOTES

1. Present address: Amoco Chemicals Co., Amoco Research Center, Naperville, Illinois 60566.

2. Federal Register, Vol. 49, p.2058, 1984

3. Byrne, J. W.; Spernello, B. K.; Leuenberger, E. L. Oil and Gas J. 1984, 101, Oct. 15.

4. Yoo, J.S.; Jaecker, J.A.; U.S. Patent 4,469,589, Sept. 4, 1984

5. Bhattacharyya, H.; Samaddar, B. N. J. Am. Ceram. Soc. 1978, 61, 279

6. Mukherjee, S. G.; Samaddar, B. N. Trans Indian Ceram. Soc. 1966, 25, 33

7. Baron, K.; Wu, A.H.; Krenzke, L.D. Proc. Symp. on Advances in Cat. Cracking, A.C.S. Washington D.C. 1983, Aug. 28.

8. Magee, J.S.; Ritter, R.E.; Rheaume, L. Hydrocarbon Processing 1979, 58, 123

9. Thiel, P.G.; Blazek, J.J.; Rheaume, L.; Ritter, R.E.; Additive R by Davison Chemical, private publication.

10. McArthur, D.P.; Simpson, H.D.; Baron K. Oil and Gas J. 1981, p. 55, Feb. 23

11. Bertolacini, R.; Lehman, G.; Wollaston, E. U.S. Patent 3,835,031, Sept. 10, 1974

12. Habib, E.T. Oil and Gas J. 1983, p. 111, Aug. 8

13. Mars, P. Masessen, J.G.H. J. Catal. 1968, 10, 1

14. Powell, J.W. Personal communications.

15. Lowell, P.S.; Schwitzgebel, K.; Parsons, T.B.; Sladek, K.J. Ind. Eng. Chem. Process Des. Dev. 1971, 10, 384

16. Mu, Jacob; Perlmutter, D.D.. Ind. Eng. Chem. Process Des. Dev. 1981, 20, 640

17. SOAI = SO_2 Oxidation and Absorption Index; defined as the percentage of absorbent that is involved in picking up SO_3 which is produced by the oxidation of SO_2 in presence of the catalyst in 15 min. at a standard TGA condition

Table 1

Sulfur Picked Up And Removed at 732°C
On Virgin 12.3% CeO_2 On $Mg_2Al_2O_5$

SOx Pickup-H_2-Reduction	Mg Sulfur Theoritical Maximum	Mg Sulfur Picked Up	Mg Sulfur Removed
First Cycle	79	44	45
Second Cycle		42	44
Third Cycle		39	39
Fourth Cycle		37	37
Fifth Cycle		38	40
Sixth Cycle		37	-

Table 2

Sulfur Picked Up And Removed At 732°C
On Steamed 12.3% CeO_2 On $Mg_2Al_2O_5$

SOx Pickup-H_2-Reduction	Mg Sulfur Theoritical Maximum	Mg Sulfur Picked Up	Mg Sulfur Removed
First Cycle	79	39	38
Second Cycle		36	36
Third Cycle		34	35
Fourth Cycle		31	35
Fifth Cycle		28	-

FIGURE 1

SCHEMATIC DIAGRAM OF A TYPICAL FCC UNIT

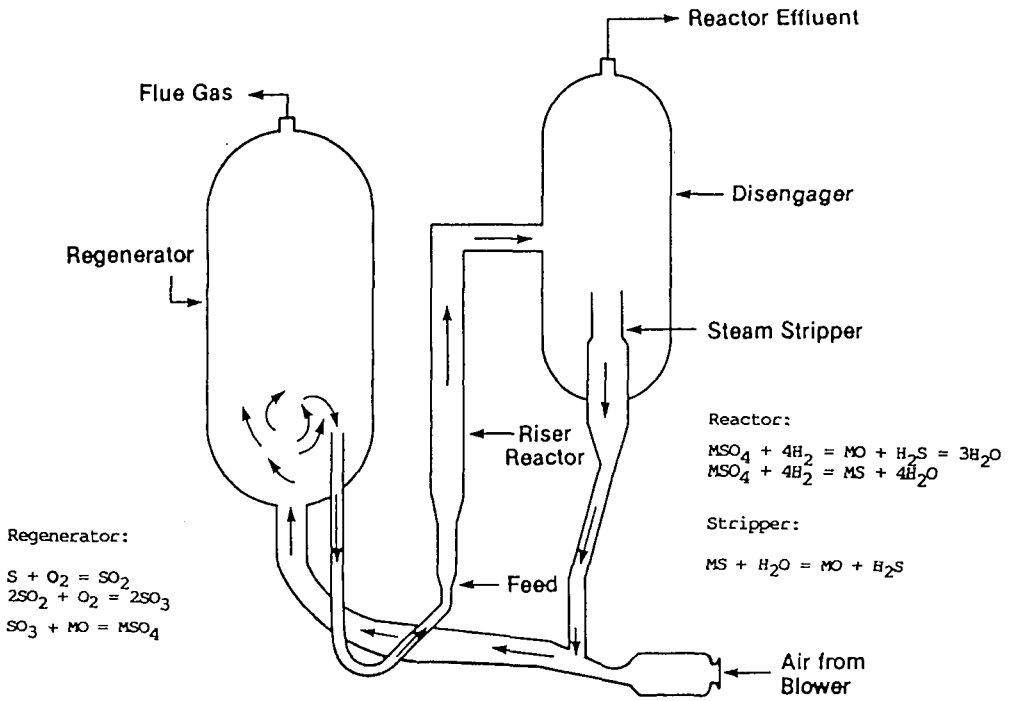

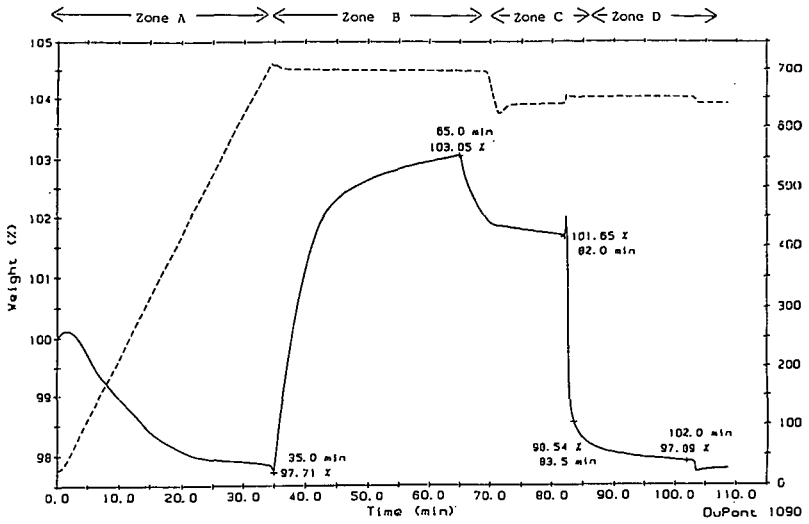

Figure 2. TGA Test of a CeO_2/Al_2O_3 Catalyst

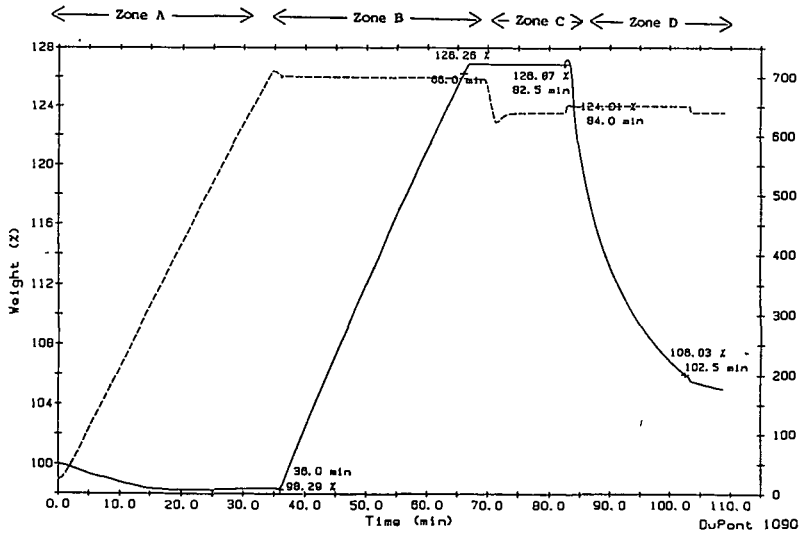

Figure 3. TGA Test of a CeO_2/MgO Catalyst

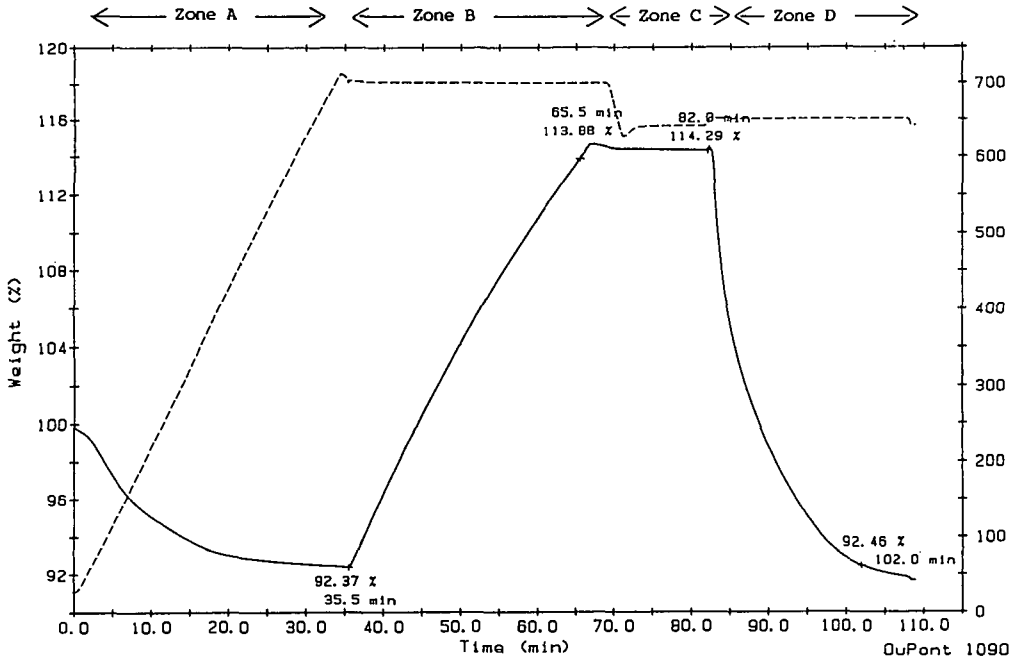

Figure 4. TGA Test of a $CeO_2/Mg_2Al_2O_5$ Catalyst

Figure 5

A Laboratory Scale Fixed Fluidized Bed Reactor System

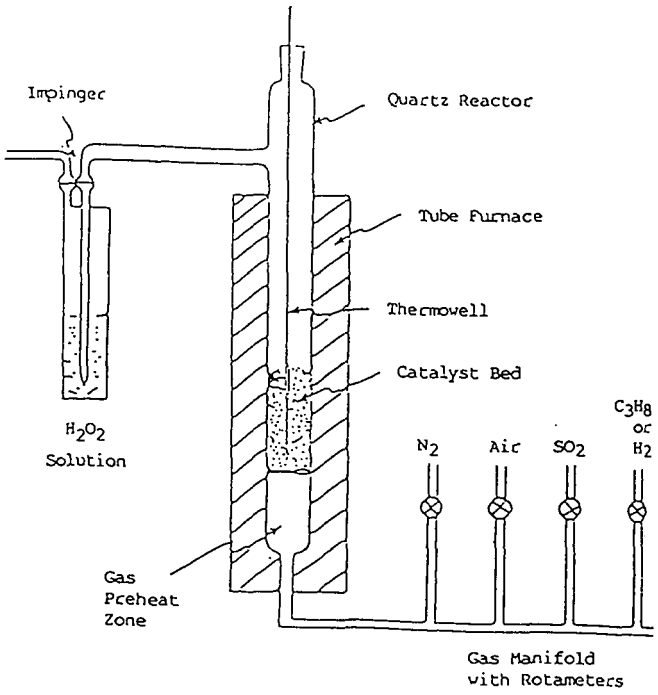

Figure 6

Adsorption And Reduction Half Cycle

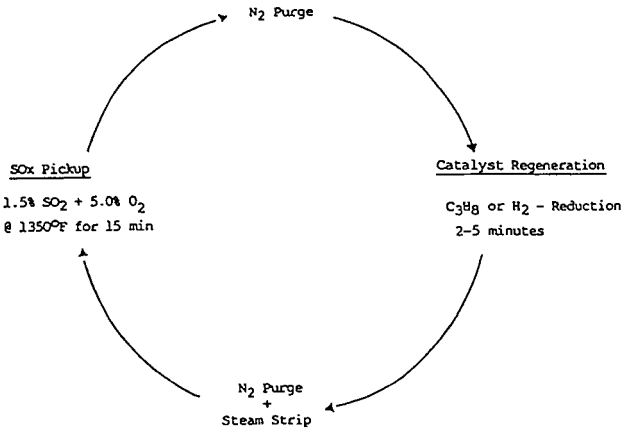

Figure 7

DeSOx Mechanistic Cycle

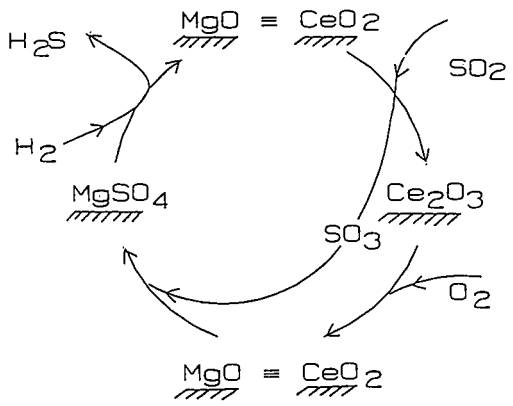

$CeO_2/Mg_2Al_2O_5$ = MgO = CeO_2

Agglomeration of Athabasca Petroleum Cokes in the Presence of Various Additives as as means of Reducing Sulfur Emissions during Combustion.

Abdul Majid, V.P. Clancy and Bryan D. Sparks

Division of Chemistry,
National Research Council of Canada
Ottawa, Ontario K1A 0R9

The relatively high sulfur content of coke produced during the upgrading of Athabasca bitumen, makes it environmentally unsuitable as a fuel. We have attempted to coagglomerate these cokes with sulphur dioxide capture agents such as: lime, hydrated lime and limestone in an attempt to reduce emissions during combustion. By providing an environment where there is intimate contact between fuel and sorbent it was hoped that greater utilisation of the sorbent could be achieved, compared to fluid bed combustion, where the sorbent is added separately to the bed. Cokes from both Suncor and Syncrude operations were used in this investigation. The effect of conditioning agents such as sodium hydroxide, sodium oleate, and a petroleum sulfonate on the formation of coke oil agglomerates as well as on the efficiency of sulfur dioxide capture was also investigated. Sulfur dioxide capture was found to depend mainly on the calcium to sulfur mole ratio in the agglomerates, the combustion temperature, partial pressure of oxygen, and the type of coke and sorbent. The efficiency of the three capture agents in the reduction of sulfur dioxide emissions, has been compared.

Upgrading of Athabasca oil sands bitumen to form a synthetic crude oil produces a solid carbonaceous material, known as "Coke". The two commercial oil sands plants operating in Alberta produce approximately 4,000 tons of coke per day [1]. This coke contains 6-8% sulfur almost entirely in the form of organic sulfur compounds such as thiophenes, sulfides, disulfides and thiols [2]. Due to serious environmental and corrosion problems associated with the combustion of this coke, its use as a boiler fuel is limited and a significant portion of the coke is being stockpiled as a waste product. However, oil sands coke with a calorific value of about 33 MJ/Kg [3] would be an attractive boiler fuel if it could be desulfurized economically.

Although considerable work has been done on various methods of desulfurizing coal and coal chars, comparatively few studies appear in the literature on the desulfurization of petroleum coke, particularly coke derived from Athabasca oil sand bitumen. There have been some attempts at desulfurization of these cokes employing such methods as hydrodesulfurization, combustion with limestone addition, impregnation with high base loadings followed by calcination in an inert atmosphere and subsequent leaching, chemical oxidation, and solvent extraction [2-5]. However, most of these methods are said to be uneconomical [1]. Fluidized-bed combustion of coal in the presence of limestone is emerging as a promising technology that can achieve high combustion efficiency with aignificantly reduced sulfur dioxide emissions [6]. The disadvantage of the process is the high calcium to sulfur mole ratios required for acceptable reductions in sulfur dioxide emissions. For example, using limestone as a sulfur sorbent in a fluidized bed for Suncor delayed coking coke, a Ca/S ratio of 3:1 was required to achieve 80% reduction in SO_2 emissions [5].

The objective of this investigation was to develop an economically attractive method by which the oil sands coke may be utilized directly as a boiler fuel without serious environmental damage. To the best of our knowledge there are no reports regarding the coagglomeration of coal, coke or char with sulfur sorbents. The present program was designed to study the feasibility of co-agglomerating sulfur capture agents such as limestone, lime and slaked lime with oil sands bitumen coke as a means of increasing the utilisation of these agents during sulfur dioxide removal on combustion.

Experimental Methods

Materials. Suncor delayed coking coke and Syncrude fluid coke samples were obtained from the Alberta Research Council sample bank. The coke was ground to 150 μm size using a Brinkman ZM-1 Centrifugal Grinding Mill. The composition and Calorific value of these samples are listed in Table I.

TABLE I
Composition and Physical Data for Cokes

	Suncor Delayed Coke	Syncrude Fluid Coke
Proximate Analysis* (Dry Basis)		
Ash	6.0	8.7
Volatile Matter	11.6	7.3
Fixed Carbon	82.4	84.0
Ultimate Analysis (Dry Basis)		
Carbon	83.0	76.8
Hydrogen	3.4	1.6
Nitrogen	1.5	1.5
Sulfur	5.9	6.9
Oxygen	2.9	4.4
Ash	3.4	8.0
Calorific Value* MJ/Kg	33.4	32.6

* Alberta Research Council (Fuel Sciences Division)

Bridging liquid used for agglomeration of coke particles was a sample of bitumen obtained from the Alberta Research Council sample bank. This was a sample of coker feed bitumen from Suncor, prepared for use in a round robin study of bitumen analyses [7].

A number of sulfur dioxide capture agents were tried including: limestone, lime and slaked lime. The sample of limestone used was pulverized agricultural limestone (Domtar). It contained approximately 97% $CaCO_3$. A partial size distribution of this sample is given in Table II. Lime was a laboratory grade CaO sample. Various samples of slaked lime were prepared as shown in Table III.

Petroleum sulfonate (TRS-10-80), used as a conditioning agent, was obtained from Witco Chemicals Corporation.

TABLE II
Size Distribution of Limestone

Sieve Size (μm)	Cumulative Weight Percent Passing
44	67.0
53	74.7
74	91.8

Procedure. 20 g of coke was mixed with known amounts of sorbent and the mixture dispersed in 100 ml of tap water contained in a Waring Blendor. An appropriate amount of a conditioning agent was then added and the contents agitated at 250 rps for 15 seconds. At this stage the blending speed was lowered to 120 rps. Bitumen was added slowly while continuing blending until discrete agglomerates or a unitary phase was obtained (5-15 minutes). Coke oil agglomerates/oil phase were then separated from the aqueous phase by screening. A portion of the agglomerates were used for analysis of bitumen, coke and ash content using a procedure described elsewhere [8]. The second portion of the agglomerates was dried at 100°C to a constant weight.

TABLE III
Experimental Conditions for Various Hydrated Lime Sample Preparation

Sample #	Experimental Conditions
1.	Laboratory grade CaO was mixed with distilled water in the ratio of 1:4 and then air dried at 90°C.
2.	20 g of CaO was mixed with 80 g of distilled water and 740 ml of isopropyl alcohol. The slurry was then dried at 90°C on a rotary evaporator under vacuum.
3.	Same as above, except the excess liquid was removed under atmospheric pressure at 90°C.
4.	10 g of CaO was mixed with 40 g of 0.5% aqueous solution of sodium sulfonate (Witco TRS-10-80) and 370 ml of isopropyl alcohol. Contents were mixed into a slurry and then dried on a rotary evaporator at 90°C under vacuum.
5.	Same as above, except the excess liquid was removed under atmospheric pressure at 90°C.
6.	Same as sample 1 except that the sample was freeze dried.
7.	Same as sample 1 except that the sample was dried in a vacuum oven at 90°C.

Combustion of Oil Agglomerates/Oil Phase. Before combustion wet agglomerates were first dried in an oven at 100°C to a constant weight to facilitate analytical calculations. However, because of the economic advantage in burning wet agglomerates, a separate investigation involving the combustion of wet agglomerates is in progress. The results of this study will be reported elsewhere. Two procedures were used for the ashing of dried coke-oil agglomerates/oil phase. The first procedure involved weighing an agglomerate sample into a porcelain crucible, and placing it directly into a muffle furnace preset at the desired temperature. This technique has been referred to as combustion with limited air. The second procedure involved burning the sample over a bunsen burner in the open air followed by completion of the ashing process in the muffle furnace at an appropriate temperature. This has been referred to as combustion with excess air.

Sulfur Analysis. Attempts were made to measure the sulfur dioxide emissions from coke-oil agglomerates by burning ≈ 1.0 g of the sample in a porcelain boat placed inside a quartz tube contained in a tube furnace (ASTM method D4239-83). This method is specifically designed for the determination of sulfur in coke and coal. Sulfur dioxide in the combustion gases was absorbed by 1% hydrogen peroxide solution and the resulting sulfuric acid titrated against 0.05N-NaOH solution to pH 5.0, see equation [1].

$$SO_2 + H_2O_2 \longrightarrow H_2SO_4 \qquad [1]$$

The sulfur content of the coke, coke-oil agglomerates and coke-sorbent-oil agglomerates was also determined independently using a Leco sulfur analyzer and by x-ray fluorescence spectrometry. Excellent agreement between the results for sulfur content for coke and coke-oil agglomerates was obtained by the three methods. However, each method gave a different result for the sulfur content of coke-sorbent-oil agglomerates. Reproducibility was extremely poor for these samples when using the ASTM method. Results from the Leco sulfur analyzer were reproducible within ±5% but gave significally lower sulfur contents than x-ray fluorescence spectrometry. Results from x-ray fluorescence spectrometry were much closer to the expected values than the results from the other two methods. Total sulfur in the ash obtained from the combustion of coke-oil and coke-sorbent-oil agglomerates was also determined using x-ray

fluorescence spectrometry.

The sulfur fixed in the ash during combustion is expressed as a percentage of the total sulfur in the original coke. It was calculated from the equation:

$$\text{Percentage sulfur fixed} = \frac{\text{wt. of sulfur in ash from y g of agglomerates}}{\text{wt. of sulfur in y g of agglomerates}} \times 100 \qquad (2)$$

$$\text{wt. of sulfur in ash} = \frac{\text{wt. ash} \times \% \text{ sulfur in ash}}{100}$$

$$\text{wt. of sulfur in agglomerates} = \frac{\text{wt. agglomerates} \times \% \text{ sulfur in agglomerates}}{100}$$

Results and Discussion

Sulfur Determination. Sulfur contents of coke and coke agglomerates as determined by: ASTM method D4239-83, Leco sulfur analyzer and x-ray fluorescence spectrometry are listed in Table IV. The three methods gave similar results for coke and coke oil agglomerates, but each method gave a different result for coke- limestone-oil agglomerates with the most scatter being obtained with the ASTM method. The reproducibility of the other two methods was similar. However, the Leco sulfur analyzer gave lower sulfur values compared with the x-ray fluorescence method. Sulfur content, determined using x-ray fluorescence spectrometry, was much closer to the expected values. Hence, all the results discussed in this report are based on the x-ray fluorescence spectrometry method.

TABLE IV
Comparison of Sulfur Results Obtained Using Different Methods.

Sample	Total oxidisable sulfur (SO_2 emitted) by ASTM Method				Total sulfur (as w/w% of agglomerates)		Total oxidisable sulfur from ash* analysis	
	460°C	750°C	840°C	1000°C	x-ray method	Leco method	460°C	1000°C
Suncor Coke	5.5±0.1 (4)	5.3±0.2 (3)	-	-	5.9±0.2 (4)	5.8±0.1 (4)	-	-
Suncor Coke-Bitumen Agglomerates	5.8±0.1 (2)	5.9±0.2 (2)	-	5.6±0.2 (2)	5.7	5.9±0.1 (3)	5.8	5.7
Suncor Coke-Limestone-Bitumen Agglomerates Ca:S Mole ratio 0.6	3.2±0.7 (3)	2.8±0.7 (3)	3.3±0.1 (2)	4.1±0 (2)	4.75±0.3	3.7±0.2 (3)	3.2	1.3
" " Ca:S Mole ratio 0.8	1.8	2.9	-	3.1	4.2±0.3	3.5±0.4 (3)	3.2	1.3
" " Ca:S Mole ratio 2.6	1.40±0.1 (2)	3.0±0.5 (3)	1.3	2.1±1.0 (2)	3.5±0.3	2.6±0.1 (10)	2.2	0.9

* by x-ray fluorescence spectrometry.
Values is paranthesis are number of determinations.

Sulfur Retention by the Ash from Suncor Coke-Oil Agglomerates. Tests on several lignites at various laboratories have shown that with no limestone injection, highly variable sulfur retention by the ash is achieved during combustion in a fluidized bed. In some cases the retention of sulfur by the ash alone have been quite significant [9]. Mineral composition of the ash is said to be important in determining the extent of sulfur retention. Iron in particular has been

reported to catalyze the sulfation reaction between CaO(s) and SO_2(g) [10]. Ash analyses of the Suncor delayed coking coke and Syncrude fluid coke are presented in Table V below:

TABLE V
Ash analyses of the Cokes (w/w% of Ash)

Component	Suncor delayed Coking Coke	Syncrude Fluid Coke
Total Ash	3.4	8.0
SiO_2	42	41
Al_2O_3	19	22
Fe_2O_3	23	12
NiO	2	1
V_2O_5	5	3
TiO_2	2	3
CaO	3	5
MgO	2	2
Na_2O	1	2
K_2O	2	2

As Fe_2O_3 is one of the major components of the ash from both cokes, significant amounts of sulfur retention by the ash from these cokes might be expected. However, no significant sulfur retention by the ash from either coke was observed. Sulfur retention by the ash from Suncor coke ranges from 1-3% and for Syncrude coke it is in the 3-5% range. Although the Fe_2O_3 content of the ash from Suncor coke is about double that of the Syncrude coke, its sulfur retention is only half that of the Syncrude coke ash. This appears to be more consistent with the CaO content of the two ashes and suggests that CaO is the only reactive ingredient for sulfur retention in the coke ash.

Conditioning agents used did not affect the retention of sulfur by ash. However, conditioning agents were found to facilitate agglomeration, probably by increasing the wettability of the coke particles with respect to the bridging oil. The effect was more pronounced for Syncrude coke than for Suncor coke. This was evident from the lower amount of bridging liquid required to agglomerate Syncrude coke in the presence of conditioning agents, in particular oleic acid and sodium oleate. This is consistent with the fact that Suncor delayed coke is more hydrophobic than Syncrude fluid coke because of the presence of a small amount (0.4% by weight) of a benzene extractable material [11].

Coagglomeration of Limestone with Suncor Coke in the absence of a conditioning Agent.

Suncor coke can be easily coagglomerated with limestone. However, individual agglomerates were only obtained when the Ca to sulfur ratio was < 1.2; beyond this ratio a unitary phase resulted.

Figure 1, is a plot of the percentage of the sulfur retention versus calcium to sulfur molar ratio. It is obvious from these plots that the efficiency of sulfur dioxide capture mainly depends on the calcium to sulfur mole ratio in the agglomerates, and the combustion temperature. Considerably more sulfur dioxide retention was obtained at 1000°C than at 460°C. This is consistent with various published reports [9,12-15]. This greater reactivity of limestone at higher temperatures has been explained on the basis of several mechanisms [9].

The detailed kinetic mechanism of the reaction between carbonate rock and sulfur dioxide is not well understood [16-17]. However it is generally accepted that the reaction involves two steps. The first step is the decomposition of calcium carbonate (calcination) to carbon dioxide and calcium oxide:

$$CaCO_3(s) \longrightarrow CaO(s) + CO_2\ (g) \qquad (3)$$

The second step is the reaction of sulfur dioxide and calcium oxide. In the presence of excess air this reaction produces $CaSO_4$(s):

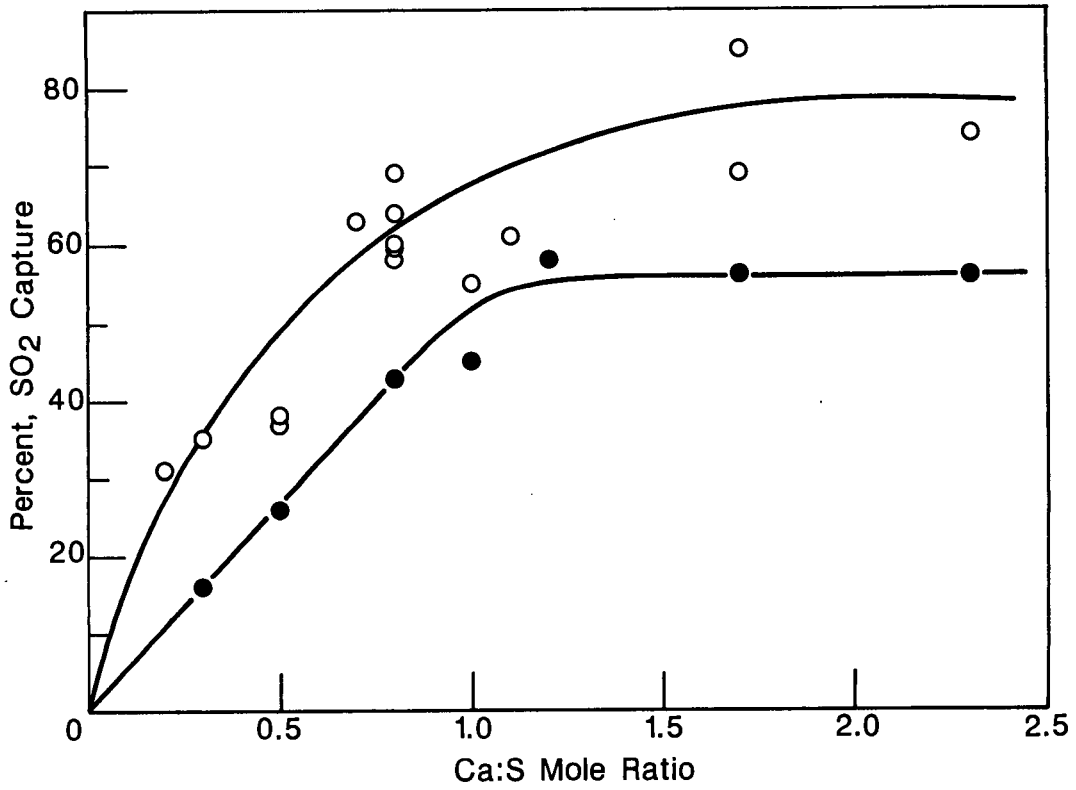
Percent, SO_2 Capture
80
60
40
20
0
0.5
1.0
1.5
2.0
2.5
Ca:S Mole Ratio

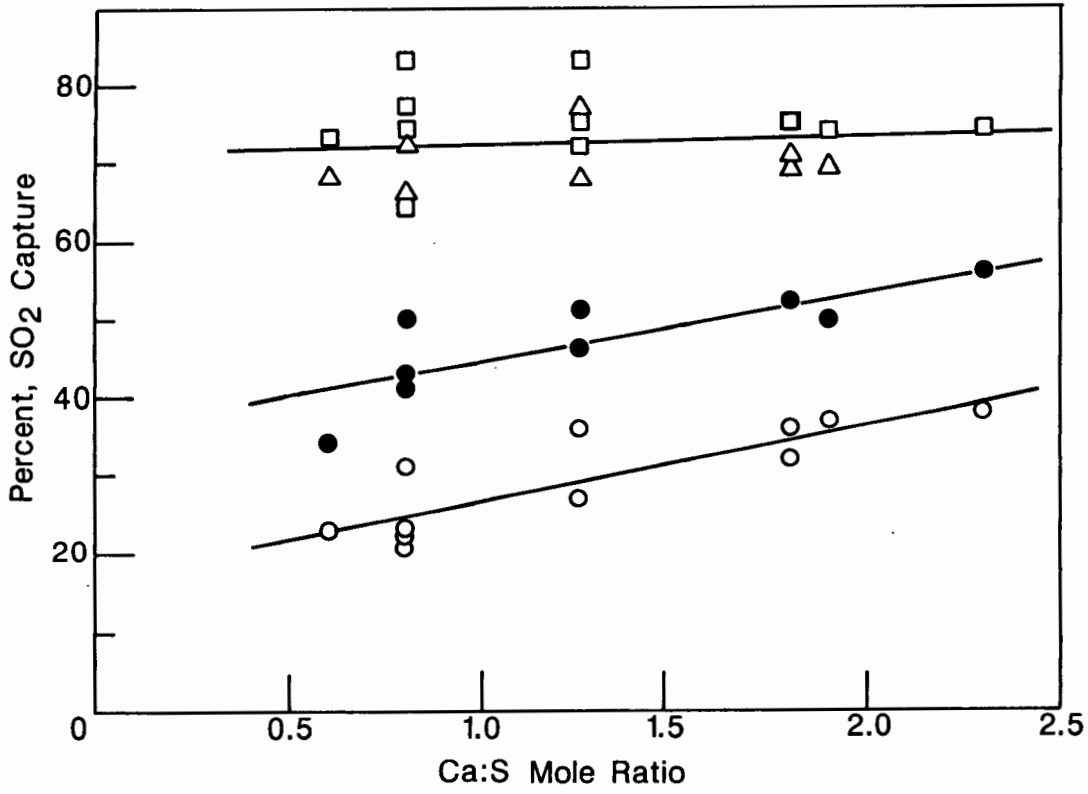
Percent, SO_2 Capture
80
60
40
20
0
0.5
1.0
1.5
2.0
2.5
Ca:S Mole Ratio

$$CaO(s) + SO_2(g) + \tfrac{1}{2}O_2 \longrightarrow CaSO_4(s) \qquad (4)$$

However, with limited amounts or no air present the preferred product was temperature dependent [12]. At lower temperatures $CaSO_3$ was formed whereas the more thermodynamically stable $CaSO_4 \cdot CaS$ was formed at higher temperatures as shown in reactions 5-7 below.

$$CaO(s) + SO_2(g) \longrightarrow CaSO_3(s) \qquad (5)$$

$$4\ CaO(s) + 4\ SO_2(g) \rightleftharpoons 3\ CaSO_4(s) + CaS(s) \qquad (6)$$

$$CaS(s) + 2\ O_2(g) \longrightarrow CaSO_4 \qquad (7)$$

The capacity of limestone to react with SO_2 in a fixed bed reactor has been studied by various workers [9,12-15]. It has been found that the calcination reaction is the controlling step at low temperatures, and the sulfation reaction is the controlling step at high temperatures. At low temperatures calcination is slow and hence overall conversion of limestone to $CaSO_4$ will be low. As the temperature is raised the calcination rate will increase [18]. At the optimum temperature the rate of calcination is so fast that the rate of sulfation dominates the overall reaction resulting in higher utilisation of sorbent.

Results summarized in Figure 1 demonstrate that as the limestone content of the agglomerates is increased a corresponding decrease in sulfur dioxide emissions during combustion of Suncor coke is achieved. For small values of the calcium to sulfur ratio there appears to be a linear correlation between sulfur dioxide capture and the calcium to sulfur mole ratio. This is consistent with the fluidized bed combustion studies of coals in presence of limestone.In this range, sulfur retention has been found to be related to the capacity of the stone and not its reactivity [6].

It has been suggested that the rate of reaction between sulfur dioxide and limestone is strongly affected by the diffusion of the gaseous reactants [16,17]. Because calcium sulfate has a molar volume about 3 times larger than that of calcium oxide, the accumulation of reaction product causes the sorbent porosity to decrease and the diffusional resistance to increase. When the pore mouths are filled with the reaction product, a considerable percentage of the interior of the pores become inaccessible to the gaseous reactants and the reaction stops. In addition it has been shown that the pore size distribution is affected by the temperature and CO_2 partial pressure during calcination [14]. At higher temperatures and under higher partial pressures of CO_2 higher rates of reactions between SO_2 and CaO have been reported [19]. This is consistent with the observed lower degree of sulfur fixation at 460°C than at 1000°C.

The sulfur retention by limestone was also found to be affected by the oxygen partial pressure during combustion at a particular temperature. Much higher sulfur retention values were obtained under excess air than under limited air at the same combustion temperature (460°C). This is because at lower temperatures, in the presence of excess air $CaSO_4$ is formed which is thermodynamically more stable than the $CaSO_3$ preferentially formed in the presence of limited air. However, it is noteworthy that the results under discussion were obtained from two stage combustion as described in the experimental section. The initial combustion was carried out on a bunsen burner where the effective combustion temperature could have been considerably higher than 460°C, the temperature of the furnace for second stage of combustion. Hence, the effect noted above could be due to a combination of excess air and higher initial combustion temperature.

With increasing amounts of limestone, greater quantities of bitumen were required for agglomeration. However, the ratio of coke to bitumen does not affect the extent of sulfur retention by limestone. This suggests that limestone is a good sorbent for sulfur emissions from both bitumen and coke.

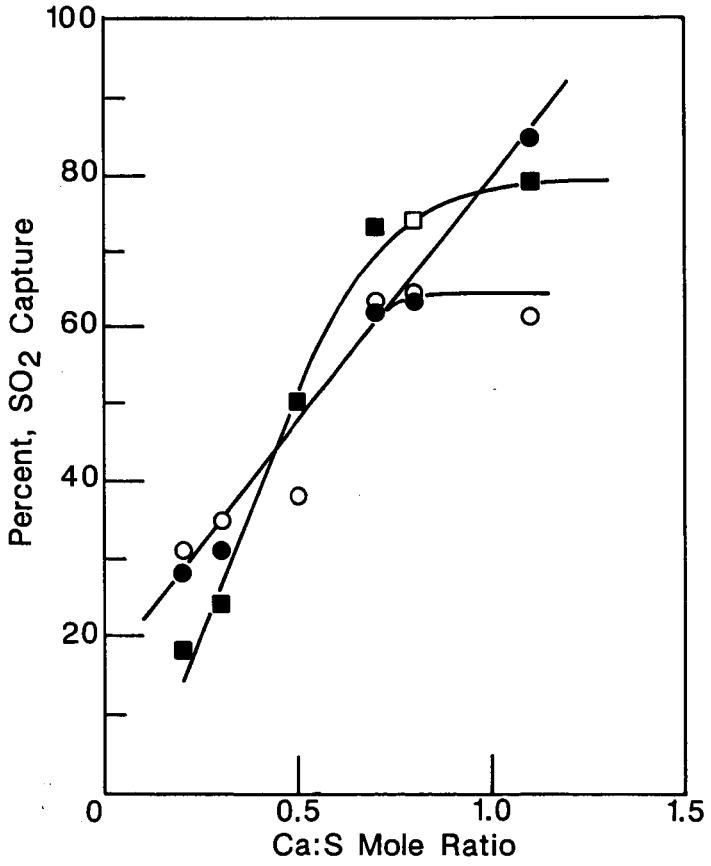
100
80
60
40
20
0
0.5
1.0
1.5
Percent, SO_2 Capture
Ca:S Mole Ratio

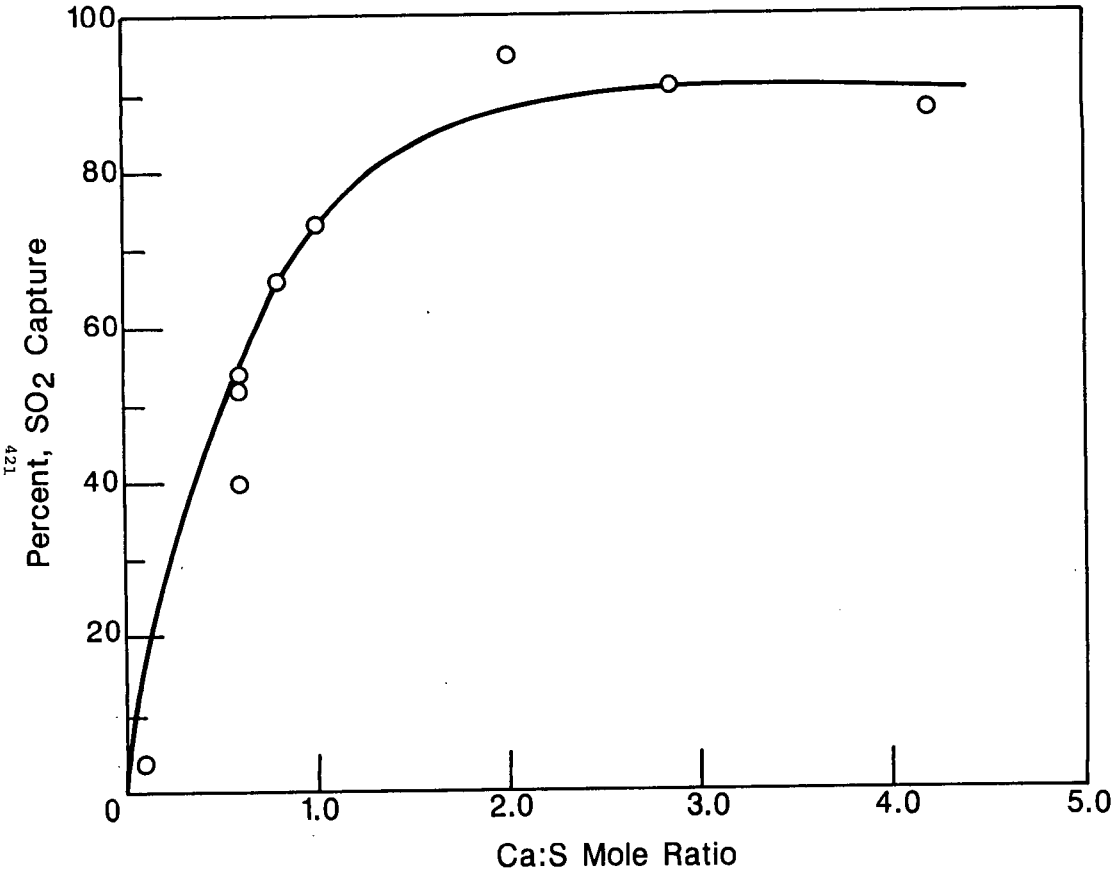
100
80
60
40
20
0
Percent, SO_2 Capture
1.0
2.0
3.0
4.0
5.0
Ca:S Mole Ratio

The Effect of Combustion Temperature on the Retention of SO_2 by Ash from Suncor Coke-Limestone Agglomerates.

As discussed above, the capture of sulfur dioxide by the sorbent is affected by the combustion temperature. The samples of coke agglomerates containing limestone were ashed at 460°C, 750°C and 1000°C in order to find the optimum combustion temperature for maximum sulfur retention. Results are summarized in Figure 2. These results are different from the results shown in Figure 1 in that these were obtained using sodium hydroxide as a conditioning agent. It is obvious from these results that maximum retention is achieved around 750°C to 1000°C. However, an ashing temperature of 1000°C was selected for subsequent work because this is closer to the temperatures used in actual combustion equipment.

At higher temperature sulfur retention is almost independent of the calcium to sulfur mole ratio in the range investigated. Almost 70% sulfur retention can be achieved with a Ca to sulfur mole ratio of 0.6. This can be explained on the basis of much faster rates of reactions for both calcination and sulfation as well as pore plugging at higher temperatures as discussed above [14,16-17,19]. For lower temperatures, sulfur retention is proportional to the Ca to S mole ratio. This could have been due to the greater thermal stability of $CaSO_4$ at lower temperatures.

At 460°C, for a particular Ca to S mole ratio the extent of sulfur retention was much higher in excess air than in limited air. The effect of oxygen partial pressure at higher temperatures was insignificant. This can be explained on the basis of the formation of thermodynamically more stable $CaSO_4$ in excess air at low temperature and under any conditions at higher temperatures as against thermodynamically less stable $CaSO_3$ obtained at low temperatures in limited air. Calcium sulfite will decompose above 400°C according to the equation:

$$CaSO_3(s) \rightleftharpoons CaO(s) + SO_2(g) \qquad (8)$$

The Effect of Conditioning Agents on Sulfur Dioxide Capture by Limestone.

In a recent publication it has been reported that when sodium was deposited on CaO, there was a significant increase in SO_2 adsorption, and adsorption increased with increasing sodium deposition [20]. The presence of sodium was suggested to have activated the CaO surface for SO_2 adsorption due to the formation of Na-O-Ca species. In order to investigate the effect of sodium on SO_2 capture by limestone, Suncor coke was coagglomerated with limestone in the presence of various concentrations of sodium hydroxide, sodium oleate and a sodium salt of a petroleum sulfonate (Witco TRS 10/80). The effect of these additives on the retention of sulfur dioxide by limestone has been illustrated in Figure 3.

The addition of all three conditioning agents improved the coagglomeration of the components, resulting in the use of smaller quantities of bitumen, especially at higher Ca to sulfur mole ratios. This could have been due to the improved wettability of the components towards the bridging oil as a result of the use of surfactants or by in situ formation of surfactants by reaction between the alkali and certain bitumen components.

As can be seen from the plots in Figure 3, better sulfur capture was achieved when the agglomerates were prepared in the presence of these additives. This effect was more pronounced for the higher Ca to sulfur ratios. The relative effectiveness of the three additives was essentially identical. As all three additives were sodium salts it is possible that the observed improvement was owing to sodium activation of calcined limestone [20].

It is also apparent that there is a reduced scatter in the data points for experiments carried out in the presence of additives, compared with the blank experiments. It appears that the three additives all have the ability to distribute limestone uniformly within the agglomerates. Overall sulfur capture by limestone was independent of the concentration of the various additives. This is consistent with the presumed catalytic nature of these additives.

Coagglomeration of Suncor Coke with Lime.

Coagglomeration of Suncor coke with lime was also attempted. This procedure was considerably more difficult than with limestone, resulting in a unitary phase in most cases. Certain bitumen components (carboxylic acids) are known to interact

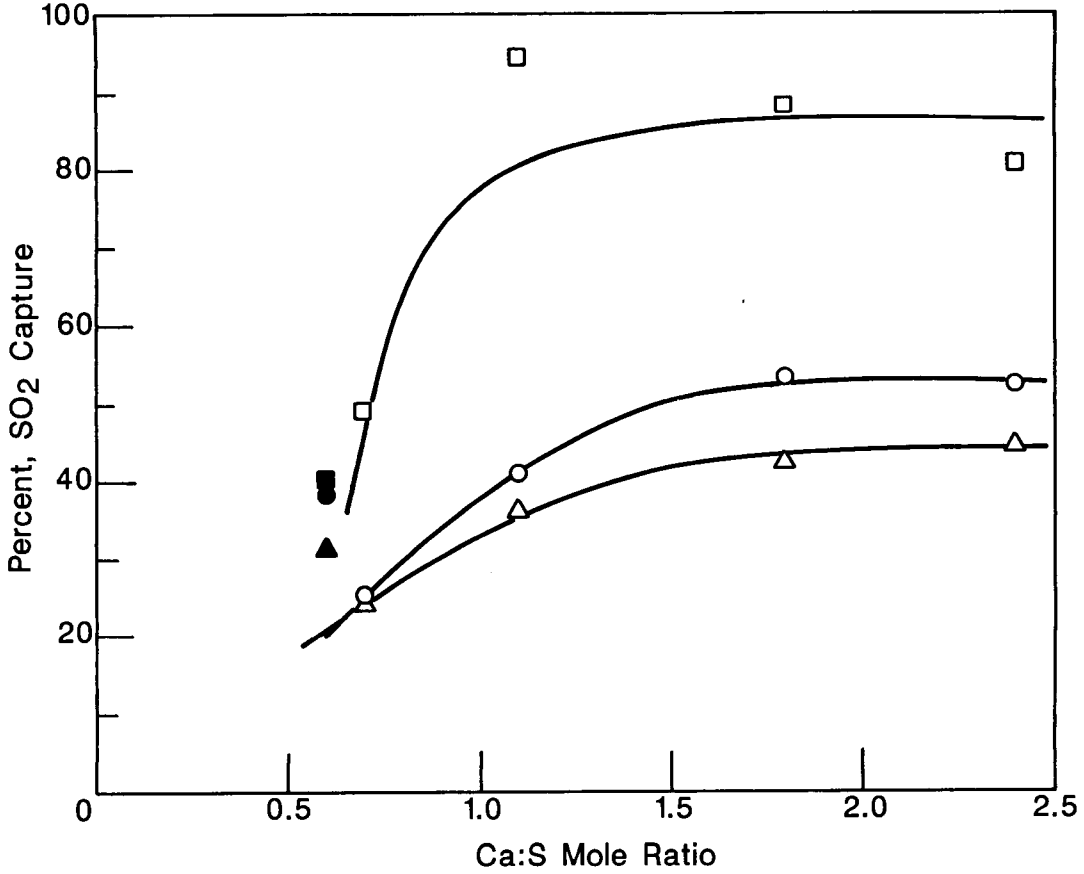
100
80
60
40
20
0
0.5
1.0
1.5
2.0
2.5
Percent, SO_2 Capture
Ca:S Mole Ratio

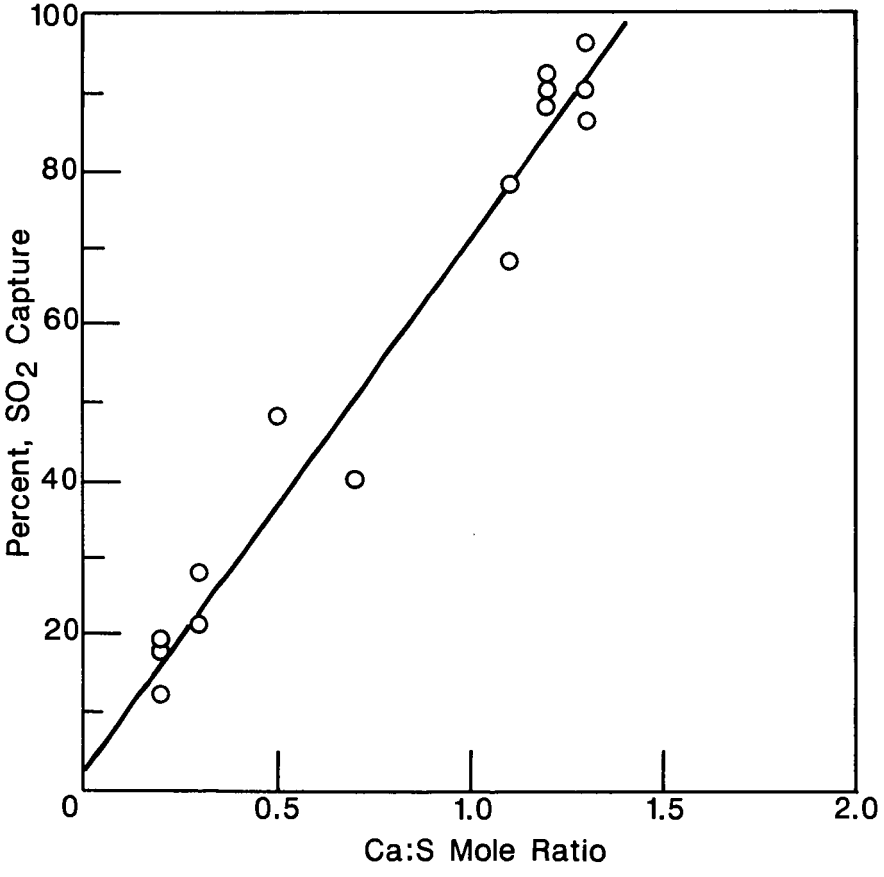
100
80
60
40
20
0
Percent, SO_2 Capture
0.5
1.0
1.5
2.0
Ca:S Mole Ratio

strongly with calcium ions. For limestone, chemisorption of these components to calcium atoms at the solid surface appears to occur readily. This results in a hydrophobic surface easily wettable by the oil, allowing co-agglomeration with the naturally hydrophobic coke. Lime, however, reacts strongly with water and this reaction probably occurs in preference to interaction with the acidic bitumen components. Thus, the lime surface does not become properly conditioned by the bitumen and co-agglomeration does not readily occur.

The effect of calcium to sulfur mole ratio on the retention of sulfur dioxide by lime is illustrated in Figure 4. As is evident the degree of sulfur dioxide retention increases with increasing amounts of lime in the agglomerates up to about 90% at a calcium to sulfur mole ratio of about 2. Relatively low data scatter in Figure 4 suggests a uniform distribution of lime within the agglomerates.

Figure 5 demonstrates the effect of combustion temperature and amount of excess air on the retention of sulfur by lime. Again, considerably higher sulfur retentions were achieved at 1000°C than at 460°C. This effect is identical to the one noted for limestone. It is also consistent with the published results for the fluidized bed combustion studies with similar systems [9,12-15]. However, contrary to the limestone case, where sulfur capture was found to be independent of the calcium to sulfur mole ratio in the higher ratio range, sulfur capture by lime is dependent on the calcium to sulfur mole ratio at a combustion temperature of 1000°C. This could be partly due to the difference in the reactivities of uncalcined and precalcined limestone at higher temperatures [13]. It has been found that the capacity of uncalcined limestone to react with $SO_2(g)$ reached an optimum near 900°C while the capacity of precalcined limestone decreased with increasing temperature above 700°C. Higher reactivity of uncalcined limestone at higher temperatures is said to be due to the higher partial pressure of $CO_2(g)$ produced from the calcination reaction [21].

The temperature effect for sulfur dioxide retention by lime is more pronounced for the Syncrude fluid coke-lime system than for the Suncor delayed coking coke-lime system. This reflects the differences in the conditions during formation of the cokes. During fluid coking (FC), more volatile matter is removed from the bitumen feed than during delayed coking (DC) [22]. As a result DC coke may require lower combustion temperatures than the FC coke.

Another important observation relating to the temperature effect is that maximum sulfur dioxide retention was obtained near 750°C for lime in contrast to a value of 1000°C for limestone. This is consistent with the published data of various authors who found that the optimum sulfation temperature for uncalcined particles is generally higher than that for calcined particles of the same material [9,13].

Excess air had a negative effect on the retention of sulfur dioxide by lime at a combustion temperature of 460°C. This is contrary to the effect noted for limestone. The presence of excess air will lead to the formation of thermodynamically stable $CaSO_4$ in both cases. However, the rate of sulfation reaction will decrease with the extent of reaction due to pore plugging [16-17]. It is probable that this pore plugging is slower in the presence of CO_2 produced from the calcination of limestone.

Coagglomeration of Suncor Coke with Hydrated Lime.

It was relatively easy to coagglomerate the samples of hydrated lime prepared in the laboratory under different conditions as listed in Table III, compared with the reagent grade $Ca(OH)_2$. The results for the retention of sulfur dioxide from Suncor coke by hydrated lime lead to various observations.

As with lime maximum sulfur dioxide retention was achieved near 750°C for reagent grade $Ca(OH)_2$ in contrast to the maximum near 1000°C for the laboratory prepared samples of hydrated lime. The reason for this difference in behavior of the same sorbent obtained from different sources is not well understood. However, this behavior is consistent with the fluidized bed combustion studies of sulfur retention by limestone and dolomite. It has been reported that the maximum in sulfur retention in fluidized bed combuation depends on the specific limestone or dolomite employed [23].

Whereas sodium oleate was found to be beneficial in the agglomeration of laboratory prepared samples of hydrated lime, none of the additives affected either the retention of SO_2 or agglomeration of the reagent grade $Ca(OH)_2$. This suggests

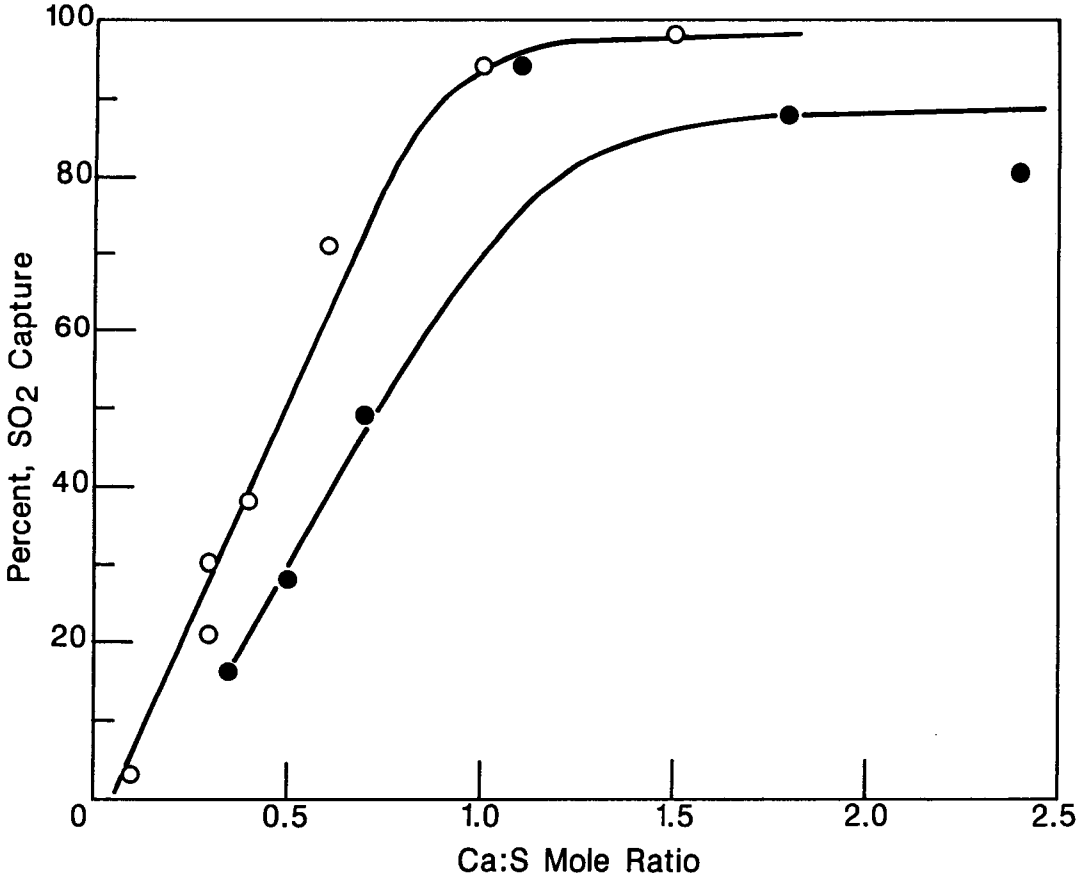
100
80
60
40
20
0
Percent, SO_2 Capture
0.5
1.0
1.5
2.0
2.5
Ca:S Mole Ratio

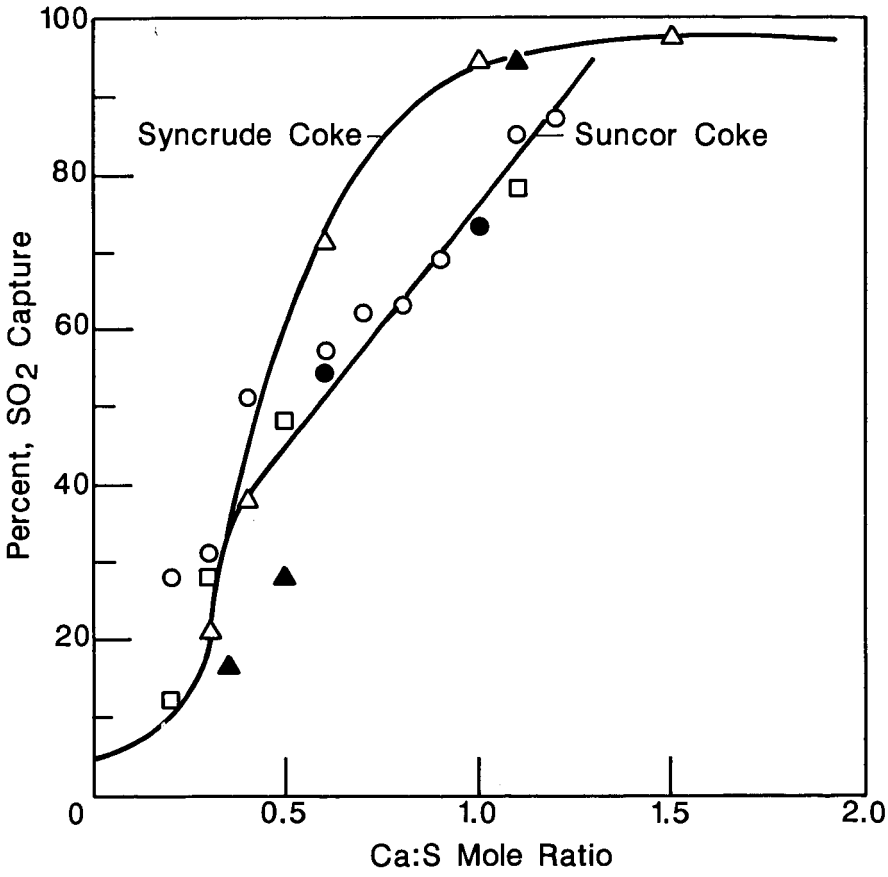
100
80
60
40
20
0
Percent, SO_2 Capture
Syncrude Coke
Suncor Coke
0.5
1.0
1.5
2.0
Ca:S Mole Ratio

that reagent grade $Ca(OH)_2$ is the least hydrophobic among the sorbents investigated in this work.

Also, decomposition of $Ca(OH)_2$ possibly produced reactive CaO

$$Ca(OH)_2(s) \longrightarrow CaO(s) + H_2O(g) \qquad [9]$$

Water vapour and oxygen have been found to show a similar effect on the oxidation rate of $CaSO_3$ to $CaSO_4$ [24]. Figure 6 is a graphic representation of these results. There is a linear correlation between the amount of sulfur retention and the mole ratio of calcium to sulfur in the agglomerates. About 90% sulfur retention can be achieved with a calcium to sulfur mole ratio of 1.2. Coke to bitumen ratio does not appear to affect the reactivity or capacity of hydrated lime for SO_2 capture. This suggests that hydrated lime is an effective sorbent for sulfur dioxide from bitumen as well as from coke.

The presence of excess air does not have any significant effect on the overall retention of sulfur dioxide by hydrated lime. This is contrary to the effect noted for CaO and limestone. Since water vapor and oxygen have a similar effect on the oxidation rate of $CaSO_3$ to $CaSO_4$ [24], the need for additional air will be eliminated. Also, it could be possible that water vapor prevents the pore plugging that produced a negative effect for CaO in the presence of excess air, leading to almost stoichiometric utilisation of the sorbent. This will also explain the linear relationship between the extent of sulfur dioxide retention and the amount of hydrated lime in the agglomerates.

Coagglomeration of Syncrude Fluid Coke with Lime/Limestone.

In order to assess the efficiency of this process for controlling sulfur dioxide emissions from the combustion of various types of cokes, coagglomeration of Syncrude fluid coke with lime or limestone was also attempted. The results were essentially identical to those observed for Suncor coke. The efficiencies of sulfur dioxide retention from the combustion of Syncrude coke by limestone and lime can be compared with the results presented in Figure 7. Although, both curves follow essentially the same trend, it is obvious from the results that limestone is a more efficient sorbent, compared with lime, over the entire range of calcium to sulfur ratios. This could be attributed to the higher porosity and reactivity produced by the in situ calcination reaction [16,17]. The effect of pore size is known to be significant in determining the rate as well as the extent of reaction between SO_2 and CaO. It has been found that small pores in the calcines resulted in high rates of reactions and low overall conversions due to pore plugging, while large pores caused lower rates of reaction with higher conversions [17,21,25]. It is probable that the freshly calcined limestone particles have bigger pores than the CaO used. This is a very important result as the ability to use a cheap and readily available material in its natural form has a considerable economic significance. The cost ratio of lime to limestone on a molar basis may vary from 2 to 4 depending on the transportation distance [26]. Even the costs for transportation and handling of limestone tends to be lower than for lime since it can be transported in open trucks.

Results discussed so far have demonstrated that coagglomerating cokes with such sulfur capture agents as limestone, lime and hydrated lime could be an effective way for controlling sulfur dioxide emissions from the combustion of these cokes. In Figure 8 a comparison of the efficiency of this process in terms of sulfur retention by the ash has been made for the two cokes investigated. It is obvious from the plots that although this process is effective for both cokes it is slightly more efficient for Syncrude coke compared with Suncor coke specially at higher calcium to sulfur ratios. Thus, at a calcium to sulfur mole ratio of about 1:1 over 90% sulfur retention can be achieved for Syncrude coke compared with over 80% sulfur retention for Suncor coke. This difference may be due to the reportedly higher bulk gasification reactivity of Syncrude fluid coking coke compared with that of Suncor delayed coking coke [22]. Higher reactivity of fluid coke, compared with delayed coke, is surprising as the former was subjected to more severe treatment in the coking process. However, no reason for this reactivity difference has been suggested.

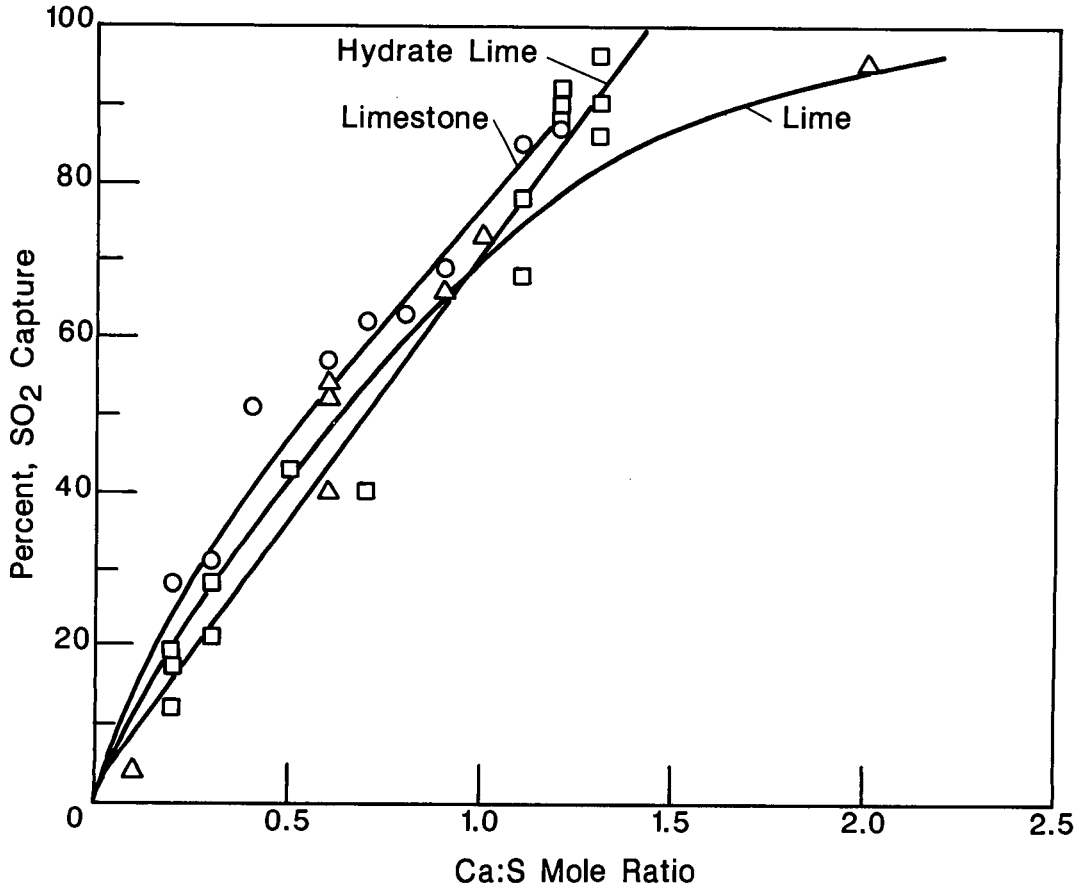
Hydrate Lime
Limestone
Lime
Percent, SO_2 Capture
Ca:S Mole Ratio
100
80
60
40
20
0
0.5
1.0
1.5
2.0
2.5

Comparative efficiencies of the three sorbents investigated; lime, hydrated lime and limestone have been illustrated in the plots shown in Figure 9. These results were obtained in the presence of conditioning agents that activate the sorbent as discussed above. It is obvious from these plots that activated limestone is the most efficient in its capacity to retain SO_2. Lime and hydrated lime both have comparable efficiencies for low calcium to sulfur ratios (up to ≈ 1.0). However, in the range of Ca to S ratios beyond 1, hydrated lime appears to be more efficient than lime, approaching in efficiency to that observed for activated limestone. The observed higher efficiency of activated limestone for SO_2 retention is of considerable significance because of its already mentioned economic advantage over the other sorbents.

According to the findings of Schneider and George [27] calcium has a beneficial effect on the leaching of nickel and vanadium from coke ash using hydrochloric acid. Hence, coagglomeration of coke with calcium compounds will have the added advantage that the ash from these agglomerates would be more suitable for mild acid leaching than the ash from coke alone.

In a fluidized bed combustion of coal the amount of sorbent required to achieve a given reduction in sulfur dioxide emissions mainly depends on the gas retention time in the bed and consequently the flow rate of air. However, in the present case, where there is intimate contact between fuel and sorbent within an agglomerate matrix, sulfur dioxide has to diffuse out through the agglomerate pores, contacting sorbent during its passage, before coming in contact with the fluidizing air. Hence, one might expect greater utilization of the sorbent in this latter case compared to fluidized bed combustion where sorbent is added separately to the bed. A comparison of the results from this investigation with the data from some preliminary experiments on the simulated fluidized bed combustion of Suncor coke does suggest a greater efficiency for coagglomerated sorbents compared to a simple mixture of components. Details of these findings will be presented elsewhere.

Conclusions

(1) There is no significant sulfur retention by the original ash from the Athabasca bitumen cokes.

(2) Cokes produced during the upgrading of Athabasca bitumen can be successfully coagglomerated with sulfur dioxide capture agents such as: lime, hydrated lime and limestone as a means of reducing sulfur emissions. On combustion, most of the sulfur remains in the recovered ash from these agglomerates instead of escaping to the atmosphere as SO_2.

(3) ASTM method D 4239-83 is not satisfactory for measuring the sulfur dioxide emissions from the combustion of coke-limestone agglomerates.

(4) Decrease in the sulfur dioxide emitted on combustion of the coke-sorbent agglomerates depends on such variables as the calcium to sulfur mole ratio, combustion temperature, partial pressure of oxygen, conditioning agents and the type of coke and sorbent.

(5) The quantity of the sulfur dioxide capture agents required for coagglomeration with coke depends on the degree of sulfur removal desired. The decrease in the sulfur dioxide formed on combustion increases with increasing quantities of additive, until further additive confers no additional benefit. Thus over 80-90% reductions in sulfur dioxide emissions can be achieved with a calcium to sulfur mole ratio of approximately 1:1.

(6) Combustion temperature had a profound effect on the retention of sulfur dioxide by sorbents. In general, at higher temperatures more sulfur dioxide retention was achieved than at lower temperatures. However, the optimum temperature at which maximum sulfur retention could be obtained varies with the type of sorbent.

(7) At lower combustion temperatures, the presence of excess air had a beneficial effect on the retention of sulfur in the coke-limestone system, and a negative effect in the coke-lime system. For the coke-hydrated lime, presence of excess air does not affect the overall conversion.

(8) Conditioning agents such as sodium hydroxide, sodium oleate and a petroleum sulfonate had a beneficial effect both on agglomeration and on the extent of sulfur dioxide capture.

(9) Coagglomeraion of Athabasca bitumen cokes with lime, hydrated lime or limestone is an effective desulfurization method. However, Syncrude fluid coke gave slightly better results than Suncor delayed coke.

(10) Activated limestone is a slightly more efficient sorbent than lime. This has an economic advantage as limestone is 2-4 times cheaper than lime.

Acknowledgments

The authors wish to thank P. Maxwell, Martin Lepage, Mrs. M.R. Miedema and F.W. Meadus for some technical assistance; R.D. Coleman and Roger Lafleur of EMR for kindly providing access to a Leco sulfur analyzer.

Literature Cited

1. George, Z.M.; Kessick, M.A. Prep. 32nd Can. Chem. Engin. Conf. 1982, 712.
2. Parmar, B.S. and Tollefson, E.L. Can. J. Chem. Engin. 1977, 55, 185.
3. Hall, E.S.; Tollefson, E.L.; George, Z.M. and Schneider, L., Can. J. Chem. Engin. 1982, 60, 418.
4. Phillips, R.C.,; Chao, K.S. Fuel, 1977, 56, 70.
5. Anthony, E.J.; Desai, D.L.; Friedrich, F.D. Canmet Report No. ERP/ERL 81-27, 1981.
6. Lee, D.C.; Georgakis, C. AIChem. Engin. J., 1981, 472.
7. Alberta Committee on Oil Sands Analysis. Bitumen Round Robin No. 2. Dean Wallace, Chairman, Alberta Research Council, February, 1983.
8. Majid, A.; Ripmeester, J.A. and Sparks, B.D. Proc. 4th International Symposium on Agglomeration, 1985, 927.
9. Christman, P.G. Ph.D. Thesis, The University of Texas at Austin, 1981.
10. Yang, R.T.; Shen, M.; Sheinberg, M. Environ. Sci. Technol., 1978, 12 (8), 915.
11. Jack, T.R.; Sullivan, E.A. and Zajic, J.E. CIM Bulletin, 1980, 151.
12. Hatfield, J.D.; Kim, Y.K.; Mullins, R.C. and McClellan, G.H. NTIS Publication, no PB202407, 1970.
13. Potter, A.E., Ceramic Bulletin, 1969, 48(9), 855.
14. O'Neill, E.P.; Kearns, D.L. and Kittle, W.F. Thermochimica Acta, 1976, 14, 209.
15. Roberts, A.G.; Stanton, J.E.; Wilkins, J.M.; Beacham, B. and Hoy, H.R. Proc. Fluidized Combustion Conference, 1975.
16. Borgwardt, R.H. Environ. Sci. and Techn., 1970, 4(1), 59.
17. Borgwardt, R.H. and Harvey, R.D. Environ. Sci. and Techn., 1972, 6(4), 350.
18. Hills, A.W.D. Chem. Engin. Sci., 1968, 23, 297.
19. Hoke, R.C.; Nutkis, M.S. and Kinzler, D.D. Proc. Fluidized Bed Technology Exchange Workshop, 1977, 157.
20. R.V. Siriwardane and J.M. Cook, J. Coll. Interface Sci., 1986, 114, 525.
21. Ulerich, N.H.; O'Neill, E.P. and Keairns, D.L., Thermochimica Acta, 1978, 26, 269.
22. Furimsky, E. Fuel Processing Technology, 1985, 11, 167.
23. Berenak, J., Proc. of Control of gaseous sulfur compound emissions, Intr. Conf., 1973, 2.
24. Karlsson, H.T.; Bengtsson, S.; Bjerle, I.; Klingsper, J.; Nilsson, L.I. and Stronberg, A.M. Proc. International Conference on Processing and Utilization of High Sulfur Coals, 1985, 389.
25. O'Neill, E.P.; Ulerich, J.H.; Keairns, D.L.; Newby, R.A. and Archer, D.H. Proc. Fluidized Bed Technology Exchange Workshop, 1977, 371.
26. Miller, J.F.; Oxley, J.H.; Rosenberg, H.S. and Nusum, H.K. Proc. I. International Conference on Processing and Utilization of High Sulfur Coals, 1985, 575.
27. Schneider, L.G. and George, Z.M. Ext. Metal. Conf. 81, Instite Min. Metall. London, 1981.

Figure Captions.

Figure 1. Calcium to sulfur ratio effect on SO_2 capture by limestone ● Ashing temperature 460°C in excess air; ○ ashing temperature 1000°C in limited air.

Figure 2. The effect of ashing temperature on SO_2 capture by limestone. ○ 460°C, limited air, ● 460°C, excess air, △ 750°C, excess air and □ 1000°C limited air.

Figure 3. The effect of various conditioning agents on the retention of sulfur dioxide by limestone.
○, blank; ●, NaOH; □, sodium oleate and ■, TRS 10/80.

Figure 4. Calcium to sulfur ratio effects on the retention of sulfur dioxide by lime.

Figure 5. The effect of ashing temperature on SO_2 capture by lime. ○, ●, 460°C limited air; △, ▲, 460°C, excess air and □, ■, 1000°C limited air. Open symbols for Syncrude coke; close symbols, Suncor coke.

Figure 6. Calcium to sulfur ratio effect on SO_2 capture by hydrated lime.

Figure 7. The SO_2 capture efficiencies of limestone vs lime ○, limestone; ● Lime; from Syncrude coke.

Figure 8. Efficiency of SO_2 capture; Suncor coke vs Syncrude coke. ○, △, limestone; ●, ▲, lime; □, hydrated lime; △, ▲, Syncrude coke; ○, ●, □, Suncor coke.

Figure 9. Comparative SO_2 capture efficiencies of various sorbents for Suncor coke. ○, limestone; △, lime; □, hydrated lime.

KINETICS AND MECHANISM OF THERMAL DeNOx: A REVIEW

Richard K. Lyon

Energy and Environmental Research Corp.
1090 King Georges Post Road
Edison, NJ 08837

In 1972 the author, then with Exxon Research and Eng. Co. (ERE), discovered a new chemical reaction, the gas phase homogeneous reduction of NO to N2 and H2O by NH3, in the presence of O2 (1,2,3). This reaction was both rapid and highly selective, i.e. with reaction times of 0.1 sec or less NO could be nearly quantitatively reduced by equimolar amounts of NH3 in the presence of O2 concentrations orders of magnitude greater than the NO. The discovery of this reaction made possible a new and remarkably simple method of controlling the emissions of NOx from stationary sources such as utility boilers and industrial process furnaces, the Thermal DeNOx process. One simply found the location in the unit at which the temperature was appropriate to the reaction and installed there a grid to inject NH3 into the hot flue gas. To date this process has had upwards of 60 commercial applications and in recent instances NO reductions in excess of 90% have been achieved.

One factor which helped make this success possible was the development of a predictive kinetic model, i.e. a model which described the kinetics of the reaction in terms of elementary reaction rate constants and which could be used to accurately predict the performance of the process in any given practical application. The model is routinely used in the engineering design of new Thermal DeNOx installation. To the author's knowledge this is the first instance in which a model based on elementary reaction rate constants has been so used. This success was the culmination of the efforts of workers both within and outside of ERE but this success has recieved less attention than it might have otherwise. Several papers and meeting presentations have outlined the general nature of the model (4,5,6,7,8), but the actual model itself has been disclosed only in one somewhat obscure patent (9). In this review the DDHL model will be discussed and compaared with models published by others.

The other models of interest were developed by Hanson and Salimian with subsequent refinement by Hanson and Kimball-Linne (10,11), by Miller, Branch and Kee (12), and by Silver, Gozewski and Kolb (13), hereinafter the H&K, MBK, and SGK models, respectively. Silver and Kolb (14) also measured the rate constant of the NH2 + NO reaction at elevated temperatures. Miller et al. are to be credited with proposing on purely theoretical grounds that the second channel of the NH2 + NO reaction does not directly yield N2 + H + OH but rather N2H + OH, a suggestion later supported experimentally by Andresen et al. (15). It is to be noted that both of these contributions were incorporated into the DDHL model.

A principal difference among these modeling efforts was the extent to which experimental data on the kinetics of the NO - NH3 - O2 reaction were available to the modelers. The MBK and SGK models are a prior models, i.e. in the development of these models if the rate constant of a reaction was unknown, it was estimated on purely theoretical grounds without any effort to choose a value that would make the model fit the data. Both these models were successful in qualitative terms in that they showed the appropriate trends when compared to the limited data of Muzio et al. (16). In the H&K model, however, the model seeks to provide a truly quantitative description of the reaction kinetics. Hanson and Kimball-Linne set up a laboratory scale combustor and generated a block of data showing the kinetics of the Thermal DeNOx process for initial temperatures ranging from 1258 K to 1548 K and initial [NO] and [NH3] ranging from 141 to 387 ppm and 78 to 556 ppm, respectively. Since the combustor was operated at a constant air/fuel equivalence ratio of 0.9, neither [O2] nor [H2O] were varied. Sensitivity analysis was done on the model and the rate constants of reactions which were uncertain and sensitive were adjusted to fit the data. Figure 1 shows an example of the model's fit to the data.

The DDHL model was developed in a similar manner, i.e. flow tube experiments were done with synthetic gas mixtures to develop two data bases, one relating to the oxidation of NH3 in the initial absence of NO (T = 1279 to 1323 K, [NH3] = 900 ppm, [O2] = 2 to 8% and [H2O] = 0 or 1%) and the second larger data base relating to the reduction of NO by NH3 (T = 1120 to 1390 K, [O2] = 2 to 8%, [H2O] = 0 to 15%, [NO] = 100 to 460 ppm, [NH3] = 270 to 530 ppm, a total of 742 data points). A kinetic model was developed which gave excellent fit to the former data base and with minor modifications which didn't damage the fit to the NH3 oxidation data base it proved possible to fit the NO reduction data base within 7%, which is within the experimental uncertainty. Figure 2 shows examples of this model's fit to laboratory data (5) while Figure 3 shows a comparison between the model's predicted performance for the Thermal DeNOx process in commercial application and what was obtained.(9)

Since then the DDHL and HSK models were derived in general similar manners, the comparison between them is particularly interesting. While the DDHL model uses 31 elementary reactions of H/N/O species, the H&K model uses 52. Of these 30 reactions are common to the two models, DDHL includes one radical radical reaction which is probably unimportant under Thermal DeNOx conditions and which the H&K model omits. The H&K model includes ten such radical radical reactions. The other reactions which are used in H&K and omitted in DDHL includes three reactions which form nitrogen atoms and four reactions of N2O. The former have high activation energies and will be important only at temperatures well above the Thermal DeNOx range. Since Thermal DeNOx does not make significant amounts of N2O, the latter will be unimportant in the initial absence of N2O. While the DDHL model show the interaction of NH2 and NO as a two channel reaction, capable of yielding N2H + OH and N2 + H2O, the H&K model shows it as having a third far less probable channel yielding HNO + NH. DDHL shows the reactions of NH2 + O, NH + O2, and

NO + HO2 as single channel processes, each making only one pair of products. While the H&K model agrees that these are the dominant raction pathways, it does includes a second less important channel for each. The H&K model also includes the reaction N2H+O2=N2+HO2 with a rate constant that is 1000 times less at 1200 K than the rate constant which H&K assumes for the competing N2H+NO=N2+HNO reaction. Thus the omission of this reaction by DDHL does not appear to be a serious disagreement.

Indeed there does not seem to be any disagreement between the two models as to which reactions are central to the Thermal DeNOx chemistry. There is also much agreement as to the roles which these reactions play in deciding the overall kinetics of the Thermal DeNOx reaction. In both models the overall reaction mechanism may be divided into two submechanisms, a chain reaction in which NH3 reduces NO and a chain reaction in which NH3 is oxidized to form NO. In both submechanisms the first step is the attack on NH3 by O and OH to form NH2. In the reduction submechanism the NH2 reacts with NO yielding either N2 and H2O (a chain terminating step) or yielding NNH and OH. If the latter step is followed by the reactions NNH+M=N2+H+M and H+O2=OH+O it is strongly chain branching. If, however, the subsequent reaction is NNH+NH2=N2+NH3 or NNH+OH=N2+H2O the result is chain termination. Consequently the NO reduction submechanism is a self controlling explosion. Initially the chain branching sequence is dominant and the concentration of chain carriers grows exponentially, i.e. at a rate that is proportional to the concentration of chain carriers. Since chain termination processes have rates that are proportional to the square of the chain carrier concentration, they soon limit the increase in chain carrier concentration. Thus in the NO reduction submechanism the rate of the overall reaction rapidly grows to a finite limit and proceeds smoothly thereafter.

In the NO formation submechanism NH2 reacts with O, OH and O2. The latter reaction directly produces HNO while the former two reactions produce NH which reacts with O2 to yield HNO. The function of HNO in the oxidation submechanism is similar to NNH, i.e. dissocation of HNO to yield H atoms causes chain branching while reaction with NH2 or OH causes chain termination. Thus the oxidation submechanism, left to its own devices, would regulate the chain carrier concentration and overall reaction rate to finite values, though not necessarily the same values as those dicatated by the reduction submechanism. This conflict helps make the kinetics of the Thermal DeNOx reaction more complex than one might expect from the number of reactions involved.

While there is agreement between the DDHL and H&K models as to which reactions are important, there is significant disagreement as to the roles those reactions play. In table 1 the rate constants of the thirty reactions the two models have in common are listed along with the ratios of those rate constants at 1200 K. Numerically the largest disagreement relates to the NH+O2=HNO+O reaction but this is actually trivial since neither model assumes any reaction of NH which could compete effectively with NH+O2=HNO+O. The disagreement as to the rate constant for the NNH+NO=N2+HNO reaction is more important.

In the DDHL model control of the overall rate is shared between the submechanisms while the high rate constant assumed by H&K for this reaction tends to transfer control of the overall rate from the reduction submechanism to the oxidation submechanism.

Another important disagreement between the models relates to the balance between chain branching and chain termination. In the DDHL model the rate of the chain terminating reaction NH2+HNO=NH3+NO is faster by a factor of 15.8 than in the H&K model. This disagreement is compounded by the fact that in the H&K model the N2+H2O and NNH+OH channels in the NH2+NO reaction are assumed to have equal rate constants while in the DDHL model the former is 1.5 times as fast as the latter. This rate constant ratio is very critical to the kinetics since it controls the chain branching factor.

Finally it is to be noted that in the DDHL model the rate constant for the NH3+O=NH2+OH reaction is a factor of five slower than that used in the H&K model. A recent review of the literature by Cohen (17) recommends a rate constant for NH3+O=NH2+OH that is midway between the H&K and DDHL values with an uncertainty large enough to include both. The result of this and to a lesser extent the other disagreements between the models is that the concentration of O atoms during the deNOx reaction is much lower in the H&K model than it is in the DDHL model. Within DDHL NH2 is oxidized to NO chiefly by reaction with O atom but in H&K the NH2+OH=NH+H2O is more important. This leads the two models to rather different predictions of the effect of water vapor on the kinetics of the Thermal DeNOx reaction. Figures 4 and 5 show calculations of the extent of NO reductions as a function of reaction temperature done with the DDHL and H&K models. In the DDHL model adding water vapor shifts the optimum reaction to higher values, i.e. in the DDHL model added water removes O atom via the reaction O+H2O=2OH and since O is the critical chain carrier removing it with added water retards the reaction. In the H&K model, however, adding water shifts the optimum reaction temperature to lower values because the added water increases the concentration of OH, the critical chain carrier for H&K.

Since the retarding effect of water has been demonstrated experimentally (compare figures 3c and 3d, also see reference 6), this would seem to be a limitation on the H&K model. Such limitations are to be expected when an empirical model is pushed beyond the range of its data base. The DDHL model has the advantage resting on a much broader data base, one that covers all the parameters of practical importance in applications of the Thermal DeNOx process. This makes the model a useful tool in commercial application of the process, but it is to be recognized that when the model "predicts" the extent of NO reduction to be expected in a given boiler or furnace, it is merely interpolating within the base of laboratory data. When one develops a kinetic model by using the rate constants of unknown reactions as adjustable parameters, two kinds of failure are possible. The model can fail to predict kinetics for conditions outside the range of its data base because for these conditions reactions which were unimportant within the conditions of the data base become important. Such failure is less serious since it does not imply that the model is

essentially wrong, merely that it needs extension. It is also possible, however, for the adjustable parameters to produce a compensating set of errors. It is interesting to ask what experiments could be done to test the DDHL model for the latter problem.

A number of fair tests of the model are possible, i.e. in several instances the information in the model is sufficient to make unambiguous predictions about what should happen for conditions significantly different from the data base. Thus, for example, all the observations in the data base were at one atmosphere pressure and it would be interesting to see whether or not the model could correctly predict the effect of varying the pressure while holding [NH3], [NO], [H2O], and [O2] constant. Similarly the model contains the reactions known to be important during the oxidation of H2 and those which occur during CO oxidation could readily be added. Thus the model's ability to predict the extent to which adding H2 or CO shifts the optimum reaction temperature to lower values is another interesting test.

Another test of the model, one which has been carried out, involves the oxidation of NH3 at trace concentrations (19). The model's data base includes experiments in which NH3 at an initial concentration of 900 ppm was oxidized with NO initially absent. The observed decay of NH3 was zero order in NH3. This somewhat surprising behavior is a result of the balance between chain carrier production and removal. If the production of free radicals by the reaction sequence HNO+M=H+NO+M, H+O2=OH+O is balanced by their consumption by HNO+NH2=NO+NH3, it follows that [NH2] is independent of NH3 and the rate of NH3 disappearance is zero order. Obviously, however, if one starts with a sufficiently small initial concentration of NH3 this mechanism for maintaining [NH2] constant has to become ineffective and the rate of NH3 oxidation must become dependent on [NH3]. Specifically using the DDHL model one can calculate that for the conditions shown in figure 6 the decay of NH3 should be first order in NH3 and the decay constant should be 5.61/sec in contrast to the observed value of 5.65/sec. Thus in this instance, at least, the extrapolation of the DDHL model to conditions quite different from its data base is valid.

REFERENCES

1 R. K. Lyon, U.S. Patent 3,900,554, 1975

2 R. K. Lyon, Int. J. Chem. Kinet., 8, 315, 1976

3 R. K. Lyon and D. Benn, Symp. (Int.) Combust., [Proc], 17th, 1978, 1979, 601

4 R. K. Lyon and J. E. Hardy, I&EC Fundamentals, 1986, 25, 19

5 A. M. Dean, A.J. DeGregoria, J. E. Hardy, and R. K. Lyon, 7th International Symposium on Gas Kinetics, Gottingen, Germany, August 1982

6 A. M. Dean, J. E. Hardy, and R. K. Lyon, Symp. (Int.) Combust., [Proc], 19th, 1982, 1983, 97

7 R. K. Lyon, Envr 44 Paper Presented at the 187th National Meeting of the American Chemical Society, St. Louis, April 1984

8 B. E. Hurst, Glass Techno. 24, 97 (1983)

9 A. M. Dean, A. DeGregoria, J. E. Hardy, B. E. Hurst, and R. K. Lyon, U. S. Patent, 4,507,269, 1985

10 S. Salimain and R. K. Hanson, Comb. Sci. and Technol. 23, 225, (1980)

11 M. A. Kimball-Linne and R. K. Hanson, Comb. and Flame, 64, 337, (1986) also see M. A. Kimball-Linne, Report T244 High Temperature Gas Dynamics Laboratory, Stanford University

12 J. A. Miller, M. C. Branch, and R. J. Kee, Comb. and Flame, 44, 181 (1981)

13 J. A. Silver, C. M. Gozewski and C. E. Kolb, Aerodyne Report NO ARI-RR-66; also see J. A. Silver, Comb. and Flame 53, 17 (1983)

14 J. A. Silver and C. E. Kolb, Chem. Phys. Lett. 75, 191, (1980)

15 P. Andresen, A. Jacobs, C. Kleinermanns, and J. Wolfrum, Symp. (Int.) Combust., [Proc], 19th, 1982, 1983, 11

16 L. J. Muzio, J. K. Arand and D. P. Tierxeria, Symp. (Int.) Combust., [Proc], 16th, 1976, 1977, 199

17 N. Cohen, Int. J. Chem. Kinet. 19, 319, 1987

18 A. C. Lloyd, Int. J. Chem. Kinet. 6, 169, 1974

19 R. K. Lyon and J. E. Hardy, Poster Session at 20th Symposium, (Int.) on Combustion, Ann Arbor, 1984

TABLE 1

COMPARISON OF THE RATE CONSTANTS USED IN THE DDHL AND H&K MODELS

(In this table R denotes the ratio of the DDHL rate constant to the H&K rate constant at 1200 K. * indicates reactions which were found to be kinetically sensitive.)

			A	n	E,kcal	R**
1)	DDHL	H+O2=O+OH	2.2E+14	-0.	16.80	0.97
	H&K	H+O2=O+OH	3.7E+17	-1.00	17.5	
2)	DDHL	O+H2=H+OH	1.8E+10	1.0	8.90	1.0
	H&K	O+H2=H+OH	1.8E+10	1.00	8.90	
3)	DDHL	H2+OH=H2O+H	2.2E+13	0.0	5.15	0.97
	H&K	H2+OH=H2O+H	1.17E+09	1.30	3.626	
4)	DDHL	OH+OH=O+H2O	6.3E+12	0.0	1.09	0.95
	H&K	O+H2O=OH+OH	4.60E+09	1.3	17.10	
5)	DDHL	H+O2+M=HO2+M	1.5E+E15	0.0	-0.995	1.45
(For M=H2O the quoted rate constant is increased by x21)						
	H&K	H+O2+M=HO2+M	7.3E+18	-1.0	0.0	
(For M = N2 or O2 the quoted A factor is changed to 6.7E+19 and n changed to -1.42)						
6)	DDHL	H+HO2=OH+OH	2.5E+14	0.0	1.90	1.0
	H&K	H+HO2=OH+OH	2.5E+14	0.0	1.90	
7)	DDHL	HO2+OH=H2O+O2	5.0E+13	0.0	1.00	1.0
	H&K	HO2+OH=H2O+O2	5.0E+13	0.0	1.00	
8)	DDHL	HO2+O=O2+OH	5.0E+13	0.0	1.00	1.0
	H&K	HO2+O=O2+OH	5.0E+13	0.0	1.00	
9)	DDHL	NH3+M ◘ NH2+H+M	4.8E+16	0.00	93.90	1.83
	H&K	NH3+M ◘ NH2+H+M	2.5E+16	0.0	93.79	
10)	DDHL	NH3+H=NH2+H2	2.5E+13	0.0	17.10	1.22
	H&K	NH3+H=NH2+H2	1.3E+14	0.0	21.50	
11)	DDHL	NH3+O=NH2+OH	1.5E+12	0.0	6.04	0.23
	H&K	NH3+O=NH2+OH	2.19E+13	0.0	8.94	
12)	DDHL	NH3+OH=NH2+H2O	3.3E+12	0.0	2.12	0.71
	H&K	NH3+OH=NH2+H2O	5.75+13	0.0	8.11	
13)	DDHL	NH2+O=NH+OH*	1.7E+13	0.	1.00	0.71
	H&K	NH2+O=NH+OH	6.75E+12	0.0	0.0	

Table 1 (continued)

14)	DDHL	NH2+OH=NH+H2O*	5.5E+10	0.68	1.29	0.66
	H&K	NH2+OH=NH+H2O	6.0E+12	0.0	0.0	
15)	DDHL	NH2+H=NH+H2	5.0E+10	0.5	2.00	0.39
	H&K	NH2+H=NH+H2	1.9E+13	0.0	0.0	
16)	DDHL	NH2+HNO=NH3+NO*	1.8E+14	0	1.00	15.8
	H&K	NH2+HNO=NH3+NO	5.0E+11	0.5	2.00	
17)	DDHL	NH+O2=HNO+O	3.0E+13	0.0	3.40	110.6
	H&K	NH+O2=HNO+O	1.0E+13	0.0	12.00	
18)	DDHL	HNO+OH=NO+H2O	3.6E+13	0.0	0.0	0.5
	H&K	HNO+OH=NO+H2O	1.26E+12	0.5	2.0	
19)	DDHL	HNO+M=H+NO+M*	1.9E+16	0.0	48.68	0.4
	H&K	H+NO+M=HNO+M	7.56E+15	0.0	-0.6	
20)	DDHL	NO+HO2=NO2+OH	3.4E+12	0.0	-.26	1.8
	H&K	NO+HO2=NO2+OH	2.09E+12	0.0	-.48	
21)	DDHL	NH2+NO=NNH+OH*	6.1E+19	-2.46	1.87	0.4
	H&K	NH2+NO=NNH+OH	1.26E+16	-1.25	0.0	
22)	DDHL	NH2+NO=N2+H2O*	9.1E+19	-2.46	1.87	0.6
	H&K	NH2+NO=N2+H2O	1.26E+16	1.25	0.0	
23)	DDHL	O+NO2=NO+O2	1.0E+13	0.0	0.6	1.0
	H&K	O+NO2=NO+O2	1.0E+13	0.0	0.6	
24)	DDHL	NO2+H=NO+OH	3.5E+14	0.0	1.50	0.99
	H&K	NO2+H=NO+OH	3.5E+14	0.0	1.48	
25)	DDHL	NO2+M=NO+O+M	1.1E16	0.0	66.00	1.6
	H&K	NO+O+M=NO2+M	2.00E+15	0.0	1.88	
26)	DDHL	NNH+NH2=N2+NH3*	1.0E+13	0.0	0.	1.0
	H&K	NNH+NH2=N2+NH3	1.0E+13	0.0	0.0	
27)	DDHL	NNH+M=N2+H+M*	2.0E+14	0.0	30.00	0.4
	H&K	NNH+M=N2+H+M	2.0E+14	0.0	28.00	
28)	DDHL	NNH+OH=N2+H2O	3.0E+13	0.0	0.0	1.0
	H&K	NNH+OH=N2+H2O	3.0E+13	0.0	0.0	
29)	DDHL	NNH+NO=N2+HNO*	9.1E+11	0.0	0.0	0.02
	H&K	NNH+NO=N2+HNO	5.0E+13	0.0	0.0	
30)	DDHL	NH2+O2=HNO+OH*	5.1E+13	0.0	30.00	1.4
	H&K	NH2+O2=HNO+OH	4.5E+12	0.0	25.00	

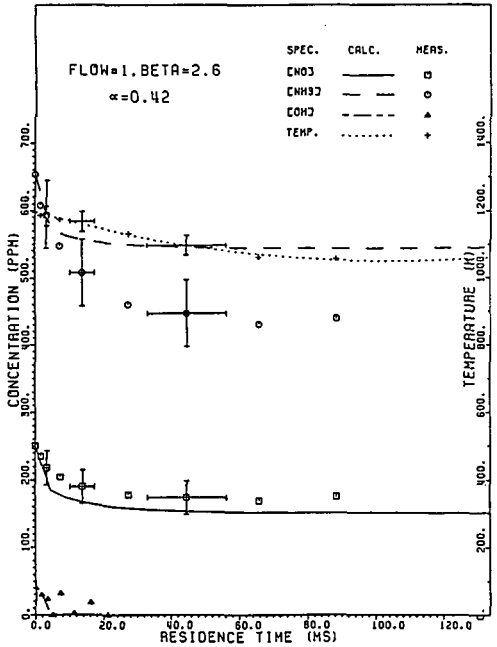

Figure 1. Comparison of H&K Model Predictions with Experiment. $NH_3/NO=2.6$

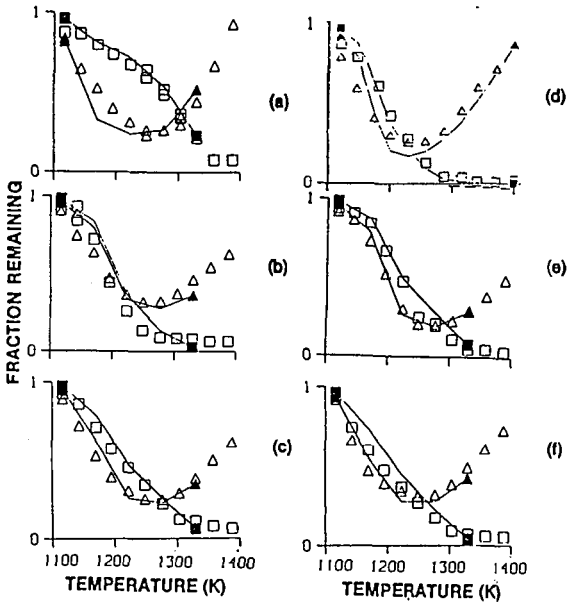

Figure 2. Comparison of DDHL Model Predictions (Lines Terminated by ■ for NO and by ▲ for NH_3) with Experiment. □ =NO, △ = NH_3, t=0.1 sec, p=1.2 atm, O_2=4% (a,b,c,d), 2%(e), 8% f, NH_3=385 ppm NO=100 ppm(a), 325 ppm (b), 225 ppm (c,d, e,f), H_2O=10% (a,b,c,e,f) or 0%(c).

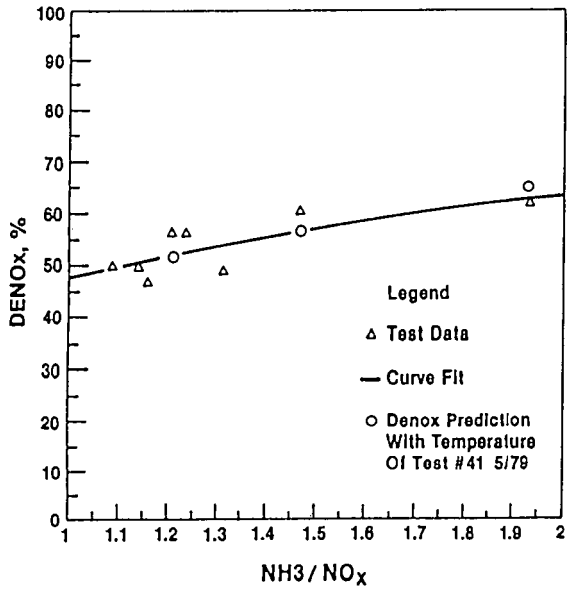

Figure 3. Comparison of DDHL Model Prediction with Observed NO Reduction in a Utility Boiler, LADWP Haynes #4. Curve Fit is to Test Data.

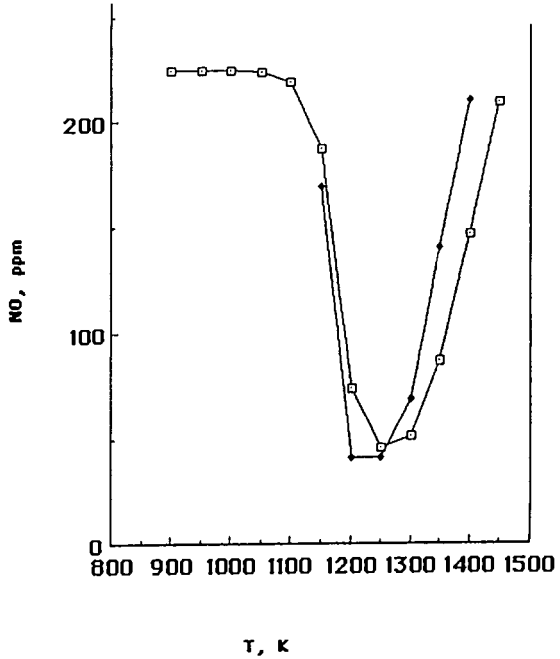

Figure 4. Effect of H_2O on $DeNO_x$ as Predicted by DDHL Model, 4% O_2, 225 ppm NO, 385 ppm NH_3, 0.1 sec reaction time ⊡=10% H_2O, ◆ = 0% H_2O.

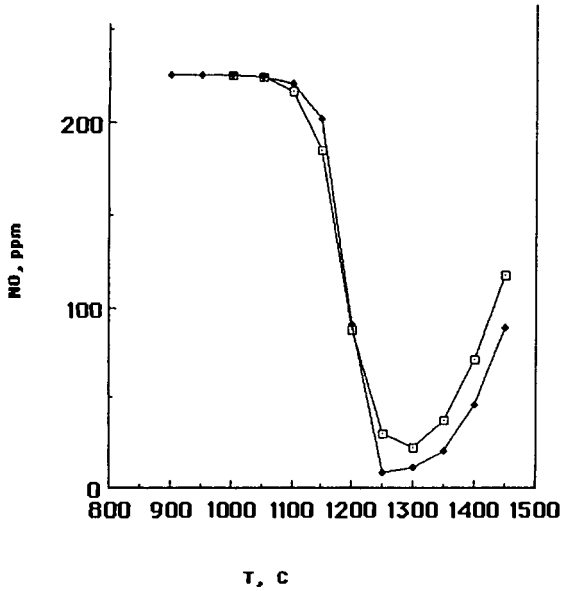

Figure 5. Effect of H_2O on $DeNO_x$ as Predicted by H&K Model, 4% O_2, 225 ppm NO, 385 ppm NH_3, 0.1 sec Reaction Time ⊡=10% H_2O, ◆=0% H_2O.

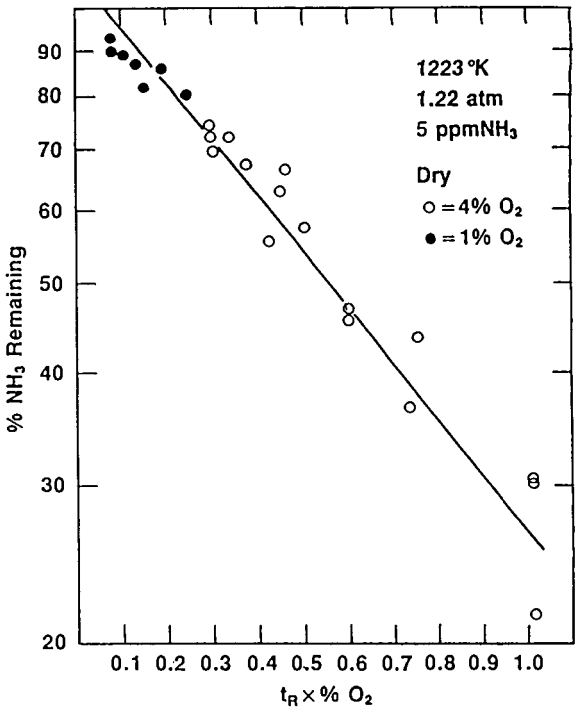

Figure 6. First Order Decay of NH_3 During the Oxidation of NH_3 at Trace Concentrations

Combined NO_x/SO_2 Removal from Flue Gas Using Ferrous Chelates of SH-Containing Amino Acids and Alkali

David K. Liu and S. G. Chang

Applied Science Division
Lawrence Berkeley Laboratory
University of California
Berkeley, CA 94720

ABSTRACT

We report herein the use of ferrous chelates of SH-containing amino acids including cysteine, penicillamine, N-acetylcysteine, and N-acetylpenicillamine in neutral or alkaline solutions for the combined removal of NO and SO_2 in wet flue gas clean-up systems. These SH-containing amino acids not only can stabilize ferrous ions in alkaline solutions to promote the absorption of NO, but are also capable of rapidly reducing ferric ions formed during the scrubbing process back to ferrous ions. The disulfide from of the above amino acids can be reduced by SO_2 and H_2S to regenerate the starting monomeric species. The chemistry relevant to the absorption of NO by the above ferrous chelates and the ligand regeneration process will be discussed.

INTRODUCTION

A large number of wet flue gas clean-up processes using iron chelates to simultaneously remove NO_x and SO_2 from combustion flue gas have been developed over the past fifteen years. The mechanism for NO absorption using these Fe^{2+}(EDTA) type chelates involves the formation and subsequent reaction of a ferrous nitrosyl complex with dissolved SO_2 and O_2 to produce N_2, N_2O, dithionate, sulfate, nitrogen-sulfur compounds, and ferric chelates which are unreactive towards NO (1). The regeneration of scrubbing liquors and ferrous chelates associated with such processes is very costly (2). Therefore, these wet absorption processes, even though very efficient in SO_2 and NO_x removal, have not yet reached the commercial stage.

We wish to report the use of ferrous chelates of SH-containing amino acids (or thioamino acids) in neutral or alkaline solutions for the simultaneous removal of NO_x and SO_2 from flue gas. The ferrous chelates investigated in this study include those of L-cysteine (CySH), DL-penicillamine (Pen), N-acetyl-L-cysteine (AcCySH), and N-acetyl-DL-penicillamine (AcPen).

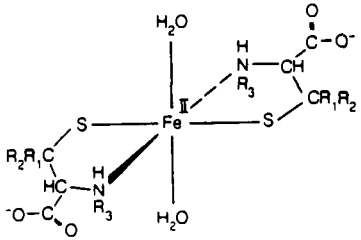

$Fe(CyS)_2(H_2O)_2$	$R_1 = R_2 = R_3 = H$
$Fe(Pen)_2(H_2O)_2$	$R_1 = R_2 = CH_3$ $R_3 = H$
$Fe(AcCyS)_2(H_2O)_2$	$R_1 = R_2 = H$ $R_3 = C(O)CH_3$
$Fe(AcPen)_2(H_2O)_2$	$R_1 = R_2 = CH_3$ $R_3 = C(O)CH_3$

The stereoisomers or racemates of the thioamino acids employed represent the most common and therefore least expensive forms; other stereoisomers or racemates can also be used since they should have identical chemical reactivities. Recent reports from our laboratory have addressed some the chemistry involved in the absorption of NO by ferrous cysteine (3,4). We have also recently communicated preliminary results concerning the use of ferrous chelates of certain cysteine derivatives in the removal of NO from the gas (5). This paper presents a full account of the scrubber chemistry of NO and SO_2 removal by alkaline solutions containing ferrous chelates of the aforementioned SH-containing amino acids, as well as subsequent regeneration of the thioamino acids for recycling in the scrubber system.

EXPERIMENTAL

The absorption of NO by neutral or alkaline solutions of ferrous thioamino acid complexes was studied using a bench-scale gas scrubber and a Thermoelectron Model 14A chemiluminescent NO_x analyzer (3). For the reduction of the disulfide form of the

thioamino acids, a method similar to that developed for the regeneration of cysteine from cystine was used (4). The identification of all thioamino acids and their derivatives was performed on an amino acid analyzer built in-house (6). The determination of iron-, nitrogen-, and thioamino acid-containing products was based on analytical techniques described previously (3,4).

RESULTS AND DISCUSSION

The removal of NO from oxygen-containing flue gas can be effected by aqueous solutions containing ferrous chelates of SH-containing amino acids, as shown in Figure 1. It is clear that all the ferrous thioamino acid complexes we tested are much more effective in absorbing NO than Fe^{2+}(EDTA) under the same conditions. The greater NO absorption capacity in the cases of ferrous thioamino acid complexes may be accounted for by the ability of the thiol groups to reduce any ferric ion formed upon oxidation of the ferrous chelate by residual O_2 in flue gas (Equation 1):

$$Fe^{2+}(RS^-)_2 \xrightarrow[O_2]{RSH \quad H^+} Fe^{3+}(RS^-)_3 \longrightarrow Fe^{2+}(RS^-)_2(RS\cdot) \qquad 1)$$

$$\uparrow \qquad\qquad \downarrow$$

$$\tfrac{1}{2}RSSR$$

This mechanism is well established for $Fe^{2+}(CyS)_2$ (7) and is likely also applicable to $Fe^{2+}(AcCyS)_2$. In the case of Pen, it has been suggested that the two β-methyl groups serve to inhibit the oxidation-reduction reactions (8). It is therefore likely that the enhanced NO absorption capacity using $Fe^{2+}(Pen)_2$ and $Fe^{2+}(AcPen)_2$ is the result of the stability of ferrous chelates towards O_2. In any case, the concentration of ferrous thioamino acid complex in the absorber is maintained, and NO removal can therefore be sustained. On the contrary, the Fe^{3+} (EDTA) complex formed upon oxidation is inactive towards NO. A further advantage of the ferrous thioamino acid systems is that the rapid intramolecular reduction of Fe^{3+} to Fe^{2+} can prevent thef formation of dithionate ion resulting from the reaction between Fe^{3+} and HSO_3^-.

The effect of pH on the NO absorption capacity of ferrous thioamino acid complexes, as represented by the number of moles of NO absorbed per mole of Fe^{2+} used (nNO/nFe^{2+}), is shown in Figure 2. While the NO absorption capacity of $Fe^{2+}(CyS)_2$ is fairly insensitive to pH, $Fe^{2+}(Pen)_2$, $Fe^{2+}(AcCyS)_2$, and $Fe^{2+}(AcPen)_2$ are more efficient as the solutions become less basic, up to pH $\sim$ 6. The influence of pH on NO absorption can be attributed to the presence of various ionic forms of thioamino acid, the stability constants of ferrous thioamino acid complexes and ferrous hydroxide, and the rate of Fe^{2+}-catalyzed oxidation of the thioamino acids by O_2.

The effects of several additives on the NO removal efficiency of $Fe(CyS)_2$ were examined, and the results are summarized in Table I (below). Power plant flue gas typically contains several thousand ppm SO_2, which dissolves in scrubbing liquors to form primarily SO_3^{2-} at pH $>$ 9. The effect of SO_2 on the NO absorption capacity can therefore be studied by the addition of SO_3^{2-} to the ferrous cysteine solution. Our results show that SO_3^{2-} can improve the NO removal efficiency of $Fe^{2+}(CyS)_2$. Such enhancement could be a result of the reaction of SO_3^{2-} with O_2 to form SO_4^{2-}, and/or the reaction of SO_3^{2-} with the oxidized product cystine (CySSCy) to form CySH and cysteine sulfonate ($CySSO_3^-$), *vide infra*. High concentrations of $S_2O_3^{2-}$ can also enhance the NO removal efficiency of $Fe^{2+}(CyS)_2$, probably because $S_2O_3^{2-}$ can serve as an oxidation inhibitor. It is expected

Table I. Effects of Various Additives on NO Absorption Capacity of Ferrous Cysteine[a]		
Additive	Concentration, M	nNO/nFe^{2+}
none	—	0.023
Na_2SO_3	0.05	0.040
	0.10	0.050
	0.50	0.068
$Na_2S_2O_3$	0.05	0.030
	1.00	0.080

[a] The concentrations of Fe^{2+} and CySH were 0.01 M and 0.04 M, respectively. The reaction was carried out at pH 9.5 (borate buffer) and 55 °C using a gas mixture of 500 ppm NO, 4% O_2 and the balance N_2.

that SO_3^{2-} and $S_2O_3^{2-}$ will also improve the NO removal efficiency for other ferrous thioamino acid complexes. However, the extent of the improvement may not be as much as that in the $Fe^{2+}(CyS)_2$, since the adverse effect of O_2 is not as pronounced in those systems (5).

The reaction products collected from the NO absorption reactions by $Fe^{2+}(CyS)_2$ and $Fe^{2+}(Pen)_2$ were analyzed. It has been shown (3) that an iron dinitrosyl complex with an empirical formula $[Fe(CySSCy)(NO)_2]$ can be isolated when the reaction of NO and $Fe^{2+}(CyS)_2$ was carried out in the absence of O_2. The same dinitrosyl complex was not found in the presence of 4% O_2, nor could an analogous iron nitrosyl complex be detected in the case of $Fe^{2+}(Pen)_2$, whether or not O_2 was present. In both the $Fe^{2+}(CyS)_2$ and $Fe^{2+}(Pen)_2$ systems, most of the absorbed NO was reduced to N_2 and N_2O, and a small amount ($<10\%$ of the NO absorbed) of NO_2^- was also detected in solution. As a result, minimal formation of of nitrogen-sulfur compounds is expected from the reaction between NO_2^- and HSO_3^- in the ferrous thioamino acid systems. On the other hand, $> 90\%$ of the iron was recovered as insoluble hydroxides in the solid residue, of which $\sim 80\%$ was Fe (II) and $\sim 20\%$ was Fe (III), The mass balance for the thioamino acid in the NO absorption reaction by $Fe^{2+}(CyS)_2$ was also studied. In the absence of SO_3^{2-}, all of the CySH were recovered as CySSCy, as shown in Figure 3. However, if SO_3^{2-} as added to the $Fe^{2+}(CyS)_2$ solution, $CySSO_3^-$ was also formed. It appears that the decrease in [CySSCy] and the increase in $[CySSO_3^-]$ are linear with respect to increasing $[SO_3^{2-}]$. In each case, $96 \pm 2\%$ of the CySH can be recovered as a combination of CySSCy and $CySSO_3^-$. It is clear from Figure 3 that unless high concentrations (> 0.5 M) of SO_3^{2-} are present, most of the CySH would end up as CySSCy. It is therefore necessary to convert CySSCy back to CySH in order to make this process recyclable and cost-effective.

Existing methods for converting CySSCy to CySH require the use of electric energy or expensive reagents, which are not suitable for large-scale applications in flue gas clean up systems. We have discovered a simple and potentially cost-effective method for the regeneration of CySH from CySSCy using H_2S (or sulfide/hydrogen sulfide ion) and SO_2 (or sulfite/bisulfite) (4). The results for the regeneration of CySH from CySSCy are presented in Table II (below). Methods I (sequential) and II (simultaneous) involve the treatment of a 40 mM CySSCy solution with two equivalents of $Na_2S{\cdot}9H_2O$ and three equivalents of Na_2SO_3. Similarly, H_2S and SO_2 were used to treat the same CySSCy solution, sequentially in Method III and simultaneously in Method IV. The best result was obtained from the reaction of CySSCy with H_2S and then SO_2 at pH 10 and 60 °C (Method III). The concentrations of HS^- and SO_3^{2-} in solution were estimated to be 0.04

Table II. Regeneration of CySH from CySSCy under Various Conditions					
Method[a]	pH	T°, °C	CySH, %	$CySSO_3^-$,%	CySSCy, %
I	10	60	59	17	15
II	10	60	36	3	58
III	10	60	90	5	4
IVa	10	60	85	8	6
IVb	10	80	84	10	6
IVc	12	60	84	6	5

[a]See text for description of experimental methods.

M and 0.22 M, respectively. In this case, a 90% yield of CySH was attained, which increased to 95% upon neutralization of the reaction mixture to pH ~ 7. The concentration-time profile of this reaction is shown in Figure 4. The mechanism for the conversion of CySSCy to CySH can be summarized by the following equations:

$$CySSCy + HS^- \rightleftharpoons CySH + CySS^- \quad 2)$$

$$CySS^- + HS^- \rightleftharpoons CySH + S_2^{2-} \quad 3)$$

$$CySS^- + SO_3^{2-} \rightleftharpoons CyS^- + S_2O_3^{2-} \quad 4)$$

$$CySSCy + SO_3^{2-} \rightleftharpoons CyS^- + CySSO_3^- \quad 5)$$

$$CySSO_3^- + HS^- \rightleftharpoons CySH + S_2O_3^{2-} \quad 6)$$

where $CySS^-$ represents S-thiocysteine.

In the present study, we have determined that the disulfides of AcCySH and Pen were formed upon the reaction of respective thioamino acid and Fe^{3+}. The same $H_2S/SO_2/OH^-$ treatment for the regeneration of CySH from CySSCy can be successfully applied to the regeneration of AcCySH from its disulfide. However, the reduction of Pen disulfide did not occur under the same conditions even after 48 hours. As mentioned above, this could be due to the steric effects of the two β-methyl groups in Pen. Therefore, development of a new method to regenerate Pen, and possibly AcPen, from the scrubbing liquor is needed.

The overall reaction for the regeneration of CySH from CySSCy using HS^- and SO_3^{2-} can be expressed as

$$CySSCy + HS^- + SO_3^{2-} \rightleftharpoons 2CyS^- + S_2O_3^{2-} + H^+ \quad 7)$$

In an acidic medium, $S_2O_3^{2-}$ decomposes to form HSO_3^- (and/or SO_2) and colloidal sulfur, as shown in Equation 8.

$$S_2O_3^{2-} + H^+ \rightarrow HSO_3^- + S\downarrow \quad 8)$$

By adding equations 7 and 8 and taking into account the equilibrium between SO_3^{2-} and HSO_3^-, we obtain the net equation

$$CySSCy + HS^- \rightleftharpoons 2CyS^- + S\downarrow + H^+ \quad 9)$$

Thus, the only reagent consumed in the conversion of CySSCy to CySH is HS^-, and elemental sulfur is formed as a product. The latter can be converted back to H_2S by reaction with H_2, which can be derived from CO and H_2O (9). Therefore, in essence, the reducing agent consumed in this CySH and the corresponding AcCySH regeneration scheme is CO, which can be easily obtained from the incomplete combustion of coal. It can be inferred from Equation 9 that one mole of CO is required for the regeneration of two moles of CySH or AcCySH.

CONCLUSIONS

Wet flue gas clean-up systems based on ferrous chelates of thioamino acids possess several major advantages over the conventional Fe^{2+} (EDTA) type chelates. These include higher NO absorption capacities, the suppression of dithionate and N-S compound formations, and the ability of the thioamino acids to reduce Fe^{3+} to Fe^{2+} ion, thus eliminating the need to regenerate ferric chelates from the scrubbing liquor. Reduction of the oxidation products cystine and N-acetylcystine can be accomplished by treatment with H_2S and SO_2 in basic solutions. However, the same process is not applicable to penicillamine, and possibly N-acetylpenicillamine, due to steric effects. Unfortunately, the application of these ferrous thioamino acid chelates in spray drying systems is limited by the larger stoichiometric ratio of the ferrous chelates to NO (Figure 2) required for obtaining a high ($\geq 50\%$) NO removal efficiency.

ACKNOWLEDGEMENT

This work was supported by the Assistant Secretary for Fossil Energy, U.S. Department of Energy under Contract No. DE-AC03-76SF00098 through the Pittsburgh Energy Technology Center, Pittsburgh, PA.

REFERENCES

1. Chang, S.G., *ACS Symp. Ser. No. 919,* 159 (1986), and references therein.
2. Faucett, H.L., Maxwell, J.D., and Burnett, T.A., *EPRI Report AF-568,* (1978).
3. Tu, M.D. and Chang, S.G., *AIChE Environ. Progr., 6,* 51 (1987).
4. Liu, D.K., Frick, L.P. and Chang, S.G., submitted to *Environ. Sci. & Tech.* (1987).
5. Chang, S.G., Liu, D.K. and Littlejohn, D., Paper No. 76b presented at the AIChE National Meeting in Houston, TX, March 29-April 2, 1987.
6. Liu, D.K. and Chang, S.G., *Can. J. Chem. 65,* 770 (1987).
7. Gilmour, A.D. and McAuley, A., *J. Chem. Soc., (A),* 1006 (1970).
8. Stadther, L.G. and Martin, R.B., *Inorg. Chem., 11,* 92 (1972).
9. Kent, J.A., Ed., Riegels Handbook of Industrial Chemistry, 7th ed., Van Nostrand Reinhold, New York, NY, 1972, p. 87.

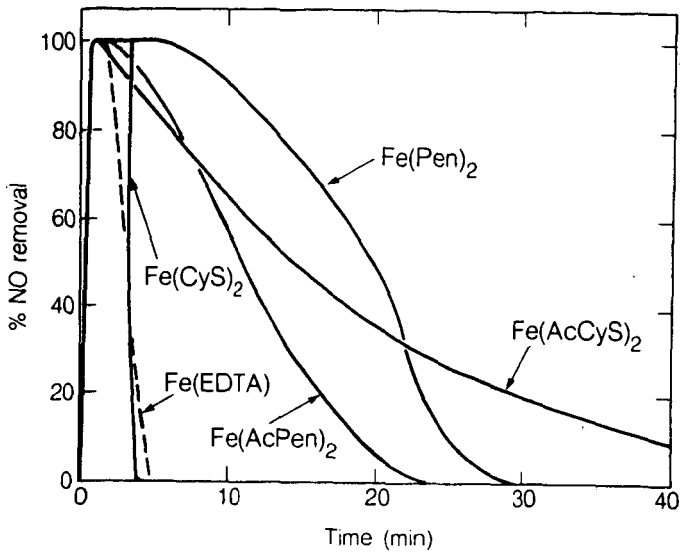

Figure 1. The NO removal efficiency of ferrous thioamino acid and Fe^{2+} (EDTA) chelates. Reaction conditions were: $[Fe^{2+}]$ = 0.01 M; [thioamino acid] = [EDTA] = 0.04 M; $[B_4O_7^{2-}]$ = 1.18 M; P_{NO} = 500 ppm; P_{O_2} = 4%; pH = 7.0; T° = 55 °C.

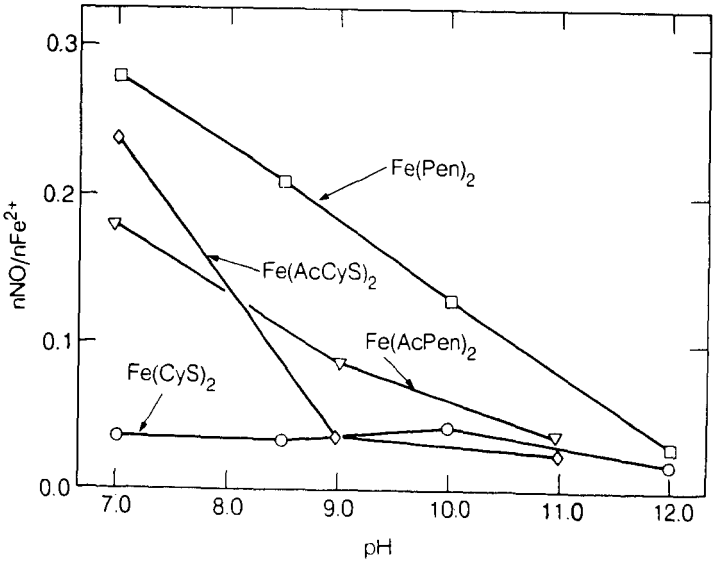

Figure 2. The NO absorption capacity of ferrous thioamino acid chelates as a function of pH. Reaction conditions were: $[Fe^{2+}]$ = 0.01 M; [CySH] = 0.04 M; $[B_4O_7^{2-}]$ = 0.09 M; P_{NO} = 500 ppm; T° = 55 °C.

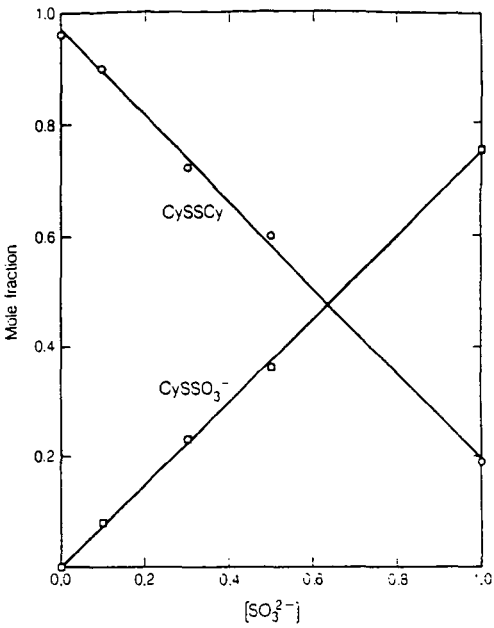

Figure 3. Recovery of CySH as CySSCy and $CySSO_3^-$ at various $[SO_3^{2-}]$. Reaction conditions were: $[Fe^{2+}]$ = 0.1 M, [CySH] = 1.0 M; $[B_4O_7^{2-}]$ = 0.2 M; P_{NO} = 500 ppm; PO_2 = 4%; pH = 9.0; T° = 55 °C.

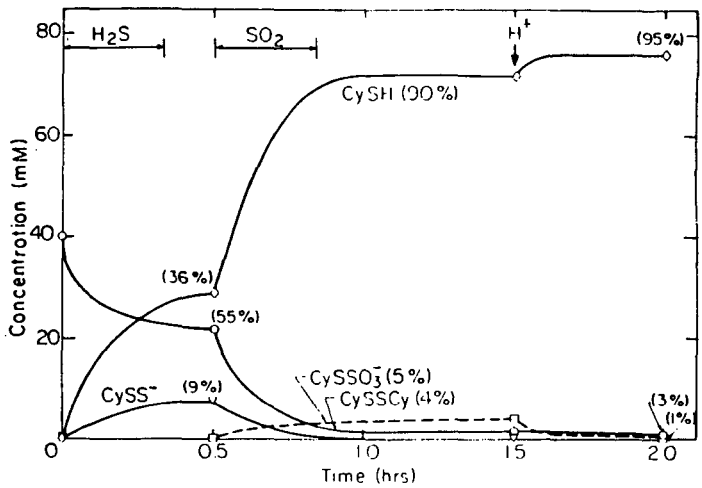

Figure 4. The concentration-time profile of the regeneration of CySH from CySSCy at pH 10 and 60° C by the reaction of CySSCy first with H_2S and then SO_2, followed by neutralization to pH ~ 7.

NO_x and SO_2 Removal From Flue Gas by Ferrous Ion-Peptide Solutions

D. Littlejohn and S. G. Chang

Applied Science Division
Lawrence Berkeley Laboratory
University of California
Berkeley, CA 94720

SO_2 and NO_x generated by combustion are believed to oxidize in the atmosphere to form H_2SO_4 and HNO_2/HNO_3. The main removal mechanism of these acids from the atmosphere is precipitation, popularly referred to as acid rain. Considerable research is being done to develop efficient, cost-effective procedures to remove SO_2 and NO_x from power plant flue gases (1). SO_2 can be removed more readily than NO_x since it is highly soluble in aqueous solutions and can be oxidized to form SO_4^{2-}. The sulfate ion can then be precipitated with calcium ions, if desired. Most of the NO_x is in the form of NO, which has limited solubility in water. Many control strategies for NO_x have focussed on compounds which enhance the solubility of NO. These systems are usually based on ferrous ion-chelate compounds which readily form nitrosyl complexes (2). Early systems used aminocarboxylic acid chelates such as EDTA, because of their large equilibrium constants for the formation of nitrosyl complexes. However, these systems were very sensitive to the presence of oxygen. In oxygen-free systems, solutions of these compounds can remove significant amounts of NO (3). With oxygen present, the ferrous ion is rapidly oxidized to ferric ion, which does not absorb NO. The oxidized metal ion must then be chemically or electrically reduced to the +2 state. This adds to the cost and complexity of processes using these compounds. The recovery or removal of the absorbed NO is not straightforward in these systems, and it would be desirable to develop a chemical system in which this could be done more easily.

In a search for more suitable iron-chelate combinations, the ferrous ion-cysteine combination was studied (4). It was found that cysteine would readily reduce ferric ion to ferrous ion, and in so doing, keep most of the iron in the ferrous state when exposed to oxygen. The ferrous ion-cysteine system was found to be capable of absorbing significant amounts of NO, with or without the presence of oxygen. Cystine, the oxidized form of cysteine, can be reduced back to cysteine by the appropriate application of HS^- and SO_3^{2-} (5). These compounds can be obtained from the SO_2 removed from the flue gas.

Various cysteine derivatives have been studied to determine if they would be superior to cysteine in removing NO from flue gas. These include glutathione (a tripeptide) and glyclcysteine (a dipeptide) which are the subject of this study. Glutathione (glutamylcysteinylglycine, abbreviated GSH) is a thiol compound that is abundant in living cells. It is composed of the amino acids glutamic acid, cysteine and glycine linked by peptide bonds. Cysteine is the central amino acid. In a manner similar to cysteine, GSH can be oxidized to the disulfide (noted as GSSG).

Glyclcysteine is readily produced by the acid hydrolysis of GSH (6). It also forms a disulfide when oxidized.

EXPERIMENTAL

Glutathione (Sigma Chemical, 99%) was used without further purification. Glyclcysteine was prepared by hydrolyzing glutathione in 1.2N HCl at 95 °C for 60-90 min. under a nitrogen atmosphere. Yield was in excess of 95%. Pyrrolidone carboxylic acid (pyroglutamic acid) is a co-product of the hydrolysis. It was prepared independently by heating glutamic acid with an equal amount of water in a sealed tube to 140 °C for 3 hours (7). The compounds used for preparing the acetate and borate, as well as the ferrous ammonium sulfate, were of reagent grade quality.

Two types of experiments were done with the ferrous ion - peptide systems in aqueous solutions to study their effectiveness in removing NO from the gas phase. In the first set of experiments, buffered ferrous ion - peptide solutions were prepared on a vacuum line. A bulb of known volume was filled with NO and expanded into the evacuated bulb with the ferrous ion - peptide solution. The pressure was noted and vigorous stirring of the solution was initiated. Once the pressure stabilized, the pressure drop was used to calculate the amount of NO absorbed by the solution. Corrections were made for water vapor pressure and the solubility of NO in water. Runs were done with the pH of the solution ranging from acidic to alkaline. All runs were done with the peptide concentration four times that of the ferrous ion concentration.

The second type of experiment is designed to determine the ability of ferrous ion - peptide to remove NO from the gas phase under realistic conditions. Simulated flue gas was prepared by mixing nitrogen, oxygen, nitric oxide and, in some cases, sulfur dioxide. The gas mixture was passed through the buffered ferrous ion - peptide solution, which had been heated to 55 °C. NO removal was determined by measuring the fraction of NO not absorbed by the solution using a chemiluminescent NO_x analyzer. The plot of NO absorbed vs. time, was graphically integrated to obtain the total quantity of NO removed by the solution. When SO_2 was used, the amount of SO_2 removed was obtained in a similar manner using a pulsed fluorescent SO_2 analyzer.

The solutions were saved for analysis after the experiments were complete. Ferrous ion was analyzed by the 1,10 phenanthroline method. Nitrate and nitrite ions were analyzed by ion chromatography. An amino acid analyzer was used to measure the amounts of the reduced and oxidized forms of the peptides that were present.

RESULTS AND DISCUSSION

The NO absorption experiments with glutathione were done over a pH range from 3.0 to 8.5. The ferrous ion concentrations were .02M. The NO:Fe stoichiometry was 2:1 or higher over the pH range studied. The stoichiometric ratio increased as the pH increased. In solutions with pH <7, the nitrosyl complex formed a rust-colored precipitate. This is similar to what is observed in ferrous cysteine solutions when treated with NO. In alkaline solutions, no precipitate was observed.

NO absorption by ferrous ion - glyclcysteine solution was studied over a pH range from 4 to 9. Again, a NO:Fe stoichiometry in excess of 2:1 was found. With glyclcysteine, a solid nitrosyl complex formed at all pH conditions. The appearance of the precipitates was similar to the solids obtained with GSH.

To confirm that glyclcysteine, not pyroglutamic acid, was responsible for the NO absorption observed, separate experiments were run with glutamic acid and pyroglutamic acid. Solutions of these compounds mixed with ferrous ions absorbed NO only marginally better than solutions of ferrous ions alone. This suggests that the peptide forming the complex with the ferous ion needs to contain cysteine to efficiently bind NO.

The NO absorption experiments discussed above were done with approximately one atmosphere of NO. The second set of experiments, in which the NO-containing gas was bubbled through the heated solution, were done at much lower concentrations. The gas mixture was typically 96% N_2, 4% O_2 and 500 ppm NO. SO_2, when included, was typically at 2500 ppm. The ferrous ion concentration used in these experiments was 0.01M, and the peptide concentration was four times higher. The ferrous ion - GSH solutions were studied over a pH range of 4.3 to 10.9, and the ferrous ion - glyclcysteine solutions were studied at pH 4.3 to 9.2.

Essentially no NO was absorbed by the Fe(II)-GSH solution at pH 4.3, suggesting the equilibrium constant for the formation of the nitrosyl complex is small under these conditions. At slightly less acidic conditions (pH 5.4), the best NO removal was found. An NO:Fe stoichiometry of 0.54:1.0 was obtained. This stoichiometry decreased as the pH rose, ending with NO:Fe = 0.17:1.0 at pH 10.9. The decrease with increasing pH is presumably due to the increasing role of oxidation of GSH and Fe(II) with the increase in pH. The rate of NO absorption was found to be highest in neutral and slightly alkaline solutions, and the rate was slowest in the acid solutions. SO_2 was less difficult than NO to remove. It was removed most efficiently by alkaline solutions.

In the alkaline solutions, almost all the NO absorbed was converted to nitrite and nitrate ions. Almost all of the iron in the solution precipitated out in Fe(III) form. Much of the GSH was oxidized to GSSG. Under very alkaline conditions, there was some decomposition of the GSH.

The ferrous ion - glyclcysteine solutions absorbed NO at all conditions studied. The NO:Fe stoichiometry was about 0.3:1.0 in acidic conditions and rose to 0.87:1.0 at pH 7.3. It then dropped off rapidly as the pH increased, falling to 0.05:1.0 at pH 9.2. The rate of NO absorption was slowest under acidic conditions. In neutral or alkaline conditions, the rate of NO absorption was considerably higher than with the corresponding GSH solutions. It appears that oxidation of the Fe(III) and glyclcysteine is significant in alkaline conditions, and this limits how much NO can be absorbed. In acidic conditions the oxidation is slower, but the NO absorption is also slow.

A rust-colored precipitate formed in all of the solution, apparently containing most of the iron as Fe(III). Most of the glyclcysteine was oxidized to the disulfide form.

Both GSH and glyclcysteine are capable of reducing Fe(III) to Fe(II) in solution. Thus, they enhance the NO removal capabilities of an Fe(II) solution not only by forming an effective ferrous nitrosyl complex, but also by maintaining the iron in the ferrous state. Of course, the peptides will be oxidized as a result. The oxidized peptides can be reduced to their original form by several methods. These include the technique developed for cysteine in which the oxidized material is sequentially treated with H_2S and SO_2 (5).

These compounds have been found to be considerably more effective than cysteine in ferrous ion - based NO removal systems operating at pH 5 to 7. Other cysteine-based peptides might be equally effective. To be commercially useful, however, the compounds must not be excessively expensive and capable of being regenerated without large losses.

REFERENCES

1. A.E. Martin, ed. *Emission Control Technology for Industrial Boilers* (1981), Noyes Data Corp., Park Ridge, NJ.

2. S.G. Chang, D. Littlejohn and S. Lynn *Environ. Sci. Tech.* (1983) *17*, 649.

3. N. Lin, D. Littlejohn and S.G. Chang *I&EC Proc. Des. Dev.* (1982) *21*, 725.

4. M.D. Tu and S.G. Chang *Environ. Prog.* (1987) *6*, 51.

5. P.C. Jocelyn *Biochemistry of the SH Group* (1972) Academic Press, New York City, NY.

5b. D.K. Liu and S.G. Chang *Can J. Chem.* (1987) *65*, 770.

6. C.K. Olson and F. Binkley *J. Biol. Chem.* (1950) *186*, 731.

7. M. Windholz, ed. *Merck Index* (1976) Merck & Co., Inc., Rahway, NJ.

REDUCTION OF NO WITH NH_3 ON TiO_2-, Al_2O_3- AND Fe_2O_3-SUPPORTED METAL OXIDE CATALYSTS

T.I. Maunula and M.A. Hiltunen
R&D Center, A.Ahlström Co., P.O. Box 18, SF-48601 Karhula, Finland

J.B-son Bredenberg
Department of Chemical Engineering, Helsinki University of Technology, SF-02150 Espoo, Finland

INTRODUCTION

The pollution of the atmosphere by nitrogen oxides (NO_x=NO+NO_2) has been a subject of growing concern during the past decade. During combustion, NO_x is formed either by reaction of oxygen and atmospheric nitrogen (thermal NO_x) or conversion of chemically bound nitrogen in the fuel (fuel-NO_x).The major fraction of these emissions results from the fuel-NO_x during combustion in industrial and utility boilers. The formation of NO_x in the boilers can be reduced to a considerable extent by modification in the combustion technique, for example by applying fluidized bed combustion boilers. There still will remain some NO_x in the flue gases. Hence, other additional methods have been introduced for NO_x-removal .

The most widely applied method for decreasing NO_x emissions from existing stationary sources is selective catalytic reduction (SCR) by NH_3. The most commonly proposed overall reactions between NO and NH_3 are (Odenbrand et. al. 1985, Matsuda et. al. 1978):

$$4\ NH_3 + 4\ NO + O_2 \longrightarrow 4\ N_2 + 6\ H_2O \qquad (1)$$

$$4\ NH_3 + 6\ NO \longrightarrow 5\ N_2 + 6\ H_2O \qquad (2)$$

The catalyst used in a commercial plant must possess high activity and selectivity, since the volume of flue gas to be treated is large. In addition, the catalyst must be resistant to SO_x poisoning (Matsuda et al. 1982,Nam et al.1986). The purpose of the present study was to examine the kinetics of NO-NH_3-O_2 reactions on several catalysts promoting the SCR of NO_x.

EXPERIMENTAL

Catalysts.
The catalysts and their main characteristics are shown in Table 1.The catalysts were supported base metal oxides.Some other materials were also tested for their catalytic activity.

Table 1. Catalysts in experiments.

Catalyst	Pellet size(mm)	Specific surface area(m^2/g)	Bulk density(g/ml)
1. V(4%)/TiO_2	>2.0	7	1.1
2. Cu(5%)/TiO_2	>2.0	7	1.0
3. Fe(6%)/TiO_2	>2.0	14	1.1
4. Ni(5%)/TiO_2	>2.0	6	0.8
5. Cu(7%)/Al_2O_3	3.2	140	1.0
6. Cr(14%)/Al_2O_3	4.0	60	1.1
7. Ni(11%)/Al_2O_3 (Ni P)	3.2	80	1.1
8. Ni(16%)/Al_2O_3 (Ni T)	2.0-4.0	210	0.8
9. Slag A (13% Fe)	>1.0	1.4	1.6
10.Slag B (0.4% Fe)	>1.0	0.2	1.1
11.Hematite (66% Fe)	0.2-1.0	<0.1	3.1
12.Ilmenite (36% Fe)	>2.0	0.6	1.1
13.Ilmenite+TiO_2(5% Fe)	>2.0	-	1.0

The TiO_2-based catalysts were prepared according to methods developed by Matsuda et al. (1982), Saleh et al. (1986) and Skvortsov et al. (1977). TiO_2 (anatase) was wet-impregnated in a solution of a salt of the active material (V,Cu, Fe, Ni). After drying for 24 hours at 110 °C the catalyst was calcined in air at 400 °C. The Al_2O_3-supported catalysts were commercially available materials. The other materials in the experiments were inexpensive iron-containing slags and ores.

The total specific surface areas of the fresh materials were obtained with a Perkin-Elmer 212 C Sorptometer.

Apparatus and reactant gases

The schematic diagram of the experimental apparatus is presented in Figure 1. The fixed bed reactor and a pre-heater were made of quartz.The reactor was heated in a Heraeus ROK 4/60 oven and the temperature in the catalyst bed was measured with a Ni-NiCr-thermocouple. The gases were supplied from pressure bottles via high precision Hi-Tech massflowmeters. Gas lines before the pre-heater were made of stainless steel. The mixing of NH_3 with the simulated flue gas took place after the pre-heater, just in front of the reactor, in order to avoid any homogeneous reactions between the components.

Two teflon sampling lines were connected to the reactor.The gas mixture was transported through a EPM 797 diluting unit to a Monitor Labs 8840 chemiluminescent NO_x-analyser. The analyser was equipped with a thermodynamic converter (Monitor Labs 8750) and it measured NO_x and NO_x+NH_3. NH_3 was calculated by difference. The equipment was calibrated with a gas having 200 ppm NO.

Procedures

The $NO-NH_3-O_2$ reaction was studied in both an empty tubular reactor and a packed bed reactor with different catalysts. After the temperatures of flue gas in the catalyst bed reached the set value, the concentration of NO_x was measured until a steady-state reading was obtained. The experimental operating conditions are summarized in Table 2.

Table 2. Experimental operating conditions.

Inlet concentration	NO	0-2000 ppm
	NH_3	0-2000 ppm
	O_2	0-5 %
	CO_2	0 or 10 %
	SO_2	0 or 500 ppm
	N_2	carrier gas
Volumetric flow rate		0.57-0.64 m^3(NTP)/h
Catalyst bed volume		50 cm^3
Space velocity (SV)		3.2-3.6 m^3 flue gas(NTP)/m^3(cat)s
Temperature		200-900 °C
Duration of the test		0.25 - 6 h

The SO_x poisoning experiments were performed with a test gas containing 500 ppm SO_2 using the Cu/Al_2O_3, Cr/Al_2O_3, Cu/TiO_2 and V/TiO_2 catalysts.

RESULTS AND DISCUSSION

Empty reactor

Figure 2 shows the plot of NO_x conversion versus temperature from 300 to 900 °C. The empty reactor had neglible effects on the NO decomposition. The wall effect of the quartz tube on the reaction between NO and NH_3 was also small. The thermal reduction of NO by NH_3 increased once the temperature reached 900 °C. At this temperature the NO conversion was 26 %.

TiO_2-supported catalysts

The concentrations of NO_x after a one hour operation with the Cu, V, Ni and Fe catalysts are shown in Figure 6 as a function of the catalyst temperature. The conversion of NO increased rapidly until about 300 °C which seemed to be the optimal temperature for all these catalysts. Above this temperature the NO_x concentrations increased. This was due either to the incomplete reduction of NO with NH_3 or direct oxidation of NH_3 with the excess oxygen present or a combination of both factors.

The V/TiO_2 catalyst showed high activity and resistance to SO_2 poisoning (Figure 7). The Cu catalyst lost its activity under 350 °C in the presence of SO_2 (Figure 8). Sulfur was not found to accumulate in great degree on this catalyst at 350 °C (Fresh: 0.23 % S; After SO_2-test: 0.40 % S). The Fe and Ni catalysts were less active than the V and Cu catalysts. Wong et al. (1986) have shown that the activity of TiO_2-based iron oxide catalysts is strongly affected by the preparation procedure.

Al_2O_3-supported catalysts

Four commercial Al_2O_3-supported catalysts were investigated. These catalysts had large specific surface areas (between 60 and 140 m^2/g). The results with these catalysts are shown in Figure 3. The optimal operation temperatures were between 300 and 350 °C in the absence of SO_2. The highest measured conversions were 80 (Cu), 74 (Ni P), 56 (Cr) and 40 % (Ni T) after a one hour operation.

The activity of the Cu catalyst improved in the presence of SO_2 at temperatures above 350 °C (Figure 4). Nam et al. 1986 have found with a V/Al_2O_3 catalyst similar results. They proposed that the sulfur contamination as, $Al_2(SO_4)_3$, increased the NO conversion at temperatures above 400 °C, presumably due to the moderation of the competing reaction of the NH_3 oxidation to NO. Another reason for the behavior can be the formation of $CuSO_4$, which is also known to catalyze the reaction concerned (Schrod 1986). Sulfur was accumulated on our Cu/Al_2O_3 catalyst at 350 °C (Fresh: 0.02 % S; After SO_2-test: 3.32 % S). Compared with the results with TiO_2-supported catalysts, it can be concluded that the formation of $Al_2(SO_4)_3$ is probable on Al_2O_3-supported catalysts.

The activity of the Cr catalyst decreased at temperatures under 350 °C when SO_2 was present (Figure 5). The life of this catalyst seemed to be short under these circumstances. According to Ando (1983) a portion of SO_2 oxidizes to SO_3 on the catalyst surface to form NH_4HSO_4. The SO_2 poisoning test time was too short to make any accurate conclusions about the effects of SO_2.

It could be concluded that NO reacts with NH_3 at a 1:1 mole ratio at the optimal operation temperature as proposed by Kato et al. (1981). The NH_3 concentration decreased in a similar way than the NO_x concentration until about 350 °C. Above that temperature the concentration stayed under 100 ppm. The degree of NH_3 oxidation by O_2 increased when the temperature rose over 350 °C.

Other materials tested.

Iron oxide containing materials vary widely in catalytic activity depending on the composition (Moriguchi et al. 1978). The results of our tests are shown in Figure 9.

At low temperatures (200 - 350 °C) reaction kinetics has a decisive role. In the case that the catalytic material is poorly distributed or the available surface is low, no discernible reaction is observed. When the temperature is increased all reactions, e.g. also the NH_3 oxidation reaction, are speeded up and the final result in a NH_3-NO-O_2 -system may be either a balance between the competing reactions or, in the worst case, an increase of NO_x from NH_3 oxidation. The above explanations apply to some of the slag catalysts. The specific surface areas of the investigated materials were probably not sufficient for a measurable selective catalytic reduction.

For the $NO-NH_3-O_2$ reaction the investigated materials can be divided in four groups:

A. Good catalysts (V/TiO_2, Cu/TiO_2, Cu/Al_2O_3 and Cr/Al_2O_3)
B. Inferior catalysts ($Ni\ T/Al_2O_3$)
C. NH_3 oxidation catalysts (Fe/TiO_2, Ni/TiO_2, slag A and iron containing ores)
D. Noncatalytic materials (Slag B)

Good catalysts are predicted to be promoting both competitive reactions: NO reduction and straight NH_3 oxidation.

Influence of oxygen.

The role of oxygen in SCR becomes greater when the O_2 concentration falls below 1 % (Figure 10, 11 and 12). The oxygen affects the reaction rate of NO with NH_3 as found also by Matsuda and Kato (1983). An O_2 concentration of 0.1 % was near to the critical value for the NO conversion with the Cu/Al_2O_3 catalyst (Figure 10). Kotter et al. (1986) have also shown that an O_2 concentration below 0.2 % changes the reaction rate markedly.

The NO reduction using the Cu/Al_2O_3 catalyst has an optimal operation temperature at about 300 to 350 °C in the presence of 1 to 5 % O_2. In the absence of oxygen the NO reduction proceeds according to the reaction (2) at higher temperatures (>350 °C). There exists no oxidation of NH_3 to NO and the higher temperatures favour this reaction kinetically.

The absence of O_2 inhibits the NO reduction on TiO_2-supported catalysts at 300 to 350 °C. Oxygen concentrations between 1 to 5 % were shown to have some influence only at temperatures below 300 °C especially with V/TiO_2 catalyst. The possibilities of the formation of N_2O become greater when oxygen is absent (Otto and Shelef 1972).

The influence of inlet NO concentration.

The conversions with Cu/Al_2O_3 catalyst at different inlet NO concentrations are shown in Figure 12. The degree of NO reduction increases with NO inlet concentration. It is easier to reach the low outlet concentration if the inlet concentration is as low as possible. When the reactant concentration (NO and NH_3) falls below 100 ppm the reaction rate of SCR, however, decreases sharply.

CONCLUSIONS

Thirteen different SCR catalysts were investigated at temperatures between 200 to 900 °C. Oxygen affects the reaction rate of NO with NH_3. In the presence of O_2 the NO reduction has an optimum temperature between about 300 to 400 °C. In the absence of O_2 the NO reduction is shifted to higher temperatures. The V/TiO_2 catalyst is resistant to SO_2. The activities of the other catalysts investigated are affected by SO_2. There is a clear difference between the Al_2O_3- and TiO_2-supported catalysts in regard to the influence of SO_2.

ACKNOWLEDGMENTS

This work was done at the Laboratory of Industrial Chemistry in Helsinki University of Technology in co-operation with Ahlstrom Co. Research and Development Center. The work was partly funded by Ministry of Trade and Industry in Finland.

REFERENCES

1 Ando,J., Technical report, EPA-600/7-83-027, May 1983.
2. Bosch, H., Janssen,F.J.J.G., Kerkhof van den,F.M.G.,Oldenziel,J.,Ommen van,J.G. and Ross, J.R.H., Appl. Cat., 25(1986) pp 239-248.
3. Kato,A.,Matsuda,S.,Nakajima,F.,Imanari,M. and Watanabe,Y., J.Phys.Chem., 85(1981) No 12 pp 1710-1713.

4. Kotter,M.,Lintz,H-G and Weyland,F., Chem.-Ing.-Tech., 58(1986) No 8 pp 617-623.
5. Matsuda,S.,Kato,A.,Uno,S.,Sakuta,Y.,Nakajima,F.,US Pat. 4,351,811 Sept 28,1982.
6. Matsuda,S.,Kamo,T.,Kato,A.,Nakajima,F.,Kumura,T.and Kuroda,H.,Ind. Eng.Chem.Prod.Res.Dev.,1982 21 pp 48-52.
7. Matsuda,S. and Kato,A., Appl.Cat.,8(1983) No 2 pp 149-165.
8. Moriguchi,S.,Abe,H:,Takenaka,J.,Yoshikoski,H. and Komatsu,U., US Pat. 4,070,440 Jan. 24,1978.
9. Nam,I-S,Eldridge,J.W. and Kittrell,J.R., Ind.Eng.Chem.Prod.Res.Dev.,25(1 986) No 2 pp 186-192.
10. Odenbrand,C.U.I.,Lundin,S.T. and Andersson,L.A.H.,Appl. Cat. 18(1985) pp 335 352.
11. Otto,K. and Shelef,M., J.Phys.Chem.,76(1972) No 1 pp 37-43.
12. Saleh,R.Y.,Wachs,I.E.,Chaw,S.S and Chersich,C.C.,J.Cat., 98(1986) No 1 pp 102-114.
13. Skvortsov,G.A.,Nizeeva,N.N.,Podzharsky,A.I. and Dobrovolskaya,I.V., US Pat. 4,056,600 Nov. 1,1977.
14. Wong,W.C. and Nobe,K., Ind.Eng.Chem.Prod.Res.Dev., 25(1986) No 2 pp 179-186.

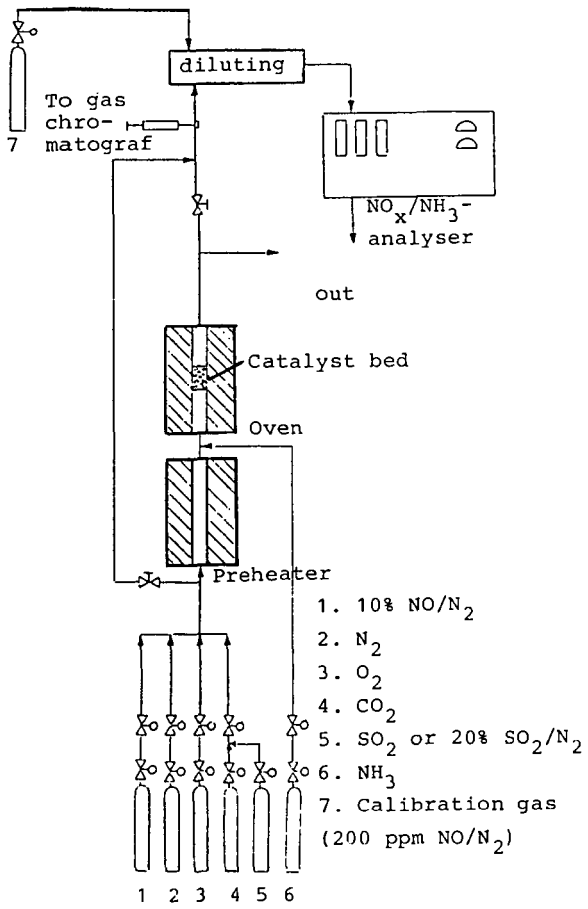

Figure 1. A schematic diagram of the experimental apparatus.

Figure 2. Thermal NO conversion in the quartz tube (NO_o=500 ppm, O_2=5 %, SV=3.6 s^{-1}, SO_2=0).

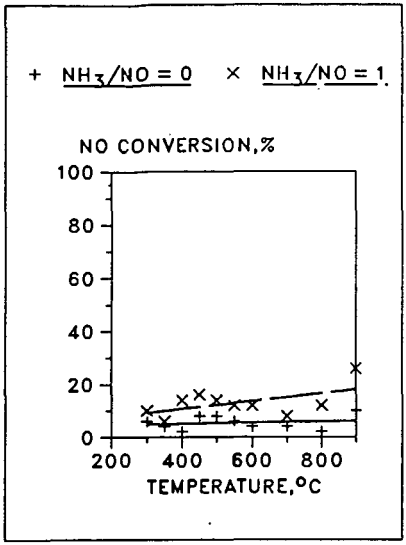

Figure 3. NO conversion with the TiO_2-supported catalysts (NO_o=500 ppm, NH_3/NO=1, SV=3.6 s^{-1}, SO_2=0).

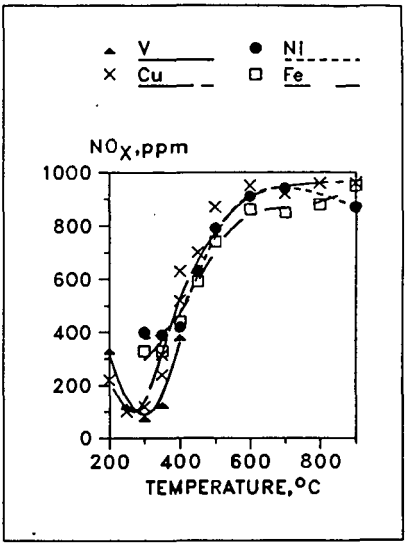

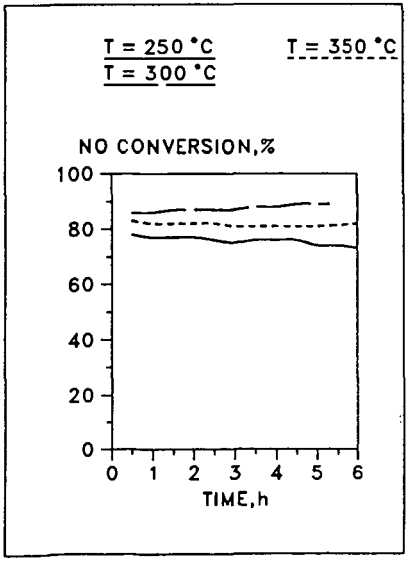

Figure 4. The influence of SO_2 on the NO conversion with the V/TiO_2 catalyst (NO_o=500 ppm, NH_3/NO=1, SV=3.2 s^{-1}, SO_2=500 ppm).

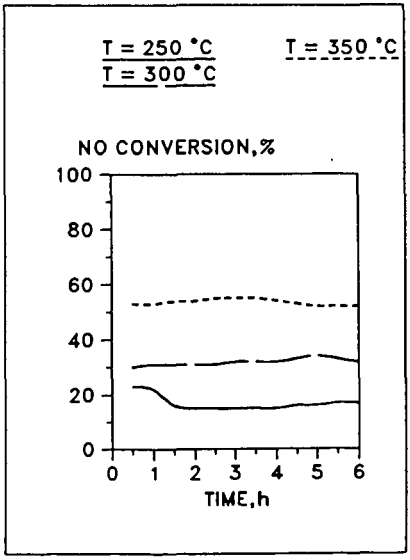

Figure 5. The influence of SO_2 on the NO conversion with the Cu/TiO_2 catalyst (NO_o=500 ppm, NH_3/NO=1, SV=3.2 s^{-1}, SO_2=500 ppm).

Figure 6. NO conversion with the Al_2O_3 -supported catalysts (NO_o=500 ppm, NH_3/NO=1, SV=3.6 s^{-1}, SO_2=0).

Figure 7. The influence of SO_2 on the NO conversion with the Cu/Al_2O_3 catalyst (NO_o=500 ppm, NH_3/NO=1, SV=3.2 s^{-1}, SO_2=500 ppm).

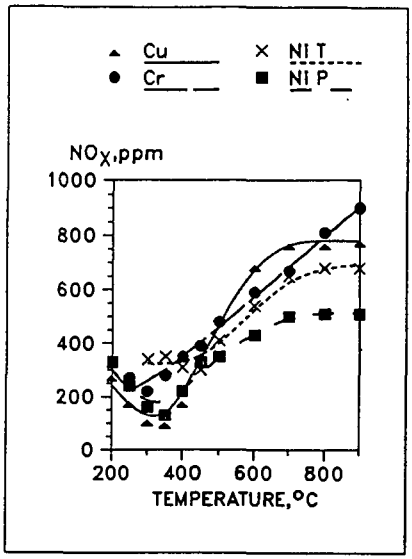

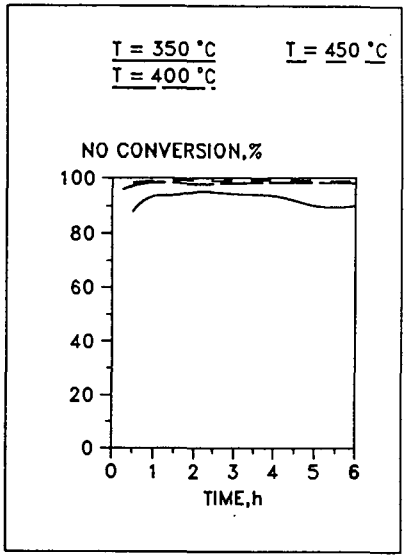

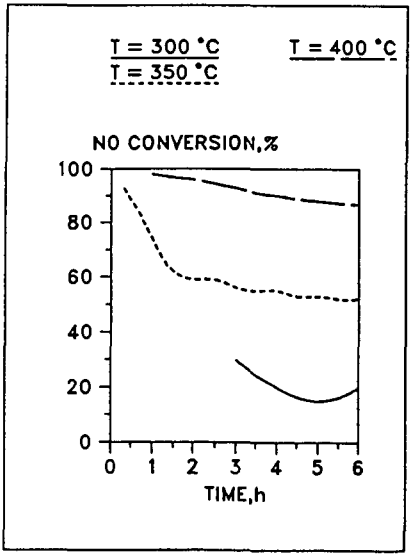

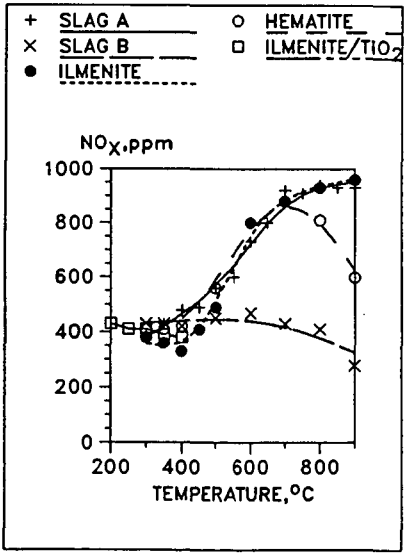

Figure 8. The influence of SO_2 on the NO conversion with the Cr/Al_2O_3 catalyst (NO_o=500 ppm, NH_3/NO=1, SV=3.2 s^{-1}, SO_2=500 ppm).

Figure 9. NO conversion with the other catalysts (NO_o=500 ppm, NH_3/NO=1, SV=3.6 s^{-1}, SO_2=0).

Figure 10. The influence of the O_2 concentration on the NO conversion with the V/TiO_2 catalyst (NO_o=500 ppm, NH_3/NO=1, SV=3.4-3.6 s^{-1}, SO_2 =0).

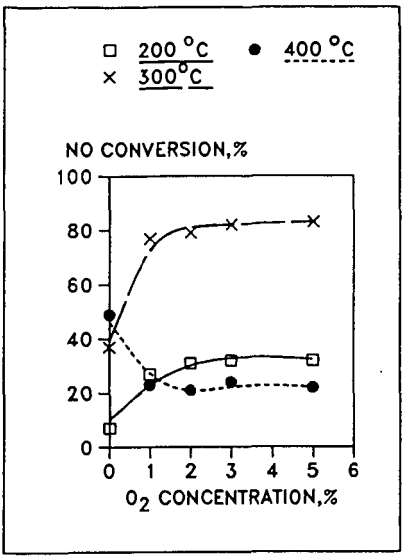

Figure 11. The influence of the O_2 concentration on the NO conversion with the Cu/TiO_2 catalyst (NO_o=500 ppm, NH_3/NO=1, SV=3.4-3.6 s^{-1}, SO_2 =0).

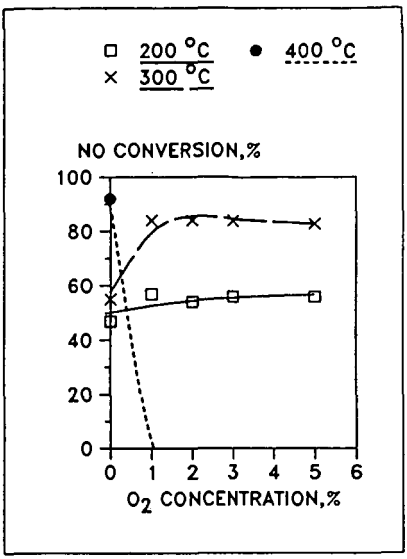

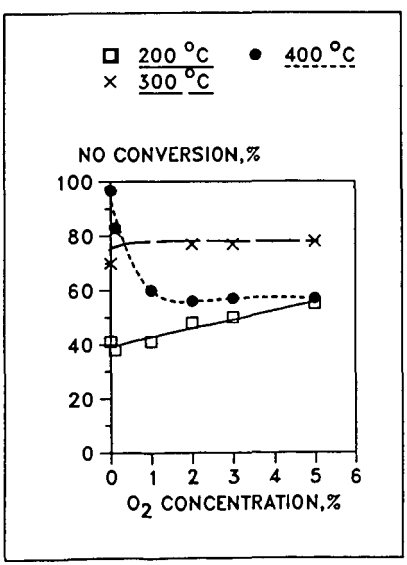

Figure 12. The influence of the O_2 concentration on the NO conversion with the Cu/Al_2O_3 catalyst (NO_o=500 ppm, NH_3/NO=1, SV=3.4-3.6 s^{-1}, SO_2=0).

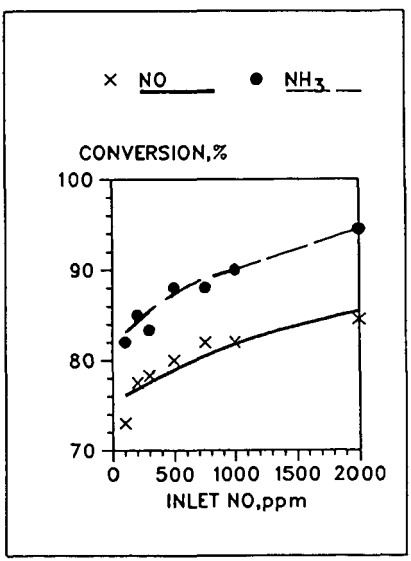

Figure 13. The influence of the NO inlet concentration on the NO conversion with the Cu/Al_2O_3 catalyst (NH_3/NO=1, O_2=5 %, SV=3.6 s^{-1}, SO_2=0).

Activation of Flue Gas Nitrogen Oxides by Transition Metal Complexes

Michael E. Miller*, Dennis H. Finseth, and Henry W. Pennline

Pittsburgh Energy Technology Center
U.S. Department of Energy
P.O. Box 10940
Pittsburgh, PA 15236

Introduction

Sulfur and nitrogen oxides are major flue gas pollutants released by coal-fired electric power plants. In the atmosphere these oxides are converted to sulfuric and nitric acids, which contribute to the acid rain problem [1]. Most of the nitrogen oxides (90%-95%) present in coal-derived flue gas exist as the relatively inert and water-insoluble nitric oxide (NO), thus presenting a difficult removal problem.

Nitric oxide reacts with oxygen to form the more reactive nitrogen dioxide:

$$2NO + O_2 \rightleftarrows 2NO_2$$

The equilibrium constant is about 400 at a typical flue gas temperature of 200°C (e.g., after the air preheater). However, the rate law

$$-\frac{d[NO]}{dt} = k[NO]^2[O_2]; \qquad k(197°C) = 3{,}340\ M^{-2}sec^{-1}$$

predicts very slow conversion to NO_2 under normal flue gas conditions (500 ppm NO and 4% O_2). About 2.5 hours would be required for 50% conversion of the NO to NO_2 [2]. Catalysis would be necessary to increase the rate of this oxidation reaction. Gaseous nitric oxide attacks a wide variety of transition metal complexes to produce nitrosyl compounds [3-5]. Thus transition metal complexes are candidate systems for control of nitrogen oxides via sorption, as well as candidate systems for catalysis of NO transformations.

A practical strategy for nitrogen oxides removal might utilize a solid support that has been impregnated with an active transition metal complex. Some supported transition metals are expected to remove NO_x by sorption, with regeneration of the sorbent being a necessary property. Others catalyze NO oxidation to the more soluble NO_2 and N_2O_5, which has been demonstrated for certain transition metal species [6]. These activated nitrogen oxides can be more efficiently removed along with SO_2 in conventional scrubbing or spray-drying processes, in which an aqueous slurry of sorbent, such as hydrated lime, is injected into the hot flue gas [7,8].

*Oak Ridge Associated Universities Appointee, Postgraduate Research Training Program.

We present here preliminary studies intended to establish basic homogeneous chemistry of transition metal complexes with nitrogen oxides. The transition metals considered in this work are volatile carbonyl complexes. This work is the first step in the development of supported metal species for enhanced nitrogen oxides removal.

Experimental Methods

Reaction mixtures are prepared on a standard glass vacuum manifold. A mercury manometer measures the pressure of each gaseous component of the sample ($\pm$1 torr). The reactions take place inside Pyrex reaction cells with KBr or CaF_2 windows. The cells are mountable inside a Digilab FTS-20C FTIR instrument that records the IR spectra of reacting mixtures. In photochemical experiments, a Hanovia 901B0011 200-watt mercury arc lamp irradiates the sample for periods of 15 or 30 seconds.

Metal carbonyls are obtained from Strem Chemicals and transferred to Pyrex vacuum cells inside a dry nitrogen-purged glove bag. Gases (NO, NO_2, and O_2) are used as received from Scott Specialty Gases. Small amounts (<5 torr) of certain gases are taken from previously made dilution mixtures of each gas in nitrogen.

Results and Discussion

Irradiation of a mixture of 0.3 torr $Fe(CO)_5$ and 20 torr NO produces new infrared bands in the carbonyl-stretching region (2092 and 2049 cm^{-1}) and in the nitrosyl-stretching region (1822 and 1787 cm^{-1}). The new IR spectrum (see Table 1) agrees with published $Fe(CO)_2(NO)_2$ spectra after taking solvent shifts into account [9-11].

Addition of nitrogen dioxide to $Fe(CO)_5$ results in the loss of all iron carbonyl spectral features and the appearance of free CO (see Table 2). The reaction produces an orange film on the bottom of the cell, whose IR spectrum was recorded after depositing this coating on a KBr plate. This solid exhibits a weak band in the terminal CO-stretch region (1910 cm^{-1}) and a strong band at 1805 cm^{-1}, which is probably due to a bridging carbonyl. Infrared bands are also observed at 1485, 1355, 1315, and 1220 cm^{-1}. The highest frequency absorbance may be a bridging nitrosyl, while the others are probably coordinated NO_2 or nitrite (NO_2^-) groups [5]. The formation of a solid containing bridging ligands indicates that iron clustering results from reaction with NO_2. Free CO is generated as this ligand is eliminated between clustering metal centers.

A sequence of chemical changes, which are followed by FTIR, occurs upon addition of 16 torr of oxygen to a mixture of 0.3 torr $Fe(CO)_5$ and 25 torr NO. Five minutes after mixing, the $Fe(CO)_5$ concentration is reduced by 72%, free carbon monoxide appears, and a small amount of $Fe(CO)_2(NO)_2$ is observed. Eight minutes following mixing, iron pentacarbonyl is gone, while the $Fe(CO)_2(NO)_2$ concentration is halved. Nitrogen dioxide is not observed until eleven minutes after mixing, when all of the iron carbonyls have left the gas phase (see Figure 1). (We observe that binary samples of NO + O_2 begin producing NO_2 immediately upon mixing; see Figure 2.) An orange film results, such as in the reaction of $Fe(CO)_5$ + NO_2. Our interpretation is that the initial NO_2 formed by NO oxidation reacts with the iron carbonyls

to produce iron clusters, and only after this reaction is complete does free NO_2 appear.

The next set of experiments involves dicobalt octacarbonyl. Upon addition of NO, $Co_2(CO)_8$ is quickly converted to $Co(CO)_3NO$, as determined by FTIR (see Table 1) [9-12]. No irradiation is necessary to initiate this reaction. Pure $Co(CO)_3NO$, produced by the introduction of NO into a cell containing a crystal of $Co_2(CO)_8$, exhibits no reactivity toward oxygen. Upon addition of NO_2, both $Co_2(CO)_8$ and $Co(CO)_3NO$ leave the gas phase, and free carbon monoxide is produced. We believe that cobalt clustering results from the interaction with NO_2, much as with $Fe(CO)_5$ (see above).

Summary and Conclusions

The metal carbonyls studied take up nitric oxide homogeneously in the gas phase. Iron requires UV light for reaction with NO, but the same result is expected with the application of heat. The metal carbonyls also react with nitrogen dioxide but in this case produce polynuclear metal species. Oxygen does not attack the carbonyl or nitrosyl complexes.

The results indicate high potential for NO_x removal from stack gases by sorption onto supported metal carbonyl complexes. The solid form allows ease in separation from the flue gas. Regeneration of the sorbent might be achieved by treating with CO to liberate NO_x by displacement or by heating to decompose and drive off NO_x.

Experiments conducted between the time of this writing and the 194th ACS National Meeting will focus on efforts to produce supported transition metal complexes and to conduct fundamental studies involving their testing as NO_x sorbents and as catalysts for nitrogen oxide transformations. Support materials will include alumina and titania. Transition metal sources will be metal carbonyls and metal salts, such as the nitrates.

Acknowledgment

This research was supported in part by an appointment to the U.S. Department of Energy Postgraduate Research Training Program administered by Oak Ridge Associated Universities. Michael Miller wishes to thank Charles Drummond and Richard Walker for helpful discussions.

Disclaimer

Reference in this report to any specific commercial product, process, or service is to facilitate understanding and does not necessarily imply its endorsement or favoring by the United States Department of Energy.

References

1. National Research Council, Acid Deposition: Atmospheric Processes in Eastern North America, National Academy Press: Washington, D.C., 1983.

2. W.L. Jolly, The Inorganic Chemistry of Nitrogen, W.A. Benjamin, Inc.: New York, 1964.

3. K.G. Caulton, Coord. Chem. Rev. 1975, 14, 317-355.

4. J.P. Collman and L.S. Hegedus, Principles and Applications of Organotransition Metal Chemistry, University Science Books: Mill Valley, Calif., 1980.

5. F.A. Cotton and G. Wilkinson, Advanced Inorganic Chemistry, 3rd Edition, Interscience Publishers: New York, 1972.

6. H.T. Karisson and H.S. Rosenberg, Ind. Eng. Chem., Process Des. Dev. 1984, 23, 808-814.

7. J. Ratafia-Brown, Assessment of Advanced NO_x Control Technologies, PETC Report, Burns and Roe Services Corp. Contract Number DE-AC22-84PC72571, June 1986.

8. H.S. Rosenberg, L.M. Curran, A.V. Slack, J. Ando, and J.H. Oxley, Control of NO_x Emission by Stack Gas Treatment, EPRI Final Report-925, Project 783-1, Battelle Columbus Laboratories, October 1978.

9. P.S. Braterman, Metal Carbonyl Spectra, Academic Press: New York, 1975.

10. W. Beck and K. Lottes, Chem. Ber. 1965, 98, 2657-2673.

11. H. Behrens, E. Lindner, and H. Schindler, Chem. Ber. 1966, 99, 2399-2406.

12. W.D. Horrocks, Jr., and R.C. Taylor, Inorg. Chem. 1963, 2, 723-727.

Table 1. Gas Phase FTIR Spectra of Some Metal Complexes as Measured in this Work.

Compound	Absorbance maxima, cm^{-1} (relative intensity)
$Fe(CO)_5$	2034(.58), 2014(1.0), 1976(.02)
$Fe(CO)_2(NO)_2$	2092(.34), 2049(.76), 1822(.54), 1787(1.0)
$Co_2(CO)_8$	2075(.64), 2052(1.0), 2037(.69), 2002(.07), 1867(.21), 1825(weak)
$Co(CO)_3NO$	2108(.12), 2045(1.0), 2010(.02), 1821(.52)

Table 2. Gas Phase FTIR Spectra of Simple Nitrogen and Carbon Oxides as Measured in this Work.

Compound	Absorbance maxima, cm^{-1} (relative intensity)
NO_2	2920(.07), 2890(.05), 1625(1.0), 1605(.74)
NO	1910(1.0), 1855(.88)
N_2O	2238(1.0), 2212(.72), 1302(.17), 1275(.14)
CO	2170, 2115
CO_2	2365(1.0), 2335(.76)

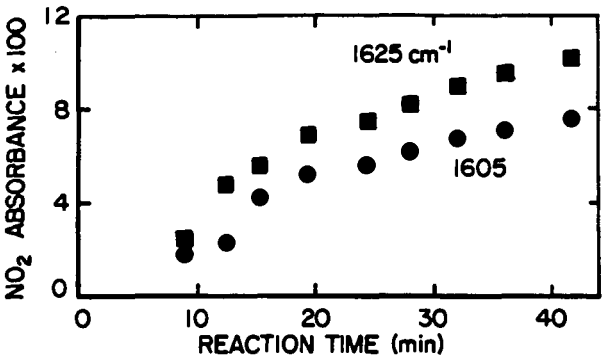

Figure 1. ***Evolution of NO_2 in the presence of $Fe(CO)_5$ as monitored by FTIR.*** **Initial pressures: 0.18 torr $Fe(CO)_5$, 1.1 torr NO, and 18 torr oxygen. Note: these initial pressures are different from the experiment described in the text, but the overall chemical behavior is the same.**

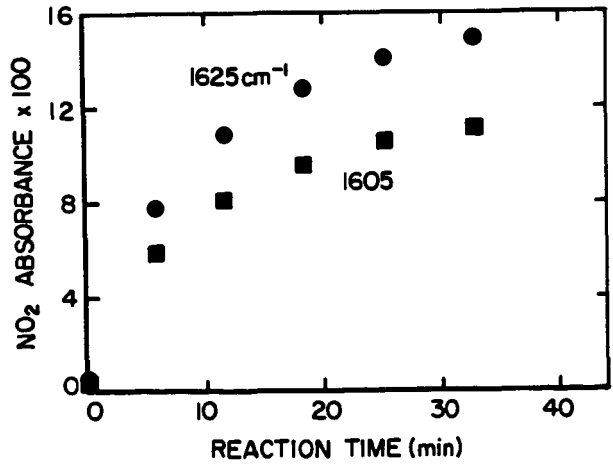

Figure 2. ***Oxidation of nitric oxide as followed by FTIR.*** **Initial pressures: 1.1 torr NO and 20 torr oxygen.**

NO/13,999

NEW STRATEGY TO DECOMPOSE NITROGEN OXIDES FROM REGENERABLE FLUE GAS CLEANUP PROCESSES

James T. Yeh, James M. Ekmann, Henry W. Pennline, and Charles J. Drummond

U.S. Department of Energy
Pittsburgh Energy Technology Center
Pittsburgh, Pennsylvania 15236

INTRODUCTION

Nitrogen oxides (NO_x) emitted from stationary combustion sources have been identified as important precursors of acid rain formation. Nitric oxide is a precursor to the formation of nitrogen dioxide and is an active compound in photochemical smog formation as well. It initiates reactions in which the products are air pollutants. Consequently, the control of NO emissions is an important factor in reducing air pollution. Well over 90 percent of all the man-made nitrogen oxides that enter the atmosphere are produced by the combustion of various fuels. On a nationwide basis, about one-half of the NO_x is from stationary sources.

Two sources of nitrogen contribute to the formation of oxides of nitrogen in the combustion reaction: molecular nitrogen from the combustion air and bound nitrogen from the fuel. Two ways exist to reduce the quantity of NO_x dispersed into the atmosphere. One method is control over the combustion reaction that produces the pollutant (combustion modification). Recent experience with combustion modification techniques for coal combustion indicate that NO_x emissions for combustion when low-NO_x burners are used can be 50%-60% lower than when employing conventional burners under otherwise identical conditions [1]. Similarly, NO_x reductions approaching 70% have been reported in pilot-scale reburning studies [2]. The second method is to remove the pollutant downstream after it is formed (postcombustion cleanup). Postcombustion techniques, which tend to be more complex and expensive, may be necessary when high levels (>70%) of NO_x reduction are required or when installing new facilities for which both NO_x and SO_x controls are mandated.

In certain regenerable, postcombustion cleanup processes, such as the NOXSO process [3], a sorbent is used to remove the NO_x from the flue gas. In the regeneration step, a concentrated stream of NO_x is produced. This stream would be "recycled" as part of the combustion air back to the coal combustor, where a portion of the NO_x would be destroyed. Theoretically, the NO_x returned to the coal combustor would cause little change in the concentration of NO_x in the exiting flue gas. Thermodynamic equilibrium calculations for NO_x formation from combustion indicate that NO_x injected into the flame zone of a combustor would be destroyed to a large extent. The formation of NO_x and its destruction in practical systems are kinetically controlled, and final concentrations of NO_x in flue gas substantially exceed equilibrium values. To assess the extent of the reduction of recycled NO_x, experimental tests in practical systems are required.

Simulated NO_x recycle tests were recently conducted at the Pittsburgh Energy Technology Center (PETC), U.S. Department of Energy, with excellent results [3]. However, the NO_x-recycle technique needs improvement if steady-state removal of 90% of the NO_x produced from the combustor is required. This paper reports experimental results for two new techniques to improve the destruction of externally injected NO_x into a combustor. The first technique involves doping the NO_x gas stream to the combustor with methane (other reductants might also be effective). The second technique is injecting the recycled NO_x stream at the optimum location (with and without methane doping) for maximum reduction. Test data showed 100% reduction of injected NO_x is possible with this technique. A third approach is proposed using a low-NO_x burner in combination with the NO_x recycle technique to achieve a steady-state 90% NO_x removal in the flue gas. The projected results of the third process scheme are based on material balance computations and reasonable expectations of the performance of each component of the process.

THEORETICAL BACKGROUND

The NO_x control techniques described above are based on concepts utilized in other in-furnace NO_x reduction processes. The techniques involve kinetically controlled reduction of NO_x based in part on increased residence time at high temperatures and in part on the presence of chemical species that reduce the NO_x to N_2, particularly doping the externally added NO_x with methane (CH_4). Doping recycled NO_x with a fuel may appear similar to the reburning technique, a term coined by Wendt et al. [4] to describe the process of NO_x reduction by injection of a secondary fuel stream to create a large fuel-rich zone in the combustor. The approach described in this paper, tentatively called "hydrocarbon doping," differs from reburning in that small amounts of secondary fuel are used (approximately 20% of that used in reburning for effective control), and no downstream injection ports are required.

Thermodynamic Equilibrium

The thermodynamic feasibility of in-furnace NO_x reduction was studied using the PETC Multi-Phase Thermodynamic Equilibrium computer code and Sandia National Laboratory's CHEMKIN computer code. Results of the thermodynamic study show the equilibrium concentration of NO at various flame temperatures (see Figure 1). The thermodynamic model simulates pulverized-coal combustion at 20% excess air. Injection of additional NO (referred to as recycle ratio, expressed as the ratio of moles of NO injected to moles of NO formed in the combustion process) was studied at levels of 0%, 90%, and 100%. The calculated data show that at NO recycle ratios as high as 1, virtually no net increase of NO occurs. However, although thermodynamics indicates nearly total destruction of injected NO is feasible (up to a recycle ratio equal to 1), chemical kinetics reaction rates will dictate the final product mix. At a NO recycle ratio equal to 4, the CHEMKIN equilibrium code predicts a 1.8% increase in NO concentration compared to the case with no recycle.

Hydrocarbon Doping

The global reactions involved in doping the injected NO_x with CH_4 for NO_x reduction are believed to be as follows:

$$CH_4 + 4\ NO_2 \rightarrow 4NO + CO_2 + 2\ H_2O \quad (1)$$

and

$$CH_4 + 4NO \rightarrow 2\ N_2 + CO_2 + 2\ H_2O \quad (2)$$

However, these reactions compete with the methane combustion reaction:

$$CH_4 + 2\ O_2 \rightarrow CO_2 + 2\ H_2O \quad (3)$$

Figure 2 (taken from Chen et al. [5]) describes the chemical mechanism for NO_x destruction by hydrocarbons. The key steps include initial NO destruction by reaction with the methylidyne radical (CH) to form HCN. Subsequent reactions lead to ammonia (or NH_i radicals) and eventually to the formation of N_2.

EXPERIMENTAL APPROACH

Test Facilities

The experimental work was conducted at PETC using a tunnel furnace and a 227-kg/hr pulverized-coal combustor. The tunnel furnace is a hot-walled, refractory-lined box with dimensions of 0.97 x 0.97 x 2.80 m and has a single burner in the front wall (interchangeable). It was designed to burn gas, coal-water slurry, or pulverized fuels. Combustion air can be preheated to 400°C (750°F). The burner is supplied with separate flows of combustion air, atomizing air, center-fire air, and natural gas (separate ring). The typical firing rate for the coal-water-mixture is approximately 0.5×10^6 W (1.7 MMBtu/hr).

The 227-kg/h (500-lb/h) pulverized-coal combustion test facility is shown schematically in Figure 3. The furnace walls are refractory-lined and water-cooled. The unit is 2.13-m (7-ft)-wide, 1.52-m (5-ft)-deep, and 3.66-m (12-ft)-high, and has a volumetric heat liberation rate of about 165,662 W/m^3 (16,000 Btu/hr-ft^3) at a thermal input of 1.9×10^6 W (6.5 MMBtu/h). The flue gas flow rate is approximately 0.613 cubic meters per second at standard conditions (1300 scfm) (standard condition is 1 atm and 0°C). Coal is charged to the hopper, pulverized to a size consist of 70% minus-200 mesh, and then conveyed by the primary air into a recycle coal loop, where intimate mixing of coal and air occurs. Four adjustable exit tubes are connected to the recycle loop; these convey the primary air-coal mixtures to each of the four burners. It should be noted that the primary air swirl inducer is no longer being used. Secondary air at 315°C (600°F) is fed through swirl vanes surrounding each burner. The flue gas exits the furnace at about 1090°C (2000°F) and passes through a convective heat transfer section and an air preheater.

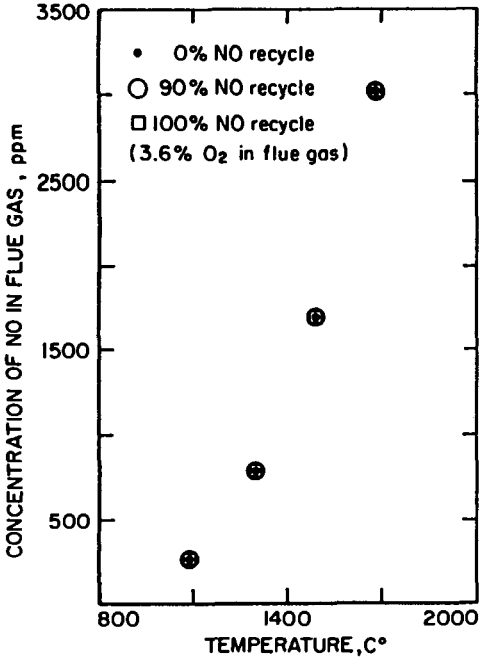

FIGURE 1. THERMODYNAMIC EQUILIBRIUM OF NO IN FLUE GAS.

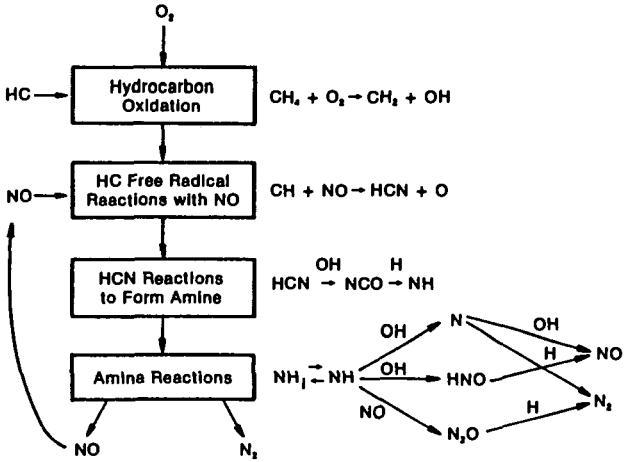

FIGURE 2. REACTION MECHANISM FOR NO_X DESTRUCTION BY HYDROCARBONS.

NO./8116

NO./14,186

Test Procedure

To simulate the recycle of NO_x from a regenerable NO_x control process, nitric oxide (NO) from a compressed-gas cylinder was injected into the combustor through the burner(s). Initial NO_x concentration at the exit of the combustor was recorded. Nitric oxide gas was then injected into the burner. The NO_x concentration in the exiting flue gas reached a steady-state level. In the case of the 227-kg/h pulverized-coal combustor, the point of NO_x injection into the burner could be varied. Also, natural gas could be added to the NO_x stream. The burner used in the 227-kg/h combustor is shown in Figure 4.

RESULTS AND DISCUSSION

The test results of in-furnace reduction of recycle NO_x with and without assistance from hydrocarbon doping are given in Tables 1 and 2. Table 1 results were obtained from the tunnel furnace tests while burning natural gas and while burning coal-water mixtures. Table 2 contains test results obtained from the 227-kg/h pulverized-coal combustor. The initial NO_x concentration is defined as the NO_x concentration in the furnace exit without any NO injection into the furnace (base line). The final NO_x concentration is that in the exiting furnace flue gas during injection of NO at steady-state conditions. The net NO_x increase is the difference between the concentrations during NO injection and the base-line condition. The reduction of recycled NO_x is the difference between the calculated final NO_x (assuming no in-furnace reduction) and the final NO_x concentration, divided by the difference between the calculated final NO_x and the initial NO_x concentration. A discussion of the results from the two test series follows.

Tunnel Furnace

Simulated NO_x recycle tests were conducted by injecting nitric oxide (NO) into the combustion air stream. The pure NO was delivered from a compressed-gas cylinder. The NO was diluted by the air stream before entering the furnace.

The recycled NO_x reductions were in the range of 59% to 79%. The data show a nearly linear relationship between NO_x recycle ratio and NO_x reduction in moles per minute. This indicates that the higher the NO_x concentration in the furnace, the more NO_x that is being decomposed. The linear relationship perhaps indicates the decomposition of NO_x is a first-order kinetics reaction. Since the reduction of NO_x returned to the furnace is not complete, thermodynamic equilibrium among all the reactions species is not being reached within the furnace.

Pulverized-Coal Combustor

Several parameters were studied during this series of tests. The objective was to maximize the reduction of NO_x injected into the combustor.

Table 1. In-Furnace Reduction of Recycled NO_x, Tunnel Furnace Tests

	Test No.						
	1	2	3	4	5	6	7
Fuel Type	natural gas			coal-water slurry			
Initial NO_x, ppm	31	31	31	510	510	510	510
Final NO_x, ppm	80	134	51	580	546	720	840
NO_x recycle ratio	6.3	12.0	3.0	0.6	0.3	1.0	2.0
Calculated final NO_x, ppm, if in-furnace reduction efficiency = 0	227	403	124	816	663	1020	1530
Net NO_x increase, ppm	49	103	20	70	36	210	330
Reduction of recycled NO_x, %	75	72.3	78.5	77.0	76.0	59.0	68.0
NO_x reduction, 10^{-3} mol/min	0.061	0.13	0.03	0.2	0.1	0.26	0.6

Table 2. In-Furnace Reduction of Recycled NO_x, 227 kg/h Coal Combustor Tests

	Test No.					
	8	9	10	11	12	13
Initial NO_x, ppm	700	700	700	550	550	550
Final NO_x, ppm	770	910	980	980	740	750
NO_x recycle ratio	1.48	1.47	1.47	1.90	1.87	1.77
Calculated final NO_x, ppm, if in-furnace reduction = 0	1739	1731	1731	1596	1579	1523
Net NO_x increase, ppm	70	210	280	430	190	200
Reduction of recycled NO_x, %	93.3	79.6	72.8	58.9	81.5	79.4
No. of burners used for NO_x injection	2	2	2	4	4	4
Location of NO_x entering into burners	auxiliary gas line		primary air	secondary air		primary air
NO_x reduction, 10^{-3} mol/min	2.85	2.44	2.23	1.90	2.58	2.38
mol CH_4/mol NO_x reduced	10.1	0	0	0	14.9	0
CH_4 to coal calorie ratio	0.107				0.135	

Table 2 (continued). In-Furnace Reduction of Recycled NO_x, 227 kg/h Coal Combustor Tests

	Test No.					
	14	15	16	17	18	19
Initial NO_x, ppm	550	480	510	510	490	490
Final NO_x, ppm	650	685	590	570	490	490
NO_x recycle ratio	1.77	2.04	1.92	1.92	2.05	2.05
Calculated final NO_x, ppm, if in-furnace reduction = 0	1523	1460	1490	1490	1492	1492
Reduction of recycled NO_x, %	89.7	79.1	91.8	93.9	100	100
No. of burners used for NO_x injection	4	4	4	2	2	2
Location of NO_x entering into burners		primary air		auxiliary gas line		primary air
NO_x reduction, 10^{-3} mol/min	2.68	2.37	2.75	2.81	3.1	3.1
mol CH_4/mol NO_x reduced	12.5	0	4.4	0	3.9	3.9
CH_4 to coal calorie ratio	0.118		0.043		0.043	0.043

The approaches evaluated included variation of the NO_x injection location in the burner and the use of hydrocarbon doping of the NO_x stream.

The NO_x can be injected into the burner and then subsequently into the combustor by three possible routes: (1) with the secondary air (this represents about 80% of total combustion air), (2) with the primary air and coal stream, or (3) through the auxiliary gas lines (see Figure 4). Four wall-mounted burners are at two different vertical elevations. The NO_x may be injected through all four burners or just through the two lower burners.

The location of the injection of NO_x within the burner is important. The data indicate that the extent of NO_x reduction varies in a manner consistent with other kinetically based NO_x reduction schemes, such as air staging or reburning. It is reasonable to assume that the concentration of NO_x would be lower at the exit of the furnace if the NO_x is injected into the combustor in a more concentrated form. A comparison of NO_x reduction efficiency can be made when the NO_x is injected with the secondary air (test 11) and with the primary air (tests 13 and 15). Tests 13 and 15 show a greater NO_x reduction efficiency because the primary air carried the NO_x into the combustor at a higher concentration than did the secondary air. The flow rate of secondary air is about four times that of the primary air. The NO_x reduction efficiency would be expected to be higher if the NO_x is injected into the combustor through the auxiliary gas line (tests 9 and 17) rather than through the primary air line (test 10). By use of the auxiliary gas line to inject the NO_x, no other gas is there to dilute the pure NO delivered from the gas cylinder. The highest NO_x reduction efficiency obtained was when the NO_x was injected into the furnace through the auxiliary gas line. Test 17 showed a 93.9% reduction of the externally injected NO_x. This is a very substantial improvement over the previously reported results obtained in the same furnace [3].

Methane doping of the NO_x stream, especially when the NO_x is concentrated, is believed to cause reburning reactions leading to NO_x reduction, as shown in Equations (1) and (2) and in Figure 2. The data indicate that the addition of a small amount of methane to the NO_x stream greatly improves the in-furnace NO_x reduction efficiency. Tests 18 and 19 show 100% reduction of recycled NO_x. At this condition, the methane to NO_x mole ratio was only 3.9. Other hydrocarbons or reducing gases could also be good candidates as doping reagents for in-furnace NO_x reduction.

System Material Balance for In-Furnace Decomposition of Recycled Nitrogen Oxides

Figure 5 shows a schematic diagram of a regenerable NO_x control process in which the NO_x is reinjected into the coal combustor for in-furnace disposal. A number of regenerable NO_x control processes now under development employ this approach. In the combustor, "a" mol/h of NO_x is being produced and is partially removed downstream by the sorbent within the reactor (absorber). The remaining NO_x, $(100 - E_1)a/100$ mol/h, is emitted into the atmosphere. The NO_x absorbed in the absorber reactor is separated from the sorbent through a regeneration process and is then recycled back to the combustor for in-furnace disposal.

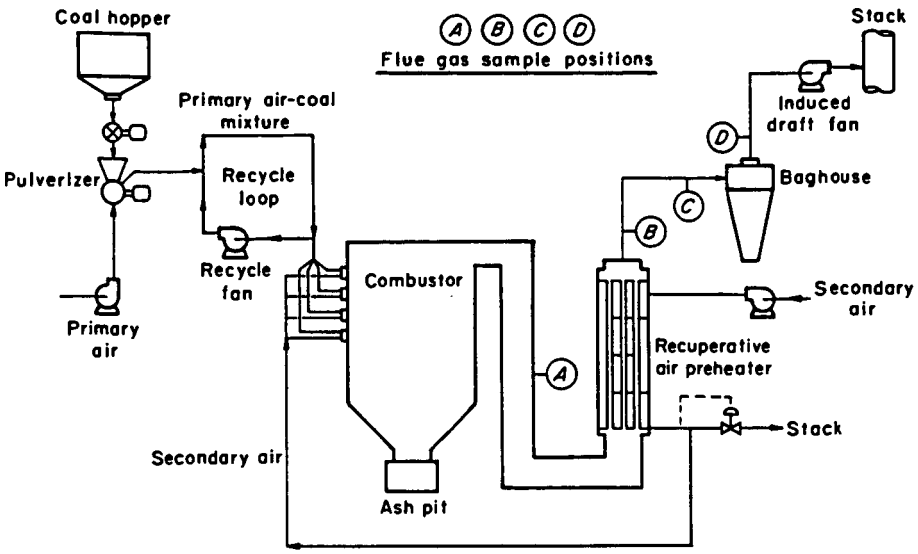

FIGURE 3. SIMPLIFIED FLOWSHEET OF 227 kg/h PULVERIZED-COAL-FIRED FURNACE.

L-81017

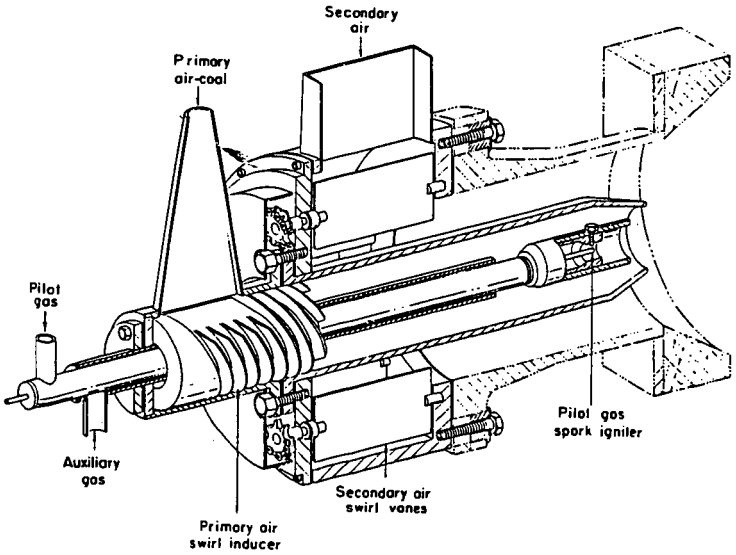

FIGURE 4. MULTI-FUEL BURNER ASSEMBLY.

L-11647

If the in-furnace NO_x decomposition efficiency is not 100%, it would be desirable to determine if the NO_x concentration at the outlet of the combustor would reach steady state when the in-furnace NO_x disposal concept is applied to the overall operation.

At steady state, a material balance around the absorber may be defined as follows:

$$a + [\frac{(100 - c)x}{100}] = [\frac{(100 - E_1)a}{100}] + x \quad (4)$$

Therefore,

$$x = aE_1/c \quad (5)$$

Here, E_2 is defined as the absorber NO_x removal efficiency relative to the net mass flow of NO_x entering the absorber.

$$E_2 = 100x/(a + [\frac{(100 - c)x}{100}]) \quad (6)$$

Equations (4) and (6) indicate that the NO_x recycle system will reach a steady state of NO_x concentration at each stage of the system. For example, given a = 100 mol/h, c = 70%, and E_1 = 90%, the steady-state recycle rate x can be found. From Equation (5), x = 128.6 mol/h of NO_x. This implies that if the absorber is designed for steady-state 90% NO_x removal from the flue gas produced from the combustor in a recycle mode, the NO_x removal capacity of this reactor (absorber) must be 128.6 mol/h of NO_x.

Low-NO_x Burner and NO_x Recycle Combination Process Scheme

Other possibilities also exist to reduce recycled NO_x. One technique couples a low-NO_x burner and in-furnace NO_x reduction without the use of hydrocarbon doping (see Figure 5). The low-NO_x burner first reduces the NO_x produced from the combustor, thus reducing the burden on the absorber; this is then followed by the recycle of the regenerated NO_x for in-furnace reduction.

An example of this technique is demonstrated as follows (refer to Figure 5 and the previous sample calculations): Given a = 73 mol/h NO_x (assuming a low-NO_x burner with 27% NO_x reducing efficiency is in place), c=70% (percent of in-furnace reduction of recycled NO_x), and the NO_x emission control is 90% removal of the NO_x produced in the combustor before the use of a low-NO_x burner, determine if the combined NO_x reduction through the coupling of low-NO_x burner and in-furnace reduction of recycled NO_x can meet the 90% NO_x reduction requirement.

The answer may best be illustrated in a tabulated form (see Table 3) by comparing overall NO_x removal efficiencies at various NO_x recycle rates.

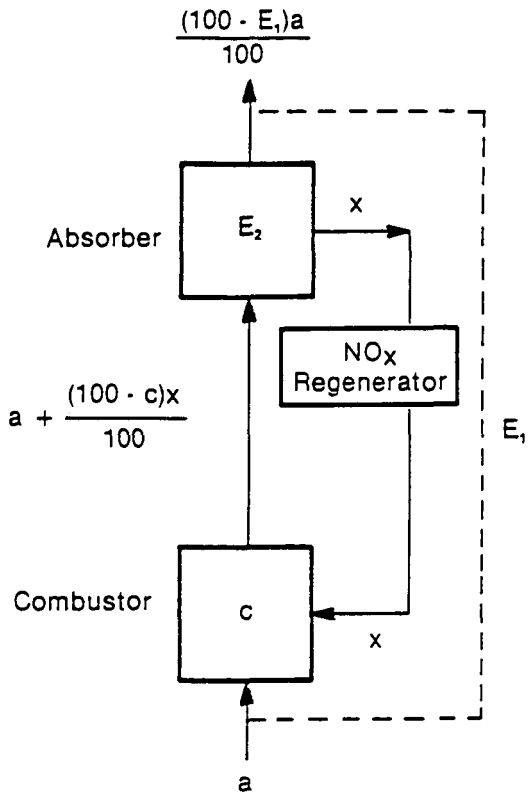

a = NO_X produced in the combustor, mol/h

E_1 = system NO_X removal efficiency, in relation to "a", %

E_2 = absorber NO_X removal (with NO_X recycle) efficiency, in relation to "a + (100 - c)x/100", %

c = destruction efficiency of recycled NO_X in the combustor, %

x = flow of NO_X recycled to combustor, mol/hr

FIGURE 5. SCHEMATIC DIAGRAM OF NITROGEN OXIDE RECYCLE.

Table 3. Combined NO_x Reduction Scheme

x	a + (100-c)x/100	(100-E_1)a/100	E_1
NO_x absorbed and then recycled, mol/h	NO_x entering absorber, mol/h	NO_x exiting absorber to stack, mol/h	Overall efficiency, %
60	91	31	69
70	94	24	76
80	97	17	83
90	100	10	90

The calculated results show that given a low-NO_x burner with 27% NO_x reduction efficiency combined with in-furnace reduction of recycled NO_x at 70% efficiency, 90% overall NO_x reduction could be maintained.

CONCLUSIONS

The location of injection of recycled NO_x into the combustor is important. A high degree of mixing between the recycled NO_x and the entire body of oxidizer and/or combustion gas should be avoided. Doping the recycled NO_x stream with methane is very effective in destroying the injected NO_x. It is kinetically advantageous to keep the NO_x in a concentrated form when it comes in contact with the reducing gas. It appears that this approach generates a locally fuel-rich zone, minimizes the oxidation of methane, and probably creates a pool of hydrocarbon radicals that contribute to the destruction of NO_x.

Recirculation of NO_x to the combustor after the regeneration step, plus th use of either hydrocarbon doping or a low-NO_x burner, can destruct most or all the recycled NO_x. These techniques should contribute to the development of cost-effective systems in which greater than 90% NO_x removal efficiencies can be obtained.

DISCLAIMER

Reference in this paper to any specific commercial product, process, or service is to facilitate understanding and does not necessarily imply its endorsement or favoring by the United States Department of Energy.

REFERENCES

1. Mulholland, J.A.; Lanier, W.S. Application of Reburning for NO_x Control to a Firetube Package Boiler, Journal of Engineering for Gas Turbines and Power, Vol. 107, p. 739, July 1985.

2. McCarthy, J.M.; Chen, S.L.; Seeker, W.R.; Pershing, D.W. Pilot Scale Studies on the Application of Reburning for NO_x Control, presented at the Joint Symposium on Stationary Combustion NO_x Control, New Orleans, La., March 1987.

3. Yeh, J.T.; Drummond, C.J.; Haslbeck, J.L.; Neal, L.G. The NOXSO Process: Simultaneous Removal of SO_2 and NO_x from Flue Gas, presented at the AIChE 1987 Spring National Meeting, Houston, Texas, March 29 - April 2, 1987.

4. Wendt, J.O.L.; Sterling, C.V.; Matovich, M.A. Reduction of Sulfur Trioxide and Nitrogen Oxides by Secondary Fuel Injection, 14th Symposium (International) on Combustion, The Combustion Institute, 1973, p. 897.

5. Chen, S.L.; Clark, W.C.; Heap, M.P.; Pershing, D.W.; Seeker, W.R. NO_x Reduction by Reburning With Gas and Coal: Bench Scale Studies, Proceedings of the 1982 Joint Symposium on Stationary Combustion NO_x Control, Vol. 1, Utility Boiler Applications. EPRI Report No. CS-3182, July 1983.

COOLSIDE DESULFURIZATION REACTIONS AND MECHANISMS

H. Yoon, M. R. Stouffer and F. P. Burke

Research & Development Department
Consolidation Coal Company
4000 Brownsville Road
Library, PA 15129

ABSTRACT

Coolside desulfurization is an emerging SO_2 control technology, involving injection of a dry sorbent such as hydrated lime and flue gas humidification by water spraying, downstream of the air preheater in a coal-fired boiler unit. The sorbent entrained in the flue gas removes SO_2 in the humidification zone. It also removes SO_2 in the particulate layer collected by the ESP or baghouse. Based on pilot-scale data, the desulfurization mechanism in the humidifier is highly complex. Hydrated lime entrained in the flue gas rapidly reacts with SO_2 at high relative humidity conditions but, in the absence of liquid water, the reaction utilizes only a small fraction of the sorbent. The presence of water droplets in the humidifier significantly increases the sorbent efficiency and the SO_2 removal level by making the sorbent-SO_2 reaction more effective. Increasing the water droplet size also increases the SO_2 removal in the humidifier.

This paper discusses the results of pilot tests which studied the mechanisms of SO_2 capture by hydrated lime in the presence and absence of water droplets in the flue gas.

INTRODUCTION

Coolside desulfurization involves injection of a dry sorbent (typically hydrated lime) followed by flue gas humidification with liquid water sprays in the ductwork downstream of the air preheater in a coal-fired boiler. SO_2 is removed by the entrained sorbent particles in the humidification zone and by the sorbent bed in the particulate collector. Since sorbent residence time in the humidifier is very short (typically 1-3 seconds), a highly active sorbent is needed for a significant humidifier SO_2 removal. Water-soluble additives can be injected with the humidification water to enhance the sorbent activity.

The concept of Coolside technology was successfully demonstrated by Consolidation Coal Company (Consol) in 1 MW field tests at Martinsville, Virginia, in 1984 (1,2). In the field tests, SO_2 removals up to 75-80% were achieved across a pilot humidifier and ESP at sorbent utilizations ranging up to 35-40%, using commercial hydrated lime with NaOH as the additive. The field results indicate that the presence of liquid water droplets plays a key role for high humidifier SO_2 removal. The sorbent activities in the field tests were significantly higher than those observed in laboratory differential reactor tests under humid flue gas conditions without evaporating water droplets (1).

To improve the process performance through process optimization and improved sorbent development, Consol constructed a 0.15 MW pilot test unit (3). A first series of process variable tests made in the pilot unit (3) confirmed the consistency of the pilot SO_2 removal data with the removals observed in the 1 MW field tests.

This paper describes the results of a subsequent pilot research program, which studied the SO_2 removal mechanisms in the humidifier. Two types of tests were conducted:

- Tests with steam humidification, to study sorbent-SO_2 reactions at close approach to adiabatic saturation and short contact times, but in the absence of water droplets.
- Tests with water spray humidification downstream of the lime injection (Coolside humidification), with varying nozzle atomizing conditions to produce different droplet sizes and drying times.

TEST METHODS

The tests of humidifier SO_2 removal mechanisms were made using the 0.15 MW Coolside pilot unit. Both the steam humidification tests and the water spray humidification tests were conducted in this unit.

Pilot Unit

Figure 1 shows a schematic of the pilot unit. The unit consists of a flue gas generation system, Coolside process system (including lime injector and humidifier), a baghouse, and continuous flue gas sampling and analysis systems. The flue gas leaving the baghouse is recycled after removal of excess moisture by a condenser/separator, providing about 80% of the flue gas requirement. The recycle gas is mixed with the flue gas introduced from a natural gas burner. By injecting CO_2, H_2O, SO_2 and fly ash into this combined gas, the inlet flue gas conditions can be matched to the flue gas conditions downstream of the air preheater in a coal-fired boiler. The fly ash content was about 4 grains/scf flue gas and the SO_2 content was 1500 ppm in the tests reported here. The pilot humidifier is a vertical, 8.3-inch ID, cylindrical duct and provides a 20-foot down-flow humidification zone. The flue gas velocity is variable from 8 to 25 ft/sec, giving 0.8-2.5 sec residence times. The humidifier has thermocouples and observation ports every two feet along its length. Hydrated lime (Table 1) is injected into the flue gas at the top of the humidifier. A series of distribution plates is placed between the lime injector and the spray nozzle locations to provide solids mixing and uniform gas flow. In all the tests with water spraying, commercial two-fluid (air/H_2O) nozzles were used. The nozzle water flow controls the humidifier exit gas temperature for the desired approach to saturation. A water soluble additive such as NaOH can be fed as an aqueous solution into the humidification water stream.

The pilot baghouse has a total cloth area of 115 ft^2, giving a maximum air/cloth ratio of 4.1 acfm/ft^2 at 150°F.

The pilot unit is installed with two continuous SO_2/O_2 flue gas analysis systems to measure the process SO_2 removal. The O_2 analyses are used to correct for air in-leakage. The SO_2 removal can be measured across the humidifier only or across the humidifier and baghouse. The humidifier exit gas sampling system was specially designed to prevent further SO_2 reaction with reactive solids in the sample system.

Steam Humidification Tests

In the steam humidification tests, a low-temperature (<180°F) gas stream was produced by running the combustor at very low load and operating with a high recycle. The gas was then humidified with steam upstream of the hydrated lime injection point. The humidifier inlet flue gas in the steam humidification tests was equivalent to the flue gas after complete droplet evaporation with water spray humidification. Since the flue gas was free of water droplets, the tests measured SO_2 removal in a dry but humidified environment. Experimental variables were approach to saturation (10-60°F), and Ca/S molar ratio (1-2).

Water Spray Humidification Tests

In the water spray humidification tests, a high-temperature (ca. 300°F) simulated flue gas was humidified to a close approach to adiabatic saturation (20-25°F) by spraying liquid water in the humidifier downstream of the lime injection point. Therefore, liquid water droplets were present with the entrained sorbent until they evaporated completely. In these tests, three different atomizing nozzles were tested, each under widely varying atomizing air pressures/flows. The varying degrees of atomization yielded sprays with widely varying droplet size distributions and drying times (0.7-2.1 sec at 30°F approach). Other experimental variables were approach (20-60°F), Ca/S (1 to 2 by mol) and $NaOH/Ca(OH)_2$ additive ratio (0 to 0.1 by mass).

RESULTS AND DISCUSSION

Reactivity of Entrained Lime Particles in Humidified Flue Gas

Tests with steam humidification (Figure 2) revealed that entrained hydrated lime particles have a substantial activity for SO_2 capture under humidified flue gas conditions (at low approach to saturation without the presence of liquid water droplets). At 25°F approach to saturation, 2 Ca/S molar ratio and 2 second contact time, the SO_2 removal was 23%. This level of SO_2 removal in the short contact time shows that hydrated lime particles have a high intrinsic activity under the humidified conditions, even in the absence of water droplets. This result indicates that a significant SO_2 reduction is possible in the humidifier by lime which is not directly wetted by water droplets. It also indicates that the lime can continue to capture a significant amount of SO_2 even after complete evaporation of water sprays.

The activity of entrained lime particles under humidified conditions increased significantly with increasing relative humidity (Figure 2). The SO_2 removal at 2 Ca/S mole ratio increased from 12% to 40% as the approach to adiabatic saturation (ca. 125°F) decreased from 60°F (about 20% relative humidity) to 10°F (about 75% relative humidity). At 1 Ca/S ratio, the SO_2 removal increased from 7% to 20% with the same change in the approach.

At higher approaches, the SO_2 removal was not as sensitive to the level of approach. As shown in the figure, there was little drop in removal from 45°F to 60°F approach. At very high approach (130°F), the removal was still 5 to 6% at 2 Ca/S ratio.

The observed effect of the approach to adiabatic saturation (or flue gas humidity) on the SO_2 removal may be due to the positive role of physically adsorbed water on the internal and external surfaces of porous lime particles. The amount of water adsorbed at equilibrium on the lime surfaces increases strongly with increasing humidity (4). Figure 3 shows that the observed SO_2 removals at varying humidities (data from Figure 2) can be correlated nearly linearly with the calculated number of monolayers of absorbed water (Table 2), based on data from a published study of water vapor equilibrium adsorption on six different hydrated limes as a function of humidity. The study showed that the adsorption per unit lime surface area (or equivalently the number of H_2O layers) was independent of the lime source. For example, the equilibrium amounts of H_2O adsorption on lime are roughly 1.3 and 1.9 monolayers at 50°F and 25°F approaches, respectively. In the steam humidification tests, it is not clear whether the lime rapidly adsorbed water to near the equilibrium level after injection into the flue gas or if the close approach allowed retention of the original surface moisture on the lime. Pilot tests with varying initial lime surface moisture contents can address this question.

The SO_2 removal by lime particles in steam humidified flue gas increased with increasing lime feed rate in almost direct proportion with the Ca/S mol ratio. Thus, the observed sorbent utilization efficiency remained nearly constant with increasing Ca/S. Figure 2 shows that the SO_2 removal at each approach roughly doubled as the Ca/S mol ratio doubled from 1 to 2. These results are consistent with the fact that the increased sorbent loading did not change significantly the environment for sulfur capture for individual sorbent particles. Except for the 10°F approach tests, the differences in the flue gas SO_2 partial pressure were not significant at the two different Ca/S mol ratios because of the relatively low levels of SO_2 removal. In the 10°F approach tests, the SO_2 partial pressure was appreciably lower at the higher Ca/S mol ratio, but this did not affect the performance of individual sorbent particles.

Effect of Water Droplets

Tests with water spray (Coolside) humidification clearly indicate that the presence of liquid water droplets substantially enhances desulfurization performance. Figure 4 shows that at the same final approach to saturation, humidifier SO_2 removals with water spray humidification significantly exceeds that with steam humidification. At 25°F approach and 1 Ca/S ratio, the humidifier removal was 30% with Coolside humidification, as compared with 12% with steam humidification. At 45°F approach, the respective removals were 13% and 6%. The flue gas residence time in the humidifier in Coolside tests was 1.7-2.0 seconds, similar to that in the steam humidification tests. Water was atomized using the Spraying Systems J-12 nozzle with 100 psig atomizing air pressure.

The significant enhancement of the sorbent performance in the presence of evaporating water droplets must result from the wetting of lime particles by water droplets through droplet-particle collisions. This wetting by water droplets would be very efficient in supplying moisture to the lime surfaces and would increase the water content in the lime particles well above that possible by physical adsorption alone.

The humidifier SO_2 removal under conditions of water spraying increased significantly with closer approaches to saturation (Figures 4 and 5). The removal at 1 Ca/S increased from 13% to 31% as the approach decreased from 45°F to 25°F. Above 45°F approach, the removal was less sensitive to the approach.

A lower approach to saturation can enhance SO_2 removal under Coolside humidifying conditions in two ways. First, a higher liquid water feed rate is required at a lower humidifier exit temperature. The theoretical water requirements for cooling to 45°F, 30°F and 25°F approaches in the above runs were 0.288, 0.329, and 0.354 gal/1000 scf flue gas, respectively. The increased water spraying capacity increases the probability of sorbent/droplet interactions. Secondly, the lower approach increases water evaporation time. This allows the wetted lime particles to retain moisture longer on the particle surfaces.

The effect of Ca/S mol ratio observed in the Coolside tests with water droplets present was somewhat different from that observed in steam humidification tests. In the Coolside tests, increasing the lime feed increased humidifier SO_2 removals, but not in direct proportion to the increasing Ca/S ratio (Figure 5). The incremental effect of additional sorbent diminished with increasing Ca/S ratio, particularly at the very close (25°F) approach. Therefore, sorbent utilization efficiency decreased with increasing Ca/S ratio. As shown in Figure 5, humidifier SO_2 removal at 25°F approach was rather insensitive to Ca/S ratio from 1 to 2, increasing from 30 to only 34%. Additional study is required to identify the causes or mechanisms for the

reduced sorbent utilization efficiency with increasing sorbent loading. One possible explanation is that the fraction of the total sorbent particles impacted by the water droplets may be smaller at a higher sorbent particle loading.

Effect of Droplet Size and Evaporation Time

Tests with Coolside humidification with widely varying degrees of water atomization showed that SO_2 removal in the humidifier was higher with larger water droplets and longer droplet drying times at the same final approach to saturation. This result indicates that larger droplets may provide more sorbent-droplet interaction because of either their longer drying times or higher collection efficiencies. The effect of droplet size further confirms the important role of water droplets in the Coolside desulfurization mechanism.

In the Coolside atomization tests, three different nozzles (Spraying Systems J-12, Caldyne 2 mm, and Heat Systems Sonimist 700-3) were tested under widely varying atomizing air pressures and flows. The variation in nozzle type and atomizing pressure produced a wide variation in the drying time in the humidifier (Table 3). The drying time variation resulted primarily from differences in water droplet size distributions produced at different atomizing air pressures, although droplet sizes were not experimentally measured in this study. Humidifier center-line gas temperature profiles were used to estimate drying times in the tests. Figure 6 shows such profiles for the Spraying Systems J-12 nozzle humidifying a 300°F flue gas to 30°F approach at different atomizing air pressures. When enough unevaporated water droplets were present in the flue gas to wet the center-line thermocouples, they read at or close to the adiabatic saturation (wet bulb) temperature. As complete evaporation was approached the thermocouple readings approached the humidifier exit bulk gas (dry bulb) temperature. Thus drying time was estimated from the point at which the profile leveled out at the humidifier exit temperature to within thermocouple error (±3°F). The residence time is based on the plug flow gas velocity at the average humidifier temperature. Based on the temperature profiles, the drying time with the Spraying Systems J-12 nozzle at 30°F approach increased from roughly 0.8 to 2.0 seconds as atomizing air pressure decreased from 115 psig to 45 psig. This reduction in the atomizing air pressure reduced the atomizing air flow through the nozzle. Drying time with the Caldyne nozzle was variable from 0.8-1.2 sec at 30°F by changing the air pressure from 90 to 70 psig (Table 3). The Heat Systems nozzle showed little or no variation in the drying time with air pressure (Figure 7).

Figure 8 shows that the humidifier SO_2 removal with the Spraying Systems J-12 nozzle increased significantly with decreasing atomizing air pressure and increasing drying time. The removal at 30°F approach and 1.5 Ca/S ratio increased from 20% to 28% as atomizing pressure dropped from 115 psig to 55 psig. A similar effect was observed at 45°F approach, the removal increasing from 15 to 19% over 115 to 45 psig air pressures (Table 3). With 0.1 $NaOH/Ca(OH)_2$ additive injection, the increase was from 34% to 41% from 115 to 55 psig air pressure, at 30°F approach and 1.5 Ca/S ratio.

Using the Caldyne nozzle, the humidifier SO_2 removal at 45°F approach increased from 15% to 25% with decreasing atomizing air pressure from 90 psig to 50 psig. At 30°F approach, there was not as much variation in drying time (Table 3) with air pressure (90-70 psig) and thus less variation in the SO_2 removal (23 to 26%).

The observed SO_2 removal using the Heat Systems nozzle was lower than with the other two nozzles tested, because it produced very small rapidly evaporating droplets, independent of the atomizing air pressure (Figure 7). At 30°F approach

and 1.5 Ca/S, the removals were 19-21%, independent of the atomizing air pressure, as compared with the 20-28% range observed with the other nozzles. At 45°F approach, removals ranged 10-12%, compared with 15-25% observed with the other nozzles.

SO_2 Removal in Baghouse

The baghouse provided significant SO_2 capture in both the steam humidification and Coolside humidification tests. The relative baghouse SO_2 removals, based on the SO_2 content at the baghouse inlet, depended heavily on approach to saturation. In the steam humidification tests, the relative removal at 1 Ca/S increased from 9% to 48% with decreasing approach from 60°F to 10°F. The relative removal also depended on Ca/S ratio, roughly doubling as Ca/S increased from 1 to 2, at lower approaches in the steam humidification tests. The relative baghouse SO_2 removals observed during Coolside testing were about the same or a little less than during steam humidification tests. The total SO_2 removals (across the humidifier and baghouse) were 38% and 21% with Coolside humidification and steam humidification, respectively, at 25°F approach and 1 Ca/S without NaOH (additive) injection. The residence time of solids in the baghouse during the pilot tests ranged 1-2 hours. Because the average solid residence time in the baghouse varied and because some solids dropped out in the baghouse hopper before reaching the bags, observed baghouse removals provide only qualitative desulfurization data.

CONCLUSIONS

Pilot test results with steam and water humidification indicate that the SO_2 capture mechanisms by entrained hydrated lime are highly complex and strongly dependent on the humidification level (approach to adiabatic saturation). Hydrated lime particles have a significant activity and thus provide considerable SO_2 removal in only a few seconds of entrainment in the flue gas under highly humidified flue gas conditions with no water droplets. The adsorbed lime surface moisture may play a key role for the desulfurization reaction based on the strong positive effect of the approach to saturation on SO_2 removal. The presence of evaporating water droplets enhanced the SO_2 removal by the entrained hydrated lime particles significantly. The wetting of lime particles by water droplets may play a key role in the enhanced performance. The beneficial effect of the water was greater at a lower approach to saturation and with larger droplets. The above results indicate that lime injection prior to water spraying, as in the Coolside process, is important for maximum sorbent utilization efficiency and SO_2 removal. Additionally, the sorbent efficiency of the Coolside process may be increased by modifying the lime properties for improved activity under humidified flue gas conditions and by increasing the lime particle-water droplet interactions for enhanced wetting of the particles.

REFERENCES

1. Yoon, H., Stouffer, M. R., Rosenhoover, W. A., and Statnick, R. M., "Laboratory and Field Development of Coolside SO_2 Abatement Technology", Second Annual Pittsburgh Coal Conference, Pittsburgh, PA, September 16-20, 1985.

2. Yoon, H., Ring, P. A. and Burke, F. P., "Coolside SO_2 Abatement Technology: 1 MW Field Tests", Coal Technology '85 Conference, Pittsburgh, PA, November 12-14, 1985.

3. Yoon, H. Stouffer, M. R., Rosenhoover, W. A., Withum, J. A., and Burke, F. P., "Pilot Process Variable Study of Coolside Desulfurization", AIChE 1987 Spring National Meeting, Houston, Texas, March 1987.

REFERENCES (Continued)

4. Klingspor, J., "Kinetic and Engineering Aspects on the Wet-Dry FGD Process", Department of Chemical Engineering II, Lund Institute of Technology, Lund, Sweden, 1983.

TABLE 1

CHEMICAL AND PHYSICAL ANALYSES
OF DRAVO LONGVIEW HYDRATED LIME (a)

Chemical Analyses, wt %		Particle Size Analyses, wt %	
Moisture	0.21	+325 mesh	21.6
Ash	75.59	-325 mesh	78.4
Carbonate	1.75		
Ash Elemental, wt %		**BET Analyses**	
Na_2O	0.01	Surface Area, m^2/g	17.3-20.3
K_2O	0.02		
CaO	97.42		
MgO	2.25		
Fe_2O_3	0.10		
TiO_2	0.02		
P_2O_5	0.01		
SiO_2	0.54		
Al_2O_3	0.57		
SO_3	0.07		
Total	101.01		

(a) Typical analysis of batch used in pilot testing.

TABLE 2

APPROXIMATE EQUILIBRIUM WATER ADSORPTION FOR HYDRATED LIME
BASED ON PUBLISHED DATA (4)

Approach to Saturation	Water Adsorbed at Equilibrium	
	g H_2O/m^2 Lime	No. Monolayers
60	0.00053	1.3
45	0.00059	1.5
30	0.00069	1.7
25	0.00075	1.9
15	0.00087	2.2
10	0.00100	2.5

Based on data at 158°F for six different hydrated limes.

TABLE 3

ATOMIZATION TEST RESULTS

Nozzle	Approach °F	NaOH/ $Ca(OH)_2$, mass	Atomizing Air psig	Atomizing Air scf/ gal H_2O	Estimated Drying Time, sec	Humidifier SO_2 Removal %
Spraying Systems J-12	45	0	115	78	0.5-0.7	15 (15)
	45	0	100	69	0.9-1.1	15 (14)
	45	0	85	57	-	17 (16)
	45	0	70	51	1.1-1.5	17 (18)
	45	0	55	44	1.5-1.9	19
	45	0	45	38	1.7-1.9	19
	30	0	115	74	0.7-0.8	20 (20)
	30	0	100	63	0.8	23
	30	0	85	56	1.0	24 (24)
	30	0	70	46	1.9-2.1	27
	30	0	55	40	1.9-2.1	28
	30	0.1	115	62	0.7-0.8	34 (36)
	30	0.1	100	54	0.8	39
	30	0.1	85	47	1.0	41
	30	0.1	70	39	1.9-2.1	40 (41)
	30	0.1	55	34	1.9-2.1	41
Caldyne	30	0	90	131	0.8	23 (23)
	30	0	80	119	0.9-1.1	24 (26)
	30	0	70	101	1.0-1.4	26
	45	0	90	159	0.5-0.8	15 (14)
	45	0	80	139	0.7-0.7	18
	45	0	60	108	1.0-1.2	21 (20)
	45	0	50	92	1.5-1.8	25
Heat Systems	45	0	70	---	0.6-0.8	10
	45	0	60	295	0.6-0.8	10
	45	0	55	273	0.6-0.8	11 (12)
	45	0	45	213	0.6-0.8	--
	30	0	70	---	0.7-0.8	19
	30	0	60	271	0.7-0.8	19
	30	0	55	260	0.7-0.8	21
	30	0	45	212	0.7-0.8	23

Numbers in parentheses are repeat tests.

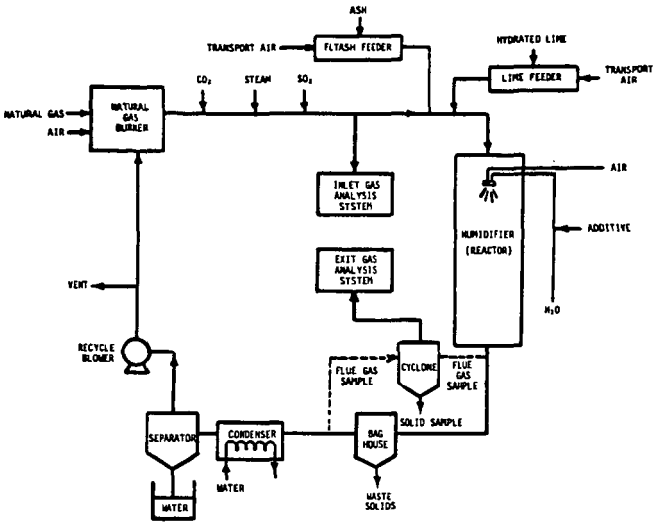

Figure 1. Schematic of Pilot Unit.

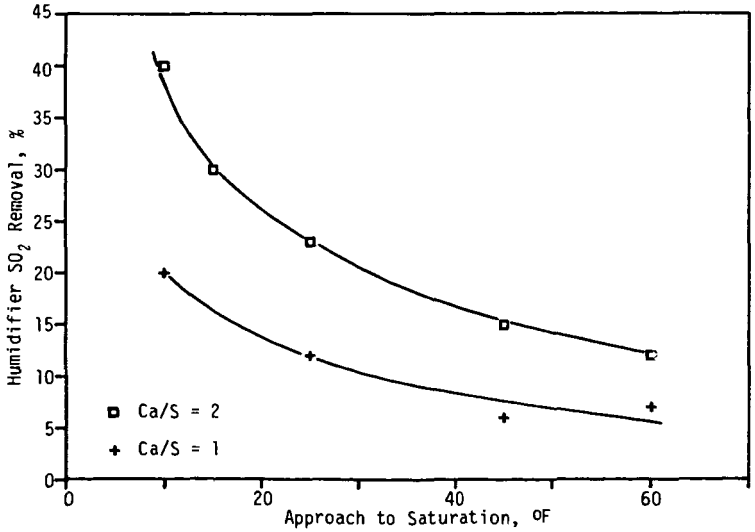

Figure 2. Steam Humidification Tests. Humidifier Removal: 2 sec residence time, 1500 ppm SO_2.

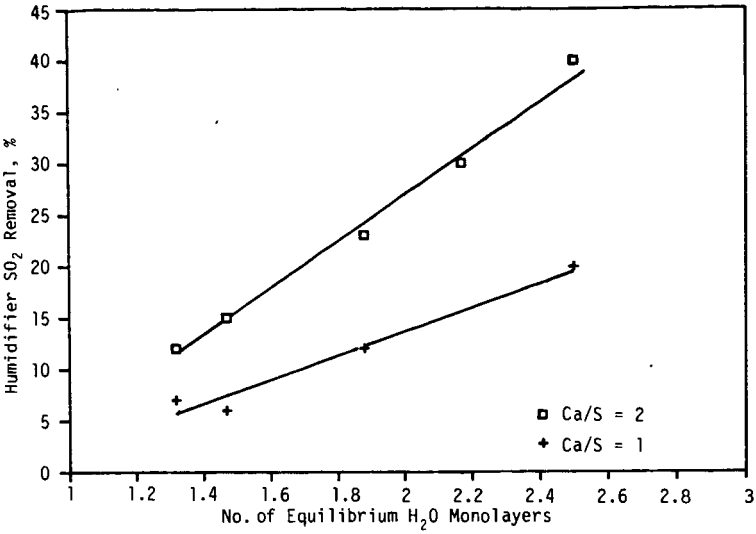

Figure 3. Steam Humidification Tests. Humidifier Removal: 2 sec, 1500 ppm SO_2.

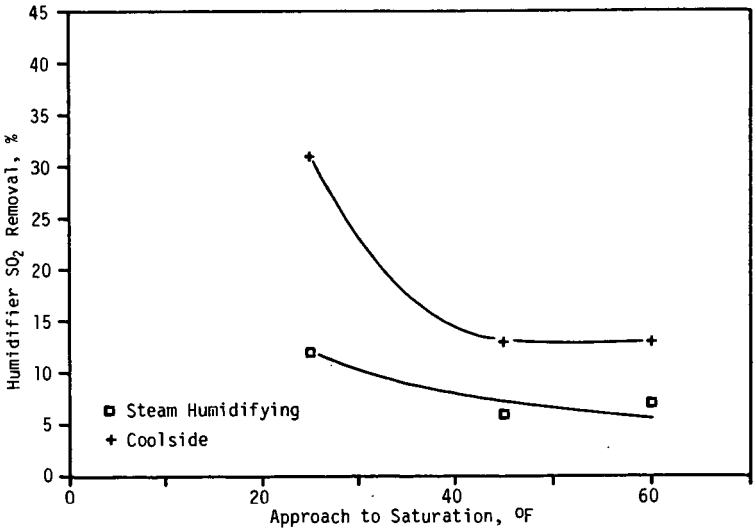

Figure 4. Comparison of Coolside Process and Steam Humidification Test Results. 1 Ca/S, 0 NaOH, 1500 ppm SO_2.

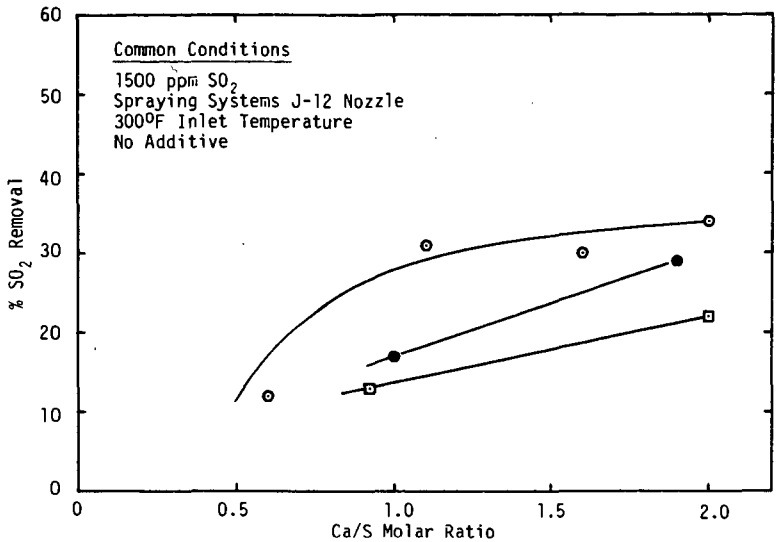

Figure 5. Effect of Ca/S Ratio and Approach on Humidifier SO_2 Removal in Coolside Humidification Tests. ⊙ 25°F ● 30°F ⊡ 48°F Approach.

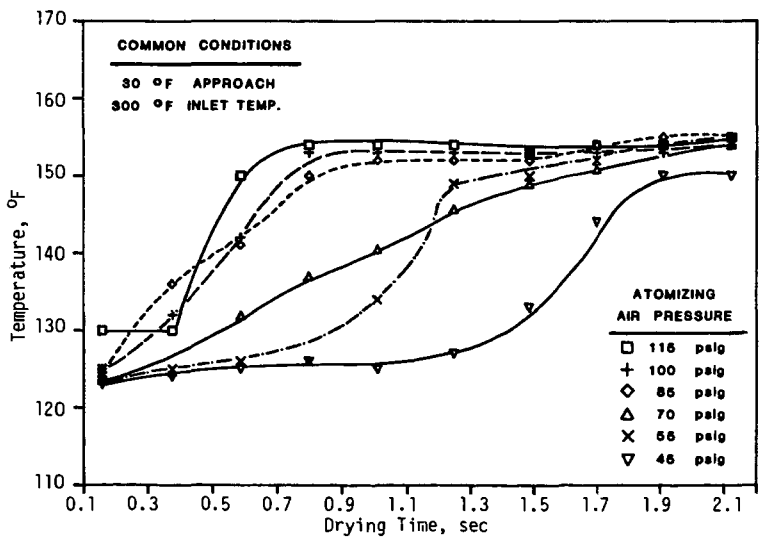

Figure 6. Humidifier Temperature Profile. Spraying Systems J-12 Nozzle.

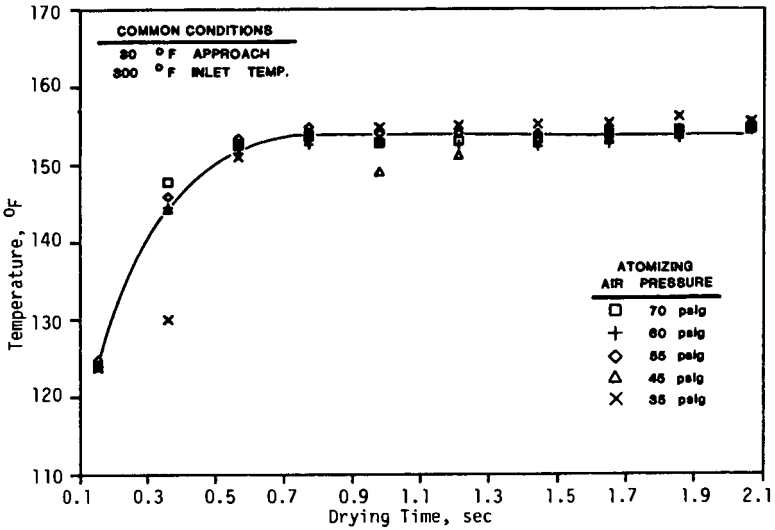

Figure 7. Humidifier Temperature Profile. Heat Systems 700-3 Nozzle.

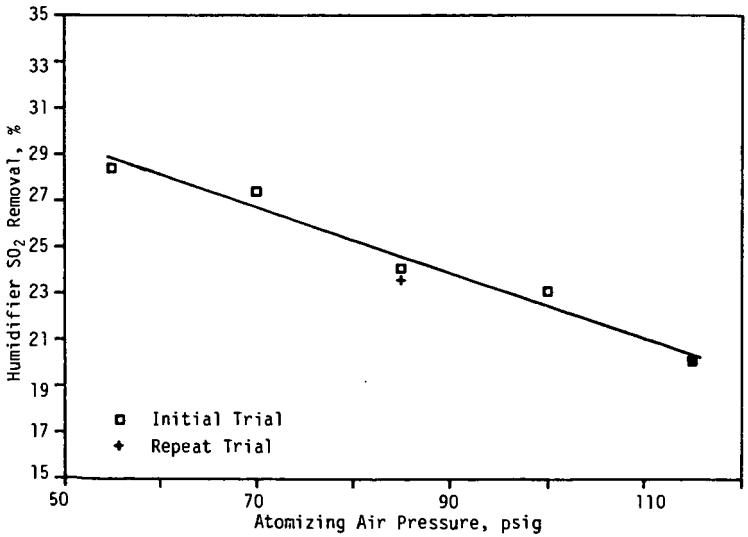

Figure 8. Effect of Atomization on SO_2 Removal. Spraying Systems J-12 Nozzle.

THE MECHANISM OF CaO SULFATION IN BOILER LIMESTONE INJECTION

M. R. Stouffer, H. Yoon and F. P. Burke

CONSOLIDATION COAL COMPANY
Research & Development Department
4000 Brownsville Road
Library, PA 15129

ABSTRACT

Pilot and industrial-scale tests of boiler limestone injection (BLI) have demonstrated flue gas SO_2 reductions of around 50% at sorbent utilization efficiencies of 15-20%. The objective of the laboratory research program described in this paper was to improve BLI sorbent utilization through an understanding of the limestone calcination and CaO sulfation reaction mechanisms. This paper describes the laboratory sulfation studies. The laboratory work used a differential reactor operated at 700-1000°C and lab-produced calcines from limestones, dolomites, and hydrated limes, having particle sizes in a range applicable to BLI. The lab work determined the intrinsic sulfation reaction rate and rate-controlling steps over this temperature range. The intrinsic rate increased with the square of calcine surface area and was rate controlling only at temperatures below 800°C. At the higher temperatures more applicable to BLI, the sulfation rate was limited by pore diffusion of SO_2 and pore plugging by the sulfate product. Therefore, the reaction rate and the saturated sorbent efficiency depended strongly on particle size and calcine pore structure. The lab data indicate that an optimum calcine pore structure can be obtained by appropriately evaluating sorbents, controlling calcination conditions and incorporating alkali additives in the sorbent.

INTRODUCTION

Boiler limestone injection is a low capital cost SO_2 control technology, involving injection of pulverized limestone into the high-temperature (1000-1300°C) regions of a coal-fired furnace. Alternate calcium sorbents, such as hydrated lime and dolomite, can also be used. In 1984, Consolidation Coal Company (Consol) successfully demonstrated the technology using a 15 MW industrial boiler at Du Pont's Martinsville nylon plant (1). The target 50% SO_2 removal was achieved by injecting limestone at 2.5-2.75 Ca/S molar ratios, corresponding to 18-20% sorbent utilization efficiencies. Since then, Consol has conducted an extensive laboratory program studying the fundamental mechanisms involved in BLI. The objective has been to significantly improve the sorbent utilization by applying the fundamental information for process improvement.

SO_2 removal by BLI involves sequential calcination and sulfation reactions:

Calcination: $CaCO_3 \longrightarrow CaO + CO_2$

Sulfation: $CaO + SO_2 + 1/2\ O_2 \longrightarrow CaSO_4$

These reactions have been widely studied; however, much of the published work has been limited to low surface area (<5 m^2/g), large particle size (ca. 1 mm) calcines (CaO), applicable to fluidized bed combustion. The reactivities observed with these calcines are too low to provide significant SO_2 reduction in BLI (2). More recent studies at EPA (3-6) using very fine (ca. 1 micron) limestone particles have shown that very high surface area calcines (up to 80 m^2/g) could be produced by differential calcination in a dispersed-phase system. In these studies, the intrinsic sulfation activity of the very fine calcine particles was proportional to the square of the calcine BET surface area. This result suggests that production of a high

surface area calcine may be critical for BLI processes. However, the 1 micron limestone particle size used in the EPA studies is much smaller than practical sizes for BLI.

This paper reports a laboratory study of calcination and sulfation for sorbent samples having a range of particle sizes applicable to BLI. Detailed results of the calcination study were previously reported (7). In this work, calcines having up to 70 m^2/g surface area were produced under differential and dispersed conditions from pulverized limestone samples applicable to BLI. Calcine surface area depended on exposure time, temperature, CO_2 partial pressure, and stone properties. A kinetic model derived for the calcination reaction indicated that calcination occurs very rapidly (<0.1 sec) at BLI temperatures.

In the sulfation study, the intrinsic sulfation kinetics and rate-controlling steps were determined with lab-produced calcines from limestones, dolomites, and hydrated sorbents. In addition, the effect of alkali additive incorporation on limestone was studied as a means of enhancing sulfation performance of calcines. The temperature range of 700-1000°C, limited by the experimental apparatus, was lower than the BLI temperature range of 1000-1300°C. However, the lab data provided valuable insight into BLI sulfur capture mechanisms and comparison of different sorbent performance.

EXPERIMENTAL

Test Sorbents

Twelve test sorbents were evaluated including eight different limestones, two dolomitic stones, a hydrated lime and a pressure-hydrated dolomite (Table 2). These sorbents varied widely in particle size as indicated by their specific surface mean diameters, and yielded calcines with widely varying BET surface areas (35-70 m^2/g). Most of the kinetic data were obtained for calcines produced from one stone, the Dravo Maysville -100 (#1). The other stones in Table 1 were tested for comparison.

Differential Reactor

A differential reactor (Figure 1) was used to calcine sorbent samples and to measure the sulfation performance of the calcines. This unit allowed control of reaction temperature to within ±3°C and sorbent/SO_2 contact time to within ±1 sec. To maintain differential sulfation conditions with respect to SO_2 partial pressure and temperature and to eliminate bulk mass transfer resistance, very small sorbent samples (down to 8 mg) well-dispersed in quartz wool and large flows (up to 70 scfh) of SO_2-containing sweep gas were used. Differential sulfation conditions were confirmed up to 900-950°C. Differential conditions were not possible above 950°C because of the extremely high sulfation rate. A few tests at 1000°C provided saturated sorbent utilization data, but no accurate rate data.

Test Procedures

Before sulfation, the sorbent was calcined in the differential reactor, under a purge flow of air at the same temperature as the subsequent sulfation. The calcination contact time was set to control the calcine surface area. For runs with low surface area calcines, the sorbent was calcined externally in a muffle furnace. After calcination was complete, the purge gas was switched immediately to an SO_2-containing gas containing 80% N_2, 15% CO_2, 5% O_2 and 750-3000 ppm SO_2. Immediately after a set reaction time between 5 and 600 sec, the SO_2-containing gas was shut off and the sorbent sample removed from the reactor. The conversion of CaO to $CaSO_4$ was determined by the Ca and S contents in the recovered sample

measured by atomic adsorption spectroscopy and combustion infrared detection, respectively.

Surface area and pore volume distributions of the calcine intermediates were measured separately by producing calcine samples under conditions duplicating those used prior to sulfation. Calcine surface areas were determined by N_2 adsorption at 77K (liquid N_2) and the one-point BET method. Pore distributions were determined from N_2 desorption isotherms (at 77K) following the methods detailed in References 8 and 9.

DISCUSSION OF RESULTS

Intrinsic Sulfation Kinetics

Intrinsic sulfation rate data measured for calcines from Dravo -100 mesh limestone were correlated by a kinetic model, originally proposed by Borgwardt (6). Based on the classical unreacted core model or grain model, this model relates fractional calcium conversion (x) to the SO_2 contact time (t, sec), absolute temperature (T, K), SO_2 partial pressure (P_{SO_2}, mmHg), and calcine specific surface area (A, m^2/g) as follows:

$$1 - 3\,(1-x)^{2/3} + 2\,(1-x) = k_d \cdot t \qquad (1)$$

$$k_d = K\,(A)^m\,(P_{SO_2})^n \exp\,(-E/RT) \qquad (2)$$

where the constants are

E = 37 kcal/mol, the activation energy
m = 2.0
n = 0.62
K = 50

The model equation is applicable to any calcine (CaO), since it includes a calcine property, the specific surface area, A. The intrinsic rate increased with the square of the surface area.

In the original development of this kinetic model, Borgwardt (6) used extremely small (95 wt % <2 micron, 30 wt % <1 micron) calcine particles, in order to eliminate pore diffusion limitation. Because of the much larger particle sizes used in the current study (13.4 micron specific surface mean diameter and 28.3 mass median diameter for the Dravo stone, #1), intrinsic rate data without pore diffusion limitation were measured only at low temperatures (≤800°C) and with low surface area calcines (<15 m^2/g). Figure 2 shows the good agreement of laboratory data at 800°C with the kinetic model predictions.

Pore Diffusion Limitation

With calcines produced from sorbent samples having particle sizes applicable to BLI (Table 1), pore diffusion was rate limiting at higher temperatures (>800°C) and with higher surface area calcines (>15 m^2/g). As a result, observed sulfation rates were significantly lower than the intrinsic rate predicted by the above model. As discussed below, pore diffusion limitation was evidenced by the observed reaction rate dependence on temperature, SO_2 partial pressure, particle size, and calcine surface area and pore structure.

Figure 3 shows that for higher surface area calcines, the apparent activation energy dropped from 37 kcal/mol to 15-20 kcal/mol at higher temperatures, indicative of transition to pore diffusion control. This agrees with the theoretical prediction that

$$E_{apparent} = \frac{E + E_{diffusion}}{2} \doteq E/2 \text{ under strong pore diffusion control.}$$

The onset of pore diffusion limitation for higher surface area calcines was around 800°C, based on the changes in slope in the Arrhenius plots. For a low surface area calcine (4 m^2/g), pore diffusion limitation was not evident up to 950°C, based on the activation energy.

The reaction order (n) in SO_2 partial pressure, measured at 900°C with a 55 m^2/g calcine, was 0.80 over 750-3000 ppm SO_2 concentrations, as compared with 0.62 according to the intrinsic kinetics. This change in the reaction order was also indicative of the pore diffusion control.

Because of the pore diffusion limitation, the initial sulfation rate observed at 900°C varied inversely with particle size (Figure 4). The different stone samples (#1-10) in Table 1 provided the variations in the particle size in the figure.

Under pore diffusion control, the effect of calcine surface area was diminished and high surface area calcines did not necessarily give high reactivity. This is because a calcine with very high surface area contains predominantly very fine pores which are more subject to pore diffusional resistance as well as pore mouth plugging, as discussed below.

Calcine Pore Plugging

Calcine pore mouth plugging by product $CaSO_4$ limited sulfation of highly porous calcines at higher temperatures. Limitation by pore plugging was evident in the lab tests from the exceptionally low apparent activation energies (<10 kcal/mol) observed with some very high surface area calcines and from the reduction in the saturated calcium utilization with increasing sulfation temperature for most of the calcines.

Porous calcines are subject to pore plugging by product sulfate because the molar volume of $CaSO_4$ (46.0 cm^3/mol) is considerably greater than that of CaO (16.5 cm^3/mol). If the mouth of a pore plugs before the interior undergoes reaction, the sorbent utilization is reduced. Further, pore mouth plugging by $CaSO_4$ can reduce the rate of sulfation by reducing available surface area and by increasing the pore diffusional resistance. Severe product pore mouth plugging is most likely when the rate of sulfation exceeds the rate of diffusion through the pores. Therefore, the degree of deactivation by pore plugging can be expected to increase with increasing temperature because the intrinsic sulfation rate increases more rapidly with temperature than the diffusion rate. Because of this temperature effect, pore plugging can reduce the apparent activation energy for sulfation. Deactivation by pore plugging can be expected to be most severe for smaller pores because the diffusion rate is slower and less $CaSO_4$ is required for complete pore blockage.

The degree of limitation of sulfation by pore plugging varied widely among calcines produced from different sorbents (Table 2). The apparent sulfation activation energies (based on initial reaction rates) among the different calcines ranged from negative values up to 22 kcal/mol. The activation energies below 15 kcal/mol indicate a rapid pore plugging at a higher temperature since the activation energies are lower than that under pore diffusion control. The wide variation in the activation energy among calcines indicates varying severity of pore plugging with these calcines. The saturated utilizations also varied widely among different calcines (17-80% at 900°C), as did the degree of temperature dependence of the saturated conversion.

The test data confirmed the more severe limitations by pore plugging for calcines with smaller pores. Figure 5 shows that a calcine from Genstar (#6) limestone had

significantly finer pores (mostly 3-10 nm) and less total pore volume than a calcine from the Dravo limestone (#1). The Dravo calcine had many pores in the 8-30 nm range. The apparent activation energy with the Genstar calcine was only 1.4 kcal/mol, significantly lower than the 15 kcal/mol observed for the Dravo calcine. Further, the Genstar calcine showed a more severe drop in final (saturation) calcium utilization with increasing temperature, from 36% to 27% to 18%, at 800°C, 900°C and 1000°C, respectively. The final utilizations with the Dravo calcine were 37%, 36% and 33% at these temperatures.

Performance of Different Stones/Sorbents

Limestones: Eight different limestones tested exhibited widely varying sulfation performance (Table 2). Saturation utilizations at 900°C varied from 17% to 50% and apparent activation energies varied from 1.4 to 22 kcal/mol over 800-950°C. These differences resulted from differences in both the stone particle size (Table 1) and the calcine intermediate pore structure. Calcine intermediate pore structure (surface area and pore size distribution) varied widely with limestone source. However, the specific properties of the original limestone which lead to a favorable calcine pore structure were not clearly identified.

Dolomitic Stones: Calcines from two dolomitic stones (Tables 1, 2) tested showed poor sulfation performance, presumably due to the presence of very small pores. Both showed negative apparent sulfation activation energies and low saturated calcium utilizations (22% at 900°C), indicative of premature pore plugging. Both calcines had very high surface areas (70 m^2/g). Pore volume analysis of the calcine from the Hommel dolomite (#9) showed that it had over 85% of its pore volume in small pores, 2-10 nm in diameter.

Hydrated Sorbents: Calcines derived from a hydrated lime and a pressure-hydrated dolomitic lime showed better sulfation performance, in terms of both rate and saturation calcium utilization, than those derived from most limestones or dolomites. For the Dravo Longview hydrated lime (#11), saturated utilization was 55% at 800°C and dropped only to 53% at 900°C (Table 2). The apparent activation was 20 kcal/mol. Figure 6 clearly shows the superior sulfation performance of a calcine from a pressure hydrated dolomite (#12) to that from a dolomitic limestone (#9), the two calcines having roughly the same chemical composition. Saturated calcium utilizations were 80% and 22% for the pressure dolomitic hydrate and the dolomitic stone, respectively. Also, the saturated calcium utilization with the pressure hydrate did not drop at higher temperature. The excellent performance of the pressure hydrated dolomite again can be attributed to the formation of a very favorable calcine pore structure. Pore volume analysis showed that the calcine from the pressure hydrate had a broad pore size distribution (4-40 nm diameter) with about 60% of its total pore volume contributed by pores of 10 nm diameter and larger, as compared with the predominance of very small pores found in the calcined dolomite.

Sulfation Enhancement by Additive Promotion

Of several salts (Na_2CO_3, NaCl, $CaCl_2$, $FeCl_3$) tested, Na_2CO_3 was found to be the most effective in enhancing the desulfurization performance of limestone. Additives were incorporated in small amounts (0.25-5 wt %) in the limestone sample prior to calcination. The results indicate that the enhancement was primarily due to physical effects, increasing the pore size of the calcine to a range more favorable for pore diffusion. This agrees with the alkali additive effects on calcine porosity in FBC (10-13). The degree of enhancement increased with the Na_2CO_3 dosage up to 2 wt %.

For this additive study, additive effects were studied for two different limestones, the Dravo limestone (#1) and the Genstar limestone (#6) (Table 1). To produce an

additive promoted limestone sample, limestone was slurried in an aqueous additive solution. Water was then evaporated from the slurry. After preparation, the dry additive-enhanced limestone was charged in the differential reactor and calcined and sulfated in the usual manner.

Figure 7 shows that sodium carbonate promotion of the Dravo stone significantly increased pore size of the calcine intermediate. With no additive, a calcine produced at 900°C had pores mostly in the 6-20 nm diameter range. With 0.5 wt % and 2 wt % Na_2CO_3 in the stone, the 900°C calcines had pores mostly in the 6-40 nm and 10-70 nm ranges, respectively. Because of the increased pore size, calcine surface areas decreased. The BET surface areas for these calcines were 52, 21 and 10 m^2/g, with Na_2CO_3 concentrations of 0, 0.5 and 2 wt %, respectively.

With the increase in calcine pore size with Na_2CO_3, the sulfation performance of the Dravo calcine was significantly enhanced (Figure 8). At 0.5 and 2 wt % additive dosages, saturated calcium utilizations at 900°C increased from 36% (with no additive) to 47% and 52%, respectively. Observed initial sulfation rates were also increased substantially. Similar enhancement was observed at 800°C and 1000°C. Further increase in the additive dosage above 2 wt % did not give additional sulfation enhancement. With 5 wt % Na_2CO_3 sulfation, performance of the Dravo calcine was not as good as with 2 wt % Na_2CO_3. The calcine with 5 wt % Na_2CO_3 had a low surface area (7 m^2/g) and thus a lower intrinsic reaction rate. This result indicates that the pore size was increased excessively above an optimum level.

With Genstar limestone (#6), Na_2CO_3 showed similar positive effects. The saturated calcium utilization at 900°C was increased to 60% with 2 wt % Na_2CO_3, a substantial improvement over the 27% utilization with no additive. Initial reaction rate was likewise enhanced.

Other additives tested were not as effective as Na_2CO_3 in promoting sulfation. Sodium chloride (NaCl) showed some enhancing effect. The saturation conversion with calcined Dravo stone (#1) at 900°C increased from 36% to 42% at 2 wt % NaCl. Calcium chloride ($CaCl_2$) and ferric chloride ($FeCl_3$) showed no significant enhancement of sulfation performance.

CONCLUSIONS

Sulfur capture by boiler limestone injection involves complex calcination and sulfation phenomena and is limited by both chemical and physical processes including intrinsic sulfation reaction, SO_2 pore diffusion in the calcine, and pore plugging by the product $CaSO_4$.

An intrinsic sulfation kinetic model, developed by Borgwardt of EPA, was experimentally confirmed. The intrinsic reaction rate increased with the square of calcine surface area and the 0.6 power of SO_2 partial pressure, and had an activation energy of 37 kcal/mol. The intrinsic reaction was rate limiting only at lower temperatures (≤800°C) and with lower surface area calcines (<15 m^2/g).

Under conditions applicable to BLI, sulfation is limited by pore diffusion and by product pore mouth plugging. Observed sulfation rates at 900°C with high surface area calcines varied inversely with sorbent particle size because of the pore diffusion limitation. Because of the pore plugging effect, the capacity for sulfation was lower for calcines with finer pore structures. These results indicate that an optimum calcine pore structure (in terms of surface area and pore size) may exist for effective sulfation. The lab data indicate that the pore structure of a calcine depends on sorbent source and calcination conditions. Different limestones gave widely varying sulfation performances because they produced calcines having different pore structures. Hydrated sorbents gave significantly better sulfation performance

than limestones, because they yielded a more favorable calcine structure. These results indicate that sorbent selection for BLI may be very important.

Small amounts of sodium carbonate added to limestones prior to calcination yielded calcines with larger pores and thus significantly enhanced desulfurization performance.

REFERENCES

1. Fink, C. E., Harding, N. S., Koch, B. J., McCoy, D. C., Statnick, R. M. and Hassell, T. J., "Demonstration of Boiler Limestone Injection in an Industrial Boiler", 1st Joint Symposium on Dry SO_2 and Simultaneous SO_2/NOx Control Technologies, San Diego, California, November 13-16, 1984.

2. Borgwardt, R. H., "Kinetics of the Reaction of SO_2 with Calcined Limestone", Environmental Science and Technology 4, 59 (1970).

3. Borgwardt, R. H., Bruce, K. R. and Blake, J., "EPA Experimental Studies of the Mechanisms of Sulfur Capture by Limestone", Proceedings: 1st Joint Symposium on Dry SO_2 and Simultaneous SO_2/NOx Control Technologies, San Diego, California, November 13-16, 1984.

4. Borgwardt, R. H., "Calcination Kinetics and Surface Area of Dispersed Limestone Particles, "AIChE Journal, 31, 103 (1985).

5. Borgwardt, R. H., Roach, N. F. and Bruce, K. R., "Method for Variation of Grain Size in Studies of Gas-Solid Reactions Involving CaO", Ind. Eng. Chem. Fund., 25 (1), 1986.

6. Borgwardt, R. H. and Bruce, K. R., "Effect of Specific Surface Area on the Reactivity of CaO with SO_2", AIChE Journal, 32, 2 (1986).

7. Stouffer, M. R. and Yoon, H., "Laboratory Calcination and Sulfation Studies for Boiler Limestone Injection", presented at 6th Workshop on Coal Liquid and Alternate Fuels Technology, Halifax, Nova Scotia, September 1986.

8. Barrett, E. P., et al., "Determination of Pore Volume and Area Distributions in Porous Substances, I. Computations from Nitrogen Isotherms", Journal of American Chemical Society, 73, 3155, 1951.

9. Pierce, C., "Computation of Pore Sizes from Physical Adsorption Data", Journal of Physical Chemistry, 57, 147, 1953.

10. Shearer, J. A., Lenc, J. F., Johnson, I. and Turner, C. B., "The Effect of Sodium Carbonate Additive on the Reaction of SO_2/O_2 Mixtures with Carbonate Rocks", Argonne National Laboratory, Report ANL/CEN/FE-79-11, July 1979

11. Shearer, J. A., "The Effect of $CaCl_2$ Additive on the Reaction of SO_2/O_2 Mixtures with Carbonate Rocks", Argonne National Laboratory, Report ANL/CEN/FE-79-7, 1979.

12. Gasner, L. L., "The Addition of Salt to Fluidized Bed Combustors", Proc. Fifth Intl. Symposium on Salt - No. Ohio Geological Society, 439-445.

13. Shearer, J. A., Johnson, I. and Turner, C. B., "The Effects of Sodium Chloride on Limestone Calcination and Sulfation in Fluidized-Bed Combustion, Journal of Environmental Science and Technology.

TABLE 1

TEST SORBENTS

No.	Sorbent	Elemental Analysis CaO, wt %	Elemental Analysis MgO, wt %	Avg Particle Diameter, (a) micron Mass Median	Avg Particle Diameter, (a) micron Specific Surface Mean(b)	BET Surface Area of Raw Stone, m^2/g	Maximum BET Surface Area of Calcine, m^2/g
1	Dravo Maysville Limestone, -100 mesh	50.82	2.74	28.3	13.4	1.4	55
2	Dravo Maysville Limestone, -325 mesh	51.86	2.81	7.2	8.5	6.3	35
3	Pfizer Marble White 200 Limestone	54.79	0.36	23.1	14.6	0.7	60
4	Warner Bell Mine Limestone	54.71	0.58	25.9	15.8	1.8	45
5	Mississippi R-1 Limestone	55.20	0.30	300.0	112.0	0.9	70
6	Genstar Apex Limestone	56.53	0.46	28.3	16.1	1.0	60
7	Utah Marblehead Limestone	56.55	0.29	48.0	27.0	0.9	65
8	Baker Reagent $CaCO_3$	56.54	0.01	13.2	11.2	0.5	55
9	Hommel #1974 FF Dolomite	32.00	20.11	32.9	22.0	0.8	70
10	Warner Dolomite	28.90	21.96	98.2	55.8	0.3	70
11	Dravo Longview Hydrated Lime	72.01	2.44	12.0	12.0	21.1	40
12	Pressure Hydrated Dolomite	41.70	30.38	39.2	24.9	23.3	45

(a) Particle size determined by wet screening in CH_3OH and by Coulter Counter.

(b) Specific surface mean, $D_p = \frac{\Sigma Yi}{\Sigma YiDi}$

where Yi = weight fraction of size cut, Di = Average diameter of size cut.

TABLE 2

SULFATION PERFORMANCE OF HIGH SURFACE AREA CALCINES FROM TWELVE TEST SORBENTS

No.	Sorbent	D_p micron (a)	Calcine Surface Area, m^2/g	$E_{apparent}$ (b)	Saturation Ca Conversion, % 800°C	900°C	1000°C (c)
1	Dravo Maysville Limestone, -100 mesh	24.5	55	15	39	36	33
2	Dravo Maysville Limestone, -325 mesh	8.5	35	15	50	50	36
3	Pfizer Marble White 200 Limestone	14.6	60	4.1	23	21	--
4	Warner, Bell Mine Limestone	15.8	45	15	37	33	23
5	Mississippi R-1 Limestone	112.0	70	4.1	20	17	9
6	Genstar Apex Limestone	16.1	60	1.4	36	27	18
7	Utah Marblehead Limestone	27.0	65	15	31	20	11
8	Baker Precipitated $CaCO_3$	11.2	55	22	45	36	--
9	Hommel #1974 Dolomite	22.0	70	Negative	32	22	--
10	Warner Dolomite	55.8	70	Negative	30	22	--
11	Dravo Longview Hydrated Lime	12.0	40	20	55	53	--
12	Pressure Hydrated Dolomite	24.9	45	21	80	80	--

(a) Specific surface mean particle diameter, as defined in Table 1.
(b) Apparent sulfation activation energy over 800-950°C.
(c) Runs at 1000°C deviated from differential conditions.

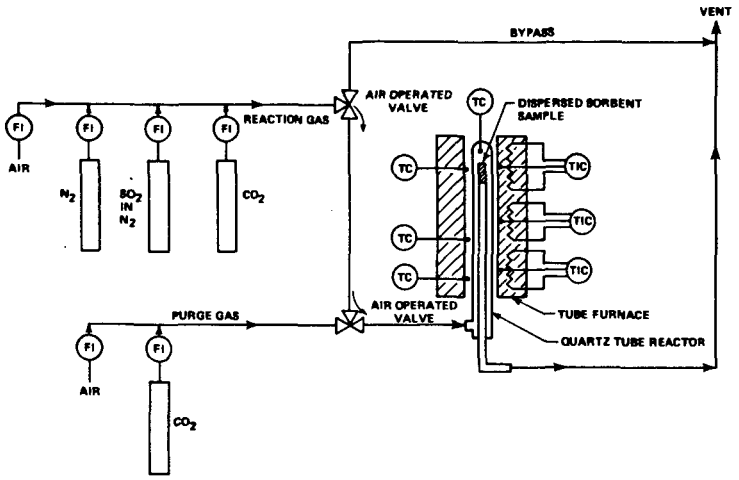

Figure 1. Schematic of Differential Reactor Unit.

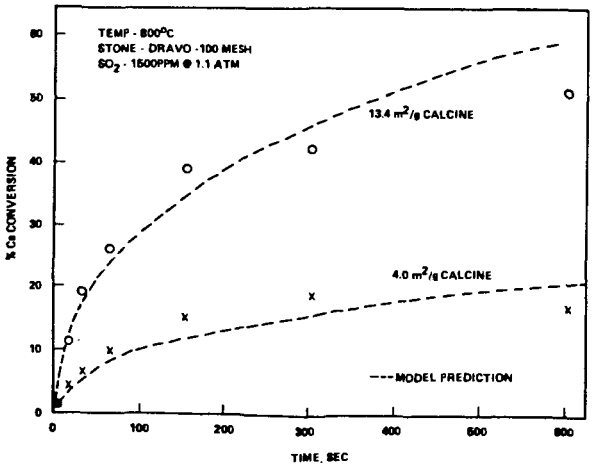

Figure 2. Comparison of Sulfation Rate Data with Intrinsic Sulfation Kinetic Model.

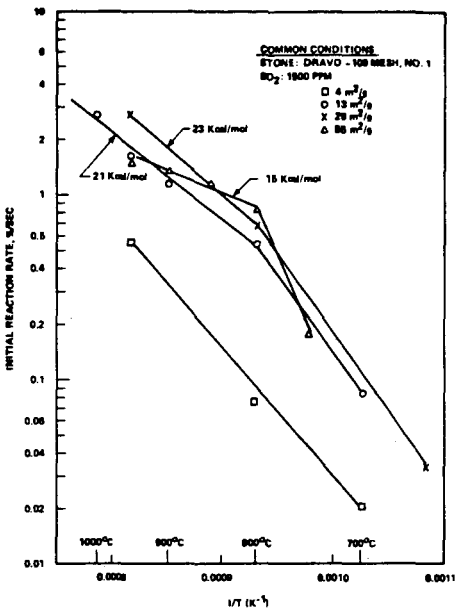

Figure 3. Initial Sulfation Rate vs Temperature.

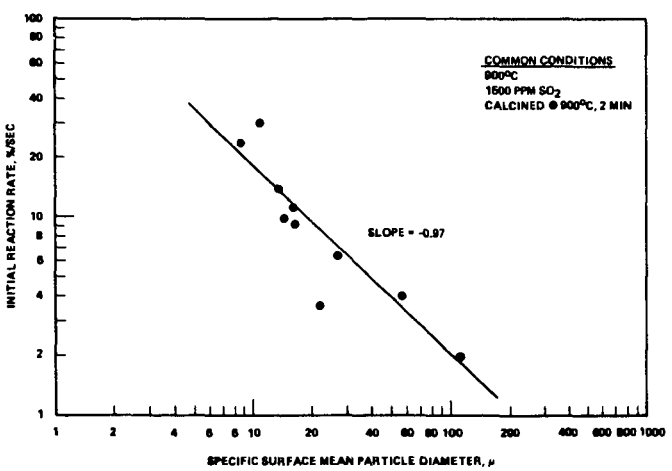

Figure 4. Effect of Stone Particle Size on Sulfation Rate.

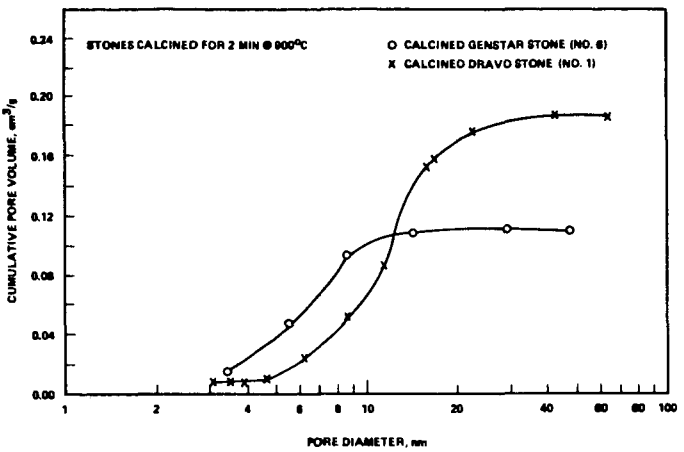

Figure 5. Cumulative Pore Volume Distribution for Two Calcined Limestones.

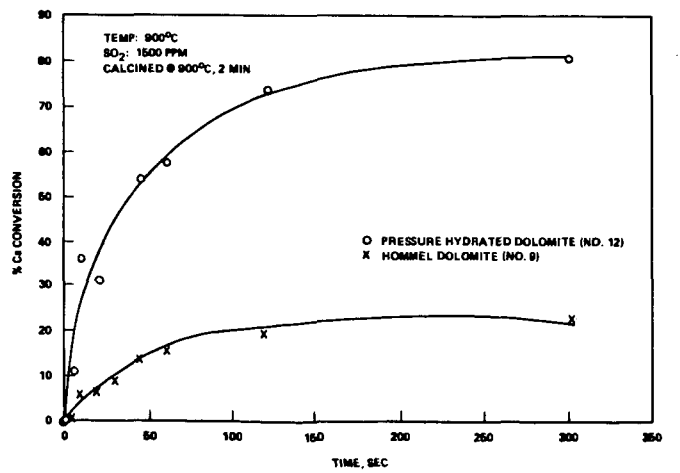

Figure 6. Performance Comparison of Pressure Hydrated Lime and Dolomitic Stone.

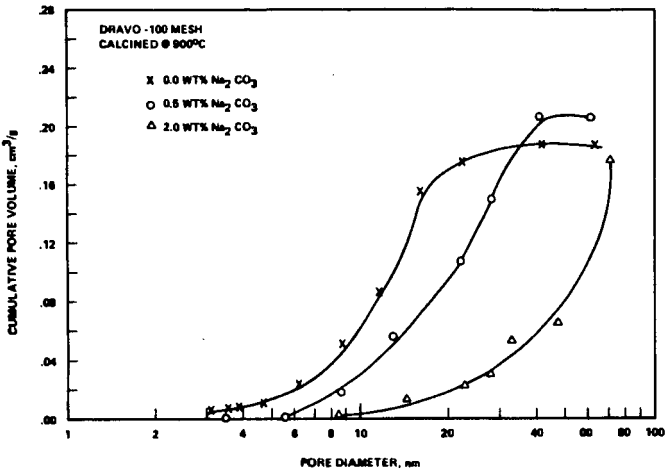

Figure 7. Effect of Na_2CO_3 Additive on Calcine Pore Distribution.

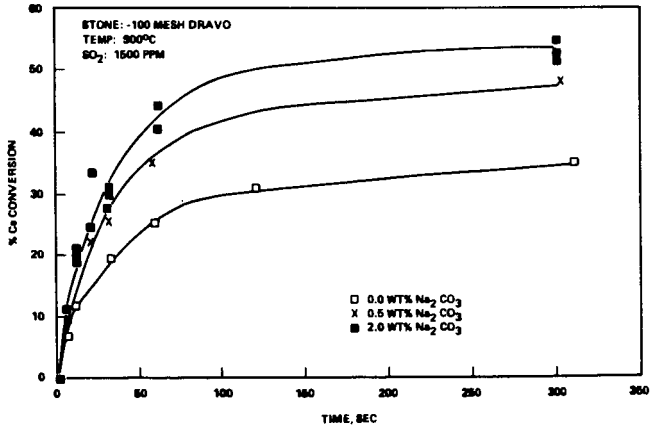

Figure 8. Sulfation Enhancement by Na_2CO_3 Additive.

SULFUR DIOXIDE SORPTION REACTIVITY OF HYDRATED LIME: EFFECT OF HYDRATION METHOD

D. L. Moran, M. Rostam-Abadi, R. D. Harvey, and R. R. Frost
Illinois State Geological Survey, Champaign, Illinois 61820

and

G. C. Sresty
Illinois Institute of Technology Research Institute

INTRODUCTION

The Furnace Sorbent Injection (FSI) process is a relatively low capital cost technology for control of SO_2 emissions produced during combustion of high sulfur coal. A major factor in the total cost of the FSI concept is the effective utilization of the sorbent. In pilot plant tests performed by previous investigators, calcium utilization efficiencies (at Ca/S feed ratio of 2:1) ranged from 15 to 20% for limestone, 25 to 30% for dolomitic limestone, 20 to 30% for hydrated lime, and 35 to 40% for pressure-hydrated dolomitic lime (1,2,3,4). The low calcium utilizations observed in these and many other studies have motivated researchers to develop methods of producing more reactive calcium-based sorbents with the goal of reducing SO_2 removal costs.

The hydration method has received considerable attention in recent years because it appears to be the least expensive method of producing fine (<10 micrometer) lime particles with high surface area. Particles of this size range are more reactive than larger particles because they lack significant resistance to pore diffusion. Recent hydration studies have focused on developing sorbents with higher surface areas than those of commercial hydrates. In laboratory-scale hydrators, under controlled processing conditions, hydroxides having surface areas ranging from 42 to 50 m^2/g (2 to 3 times greater than those of commercial hydrates) have been produced (4,5,6,7). Materials with surface areas up to 45 m^2/g have been produced by hydration with methanol-water solutions (7,8).

The objective of this investigation was to produce hydrated lime with high surface area. Three hydration methods were studied: 1) lime was hydrated with water or alcohol-water solutions, 2) lime was reacted with water at pressures and temperatures up to and exceeding supercritical conditions and the hydrated lime produced was ejected to atmospheric conditions, 3) lime was hydrated with steam. Sulfur dioxide sorption capacities were obtained by thermogravimetry and surface areas were determined by the BET (N_2) technique.

EXPERIMENTAL

Materials

Two different limestones were calcined for the experiments (table 1). Both consisted of more than 95% $CaCO_3$ (calcite). Limestone A is characterized as coarse grained and low specific gravity and limestone B as fine grained and somewhat higher specific gravity.

Calcination

The limestones were calcined in a 2.5-cm I.D. batch fluidized bed reactor constructed from a type 316 stainless steel pipe. Twenty to fifty grams of limestone (100-150 micrometer particles) were heated at a rate of 20°C/min to 850°C. The sample was held at this temperature for 30 minutes to assure complete conversion of carbonate to lime. Nitrogen was the fluidizing gas flowing at a rate of 1000 cc/min (STP).

Hydration

A 500 ml, three-neck flask was used to hydrate the lime at atmospheric pressure with water or alcohol-water mixtures. Two methods were used: 1) dry hydration (twice stoichiometric water or less) and 2) wet hydration (five times stoichiometric water or more). The hydrate was prepared by adding hydrating solution to one gram of lime while stirring the mixture. The temperature of the mixture increased from ambient to between 50 and 90°C due to the exothermic nature of the hydration reaction. Some of the hydrating solution boiled off during dry hydration runs as a result of localized overheating. The reaction was assumed to be complete after the sample had cooled to room temperature. The hydrated lime product was dried under vacuum and gently crushed for one to two minutes to break up loosely agglomerated particles. Some of the products were filtered and washed with 3 to 25 ml of alcohol prior to vacuum drying. The products were stored in vials under nitrogen to avoid recarbonation.

Pressure-hydrated lime was prepared at the Illinois Institute of Technology Research Institute in a batch reactor constructed of 1.3-cm I.D. stainless steel pipe. The reactor consisted of two sections separated by a metal disk that was designed to rupture at a specific pressure. The upper portion of the reactor (6.4 cm) was charged with one gram of lime and three to four grams of water, capped, and quickly heated using a torch. During the heating period (4 to 5 minutes), the pressure and temperature of the reactor simultaneously increased until the disk ruptured. During this rupturing period (on the order of milliseconds) the reactor pressure dropped to one atmosphere. The pressure-hydrated lime slurry was collected in the lower portion of the reactor (30 cm). The product was vacuum-dried prior to testing for sulfation reactivity.

Lime was hydrated with steam at 200°C for 30 to 60 minutes in a thermogravimetric analyzer system. The partial pressure of steam in the reactor was 0.13 atmospheres. The hydration was assumed to be complete when no further increase in weight was observed. The product was then heated in nitrogen at 20°C/min to 850°C and was tested for sulfation reactivity.

SO_2 reactivity

Reactivity data were obtained by Thermogravimetry (TG) using a Cahn RG balance. The sample holder (1-cm diameter and 0.5-cm height) was constructed of 100 mesh platinum gauze and was suspended from the microbalance by a platinum wire (0.01-cm diameter). The reaction temperature was measured by a Pt/Pt-13% Rh thermocouple located 5 mm below the sample holder. The reactant gas was passed upward through the reactor tube (3.2-cm I.D.). The lower portion of the reactor (10 cm) was filled with 0.64-cm ceramic raschig rings which served as a gas mixing and preheating zone and as a gas distributor. The system was interfaced with an IBM-PC to provide automated collection and storage of the microbalance and thermocouple outputs.

In a typical run, sample particles were dispersed in layers of quartz wool located in the sample holder. The sample was heated in nitrogen at a rate of 20°C/min to 850°C. The reaction gas containing 0.5% SO_2, 5% O_2, 20% CO_2, and balance N_2 (which simulated the flue gas from combustion of a high sulfur coal) was introduced to the reactor and the increase in weight due to sulfation and the reaction temperature were recorded at 10 second intervals for 60 minutes. Results of preliminary experiments revealed that sulfation rates were not affected when sample weights of less than 10 mg and gas flow rates between 300 and 900 cc/min (STP) were used. Sample weights of 8 mg and flow rates of 300 cc/min were used in subsequent experiments.

RESULTS AND DISCUSSION

Physical characteristics of hydrates

Hydrated lime products were examined under a light microscope. Dry-hydrated (atmospheric) lime and a commercial pressure-hydrated lime prepared from limestone B consisted of particles which were predominantly less than 10 micrometers in diameter. However, some 10 to 50 micrometer particles were present in the atmospheric hydrate. Reduction in particle size (mmd=2 to 4 micrometers) is achieved in commercial pressure hydration processes due to the ejection of the products through an orifice (9). The surface area, BET (N_2), of the pressure-hydrated lime was 17.2 m^2/g compared to 34.3 m^2/g for the atmospheric product (table 2).

Wet hydration produced agglomerated particles with clusters as large as 0.5 cm. The agglomerates were easily reduced in size by gently crushing with a spatula. However, several large particles were observed in the samples even after crushing. Examination of lime A hydrated with twenty times stoichiometric water followed by vacuum-drying and mild crushing showed that particles were predominantly less than 20 micrometers in diameter, although some as large as 150 micrometers were also present.

Hydration with methanol-water solutions generally produced hydroxides with particles that were finer and more uniform than those prepared with water alone. Few particles greater than 20 microns were observed in these samples. Depending on the amount of methanol used, surface areas ranging from 43 to 70 m^2/g were obtained (table 3). Comparable surface areas were obtained for products hydrated with ethanol-water solutions. These values show improvement over surface areas of hydrates prepared in water alone and are three to five times greater than those of commercially available hydrates.

SO_2 reactivity

As described earlier, the hydrated samples were heated in nitrogen to 850°C prior to sulfation. A weight loss of 21-23% was observed between 350 and 500°C due to the dehydration reaction. The theoretical weight loss for the dehydration of pure calcium hydroxide is 24%. The samples lost an additional 1-3% weight between 500 and 700°C. This weight loss was attributed to the calcination of any residual carbonate material in the sample.

The progressive increase in weight during sulfation was attributed to the reaction of the calcined product with oxygen and sulfur dioxide according to:

$$CaO + SO_2 + 1/2\ O_2 \text{ ------> } CaSO_4 \qquad 1)$$

X-ray diffraction analyses of samples exposed to the reaction gas mixture confirmed that calcium sulfate was the sole product formed. The following relationship was used to calculate the percent conversion (calcium utilization) of the sorbent as a function of reaction time:

$$\text{Percent conversion} = X_t = \frac{W_t - W_o}{YW_o} \frac{M_{CaO}}{M_{SO_3}} \times 100 \qquad 2)$$

where:
W_t = weight of sorbent at time t
W_o = initial weight of sorbent at 850°C
Y = weight fraction of calcium oxide in sample at 850°C
M_{CaO} = molecular weight of calcium oxide
M_{SO_3} = molecular weight of sulfur trioxide

Reactivity curves were obtained by plotting X_t against sulfation time.

Hydration with water

The sorption capacities of hydrates prepared at atmospheric pressure depended on the method of hydration (dry or wet) and the parent limestone (figure 1). The surface areas of the dry and wet hydrates produced from lime A were 37 and 46 m^2/g compared to the value of 13 m^2/g for the starting lime (100x150 micrometers). The calcium utilizations of these samples were 59, 69 and 37%, respectively. No improvement in utilization was achieved for samples hydrated with five times stoichiometric water or more. Dry and wet hydrates produced from lime B had surface areas which were similar to those obtained for hydrates prepared from lime A (table 2). However, hydrates prepared from lime B had calcium utilizations exceeding 90%.

The results of a recent study showed that calcination conditions, i.e. temperature and sintering time, were not important in producing hydroxides with high surface areas (6). The effect of calcination atmosphere was not investigated in that study. A sample was prepared by calcination of limestone A in one atmosphere carbon dioxide followed by hydration with twenty times stiochiometric water. This treatment increased the utilization of wet hydrate to 78% (vs 69% for hydrate produced from limestone calcined in nitrogen). The sorbent surface area was 33 m^2/g, surprisingly lower than that of the hydrate produced from lime prepared in nitrogen atmosphere (46 m^2/g).

Sulfation data for the -325 mesh (<45 micrometers) and 100x150 micrometer limes are also shown in figure 1 for comparison. These samples were calcined in the TGA system prior to sulfation. It is interesting to note that although hydrates made from limestone B were more reactive than those made from limestone A, the -325 mesh calcine of the latter (surface area of 20 m^2/g) was more reactive than that of the former. Little difference in reactivity was observed for the 100x150 micrometer particles.

Hydration with methanol-water solution

Hydration of lime with alcohol-water solution was tested because a previous study had shown that this method of hydration produced samples with surface areas as high as 50 m2/g (10). Alcohol affects the solubility and interfacial tension of hydrates in water and acts as a dispersing agent, thus minimizing particle agglomeration. The reactivity data for lime B hydrated with a 50% methanol-water solution and washed with ten grams of methanol are shown in figure 1. This sample had a sulfation capacity which was greater than that of the commercially prepared pressure-hydrated lime. A sorption capacity of 100% was observed for this sample as compared to 95% for the commercial hydrate. High calcium utilizations were also observed for samples prepared by hydration of lime A with methanol or ethanol-water solutions (see table 3). This indicates that costs associated with pressure hydration can be eliminated by hydration with methanol-water solution at atmospheric pressure.

Limestone A was subjected to a more extensive study on this method of hydration. The objective was to evaluate the effects of the concentration of alcohol in the hydrating solution and the amount of alcohol used in the post-hydration washing step on the reactivity of the products. The hydration conditions, calcium utilizations and surface areas of the hydrates are summarized in table 3. Reactivity data are shown in figure 2. Increasing the concentration of methanol in the hydrating solution and the amount used in the post-hydration wash resulted in increased calcium utilizations. This is clearly shown in figure 3 where the calcium conversions after 60 minutes are plotted as a function of methanol concentration.

The relationship between the surface area and calcium utilization for the hydrates prepared in methanol-water solution is shown in figure 4. BET (N_2) surface areas of hydrates (prior to dehydration) correlated well with ultimate sorption capacities.

Pressure hydration

The sulfation data for the pressure-hydrated products (Lime A) are shown in figure 5. The calcium conversion of the product prepared at 475 atmospheres and 480°C was 76%. The surface area of this sorbent was 15.4 m^2/g. A conversion of 91% was achieved for the sample prepared at 120 atmospheres and 290°C. The reason for the higher capacity observed for this sample is not known. Although the sulfation capacities of the products prepared under pressure were higher than those of the wet hydrates, their surface areas were lower (see table 2).

Steam hydration

The reactivity of the steam-hydrated lime A is also shown in figure 5. A calcium utilization of 68 % was observed for the hydrated sorbent. This is comparable to the utilization observed for the lime hydrated with water (wet method) at atmospheric pressure. Calcination of limestone under a carbon dioxide atmosphere prior to steam hydration did not influence the reactivity of the sorbent.

CONCLUSIONS

Hydration of lime with alcohol-water solution (ethanol or methanol) at atmospheric pressure produced sorbents with surface areas as high as 75 m^2/g. The hydrates had sulfur dioxide sorption capacities equal to or greater than those of commercially prepared pressure-hydrated limes. Calcium utilization depended on the parent limestone, the concentration of alcohol in the hydrating solution and the amount of alcohol used during the post-hydration step. A linear relationship was obtained between calcium utilization and BET (N_2) surface area. Reactivities of the samples tested showed the following trend:

Ethanol-water hydration = methanol-water hydration > pressure hydration > steam hydration = hydration with water > lime

Finally, it should be noted that the calcium utilizations were obtained at 850°C for sulfation times of 60 minutes. For practical application of results, reactivity data should be evaluated under conditions representative of coal-fired boilers, i.e. high temperature, short residence time.

ACKNOWLEDGEMENTS

We gratefully acknowledge the Illinois Coal Industry Committee and the Center for Research on Sulfur in Coal for their financial support of this project.

REFERENCES

1. Attig, R. C., and Sedor, P., Additive Injection for Sulfur Dioxide Control: EPA report APTD 1176 (NTIS PB 226-761) March, 1970.

2. Beittel, R., Gooch, J. P., Dismukes, E. B., and Muzio, L. J., Studies of Sorbent Calcination and SO_2-Sorbent Reactions in a Pilot-Scale Furnace. Proceedings: First Joint Symposium on Dry SO_2 and Simultaneous SO_2/NO_x Control Technologies, Volume I, p. 16-1, July, 1985.

3. Payne, R., and Abele, A. R., Evaluation of Low-NO_x Burners for SO_2 Control. Proceedings: First Joint Symposium on Dry SO_2 and Simultaneous SO_2/NO_x Control Technologies, Volume 1, p. 21-1, July, 1985.

4. McCarthy, J. M., Chen, S. L., Kramlich, J. C., Seeker, W. R., and Pershing, D. W., Reactivity of Atmospheric and Pressure Hydrated Sorbents for SO_2 Control. Proceedings: 1986 Joint Symposium on Dry SO_2 and Simultaneous SO_2/NO_x Control Technologies, Volume 1, p. 10-1, December, 1986.

5. Yoon, H., Stouffer, M. R., Rosenhoover, W. A., and Statnick, R. M., Laboratory and Field Development of Coolside SO_2 Abatement Technology. Proceedings of the Second Pittsburg Coal Conference, U. S. DOE, Pittsburgh, PA, p.223, 1985.

6. Borgwardt, R. H., and Bruce, K. R., EPA Study of Hydroxide Reactivity in a Differential Reactor. Proceedings: 1986 Joint Symposium on Dry SO_2 and Simultaneous SO_2/NO_x Control Technologies, Volume 1, p. 15-1, December, 1986.

7. Gooch, J. P., Dismukes, E.B., Beittel, R., Thompson, J. L., and Rakes, S. L., Sorbent Development and Production Studies. Proceedings: 1986 Joint Symposium on Dry SO_2 and Simultaneous SO_2/NO_x Control Technologies, Volume 1, p. 11-1, December, 1986.

8. Muzio, L. J., Offen, G. R., Boni, A. A., and Beittel, R., The Effectiveness of Additives for Enhancing SO_2 Removal with Calcium Based Sorbents. Proceedings: 1986 Joint Symposium on Dry SO_2 and Simultaneous SO_2/NO_x Control Technologies, Volume 1, p. 13-1, December, 1986.

9. Weber, G. F., Schelkoph, G. L., and Ness, H. M., Pilot Scale Studies of Simultaneous Control of SO_x/NO_x Emissions Derived from the Combustion of Low-Rank Coal. Proceedings: 1st Annual Pittsburgh Coal Conference, p.241, Sept, 1984.

10. Staley, H., Micrometrics of Lime, Research Report to National Lime Association, 1946.

Table 1. Characterization of limestones *

Sample ID Location	Geologic unit Grain-size	Spec. grav.	CaO	MgO	CO_2	Al_2O_3	Fe_2O_3	SiO_2	Na_2O
Limestone A Western Ill.	Burlington Ls. Coarse	2.61	53.8	0.3	42.6	0.1	tr+	1.1	0.02
Limestone B Upper Mich.	Fiborn Ls. Fine	2.64	54.3	0.9	43.8	0.2	0.2	0.7	nil

* Analyses in weight percent.
+ trace

Table 2. Summary of sulfation data of hydrates

Limestone	Particle size[a] (mesh)	Calcination atmosphere	Hydration method	Calcium conversion[b] %	Surface area (m^2/g)
B[c]	-100	---	---	95	17.2
A	100x150	N_2	steam	68	---
A	100x150	N_2	475 atm	76	15.4
A	100x150	N_2	120 atm	91	21.4
A	-325	N_2	none	85	20.7
B	-325	N_2	none	75	---
B	100x150	N_2	dry	93	34.3
A	100x150	N_2	dry	59	37.4
A	100x150	N_2	wet (20xstoich)	67	47.3
B	100x150	N_2	wet (20xstoich)	94	49.0
A	100x150	N_2	none	37	12.9
A	100x150	N_2	wet (5xstoich)	69	46.1
A	100x150	CO_2	wet (20xstoich)	78	33.3
A	100x150	CO_2	steam	68	10.5
B	100x150	N_2	none	33	---

[a]particle size prior to hydration step
[b]after 60 minutes
[c]commercial hydrate

Table 3. Summary of sulfation data of alcohol-water hydrates[a,b]

TG No.	Hydration method	Concentration of alcohol in solution weight %	Amount of alcohol wash gm/gm lime	Calcium conversion[c] %	Surface area (m^2/g)
91	dry (2xstoich)	0	0	59	37.4
92	dry (2xstoich)	10	0	67	43.5
98	dry (2xstoich)	50	0	79	64.3
106	wet (5xstoich)	0	0	69	46.1
104	wet (5xstoich)	0	7	79	49.1
105	wet (5xstoich)	30	0	79	44.7
96	wet (5xstoich)	30	3	86	66.4
100	wet (5xstoich)	30	7	93	70.1
95	wet (20xstoich)	0	0	67	47.3
93	wet (15xstoich)	14	10	94	59.4
97	wet (10xstoich)	10	3	78	53.9
89	wet (10xstoich)	50	25	96	63.7
90	wet (10xstoich)	50	25	94	75.3
108	wet (10xstoich)	50	10	100	---

[a]hydrates were produced from lime A except TG 108 which was prepared from Lime B
[b]methanol was used for alcohol-water hydration tests except for TG 90 ethanol was used
[c]after 60 minutes

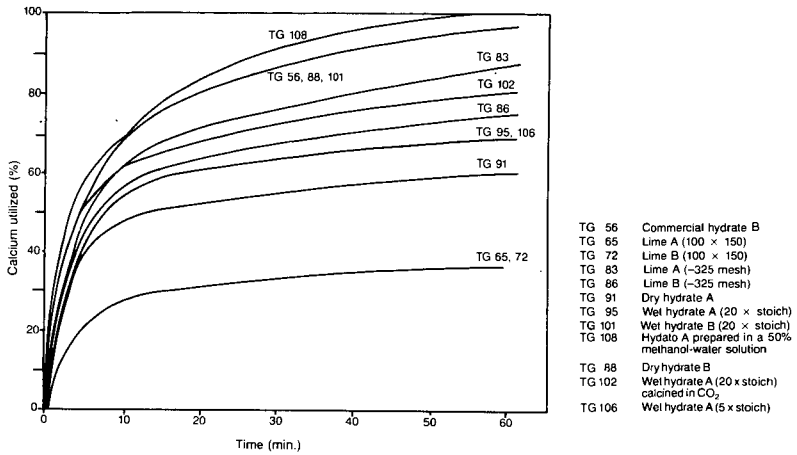

Figure 1. The effects of hydration method, parent limestone, and calcination atmosphere on the reactivity of hydrates.

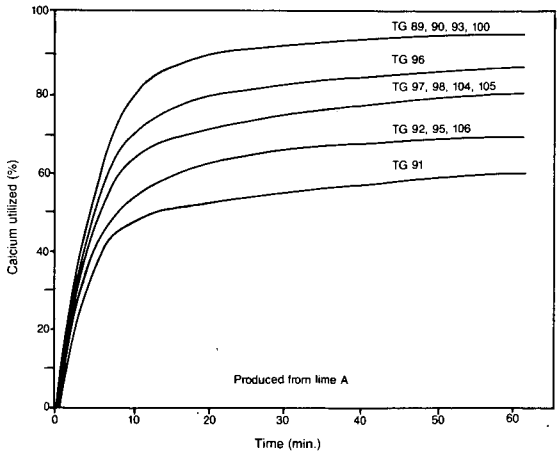

Figure 2. Sulfation reactivities of alcohol-water hydrates.

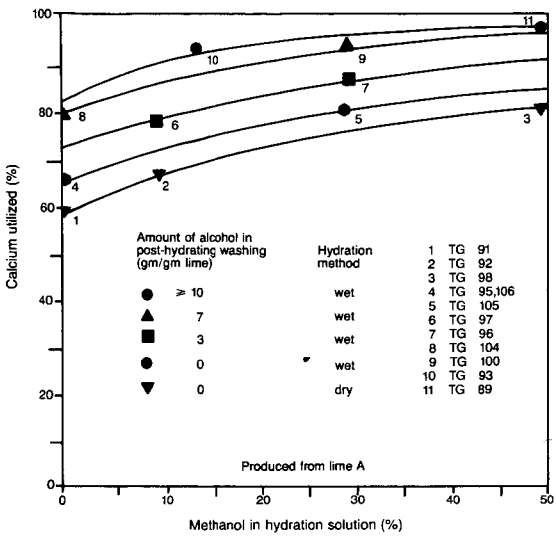

Figure 3. The influence of methanol on hydrated products.

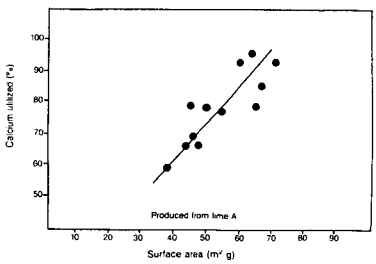

Figure 4. Relationship between calcium utilization and surface area for methanol-water hydrates.

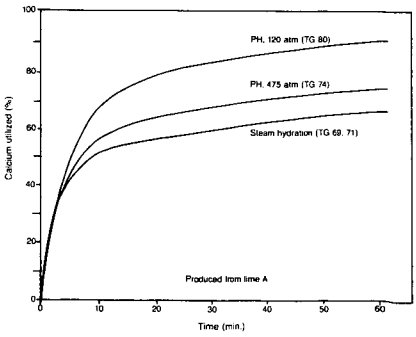

Figure 5. Sulfation reactivities of samples prepared by steam and pressure hydration (PH) methods.

REACTION OF ACID GASES WITH SOLID ALKALI FLOWING IN A DUCT: SO_2 REACTION WITH LIME

BRUCE WEINSTEIN

RESEARCH COTTRELL INC.
ROUTE 22 WEST
BRANCHBURG, NJ 08876

ABSTRACT

Many new flue gas desulfurization processes are being developed where an acid gas and alkali are reacted cocurrently in a duct. Solutions to the material balance equations for cocurrent flow processes have been solved for the cases when the conversion is limited by gas phase diffusion, reaction kinetics, or diffusion thru the product layer. The solutions are presented in a graphical form and can be used to determine the residence time required to achieve a specified conversion of the gaseous component providing the appropriate rate constant is known. The curves can also be used to determine a rate controlling step from conversion versus time data taken in an isothermal flow reactor. This method is applied to the application of the high temperature reaction of lime with SO_2 for conditions that would occur in the duct downstream of a direct coal fired heat engine combustor.

INTRODUCTION

Low capital cost flue gas desulfurization processes are being developed to address the potential market for retrofit systems on existing boilers burning medium to high sulfur coal. Many of these new systems involve the injection of a dry solid of calcium or sodium alkali in the duct to react with the SO_2 in the flue gas. Calcium alkali tend to be the preferred reagents compared to those of sodium because of the availability and lower cost.

The stoichiometry ratio of moles of calcium fed to the moles of SO_2 is often in the range of 2 to 3 for the in-duct processes. Attempts to improve the utilization of reagent have stressed the need for small particles of high BET surface area and porosity. Calcium hydroxide, commercially produced, with those properties has achieved the highest utilizations compared to other calcium alkali.

Injection processes may also be feasible for removing SO_2 from flue gas produced by a direct coal fired heat engine combustor. In this application the gas is expected to be at a high temperature and pressure. This paper presents estimates of the reaction time required for a variety of operating conditions where the reagent is calcium hydroxide.

PREVIOUS WORK

Borgwardt, et al.(2) have shown that the utilization of calcium oxide particles with a BET surface area of 32 m^2/g reacting with COS at 5000 ppm at 700°C is independent over a particle size range of 1 to 9.4 microns. They concluded that the reaction occurs equally throughout the particle and that pore diffusion resistance must be insignificant.

In a later study Borgwardt and Bruce (1) measured the conversion of 1 micron calcium oxide particles by reaction with SO_2 at a concentration of 3000 ppm in a differential reactor over a temperature range of 760 to 1125°C. The primary

resistance to SO_2 absorption was ionic diffusion thru the product layer. A conventional grain model accurately correlated the data when the concentration of the diffusing ion was computed to be proportional to the gas concentration to the 0.62 power.

Bortz, et al.(3) has studied the reaction of small particles of calcium hydroxide at temperatures of 450 to 600°C which are typical of economizers on utility boilers. These tests were done in an isothermal flow reactor. With particles in the range of 1 to 5 microns with BET surface areas greater that 20 m^2/gm, the absorption of SO_2 was dependent on the gas phase mass transfer rates of SO_2 relative to the kinetic rate of CO_2 with the hydroxide. Pore diffusion resistance was negligible.

THEORY

A generalized reaction of a single gas A reacting irreversible with solid B is given by Equation 1 where a and b are the stoichiometric coefficients.

$$a\ A\ (gas) + b\ B\ (solid) \longrightarrow Products \qquad 1)$$

When the reaction rate is controlled by diffusion of the gaseous reactant thru the inert layer of product formed over the unreacted core of solid reagent, the radius of the unreacted core, r, at any time is given by (4):

$$-\rho \frac{r^2 dr}{M}\left(\frac{1}{r} - \frac{1}{R}\right) = D_d C_A (b/a) dt \qquad 2)$$

Following the approach used by Borgwardt and Bruce (1) the initial grain radius of the solid, R, is related to the BET area by:

$$R = 3/(S_a \rho) = 3/(10^4 S_g \rho) \qquad 3)$$

By expressing the moles of solid reactant reamaining at any time per mole of gas reactant at the inlet to the fraction of reactant A remaining the partial pressure of reactant A can be expressed as:

$$P_A = P_{Ain}\left[\frac{Fa}{b}\left(\frac{r}{R}\right)^3 + 1 - \frac{Fa}{b}\right] = P_{Ain}\left[S\left(\frac{r}{R}\right)^3 + 1 - S\right] \qquad 4)$$

where F is the moles of solid reactant B fed/moles of gas reactant A.

The fraction removal efficiency is related to the partial pressure of reactant A by:

$$1 - E = P_A / P_{Ain} \qquad 5)$$

Combining Equations 4 and 5 gives the grain radius at any time in terms of the fractional removal efficiency:

$$(r/R) = \left[1 - (E/S)\right]^{1/3} \qquad 6)$$

The concentration term C_A in Equation 2 is that of the specie that diffuses thru the product layer. Borgwardt and Bruce (1) expressed the concentration in terms of the partial pressure of the gas as:

$$C_A = k_o P_A^m \qquad 7)$$

Substitution of Equation 4 into Equation 7, and then substiution of the result into Equation 1 and integrating from the initial condition r/R equal 1.0 at time zero gives:

$$I_d = \int_1^{xf} \frac{(x^2 - x)dx}{[Sx^3 + 1\text{-}S]^m} = k_g dt \qquad 8)$$

where x is set equal to r/R and k_d is the lumped constant:

$$k_d = (k_o D_d M b)/(\rho R^2 a) p_{Ain}{}^m = 10^8 k_o D_d M S_g{}^2 \rho (b/a) p_{Ain}{}^m/9 \qquad 9)$$

Assuming m is fixed the value of the integral is determined for any specified feed ratio and final fractional conversion efficiency. The upper limit on the integral is found from Equation 6. Analytical solutions for the integral for all real value of m when S equals 1.0 and for all values of S when m equals 1.0 are listed in Table 1.

When the conversion of reactant A is controlled by a first order reaction with respect to A at the surface of the unreacted core, the radius of the unreacted core is given by (4):

$$\frac{-\rho}{M} \frac{dr}{dt} = k_r C_A (b/a) \qquad 10)$$

By utilizing Equations 3 to 7 in an analagous manner, with m set equal to 1.0 the Equation 10 can be expressed as:

$$I_c = -\int_1^{xf} \frac{dx}{Sx^3 + 1\text{-}S} = k_r dt \qquad 11)$$

where k_c is:

$$k_c = 10^4 k_r k_o M S_g (b/a) p_{Ain}/3 \qquad 12)$$

The analytical solution of the integral in Equation 11 is given in Table 1.

If the conversion of reactant A is controlled by diffusion from the bulk gas to the outer surface of the grain, the radius of the unreacted core is given by (4):

$$\frac{\rho}{M} \left(\frac{r}{R}\right)^2 \frac{dr}{dt} = k_G C_A (b/a) \qquad 13)$$

With m equal to 1.0, Equation 13 can be expressed as:

$$I_g = -\int_1^{xf} \frac{x^2 dx}{Sx^3 + 1\text{-}S} = k_g dt \qquad 14)$$

where k_g is:

$$k_g = 10^4 k_G k_o p_{Ain} M (b/a) S_g/3 \qquad 15)$$

The analytical solution of the integral is given in Table 1.

The values of the integrals given by Equations 8 for m=1 and Equations 11 and 14 are plotted on Figures 1, 2, and 3, respectively. These relationships do not account for expansion or contraction of the outer radius of the grain from the differences in the molar volumes of the reactant and product.

APPLICATION OF THE GRAPHICAL SOLUTIONS

With conversion versus time data taken in a flow reactor the graphical solutions provide a rapid method of determining if the conversion is controlled by one of the three assumed mechanisms. For the known value of S and measured value of E, a value of I is read from each curve and divided by the residence time to get values for the constants k_d, k_c, and k_g. This process is repeated for each set of data taken. If the lumped parameter for any one of the mechanisms is constant then that mechanism is applicable to the process. If some test runs used different initial gas concentrations that effect can be isolated from the computed constants.

For a known reaction system where one of the three assumed mechanisms is applicable and if the rate constant is also known then the graphical solution can be used to compute the residence time in a flow reactor. For example, assume a reaction is controlled by diffusion of the gas thru the product layer, so that m is 1.0, the BET area is known, and the diffusion coefficient had been determined from a data on a differential reactor. The lumped parameter k_d can be computed from Equation 9. Figure 1 would then be used to read a value of the integral for any values of S and E selected. The required residence time can be easily computed for each case by dividing the value of the integral by the lumped constant.

SO_2 REACTION WITH LIME AT HIGH TEMPERATURE

If calcium hydroxide is injected into a hot flue gas where the temperature exceeds 700°C dehydration of the particle occurs very rapidly. The calcium oxide that forms is a small particle with about 50 % porosity and a high surface area. For this application the grain model should be applicable. The reaction of the SO_2 with the lime at these conditions produces calcium sulfate, and can be expressed as:

$$SO_2 \text{ (gas)} + CaO \text{ (solid)} \longrightarrow \text{Products} \qquad 16)$$

For this reaction a and b are both 1.0.

One such commercial application may be in the removal of SO_2 from the combustion gas from a direct coal fired turbine operating at temperatures in the range of 950 to 1200°C at pressures of 1013 to 1520 kPa (10 to 15 atm). By removing the SO_2 at the high pressure the volume of the gas being treated is much less than downstream of the turbine. The feasibilty of using calcium hydroxide injection upstream of the turbine to remove the SO_2 depends on the reaction time required.

The data of Borgwardt and Bruce (1) can be used in conjunction with Equation 8 to estimate the residence time. They concluded the conversion of lime at these temperatures is controlled by ionic diffusion thru the product layer, where m is 0.62 and the diffusion coefficient in Equation 9 is expressed as:

$$D_d = D_o * \exp(-E'/RT) \qquad 17)$$

where E' in Equation 17 is the activation energy of 36,600 kcal/mol and T is the temperature in °K. Substitution of Equation 17 into Equation 9 yields:

$$k_d = (10^8 M k_o D_o \rho/9)(S_g^2 p_{SO_2 in}^{.62} \exp(-E'/RT)) \qquad 18)$$

Borgwardt and Bruce correlated k_d by:

$$k_d=(10^8 M k_o D_o \rho/9)(6 S_g^2 p_{SO_2 in}^{.62})*\exp(-E'/RT)=2.65 S_g^2 p_{SO_2 in}^{.62} \exp(-E'/RT) \qquad 19)$$

Equating the second and third terms in Equation 19 gives:

$$10^8 * M * k_0 * D_0 * / 9 = 2.65/6 = 0.4417 \qquad 20)$$

Equation 18 can now be written as:

$$k_d = 0.442 * S_g^2 p_{SO_2 in}^{.62} * \exp(-36{,}600/RT) \qquad 21)$$

Since m equals 0.62, Equation 8 must be solved numerically except when S equals 1.0. The values for the integral are given in Figure 4. To compute the conversion time, the temperature, feed ratio, inlet SO_2 concentration and operating pressure must be specified. The inlet partial pressure of SO_2 is then computed and Equation 19 is used to compute k_d. For the specified fractional removal efficiency a value of I_d is read fom Figure 4 and divided by k_d to obtain the reaction time. Table 2 summarizes calculations for the reaction time when the operating pressure is set at 1520 kPa (15 atm). At the higher temperature a lower BET area was assumed to account for sintering.

CONCLUSIONS

For dry injection FGD processes utilizing small particles of calcium hydroxide or calcium oxide a grain model can be used to represent the reagent utilization.

The reaction time required for the high temperature, high pressure conversion of SO_2 with small lime particles can be predicted with a modified grain model that accounts for the changing SO_2 partial pressure when the rate controlling step is diffusion thru the product layer.

NOMENCLATURE

A	- gaseous reactant
a	- stoichiometric coefficient for gas A
B	- solid reactant
b	- stoichiometric coefficient for solid reactant B
C	- concentration of diffusing specie, gmol/cm
D_d	- diffusion coefficient in product layer, cm /sec
D_o	- Arrhenius pre-exponential factor
E	- fraction conversion efficiency of gaseous reactant
E'	- apparent activation energy taken as 36,600 cal/gmol
F	- moles of reactant solid fed/mole of gas reactant fed
I_c	- integral defined by Equation 11
I_d	- integral defined by Equation 8
I_g	- integral defined by Equation 14
k	- $((1-S)/S)^{1/3}$
k_c	- constant defined by Equation 12
k_d	- constant defined by Equation 9
k_g	- constant defined by Equation 15
k_G	- gas phase coefficient in Equation 13, cm/sec
k_o	- constant defined by Equation 7
k_r	- reaction rate constant in Equation 10, cm/sec
M	- molecular weight of reactant solid
m	- constant defined by Equation 7
P_A	- partial pressure of gas A, Pa
P_{Ain}	- partial pressure of gas A at inlet conditions, Pa
P_{SO_2}	- partial pressure of SO2, Pa
P_{SO_2in}	- partial pressure of SO2 at inlet conditions, Pa
R	- initial grain radius defined by Equation 3, cm; the gas constant in Equations 17, 18, 19 and 20, 1.987 cal/gmol- K
S	- Fa/b
S_a	- BET area of solid, cm^2/g
S_g	- BET area of solid, m^2/g
T	- temperature, ^oK
t	- time, sec
x	- r/R where R is the initial grain radius
x_f	- r/R at the end of the reaction time
$\int$	- mass per unit volume of grain, g/cm^3

LITERATURE CITED

1. Borgwardt, R.H, and Bruce, K.R., AIChEJ. 1986 32, 239.

2. Borgwardt, R.H., Roache, N.R., and Bruce, K.R., Environ. Prog. 1984a, 3, 129.

3. Bortz, S., Roman V. P., Yang, R. J., and Offen, G. R., EPA/EPRI Dry SO_2 and Simultaneous SO_2/NO_x Control Technology, 1986, Paper 6C, Raleigh, NC.

4. Levenspiel, O. "Chemical Reacting Engineering", Wiley, New York, NY, 1062.

TABLE 1: ANALYTICAL SOLUTIONS TO THE INTEGRALS IN EQUATIONS 8, 11 AND 14

$m = 1, \quad S \neq 1$

$$I_d = \frac{1}{3S}\ln(Sx_f^3+1-S) - \frac{1}{6Sk}\ln\left[\left(\frac{k+x_f}{k+1}\right)^3(Sx_f^3+1-S)\right] - \frac{1}{3.^5Sk}\left[\tan^{-1}\left(\frac{2-k}{k-3}\right) - \tan^{-1}\frac{2x_f-k}{k-3}\right]$$

$S = 1, \; m \neq 1$:

$$I_d = \frac{1}{S}\left[\frac{x_f^{3(1-m)}-1}{3(1-m)} - \frac{x_f^{2-3m}-1}{2-3m}\right]$$

$S = 1, \; m = 1$:

$$I_d = \ln(x_f) + (1/x_f) - 1$$

$S \neq 1$:

$$I_r = \frac{k}{6(1-S)}\ln\left[\left(\frac{k+1}{k+x_f}\right)^3(Sx_f^3+1-s)\right] - \frac{k}{3.^5(1-S)}\left[\tan^{-1}\left(\frac{2x_f-k}{k3.^5}\right) - \tan^{-1}\left(\frac{2-k}{k3.^5}\right)\right]$$

$S = 1$:

$$I_r = \frac{1}{2x_f^2} - \frac{1}{2}$$

$$I_g = -\frac{1}{3S}\left[\ln(Sx_f^3+1-S)\right]$$

TABLE 2

PREDICTION OF REACTION TIME AT
A TOTAL PRESSURE OF 1520 kPa

Inlet SO2 ppm	Temp. deg C	BET Area sq m/g	Feed Ratio S	% Gas Absorbed	% Utilization	Reaction Time sec
2000	1149	8	2.5	90	36	1.904
1000	1149	8	2.5	80	32	1.880
500	1149	8	2.5	70	28	1.908
2000	1149	15	2.5	90	36	0.541
1000	1149	15	2.5	80	32	0.535
500	1149	15	2.5	70	28	0.543
2000	927	20	2.5	90	36	3.352
1000	927	20	2.5	80	32	3.310
500	927	20	2.5	70	28	3.360
2000	927	30	2.5	90	36	1.490
1000	927	30	2.5	80	32	1.471
500	927	30	2.5	70	28	1.493
2000	927	30	1.0	90	90	17.478
2000	927	30	1.5	90	60	5.033
2000	927	30	2.0	90	45	2.486
2000	927	30	3.0	90	30	0.994

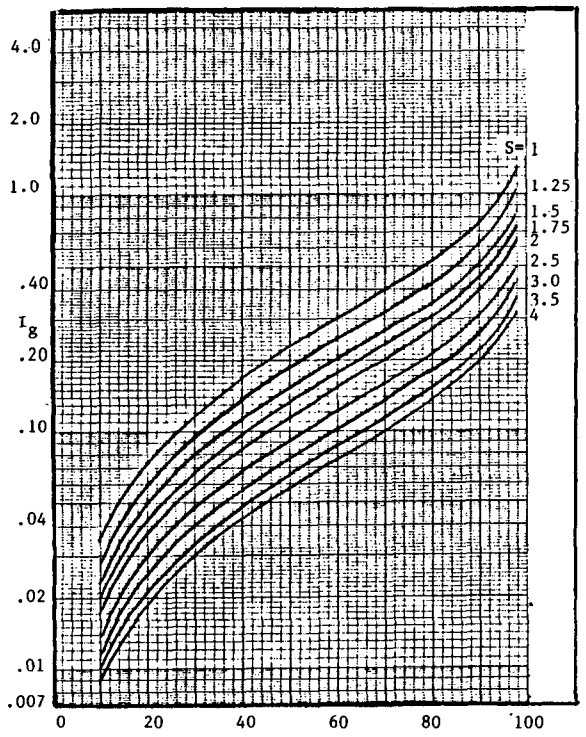

PERCENT OF GAS REACTED
FIGURE 3 VALUES OF I_g

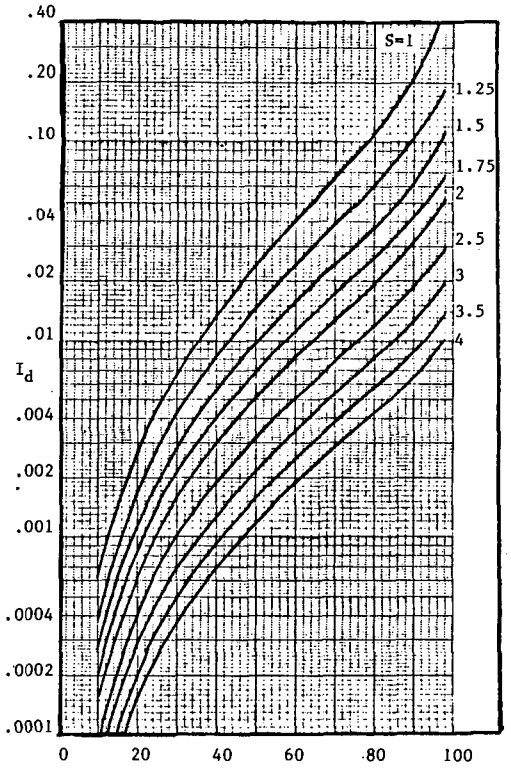

PERCENT OF GAS REACTED
FIGURE 4 VALUES OF I_d FOR m = 0.62

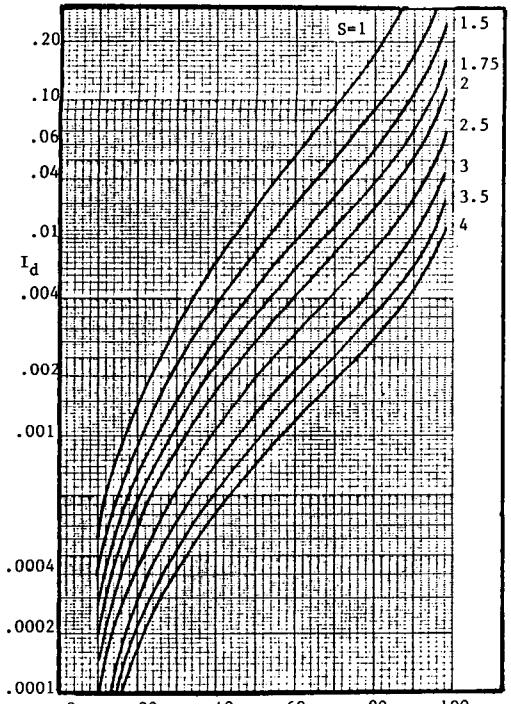

FIGURE 1 VALUES OF I_d FOR m = 1.0

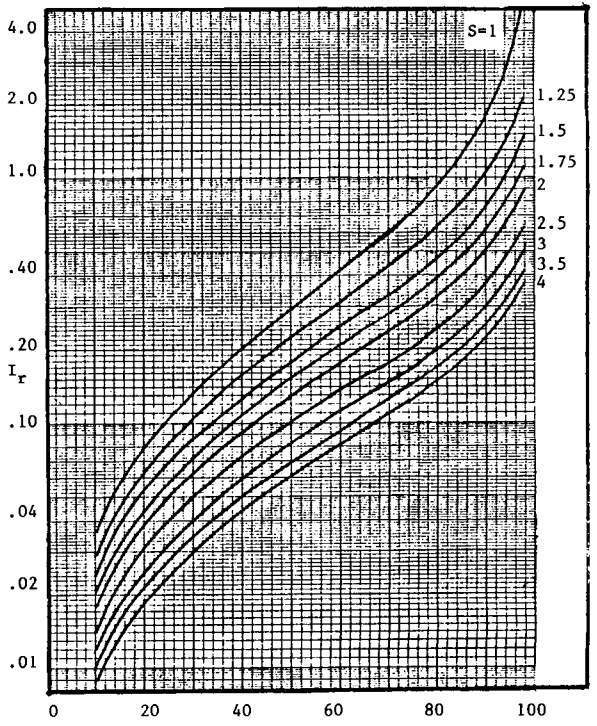

FIGURE 2 VALUES OF I_r

THE USE OF ZINC OXIDE SORBENTS TO REMOVE HYDROGEN SULFIDE FROM COAL GASES

Aysel T. ATIMTAY and Susan L. LITTLEFIELD
Department of Chemical Engineering, Tulane University,
New Orleans, LA 70118

It is anticipated in the future that synthetic fuels derived from coal will be needed to replace the limited resources of petroleum and natural gas. Coal gasification is a necessary step in the production of these synthetic fuels. During coal gasification hydrogen sulfide is produced in oxygen deficient systems due to the sulfur compounds present in coal. In order to be able to use coal gas in molten carbonate fuel cells (MCFC) for electric power generation, hydrogen sulfide needs to be removed down to 1 ppm level. Therefore, it is very important to develop some sorbents to remove H_2S from a few percent down to 1 ppm level at high temperatures (600 to 650°C) to obtain greater process efficiency.

Several metal oxides are capable of high temperature sulfur removal (Westmoreland and Harrison, 1976). Iron oxide is one of the metal oxides that has been used to desulfurize coke oven gases. However, thermodynamic limitations does not allow H_2S removal with iron oxide to the low partial pressures necessary for MCFC operation. But it can be done with zinc oxide. Therefore, metal oxide-based sorbents for high temperature H_2S removal has been an active research area in recent years.

There has been much study concerning reactions between zinc oxide (ZnO) and hydrogen sulfide (H_2S). Westmoreland and Harrison (1976) has reported the results of thermodynamic screening of the high-temperature desulfurization potential of 28 metal oxides by use of the free energy minimization method. According to the results of this study ZnO is among the most favorable oxides because of the high equilibrium constant for the ZnO-H_2S reaction. In 1977 Westmoreland and Harrison published the results of a comparative study of the kinetics of high-temperature reactions between H_2S and selected metal oxides. The relative magnitude of the reaction rates determined was MnO > ZnO = CaO > V_2O_3. The major reasons that ZnO is a desirable sorbent are its high reactivity, high equilibrium constant for the ZnO - H_2S reaction and ability of ZnS to be regenerated (Rao and Kumar, 1981).

Results regarding structural changes in the pure ZnO sorbent at high temperatures are reported in the literature (Ranade and Harrison, 1980). Sintering actually causes the particles to shrink radially, thus with the same mass of particles there is a smaller amount of surface available for reaction.

The solution to this problem can be proposed by supporting the zinc oxide on a support which can stand to high temperatures. Such a support can be zeolites. Thus, more reaction surface area will be available for the reactant and sorbent efficiency can be increased.

Information about zeolites is given by Maxwell (1982). Zeolites are crystalline aluminosilicates with a chemical composition of this general formula:

$$M^{n+}_{x/n}\ [(AlO_2)_x(SiO_2)_y]_z H_2O$$

M^{n+} is the cation that balances the negative charge of the framework ions, Si^{4+} and Al^{3+}. The framework ions are tetrahedrally coordinated to four oxygen anions. The three-dimensional network is formed by linking (SiO_4) and (AlO_4) tetrahedra through shared oxygen ions. The tetrahedra form rings which are entrances to channels or cages in zeolites. The cages define the pore diameter of the zeolite particle. The drawing below shows the structure of the mordenite, Z type zeolite, which has been used for this study. In general, zeolites have good thermal stability, and the framework cations, usually sodium can be exchanged for different types of cations, including zinc. The mordenite type of zeolite is silica rich; therefore its hydrothermal stability is great (stability increases with decreasing aluminum content). This stability made the mordenite the obvious choice for this study. Zeolites seem to be a good way to combat the loss of surface area of the ZnO, due to sintering, because the zeolite support will be thermally stable during the ZnO-H_2S reaction.

The objective for this paper is to determine if using zeolite supports for the zinc oxide-based sorbents improves conversion, making zinc oxide supported on zeolites a more efficient sorbent. Experimentally, the reactivity of zinc oxide-zeolite particles will be investigated, and kinetic data will be determined for the reaction. The results will then be compared with data found in the literature.

EXPERIMENTAL

The reaction of H_2S with ZnO on zeolite support, whose mean diameter was 0.442 mm, was studied in the temperature range of 500 to 700°C. A plug-flow reactor was used which was 52 cm long and had an inside diameter of 2.2 cm. Figure 2 shows the schematic diagram of the reactor system. The total gas flow rate was held at high rate (1200 cm^3/min) to eliminate the effect of external mass transfer for the gas solid reaction. The simulated gas mixture consisted of 4% H_2S, H_2 and the rest N_2. Gas analyses for each run were checked by taking samples from the sample port indicated in Figure 2 and injecting into the Gas Chromatograph.

Sorbent particles were prepared by soaking zeolite support particles in concentrated zinc sulfate solution, then drying them

about an hour at 100°C and finally roasting them for 24 hours at 500-600°C.

After zeolite particles were prepared, a sample of them was used to test for the determination of zinc loading on the particles. This test is performed by dissolving the zinc on the zeolite support in concentrated hydrochloric acid and determining the zinc content of the solution by atomic absorption spectrofotometer.

The reaction, $H_2S + ZnO \rightarrow ZnS + H_2O$ was performed in the reactor. The reactor temperature was varied in a range of 500-700°C and gas samples were taken every 2 minutes during the reaction and analyzed by GC. After the reaction is completed, the feed gas was cut off and reactor was cooled down to room temperature with N_2 gas. Finally, the samples were removed and analyzed to determine the extent of conversion of ZnO to ZnS.

The solubilization of ZnO and ZnS were different at different acidity solutions. By making use of this difference ZnO and ZnS were dissolved in solutions having different acidity and the zinc content of these solutions were determined by Atomic Absorption Spectrofotometer. Using the concentration of zinc in each solution, the conversion of ZnO to ZnS was found. A zinc balance was done for the samples to make sure that the amount of zinc (in ZnO and ZnS form) in the particles after the reaction was equal to the total amount of zinc in the particles before the reaction. This balance was met within +2%.

RESULTS AND DISCUSSIONS

The results obtained from this experimentation are presented in Figures 3 and 4. Figure 3 represents the overall solid conversion of ZnO to ZnS with respect to time for the particle size under study at 500°C, 600°C and 700°C. As can be observed from the figure, the overall solid conversion depends on temperature and reaction time. The overall solid conversion increases as the temperature and reaction time increases. The conversion reaches to 100% at 500°C in about a total reaction time of 40 minutes. The total reaction times for 100% conversion at 600° and 700°C are about 30 and 10 minutes, respectively. The reaction temperature above 700°C is not tested, because of the formation of metallic zinc vapor above 750°C. The maximum temperature in the ZnO-H_2S system is limited to about 750°C thermodynamically (Westmoreland and Harrison, 1976). Experimental results have also been reported about this temperature at somewhat higher values by Beveridge (1962). During the tests hydrogen has been added to the feed gas mixture in a ratio of 3 molH_2/mole of H_2S to prevent the decomposition of H_2S at high temperatures. It has been shown by Westmoreland and Harrison (1977) that the H_2 does not measurably alter the H_2S-ZnO kinetics at low temperatures (<500°C) where H_2S decomposition should be unimportant.

One of the important reasons to support ZnO on zeolite in this study was to provide better contact between H_2S and ZnO through increasing the surface area. The other reason was to minimize the structural changes of the ZnO particles during reaction due to sintering effects. Ranade and Harrison (1980) have found in their study of ZnO-H_2S reaction that surface area of pure ZnO particles decreases from 34 m^2/g to 16 m^2/g at 500°C (a 53% decrease in the surface area). This change is more severe at higher temperatures. Since the molar volumes of ZnO and ZnS are not very different, pore pluging could not be a problem during the reaction. Therefore, they have attributed this decrease in surface area to sintering effects which causes the particles to shrink under the effect of high temperatures, thus decreasing the available surface area for the reaction considerably.

The answer to the question "Did structural changes occur in the ZnO-zeolite particles due to reaction?" was important in this study. The BET surface area measurements on the particles before and after reaction were performed using the Accusorb apparatus (Micromeritics Model 2100E).

Table I lists the surface area of reacted and unreacted particles for the longest reaction times for each reaction temperature. The BET surface area of (an average of five batches) unreacted ZnO-zeolite particles is 31.8 m^2/g. The corresponding surface areas for particles reacted at 500° and 600°C for 50 minutes are 28.2 and 28.1 m^2/g, respectively. The change is only 11% for these temperatures. At 700°C, the change becomes a little higher, being 15%. These changes in surface area are small as compared to 53% change reported by Ranade and Harrison (1981) at 500°C. Zeolite support is not expected to sinter. It is thermally stable. Therefore, the change in surface area could be attributed to partial sintering of ZnO with zeolite, especially around 700°C. However, some in-depth surface studies are needed to answer this question correctly.

A direct comparison of the conversion versus time curves with the data obtained from literature could not be done, because of the vast difference in the systems. Ranade and Harrison (1980) have investigated the H_2S absorption with pure ZnO pellets, however our study uses ZnO supported on zeolite. Also, particle size, shape, zinc content will make the difference in comparison. Practically no information is available in the literature on the use of zinc oxide on a carrier or support to absorb hydrogen sulfide from hot coal gases.

Kinetic constants have been calculated for the reaction between H_2S and ZnO. Zeolite particles using experimental data. The rate constant has been found to obey the Arrhenius relationship.

$$k = A \exp(-E/RT)$$

The Arrhenius plot is shown on Figure 4. A least squares linear fit has been used for the data points to find the slope and the intercept. The correlation coefficient is 0.929. The frequency factor, A, has been found to be 1.781 cm^4/min-mol and the activation energy, E, has been found to be 4355.5 calories/mol. The activation energy is small. Normally, such a low value would indicate mass transfer limitations. This is expected in this system, because of use of zeolites as support for ZnO. Usually zeolites have small pores. The diffusion resistance in zeolites is high. Also, high temperature gas-solid reactions tend to be diffusion controlled. However, this is the first trial on this concept of using support material for metal oxides to increase the surface area available for reaction. Also, authors wanted to test if zeolite had any effect by itself on H_2S absorption. A base experiment has been conducted using plain zeolites (no ZnO deposits). No decrease in H_2S concentration has been observed with time.

CONCLUSIONS

Using zeolite as support material for zinc oxide does not seem to be suitable. A higher porosity and larger pores are desirable for this kind of application. Nevertheless, the results of this study showed that sintering of sorbent particles can be minimized or prevented by using this new concept of depositing metal oxides on thermally stable supports. Further research on this subject is in progress.

REFERENCES

Beveridge, G.S.G., "Agglomeration International Symposium", Interscience, New York, N.Y., 1962.

Maxwell, I.E.: Nonacid Catalysis with Zeolites, "Advances in Catalysis," Vol. 31, pp. 2-5 (1982).

Ranade, P. V. and D. P. Harrison, "The Variable Property Grain Model Applied to the Zinc Oxide-Hydrogen Sulfide Reaction," Chemical Engineering Science, Vol. 36, pp. 1079-1089 (1981).

Rao, T. R., and R. Kumar, "An Experimental Study of Oxidation of Zinc Sulfide Pellets," Chemical Engineering Science, Vol. 37, pp. 987-996 (1982).

Westmoreland, P. R., J. B. Gibson, D. P. Harrison, "Comparative Kinetics of High-Temperature Between H_2S and Selected Metal Oxides", Environmental Science and Technology, pp. 488-491 (1977).

Westmoreland, P. R. and D. P. Harrison, "Evaluation of Candidate Solids for High-Temperature Desulfurization of Low-Btu Gases", Environmental Science and Technology, Vol. 10, No. 7, pp. 659-661 (1976).

TABLE I. BET SURFACE AREAS FOR MAXIMUM REACTION TIME
(TIME = 50 MINUTES)

SAMPLE	SURFACE AREA (m^2/g)
RUN NO. 5 T=500 C	28.2
RUN NO. 10 T=600 C	28.1
RUN NO. 11 T=700 C	26.9
UNREACTED ZnO-ZEOLITE PARTICLES	31.8

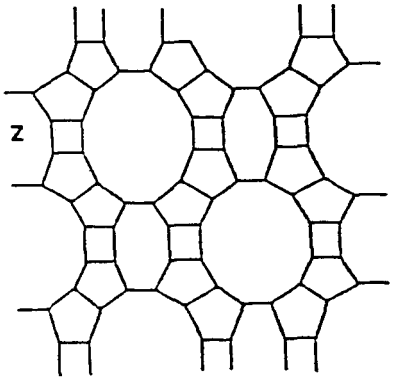

FIGURE 1. SCHEMATIC DIAGRAM OF A Z TYPE ZEOLITE

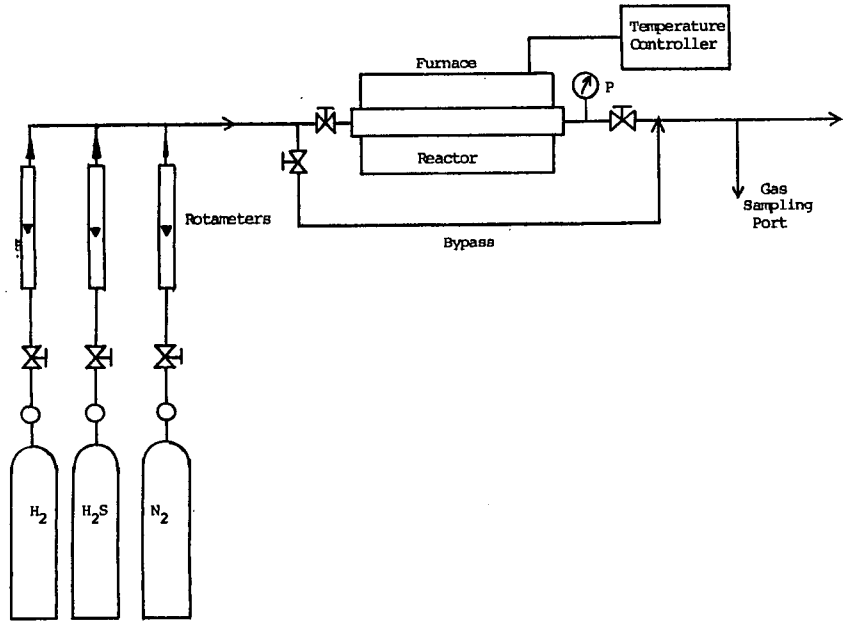

Figure 2. Schematic diagram of laboratory set up for kinetic studies.

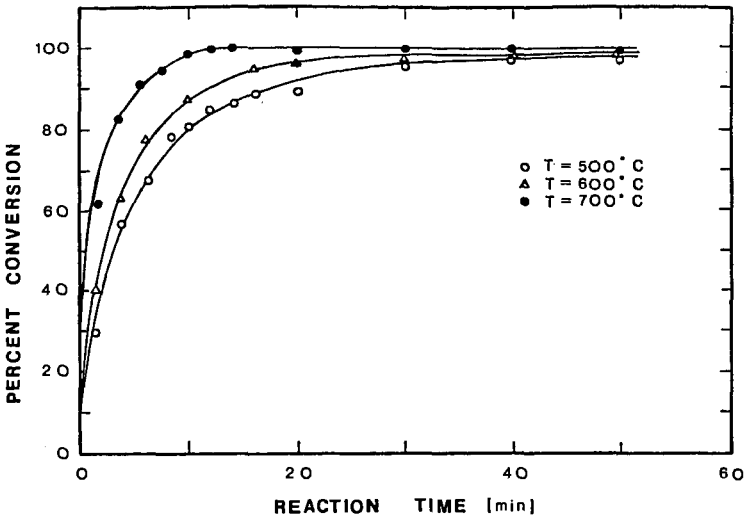

Figure 3. Conversion with reaction time, ZnO - H_2S reaction.

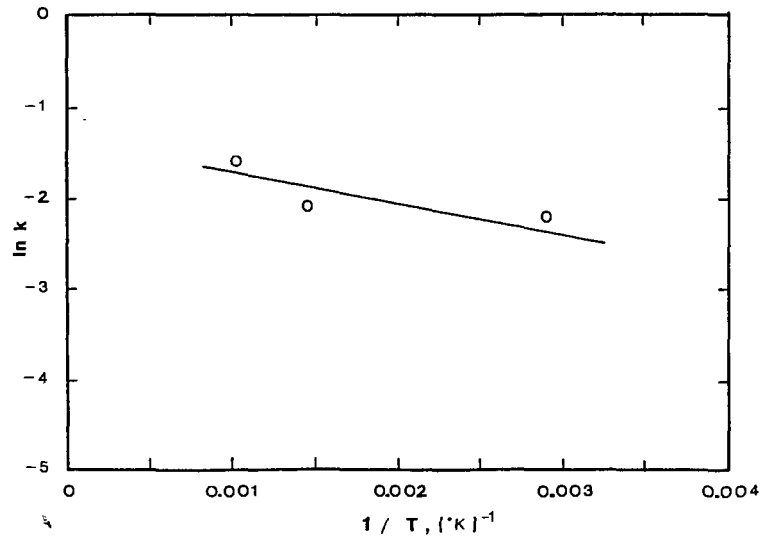

Figure 4. Arrhenius plot ZnO - H_2O reaction.